



**A University of Sussex PhD thesis**

Available online via Sussex Research Online:

<http://sro.sussex.ac.uk/>

This thesis is protected by copyright which belongs to the author.

This thesis cannot be reproduced or quoted extensively from without first obtaining permission in writing from the Author

The content must not be changed in any way or sold commercially in any format or medium without the formal permission of the Author

When referring to this work, full bibliographic details including the author, title, awarding institution and date of the thesis must be given

Please visit Sussex Research Online for more information and further details



Design and fabrication of high magnetic  
field gradients towards fault tolerant  
two-qubit gates with trapped ions  
using long-wavelength radiation

Eamon Daniel Standing

Submitted for the degree of Doctor of Philosophy  
University of Sussex, Brighton, United Kingdom.  
September 2016



# Declaration

I hereby declare that this thesis has not been and will not be submitted in whole or in part to another University for the award of any other degree.

Signature:

Eamon Daniel Standing

UNIVERSITY OF SUSSEX

EAMON DANIEL STANDING, DOCTOR OF PHILOSOPHY

DESIGN AND FABRICATION OF HIGH MAGNETIC FIELD GRADIENTS  
TOWARDS FAULT TOLERANT TWO-QUBIT GATES WITH TRAPPED  
IONS USING LONG-WAVELENGTH RADIATION

# Abstract

In this thesis, I discuss coherent manipulation of a trapped ytterbium ion using long wavelength radiation and the results of experiments towards the performance of a two-ion entanglement gate using a static magnetic field gradient of 23.3(6) T/m to create coupling between an ion's internal state and its motion.

After using these experiments to explain the requirements for high-fidelity entanglement operations, I continue by examining existing methods for creating this gradient, the current limiting factor in producing the highest fidelity operations. This includes a full characterisation of the gradients produced by symmetric scheme permanent magnets and buried current carrying wires including development of scaling laws in order to create optimum gradients for a given trap geometry.

I continue by proposing a new method by which extremely high gradients over 100 T/m can be created for planar chip traps with minimal modification to an existing experiment. These gradients are tailored for axial as well as radial entanglement schemes and aim to show that the technology exists in order to produce a two-qubit gate over the fault tolerant threshold.

Subsequently, I discuss the implementation of this new scheme in an experiment before constructing the apparatus to accurately align a chip with these magnets and documenting their installation into two new experimental setups. This includes a preliminary measurement of the gradient produced by an imperfect setup outside of vacuum which verifies those simulated at  $\sim 110$  T/m.

Lastly, I discuss the prospects of on-chip magnetic materials and propose a new method which when sufficiently developed should allow for high magnetic field gradients to be produced on-chip at higher ion heights than when solely using current carrying wires. Additionally this scheme should allow for switchable gradients with maximised stability in geometries previously not possible to create.

# Acknowledgements

## General acknowledgements

Without the help and support of many people, the work in this thesis and my life while studying for a PhD at University of Sussex would have been significantly more difficult and less fun. I will start by giving a big thanks to people involved with making my time comfortable during the course of my study before giving some more detailed acknowledgements with regards the individual chapters of this thesis and the work contained within them.

Firstly, the biggest thanks goes to my parents, Aw and Steve, my brother, Nick, and all my family and friends, especially Sam Brown, that have provided emotional, financial, and moral support over these last four to five years. You've made me able to move out but kept a home waiting for me to return to in the final stages of my study. Without you, this would have been an extremely dark and lonely experience outside of work hours and I appreciate everything you've done for me in my most trying times.

I must also acknowledge the efforts of my peers in the independent UK comics industry for keeping my legacy alive in my partial absence. Matt Dyson-Bird, Rob Cureton, Luke Surl, Emily Brady, and Ally Nuttall; your tireless efforts have kept the Comic Village Alliance alive for five tremendous years and have shaped the independent comic industry in ways I could not have envisioned when I created the group. At over 1200 strong, thank you for making this dream a reality and keeping it alive. You are the real heroes. I must also thank all my fans for their patience and support during this write up period. Tallisman Rogue, Jefferson Pugley, and The Setting will return, and I can't wait to get back in the game!

I also want to say a big thank you to all my colleagues at Clarks Burgess Hill who have made my post-submission time very enjoyable and a welcome break from the stress of thesis. You have all been so supportive and understanding of my situation, and for that I am extremely grateful. I will remember my time with you very fondly and I wish you

all the best now that my contract has come to an end.

Now onto the people who I have met during the course of my study with IQT. Dr Kimberley “Kim” Lake; words cannot express how much you’ve supported me since the day I joined the group. You are an invaluable friend who has seen me through the toughest times and your company during the night shifts will forever be remembered as the greatest way to make the most of a life with little sunlight. In you I feel I have found a friend for life from a place that at times has been more than I can bear. You are exceptional.

Similarly, Sahar Hejazi; though we only spent the first year working together, I am glad to have had you around for the two following. Your friendship and motivation has cheered me up in some very stressful times and I cannot wait to meet again so that we may eat lunch and discuss things. Okinawa was far away but not far enough to keep me from visiting you. Those two weeks were some of the best of my life and I will forever be reminded of them when I play the sanshin or hear “Shimanchu nu Takara”.

Dr Sebastian “Seb” Weidt; since my original summer placement you have always been there to point me in the right direction and steady me when the aims were not clear. Thank you for going above and beyond to make sure that our work and the team is OK and though I may not always agree with you, you will always have my respect and admiration. I don’t know when you find time to sleep, but if anyone knows what must be done to ensure the group runs smoothly, it’s you, and I couldn’t imagine it any other way. Thank you.

Dr Joseph “Joe” Randall; thank you for your help in understanding the experiment and for laying the groundwork for my PhD. We have worked together many times and your patience and expertise has always been appreciated. I can see an extremely bright future for you in whatever you choose to do. Thanks for many good laughs.

Dr Bjoern Lekitsch; your expertise in microfabrication has enabled me to pursue many magnetic designs simulated in this thesis. Thank you for always being willing to discuss ideas and for supporting me on my crazier ones with enthusiasm rather than scepticism. Whether it is discussing superhero films or optimisation of on-chip microfabricated current carrying wires, you are always there with a kindness and capability to listen which is so often lost in this field. Thank you.

Dr Simon Webster; in the beginning, I understand that we weren’t the most easy pair to work together. Having said that, after getting to know you better through the awful task of proofreading this thesis, you are well and truly the best person to do this job. You are kind, tactful and easy to talk to, for which I will be eternally grateful in what could

have been the most stressful time of my studies. Your feedback is always helpful and clear and I am truly thankful for your help in the most gruelling part of this PhD. Thank you for making sense of my scientific ramblings while being patient and cheerful throughout this process. I couldn't have done this without you.

Onto the newer batch! The unstoppable team of David Murgia and Tomas Navickas; boy it has been fun to work with you guys making the under-chip magnetic spacer a reality. Thank you for your incredibly hard work and motivation during this extremely long process. You are both extraordinary characters, fun and serious at the appropriate times. Thank you for always being understanding in all situations and making my work feel like it has worth. You deserve the very best of the intended goals of the experiments which if there is any justice in this world will be delivered. Thanks for being a great team to work with.

Anton Grounds; king of RF and microwaves! It has been truly great to work alongside you and I thank you for many discussions both work related and to do with your interests. You are kind and understanding with the ability to listen and the group would not be the same without you. Your honesty and direct discussion without fear of judgement is refreshing in this over-politically correct world and I thank you for being someone that can be talked to about anything. Thanks for always having so many interesting things to talk about.

Weikang "Fan" Fan; the ultimate source of motivation that is much more than this group deserves. You have given me so much drive and support at times where I have previously doubted myself and helped me to believe I can achieve anything I set my mind to. You are by no competition the best member of this group whose genuine kindness and interest has been unwavering since the day you started. Anyone who has the privilege of knowing you should make sure to never bring you down because you are definitely better than this world deserves. I hope everything goes well for you, always, and to know you for many years to come. Thank you for being you.

Ethan "(Only Fan gets to call me) Princess" Potter; you are by in large one of the most interesting people I have met socially, opening my eyes to a world far from my own with real honesty and clarity that I thoroughly enjoy discussing with you. You are never dull to be around and your upbeat honesty and matter-of-fact outlook is very refreshing. Thank you for giving me perspective.

Andrea Rodriguez Blanco; you bring a smile and friendliness to the group that is always present. Your passion for physics and making us all dance at a party is much needed in

this group consisting of a load of “boring Brits”. I promise one day we will learn to dance the dance of life. Thanks for pointing us in the right direction and always being someone to talk to.

Anna Webb; distilled badassery and undisputed queen of outreach. You bring a drive and attitude that is much needed in a small, tired office and you do West Sussex proud. It’s always great to discuss weekend plans with you as you always seem to be doing something new and interesting. Keep that fire burning.

Now onto the much newer people. I haven’t known you long, but you’ve made this final year worth sticking around for! Zak Romaszko; a kindred spirit born of the internet meme generation, you are always fun to hang with and I can always count on you to make me laugh. It’s nice to know someone who enjoys going to the cinema as much as I and who’ll sing along to any song lyric that works its way into conversation. Thanks for keeping those high spirits up. There’ll never be a dull day at the office with you around.

Foni Raphaël “Raph” Le Brun-Ricalens; your crude humour may enrage or gross me out at times but you are undoubtedly one of the best people to talk to and your friendship was always going to be inevitable. Thanks for so many great chats which have cheered me up with interesting content and NSFW humour. Sorry for attacking you that one time, but you have to admit, it was hilarious and really broke the ice on your arrival. Take care of yourself and keep the rest of the guys in high spirits when they get to the horrific stage of writing up. To see you again would be a gift.

Harry Bostock; selfless and forever providing us with cake. Thanks for always telling me your dreams and taking an interest in mine; I wish I could remember more of them. You’ve always looked out for everyone in the group and driven us places on social occasions. You’re a truly caring person and definitely not “the worst”. Thanks for keeping the others sensible because I know that’s not in their nature. We could always use more Harry in this world.

Nick Johnson; always good for a chat, a cup of tea, and a ridiculous awe-inspiring demonstration of gymnastic ability. Thanks for keeping the labs sensible, safe, and clean this past year and for always being upbeat and wearing a smile with a genuine interest in my work. I tremendously look forward to seeing a scalable demonstrator device and your drive is definitely up to the task. At ease, mate.

Nikolaus “Niko” Lorenz; at first I didn’t realise when you were joking, but now that I understand your humour, I’ve come to realise you are very funny and it’s been fun working with you. Thank you for all the help towards setting up the experiments and your evening

shifts. It will be very sad to see you leave but you gotta do what you gotta do and I respect that. Thank you and take care of yourself.

Adam Lawrence; although we haven't really talked much at work, it cannot be denied you really rock the mic at karaoke and it's been really fun singing with you at Zak's. Thanks for all the help with the thesis and I can honestly say you're on the right path to becoming the new Joe, which is a great thing. Keep up the good work.

Ben "Bermuda" Sayers; British from far away. It's been so fun having lunch with you while you were working on your project. Thanks for your cool and collected helpfulness in the face of a mountain of work or unreasonable requests; it has been reassuring and great to have around. I hope you enjoy your return to the group; as far as I'm concerned you were a member of the team to remember. Relax, guy, and make sure to take a rest sometimes.

Oliver Wilson, Peter Hooijschuur, Fraser Hurley, and Piotr Ewiak; though I have known you all for a much shorter time than the others, you've been nothing but kind, hard working, and fun to be around. Thanks for the upbeat conversations and joining in with the group activities. I hope your time in the group was fruitful to you.

Dr Wei "Will" Wu; it's been a pleasure to work with you and it's hard to imagine the group without you now. Thanks for coming to eat lunch with us and having a laugh with great contribution to our conversations. Hopefully you are having fun and can take some nice tips back to your group. We will miss you when you're gone.

Dr Altaf Nizamani; though we don't speak often, it's been great to have you around again. I can always count on you for a smile when cake is mentioned and your kind and cheerful attitude is much needed in this group.

This work would have also not been possible without the team members that have since moved on that I am no longer in frequent contact with; Darren De Motte; though you have left, your legacy lives on. Thanks for being a good friend and a fun to work with person, both kind and patient at all times. I hope to get a great job following this PhD and follow in your footsteps; your smile says it all.

Dr Gouri S. Giri; a true gentleman with a great attitude to work. Your kindness and patience was greatly appreciated during the first years of my PhD. Thank you for helping make it a good time.

Dr Marcus Hughes, Dr James Siversns, Dr Robin Sterling, and Dr James "Jim" McLoughlin; without your work none of this would be possible. Thank you for being patient and humorous at the very beginning of my PhD and the summer placement that preceded it.



I wish you all the best in your futures and thank you for your unwavering efforts from the very start of this group.

Karsten Roth and Konstantine Luft; the two German genius kids. It was an absolute pleasure working with you both and thank you for your work on the DDS boxes with David and Anna. You were sorely missed after your departure but it is very clear you have a bright future in physics if you choose to go down that route. I hope undergraduate life is treating you well and that I bump into you one day on a freak visit to this lab in the future.

Adrian Parra Rodriguez; though we only worked together for a year it was great to have you around and a real shock to see you go. As with Niko, I hope you have found what you were looking for and I wish you the very best in the future. Take care of yourself.

I would also like to extend my biggest thanks to all of the other people who have made this work possible and been friendly around the department; all our summer and placement students (you know who you are), my second supervisor Professor Barry Garraway, Dr Matthias Keller and his group, Dr Jose Verdu Galiana and his group, and all the members of the mechanical workshop. You’ve all made this time fun with a friendly and insightful attitude during my study. Physics isn’t all about science, it’s about community and you all make it a good one.

Finally, and I’m sure he’s waiting for it, a big thanks goes out to Professor Winfried “Winni” Hensinger; thank you for seeing potential in me and twice offering me the opportunity to study with such an amazing group, enabling me to truthfully say “I play with lasers and magnets all day”; that always makes my friends laugh. Thanks to your tireless efforts, we are never short of equipment and funding, giving us the ability to get on with the science with little worry of the cost, which really makes a difference. You have assembled a fine team of great individuals which I have no doubt will shape the field of quantum computing in years to come; it was very nice to work with such a team. Finally, thank you for your helpful discussions and introducing me to a place which makes the best quiche ever. I shall not forget my time with this group.

## Detailed acknowledgements

It goes without saying that a lot of the work in this thesis was done within a team and with the help of other people. As such I will acknowledge these contributions here with respect to each chapter of this thesis. Additional thanks goes to Dr Simon Webster, Adam Lawrence, Zak Romaszko, and Tom Whitmore for their help with corrections and

proofreading this thesis.

## Chapter 1

Special thanks to all those in the group who set up the original experiment and laid the practical and theoretical groundwork before I started my PhD. Anna Webb, David Murgia, Tomas Navickas, Dr Joseph Randall, Dr Kimberley Lake, Dr Sebastian Weidt, Dr Simon Webster, Dr Bjoern Lekitsch, Dr Marcus Hughes, Dr James Siverns, Dr Robin Sterling, Dr James McLoughlin, and almost every member of the group have all had a significant contribution to the inner workings of this experimental setup. Thank you all for your great efforts.

## Chapter 2

Again, the biggest thanks goes to everyone who has worked on this experiment prior to and following the time that I spent on it which is practically everyone in this group. Your tireless shifts make our results possible.

A massive thanks to summer student Nathan Evans for laying the groundwork on the Faraday Cage which I later finished the designs for. Your summary of shielding theory allowed me to focus on the design without having to re-evaluate the best materials. This inevitably sped up the process significantly at a time when we were desperate to minimise electrical noise. I would also like to thank the experimental team for their input on this design but more importantly, to every member of the workshop for their extremely hard work in making this Faraday Cage and the resonator shield a reality, especially Peter Henderson who served as my initial contact for many of the jobs over the course of my study. You all deserve much more credit than you receive. Also, thank you to Anton Grounds for suggesting the lowest noise way to connect power to the experimental apparatus. This was extremely helpful.

An extremely large thanks to Dr Joseph Randall for allowing me to use the graphs from his thesis as they were the best of the results that were obtained from the time that I worked on the experiment and it is unclear which data was taken by whom.

A similar thank you to all members of the team with the addition of Andrea Rodriguez Blanco for her programming of the ground state cooling code, and Adam Lawrence for his efforts with the AWG coding used for the two-ion gate result which is only mentioned in passing in this thesis. These were invaluable for the experiment and you should both be commended.

An extended thank you is required for Dr Simon Webster and Tomas Navickas for their constant efforts regarding the LabVIEW programming and laser locking respectively. Without you the experiments would not run and we all should give you our most gracious thanks.

### Chapter 3

Many thanks to Dr Joseph Randall, Dr Darren De Motte, and Dr Bjoern Lekitsch for laying the groundwork of the previous magnetic gradient production schemes and discussions of the implementation of these schemes in their own experiments. Without this I would have nothing to build on and this thesis would be very empty. An unreserved thank you should also go to summer student Tom Crane for noticing that some CST simulations had been set up incorrectly when helping to design the compensation coils which have since been moved to Chapter 4. Without you, many of the magnetic designs in this thesis would be invalid and I'd be in a lot of trouble.

Also, a big thank you to David Murgia and Tomas Navickas for many discussions about the implementation of the under-chip magnetic spacer scheme prior to the work performed in Chapter 4, and to Susan Gates, Dawn Street, and all the technical support at COMSOL for making sure the licenses were always in order and that my simulations were set up correctly when I switched over from using CST.

### Chapter 4

Firstly, but perhaps unknowingly, a big thanks to Philippa Bevan and the rest of the team at Bunting Magnetics during the ordering of the magnets. You have been so helpful every step of the way and thank you for keeping me calm when things went wrong with the order and always replying promptly when quotes were being discussed. It has been a pleasure corresponding with you.

A big thank you to Robert “Bob” Woodhouse of the workshop for his patience when creating the vacuum chip tongue. I know you had to do this quite a few times and I thoroughly appreciate your effort on the matter.

Many thanks go to John Lacy for mentioning and later letting me use his magnetic field measurement setup in order to make a preliminary measurement of the gradient using my magnetic spacer scheme. I especially want to thank him for keeping me calm after the first measurements came back with a significantly lower gradient and subsequently helping me troubleshoot the measurement before achieving a correct one.

Also, a big thank you to Alan Mayers of the workshop for his discussions on the real world implementation of the magnetic spacer for David’s system and to Ian Wallis for building the offset spacer for Tomas’ system. Without your clever ideas, I would have a much more difficult apparatus to operate. Also, thanks again to Robert “Bob” Woodhouse, Michael “Mick” Ottoway, and David “Dave” Smith for making the external magnetic compensation mounts as I know doing the same thing over and over must’ve been extremely tedious.

A massive thank you goes to David Murgia, Tomas Navickas, Dr Sebastian Weidt, and later Nikolaus Lorenz for all their hard work in setting up the two new experiments and having enough faith in my new scheme to let it be combined with their chip traps. I honestly can’t thank you enough for this work at a time where I was doing a lot a writing. You made this possible and I hope that my magnetic spacers provide you with the very best results for your theses. Other thanks go to Dr Bjoern Lekitsch and Adam Lawrence for their help on the cooling system and additional work in order to get these systems running.

Additionally, many thanks to Weikang Fan and Anton Grounds for their help in setting up and teaching me how to use EMPro. One week is not a long enough time to become an expert, so without you, these simulations would have been impossible.

## Chapter 5

Though this chapter mainly concerns simulations for future work that were not done as part of an experimental team, I’d like to thank Zak Romaszko for recommending Bleiker’s paper on implanted nickel as it allowed me to justify simulations of much thicker on-chip magnets than demonstrated by thin-film deposition techniques.

I would also like to thank Dr Bjoern Lekitsch for the many discussions regarding fabrication of nickel and current carrying wires in order to assess the reality of some of my more abstract designs.

Finally, I must thank Weikang Fan for his constant enthusiasm on my magnetic yoking schemes without which I would have probably given up on the idea as others seemed to show little interest. You are the source of motivation this group needs.

If I’ve forgotten anyone, my sincerest apologies. This work would not have been possible without you and I thoroughly appreciate your every second of help. Thank you.

# Publications

## **Generation of spin-motion entanglement in a trapped ion using long-wavelength radiation**

K. Lake, S. Weidt, J. Randall, E. D. Standing, S. C. Webster, and W. K. Hensinger

*Phys. Rev. A*, 91:012319, Jan 2015.

## **Efficient preparation and detection of microwave dressed-state qubits and qutrits with trapped ions**

J. Randall, S. Weidt, E. D. Standing, K. Lake, S. C. Webster, D. F. Murgia, T. Navickas, K. Roth, and W. K. Hensinger

*Phys. Rev. A*, 91:012322, Jan 2015

## **Ground-state cooling of a trapped ion using long-wavelength radiation**

S. Weidt, J. Randall, S. C. Webster, E. D. Standing, A. Rodriguez, A. E. Webb, B. Leikitsch, and W. K. Hensinger

*Phys. Rev. Lett.*, 115:013002, Jun 2015

# Contents

<b>List of Tables</b>	<b>xx</b>
<b>List of Figures</b>	<b>xxii</b>
<b>Introduction</b>	<b>1</b>
Quantum computing with trapped ions . . . . .	4
Thesis overview . . . . .	7
<b>1 Trapping ytterbium ions</b>	<b>10</b>
1.1 RF Paul traps . . . . .	10
1.1.1 Symmetric RF Paul traps . . . . .	15
1.1.2 Planar RF Paul traps . . . . .	17
1.1.3 The Blade trap . . . . .	20
1.1.4 The linear chip traps . . . . .	21
1.1.5 Application of trap voltages . . . . .	23
1.2 The UHV system . . . . .	25
1.3 Ytterbium . . . . .	26
1.3.1 Ionisation . . . . .	26
1.3.2 Doppler cooling $^{174}\text{Yb}^+$ . . . . .	27
1.3.3 $^{171}\text{Yb}^+$ . . . . .	29
1.4 Magnetic field gradient setup . . . . .	31
1.4.1 Post-trapping procedures for the Blade trap equipped with a mag- netic field gradient retrofit . . . . .	36
1.5 Imaging, lasers, microwaves, and RF setup . . . . .	37
1.5.1 Imaging . . . . .	37
1.5.2 Laser light delivery . . . . .	38
1.5.3 Microwave and RF fields . . . . .	39
1.5.4 Computer control . . . . .	43

<b>2</b>	<b>Experimental single-qubit coherent manipulation using microwave and RF fields</b>	<b>45</b>
2.1	State preparation and detection . . . . .	47
2.2	Obstacles towards high fidelity . . . . .	50
2.2.1	External electrical noise minimisation techniques . . . . .	50
2.2.2	Anomalous RF coupling and the Theremin effect . . . . .	57
2.2.3	Minimisation of microwave intermodulations . . . . .	62
2.3	Bare state ion manipulation . . . . .	65
2.3.1	Rabi flopping and coherence time . . . . .	66
2.3.2	Resolving motional sidebands . . . . .	72
2.3.3	Spin-motional entangled states . . . . .	75
2.4	Dressed state qubits . . . . .	79
2.4.1	Preparation of the dressed states . . . . .	82
2.4.2	Rabi flopping . . . . .	83
2.4.3	Spin-motional entangled states . . . . .	84
2.5	Ground state cooling using motional sidebands . . . . .	85
2.6	Subsequent achievements using the Blade trap microwave entanglement experimental setup . . . . .	89
<b>3</b>	<b>In-vacuum high magnetic field gradients</b>	<b>91</b>
3.1	Magnetic nilling . . . . .	92
3.2	Simulating magnetic geometries . . . . .	94
3.3	Magnetic materials and coatings . . . . .	98
3.3.1	Selecting a permanent magnetic material . . . . .	98
3.3.2	Protective magnet coatings . . . . .	100
3.4	Symmetric scheme in-vacuum permanent magnets . . . . .	103
3.4.1	Basic principles of a symmetric magnet setup . . . . .	103
3.4.2	Optimising the symmetric scheme permanent magnet setup . . . . .	106
3.5	On-chip current carrying wires . . . . .	109
3.5.1	Analytical calculation of the magnetic field produced by a pair of current carrying wires . . . . .	111
3.5.2	Analysis of gradient production using current carrying wires . . . . .	114
3.5.3	Optimisation of the nilled anti-parallel current carrying wire scheme . . . . .	134
3.5.4	Closing thoughts on gradient production using on-chip current carrying wires . . . . .	140

3.6	In-vacuum under-chip magnetic spacer . . . . .	141
3.6.1	An asymmetric approach to creating high magnetic field gradients using permanent magnets . . . . .	142
3.6.2	Re-purposing this approach for our ion traps using macroscopic mag- nets . . . . .	145
3.6.3	Designing an under-chip high magnetic field gradient structure . . .	154
3.6.4	An offset magnetic spacer design for a high radial, low axial gradient scheme . . . . .	166
3.6.5	Advanced designs for x-junction traps . . . . .	170
3.6.6	Comparison of gradients produced by an under-chip magnetic spacer with other schemes . . . . .	174
<b>4</b>	<b>Installation of a high magnetic field gradient under-chip spacer into a vacuum system</b>	<b>176</b>
4.1	Vacuum systems and experimental setup . . . . .	177
4.1.1	Axial gradient system . . . . .	177
4.1.2	Radial gradient system . . . . .	177
4.2	Offset field compensation using current coils and large external permanent magnets . . . . .	180
4.2.1	Designing a compensation coil setup . . . . .	180
4.2.2	Compensation coil setups for each vacuum system . . . . .	183
4.2.3	Designing an external permanent magnet setup . . . . .	188
4.2.4	Finalised magnetic field compensation setups . . . . .	191
4.3	Alignment of the under-chip magnetic spacer with an ion chip trap . . . . .	193
4.3.1	Designing and building a high precision alignment system . . . . .	194
4.3.2	Heating plate and determination of glue thickness . . . . .	198
4.3.3	Finalised alignment stage . . . . .	200
4.3.4	Pre-alignment preparation procedure . . . . .	202
4.3.5	Alignment procedure . . . . .	207
4.4	Preliminary external measurement of the magnetic field gradient . . . . .	218
4.5	Installation of the under-chip magnetic spacers . . . . .	222
4.5.1	Magnetic spacer for the axial gradient system . . . . .	223
4.5.2	Magnetic spacer for the radial gradient system . . . . .	226
4.5.3	Alignment of the chip and magnetic spacer . . . . .	227
4.5.4	Installing the aligned spacer into the vacuum system . . . . .	235



4.6	Experimental table setup . . . . .	236
4.6.1	Ion imaging and camera setup . . . . .	237
4.6.2	Laser setup . . . . .	237
4.6.3	Microwave and RF setup . . . . .	239
4.6.4	Trapping RF and helical resonator . . . . .	250
4.6.5	DC voltages . . . . .	251
4.7	Initial trapping of $^{174}\text{Yb}^+$ ions . . . . .	252
<b>5</b>	<b>On-chip production of gradients using microfabricated magnets, yoking, and hybrid systems</b>	<b>254</b>
5.1	On-chip permanent magnetic materials . . . . .	255
5.1.1	Linear magnetic high gradient regions . . . . .	257
5.1.2	Radial gradients on a ring shaped trap . . . . .	260
5.1.3	Magnetisation of on-chip magnets for a scalable system. . . . .	261
5.1.4	Reflections on gradients produced by on-chip permanent magnets . .	263
5.2	On-chip magnetic field gradients using locally excited yokes . . . . .	264
5.2.1	Macroscopic demonstration of electromagnetic yoking . . . . .	264
5.2.2	Redirection of magnetic fields using on-chip yokes in order to create high magnetic field gradients . . . . .	265
5.2.3	Microfabrication of high-permeability yokes . . . . .	267
5.2.4	Linear magnetic high gradient regions . . . . .	268
5.2.5	High gradient regions on a junction . . . . .	278
5.2.6	Remote yoke excitation using electromagnets . . . . .	283
5.2.7	On-chip yoke excitation using current carrying wires . . . . .	285
5.2.8	Reflections on gradients produced by on-chip yoking . . . . .	292
5.3	Self-compensation of current carrying wires using simultaneously driven yoked electromagnets . . . . .	293
5.3.1	How self-compensation works . . . . .	293
5.3.2	Initial simulation results . . . . .	295
5.3.3	Design and fabrication factors for the self-compensating scheme . .	295
5.3.4	Additional offset field compensation using the self-compensating scheme . . . . .	300
5.3.5	Advantages of the self-compensating scheme . . . . .	301
5.3.6	Summary of discussions regarding the self-compensating current car- rying wire scheme . . . . .	304

5.4	Reflections on the production of magnetic field gradients for implementation with trapped ions using long-wavelength coherent manipulation techniques . . . . .	307
5.4.1	Pros and cons of each gradient production method . . . . .	307
5.4.2	Direct comparison of gradients discussed in this thesis . . . . .	311
<b>Conclusion</b>		<b>313</b>
<b>Bibliography</b>		<b>316</b>
<b>A Supplementary information for the current carrying wires gradient pro- duction scheme</b>		<b>323</b>
A.1	Derivation of the equation for the magnetic field above two infinite straight current wires . . . . .	323
A.2	Reference data for current carrying wire schemes . . . . .	327
<b>B Technical drawings</b>		<b>334</b>
B.1	The Faraday cage . . . . .	334
B.2	The alignment stage . . . . .	365
B.3	Magnetic spacers, compensation magnetics, and coil mounts . . . . .	371

# List of Tables

1.1	Transition wavelengths of several ytterbium isotopes in vacuum corresponding to the selective ionisation transition $^1S_0 \leftrightarrow ^1P_1$ (for an angle of 63 degrees between the atomic beam and laser beam) and the primary cooling transition $^2S_{\frac{1}{2}} \leftrightarrow ^2P_{\frac{1}{2}}$ [36]. . . . .	27
2.1	Some important properties of prospective Faraday cage materials [53] [54] [55] [56] [57]. . . . .	54
2.2	The skin depths of prospective Faraday cage materials for a range of frequencies calculated using the average value of relative permeability from the ranges shown in Table 2.1. . . . .	54
3.1	The approximate values for some magnetic properties of material candidates for my scheme. . . . .	100
3.2	Optimum wire separations and the resulting vertical and planar gradients for the compensated anti-parallel current carrying wire scheme. . . . .	138
3.3	Simulated results of the magnetic field gradient at a given nil height above the magnets for width leeways of 0.3 mm and 0.7 mm from a 10 mm by 10 mm magnetic footprint. . . . .	161
3.4	Simulated results to compare the gradients produced by a constant magnet size and a constant footprint size. . . . .	162
4.1	A summary table showing the general properties of the coils for the axial gradient system. . . . .	184
4.2	A summary table showing the general properties of the coils for the radial gradient system. . . . .	185
4.3	The current-temperature profile for a pair of the primary 2a-2b coils. . . .	186
4.4	The current-temperature profile for a pair of the secondary 4a-4b coils. . . .	186

5.1	The simulated gradients for two different pairs of on-chip magnets. . . . .	259
5.2	Simulation results for a set of yokes driven by a magnet for a variety of under-chip distances. . . . .	274
5.3	Simulation results for another set of yokes driven by a magnet for a variety of under-chip distances. . . . .	274
5.4	Simulation results for a pair of yokes driven by a magnet for several different yoke permeabilities. . . . .	277
5.5	Simulation results for a pair of yokes driven by a magnet for several different yoke thicknesses. . . . .	278
5.6	The simulation results for a set of three yokes driven by a magnet for use with a junction trap. . . . .	282
5.7	Simulated gradients for a pair of yokes driven by an electromagnet. . . . .	285
5.8	Simulation results for a pair of yokes driven by a pair of on-chip wires. . . .	290
5.9	Simulation results for a pair of yokes driven by a single on-chip wire. . . .	291
5.10	The simulated results for two self-compensating current carrying wire schemes with different wire dimensions and yoke proximities. . . . .	306
A.1	Summary of current wire planar gradient results for two parallel current carrying wire schemes. . . . .	329
A.2	Summary of current wire vertical gradient results for two parallel current carrying wire schemes. . . . .	330
A.3	Summary of current wire planar gradient results for two anti-parallel current carrying wire schemes. . . . .	331
A.4	Summary of current wire vertical and “vertical tailored” gradient results for two anti-parallel current carrying wire schemes. . . . .	332
A.5	Summary of current wire “planar tailored” gradient results for two anti-parallel current carrying wire schemes. . . . .	333

# List of Figures

1.1	A very simple linear Paul trap geometry that can be used to trap ions. . . .	11
1.2	The trapping potential in two-dimensions of an RF Paul trap as defined by Equation 1.1. . . . .	12
1.3	The $x$ -axis ion motion for $q_x = 0.1$ and $\Omega_T = 2\pi \times 35$ MHz, resulting in a secular frequency $\nu_x = 2\pi \times 1.24$ MHz. . . . .	14
1.4	Several symmetric trap designs. . . . .	16
1.5	Several planar trap designs. . . . .	17
1.6	The Blade trap used for the trapped ion coherent manipulation experiments discussed in this thesis. . . . .	20
1.7	An example chip trap used in our experiments. . . . .	22
1.8	An illustration of the layer structure of the microfabricated chips. . . . .	23
1.9	A cut-through diagram of a helical resonator. . . . .	24
1.10	A partial energy level diagram for neutral ytterbium showing the two-stage photo-ionisation scheme that we use [35]. . . . .	27
1.11	A partial energy level diagram for $^{174}\text{Yb}^+$ showing the relevant states used during our trapping experiments [25]. . . . .	29
1.12	The energy level diagram for $^{171}\text{Yb}^+$ . . . . .	30
1.13	Individual addressing of two ions through the use of the different $^2\text{S}_{\frac{1}{2}}$ , $F = 1$ Zeeman splittings for two ions sitting in a magnetic field gradient. . . . .	33
1.14	The Blade trap illustrated in Figure 1.6 as retrofitted with the magnets designed by Dr Joseph Randall. . . . .	35
1.15	The compensation magnetics as they sit around the vacuum system hemisphere. . . . .	36
1.16	The RF and microwave setup used for coherent manipulation for the Blade trap experimental setup. . . . .	41
1.17	An illustration of the microwave frequencies used for our experiments. . . .	42

1.18	A top-view illustration of the hemisphere for the Blade trap system. . . . .	43
2.1	Partial cooling cycles for $^{171}\text{Yb}^+$ in the presence of a small magnetic field during the state preparation and detection pulses of our experiment. . . . .	48
2.2	A state preparation graph showing the probability of the number of photons collected by the PMT for an ion prepared in $^2\text{S}_{\frac{1}{2}}, F=0$ and $^2\text{S}_{\frac{1}{2}}, F=1$ . . .	49
2.3	Illustrations of the mechanisms that result in shielding from external static electric fields and high frequency electromagnetic radiation. . . . .	53
2.4	Pictures of the Faraday cage that was constructed around the Blade trap experimental setup. . . . .	56
2.5	An illustration showing the capacitance terms that determine the resonant frequency of the resonator and the dimensions used in order to calculate the Theremin effect alterations. . . . .	59
2.6	A cut-through illustration of the modification fitted to the resonator in order to shield the trap RF from external coupling between the resonator and the feedthrough. . . . .	61
2.7	An example of some of the intermodulation frequencies created when two signals with frequency $f_1$ and $f_2$ are mixed or amplified in a non-linear medium. . .	62
2.8	An example spectrum of our $\sim 12.6$ GHz carrier mixed with three RF modulator signals of 10 MHz, 24 MHz, and 27 MHz using Equation 2.6. . .	64
2.9	The “bare state” basis within the ground state $^2\text{S}_{\frac{1}{2}}$ manifold. . . . .	65
2.10	Rabi flopping between $ 0\rangle$ and $ 0'\rangle$ . . . . .	67
2.11	Rabi flopping between $ 0\rangle$ and $ +1\rangle$ . . . . .	68
2.12	Individual addressing of each ion through the $ 0\rangle$ to $ +1\rangle$ transition with a different splitting from $ 0'\rangle$ due to the static axial magnetic field gradient. .	71
2.13	A frequency scan over the $ 0\rangle$ to $ +1\rangle$ transition with both the carrier transition $\omega_+$ and its red and blue motional sidebands. . . . .	73
2.14	An illustration showing the COM and stretch modes of motion for two ions trapped along the $z$ -axis. . . . .	74
2.15	Diagrams detailing a spin motional entanglement experiment. . . . .	76
2.16	The probability of an ion initially in $ 0\rangle$ being in $ +1\rangle$ after simultaneously driving the (single-ion) red and blue sidebands at a given detuning for 180 $\mu\text{s}$ . . . . .	77
2.17	A spin motional entanglement time scan using the (single-ion) red and blue sidebands of $  -1\rangle$ at a symmetric detuning of $\frac{\delta}{2\pi} \approx 5$ kHz. . . . .	78

2.18	The change of basis from the bare states to the dressed states. . . . .	79
2.19	A frequency scan over the dressed state peaks using a single RF field applied for 800 $\mu$ s after the ion is initially prepared in $ 0'\rangle$ and the dressing fields are applied. . . . .	81
2.20	The experimental pulse sequence used to prepare an ion in the dressed state basis and detect the result. . . . .	82
2.21	A Rabi flop between $ 0'\rangle$ and $ D\rangle$ showing the extended coherence time in comparison to the magnetically sensitive bare states. . . . .	83
2.22	A single Rabi oscillation between $ 0'\rangle$ and each of the dressed states $ u\rangle$ , $ D\rangle$ , and $ d\rangle$ . . . . .	84
2.23	Spin-motional entanglement state probability in the dressed state as a function of symmetric detuning $\delta$ for a pulse time of 1 ms and pulse time $t$ for a fixed symmetric detuning of $\frac{\delta}{2\pi} = 1.32$ kHz. . . . .	85
2.24	A post sideband cooling, dressed state frequency scan over the red sideband and blue sidebands of $ D\rangle$ . . . . .	87
2.25	The ion motional temperature $\bar{n}$ as a function of delay time in order to measure the heating rate. . . . .	88
2.26	An illustration showing the current and minimised magnet spacings using a Blade trap geometry. . . . .	90
3.1	The real and effective positions of six ions sitting near to a magnetic nil point with high surrounding gradient. . . . .	93
3.2	A diagram to show the meshing used in a simulation of a pair of magnets. .	94
3.3	An example of aliasing in simulation data around a point $x_0$ and how the true field can be determined. . . . .	95
3.4	Diagram to define the axial and radial directions with respect to a string of trapped ions. . . . .	97
3.5	The coordinate orientation used in order to define gradients. . . . .	97
3.6	An illustration to show the nickel-copper-nickel coating finish available on the custom magnets. . . . .	101
3.7	The magnetic geometry designed by Dr Joseph Randall as used in the Blade trap experimental setup. . . . .	102
3.8	Field plots for both an uncoated and coated magnet setup as shown in Figure 3.7. . . . .	102
3.9	A typical symmetric magnet scheme geometry. . . . .	104

3.10	The axial gradient as a function of the inner separation distance of the magnets shown in Figure 3.9. . . . .	104
3.11	Line graphs showing the magnetic field at a given displacement from the centre of the magnetic setup shown in Figure 3.9. . . . .	105
3.12	The simulated axial gradient as a function of the side length of the pole faces of two magnets in symmetric configuration. . . . .	107
3.13	The simulated axial gradient as a function of the magnet length for two magnets in symmetric configuration with a pole face side length equal to their separation. . . . .	108
3.14	The axial magnetic field gradient produced by a pair of idealised magnets as a function of the separation between them. . . . .	108
3.15	A conceptual illustration of a typical current carrying wire chip geometry with the wires oriented for radial gradients. . . . .	110
3.16	A diagram to show the correct orientation of variables in order to use Equations 3.2, 3.3, 3.4, and 3.5. . . . .	112
3.17	The bulk current flow (black dots) in an infinitesimal wire and a real wire with many small kinks in it. . . . .	113
3.18	The field diagram for a pair of parallel current carrying wires. . . . .	115
3.19	The magnetic field produced by two parallel current carrying wires measured centrally along the vertical radial direction. . . . .	117
3.20	The magnetic field produced by two parallel current carrying wires measured at several heights above them along the planar direction. . . . .	118
3.21	The field diagram for a pair of anti-parallel current carrying wires. . . . .	119
3.22	The magnetic field produced by two anti-parallel current carrying wires measured centrally along the vertical radial direction. . . . .	121
3.23	The magnetic field produced by two anti-parallel current carrying wires measured at several heights above them along the planar direction. . . . .	121
3.24	An illustrated breakdown of the magnetic field components produced by a single current wire with current $I$ and the effect that a uniform offset field $B_x$ has on one component in shaping the total field. . . . .	123
3.25	A two-dimensional field cancellation example applicable to anti-parallel current carrying wires. . . . .	124
3.26	The field diagram for a pair of parallel current carrying wires compensated by a global magnetic field applied horizontally flowing left to right. . . . .	125



3.27	The magnetic field produced by two parallel current carrying wires with a compensation field in the $B_x$ -direction applied measured centrally along the vertical radial direction. . . . .	126
3.28	The magnetic field produced by two parallel current carrying wires with a compensation field in the $B_x$ -direction applied measured at several heights above them along the planar direction. . . . .	127
3.29	The field diagram for a pair of anti-parallel current carrying wires compensated by a global magnetic field applied vertically flowing bottom to top. . . . .	129
3.30	The magnetic field produced by two anti-parallel current carrying wires with a compensation field in the $B_z$ -direction applied measured centrally along the vertical radial direction. . . . .	130
3.31	The magnetic field produced by two anti-parallel current carrying wires with a compensation field in the $B_z$ -direction applied measured at several heights above them along the planar direction. . . . .	130
3.32	The field diagram for a pair of anti-parallel current carrying wires compensated by a global magnetic field applied horizontally flowing right to left. . . . .	132
3.33	The magnetic field produced by two anti-parallel current carrying wires with a compensation field in the $B_x$ -direction applied measured at several heights above them along the planar direction. . . . .	133
3.34	Three ways that permanent magnets can be used to create a high gradient above a magnetic geometry by using an asymmetric field approach [65]. . .	144
3.35	The magnetic structure which is placed under an ion trap chip in order to implement the magnetic field gradient production method used on Barb's atom traps. . . . .	146
3.36	Examples of the magnetisation direction's effect on the height of the magnetic nil. . . . .	147
3.37	The field diagram for a pair of permanent magnets separated by a small distance with magnetisations parallel through their separation as shown in Figure 3.36 (a). . . . .	148
3.38	The field diagram for a pair of permanent magnets separated by a small distance with magnetisations parallel but perpendicular to their separation as shown in Figure 3.36 (b). . . . .	149

3.39	The field diagram for a pair of permanent magnets separated by a larger distance with magnetisations parallel but perpendicular to their separation as shown in Figure 3.36 (c) so that the height of the magnetic nil is that of Figure 3.36 (a).	149
3.40	The vertical radial fields at the centre of the geometries in Figure 3.36.	152
3.41	The magnetic field measured along the planar direction at $760\text{ }\mu\text{m}$ above the magnet surface for the geometries in Figure 3.36.	152
3.42	Illustrations of the advantages of recessing a magnetic spacer in the under-chip copper block.	156
3.43	One must take into account all thicknesses of material between the magnet surface and the ion in order to accurately align the RF and magnetic nil in the ion height direction.	157
3.44	An offset magnetic spacer geometry in order to create a small axial gradient in addition to a large radial gradient.	167
3.45	The magnetic field produced by the magnetic geometry shown in Figure 3.44 measured centrally along the vertical radial direction.	168
3.46	The magnetic field produced by the magnetic geometry shown in Figure 3.44 measured along the planar radial direction at a height of $855\text{ }\mu\text{m}$ above the magnets.	169
3.47	The magnetic field produced by the magnetic geometry shown in Figure 3.44 measured along the axial direction at a height of $855\text{ }\mu\text{m}$ above the magnets.	169
3.48	A three-magnet design for axial gradients in opposite arms of an x-junction and a high field in arms perpendicular to those.	171
3.49	An abstract geometry proposed by Anton Grounds in which the magnets are able to be moved underneath the x-junction.	173
4.1	The exterior of the axial gradient system.	178
4.2	The exterior of the radial gradient system.	179
4.3	The cross-sectional profiles of each of the coil types and the perfect winding order for the maximum number of turns of wire.	184
4.4	The mounts constructed in order to secure the coils in place around the hemisphere of the vacuum system.	187
4.5	A single stack of four neodymium magnets for external compensation.	189
4.6	A double stack of neodymium magnets for external compensation.	189
4.7	A quadruple stack of neodymium magnets for external compensation.	190

4.8	The field at a distance from the compensation magnets. . . . .	190
4.9	The field across the compensation magnets at a distance of 100 mm from the pole faces. . . . .	191
4.10	The missing coil axis permanent magnet compensation setup. . . . .	192
4.11	The final orientation of the field compensation apparatus with respect to the ion trap. . . . .	192
4.12	Chip tongues in order to hold the chip during the alignment procedure. . .	195
4.13	A picture taken by the USB microscope of the nano-suction-cup tape after being removed from a gold coated chip. . . . .	196
4.14	The combined lower alignment stages which should allow for precise trans- lation of the chip and magnets in $x$ , $y$ , $z$ , and $r$ , the angle around the $z$ -axis. . . . .	197
4.15	The heating plate created in order to cure the silver epoxy. . . . .	199
4.16	The finalised alignment stage used in order to glue the chip and magnetic spacer to each other with high precision. . . . .	201
4.17	A CNC machine similar to the one used in order to make the magnetic measurements. . . . .	219
4.18	A schematic of the set of magnets measured using the Hall probe mounted on a CNC machine. . . . .	220
4.19	The magnetic field component $B_z$ at 865 $\mu\text{m}$ above the geometry shown in Figure 4.18. . . . .	222
4.20	An example of the venting flute arrangement as seen from the bottom face of the copper structure that holds the magnets in place for the axial gradient system. . . . .	223
4.21	The copper spacer that holds the under-chip magnets installed in the axial gradient system. . . . .	225
4.22	The offset copper spacer that holds the under-chip magnets installed in the radial gradient system. . . . .	227
4.23	The linear 165 $\mu\text{m}$ ion height chip, $IQT\ BL\ LIN4$ to be paired with the high axial gradient magnetic spacer for the axial gradient system. . . . .	228
4.24	The inner electrode structure of the $IQT\ BL\ LIN4$ chip with certain elec- trodes marked with the resistances to the relevant bond pads. . . . .	229
4.25	A schematic of the magnetic spacer to be paired with the chip to be installed in the axial gradient system as measured during the third alignment attempt.	230

4.26	A schematic of the magnetic spacer to be paired with the chip to be installed in the radial gradient system as measured during the alignment procedure.	232
4.27	The linear 250 $\mu\text{m}$ ion height chip, <i>IQT BL LIN3</i> to be paired with the high radial, low axial gradient magnetic spacer for the radial gradient system.	233
4.28	The inner electrode structure of the chip shown in Figure 4.27 with certain electrodes marked with the resistances to the relevant bond pads.	234
4.29	The internal structure of the vacuum system connecting the chip to the trapping voltages as designed by David Murgia.	235
4.30	The front in-vacuum PCB with a wirebonded chip in place as assembled and bonded by David Murgia.	236
4.31	The imaging tube lens setup used for the axial gradient system.	237
4.32	The laser setup used for the axial gradient system.	238
4.33	The simulation geometry with important components highlighted by a dotted white outline.	241
4.34	The absolute field plot for microwaves injected into the system via a horn at the front window with a mesh with a central hole in place.	242
4.35	Several simulations of the absolute field plot for 50 MHz RF injected into the system via a single turn coil at the front window.	244
4.36	Several simulations of the absolute field plot for microwaves injected through a recessed side window using a horn and a rectangular waveguide.	246
4.37	Several simulations of the absolute field plot for in-vacuum 50 MHz RF coils.	247
4.38	Several simulations of the absolute field plot for in-vacuum microwave emitters.	248
4.39	The front window with the vacuum-side mesh in place.	250
4.40	One of the resonators designed and built by Nikolaus Lorenz.	251
5.1	The linear gradient geometry of the on-chip magnets that would be situated under the main electrode layer.	257
5.2	The field diagram for a pair of on-chip permanent magnets with an in-plane magnetisation through their separation.	258
5.3	The on-chip magnet geometry resulting in the magnetic field profile shown in Figure 5.4.	261
5.4	The magnetic field for a set of two circular magnets with a central gap.	261
5.5	Magnetic writing head designs used for imprinting a magnetisation into a magnetic film.	262

5.6	An illustration of the internal magnetic field propagation due to magnetic yoking in the electromagnetic coin stacking demonstration. . . . .	265
5.7	The geometric configuration for two on-chip yokes with a small separation between them driven by an under-chip magnet. . . . .	269
5.8	The field diagram for a pair of on-chip yokes activated by an under-chip permanent magnet with a remanence parallel to the plane of the chip across the yoke separation. . . . .	270
5.9	The magnetic field measured along the planar direction for a pair of yokes driven by a magnet with an out-of-plane remanence. . . . .	271
5.10	The magnetic field measured along the planar direction for a pair of yokes driven by a magnet with an in-plane remanence. . . . .	272
5.11	An illustration of a typical field profile across a pair of activated yokes at two different heights above them. . . . .	273
5.12	The magnetic field for a pair of yokes driven by a magnet for several different yoke permeabilities. . . . .	276
5.13	The magnetic field for a pair of yokes driven by a magnet for several different yoke thicknesses. . . . .	276
5.14	An illustration of the field profiles for several different sets of yokes that may be used with an x-junction. . . . .	279
5.15	The magnetic field measured along the planar direction for a set of three yokes driven by a magnet for use with a junction trap. . . . .	280
5.16	An illustrated comparison of the field profiles on an x-junction for on-chip permanent magnet and yoking schemes when an axial gradient is used. . . .	281
5.17	A comparison of the high axial gradient schemes that can be implemented with an x-junction trap using on-chip permanent magnets or yokes. . . . .	282
5.18	The geometric configuration for the pair of yokes driven by an under-chip electromagnet which is simulated in this section. . . . .	284
5.19	The magnetic field for a pair of yokes driven by an electromagnet. . . . .	284
5.20	Three configurations of under-yoke current wires that could be used in order to activate them using solely on-chip field sources. . . . .	286
5.21	The magnetic field for a pair of yokes driven by a pair of on-chip wires on the underside of the chip. . . . .	287
5.22	The magnetic field for a pair of yokes driven by a pair of on-chip wires fabricated just under the yokes. . . . .	288

5.23	The magnetic field for a pair of yokes driven by a single on-chip wire fabricated just under the yokes. . . . .	289
5.24	An illustration of the method by which the natural nil position of two parallel current carrying wires can be displaced from their centre of separation using yokes. . . . .	294
5.25	The field diagram for a set of self-compensating buried current carrying wires using simultaneously activated yokes. . . . .	296
5.26	The field measured along the vertical radial direction and along the planar direction at a height of $55\text{ }\mu\text{m}$ across two self-compensating current wires. .	297
5.27	Two methods by which one can compensate or make small adjustments to the in-plane and out-of-plane components of the magnetic field at the ion position. . . . .	300
5.28	Three methods of field adjustment proposed for magnetic field gradient schemes involving current carrying wires. . . . .	303
A.1	The labelled geometry of the two-wire setup with both currents parallel to each other and coming out of the page. . . . .	324
A.2	The labelled geometry of the two-wire setup shown in Figure A.1 with the current in wire 2 now reversed for the explicitly anti-parallel case. . . . .	326
B.1	An assembly diagram of the Faraday cage showing the two sides which have access panels, and the lid of the system. . . . .	335
B.2	Another assembly diagram of the Faraday cage showing the two sides which do not have access panels, and the bottom frame of the system. . . . .	336
B.3	The final assembly diagram of the Faraday cage showing part of the internal frame structure of the system. . . . .	337
B.4	Inside view of Panel 1 which shows the frames on the inside of the windows into which the access panels fit. . . . .	338
B.5	Outside view of Panel 1 showing the outer window dimensions and the hole placement in order to secure the panel to the inner frame structure of the Faraday cage. . . . .	339
B.6	The smaller a-type access panels which enable access to the inside of the Faraday cage via Panels 1 and 3. . . . .	340
B.7	The larger b-type access panels which enable access to the inside of the Faraday cage via Panels 1 and 3. . . . .	341

B.8	Inside view of Panel 2 which shows the holes so that the connectors for the compensation coils and microwave cables for coherent manipulation can enter the system. . . . .	342
B.9	Outside view of Panel 2 showing the hole placement in order to secure the panel to the inner frame structure of the Faraday cage. . . . .	343
B.10	The current panel that covers the larger connector hole in Panel 2. . . . .	344
B.11	The microwave panel that covers the smaller connector hole in Panel 2. . .	345
B.12	The imaging panel that completes the cage under the slot in Panel 2 which allows it to be installed without removing the imaging tube. . . . .	346
B.13	Outside view of Panel 3 which shows the windows in order to fit the access panels and an R30 slot which allows the compensation coil water cooling pipes to exit the system. . . . .	347
B.14	Inside view of Panel 3 showing the inner frame measurements for the access panels and the hole placement in order to secure the panel to the inner frame structure of the Faraday cage. . . . .	348
B.15	The water cooling panel that completes the cage under the slot in Panel 3 which allows it to be installed without removing the water cooling piping. .	349
B.16	Outside view of Panel 4 which shows the small connector holes that allow optical fibres to enter the cage for the post-fibre laser optical setup. . . . .	350
B.17	Inside view of Panel 4 showing the hole placement in order to secure the panel to the inner frame structure of the Faraday cage. . . . .	351
B.18	The fibre panels that cover the optical fibre connector holes in Panel 4. . .	352
B.19	Bottom frame 1 with a small hole for the DC cables to enter the cage matched with the slot in Panel 1. . . . .	353
B.20	Bottom frame 2 with extra holes associated with the position of the imaging panel on Panel 2. . . . .	354
B.21	Bottom frame 3 with extra holes associated with the position of the water cooling panel on Panel 3. . . . .	355
B.22	Bottom frame 4 with a fibre connector hole matched with the position of the slot in Panel 4. . . . .	356
B.23	The corner posts of the Faraday cage. . . . .	357
B.24	The bottom corner pieces which secure the corner posts to the bottom frames of the cage. . . . .	358

B.25 The top corner pieces which secure the corner posts to the top frames of the cage. . . . .	359
B.26 Top frame 1 associated with Panel 1. . . . .	360
B.27 Top frames 2 and 4 associated with Panels 2 and 4. . . . .	361
B.28 Top frame 3 associated with Panel 3. . . . .	362
B.29 Outside view of the Faraday cage lid showing the slot dimensions so that the ion pump and gauge cables can exit the system and the near-central hole into which a BNC connector is installed for the trap RF connection. . . . .	363
B.30 Outside view of the Faraday cage lid showing the hole placement in order to secure it to the top frames of the inner frame structure. . . . .	364
B.31 The mount used in order to secure the digital USB microscope to a Thor-Labs translation stage. . . . .	365
B.32 The stand in order to raise the microscope translation stages above the chip and magnet alignment stages. . . . .	366
B.33 The original suction-cup tape chip tongue design. . . . .	367
B.34 The pump-activated chip tongue. . . . .	368
B.35 The suction hose adaptor which allows the pump-activated chip tongue to be attached to a PVC tube compatible with the suction pump. . . . .	369
B.36 The heating plate which fits on top of the alignment stages. . . . .	370
B.37 An assembly drawing of a magnetic spacer comprised of the figure-eight and bottom parts. . . . .	372
B.38 The figure-eight of the high axial gradient spacer used in the axial gradient system. . . . .	373
B.39 The figure-eight of the offset, high radial, small axial gradient spacer used in the radial gradient system. . . . .	374
B.40 The bottom/lid common to both spacers. . . . .	375
B.41 An assembly drawing of the mount for the permanent magnet compensation setup. . . . .	376
B.42 The back plate of the magnet mount. . . . .	377
B.43 The front plate of the magnet mount. . . . .	378
B.44 A full separator which goes around the outermost magnets of each stack of four. . . . .	379
B.45 A half separator which goes around the inner magnets of each stack of four. . . . .	380



B.46 An aluminium blank that can be used in place of a magnet if the stage is not required to be fully loaded. . . . .	381
B.47 The front support of the magnet mount. . . . .	382
B.48 The base plate of the magnet mount. . . . .	383
B.49 The coil former of the primary compensation coils used for both vacuum systems discussed in Chapter 4. . . . .	384
B.50 The coil formers of the secondary compensation coils used for both vacuum systems discussed in Chapter 4. . . . .	385
B.51 A knurled thumbnut that is used to set the height or separation of the compensation coils. . . . .	386
B.52 A mount used for creating a horizontal rail from brass studding which can be used in conjunction with the thumbnuts to set the separation of the primary coils for each vacuum system. . . . .	387
B.53 An optics post style mount for securing the secondary coils. . . . .	388

# Introduction

The realisation of a scalable quantum computing architecture would allow for a surge in the capability for the human race to perform calculations and computational operations which simply are not viable on a classical computer. The key to this lies in the ability for certain systems to be in a superposition of the states “0” and “1” of a classical computer, i.e. a quantum bit or “qubit” can be both 0 and 1 at the same time, the proportionality between them determined by a measurement of the state over many repetitions of the same operation. With use of the correct computing algorithms, this allows for a change in scaling of the time it takes to solve a computational problem, such as searching for an item in an unsorted list (Grover’s algorithm [1]) or factorising an extremely large number (Shor’s algorithm [2]). Though a single operation may appear to take longer than a typical household computer, by using quantum algorithms, a larger problem may be solved in much less time, not due to the speed of the operation, but rather through a different route to the answer that can only be taken through the use of a quantum bit. One can see now that the use of a quantum computer is not suitable for all problems, but in some cases makes the problems solvable within a reasonable time frame.

The requirements of a quantum computing system were suggested by DiVincenzo in 2000 [3] and to this day they are useful criteria by which a quantum system can be judged for its suitability for creating a scalable quantum computer. These criteria are as follows<sup>1</sup> [3]:

- A scalable physical system with well characterised qubits - Scalable means that the resources required to make the system larger expand, at the very most, polynomially, otherwise there is an exponential resource requirement with minimal growth in computing power. This is obviously very inefficient and ill advised for any technology. Additionally, one must be able to make the system larger in the first place; if the very largest a system can be is with only two qubits then it would be hard to build a larger system using such a scheme. A well characterised qubit would have to be

---

<sup>1</sup>These are a paraphrased for the purpose of clarity.

clearly “0” or “1” on measurement at the highest fidelity otherwise there will always be significant errors in computations as one cannot tell what state the qubit is in.

- The ability to initialise a qubit in a simple base state - This means that the qubits must be able to be easily set to a state that is known from which a “0” ( or “1”) can be clearly identified before subsequent operations cause it to remain in this initial state, switch to the other, or become a combination of the two.
- A long decoherence time when compared to the time it takes to perform a gate operation - A state will only remain in a clearly defined “0” or “1” for a relatively short amount of time due to influences from external stimuli, thermal excitation, electromagnetic field fluctuations and noise, etc. This means that as the state decoheres, i.e. starts to deviate from perfectly prepared, an error in the quantum operation is produced; for long enough times this error is large enough such that the operation result is unusable as one cannot tell what it is. However, so long as this decoherence time is much shorter than the time it takes to perform a gate-operation (manipulation of the qubit or multiple qubits), this error will be minimal and the result will still be usable and easy to interpret.
- One should be able to use a universal set of quantum gates - As with all computers, many different operations are used in order to manipulate each bit in order to perform larger computations using basic logical gates. The same goes for a quantum computer, meaning that a scalable system must be able to perform basic quantum logic gates from a universal list by which quantum computing algorithms are defined.
- The capability to measure individual and specific qubits - This means that one must have minimal crosstalk on any readout measurements from qubits near to the intended target as this would cause a loss in the operation fidelity. This also means that any manipulation of the qubit must be able to be done to each specific qubit individually without affecting others unless intended.

In addition to these criteria, a scalable quantum computer requires the ability to network with other quantum computing hardware. This means that there needs to be a clear way that one can convert a stationary qubit, for example an ion, into a “flying” qubit, for example a polarised photon. The system also requires the ability to transmit this flying qubit between specific parts of a quantum network with no loss or degradation in the information it carries.

Trapped ions have been shown to fill these criteria well using an experimental setup that isolates them from unwanted external stimuli as will be explained later in this thesis. However, there are many different ions that can be used and methods by which a qubit can be manipulated. The ions can be selected simply by their energy level structure and whether a suitable pair of states can be isolated to be used as a two-level system for the qubit. This is specific to the isotope of a given species and though calcium [4], strontium [5], magnesium [6], barium [7], and other atomic species can be used, in this thesis I will focus solely on ytterbium ions. The  $^2S_{1/2}$  hyperfine manifold of the  $^{171}\text{Yb}^+$  ion is the basis of our qubit and it will later be shown why this feature of its energy level structure, as well as the resulting cooling cycles, make this ion a good candidate for creating a scalable quantum computing architecture.

Though this thesis will focus solely on trapped ion quantum computing, there are other physical systems which have been shown to be able to perform quantum computing operations. These include, for example, linear optical, superconducting, solid state, and neutral atom quantum systems. The latter of these, like ions, stores its quantum information within the energy levels and spin states of atoms trapped in an isolated environment, usually under vacuum [8]. Solid state systems, for example, a single phosphorus atom doped into silicon [9], differ from these systems in that the atom is within a solid medium, however, the nuclear and electronic spin states still serve as the basis of quantum information storage as well as the charge degrees of freedom [9]. For superconducting qubits, Josephson junctions when integrated as part of a circuit allow for two energy levels that are not equally spaced, an effect due to the non-linear nature of the circuit, in order to create a qubit basis [10]. For linear optics the quantum information is typically stored within a dual-rail scheme where the polarisation of the photon stores its quantum state and the presence of the photon determines the existence of the qubit within the system [11]. These photons are directed by macroscopic optical apparatus in order to create the required configuration for performing gate operations.

Trapped ions have several advantages over each of these systems as a competitor for a scalable quantum technology. When compared to neutral atoms, ions can typically be trapped for a much longer time, hours to days rather than seconds [12]. Ion traps can also be operated at room temperature, a distinct advantage over superconducting and some solid state systems when it comes miniaturising a quantum computer as a cryogenic system is not required. When compared to linear optics, linear optics has the advantage that a qubit is clearly present for all detections of a state. For our qubit the ion is detected

as “light” or “dark” depending on its quantum state which means that the lack of an ion may read the same as a “dark” ion state. However, ion trap quantum computing is much easier to scale to many qubits than linear optics and can be miniaturised much more easily, thus making it a better candidate for the scalable quantum computer overall.

## Quantum computing with trapped ions

There are several methods by which one can manipulate a trapped ion based qubit. The most common method at present is laser driven operations where pulses of resonant laser light are used to manipulate the ion’s internal state and perform entanglement operations, for example by the group of Professor Christopher Monroe [13]. Another method is to use a near-field oscillating magnetic field gradient at microwave frequencies produced on certain electrodes of the trap, for example by the group of Professor David Lucas [4]. Though these methods have both been shown to produce high fidelity multiple-ion gates [14] [4], there are several complications for creating gate operations in larger systems.

For laser driven gates, the main difficulty is that each ion needs to be individually addressed by a laser beam. This requires extremely high precision optics in order to focus a laser onto a single ion at a time with near-zero crosstalk between ions. This is not impossible but difficult, particularly when it comes to miniaturising a system as laser beam shaping would have to be done fast with smaller optics. This would be extremely challenging from an engineering perspective.

The near-field oscillating magnetic field gradient scheme solves this problem by using on-chip microwave sources instead of laser light to drive qubit rotations. However, when using near-field microwaves the ions are confined to certain microwave field zones for gates and calibrated nulled zones where gates will not be driven [15]. This means that there is again a limit to the miniaturisation of this scheme as one would need to minimise crosstalk through increased zone distances or minimising microwave power.

In this thesis I will be focussing exclusively on microwave and RF based qubit manipulation in the presence of a static magnetic field gradient at the ion position. The advantages of this method over the two I have previously discussed is that with the correct choice of energy level structure, and an ion that exhibits this structural feature, a static magnetic field gradient means that there is a different Zeeman splitting of energy levels for each ion in a linear string, assuming that the gradient and string are oriented in the same direction. This means that global laser light can be used for cooling the ions and microwaves (or radio frequency depending on the transition energy) can be used to

individually address each ion qubit with minimal crosstalk. These microwaves can also be spatially global with many frequencies combined; this may seem like a bad idea on first inspection but since the ions do not occupy the same frequency space they are still individually addressed as long as each ion sits in a different magnitude of magnetic field. There is also not an issue with miniaturisation as the closeness of the ions does not create greater microwave crosstalk as long as the static magnetic field gradient can be increased. The details of this individual addressing will be explained later concerning  $^{171}\text{Yb}^+$  ions.

In order to perform entanglement operations with trapped ions, one requires the laser or microwave manipulated state to be coupled to the motion of the ion as it oscillates in the trap. From de Broglie's wave-particle relationship, the laser or microwave photon exerts a force on the ion as it flips the state of the ion qubit and this force is dependent on the qubit state as the states have different energy. Since the ions share the same trapping potential, a force exerted on one ion will be felt by the others due to their coulomb interaction. This is the basis of inter-qubit communication within a quantum bus and is what allows us to perform multiple-qubit gate operations. The coupling between the ion's secular motion (its natural oscillation within the trapping potential) and its internal state determines how fast a gate operation can be performed; if the coupling is large, only a small force is required on a single ion in order for an operation on said ion to be felt by those surrounding it. This coupling is ultimately mediated by a parameter known as the "Lamb-Dicke parameter" [16] given by [17]:

$$\eta = \frac{\Delta z 2\pi}{\lambda} \quad (1)$$

where  $\Delta z = \sqrt{\frac{\hbar}{2m\nu}}$  is the spatial extent of the atom of mass  $m$  with a secular frequency  $\nu$ , and  $\lambda$  is the wavelength of the applied radiation. Laser based qubit manipulation provides a sufficient non-zero Lamb-Dicke parameter in order to create high fidelity entanglement between the internal and motional state of a trapped ion as the laser photon momentum gives a large enough kick to the ion so that the state change is felt by other ions within the trapping potential. However, the Lamb-Dicke parameter for microwaves is extremely small due to the long wavelength and therefore much smaller photon momentum. This means that there is very little coupling between the ion's states and its motion and that it is impractical to perform two-qubit gates.

Florian Mintert and Christof Wunderlich however realised that by adding a magnetic field gradient, two-qubit gates driven by microwave fields should be possible [17]. By supplementing the microwaves with an additional high magnetic field gradient at the ion

position, the coupling between the ion's Zeeman states and its motion is strengthened [17]. This works in a similar way to the Stern-Gerlach experiment; a magnetic field gradient exerts a force on an ion which is dependent on whether its internal spin state is up or down, i.e. the “0” or “1” of our qubit. By exciting the transition in order to flip the spin of this internal state, the magnetic field gradient causes a momentum kick to the ion not unlike that produced by a laser photon. This allows an operation on one ion to be felt by nearby ions in order to create a microwave driven quantum bus. Additionally, the magnetic field gradient causes a strengthening of the coupling between the qubit transition and the ion motion; the ion is oscillating in the magnetic field gradient and the qubit transition frequency shifts with the ion's displacement from its centre of oscillation due to the Zeeman effect. This means that one is able to manipulate the ion's motional state through the motional sidebands of its internal state transitions<sup>2</sup>. This in turn gives rise to an effective Lamb-Dicke parameter given by [18]:

$$\eta_{\text{eff}} = \frac{\mu_B b_z}{\sqrt{2m\hbar\nu_z^{\frac{3}{2}}}} \quad (2)$$

where  $\mu_B$  is the Bohr magneton,  $b_z$  is the static magnetic field gradient oriented in  $z$ , and  $\nu_z$  is the secular frequency in the  $z$ -direction. This new form of the parameter is directly proportional to the magnetic field gradient, therefore by maximising the magnetic field gradient for a given setup, one can maximise the coupling between the internal states and the ion motion, to the simplest approximation. This means that microwave (or RF) radiation can be applied to the ion for a shorter time in order to perform internal state to motion entanglement operations and therefore allows for faster multiple-ion gate operations [19]. The gate speed in competition with the heating rate of the ion determines the fidelity of a gate operation. By generating high magnetic field gradients one should be able to produce gate times dominant over the heating rate to such an extent that a fault tolerant gate can be produced. This means that there is so little error in the gate operation that error correction would mean that multiple operations improve the result rather than add more error to it. This would enable long-wavelength trapped ion quantum computing to be used as a method for creating a scalable quantum computer.

In terms of the world stage, development of microwave and RF based entanglement schemes using trapped ions in the presence of a static magnetic field gradient is mainly addressed by two groups; our own and the group of Professor Christof Wunderlich, based

---

<sup>2</sup>This motion to state coupling will be explained in more detail throughout this thesis with regards state manipulation of  $^{171}\text{Yb}^+$  ions.

in Siegen, Germany. Given this small community, collaborative work between the two groups has been valuable in working to develop this entanglement scheme. This collaboration is best seen in the “Blueprint for a microwave trapped ion quantum computer” paper written by Dr Bjoern Lekitsch [20], a collaboration additionally with Klaus Mølmer who co-pioneered the two-qubit gate scheme that we use. Magnetic field gradients for this application have been shown to be possible using on-chip current carrying wires as shown in the 2013 paper by Kunert (of Wunderlich’s group), “A planar ion trap chip with integrated structures for an adjustable magnetic field gradient” [21], the first step towards the envisioned scalable architecture of the previously mentioned paper. The gradients demonstrated by this chip, however, are much smaller than those required in order to produce high fidelity entanglement operations, peaking at 1 T/m (tesla per metre) as opposed to the 23.3(6) T/m created by the permanent magnetic setup used by our group [19], albeit using a much more scalable architecture.

This thesis focusses on developing designs for much higher static magnetic field gradients, of the order 100 T/m, so that higher fidelity and ultimately fault tolerant entanglement operations with trapped ytterbium ions using microwave and RF radiation can be performed. This would enable microwave based trapped ion quantum computing to lead in the race to developing a scalable quantum computer. My work towards this goal encompasses developing gradients produced using in-vacuum permanent magnets and on-chip current carrying wires before introducing new and exciting on-chip permanent and electromagnetic gradient production methods created using microfabricated structures. The most notable of these methods is an under-chip magnetic spacer which when correctly aligned to a chip attached to the top of it, should allow for extremely high magnetic field gradients not seen before in this field. With the correct chip and peripheral equipment such as stable DC and RF electrode voltages, high power microwaves, and in-vacuum cooling systems, this should allow coherent manipulation using long-wavelength radiation with trapped ions to reach the fault tolerant regime with fast, high fidelity gates suitable for a scalable quantum computing architecture.

## Thesis overview

Chapter 1 focusses on the principles of ion trapping, the trapping potential and resultant ion motion in the trap, and the different types of ion trap that exist, including some of their advantages and disadvantages, and how an ion trap can be integrated with an ultra-high vacuum system. Next, I describe the ytterbium ion and detail the different isotopes



that have been used for experiments in this thesis, their cooling cycles, and the required laser and microwave fields to manipulate the ion’s internal state. The chapter finishes with an overview of the macroscopic “Blade” trap experimental setup used for the bulk of coherent manipulation operations by this group, the post trapping procedures that were undertaken when this system was first retrofitted with a magnetic field gradient using permanent magnets, and the laser and microwave setup, including the computer control used to sequence pulses of these fields.

Chapter 2 continues the journey of this experiment by describing the results obtained using the Blade trap setup in order to illustrate what a magnetic field gradient of 23.3(6) T/m allows us to achieve. This covers some simple experiments as well as single-ion spin-motional entangled states, preparation of a dressed state basis which allows for much longer coherence times, and ground state cooling using microwaves, all made possible using the static magnetic field gradient designed and built by Dr Joseph Randall. This then serves as the minimum required benchmark by which a magnetic field gradient used in conjunction with microfabricated planar chip traps must greatly exceed in future experiments. In addition to this I examine some potential obstacles towards high fidelity operation that can be solved by minimising noise present on the experimental setup from within and from external sources. This includes evaluation of the noise present inside the system due to electrical supplies and the construction of a Faraday cage to minimise noise from outside the system, analysis of anomalous RF coupling, and consideration of microwave intermodulations for mixed or amplified signals.

After a short overview of the magnetic and simulation terminology that will be used to evaluate the designs described in this thesis, Chapter 3 launches into a review of the currently implemented or envisioned magnetic field gradient production methods used by this group with an emphasis on their integration with planar trap geometries. This focusses on the symmetric magnetic scheme as used in the experimental setup in Chapters 1 and 2 before a thorough review on the operation and optimisation of microfabricated current carrying wires buried under the electrode layer of planar chip traps as fabricated by Dr Bjoern Lekitsch. I then propose a new under-chip scheme inspired by the work of Dr Iuliana Barb in the field of atom trapping which uses an under-chip spacer containing two magnets with a small separation between them in order to create high magnetic field gradients exceeding 100 T/m with near-zero offset field at the ion position when an appropriate planar chip trap is correctly aligned and secured atop it.

Chapter 4 continues the story of the magnetic spacer by documenting the construction

of real spacers, their alignment with real chips, and the difficulties faced during these procedures. After reviewing and quantifying currently used methods in order to compensate any offset field that may occur due to a misalignment, I continue by designing and documenting the construction of apparatus that should allow a planar chip trap to be aligned to the magnetic spacer to micron-level precision. This is followed by an initial measurement of the magnetic field gradient made using a CNC mounted Hall probe setup achieving an in-plane magnetic field gradient of  $\sim 110$  T/m at the ion position. After aligning the chips to each under-chip magnetic spacer, the new experimental setup is documented with a detailed look into the microwave and RF setup. The system in operation was built to exhibit fault tolerant two-ion gates after initial trapping and characterisation of the ion motion and the magnetic field gradient measured in situ, though this measurement is not achieved within the time-scale of this thesis.

Chapter 5 looks towards the implementation of microfabrication techniques which may enable other methods for producing on-chip magnetic field gradients. Starting with microfabricated on-chip permanent magnets, I expand to explain the benefits of planar, mask-defined magnet geometries which allow for gradients in much more abstract and complex trap designs. Following this, I propose another new scheme which uses microfabricated high permeability yokes in order to shape the magnetic field produced by a local, off-chip permanent magnetic field source. This expands to using under-chip electromagnetic coils and on-chip current carrying wires in order to activate these yokes. This led to an exciting development in which microfabricated current carrying wires may be able to create a high gradient nil at the ion position by simultaneously driving yoked electromagnets which cancel the high offset field above them that is typically associated with most current wire schemes. This new idea is explored and key concepts are highlighted in order to make this scheme a reality once an appropriate fabrication process has been identified. I finish by comparing all the major magnetic field gradient production methods described in this thesis and identify the best schemes for certain regimes and experimental setups.

The thesis ends with a simple summary of the developments in the field of ion trapping that have been discussed before moving onto the appendices which detail the derivation of the equations which describe the field produced by a pair of current carrying wires, including tabulated results obtained from initial current wire simulations, and display many technical drawings for apparatus built for the purpose of these experiments. So, without further introduction, let us begin the main body of this thesis. I hope you enjoy the sheer volume of magnetic content that follows from this point onwards.

# Chapter 1

## Trapping ytterbium ions

This thesis describes my work on an already established experimental setup as well as one that was built during the course of my PhD. This chapter describes the basics of a trapped ion quantum computing experiment and relates this to our own experimental setups which focus on long-wavelength quantum computing using trapped ytterbium ions in the presence of a static magnetic field gradient.

I first discuss the basics of RF Paul trap operation and various different types of RF Paul trap that can be created before outlining the trap designs used to obtain the results discussed in Chapters 2 and 4 and how to electrically connect to a trap. I then introduce the ytterbium ion and discuss laser ionisation, Doppler cooling, and the laser and microwave fields required to effectively perform experiments with ytterbium ions. I finish by discussing the creation of a magnetic field gradient in the experiment and how this alters the energy levels of the ion allowing for individual addressing using microwave radiation and coupling of the ion's motion to its internal states. Thereafter, I describe the remaining experimental apparatus used, including optical imaging and laser setups, microwave and RF apparatus, and computer control.

### 1.1 RF Paul traps

Earnshaw's theorem states that it is not possible to trap a charged particle using static electric fields alone [22]. This is illustrated by Laplace's equation  $\nabla^2\phi(x, y, z) = -\nabla \cdot \mathbf{E} = 0$ , where  $\phi(x, y, z)$  is a three-dimensional static electric potential and  $\mathbf{E} = -\nabla\phi$  is the resultant electric field from such a potential [23]. This indicates that with static electric fields alone it is not possible to create a point where field lines in all directions either originate or terminate in free space, i.e. without the presence of a charge at said position.

Paul traps solve this issue by creating a hyperbolic potential and time varying its amplitude at radio frequencies. This results in a time averaged potential which resembles a parabolic well in the frame of reference of a trapped ion. The RF oscillation of the hyperbolic potential therefore provides a confining potential in which an ion can be trapped. The ion oscillates within this pseudopotential well in the same way it would oscillate in a simple harmonic well. This oscillation is called the secular motion and is the main motion of an ion trapped within a Paul trap.

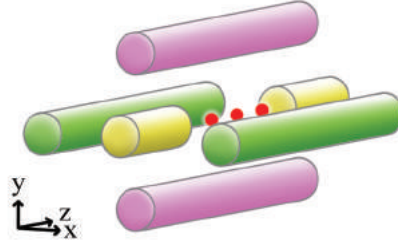


Figure 1.1: A very simple linear Paul trap geometry that can be used to trap ions. Green denotes an RF electrode, magenta denotes an RF electrode with opposite phase to the green RF electrode, and yellow denotes a DC endcap electrode. The red dots denote possible positions of trapped ions in a linear string. This diagram is not to scale.

A very simple linear Paul trap can be constructed using four RF bar electrodes arranged in a square configuration. A trapping potential is created when opposite phase RF voltages are applied to each diagonal pair of electrodes. This creates a radial potential, i.e. cylindrically perpendicular to the ion string, in which a linear string of ions can become trapped. Axial confinement, i.e. along the ion string, can be provided by using endcap electrodes with a DC potential applied to them. This electrode configuration is shown in Figure 1.1. The potential for this trap geometry is given by [24]:

$$\phi(x, y, z) = \kappa_{\text{RF}} \frac{V_{\text{RF}} \cos(\Omega_T t)}{r_0} (x^2 - y^2) + \kappa_{\text{EC}} \frac{V_{\text{EC}}}{\sigma_0} \left( z^2 - \frac{x^2 + y^2}{2} \right) \quad (1.1)$$

where  $\kappa_{\text{RF}}$  and  $\kappa_{\text{EC}}$  are a geometric factors associated with the RF and endcap electrodes respectively,  $V_{\text{RF}} \cos(\Omega_T t)$  is the RF potential varying at a drive frequency of  $\Omega_T$  with amplitude  $V_{\text{RF}}$ ,  $r_0$  is the distance between the ion and the RF electrodes,  $V_{\text{EC}}$  is the DC voltage applied to the endcap electrodes,  $\sigma_0$  is the distance between the ion and the endcap electrodes,  $x$  and  $y$  are the perpendicular radial directions defined by the lines connecting each diagonal pair of RF electrodes, and  $z$  is the axial direction defined by the line connecting the two endcap electrodes.

Figure 1.2 shows the evolution of this time-varying potential in the two-dimensional, radial trapping plane defined by the RF electrodes. At  $\Omega t = 0$  there is a high electric

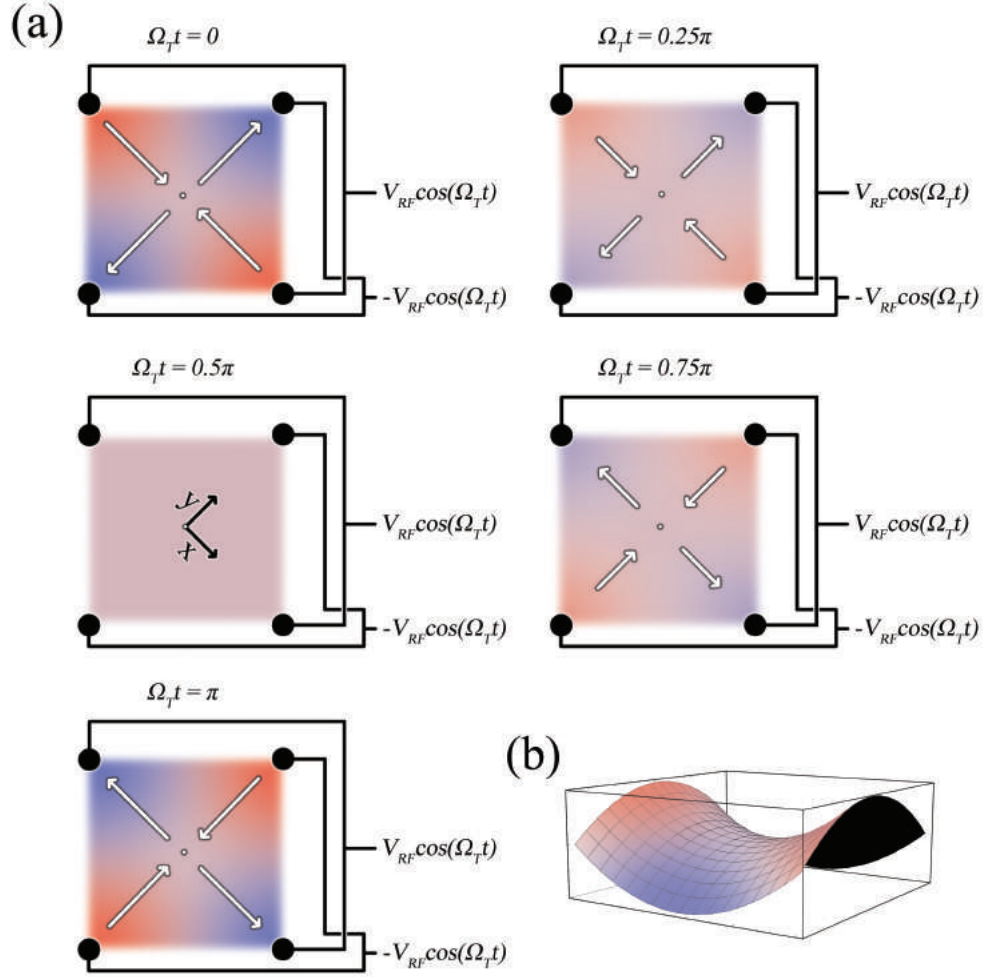


Figure 1.2: The trapping potential in two-dimensions of an RF Paul trap as defined by Equation 1.1. Red denotes high electric potential, blue denotes low electric potential, and mauve denotes zero electric potential. **(a)** - The potential landscape as it varies in time over one half-period of the driving RF (where  $\Omega_T \gg 0$  by definition). The white arrows denote the prospective trajectory of the ion if the field was static with length denoting the slope of the potential. **(b)** - A three-dimensional representation of the hyperbolic potential.

potential at two of the same phase RF electrodes and a low potential at the others. At  $\Omega t = 0.25\pi$  there is a lower electric potential at these electrodes, and at  $\Omega t = 0.5\pi$  the potential landscape is flat and equal to zero. Past this time the potential inverts until at  $\Omega t = \pi$  it is equal but in opposite direction to the potential at  $t = 0$ .

This means that the potential oscillates between trapping and anti-trapping oppositely in the  $x$  and  $y$  directions, and it can be shown that for suitable parameter values, this produces stable trapping as the average potential experienced by an ion is similar to a simple harmonic well. Suitable parameters for stable trapping in the radial directions can be determined by use of the Floquet theorem to solve the Mathieu equations of motion for

a trapped ion.  $a$  and  $q$  are two stability parameter solutions pertaining to these equations of motion. These are given by [24]:

$$a = -\frac{4e\kappa_{\text{EC}}V_{\text{EC}}}{m\sigma_0\Omega_T^2} \quad (1.2)$$

$$q = \frac{4e\kappa_{\text{RF}}V_{\text{RF}}}{mr_0\Omega_T^2} \quad (1.3)$$

where  $e$  is the charge of an electron, and  $m$  is the mass of the trapped ion. In the case of a linear Paul trap with a chain of ions in the  $z$ -direction, it is found that stable radial trapping is found where  $a_x \approx a_y \approx 0$  and  $q_x \approx q_y < 1$  [25]. These constraints can be used to select the correct driving frequency  $\Omega_T$  in order to successfully trap ions.

For  $q \ll 1$  and  $a \ll q$ , the stable radial motion of the ion in the  $x$ -direction is given by [24] [26]:

$$x(t) = A \cos(\nu_x t) \left( 1 + \frac{q_x}{2} \cos(\Omega_T t) \right) \quad (1.4)$$

A similar equation describes the motion of the ion in the radial  $y$ -direction with equivalent parameters associated with said direction. Here,  $A$  is a constant determined by the initial conditions of the trapping,  $\cos(\nu_x t)$  is the secular motion of the ion in the  $x$ -direction of the potential, and  $\nu_x$  is the radial secular frequency in the  $x$ -direction given by [24]:

$$\nu_x = \frac{\Omega_T}{2} \sqrt{\frac{q_x^2}{2} - \frac{2\nu_z^2}{\Omega_T^2}} \quad (1.5)$$

Here,  $\nu_z$  is the axial secular frequency given by [24]:

$$\nu_z = \sqrt{\frac{2e\kappa_{\text{EC}}V_{\text{EC}}}{\sigma_0 m}} \quad (1.6)$$

The axial secular frequency can be found by solving  $\mathbf{F} = -e\nabla\phi$  in the  $z$ -direction which results in the equation for a simple harmonic oscillator [24]. Lastly,  $q_x$  is the  $q$  parameter associated with the  $x$ -direction. In general, the  $q$  parameter may differ for each direction of motion due to geometric factors if the electrode geometry is not completely symmetric. If the RF electrodes are completely symmetric about the ion, the radial secular frequency can be expressed as  $\nu_r = \nu_x = \nu_y$  [24]<sup>1</sup>. One can see from the above equation that the secular frequency of the ion can be adjusted by altering the voltages  $V_{\text{RF}}$  and  $V_{\text{EC}}$  applied to the RF and endcap electrodes respectively. A higher voltage, i.e. stronger confinement of the ion, results in a higher secular frequency.

---

<sup>1</sup>This is very unlikely for most practical trap designs that we would use.

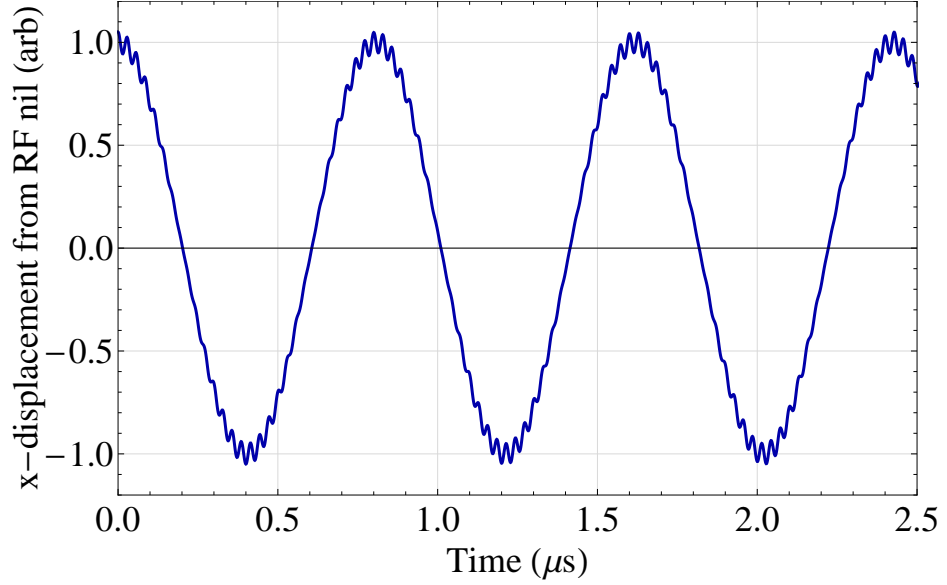


Figure 1.3: The  $x$ -axis ion motion for  $q_x = 0.1$  and  $\Omega_T = 2\pi \times 35$  MHz, resulting in a secular frequency  $\nu_x = 2\pi \times 1.24$  MHz. The amplitude of this motion is shown in arbitrary units. One can see that the further the ion sits from the RF nil, the greater the amplitude of the micromotion at the drive frequency.

The ion motion along in the  $x$ -direction as shown in Equation 1.4 is plotted in Figure 1.3. Along with the secular motion, one can also see that there is a periodic term at the driving frequency of the trap. This “micromotion” is a result of the electric field changing at the driving frequency and its amplitude is proportional to the distance of the ion from the RF potential minimum, referred to in this thesis as the “RF nil”<sup>2</sup>. Micromotion can be divided into two forms, intrinsic and excess. Intrinsic micromotion is resultant from the displacement of the ion from the centre position as it goes about its secular motion, which is unavoidable, and this is what is shown in Figure 1.3.

There are two causes of excess micromotion. The first is if the voltages on the RF electrodes are not perfectly in phase or anti-phase. If this is the case then the position of the RF minimum moves in time, so there are no points at which there is no electric field. This form of micromotion cannot be removed as long as this phase mismatch is present; this may arise due to different connection lengths to the RF electrodes. This motion is generally uncompensatable as it requires a physical change in the trap. For this reason, it is common for traps to replace the opposite phase pair RF electrodes with grounded or DC electrodes. Though this changes its definition, the potential created at the ion is very similar to the four RF electrode trap. Since the electric field lines are essentially the same shape whether the second pair of electrodes is grounded or at reverse phase with respect to

<sup>2</sup>This naming convention is chosen as RF, DC, and magnetic nils, i.e. purposely created points of zero electric and magnetic field, are discussed throughout this thesis.

the RF, the potential landscape is still suitable for trapping ions. The advantage of using a grounded pair of electrodes is that one no longer has to worry about phase matching two RF supplies in order to minimise micromotion.

For these traps, excess micromotion is mainly resultant from a bad overlapping of the nil point of the RF and DC trapping potentials. The DC nil is the zero-field position resultant from the DC and ground electrodes which the RF field lines flow to and from while oscillating. Since the RF is oscillating, this means if the two nils are not overlapped then at high RF field the ion is pulled to the RF nil and at low RF field the DC or ground field dominates. Excess micromotion can therefore be compensated for by using DC voltage electrodes to ensure these two nils are well overlapped. Since the axial secular motion of the ions is along the RF nil line, the micromotion is minimal, making this axis of motion good for high fidelity operations. The second form of excess micromotion is caused by there being a static electric field at the position of the RF nil, pushing the centre of the trapping potential into a region of oscillating electric field. This micromotion can be removed by adjusting the DC voltages to cancel the static field.

The directions of oscillation parallel to the three uncoupled components of the ion motion are known as the principal axes. It is important to know the orientation of the principal axes in order to Doppler cool the ions using laser light. This will be explained later in this chapter.

Though I have only discussed the trapping potential for a linear, four bar electrode, two endcap electrode trap, there are many different RF Paul trap designs that exist. These may use RF and DC electrode geometries that do not produce the previously defined potential but still create an electric field minimum at which an ion can be trapped with a similar secular motion. A suitable trapping potential can be created using symmetric or planar electrode geometries.

### 1.1.1 Symmetric RF Paul traps

The Paul trap described above has electrodes that sit around the ion creating a symmetric electric potential at the ion position. Traps which use electrodes that surround the ion in order to create the trapping potential are hence known as “symmetric RF Paul traps” as opposed to asymmetric (planar) traps which do not use this electrode configuration; these will be discussed momentarily. Macroscopic symmetric Paul traps can be constructed with electrodes that are hand or machine assembled into insulated mounts. Symmetric traps can also be microfabricated using lithographic and etching methods.



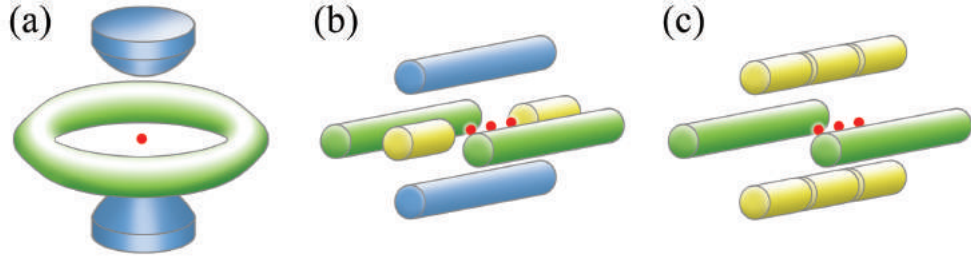


Figure 1.4: Several symmetric trap designs. **(a)** - A single point “Ring and fork” style trap. **(b)** - A four-electrode style linear trap with explicit endcap electrodes. **(c)** - A similar trap to (b) with segmented DC electrodes instead of grounded bar electrodes. Blue denotes a grounded electrode, green denotes an RF electrode, and yellow denotes an explicit DC electrode. These are required to have an explicit DC voltage in order to define the trapping position of the ion even if this voltage is zero volts. The red dots denote possible positions of trapped ions. This diagram is not to scale.

There are many different trapping geometries that can be created using a symmetric electrode geometry. The aforementioned trap is a linear geometry, i.e. it traps a linear string of ions, though this was not the first RF Paul trap design. The original “Ring and fork” RF trap design was symmetric and consists of an RF ring electrode with upper and lower grounded endcap electrodes [27] similar to the geometry shown in Figure 1.4 (a). This trap geometry creates a single-point trapping region due to the revolved electrode geometry. If one were to take the cross section of this revolved geometry and linearly extrude it, a linear trapping region is created.

A symmetric linear trap may consist of two RF bar electrodes with two DC or grounded bar electrodes on opposite diagonals of a rectangular cross section. This gives the same type of two dimensional potential as that shown in Figure 1.2. However, this will only provide trapping in the plane perpendicular to the length of the bars, thus DC endcap electrodes are required for axial confinement of the ions. This geometry is shown in Figure 1.4 (b). One can modify this by splitting each grounded bar electrode into several segmented DC electrodes, which can be used to create the required endcap potentials without an explicit electrode at the end of the axial string. Such a geometry is shown in Figure 1.4 (c). In reality, many trap geometries are possible so long as the correct potential is formed at the ion position. For example, blade shaped electrodes minimise the surface roughness seen by the ion, geometries can be extended to create junctions [28], or integrated traps can be constructed with special features such as optical fibres for ion-photon entanglement [29].

### 1.1.2 Planar RF Paul traps

It is also possible to create a Paul trap that traps ions above a set of electrodes confined to a plane. Such designs are commonly referred to as asymmetric, planar, or surface traps. For a linear trap, a planar geometry may consist of two RF rails surrounded and separated by ground or DC electrodes with DC potentials applied to outer or inner segmented electrodes in order to provide axial confinement.

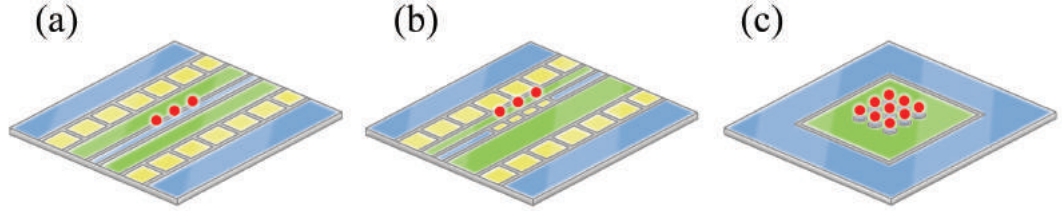


Figure 1.5: Several planar trap designs. **(a)** - A linear two-rail design with equal RF rail widths, a central grounded rail, and outer control DC electrodes. **(b)** - A linear design with unequal RF rail widths and outer and inner segmented DC electrodes for more precise control of the ion position. In this case the ions sit slightly closer above the narrower RF rail and the principal axes are rotated in this direction. **(c)** - A two-dimensional array with nine equally spaced ions in a square configuration. Blue denotes a grounded electrode, green denotes an RF electrode, and yellow denotes an explicit DC electrode. The red dots denote possible positions of trapped ions. This diagram is not to scale.

Such a geometry is shown in Figure 1.5 (a). Instead of terminating solely on the surrounding electrodes, the electric field lines also terminate above the surface trap at “infinity” thereby creating a skewed variation of the hyperbolic potential above the central separation of the RF rails but nevertheless creating an RF nil line in which a string of ions may be trapped. The height of this nil is dependant on the width and separation of the RF rails but can also be offset from the centre by making one RF rail wider than the other as shown in Figure 1.5 (b). This creates a rotation of the trapping principal axes. Later in this chapter, I discuss Doppler cooling using laser light which can be greatly affected by the direction of the principal axes. In order to cool the ion effectively, there should be a component of the beam direction along all principal axes of the ion motion. However, since the beams should be near-parallel to the surface of the trap or along the ion string, this means that it may be difficult to address all motions of the ion in order to cool it effectively. The alternative to moving the beam is to rotate the principal axes so that they are no longer perfectly in-plane or out-of-plane in orientation with regards the trap surface. Rotation allows the beam to remain parallel to the trap surface while still having a good projection on what would have previously been the out-of-plane principal axis in the absence of any rotation. Principal axis rotation can also be performed using

DC electrodes though one has to be careful to keep the DC and RF minima overlapped in order to prevent micromotion. Additionally, unequal widths of the RF electrodes can allow the ion to sit closer to an on-chip device or minimise laser photon scatter from the electrodes at the ion position which may affect state detection fidelity. This will be discussed later in this thesis.

As with symmetric linear traps, planar junction traps geometries are also possible. In addition to this, a ring trap can be created using a planar geometry with two concentric ring shaped RF electrodes in order to create a loop of linear trapping region. Use of such a trap has been demonstrated by Dr Marcus Hughes in this group, however, full loading of a trap in order to create a ring shaped ion crystal has more notably been demonstrated by Dr Boyan Tabakov [30]. The advantage of a ring trap is that the boundary conditions for every ion in a fully loaded ring are the same because, unlike a linear trap, where the endcap potentials create an ion-ion spacing that is closer at the centre of the string and further at the extremities, there is no “end” to the trapping region. This allows the ions to be spaced equally around the ring, a geometry useful for certain quantum simulations of solid-state physics that are not possible using linear geometries.

It is also possible to create a single trapping point by using a trap geometry consisting of a DC or grounded island electrode inside a larger RF electrode which subsequently is surrounded by a large ground plane. This is the planar trap equivalent of the ring and fork electrode geometry and can be used to create planar two-dimensional array traps. This is done by using an electrode geometry of grounded (or DC) islands arranged into a geometric pattern in a sea of a single RF electrode which in turn is surrounded by a grounded (or DC) electrode. The ions are trapped above each grounded island which can be arranged to create a well-defined two-dimensional ion crystal when the trap is fully loaded. Such a trap geometry is shown in Figure 1.5 (c). These two-dimensional arrays allow for a defined ion-ion spacing that can be used to investigate interactions in uniform crystalline structures [31] [32]. Alternatively, a two-dimensional ion lattice is ideal for sensing experiments as a trapped ion is extremely sensitive to magnetic fields (DC and high frequency) and the array structure ensures a high degree of spatial accuracy in order to measure minute changes in field over small distances. Quantum sensing using arrays of trapped ions is currently being developed by other members of our group. In general for both of these geometry types, the smaller the electrodes, the lower the ion height above the trap surface. It will become apparent how the ion height may affect the ion later in this thesis.

It is much more typical for planar traps to be microfabricated due to the ease of creating micron-level electrode geometries using lithographic methods. For example, conductive and insulating layers can be deposited and etched step by step in order to create an ion trap. First any necessary buried wires are fabricated onto the substrate using adhesion layers. These are then covered in an insulating layer, again with adhesion layers on top of the buried wires, which is then etched to reveal certain points on these buried wires. Vias, i.e. vertical electrical interconnects between different layers of a microfabricated chip, can then be deposited at these points in order to electrically connect the buried wires to the top layer electrodes which are subsequently deposited on the insulating layer that covers the buried wires. This allows for electric connections at the edge of the chip to electrodes that are topologically isolated. Since the ions sit directly above the chip, gaps between the electrodes can expose the dielectric substrate. This can drastically affect the trapping potential if a charge builds up (for example by scattered laser light on the trap) as this charge is likely to overwhelm the trapping potential. The effects of exposed dielectrics can be minimised by having deep trenches between the electrodes or by fabricating a small conductive layer (held at ground) at the bottom of these electrode gaps so that the dielectrics are shielded and rogue potentials are less likely to build up [26]. This and many more fabrication techniques are detailed in Dr Marcus D Hughes' paper specialising on the subject [26] and the thesis of Dr Bjoern Lekitsch [33].

These advanced fabrication techniques allow for buried wires, ground planes, and isolated electrodes, for cases when a single-layer electrode structure is insufficient for a desired experiment. On-chip features such as integrated microwaveguides and current carrying wires for creating magnetic fields have also been demonstrated using microfabricated ion traps [34] [21].

Both symmetric, planar, macroscopic, and microfabricated Paul traps have their advantages and disadvantages. While symmetric traps are generally easier to work with due to their higher trap depths, minimised background photon scatter, and lower heating rates due to larger ion-electrode distances, planar traps have the advantage that they can be more easily microfabricated with complicated structures/geometries and special features such as current carrying wires for production of a magnetic field gradient. This makes microfabricated planar traps a more viable candidate for a scalable quantum computing architecture, hence this thesis aims to show that a fault-tolerant experimental setup can be created using a microfabricated planar trap. However, in order to understand how to perform a two-ion gate, the coherent manipulation experiments discussed in this thesis are

done using a macroscopic symmetric trap due to its greater ease of operation.

### 1.1.3 The Blade trap

The ion trap used in the experiments described in Chapter 2 is the “Blade trap”, a macroscopic symmetric linear trap with split DC electrodes designed by Dr Robin Sterling which consists of two RF blade electrodes, six DC blade electrodes and three compensation bar electrodes; a single bar top compensation (TC) electrode and twin bar back compensation (BC) electrodes. This trap geometry is shown in Figure 1.6 and the dimensions are taken from the thesis of Dr Sebastian Weidt [35].

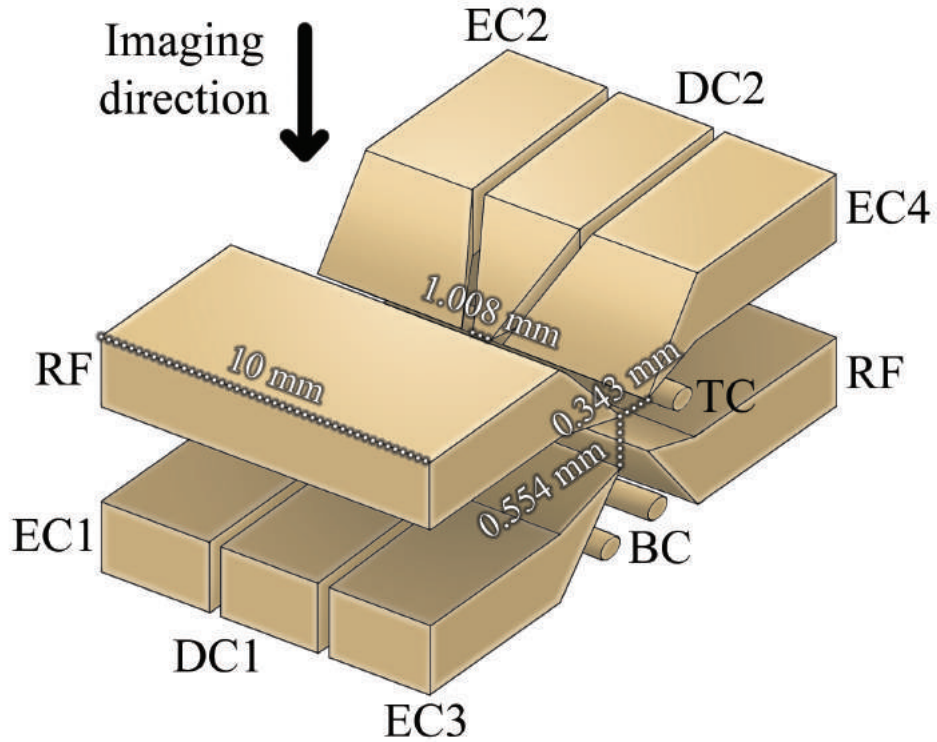


Figure 1.6: The Blade trap designed by Dr Robin Sterling used for the trapped ion coherent manipulation experiments discussed in this thesis. The two RF electrodes sit 180 degrees rotationally symmetric about the axis formed by the ion string. Opposite each RF electrode sits three DC electrodes, two endcaps for axial confinement and a central electrode for fine adjustment of the ion position. Between these main electrodes, two additional sets of electrodes are used for compensation. The inner trapping region is 1.008 mm in length allowing for many ions to be trapped with simple spacing manipulation.

The electrodes are gold plated stainless steel separated and mounted using PEEK spacers to electrically isolate the electrodes from a stainless steel “cage” [36]. As with the previously discussed symmetric trap geometries in Figure 1.4, the RF electrodes provide radial confinement to the ion string with their electric field lines terminating on the DC electrodes. By applying DC voltages to EC1, EC2, EC3, and EC4 we can axially confine

the ions and adjust their position within the 1.008 mm central trapping region. DC1, DC2, TC, and the BC pair are used to adjust the overlap of the DC and RF minima in order to compensate for micromotion. Due to construction difficulties, several DC electrodes are unfortunately shorted to each other and ground, though this does not affect the ability to trap or to compensate for excess micromotion. Unlike some other Paul traps, the endcaps are not explicitly blocking the ends of the trap, but rather are diagonally paired such that the potential that is created still provides confinement in the direction of the ion string.

#### 1.1.4 The linear chip traps

For the experimental setups described in Chapter 4, we use microfabricated linear planar chip traps designed and made by Dr Bjoern Lekitsch [33]. An example of one of these traps is illustrated in Figure 1.7 with the key features highlighted and labelled. Broadly, these traps consist of a gold coated aluminium electrode structure fabricated onto a fused silica substrate<sup>3</sup>. The gold coating is adhered to the aluminium electrodes using a titanium layer. Likewise, silicon nitride and titanium serve as adhesion layers for the aluminium electrodes onto the substrate.

Though a simpler chip can be created using a single electrode layer design, these chips use multiple layers. This allows for a large ground plane on the top surface of the chip and isolated DC electrodes, which helps to create a more uniform trapping potential by providing a good path for the RF to ground. The RF field lines can therefore terminate on the ground plane rather than on top surface DC lines that connect the DC electrodes to their bond pads; these lines are buried underneath the ground plane. Under the ground plane, buried wires connect bond pads on the outer edges of the chip to DC electrodes outside and between the two RF rail electrodes. This includes thin DC rail electrodes that run parallel to the RF rails and can be used to perform rotation of the principal axes. These buried wires are insulated from the top ground plane by a silicon dioxide layer. The top electrodes are adhered to this insulating layer by another titanium layer. These fabrication layers are illustrated in Figure 1.8.

The outer and inner DC electrodes are used to provide axial confinement to the ion string, the voltages of which should be chosen in order to centre the ion string on a certain region of the trap. The inner DCs are designed to be able to drive a potential wedge through an ion string in order to split it in two. This operation is not featured

---

<sup>3</sup>In practice, most of the gold layer of the chip traps has been stripped off those used in our experiments due to problems with shorting between electrodes. Preparation of these traps prior to use in our experiments is highly documented in the thesis of David Murgia (written in parallel to this thesis and as of yet not explicitly published).

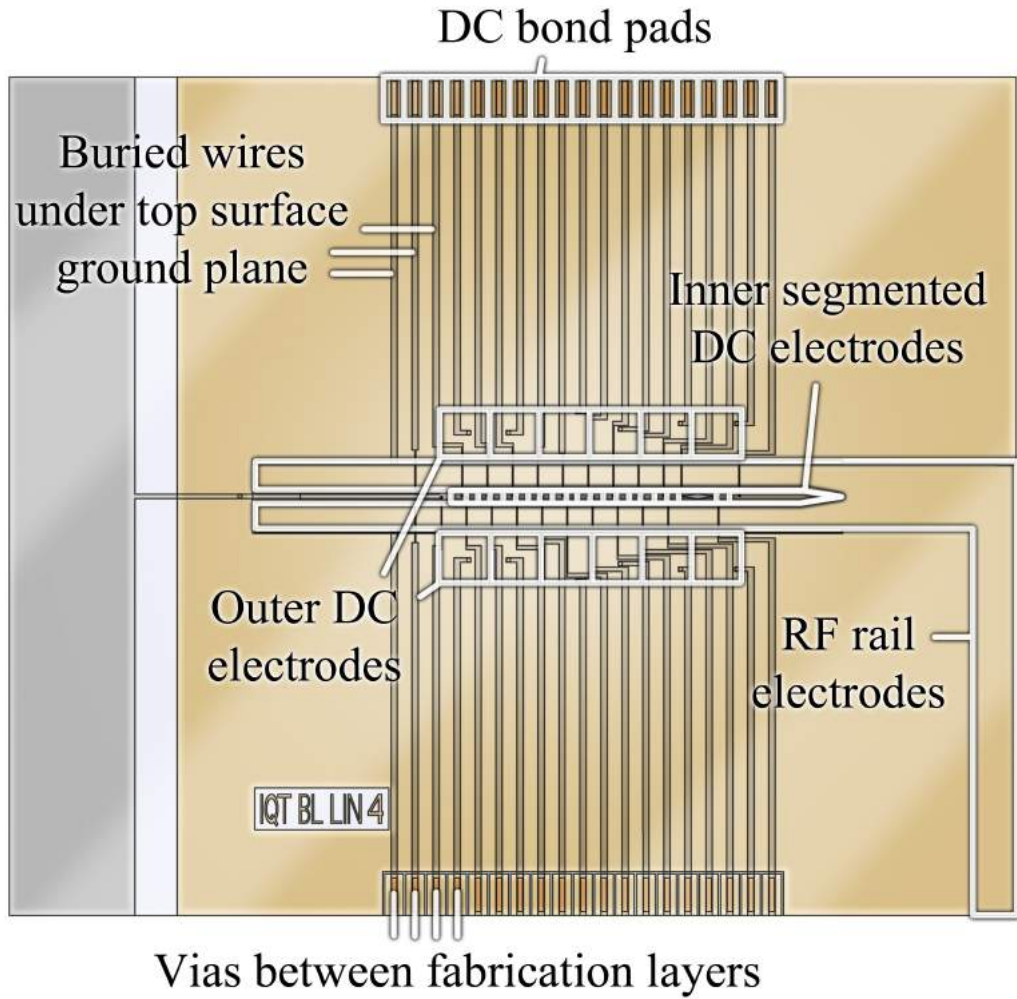


Figure 1.7: An example chip trap used in our experiments as fabricated by Dr Bjoern Lekitsch. The gold segment of the chip is approximately 10 mm by 10 mm and the silver tab on the left of the diagram is used to hold the chip without causing damage to the electrode layers. The key features of this multi-layered chip design are labelled with the exception of the inner and outer DC rail electrodes. These run between the main DC electrodes and the RF rails and can be used to make a small rotation to the principal axes or globally shift the DC potential in order to help compensate for micromotion.

in the experiments conducted in this thesis but would be used in order to combine and separate strings of ions in a large trapped ion quantum computer so that gates can be performed between different groups of ions. For the work described in this thesis, these traps are mainly used in conjunction with the new magnetic field gradient production method described in Chapter 3 in order to set up new ion trap experiments described in Chapter 4. However, once this measurement has been verified, these chips aim to be used for high-fidelity entanglement experiments in order to achieve a fault tolerant two-ion gate using a microwave entanglement scheme with a static magnetic field gradient. The specific trap geometries used in our experiments are shown in Chapter 4.

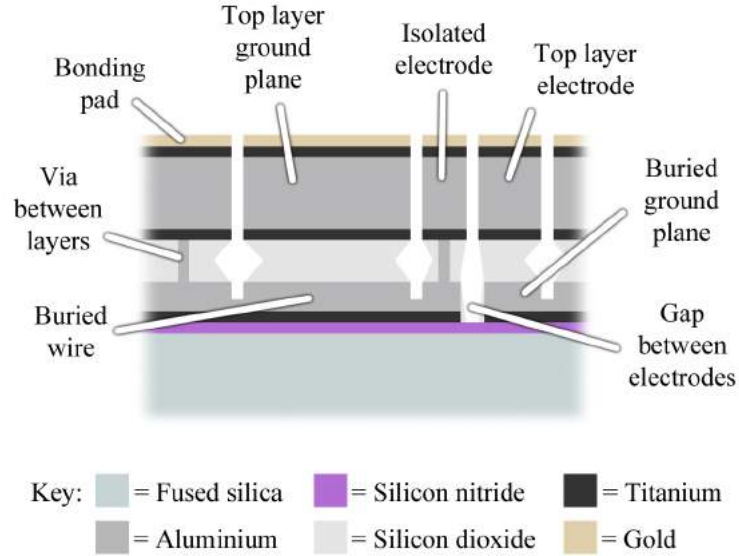


Figure 1.8: An illustration of the layer structure of the chip traps fabricated by Dr Bjoern Lekitsch [33] with some examples of key features labelled. This diagram is not to scale.

### 1.1.5 Application of trap voltages

As shown above, both DC and RF voltages have to be applied to the trap electrodes. The application of DC voltages is generally quite trivial; a DC voltage supply can be connected to a filter box which is mounted on a D-sub DC vacuum feedthrough and delivers the filtered voltages into the vacuum system. Filtering of these DC voltages is required as any electrical noise that is present on the trap electrodes will heat up the ion, which would cause infidelity in any two-ion gates performed. For the Blade trap, the DC electrodes are connected to the D-sub using in-vacuum wires. The surface traps described in Chapter 4 sit on a chip carrier which plugs into pin receptacles that are connected to the DC feedthrough. Wire bonds between the chip carrier and the edges of the chip electrode bond pads complete the connection. An additional set of low-pass filters are present at this stage, connecting the electrodes to ground via 680 pF capacitors. For the Blade trap experimental setup, the DC voltages are produced from a set of low-noise adjustable DC supplies built by Dr Bjoern Lekitsch, though in the past the DC voltages have been partially produced from analogue outputs controlled using a real-time version of LabVIEW on the secondary experimental computer. Though this made quick adjustments of electrode voltages extremely efficient, the stability of these voltages was deemed insufficient for the highest fidelity operations and thus this control was taken off computer control. The DC supply for the surface trap experiments is described in Chapter 4.



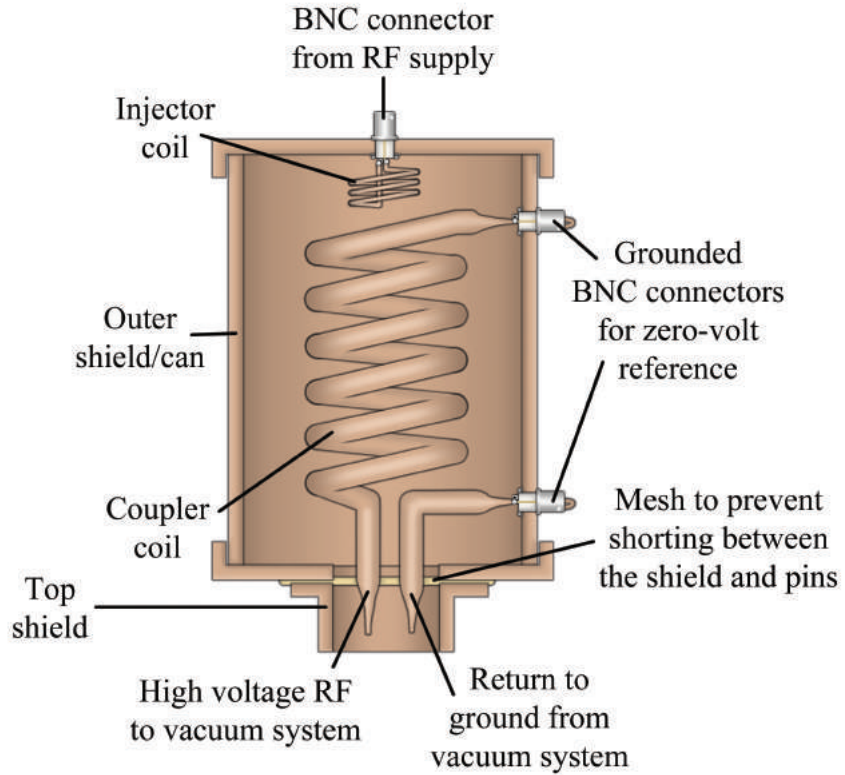


Figure 1.9: A cut-through diagram of a helical resonator as constructed by our group in order to couple an RF voltage to an ion trap. A small injector coil radiates RF which magnetically couples to a larger coil in order to impedance match the RF supply to the trap and vacuum system feedthroughs, thereby maximising RF transmission at high power.

Application of the radio frequency trapping voltage is more complicated than the DC voltages. If one were to attempt to directly apply an RF voltage to the vacuum system, it is likely that most of the voltage would be reflected at the chip due to the impedance mismatch. The impedance of the RF line including the vacuum system and the chip are matched to the supply by using a helical resonator. A helical resonator is effectively a shielded RF transformer that consists of two magnetically coupled coils inside a grounded can as shown in Figure 1.9. A small injector coil radiates the RF from a supply which is picked up by a larger coupler coil. Both of these coils are grounded at one end and float at high voltage at the other. The dimensions of the coils and their spacing in the can determine the impedance matching to the RF line inside the vacuum system at the required driving frequency. Since the coupler coil is typically wound from a rigid copper rod, this can be very difficult to adjust, meaning that alteration of the injector coil is usually preferred in order to make small adjustments to the coupling. This can be done by altering the physical properties of the injector coil such as its diameter, number of turns, or length, until the best impedance matching between the resonator and RF supply is achieved [37]. The helical resonator is then connected to a high voltage feedthrough

which is subsequently connected to the chip carrier and the trap in a similar way to the DC electrodes. In addition to impedance matching, the dimensions and material of this resonator determine the quality factor “Q” of the band of frequencies that can be applied to the trap therefore reducing noise on the RF electrodes. In order to maximise Q, the resonator is constructed from a highly conductive material, in our case copper. Due to the skin effect, the RF only propagates in the surface of the conductor meaning that the surfaces of all components of the helical resonator should be free from surface tarnishing or oxidation which would result in a higher resistance on the surfaces of the resonator and thus lower the Q [37]. Noise on the RF electrodes creates similar heating rate issues to noise on the DC electrodes. For linear ion traps, this will affect the radial confinement of the ion string and therefore the radial secular frequency. I will discuss the effects this will have on the performance of coherent manipulation operations later in this thesis, particularly in Chapter 2, where external sources of experimental noise will be examined in detail.

## 1.2 The UHV system

All ion trapping experiments in our group are done under Ultra-High Vacuum conditions of the order  $10^{-11}$  Torr (1 Torr = 1.33322 mbar). This is because we require the chances of a collision between an ion and another atom or molecule in the vacuum system to be extremely low in order to keep them trapped for long periods of time (hours or days). The low internal pressure of the system achieves this by providing an extremely long mean free path (approximately 2500 kilometres at room temperature [38]) and therefore an extremely small chance of collisions. This creates the extremely isolated environment required for high-fidelity quantum operations. This pressure is initially achieved using a combination of mechanical pumping methods while the system is baked at 200 °C in a large oven. After this bake, the vacuum system is transferred from the oven to the experimental table and this low pressure is maintained by using a Titanium Sublimation Pump (TSP) and an ion pump. The pressure is monitored/measured using an ion gauge. The details and specifications of this vacuum system are extensively documented in almost all the earlier theses by other members of this experimental group [39] [40] [36] [41] [42] [33] [35] [25] [24].

One complication of using a UHV environment in order to perform experiments is that not all materials are UHV compatible. A material that is not UHV compatible will out-gas due to the low pressure which limits the pressure that it is possible to reach due to the emission of additional particles from these materials into the vacuum system. This causes

problems for experiments due to the higher pressure and therefore a shorter mean free path and the increased chance that a collision may occur with a trapped ion. As a general rule of thumb, hydrocarbons are not vacuum compatible whereas most commonly used metals are, however there are exceptions to this rule such as zinc and zinc compounds [43]. Extensive research into the vacuum compatibility of materials has been done over the lifetime of the field of UHV applications and our main point of call when building in-vacuum apparatus has been a document known as the LIGO list [43]. This document compiled in 2011 by the “Laser Interferometer Gravitational Wave Observatory” lists the UHV compatibility of many tested materials. Though some materials are not tested or shown on this list, it is nevertheless an extremely useful document when planning to use a material in a UHV environment.

### 1.3 Ytterbium

We use two different isotopes of ytterbium ion in our experiments,  $^{171}\text{Yb}^+$  and  $^{174}\text{Yb}^+$ . The former is used for coherent manipulation experiments and is advantageous over other atomic species or ytterbium isotopes due to the magnetically sensitive hyperfine structure in the  $^2\text{S}_{\frac{1}{2}}$  manifold, the upper and lower levels of which are separated by  $\sim 12.6$  GHz making it an ideal microwave qubit for our entanglement scheme.  $^{174}\text{Yb}^+$  is used for verification of trapping parameters and other trapping experiments. Natural ytterbium consists of approximately 32 percent of mass 174 and 14 percent of mass 171 [44]. Other stable natural isotopes have masses ranging from 168 to 176 without 169 or 175 [44] and several other isotopes exist as part of radioactive decay cycles [45].

#### 1.3.1 Ionisation

The ytterbium is injected into the experiment as an atomic beam by heating a small sample of the metal in an atomic oven. This beam must be ionised in order to feel the trapping potential. Though this can be done with a single photon of wavelength 199 nm, we use a two-stage photo-ionisation technique. The first photon addresses the  $^1\text{S}_0$  to  $^1\text{P}_1$  transition in neutral ytterbium. The isotope shifts in this transition mean that the precise wavelength of 399 nm light used can be altered to selectively ionise a particular isotope. From  $^1\text{P}_1$  any photon with a shorter wavelength than 394 nm can ionise the atom. This is done using a 369 nm photon which is used in the  $^2\text{S}_{\frac{1}{2}}$  to  $^2\text{P}_{\frac{1}{2}}$  cooling cycle of the ytterbium ion. This photo-ionisation scheme is shown in Figure 1.10 and the transition wavelengths for each isotope are shown in Table 1.1.

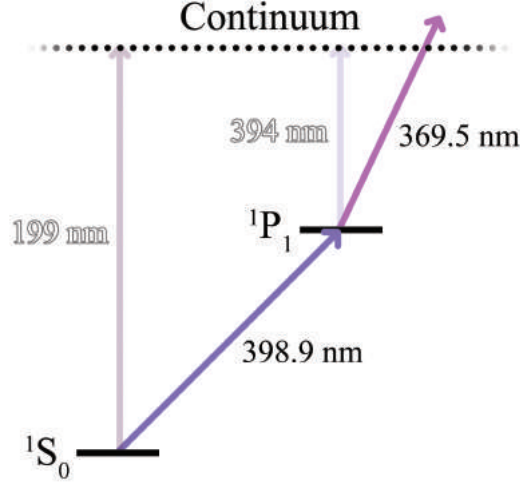


Figure 1.10: A partial energy level diagram for neutral ytterbium showing the two-stage photo-ionisation scheme that we use [35]. The faded arrows indicate the single-stage 199 nm photo-ionisation method and the 394 nm maximum wavelength that will ionise an atom with an electron in the  $^1P_1$  state.

Table 1.1: Transition wavelengths of several ytterbium isotopes in vacuum corresponding to the selective ionisation transition  $^1S_0 \leftrightarrow ^1P_1$  (for an angle of 63 degrees between the atomic beam and laser beam) and the primary cooling transition  $^2S_{\frac{1}{2}} \leftrightarrow ^2P_{\frac{1}{2}}$  [36].

Isotope	$^1S_0 \leftrightarrow ^1P_1$ transition	$^2S_{\frac{1}{2}} \leftrightarrow ^2P_{\frac{1}{2}}$ transition
	wavelength (nm)	wavelength (nm)
$^{170}\text{Yb}^+$	398.91051(6)	369.52364(6)
$^{171}\text{Yb}^+$	398.91070(6)	369.52604(6)
$^{172}\text{Yb}^+$	398.91083(6)	369.52435(6)
$^{174}\text{Yb}^+$	398.91114(6)	369.52494(6)
$^{176}\text{Yb}^+$	398.91144(6)	369.52550(6)

### 1.3.2 Doppler cooling $^{174}\text{Yb}^+$

When the ytterbium atoms from the atomic ovens are ionised they feel the electric fields of the RF Paul trap. However, these ions still have a large kinetic energy due to the temperature required for surface emission from the atomic oven and we therefore require Doppler cooling in order to crystallise the ions once they become trapped. Doppler cooling is also required in order stop heating from driving the ions out of the trap once they have crystallised. Doppler cooling utilises the Doppler effect to remove energy from the ion by absorption of photons from, in the case of ytterbium, a laser driving the  $^2S_{\frac{1}{2}}$  to  $^2P_{\frac{1}{2}}$  transition. By red-detuning the 369 nm laser from the transition, ions travelling in the opposite direction to the laser will be excited by the laser, and each photon absorbed

will reduce the ion’s momentum. After each photon absorption, a photon is also emitted but additionally, due to the isotropic nature of spontaneous emission [35], the momentum kick from these photons is averaged resulting in no net average momentum change. This therefore means that it is only a momentum kick from the absorption of the laser photon that has a defined direction which slows down the ion and hence removes some of its kinetic energy.

By orienting the laser in such a way that it has a component in all three principal trapping axes, one can ensure that the ion will travel in the opposite direction to the laser propagation at some point in its motion and therefore experience cooling. However, cooling only happens while the laser is red-detuned from the transition frequency. The closer the laser wavelength to that of the transition, the more photons are spontaneously emitted from the ion. This is the basis of how one is able to see the ion on a camera or with a PMT. The fluorescence from the ion is maximised at resonance, when the laser is at the transition frequency of the ion. The laser is very slightly detuned from this during readout of an ion’s quantum state as it ensures the highest contrast between “dark” and “light” states that an ion may be in, but also provides a small amount of cooling. As soon as the laser is blue detuned with respect to the transition, the ion ceases to visibly fluoresce as it is now heated by the laser using the reverse of the principle of Doppler cooling as a momentum kick is given in the same direction that the ion is travelling. Eventually this will lead to the ion gaining enough kinetic energy to escape the trapping potential and will thus be lost. In order to store ions for long periods of time outside of an experiment, the laser is significantly red detuned ( $\sim 659$  MHz) in order to ensure that an ion remains sufficiently laser cooled in order remain trapped but additionally that a laser that is not frequency locked to a reference will not drift over resonance during the time that the experiment is left unmonitored. This has been shown to be sufficient to keep an ion trapped overnight or over the course of a weekend to return to the experiment with little effect on the stability of the ion.

Doppler cooling can be used to continually cool a group of trapped ions but is limited by the linewidth of the transition being used. This is the Doppler limit given by  $k_B T \approx \frac{1}{2} \hbar \Gamma$  [46] where  $k_B$  is the Boltzmann constant,  $T$  is the absolute temperature,  $\hbar$  is the reduced Planck constant, and  $\Gamma$  is the natural linewidth of the transition. For the  $^{171}\text{Yb}^+$  ions used for our coherent experiments, the natural linewidth  $\frac{\Gamma}{2\pi} = 19.6$  MHz of the  $^2\text{S}_{\frac{1}{2}}$  to  $^2\text{P}_{\frac{1}{2}}$  cooling transition corresponds to a Doppler limit of  $470$   $\mu\text{K}$  [36]. The ion can be further cooled using sideband cooling with microwaves; this will be discussed in Chapter

2.

During the cooling cycle, the ion can also decay from  $^2P_{1/2}$  to the  $^3D_{3/2}$ . A 935 nm laser is used to return the ion to the  $^2S_{1/2} - ^2P_{1/2}$  cooling cycle. In addition, collisions can occasionally (on a timescale of hours) transfer the ion to  $^2F_{7/2}$ . Either a new ion can be loaded at this point, or a 638 nm laser used to return the ion to the main cooling cycle.

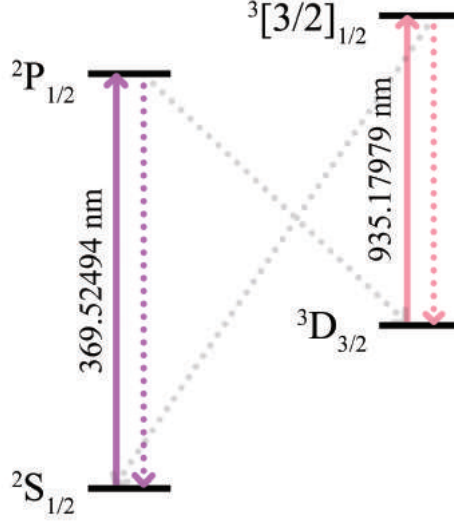


Figure 1.11: A partial energy level diagram for  $^{174}\text{Yb}^+$  showing the relevant states used during our trapping experiments [25]. The solid lines denote the lasers used to cool the ions. The dotted lines show the spontaneous emission photons, coloured denoting primary paths, and grey denoting secondary paths.

On observing the cooling cycle for  $^{174}\text{Yb}^+$ , shown in Figure 1.11, it is clear that this isotope requires only 369 nm and 935 nm laser light in order to cool the ion (ignoring transfer to  $^2F_{7/2}$ ). By interrupting the source of either of these photons, the ion will become stuck in a certain energy level and will stop fluorescing. Doppler cooling will therefore stop and the ion will begin to heat up due to electrical noise on the electrodes. Since we use this isotope mainly for verification of trapping, we typically do not require a 638 nm laser to prolong the trapping lifetime. The lasers required for using  $^{174}\text{Yb}^+$  during our trapping experiments are therefore 369 nm, 935 nm, and 399 nm.

### 1.3.3 $^{171}\text{Yb}^+$

The presence of hyperfine structure makes  $^{171}\text{Yb}^+$  more complicated to work with than  $^{174}\text{Yb}^+$ . The main cooling cycle is the  $^2S_{1/2}, F = 1$  to  $^2P_{1/2}, F = 0$  transition, where  $F = I + J$  is the total angular momentum given by the sum of the nuclear spin,  $I$  and the total electronic angular momentum,  $J = L + S$  where  $L$  and  $S$  are the electron angular momentum and spin respectively [47]. Due to the two different  $^3D_{3/2}$   $F$  states, the 935

nm repumper either has 3 GHz sidebands applied, or is sufficiently intense that power-broadening depopulates both  $F$  states. A 12.6 GHz microwave fields is used to “repump” population from  $^2S_{1/2}$ ,  $F = 0$ . Figure 1.12 shows these transitions, as well as the additional levels that are occasionally populated due to background gas collisions which requires 638 nm laser light to return to the cooling cycle.

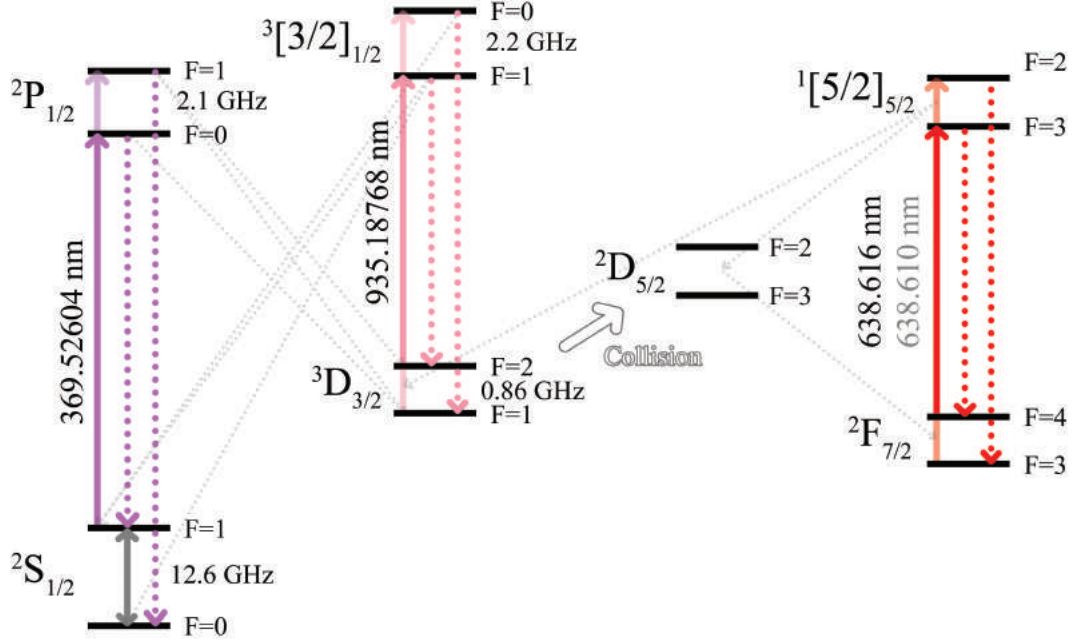


Figure 1.12: The energy level diagram for  $^{171}\text{Yb}^+$ . The solid lines denote the lasers and microwaves used to cool and manipulate the ions [35]. The faded laser lines denote power broadening, sidebands, or scanning applied to the lasers in order to broaden over additional transitions. The dotted lines show the spontaneous emission photons, coloured denoting primary paths, and grey denoting secondary paths.

For the coherent manipulation experiments discussed in this thesis, we need to use a set of well-defined states or superpositions of states as our qubit. An operation which allows us to prepare the ion in one of these well-defined states is known as a coherent operation and manipulation of the qubit in order to perform a coherent operation is called coherent manipulation. We use the  $^2S_{1/2}$  hyperfine manifold as our qubit, typically with the  $F = 0$  and  $F = 1$  states forming the “0” and “1” of our quantum binary respectively. Microwave radiation at  $\sim 12.6$  GHz can be used to transfer the ion between these two states. However, in the presence of a magnetic field the  $F = 1$  states become degenerate due to the Zeeman effect meaning that multiple microwave fields can be used to address each of the transitions for the three  $m_F$  states. The  $m_F = \pm 1$  states are first-order sensitive to the magnetic field and in the presence of a magnetic field gradient feel a strong coupling to the ion motion. I will later show that this can be used to entangle the internal spin state of an ion to its

motion, which is the first step towards performing multiple-qubit quantum gate operations. Preparation of  $^{171}\text{Yb}^+$  ions into these coherent states and coherent manipulation within the  $^2\text{S}_{\frac{1}{2}}$  hyperfine manifold is discussed and demonstrated in Chapter 2.

## 1.4 Magnetic field gradient setup

As explained in the introduction to this thesis, gate operations between trapped ions are mediated by their collective motion, and so the coupling between the ion's motion and its internal state determines how fast a gate operation can be performed. A gate operation on one ion, for example using a laser photon, should provide a state dependant force (in this example a momentum kick from the laser photon) in order for this operation to be felt by other ions in a chain through the Coulomb interaction between them. The strength of this coupling is given by the Lamb-Dicke parameter

$$\eta = \frac{\Delta z 2\pi}{\lambda} \quad (1.7)$$

where  $\Delta z = \sqrt{\frac{\hbar}{2m\nu}}$  is the spatial extent of the atom of mass  $m$  with a secular frequency  $\nu$  defined by the trapping potential, and  $\lambda$  is the wavelength of the applied radiation [17]. Laser based qubit manipulation provides a sufficient non-zero Lamb-Dicke parameter but for microwaves it is vanishingly small due to the long wavelength of the radiation, and therefore low photon momentum, used to manipulate the states [19]. This means that when using microwaves alone there is effectively zero coupling between the ion's states and its motion. This is solved by using a high magnetic field gradient at the ion position which enables transitions between states of different magnetic moment to change the motional state, enabling microwaves to be used for entanglement operations. As previously explained in the introduction, this works because, like within the Stern-Gerlach experiment, a magnetic field gradient will exert a different force on an ion based on whether its spin is oriented up or down. This means that within a magnetic field gradient, the ion will experience the required momentum kick in order for surrounding ions to feel a change in its internal state produced by a gate operation. For microwave operations in the presence of a static magnetic field gradient this coupling between the ion's internal state and external motion is described by an effective Lamb-Dicke parameter given by [18] [17]:

$$\eta_{\text{eff}} = \frac{\mu_B b_z}{\sqrt{2m\hbar\nu_z^{\frac{3}{2}}}} \quad (1.8)$$



where  $\mu_B$  is the Bohr magneton,  $b_z$  is the static magnetic field gradient oriented in  $z$ , and  $\nu_z$  is the secular frequency in the  $z$ -direction. One can see that this Lamb-Dicke parameter is proportional to the magnetic field gradient, thus the higher the magnetic field gradient that the ion sits in, the stronger the coupling between the ion motion and its internal states.

Since ions that sit in a magnetic field gradient still have the secular motion from the ion trap itself, they oscillate around a point in space, which, since the ion is sitting in a magnetic field gradient, very slightly widens and narrows the energy gap of the magnetically sensitive Zeeman states. This motion in the gradient significantly enhances the motional sidebands on these states which are spaced above and below the main transition frequency at the secular frequency associated with the mode of motion parallel to the magnetic field gradient. This allows us to use microwave pulses resonant with the sidebands of the transition to manipulate the ion's motional quanta through its internal state and additionally entangle an ion's motion with its internal state. For axial mode operations, the typical secular frequencies we use lie within the range  $2\pi \times (350 \pm 150)$  kHz. Gate operations using microwaves will be discussed and demonstrated in significantly more detail in Chapter 2.

Microwave based coherent manipulation also poses a challenge to one fundamental aspect of performing operations on many ions in a chain. Unlike laser based manipulation, which with the correct optics can be focussed to point on a single ion for individual addressing, it is extremely difficult to address a single ion with a microwave field due to its large spatial coverage. In 2013, it was demonstrated by Johanning [48] that  $^{172}\text{Yb}^+$  ions could individually addressed using long-wavelength radiation in the presence of a static magnetic field gradient using the individual degeneracies of Zeeman states in each ion of a string experiencing a different magnitude of absolute magnetic field. Using a static magnetic field gradient, one can similarly individually address a string of  $^{171}\text{Yb}^+$  ions using the transitions from  $^2\text{S}_{\frac{1}{2}}, F = 0$  to the Zeeman states of  $^2\text{S}_{\frac{1}{2}}, F = 1$ , which will be different for each ion in the chain. This splitting scheme is shown in Figure 1.13 where,  $\omega_{\text{hf}}$  is the transition frequency of the natural hyperfine splitting and primes denote the associated transition frequencies for the second ion.

In zero magnetic field, the hyperfine splitting between the  $^2\text{S}_{\frac{1}{2}}, F = 0$  and  $F = 1$  states are given by  $\omega_{\text{hf}} = 2\pi \times 12.6428121$  GHz and the  $F = 1, m_F$  states are all degenerate. However, in the presence of a magnetic field,  $B$ , the  $m_F = -1$  and  $m_F = +1$  states are first order Zeeman shifted by  $\omega_-$  and  $\omega_+$  respectively [49];

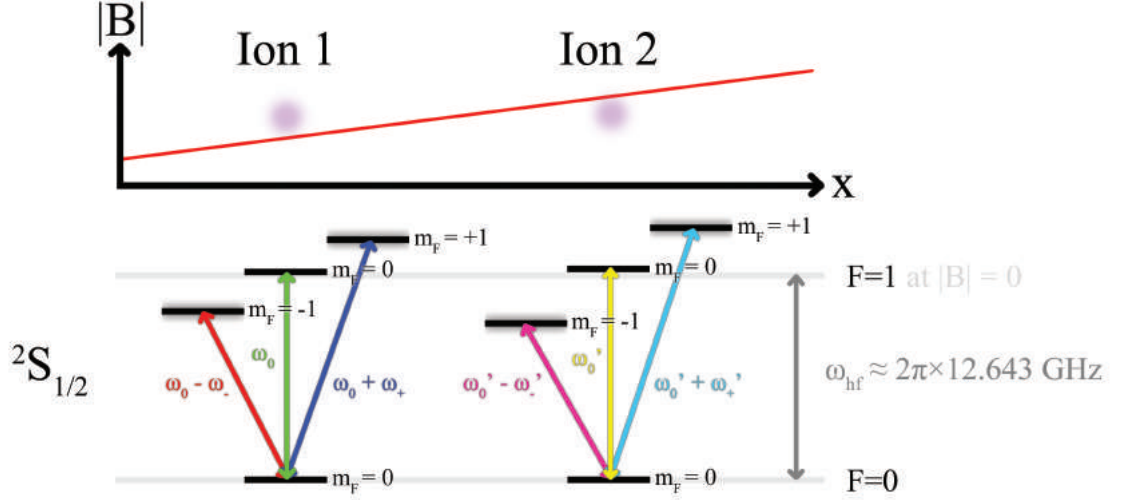


Figure 1.13: Individual addressing of two ions through the use of the different  $^2S_{1/2}$ ,  $F = 1$  Zeeman splittings for two ions sitting in a magnetic field gradient. Ion 1 and ion 2 are separated by a small distance in  $x$  in the presence of a magnetic field gradient given by  $\frac{d|B|}{dx} > 0$  where the absolute magnetic field  $|B|$  is slightly greater at the position of ion 2 than at ion 1. For both ions the  $F = 0$ ,  $m_F = 0$  to  $F = 1$ ,  $|m_F| = 1$  transitions for each ion are significantly shifted with respect to  $\omega_0$  due to the first-order Zeeman effect. The variance illustrated on each of these states denotes a strong coupling to the secular motion due to the magnetic field gradient. The  $F = 0$ ,  $m_F = 0$  to  $F = 1$ ,  $m_F = 0$  transitions are also widened by the second-order Zeeman effect. Since the energy gaps between the  $F = 0$  and  $F = 1$  states are different for all three transitions in both ions, this means that all six of these transitions can be individually addressed by using a different frequency of microwave radiation. A magnetic field gradient therefore allows for individual addressing of multiple  $^{171}\text{Yb}^+$  ions through the energy levels of the  $^2S_{1/2}$  hyperfine manifold.

$$\omega_- = -\frac{\omega_{\text{hf}}}{2}(1 - \chi - \sqrt{1 + \chi^2}) \quad (1.9)$$

$$\omega_+ = \frac{\omega_{\text{hf}}}{2}(1 + \chi - \sqrt{1 + \chi^2}) \quad (1.10)$$

where  $\chi = gJ\mu_B B / \hbar\omega_{\text{hf}}$ , and  $gJ$  and  $\mu_B$  are the Landé  $g$ -factor and the Bohr magneton respectively. The nuclear spin contribution has been ignored as  $\mu_N \ll \mu_B$  where  $\mu_N$  is the nuclear magneton. This shift is relative to  $\omega_0$  which is given by [49]:

$$\omega_0 = \omega_{\text{hf}}\sqrt{1 + \chi^2} \quad (1.11)$$

In the presence of small magnetic fields less than 30 G,  $\omega_- \approx \omega_+$  and the shift is near-linear in nature. For the magnetic field that our ions sit in, the energy splitting between these  $F = 1$ ,  $m_F$  levels corresponds to a frequency of 10 – 20 MHz. At fields greater than this, a growing difference is present due to the increased magnitude of the  $\sqrt{1 + \chi^2}$  term. This is known as the non-linear Zeeman effect. In this case,  $\omega_- > \omega_+$ . Similarly, in low

magnetic fields,  $\omega_0 \approx \omega_{\text{hf}}$  but this grows with  $\sqrt{1 + \chi^2}$  making  $\omega_0 > \omega_{\text{hf}}$ . This magnetic field gradient allows us to individually address each of the ions in a chain with minimal crosstalk.

For our experiments, we ideally desire the highest magnetic field gradient possible in order to produce the fastest gate operations and therefore highest fidelity over any sources of decoherence. In reality this gradient is limited by the maximum offset magnetic field we wish our ions to sit in. For axial mode operations this is dictated by the second ion in a chain of two; one ion will sit close to the point of zero magnetic field within the gradient and the other will sit in a much higher offset magnetic field. In order to keep the second ion in the regime where the Zeeman shift is near-linear in nature it should sit in an offset field of much less than 100 G. This ensures that the microwave transitions within  $^2\text{S}_{\frac{1}{2}}$  for each ion are well separated from each other so crosstalk between transitions is minimised. Depending on the spacing of the pair of ions, dictated by their axial secular frequency, this corresponds to a maximum desired axial magnetic field gradient of  $\sim 400$  T/m. These figures are based on calculations made within our experimental group, however, since the highest operation fidelity is a result of many factors including secular frequency, heating, ion temperature, and microwave power, higher gradients may be desired in future experiments.

The question remains as to how one is able to create a magnetic field gradient sufficient for performing the intended coherent manipulation experiments using microwaves. Gradients as low as 0.24 T/m have been shown to make individual addressing of  $^{172}\text{Yb}^+$  ions possible using RF radiation [48], however, gradients over 100 T/m would be required in order to perform a fault tolerant two-ion microwave gate using  $^{171}\text{Yb}^+$  ions and the trap architectures available to this group. There are many ways of creating a magnetic field gradient which will be discussed in extensive detail in Chapter 3, however, we will focus here on the setup that was designed by Dr Joseph Randall and retrofitted to the Blade trap in order to create the required coupling for our experiments. This setup was used to perform all experiments mentioned in Chapter 2.

The magnetic retrofit consists of four nickel-copper-nickel coated samarium cobalt<sup>4</sup> magnets using two pairs of magnets with opposing polarities pointing towards the trap centre. A smaller pair with holes for compensation electrodes to fit through are placed as close to the ion position as possible, and a larger pair further from the ion with mag-

---

<sup>4</sup>Samarium cobalt was selected due to its relatively high remanence, high coercivity, and a Curie temperature well above the temperature required for our vacuum baking process. Selection of permanent magnetic materials for a high magnetic field gradients will be discussed in more detail in Chapter 3.

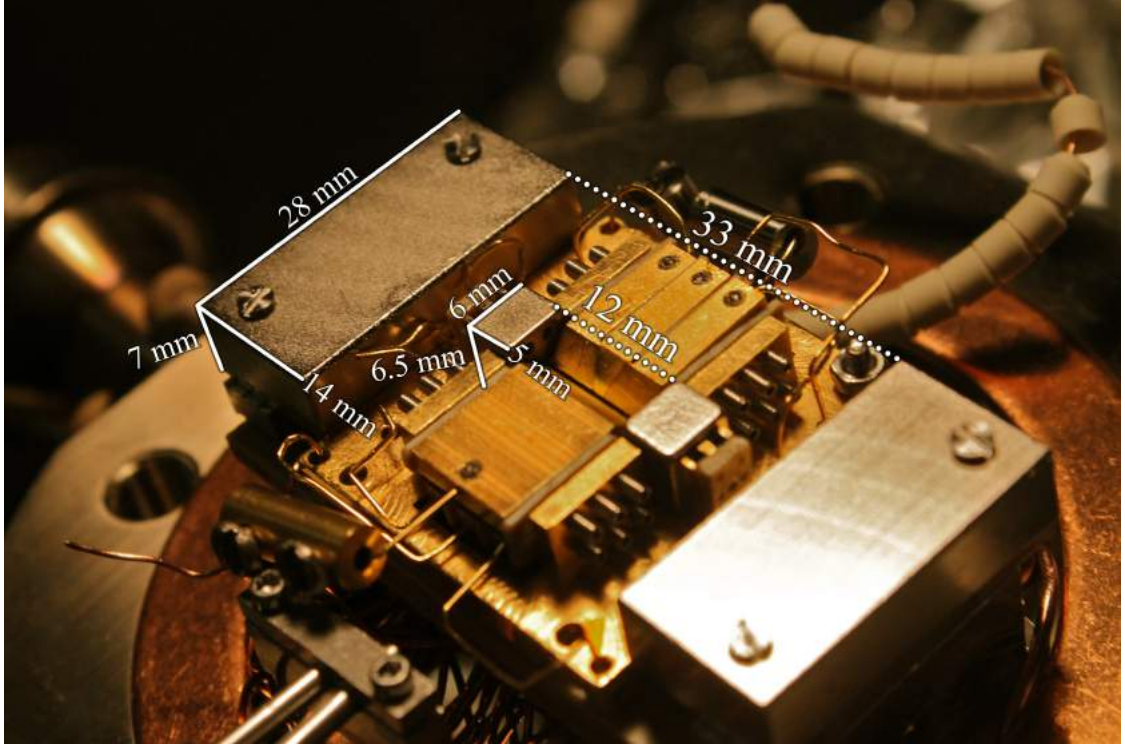


Figure 1.14: The Blade trap illustrated in Figure 1.6 as retrofitted with the magnets designed by Dr Joseph Randall. The magnetisation of each magnet points towards the central trapping region. Solid lines mark the dimensions of the cuboid magnets and dotted lines mark their face-to-face separation.

netisation parallel to their smaller counterparts serve to boost the opposing fields at the ion. This magnetic setup is shown in Figure 1.14. The ions sit almost perfectly central to the magnets for the maximum magnetic field gradient. Since these magnets are centrally repelling each other, the smaller pair are fixed in place by a mounting plate to limit their separation and the larger pair are fixed down by screws through their body. The trap was rebuilt around this magnetic setup to be as close to before the retrofit as possible. Due to the high magnetic field gradient, any slight electrode or magnet misalignment would result in the ions sitting in a high magnetic field which could lead to complications when it comes to performing coherent manipulation experiments. In the worst case scenario, this would result in a difficulty to trap due to the large detuning of the magnetically sensitive transitions and therefore an uncertainty in the laser and microwave frequencies required to effectively cool the ion. In this eventuality, a set of compensation coils (also designed by Dr Joseph Randall) were constructed for each axis to provide field compensation in all directions accounting for any reasonable misalignment. After measuring the coil temperatures as a function of the current flowing through them it was found that they became too hot to operate safely; in order to rectify this, the coils were retrofitted with water-cooling pipes so that a safe operating temperature could be maintained.

#### 1.4.1 Post-trapping procedures for the Blade trap equipped with a magnetic field gradient retrofit

Once pumped down to UHV pressure, trapping in the presence of the magnetic retrofit was achieved relatively quickly though a large offset field of approximately 100 Gauss was present at the ion position. This meant that the compensation coils required water cooling due to the high currents applied to them in order to minimise this offset field. Each coil has a copper pipe attached to its former which was supplied with a flow of cold water from a main water line into the lab. Due to water wastage, a solution was required in order to keep the experiment running constantly with the required offset fields in place.

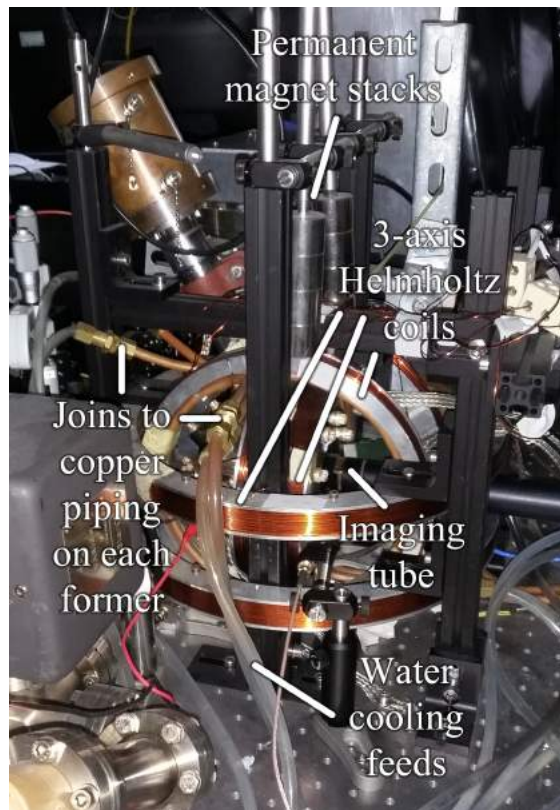


Figure 1.15: The compensation magnetics as they sit around the vacuum system hemisphere. External permanent magnets lower the current required in the compensation coils so that water cooling is no longer required. Joins to the copper piping used for heat conduction from the coils present the points of highest leak risk in the water system.

It was found that much of the field could be compensated using stacks of neodymium magnets on the relevant axes of the experiment. This allowed the coils to operate at a much lower current (1 – 3 A [24]) which meant that lower noise, low current power supplies (Delta Elektronika ES 015-10) could replace larger, noisier ones (Delta Elektronika SM 120-13). Figure 1.15 shows the compensation coils and external magnets in position around

the vacuum system hemisphere. Since the coils were now operating at a relatively safe temperature without water cooling, it was decided that due to the possibility of leaks that may not be easily visible, the water cooling would be shut off indefinitely as a precaution.

The magnetic field gradient using this setup was initially measured after field compensation was applied by moving the ion using the endcap electrodes by a small distance measured using the camera. The difference in resonant microwave frequency of a magnetically sensitive transition was then noted for the two positions yielding an approximate gradient of 24 T/m. This initial measurement was later surpassed using coherent manipulation techniques which are described in Chapter 2.<sup>5</sup>

## 1.5 Imaging, lasers, microwaves, and RF setup

The final section of this chapter discusses the experimental setup required to manipulate ions using long-wavelength radiation in order to perform the experiments discussed in Chapter 2. This includes the imaging, laser, and microwave and RF setups required in addition to computer control which sequences these aspects of the experimental setup.

### 1.5.1 Imaging

During the trapping phase of experiments, we observe the ions on an EMCCD camera. This enables us to trap the required number of ions, ensure there are no dark ions, and verify that the ion's position is stable after trapping. The results of any coherent experiments are detected using a PMT to determine the ion state, although in future we plan to also use the EMCCD for this purpose. In order to do both of these, imaging optics are required to focus this light onto the EMCCD and PMT focal planes. This consists of a light-tight imaging tube with an objective lens group, iris, and a doublet lens group, going into a light tight box with a removable 369 nm filter and a flipper mirror between the EMCCD and PMT. Due to scattered laser light from the surrounding electrodes, a small beam block was used in order to cover part of the image plane thereby minimising scatter around the ion as seen by the detectors. The iris can be closed around the image of the ion in order to further minimise background scatter.

---

<sup>5</sup>I will not display the results of this initial measurement here as the measurement process used in Chapter 2 is very similar with the exception of using computer controlled frequency scanning and readout for greater accuracy and the interleaving of measurements on two ions, their separation determined by a measurement of the axial secular frequency. This will become clear in Chapter 2.

### 1.5.2 Laser light delivery

An extensive optical setup shapes and directs the required laser beams to the position of the ion. All lasers are coupled into fibres shortly after they are produced so that they can be sampled for a wavemeter and directed via flipper mirror to be coupled to other experiments. Prior to the fibre, the 369 nm laser is produced from a 739 nm laser frequency locked via a cavity to a 780 nm laser which in turn is locked to a Rubidium cell, and 1.05 GHz sidebands are applied using an Electro-Optic Modulator (EOM). This is then frequency doubled using a bow-tie cavity to create 369 nm light with 2.1 GHz sidebands. The 369 nm laser is then switched using an Acousto-Optic Modulator (AOM). By adjusting the amplitude and frequency of the AOM driving signal, the amplitude and frequency of the laser can be adjusted. This allows one to cool the ion with high power red-detuned light and read out on resonance with a lower power optimised for the highest state detection fidelity. By doing this, one is able to efficiently cool the ion before coherent manipulation operations and read out from these operations with high contrast between a “dark” and “light” state of the ion with minimised background scatter as the laser light has lower intensity. These “dark” and “light” readout states of the ion are the basis of the “0” and “1” of the qubit and will be explained in detail in Chapter 2. The 369 nm, 399 nm, and 638 nm lasers are combined shortly prior to the ion and enter the vacuum system together.

During normal operation, the 638 nm laser is blocked unless there is a large chance that an ion may decay into the  $^2D_{\frac{5}{2}}$  state and subsequently the  $^2F_{\frac{7}{2}}$  state due to a long experimental run. In order to cover the 638.610 nm to 638.616 nm wavelengths required to address this transition, a function generator is used as an LFO applied to the piezo input of the laser controller in order to modulate this wavelength at a rate of approximately 0.5 Hz. By having the 638 nm laser modulated at all times between these two wavelengths, if an ion decays into  $^2F_{\frac{7}{2}}$ , population transfer to  $^1[5/2]_{\frac{5}{2}}$  and eventual decay back into the cooling cycle addressed by 369 nm and 936 nm laser light is possible regardless of the  $F$  state that the ion has decayed into as all transitions from these states are addressed at some point in the 638 nm laser’s range of modulation (see Figure 1.12). This slow modulation of the 638 nm laser has been shown to quickly “revive” a dark ion after a collision so that data taking can continue.

Post trapping, the experiment requires a period of time before the ion position is fixed and the magnetic field at the ion is stable, either due to an effect within the atomic oven, or charging of patch potentials on the electrodes. In our experience, a  $^{171}\text{Yb}^+$  ion is

usably stable after 60 – 120 minutes wait after initial trapping. A 638 nm laser is therefore required for experiments with  $^{171}\text{Yb}^+$  in order to keep an ion in, or return said ion to, the primary cooling cycle. If this laser is not present, an ion that has “gone dark” must be flushed from the trap and a new one must replace it in order to perform more coherent manipulation experiments. Even if such a transition only happens once a day, this creates a rather frustrating wait time and recalibration of microwave and RF fields before any worthwhile experiments can resume.

Conversely, post-trapping experiments with  $^{174}\text{Yb}^+$  typically last up to an hour maximum for an initial measurement of the secular frequency and optimisation of trapping and imaging parameters. For this time scale and isotope, one does not have to wait for the ion to settle in order to get good preliminary results and the likelihood of a collision is very low. If an ion becomes “dark” in this time period, it is much more likely that it has been lost due to unstable trapping, than to have decayed to the  $^2\text{F}_{7/2}$  state. Compared with  $^{171}\text{Yb}^+$  ions, which may be trapped for days or weeks over the course of a set of experiments, for  $^{174}\text{Yb}^+$ , a 638 nm laser is not required for our operations.

Though the 935 nm laser would ideally have 3 GHz sidebands applied to it in some way, in our setup, we power-broaden over these transitions as a higher power in the 935 nm transition does not lower the fidelity of operations. This beam enters at the opposite rear window of the vacuum system hemisphere due to the different lens required to focus the longer wavelength laser at the ion position.

The specifications and layouts of this imaging and optical table setup has been previously well-documented in several other theses from this group, and as such I will not document them here. Further information can be found in the theses of Dr Sebastian Weidt [35], Dr Kimberly Lake [25], and Dr Joseph Randall [24]<sup>6</sup>. Additionally, an example of these optical apparatus can be found in Chapter 4 as I document the construction of the new experimental setups.

### 1.5.3 Microwave and RF fields

In order to manipulate our qubit, which is based in the  $^2\text{S}_{1/2}$  hyperfine manifold of  $^{171}\text{Yb}^+$  ions, we require multiple microwave fields in order to address the  $F = 0$  to  $F = 1$  transitions for each of the  $m_F$  levels. We also require RF fields to address the transitions from  $F = 1$ ,  $m_F = 0$  to  $F = 1$ ,  $m_F = \pm 1$  as this gives us full control over this qubit subspace, which will become very useful for the coherent experiments discussed in Chapter 2.

---

<sup>6</sup>At the time that I worked on this experiment, the optical table setup most closely resembled that shown in the thesis of Dr Kimberley Lake.



## Generation of long-wavelength coherent manipulation fields

The microwave fields used for coherent manipulation are produced by a 12.6 GHz microwave generator mixed with RF signals from a set of Direct Digital Synthesis (DDS) boards designed by David Murgia [50]. DDS boards are also used to create other RF signals required for coherent manipulation<sup>7</sup>. The full RF and microwave setup is shown in Figure 1.16. In the original DDS design, each board was controlled from the computer via USB through an Arduino Leonardo, however, this has since been updated so that the synthesis boards can be directly controlled via USB<sup>8</sup>. Each DDS box contains an Analog Devices AD9959 board which produces four RF signals between 0 – 500 MHz at up to +7 dBm power using a 25 MHz reference clock. Each signal from the four DDS units is +18 dB amplified (Mini-Circuits ZFL-750+) before going to a TTL controlled switch (Mini-Circuits ZASWA-2-50DR+). These switches are controlled by the experimental computer FPGA in order to create the microwave and RF pulses required for the experiment. For each DDS box, the four RF signals are then combined by a Mini-Circuits ZMSC-4-3+ before application to the experiment. Two of these combined signals then go to another Mini-Circuits ZASWA-2-50DR+ so that each DDS can be selected in turn for the experimental pulses.

For the RF setup, the signal then goes through a directional coupler which sends a small amount of the signal to a Picoscope 2208A. The Picoscope 2208A is a USB oscilloscope used to monitor the phase of the RF pulses going to the coil. Though not covered in this thesis, these phases are extremely important for the successful performance of a high-fidelity two-ion entanglement gate. This is detailed extensively in the thesis of Dr Joseph Randall [24]. The main RF signal from the directional coupler is then split by a Mini-Circuits ZFSC-2-1-S+ before each side is +43 dB amplified by a Mini Circuits LZY-22X+ and recombined by a Werlatone D1635-102. The reason for this splitting is to reduce intermodulations in the RF signal due to the amplification of the combined frequencies. These will be discussed in more detail in Chapter 2. The RF signal is then sent to the experiment.

For the microwave setup, the combined RF signals for the DDS boxes are mixed with 12.6 GHz microwave signal in order to create the required frequencies for the different transitions of the  $^2S_{1/2}$  manifold. Over the course of my time working on the experiments discussed in Chapter 2, the 12.6 GHz microwave source has been changed from a Hewlett Packard 83712B to a Keysight E8267D Vector Signal Generator (VSG) [24]. For

---

<sup>7</sup>These DDS boxes were built by David Murgia, Karsten Roth, Konstantine Luft, and Anna Webb.

<sup>8</sup>The conversion from Arduino control to direct control was done by Anna Webb.

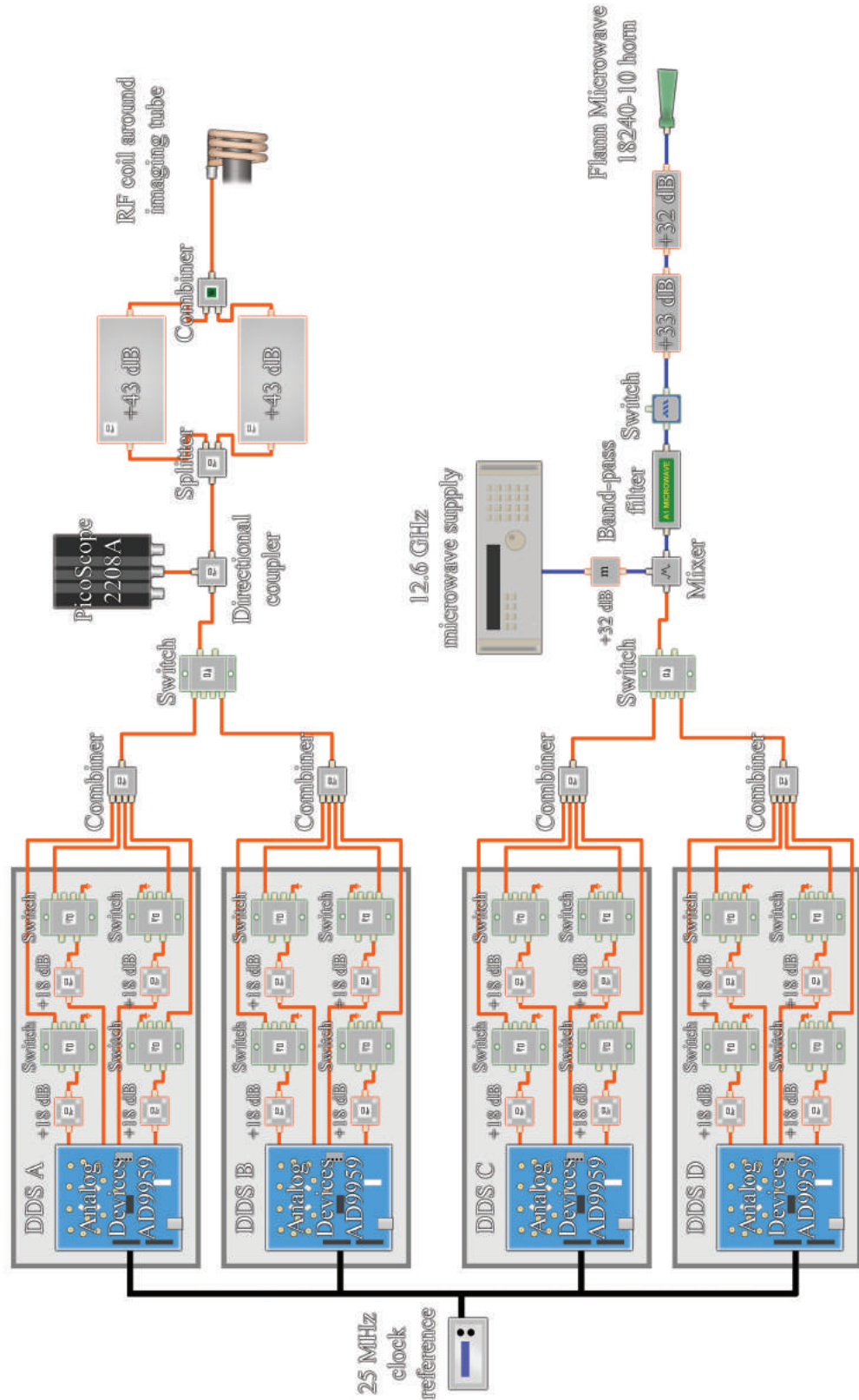


Figure 1.16: The RF and microwave setup used for coherent manipulation for the Blade trap experimental setup. Black lines indicate a clock signal, orange lines indicate RF signal connections, and blue lines indicate microwave signal connections. An orange hue around a component indicates a gain stage, and a green glow indicates a TTL pulse activated switch.

the VSG, the signal is output at -12 dBm and is +32 dB amplified (Microwave Amps AM25-12-13-30-33) before it is mixed with the DDS RF signals using a Marki Microwave T3-0316MQP mixer. As will be discussed in Chapter 2, a mixer creates RF (modulator) sidebands above and below the microwave (carrier) frequency. The carrier is offset by 100 MHz [24] so that the positive sidebands of the resultant signal are the frequencies resonant with the transitions that we require to address. In order to suppress the negative sidebands/intermodulations, the signal goes through a A1 Microwave WG 18 custom bandpass filter. A final switch (AMC SWN-218-2DT) allows us to create microwave pulses and turn off the microwaves globally in the event we want to interrupt the cooling cycle or for safety measures when rearranging apparatus near to the vacuum system hemisphere. The signal then passes through two gain stages (+33 dB Ciao Wireless CA1020-503 and +32 dB Microwave Amps AM25-12-13-30-33 amplifiers) before being sent to the experiment. This distribution of microwave frequencies and how they are produced is illustrated in Figure 1.17.

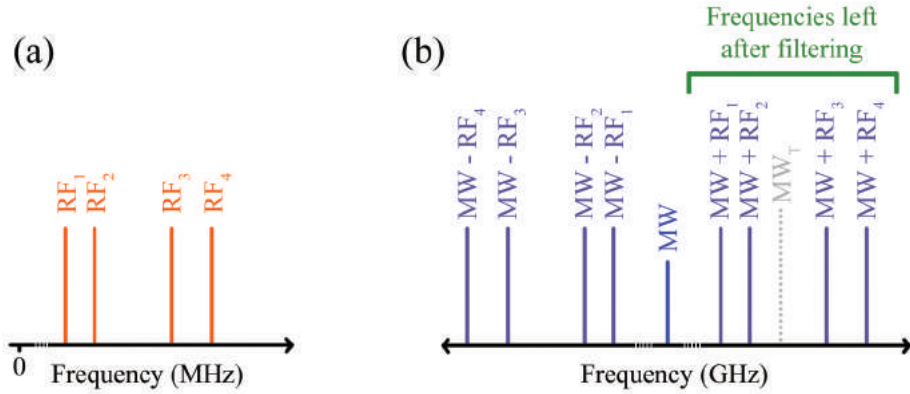


Figure 1.17: An illustration of the microwave frequencies used for our experiments. **(a)** - A set of four RF frequencies to be mixed with a single microwave source in order to create several microwave frequency peaks. **(b)** - The full set of microwave peaks resultant from mixing the four RF frequencies from (a) with a single microwave source of frequency  $MW$  which is negatively offset from our microwave transition frequency band centred on  $MW_T$ . After bandpass filtering, only the positive sidebands remain and these are used for driving transitions within the  $^2S_{1/2}$  hyperfine manifold of our  $^{171}\text{Yb}^+$  ions.

### Delivering microwave and RF radiation to the ion

At the vacuum hemisphere, for the coherent manipulation RF, the combined signal is passed through a small coil (3.35 mm diameter bare copper, three turns at 51 mm diameter) designed and built by Anna Webb which sits externally at the front viewport around the imaging tube. The microwaves used for coherent manipulation and completing the

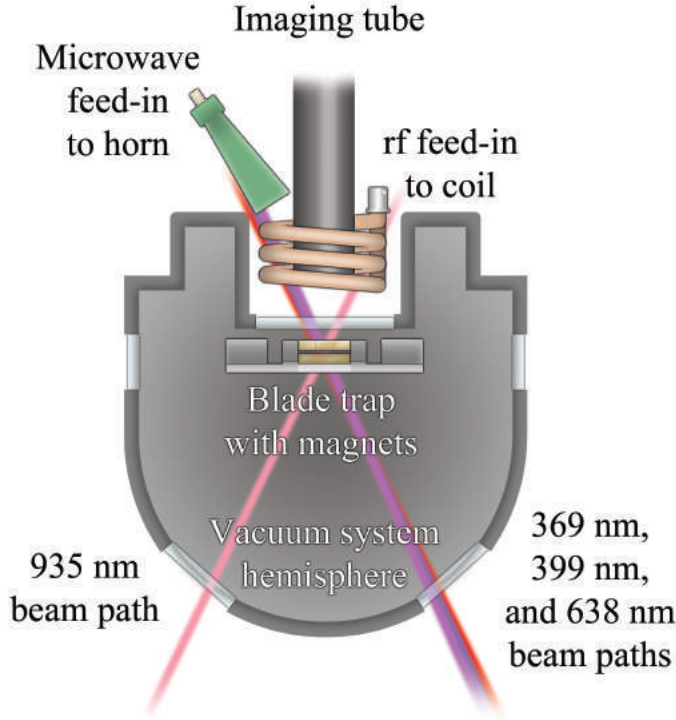


Figure 1.18: A top-view illustration of the hemisphere for the Blade trap system showing the entry points of each laser and the position of the RF coil, microwave horn, and imaging tube for coherent manipulation and detection. This diagram is not to scale and certain components of the setup have been exaggerated for clarity; in reality, the RF coil and imaging tube do not block the line of sight between the ion and microwave horn.

cooling cycle of the ion, are emitted at an angle to the imaging tube from a Flann microwave 18240-10 horn, again at the front viewport. The microwave horn is rotated with respect to the trap in order to provide polarisations of the microwave field in all directions at the ion position relative to the magnetic field polarisation. This polarisation will be discussed in more detail in Chapter 2 in the context of coherent manipulation and Chapter 4 when I discuss the microwave injection methods for the other experimental setups. The complete setup is illustrated in Figure 1.18 which shows the entry points of each laser and the position of the microwave horn, RF coil, and imaging tube. In reality there are many components behind the trap for mounting and connection of DC and RF voltages, but these and the focussing of each laser beam at the ion position have been omitted for clarity.

#### 1.5.4 Computer control

The laser beam blocks, AOMs, laser sidebands (EOM), microwave, and RF pulses required in order to perform coherent manipulation experiments with trapped ions are controlled

using digital and analogue switching pulses from the FPGA of the main experimental computer. This computer is also integrated with the DDS boxes in order to set the frequency and amplitude of the RF (and microwave) pulses used in the experiment. These switching pulses are controlled by a LabVIEW program (primarily overseen by Dr Simon Webster) which allows for sequencing of the pulses in order to create the relevant combinations that will perform the intended manipulation of the ion-based qubit.

A secondary computer running a real-time version of LabVIEW allows for remote wavemeter monitoring of the laser wavelengths as well as frequency locking for the 399 nm and 935 nm lasers, and remote fine adjustment of the 369 nm (739 nm) locking setup. In addition to this, remote control of the atomic oven current supply, trapping RF output switch, and monitoring of the vacuum pressure from the ion gauge controller allows for programmable oven sequences and flushing of the trap for the purpose of trapping experiments.

Now that we have briefly described the main principles of ion trapping, the ytterbium ion and its required laser, microwave and RF fields, the components of an Ultra-High Vacuum system, and our main coherent manipulation experimental setup, we can proceed to the next chapter which will put this apparatus to use in order to manipulate the hyperfine qubit present in a trapped  $^{171}\text{Yb}^+$  ion.

## Chapter 2

# Experimental single-qubit coherent manipulation using microwave and RF fields

In Chapter 1, I described the Blade trap experimental setup and the basis of our qubit subspace in the  $^2S_{\frac{1}{2}}$  hyperfine manifold of a trapped  $^{171}\text{Yb}^+$  ion. In this chapter, I discuss the use of this experimental apparatus in order to perform single-qubit operations on a trapped ion through the use of individual addressing with microwaves using a static magnetic field gradient. These discussions will include manipulation of the motional sidebands caused by two ions in the trapping potential as well as how one would simultaneously prepare two ions in the dressed state basis. In addition to this, I also discuss methods by which electromagnetic noise can be minimised in our experimental setup in order to increase the fidelity of qubit operations.

Concerning the experimental procedures described in this chapter, certain language is used in order to describe elements of the pulse sequence that performs the experiment. Before I go on to describe any experiments, I will clarify these terms here.

- **Pulse sequence** - This is the series of logical pulses that control the stimuli to the ion and its states. These pulse sequences are formed of a number of simultaneous pulses of different stimuli for a set time. Many of these pulse sequences will be described for different experiments performed within this chapter.
- **Run** - Typically each pulse sequence performs a single measurement of the ion state<sup>1</sup>,

---

<sup>1</sup>A pulse sequence can be expanded in order to perform multiple measurements of a group of near-simultaneous experiments within one run of the pulse sequence. This will be described later in this chapter.

however, one can only detect the ion as “dark” or “light” due to the measurement forcing the ion out of any superposition of the two. Therefore since this measurement is based on a probability, the experiment must be repeated many times in order to produce a statistical distribution of the probability that the ion will be detected in a “light” state, and therefore a measure of any superposition that has been created by the operation. By taking an average of many runs we can deduce, for example, that if the probability of being in a certain state is 50 percent for both outcomes we know that the ion is in a superposition of the two. The number of runs varies with the experiment performed as each run takes time, ergo more runs means a longer time to take a full dataset. For something such an initial frequency scan to find transitions, one might use 50 runs so a peak will be seen but not resolved with high accuracy. For an important experiment to measure a level of entanglement, such as spin-motional coupling, one may use over 400 runs in order get the best representation of the statistical distribution. These experiments will be explained later in this chapter<sup>2</sup>.

- **Step** - For each experiment (except for state preparation and detection after these have been optimised) one will typically want to vary one or more parameters in order to show the evolution of the probability that the ion is in a certain state with said parameter. Each “step” of the experiment adjusts this parameter by a given amount in the pulse sequence. This parameter is typically the frequency of one of the DDS channels or the length of a certain pulse in the pulse sequence. The former is broadly known as a frequency scan and the latter, a time scan. For each step, a set number of runs of the experiment are performed before proceeding to the next step and altering the desired values.
- **Population** - The population is the term given to the statistical chance that a single run will be in a “dark” or “light” state based on many runs. This in turn describes the ratio of superposition or entanglement of two states depending on the experiment performed and is therefore a way that one can express the measurement simply in words. For example, “in this operation, 150 out of 200 runs were measured to be have transferred to state  $|a\rangle$ ”, could be worded as, “this operation results in 75 percent of the population transfer to  $|a\rangle$ ”.

---

<sup>2</sup>Run is also used in a different sense in later chapters, for example, an experimental or trapping run is used to indicate a long series of experiments in the most general sense or a single attempt at trapping an ion based on turning the atomic oven current supply on, waiting until the vacuum pressure has increased slightly, and subsequently turning it off.

## 2.1 State preparation and detection

The ability to be able to discriminate between the “dark” and “light” states is essential for our ions to be used as a qubit since it is the basis of our measurement process after performing a coherent manipulation operation on an ion. A coherent operation is an operation which results in the ion being in a well-defined state or superposition of states and is the basis of quantum computation using trapped ions. An ion can be prepared in a dark state “0” ( $F = 0$ ) by shining 369 nm light on resonance with the  $^2S_{\frac{1}{2}}, F = 1$  to  $^2P_{\frac{1}{2}}, F = 0$  transition with 2.1 GHz applied, and 935 nm light with 3 GHz sidebands or sufficient power broadening applied. This creates an open cooling cycle which after a given time optically pumps the ion into the  $F = 0$  state of the hyperfine manifold. Once prepared in this “0” state we can apply a microwave  $\pi$ -pulse at  $\sim 12.6$  GHz to get it to a “1” state which can be  $m_F = -1$ ,  $m_F = 0$ , or  $m_F = +1$  of the  $^2S_{\frac{1}{2}}, F = 1$  manifold.

The state can then be detected by applying 369 nm and 935 nm laser light without their sidebands applied. If the ion is in  $F = 0$  then transitions to  $^2P_{\frac{1}{2}}$ , are far off-resonant, thus no 369 nm photons are scattered by the ion. However, if the state is in  $F = 1$  then the  $^2S_{\frac{1}{2}}, F = 1$  to  $^2P_{\frac{1}{2}}, F = 0$  transition is closed (barring decay to  $^3D_{\frac{3}{2}}$  and off-resonant excitation to  $^2P_{\frac{1}{2}}, F = 1$ ) and the ion will scatter 369 nm light due to repeated excitation and decay of the transition. By recording the number of counts detected by a PMT for a set length of time the  $F$  states can be distinguished. Both these preparation and detection operations are illustrated in Figure 2.1.

There are multiple sources of error in the measurement process that we use to determine the state of an ion:

- Off-resonant excitation of  $^2S_{\frac{1}{2}}, F = 0$  to  $^2P_{\frac{1}{2}}, F = 0$ , which turns a “dark” ion “light”.
- Off-resonant excitation from  $^2S_{\frac{1}{2}}, F = 1$  to  $^2P_{\frac{1}{2}}, F = 1$  or off-resonant excitation from  $^3D_{\frac{3}{2}}, F = 1$  to  $^3[3/2]_{\frac{1}{2}}, F = 1$ , which can transfer a “light” ion to a “dark” state.
- Dark counts and background light which can give PMT clicks
- The statistical variations in the photon detection process which result in a variable number of detections for identical ion states.

Due to these errors, we calibrate the detection process by recording the statistics of the numbers of PMT clicks for “light” and “dark” ions, and pick a threshold which minimises



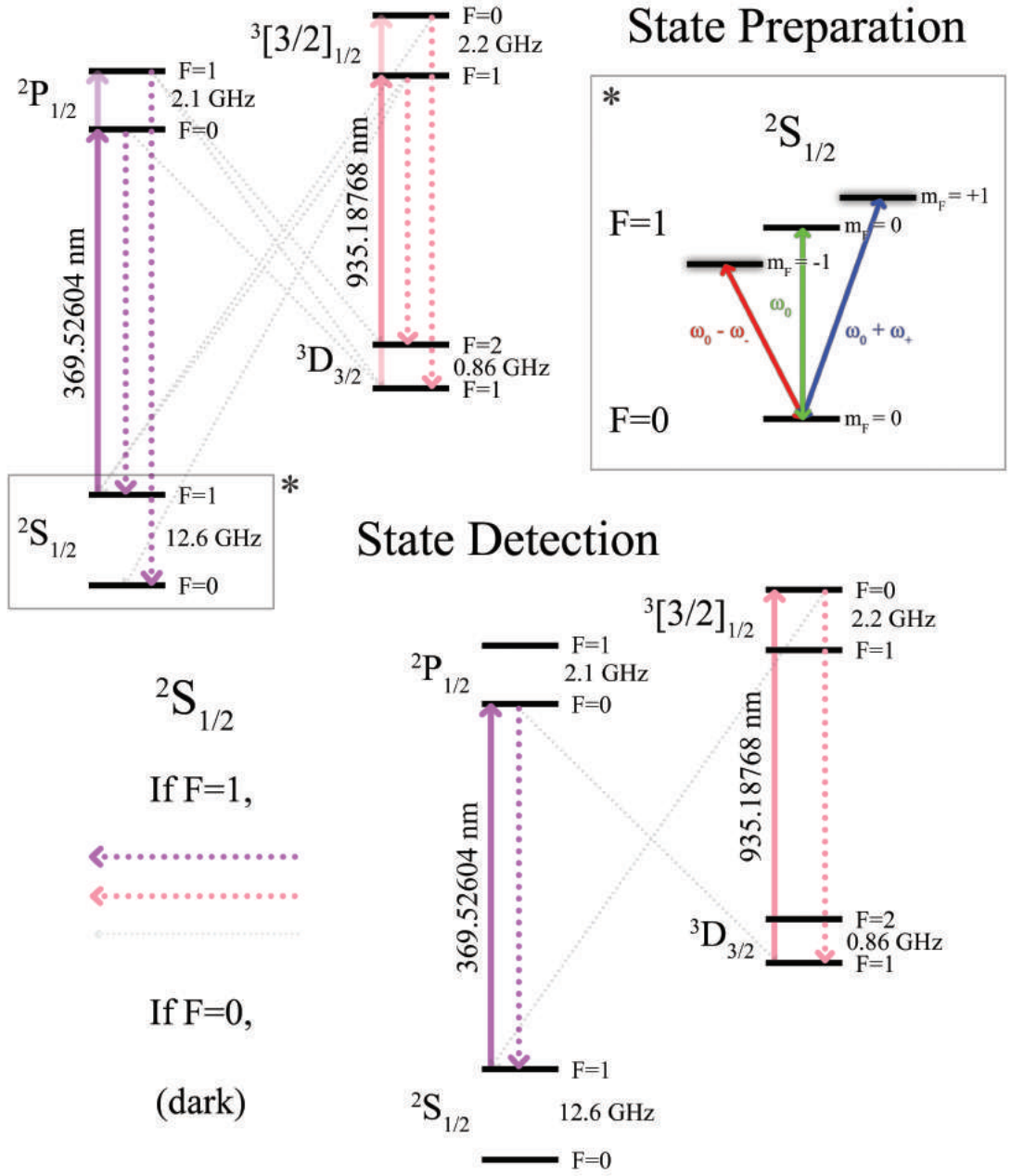


Figure 2.1: Partial cooling cycles for  $^{171}\text{Yb}^+$  in the presence of a small magnetic field during the state preparation (top) and detection (bottom) pulses of our experiment. During the preparation pulse, sidebands are applied to both lasers in order to cover all states of the cooling cycle. Without 12.6 GHz microwaves present, this forces the ion into  $^2\text{S}_{1/2}$ ,  $F=0$  after a given time. By applying microwave radiation for a small, calibrated amount of time determined by the microwave Rabi frequency, the population can be transferred to  $^2\text{S}_{1/2}$ ,  $F=1$  into of the three  $m_F$  states. This state can be detected by reapplying laser light without the sidebands present. For an ion in  $F=0$ , there will be no fluorescence as it is isolated from the cooling cycle that is being driven. For an ion in  $F=1$ , a closed cooling cycle is created which allows the emission of photons to be detected by an imaging system.

the error probability. We can then optimise laser parameters and the detection time to maximise the discrimination probability between the “light” and “dark” states.

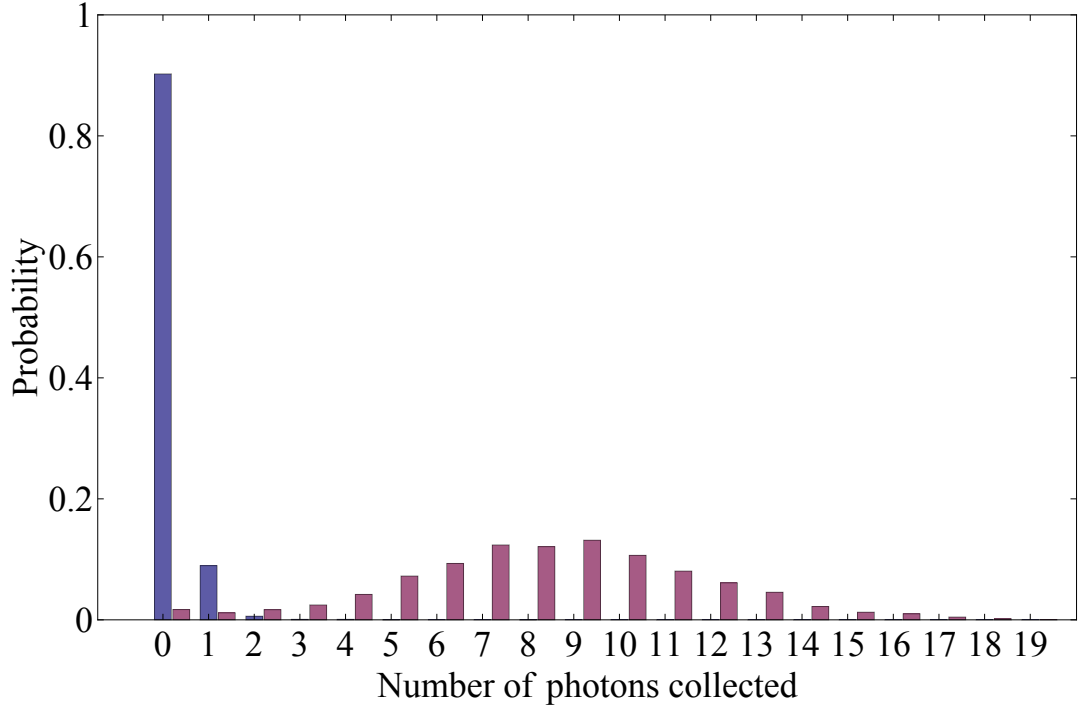


Figure 2.2: A state preparation graph showing the probability of the number of photons collected by the PMT for 1000 runs of **blue** - an ion prepared in  $^2S_{\frac{1}{2}}$ ,  $F = 0$ , and **purple** - an ion prepared in  $^2S_{\frac{1}{2}}$ ,  $F = 1$ . One can see that for an ion prepared in  $^2S_{\frac{1}{2}}$ ,  $F = 0$ , for  $\sim 10$  percent of the runs there were a small number of photons collected due to scattered laser light or dark counts causing PMT clicks, however, for  $\sim 90$  percent of the runs there were no photons detected, hence the ion is in a “dark” state. For an ion prepared in  $^2S_{\frac{1}{2}}$ ,  $F = 1$  there are a significant number of photons collected across the runs, hence the ion is in a “light” state. In reality, there is likely to be some runs that have more than 20 photons detected, however, the probability of this is low enough to not be visible on this plot, hence I have cropped the data axis at 20 counts. In this distribution, one can see that the highest number of photons detected by the ion prepared in  $^2S_{\frac{1}{2}}$ ,  $F = 0$  is 2, hence we set the threshold to “2” and count any run in which more than 2 photons are detected as an ion in a “light” state. Having said this, if a higher fidelity is observed using a different threshold, this would be the best to use for data taking.

Figure 2.2 shows a state preparation graph for a “dark” state when the ion is prepared in  $^2S_{\frac{1}{2}}$ ,  $F = 0$ , and a “light” state for the ion in  $^2S_{\frac{1}{2}}$ ,  $F = 1$ . This sequence initially cools the ion using a high intensity  $6000 \mu\text{s}$  long laser cooling pulse with the complete cooling cycle addressed. The  $369 \text{ nm}$  laser is red detuned from resonance by the natural linewidth  $\frac{\Gamma}{2\pi} = 19.6 \text{ MHz}$  [24] for optimum cooling during this pulse. The preparation pulse is  $30 \mu\text{s}$  long in order to ensure the ion is in  $|0\rangle$  and the detection pulse is  $900 \mu\text{s}$  long<sup>3</sup>. In

<sup>3</sup>These pulse lengths have been optimised in order to provide the highest preparation and detection

this case the 369 nm laser is set to a lower intensity but on resonance with the transition for maximum photon emission with minimum counts due to background scatter. This preparation and detection is the basis of “initialising” our qubit prior to performing any quantum operation with “readout” in order to determine the outcome of the operation, serving as the start and finish of all our experiments and the most basic steps of operating a quantum computer.

## 2.2 Obstacles towards high fidelity

In order to perform high fidelity operations on trapped ions, several concerns must be addressed. These concerns involve experimental setup and procedural problems that can be solved or must be taken into account when attempting microwave based coherent manipulation operations on trapped ions. In this section, I will discuss three obstacles towards high fidelity that have been investigated during my time in the lab and how they affect the ion.

### 2.2.1 External electrical noise minimisation techniques

Electrical noise can pose a large problem for performing high fidelity coherent manipulation of trapped ions as it is a major source of decoherence in our operations. Since we aim to perform microwave gate operations in the presence of a static magnetic field gradient this means that any translation of an ion results in a shift in the magnetic field and therefore the transition frequencies of our hyperfine manifold based qubit system. This detunes the ion from the radiation we use to perform coherent manipulation and therefore affects the timing in order to produce the intended population transfer from one state to another, which has a direct effect on the operation fidelity and coherence time. Electrical noise on the DC and RF electrodes leads to heating and frequency shift related decoherence due to the small drifts in the ion’s position in the gradient, therefore setting a limit to the amount of time we can manipulate the ion. In order to perform two-ion entanglement gates at high fidelity, operations must be much faster than the ion heating rate or the decoherence time of the chosen state, therefore we must make sure we can get the level of electrical noise to a minimum.

There are two main ways that noise can enter our experimental setup. Internal noise can be introduced by the power supplies that produce the DC trapping voltages, compensation coil currents, and production and amplification of coherent manipulation radiation

---

fidelity between the “dark” and “light” states of the ion(s) within our experiment.

and trapping RF voltages. External noise produced outside of the experimental setup can penetrate the vacuum system in order to get to the ion and produce unwanted population transfer and ion translation or heating. In this section I aim to discuss these effects and show how they can be minimised using noise minimisation and shielding techniques.

### Noise on electrical supplies

The first point of call in order to minimise the effects of electrical noise at the ion was to address any noise on the DC and RF trapping voltages. In terms of experimental apparatus, this involved making cleaner, more stable DC voltage supplies for the trap electrodes, making sure that everything was earthed correctly and that earth was kept as a stable zero-voltage reference. Some electronic equipment was found to affect the earth/ground voltage of the lab by introducing a spectrum of frequencies onto it in order to ensure their own clean performance. However, this contaminated earth voltage was then being used by all other equipment in the lab as the zero voltage reference. This meant that if one piece of equipment was plugged into a local earth and contaminated it, the voltages or currents produced by any power supply sharing that earth became contaminated with the same noise regardless of its connection to the experimental setup. We therefore rearranged the lab so that all power supply cables to equipment were grouped into master power points which reflected their requirement for a stable ground. In addition to this, all AC power cables were (at most) zig-zagged instead of coiled to prevent the loops from picking up any external frequencies and adding noise to them<sup>4</sup>. Any pairs of DC supply cables were also twisted around each other so that any noise induced along their lengths would be cancelled. This was important not just for the trapping voltages but also the microwave and RF supplies used for coherent manipulation of the qubit. Each piece of equipment was tested using a spectrum analyser and a noticeable reduction in unwanted frequency content was observed after this clean-up procedure.

This evaluation of the noise present on DC and RF trapping voltages therefore minimises unwanted translation of the ion which may cause decoherence. However, the current supplies to the compensation coils must also be free of noise in order to produce a stable offset magnetic field and therefore minimise any frequency shifts in the hyperfine manifold of the ion. Also, as mentioned in Chapter 1, large external permanent magnets were used in order to minimise the required currents in each of the coils and more stable low current supplies replaced larger noisier ones. This took care of the majority of electrical noise that

---

<sup>4</sup>This was done on the advice of Anton Grounds who had previously encountered these phenomena.

was present in the system due to noise on integrated equipment. Any remaining noise or external electromagnetic stimuli that could be blocked or compensated would now be coming from outside the system.

### **External electromagnetic noise and the Faraday cage**

In addition to electric field noise present on the trapping electrodes, electromagnetic fields generated outside of our experimental setup can also affect the ion. We therefore decided to build a Faraday cage to go around the vacuum system and all the surrounding optics, similar to that demonstrated by Häffner et al. [51]. While the vacuum system will partially shield the ions from external electromagnetic field noise, since there are windows for optical access, in particular the front window, this shielding is nowhere near perfect.

The effectiveness of a Faraday cage is dependent on a number of factors which depend on the frequencies of electrical noise present. A Faraday cage can be constructed from a conductive material (solid or mesh) that is electrically earthed. By placing this cage around an object one is able to protect it from electromagnetic radiation and electrostatic fields. An external electric field causes a redistribution of charge carriers on the outside of the cage creating an equal in magnitude but opposite direction field on the inside of the cage. The external and internal electric fields thus cancel creating a zero static electric field environment within the cage. However, it is possible that electromagnetic waves and static magnetic fields can penetrate the material of the Faraday cage depending on the thickness of the material and the size of any holes, gaps, or apertures in the cage. In order to block static magnetic fields, the cage material must be diamagnetic in order to oppose an external magnetic field in order to cancel it. However, this is typically only truly effective in the case of superconductors exhibiting the Meissner effect and is therefore not practical for our Faraday cage application. An alternative to directly blocking a static magnetic field is to channel (yoke) it in a high permeability medium such as mu-metal. This results in an external static magnetic field being contained within the shell of the cage but being unable to penetrate it. Magnetic yoking will be discussed in much more detail over the course of this thesis. The thickness the cage determines how much the material will allow certain frequencies of electromagnetic radiation to penetrate, due to the skin effect. When propagating electromagnetic radiation comes into contact with a conductive medium, a current is induced inside the conductor by the alternating magnetic field of said radiation. However, this changing current also induces an internal back EMF in the conductor which drives the charge carriers (electrons) to the surface. For a thin

conductor, this will attenuate the electromagnetic wave that is transmitted through the medium. The skin depth of a material at a given electromagnetic wave frequency is the depth by which the magnitude of current inside a conductor drops to  $\frac{1}{e}$  (approximately 0.37) the value from the surface of the conductor and is dependent on the resistivity and electromagnetic constants of the material. In terms of electromagnetic shielding, this corresponds to the value that the induced current due to external electromagnetic radiation, and therefore amplitude of the transmitted radiation inside the conductor, drops to  $\frac{1}{e}$  of the wave amplitude at the surface. A set of diagrams illustrating the electrostatic shielding and skin depth mechanisms of a Faraday cage is shown in Figure 2.3.

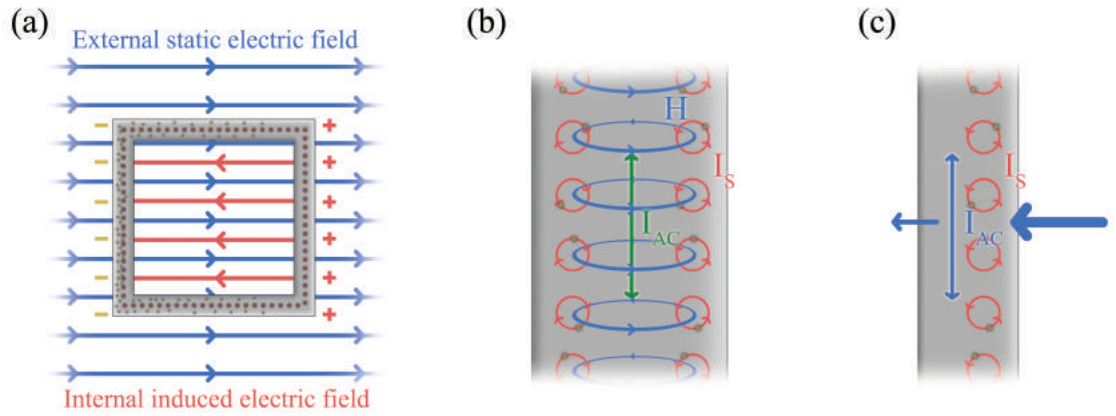


Figure 2.3: Illustrations of the mechanisms that result in shielding from external static electric fields and high frequency electromagnetic radiation. **(a)** - The charge carriers (electrons) on the outside of the cage are redistributed by the external electric field creating an equal but opposite electric field inside the cage resulting in zero net field. **(b)** - The skin effect exhibited inside a conductor with a high frequency alternating current  $I_{AC}$  inside it. The net auxiliary magnetic field  $H$  induced by the current forces the oscillating charge carriers to the surface of the conductor due to their own inherent  $H$  fields from the surface eddy-currents  $I_S$ . **(c)** - The skin effect exhibiting electromagnetic shielding in the presence of external radiation. The incident radiation induces a current  $I_{AC}$  inside the conductive shield which confines the charge carriers to the surface of the conductor. This attenuates radiation transmitted through the conductive medium as the charge carriers are unable to propagate the wave through the cage wall.

The skin depth  $\delta$  is given by [52]:

$$\delta = \sqrt{\frac{2\rho}{\omega\mu}} \sqrt{\sqrt{1 + (\rho\omega\epsilon)^2} + \rho\omega\epsilon} \quad (2.1)$$

where  $\epsilon$ ,  $\mu$ , and  $\rho$ , are the electromagnetic permittivity, electromagnetic permeability, and the resistivity of the material respectively, and  $\omega$  is the angular frequency of the incident electromagnetic radiation.

The skin depth decreases with higher frequencies and relative permeability and mul-

Table 2.1: Some important properties of prospective Faraday cage materials [53] [54] [55] [56] [57].

Material	Relative permeability	Resistivity ( $\Omega\text{m}$ )	Density ( $\text{kg}/\text{m}^3$ )
Stainless steel	750 - 1800	$6.9 \times 10^{-7}$	7480 - 8000
Aluminium	1.000 002	$2.82 \times 10^{-8}$	2712
Mu-metal	20 000 - 50 000	$5.8 \times 10^{-7}$	8747

Table 2.2: The skin depths of prospective Faraday cage materials for a range of frequencies calculated using the average value of relative permeability from the ranges shown in Table 2.1.

Material	Skin depth ( $\mu\text{m}$ ) at 1 MHz	Skin depth ( $\mu\text{m}$ ) at 10 MHz	Skin depth ( $\mu\text{m}$ ) at 100 MHz
Stainless steel	11.708	3.702	1.171
Aluminium	84.571	26.727	8.452
Mu-metal	2.049	0.648	0.205

multiple skin depths (thicker material) means that less power of the incident radiation is transmitted. For a good electrical conductor,  $\delta \approx \sqrt{\frac{2\rho}{\omega\mu}}$  for sub-terahertz frequencies where  $\rho\omega\epsilon \ll 1$ . If one compares some typical skin depths for a variety of materials and frequencies, an idea of what material would be suitable for constructing a Faraday cage can be better inferred. Important physical properties for stainless steel, aluminium, and mu-metal are shown in Table 2.1 and their skin depths for a range of frequencies are shown in Table 2.2.

However, it is important to note that though some materials may seem better in theory, in practice they may not be economically or structurally viable. Though non-austenitic stainless steel would be ideal in principle due to its high permeability and resistance to corrosion, it is heavy and at the size of Faraday cage we desire, it would be physically difficult to build around the existing experimental apparatus. It is also likely that the weight of the cage would render the vibration-proof experimental table useless as it would be significantly depressed. Mu-metal is the ideal metal in terms of shielding, however, this would not be cost effective for the size of cage we intend to build. Additionally, the required thickness for attenuation is much thinner than that required in order to create a structurally sound cage around the experiment. Aluminium is the obvious choice as it is resistant to corrosion, structurally strong but also light in weight (less than a third the density of stainless steel), is easy to machine, and has a relatively low resistivity. Though it is not the ideal material due to the relatively large skin depth, it is at least viable both structurally and economically to be used to construct a Faraday cage for our application. This structure could later be retrofitted with thin mu-metal foil at a later date if more

shielding is required.

An extensive Faraday cage was designed based around a cuboid frame onto which five panels were attached; the base panel was provided by the optical table serving as the ground reference. Four large main access panels/doors were designed on the cage for access to any optics situated inside the cage which may require adjustment. These access panels are clamped into place by “lift and turn” compression latches and an inner rim to each panel frame ensures minimal transmission of plane polarised electromagnetic radiation. For one of the main panels, this rim was welded in place which resulted in a distortion of the panel such that the doors did not fit properly and the removable panel/door itself could not be attached to the frame with all bolts in place. This was remedied by filing the through holes for the bolts and the edges of the removable panel/doors until they fit into place. The second main panel used rivets to attach the inner rim resulting in no warping of the main panel and no required modification to the removable panel/doors. All lasers are fed into the cage via fibres and there are access holes for the water cooling tubing for the current coils, imaging, trap DC voltages, trap RF (which terminates to the same earth as the Faraday cage), and microwave and RF cables for coherent manipulation experiments. These panels were each made of 4 mm thick aluminium with no explicit gaps or slit apertures wider than the 150 mm spacing of the M6 attachment bolts. Aside from plane polarised radiation going through the joins in the cage pieces and access holes, this structure should form a perfect grounded cage around the experiment as shown in Figure 2.4. The technical drawings for this Faraday cage design can be found in Appendix B.

If we assume that ten skin depths effectively nulls a given frequency of incident radiation ( $\sim 0.000045$  transmitted amplitude of the incoming radiation) then the minimum frequency that 4 mm of aluminium will “block” is  $\sim 42$  kHz, which covers all radiation in the lab that may concern our experiment except for RF fields that may come from other future setups. The main frequency that we are unable to block is the 50 Hz mains voltage, which has a skin depth of 11.6 mm for aluminium, much too large to put onto the table. However, line-triggering of the experimental pulses allows data taking in synchronisation with the mains oscillation and thus cancels the effect that this has on the results, disregarding the effect of magnetic field fluctuations on the coherence time, which will be explained later in this chapter.

There are, however, additional holes in the cage which allow for the imaging tube, water cooling tubes, and laser fibres to enter, and these will undoubtedly affect the performance



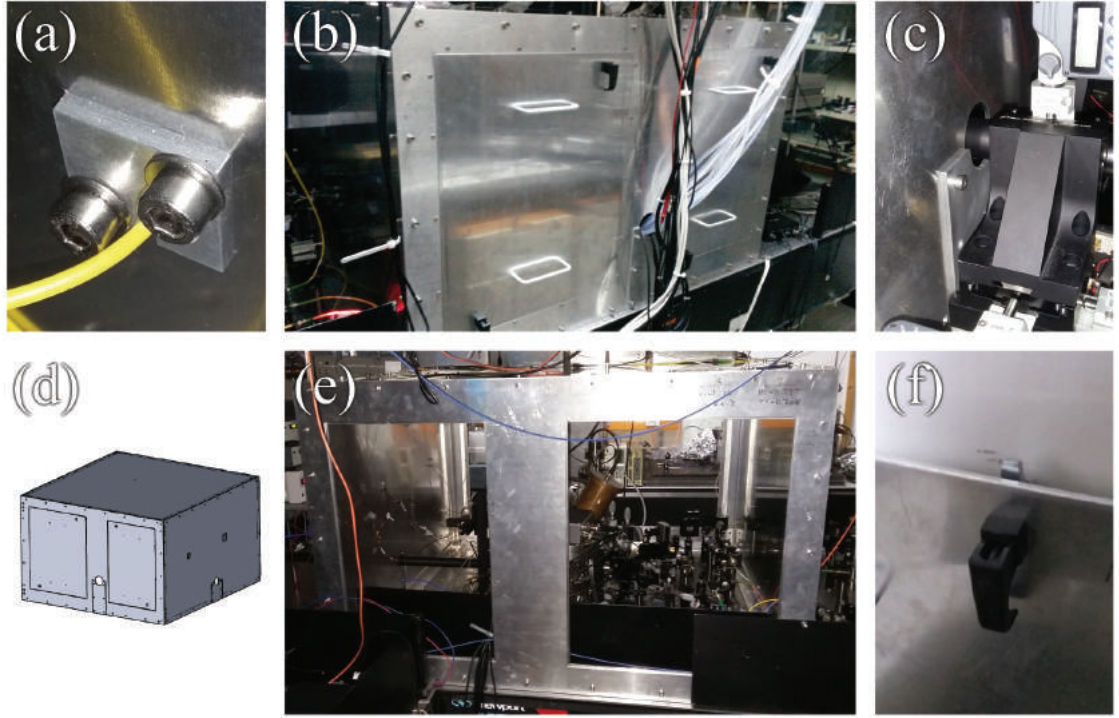


Figure 2.4: Pictures of the Faraday cage that was constructed around the Blade trap experimental setup. **(a)** - An optical fibre feed-in on the outer edge of the cage. **(b)** - The back of the cage with both removable panel/doors in place. Between them sits the feed-in for the water cooling tubes. **(c)** - A hole for the imaging tube on the side of the cage. **(d)** - A technical drawing of the completed cage showing the water cooling and imaging tube holes. **(e)** - The front view of the cage with all removable panel/doors open showing the vacuum system inside the cage. **(f)** - A “lift and turn” compression latch which secures a removable panel/door in place via the inner rim of the cage openings.

of the Faraday cage. The diameters of these holes are 3.5 mm for each laser fibre, 4.5 mm for a microwave cable, 5 mm for the current wires to the coils, 50 mm for the imaging tube, and 60 mm for the water cooling tubes. A study in 2002 by F.J. García de Abajo showed that when the radius of a hole in a metal sheet is a tenth of the wavelength of the incident radiation, the hole is effectively blocked [58]. This attenuation increases with a higher ratio of the thickness of the material to the radius of the hole in it. The results obtained by García allow one to determine the minimum wavelength that is attenuated by less than 99.9 percent.

Using García’s results as a reference, the smaller holes should sufficiently attenuate any radiation that may interfere with the experiment as the cut-off frequencies are much higher than those used in our experiments, however, the larger holes will only attenuate RF and not any noise at the 12.6 GHz microwave frequency used to manipulate our qubit subspace. This could understandably cause interference with our experiment, however, the smaller 25 mm radius imaging tube hole has the 12.7 mm radius imaging tube within

it which is also made of aluminium. This is likely to greatly reduce the effective hole radius and thus highly attenuate or reflect any incoming microwave radiation. The 30 mm radius hole contains the PVC tubing for the water cooling to the compensation coils. Though the conductive hole size remains the same, this can be broken into 4 mm radius holes by wrapping each tube in aluminium foil and packing the hole in order to block incoming radiation. In addition to the external Faraday cage, the vacuum system is grounded creating an additional Faraday cage in its own right as previously mentioned. This combination of shields should be sufficient in blocking incoming electromagnetic radiation in the frequency range that is likely to interfere with our coherent manipulation experiments.

On installation of the cage, an internal probe connected to an external spectrum analyser showed that with the main removable panels of the Faraday cage in place, the drive RF used for trapping on other experiments in the lab was no longer visible in the electromagnetic spectrum, verifying the performance of the cage<sup>5</sup>. This said, with the cage closed, a significant temperature increase of around 7 °C was observed causing concern for the lifetime of internal apparatus, particularly the microwave amplifiers. These were moved to outside the cage making the current coils the main source of heating inside, though the currents in these coils had already been minimised using large external permanent magnets. Though water cooling would further minimise the heating inside the cage, due to the risk of leaks, this was not reinstated. It was decided that the Faraday cage would remain partially open at all non-crucial times by removing two of the access panels, unfortunately drastically reducing its effectiveness. Development of sufficient cooling methods has been investigated but a viable solution is yet to be permanently installed.

### 2.2.2 Anomalous RF coupling and the Theremin effect

In addition to these main sources of electromagnetic noise, another very low frequency effect that we noticed was that if one held their hand close to the helical resonator that couples the RF to the trap, the ion(s) moved with proximity of the hand to it. This effect was originally observed and addressed prior to installation of the Faraday cage, but would likely remain if one were to adjust laser optics within the cage if left untreated. Any unwanted movement of the ion will cause the magnetic field sensitive transition frequencies to change which is a problem for high fidelity operations. Though it is not expected that one would be moving their hand near the resonator during an experiment, it is still

---

<sup>5</sup>When the cage was open, the trapping RF from other experimental setups was still observed, as before its installation.

important to address this issue.

This effect is reminiscent of the early electronic musical instrument, the theremin. Its inventor, Léon Theremin, had observed an alteration of the resonant frequency of RF circuits depending on his proximity to them. By mixing this detuned RF with a constant RF carrier, the beat frequency was in the audio range and could thus be used for making music. Though the theremin itself is not too relevant to our discussion, the theory of its operation can help us understand and quantify the effects that we observed at the unshielded feedthrough of the RF to the vacuum system.

I hypothesised that with one's hand in close proximity to the RF feedthrough of the vacuum system, the capacitance between the RF line and ground was changed, causing a detuning of the resonant frequency of the system with respect to the RF resonator which results in a change in RF voltage on the trap electrodes. This would cause a shift in the ion position in the presence of poor micromotion compensation or if the trapping RF becomes sufficiently low. Aside from the resonator and vacuum system (which includes the trap and the internal wiring), there are two other easily identified sources of capacitance in this setup that are unwanted, namely the capacitance due to the feedthrough and additional capacitances from Theremin effects. The latter can be split into two terms; the capacitance between the exposed part of the feedthrough and infinity with no close dielectric object,  $C_A(\infty)$ , and the capacitance to ground in the presence of one's hand,  $\Delta C_A$ .

The high voltage external feedthrough consists of two cylindrical prongs that are 50 mm long and 2.1 mm in diameter which are both barrel connected to the bottom pins of the resonator, one of which floats at high RF voltage. This is face separated by 10.5 mm from its grounded counterpart, however, since this by definition should be held at ground, I will operate on the assumption that there is only one RF “antenna” when calculating Theremin effects. For simplicity, I will assume that this antenna is oriented above an infinite ground plane with no surrounding objects bar the hand. Though the feedthrough has a lot of grounded objects around it and is very far from this infinite case, it is useful to consider the simplest scenario when calculating the capacitance resulting from a nearby hand.

$C_A(\infty)$  is implicit in the measured properties of the resonator as the resonator is characterised when connected to the experiment. What is important to note is how a hand modifies the circuit in order to change its resonant frequency. When there is a hand near to the feedthrough,  $C_A(\infty)$  is modified by  $\Delta C_A$  which assumes the hand is an infinite ground plane and the capacitance is that between the real antenna and an image antenna

past this ground plane. This is given by [59]:

$$\Delta C_A \approx \frac{\pi \epsilon_0 l}{10 \log\left(\frac{4x}{d}\right)} \quad (2.2)$$

where  $\epsilon_0$  is the permittivity of free space,  $l$  is the length of the antenna,  $d$  is the diameter of the antenna, and  $x$  is the distance of the feedthrough from one's hand, with 10 as a reduction factor to compensate for the non-infinite nature of a hand. This reduction factor was determined by Kenneth D. Skeldon in order to match theremin theory calculations to its operation in practice [59]. At  $x = 10$  cm, this achieves  $\Delta C_A \approx 0.026$  pF. This can be viewed as a worst case scenario as the feedthrough is surrounded by other grounded equipment and other imperfections from the single antenna above an infinite ground plane scenario on which these calculations are based. Nevertheless, it will be shown that the capacitance alteration calculated here produces an effect that is comparable to what we have observed in the lab.

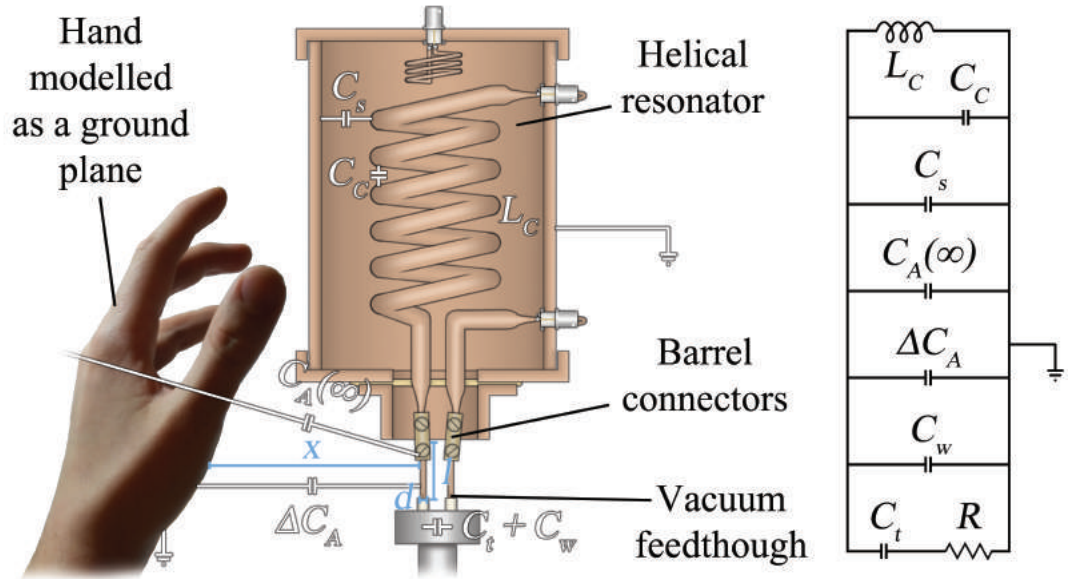


Figure 2.5: An illustration showing the capacitance terms that determine the resonant frequency of the resonator and the dimensions used in order to calculate the Theremin effect alterations. An equivalent schematic is shown to the right of this illustration; the additional  $R$  term denotes the total resistance of the resonator which is used in the calculation of the quality factor  $Q$ .

The resonant frequency of a helical resonator is described in Dr James D. Sivers' paper [37];  $C_s$ ,  $C_t$ ,  $C_w$ , and  $C_c$ , are the shield, trap, connecting wires/feedthrough, and coil self capacitances respectively [37] and the resonant frequency of the resonator,  $\Omega$  can be found using [37]:

$$\Omega = \frac{1}{\sqrt{(C_s + C_t + C_w + C_C)L_C}} \quad (2.3)$$

where  $L_C$  is the inductance of the coupler coil and  $C_A(\infty)$  is implicit in these capacitance terms. The origin of each capacitance term considered are shown in Figure 2.5 with the inclusion of those responsible for the Theremin effect. The total capacitance of our resonator was measured to be  $17 \pm 2$  pF with a resonant frequency of  $\Omega = 2\pi \times 21.895 \pm 0.010$  MHz [41], corresponding to a coil inductance  $L_C \sim 3.11$   $\mu$ H.

By modifying the capacitance term by adding  $\Delta C_A$ , we get a modified resonant frequency  $\Omega' = 2\pi \times 21.878$  MHz, a difference of  $2\pi \times 16.7$  kHz. As noted in Chapter 1, the helical resonator will also have an associated  $Q$  which will determine the band-pass filtering properties of the resonator and is given by [37]:

$$Q = \frac{1}{R} \sqrt{\frac{L}{C}} \quad (2.4)$$

where  $R$  is the resistance of the resonant circuit,  $L = L_C$ , and  $C$  is the total capacitance of the resonant circuit. The  $Q$  of this resonator was measured to be  $447 \pm 28$  [41]. One can determine the modification of  $Q$  with  $\Delta C_A$  using:

$$\frac{Q'}{Q} = \sqrt{\frac{C}{C + \Delta C_A}} \quad (2.5)$$

This gives a modified quality factor  $Q' \approx 446.65$  which is within the error of the original  $Q$ . The bandwidth at half the height of the resonance peak, is given by  $\Delta f = \frac{f_0}{Q}$  where  $f_0$  is the peak frequency. For 21.985 MHz,  $\Delta f = 49.0$  kHz (24.5 kHz either side of resonance) which is slightly less than three times the resonance shift caused by one's hand. Assuming that the resonance peak follows a Lorentzian or Gaussian profile, this would correspond to power drop of 30.8 percent or 26.5 percent respectively for a resonant trapping RF. If the trap is operating at "low" RF for the purpose of the trapping, this shift is likely to be enough to cause some movement of the ion, especially when micromotion is not adequately compensated. Additionally, if one were to move their hand closer to the exposed feedthrough, the detuning would increase resulting in a further drop in the RF voltage that reaches the trap. Despite the assumptions and simplifications made to this model, this hypothesis provides a plausible explanation of the phenomenon seen in the laboratory.

A solution to this was found by making sure that the RF line was fully shielded from the resonator to the vacuum system in order to prevent any unintended modification to

the RF coupling from external movement of objects with a connection to ground. In order to do this, I designed a modification to the bottom of the resonator which shields the RF up until the feedthrough on the vacuum system as illustrated in Figure 2.6. This piece is held at ground and extended the shielding of the resonator and vacuum system as far as the RF supply. Additionally, by using wire connections between the resonator and the feedthrough pins, disconnection/removal of the resonator is now much easier than before. Following installation of this piece, there have been no further observations of the Theremin effect within our experimental setup meaning that the ion movement is now much more decoupled from the surrounding lab environment. This should improve offset based transition frequency drift when performing coherent manipulation operations.

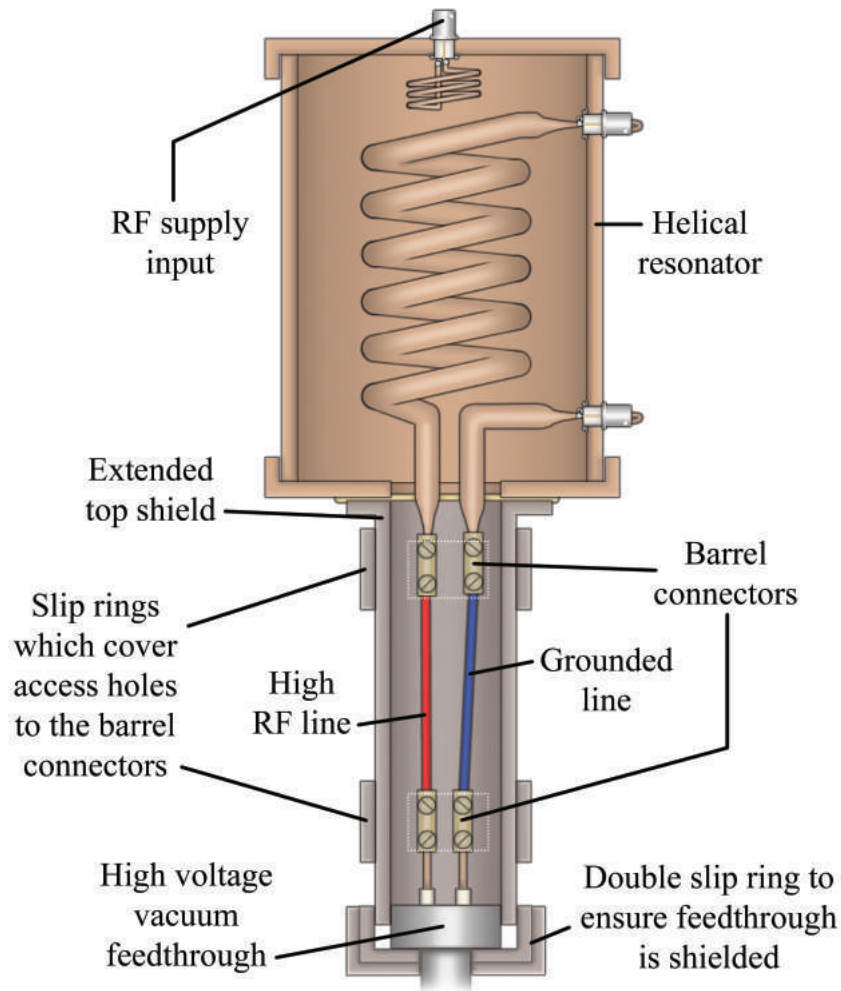


Figure 2.6: A cut-through illustration of the modification fitted to the resonator in order to shield the trap RF from external coupling between the resonator and the feedthrough. Two wires were added between the resonator and feedthrough pins in order to minimise mechanical stress on the feedthrough ceramic seal. Slip rings cover access holes to the barrel connectors and encase in the feedthrough in order to complete the shield.

### 2.2.3 Minimisation of microwave intermodulations

The last problem I will discuss that may lead to loss of fidelity concerns the generation of the many RF and microwave fields that are required for gate operations. In our experimental setup, microwave fields are generated by combining multiple pure tones generated by the DDS boxes in the low frequency ( $\sim 100$  MHz) regime, which are then mixed with a microwave source to upconvert to  $\sim 12.6$  GHz, and then amplified. Both mixing and amplification are non-linear processes, so intermodulations occur; these are the sums and differences of the individual frequencies present, including their harmonics. The amplitudes of the intermodulations are dependent on the characteristics of the mixer (or amplifier), the intermodulation order, and the original input powers of each signal.

A mixer takes in a carrier signal  $f_c$  and one or several modulator signals  $\Sigma f_i$  with the aim of outputting the carrier plus or minus each of these modulators, i.e.  $f_c \pm \Sigma f_i$ . This allows a single microwave source to be used to generate all required microwave frequency signals. However, typically it is only these first order terms that are desired, but higher order terms of many modulators are also created which becomes a problem as off-resonant fields for a given coherent manipulation pulse may affect the desired operation by driving another transition. Similarly, amplification through a non-linear medium will output all the input frequencies with the addition of these intermodulations and harmonics of the original combined signal. Examples of the higher order terms are shown in Figure 2.7 for two frequencies  $f_1$  and  $f_2$ .

1 <sup>st</sup> Order	2 <sup>nd</sup> Order	3 <sup>rd</sup> Order	...
$f_1$	$f_1 + f_2$	$2f_1 + f_2$	
$f_2$	$f_1 - f_2$	$2f_1 - f_2$	
	---	$2f_2 + f_1$	
	$2f_1$	$2f_2 - f_1$	
	$2f_2$	---	
		$3f_1$	
		$3f_2$	

Figure 2.7: An example of some of the intermodulation frequencies created when two signals with frequency  $f_1$  and  $f_2$  are mixed or amplified in a non-linear medium. The  $n^{\text{th}}$  order contains the sums and differences of  $n$  frequencies including the  $n^{\text{th}}$  harmonics of the original signals. “- -” denotes a complete set of peaks for a set of  $n$  frequencies in an order. “...” denotes that there are many more terms that are not shown in this diagram.

An ideal mixer mixing  $f_1$  and  $f_2$  with  $f_c$  outputs four tones,  $f_c \pm f_1$  and  $f_c \pm f_2$ . In practice, higher order tones are present; though the (unwanted additional) second

order tones are not so important as they are far from the frequency band of the ion, the third order tones are problematic. One can calculate the expected amplitude of the intermodulations for the mixer (or amplifier) that is intended to be used. A mixer is specified with a certain parameter known as the “two-tone, third-order input intercept point” (IP3), a theoretical point (outside of the operating range of the mixer) at which the third-order intermodulations are equal in power to the carrier and modulator signals<sup>6</sup>. The conversion loss is the reduction in the input signal power as it goes through the mixer. Another parameter that the mixer is specified with is the 1 dB compression point, the point at which this conversion loss increases by 1 dBm. This results in a 1 dB reduction in the sideband output power as the input power to output power relationship starts to become non-linear.

An estimation of the output power of the intermodulations in dBm is given by the following equation [60]:

$$P_{\text{out}} = (I_p + Z_c) - O_r(I_p - P_{\text{in}}) - C \quad (2.6)$$

where,  $P_{\text{out}}$  is the power of the intermodulations referenced to the output,  $I_p$  is the IP3 of the device,  $Z_c$  is the 1 dB compression point of the device,  $O_r$  is the order of the intermodulation, i.e. the numbers of single input frequencies that are added/subtracted from each other as shown in Figure 2.7,  $P_{\text{in}}$  is the input power of the frequencies to be mixed, and  $C$  is the conversion loss, all measured in dBm. In order to get the intermodulation power referenced to the input, do not subtract the conversion loss. This is a relatively simple equation and only assumes equal input amplitudes of the signals to be mixed, however, this still allows one to select a mixer or amplifier and the input power to such a device in order to minimise the intermodulation powers at the output.

Figure 2.8 shows an example spectrum of our 12.6 GHz carrier mixed with three RF modulator signals of 10 MHz, 24 MHz, and 27 MHz when the IP3 of the mixer is +15 dBm and all four signals are mixed at an input power of -2 dBm. From Equation 2.6 one can see that with a lower input power and/or higher IP3, the intermodulations become increasingly suppressed. Knowing this, one can choose an acceptable input power for signals being mixed or amplified by a given mixer or amplifier so that the power of intermodulations close to the ion transition frequencies are at the same level as the background electrical

---

<sup>6</sup>This point is measured by applying an input signal in the normal operating range of the device and measuring the power of the third order intermodulations of that signal. This is done for several input powers after which two linear fit lines are extended (linearly) for the input signals and the intermodulations until they intersect. This point is the IP3 of the device.



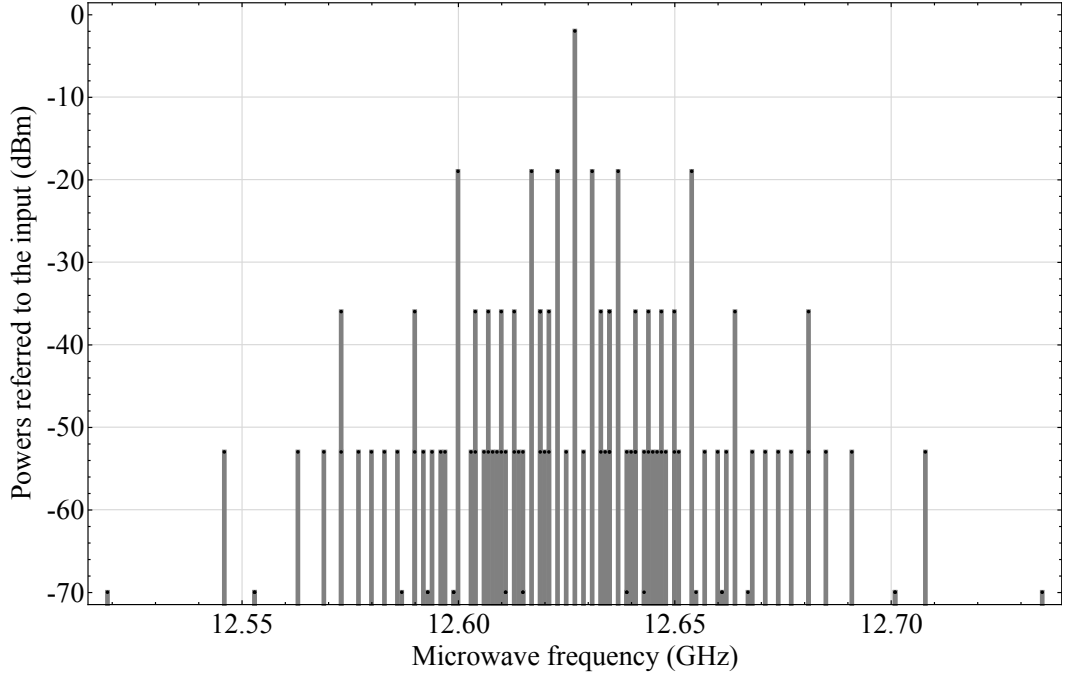


Figure 2.8: An example spectrum of our  $\sim 12.6$  GHz carrier mixed with three RF modulator signals of 10 MHz, 24 MHz, and 27 MHz using Equation 2.6. The IP3 of the mixer is +15 dBm, the 1 dB compression point is at 0 dBm, and all four signals are mixed at an input power of -2 dBm. To clarify the spectrum, the band-width of each peak, carrier suppression, and harmonics of the carrier have been ignored. These powers are referred to the input, thereby ignoring the conversion loss.

noise in the lab, otherwise known as the noise floor. In reality this is generally a trade-off which produces some third-order intermodulations at low amplitudes but still well above the noise floor. This means that one must be extremely careful when selecting the frequencies required to address certain transitions. Problems occur when multiple frequencies are used simultaneously and an intermodulation of those frequencies coincides with a transition on the ion that one is not aiming to address. Additionally one may not notice when an intermodulation is driving a transition due to its reduced power. However, if an intermodulation coincides with a transition and it is driven for a long enough time, the ion will still experience some unintended population transfer and therefore the fidelity of the intended operation will be reduced. As mentioned in Chapter 1, in order to minimise this risk, the 12.6 GHz supply is negatively offset from the hyperfine splitting by 100 MHz and a bandpass filter is used to suppress all negative sidebands so that only the positive sidebands of the microwaves are used to address transitions. Although it is unlikely that one would coincidentally use several tones which result in an intermodulation close to a transition, one must still be careful when selecting the frequencies to be mixed and check to ensure that such intermodulations are not present. This is most easily done by using a

small probe, such as an open coaxial cable, fed to a spectrum analyser and checking that no peaks coincide with each other when each channel of a DDS is switched on or off.

The appropriate cabling must also be used in order to make the most efficient use of a microwave setup. Use of the wrong cable or connector type can result in drastic loss of power between devices in the signal chain. This is important as it means that the amplifiers can be used further from their 1 dB compression point in order to maintain the required signal power with low intermodulation power. In general, SMA connectors should be used which are tightened to the specified level using an SMA torque-wrench for optimum signal transfer. One should also minimise the connection distance between components of the RF and microwave setup, particularly between the final amplifier and emitter since losses in microwave power are greater per unit length of cable than for RF.

## 2.3 Bare state ion manipulation

All coherent manipulation of the  $^{171}\text{Yb}^+$  ion is done within the ground state  $^2\text{S}_{1/2}$  manifold. The four states are distinguished by their quantum numbers  $F$  and  $m_F$ , however, for brevity we relabel the states as follows:  $|F = 0, m_F = 0\rangle \equiv |0\rangle$ ,  $|F = 1, m_F = -1\rangle \equiv |-1\rangle$ ,  $|F = 1, m_F = 0\rangle \equiv |0'\rangle$ , and  $|F = 1, m_F = +1\rangle \equiv |+1\rangle$ , where we detect the  $F = 0$  state as “dark” and the  $F = 1$  states as “light”. The labelling of these states is shown in Figure 2.9.

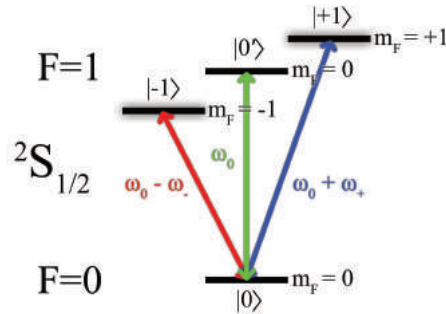


Figure 2.9: The “bare state” basis within the ground state  $^2\text{S}_{1/2}$  manifold. The ion can be transferred between the  $F = 0$  and  $F = 1$  levels using microwave radiation.

In Section 2.4 I discuss dressing these states using microwave fields to form the dressed state manifold. For all operations prior to this, dressing fields are not applied and the hyperfine manifold is referred to as the bare-state manifold.

### 2.3.1 Rabi flopping and coherence time

One can perform coherent manipulation operations on an ion by applying microwave or RF radiation. A microwave or RF pulse to the ion whose photon energy  $\hbar\omega$  matches the energy difference between a pair of states in the ion will cause the state of the ion to oscillate between these two states. The frequency at which these spin flips (also known as Rabi-flopping) occur is called the Rabi frequency, which is given by [24]:

$$\Omega_0 = -\frac{\langle \uparrow | \boldsymbol{\mu} \cdot \mathbf{B}_0 | \downarrow \rangle}{\hbar} \quad (2.7)$$

where  $\boldsymbol{\mu} = \frac{2\mu_B}{\hbar} \mathbf{S}$  is the magnetic dipole operator,  $|\uparrow\rangle$  and  $|\downarrow\rangle$  are the two states in question,  $\mathbf{S}$  is the electronic spin angular momentum, and  $\mathbf{B}_0$  is the vector magnitude of the magnetic field of the radiation used to drive the transition. The population in the  $|\uparrow\rangle$  state of a two level system initially in  $|\downarrow\rangle$  after driving it for a time,  $t$ , with radiation at a detuning  $\delta = \omega - \omega_0$  from the transition is given by [24]:

$$P_{\uparrow}(t, \delta) = \frac{\Omega_0^2}{\Omega_{\delta}^2} \sin^2 \left( \frac{\Omega_{\delta} t}{2} \right) = \frac{\Omega_0^2}{2\Omega_{\delta}^2} (1 - \cos(\Omega_{\delta} t)) \quad (2.8)$$

where,  $\omega$  is the (angular) frequency of the radiation being used to drive the transition of energy  $\hbar\omega_0$  and  $\Omega_{\delta} = \sqrt{\Omega_0^2 + \delta^2}$  [24].

Using microwave radiation at frequencies close to  $\sim 12.6$  GHz, Rabi flopping can be driven between  $|0\rangle$  and  $|-1\rangle$ ,  $|0'\rangle$ , or  $|+1\rangle$ . The Rabi frequencies of each of these transitions are dependant on the polarisation of the microwaves as well as the microwave power, and will be stated less generally later in this section. Figure 2.10 shows a Rabi flop between  $|0\rangle$  and  $|0'\rangle$ .

For a pulse length of 0, the population is in  $|0\rangle$  as this is the initially prepared state. After a pulse of  $\sim 375 \mu\text{s}$ , there is equal population in  $|0\rangle$  and  $|0'\rangle$  giving us a superposition of the two which can be written as  $\frac{1}{\sqrt{2}}(|0\rangle + |0'\rangle)$ . After  $\sim 750 \mu\text{s}$ , the population has been transferred to  $|0'\rangle$ . This time is half the period of a full Rabi oscillation and is hence known as the  $\pi$ -time, the time taken to perform a quantum bit flip in a two-level system. The Rabi frequency of the driving field is given by  $\Omega_0 = \frac{2\pi}{t_{2\pi}}$  where  $t_{2\pi}$  is the  $2\pi$ -time. For this case,  $\Omega_0 = 2\pi \times 679$  Hz.

This Rabi flop can be performed experimentally using the following pulse sequence:

- \*Cool the ion(s).
- \*Prepare the ion(s) in  $|0\rangle$ .

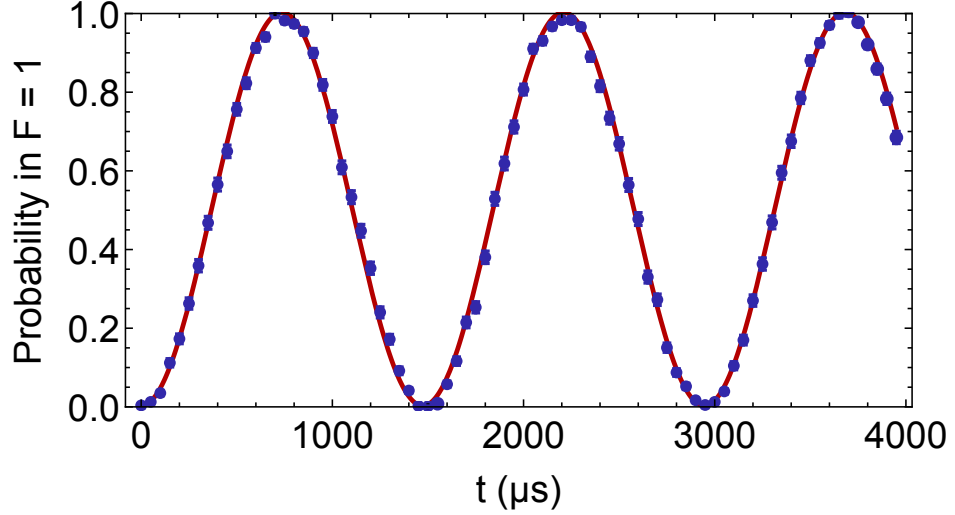


Figure 2.10: Rabi flopping between  $|0\rangle$  and  $|0'\rangle$ . Since the splitting between these two states is first-order insensitive to magnetic field fluctuations, the coherence time is on the order of hundreds of milliseconds, good for coherent manipulation operations. However, since this state is magnetically insensitive, this also means that operations are limited as it feels very little coupling to the ion motion in the presence of a static magnetic field gradient. For the purpose of this thesis, unless otherwise stated, data points will be shown in blue and a theory curve for the operation will be shown in red. In this case, the theory curve is fit to Equation 2.8 with  $\delta = 0$  and  $\frac{\Omega_0}{2\pi} = 679.0(4)$  Hz. This figure is altered from that shown in the thesis of Dr Joseph Randall [24].

- <sup>+</sup>Apply a fixed frequency microwave pulse resonant with the  $|0\rangle$  to  $|0'\rangle$  transition of the ion and scan the pulse length, increasing it with each step of the experiment.
- \*Make a detection measurement on the ion(s).

Here, I have marked a \* on steps of the experiment that are common to most pulse sequences; <sup>+</sup> denotes the main pulse that defines the experiment. From this point onwards, when discussing any experiments in this chapter, I will assume the common pulses (cool  $\rightarrow$  prep, detect) envelope the main experimental pulse <sup>+</sup> that is described.

Driving Rabi oscillations for long pulse times can help us to determine the coherence time of a qubit formed from a pair of states. The coherence time is the time that oscillations between a pair of states can be driven before the operation fidelity becomes significantly reduced. For the magnetically sensitive states this is due to magnetic field noise around the experiment which causes dephasing of superpositions of the states [24]. This decoherence causes the contrast of a Rabi flop to decay exponentially with time. One can determine the coherence time of the qubit to be the time at which the amplitude of oscillation between the two states has decayed to  $\frac{1}{e}$  of the original amplitude. If driven for a long enough time past this coherence time, the probability of being in either state will be 50 percent and the amplitude of the Rabi oscillations will be reduced to zero about this central probability.

This effect can be seen on a Rabi flop between  $|0\rangle$  and the magnetic field sensitive state  $|+1\rangle$  as shown in Figure 2.11. The population in  $|\uparrow\rangle$  after preparing in  $|\downarrow\rangle$  can be found to be [24]

$$P_{\uparrow}(t) = \frac{1}{2} \left[ 1 - e^{-\frac{\Gamma t}{2}} \left( \cos \left( \frac{\Omega_{\Gamma} t}{2} \right) + \frac{\Gamma}{\Omega_{\Gamma}} \sin \left( \frac{\Omega_{\Gamma} t}{2} \right) \right) \right] \quad (2.9)$$

where  $\Omega_{\Gamma} = \sqrt{4\Omega_0^2 - \Gamma^2}$  and  $\Gamma = \frac{1}{T_2}$  where  $T_2$  is the coherence time of the operation.

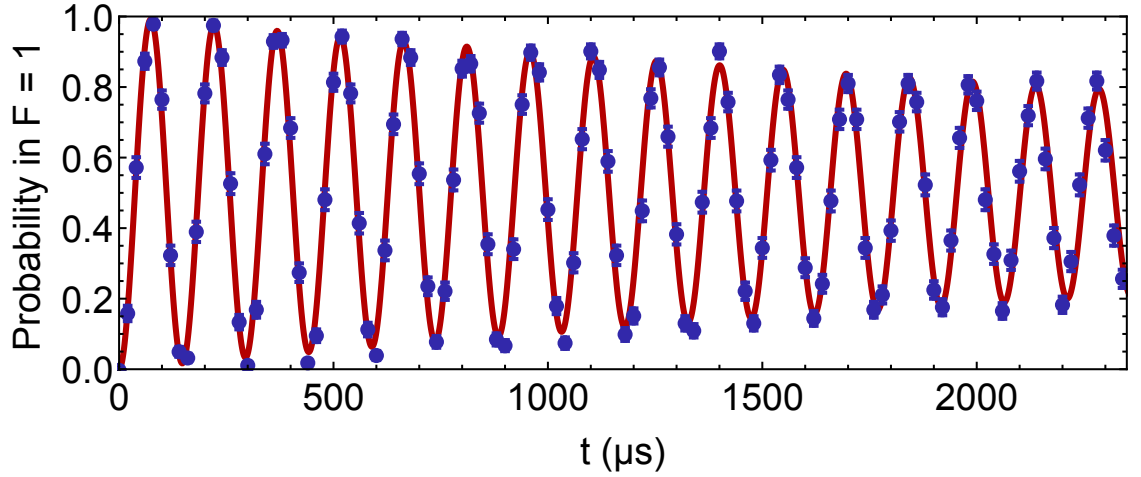


Figure 2.11: Rabi flopping between  $|0\rangle$  and  $|+1\rangle$ . The theory curve is fit to Equation 2.9 for  $\frac{\Omega_0}{2\pi} = 6.783(2)$  kHz and  $T_2 = 2.2(1)$  ms. Since  $|+1\rangle$  is extremely sensitive to magnetic field fluctuations, the coherence time is much shorter than the Rabi-flop shown in Figure 2.10 between  $|0\rangle$  and  $|0'\rangle$ . This severely limits the time one is able to perform operations using this state or its motional sidebands. This figure is altered from that shown in the thesis of Dr Joseph Randall [24].

As previously noted, the Rabi frequency is proportional to the magnetic field strength of the microwave radiation, however, the Rabi frequencies in order to drive population from  $|0\rangle$  to  $|0'\rangle$ ,  $|-1\rangle$ , and  $|+1\rangle$  are each dependent on different polarisations of this microwave magnetic field in order to drive the transition. Since the magnetic field of the microwaves couples to the magnetic moment of the electron via a dot product, as shown in Equation 2.7, this means that for each of the different states, the required microwave magnetic field polarisation will be different in order to get the highest Rabi frequency for a given transition as the angular momentum of the electron, and therefore the magnetic moment, is different. The Rabi frequencies  $\Omega_-$ ,  $\Omega_\pi$ , and  $\Omega_+$  for oscillations between  $|0\rangle$  and  $|-1\rangle$ ,  $|0'\rangle$ , and  $|+1\rangle$  respectively of the hyperfine manifold of  $^{171}\text{Yb}^+$  were derived in the thesis of Dr Anastasiya Khromova and are given by [47]:

$$\Omega_- = -\sqrt{2}\frac{\mu B}{\hbar}B_-e^{-i\phi_-} \quad (2.10)$$

$$\Omega_\pi = \frac{\mu B}{\hbar}B_\pi e^{-i\phi_\pi} \quad (2.11)$$

$$\Omega_+ = \sqrt{2}\frac{\mu B}{\hbar}B_+e^{-i\phi_+} \quad (2.12)$$

where,

$$B_-e^{-i\phi_-} = \frac{1}{2}(B_xe^{-i\phi_x} + iB_ye^{-i\phi_y}) \quad (2.13)$$

$$B_\pi e^{-i\phi_\pi} = B_z e^{-i\phi_z} \quad (2.14)$$

$$B_+e^{-i\phi_+} = \frac{1}{2}(B_xe^{-i\phi_x} - iB_ye^{-i\phi_y}) \quad (2.15)$$

where  $B_\pi$ ,  $B_-$ , and  $B_+$  are the amplitudes of the driving magnetic field linearly polarised in the  $z$ -direction and left/right-hand circularly polarised in the  $x - y$  plane respectively to the static magnetic field that the ion sits in which forms the quantisation axis in  $z$  (in this example).  $\phi_\pi$ ,  $\phi_-$ , and  $\phi_+$  are the phases of these fields and  $B_x$ ,  $B_y$ , and  $B_z$  are the three orthogonal components of the magnetic field of the microwaves in three-dimensional space. One can therefore see from these equations that in order to drive all three transitions to  $F = 1$  in the  $^2S_{\frac{1}{2}}$  manifold, the qubit manipulation fields must have components in all three directions. For a quantisation axis defined by a magnetic field oriented parallel to the  $z$ -direction, parallel microwave magnetic field polarisation components will drive population transfer from  $|0\rangle$  to  $|0'\rangle$ , and circularly polarised perpendicular components will drive population transfer from  $|0\rangle$  to  $|-1\rangle$  and  $|0\rangle$  to  $|+1\rangle$ . Additionally, circularly polarised perpendicular components of the coherent manipulation RF fields are required in order to drive population transfer from  $|0'\rangle$  to  $|-1\rangle$  and  $|0'\rangle$  to  $|+1\rangle$ . This means that the orientations of the microwave horn and RF coil are extremely important in order to get sufficient balancing of Rabi frequencies for the required transitions. This will be discussed in detail in Chapter 4 for the microwave and RF setups used in the new experiments as the quantisation axis due to the static magnetic field is very different from that used in the Blade trap experimental setup.

In order to find the transition frequency for a pair of states in order to perform Rabi flopping, we must first perform a scan over the ion in frequency space using a constant pulse time for each step of the experiment. If the frequency is resonant with a transition, we should see some population transfer from the initial state, usually  $|0\rangle$ , to one of the

$F = 1$  states if using microwave radiation. If the pulse time is equal to the  $\pi$ -time of the transition then maximum population transfer will occur at the transition frequency. Population transfer will also happen at a small detuning from the transition due to off-resonant coupling. The probability that off-resonant radiation will transfer the ion from the initial state to the final state can be shown by Equation 2.8 as a function of the detuning; this produces a peak at the transition frequency with smaller sidelobes due to off-resonant excitation. This equation also indicates that the higher the transition Rabi frequency, which can be equated to the microwave power, the greater the width of the transition. If two transitions are close to each other, the Rabi frequencies must be small enough to resolve both peaks in order to minimise crosstalk between the transitions, i.e. the width of each peak must be much smaller than their frequency separation.

Figure 2.12 shows a scan of the  $|0\rangle$  to  $|+1\rangle$  transition frequencies for a pair of ions in a magnetic field gradient. This gradient means that each ion sits in a different magnitude of magnetic field and thus they each have a different Zeeman splitting of their  $F = 1$  states. The transition peaks are well defined because the Rabi frequency of each transition is much lower than their separation in frequency space. This means that there is minimal crosstalk between ions if one decides to drive one ion to  $|+1\rangle$  while leaving the other in  $|0\rangle$ . This demonstrates how the magnetic field gradient allows for individual addressing of multiple ions using microwave radiation.

The spatial separation of the ions is determined by the axial secular frequency, which can be measured extremely accurately and the differences in magnetic field determined from the frequency separation of the two transitions. However, over the course of a single scan of the transition frequencies for both ions, the ions can drift axially in the trap due to very low frequency noise on the DC endcap electrodes. This means that a single scan is an inaccurate way to measure the frequency separation because the transition frequencies will change over the course of the scan as the ions drift in the gradient. A more accurate measurement of the frequency separation of the ions can be done by performing a near-simultaneous scan over the transition frequencies for each ion separately and interleaving the measurements. This allows us to determine the transition frequencies for each ion to within a single step of the experiment where any drift is likely to be negligible. These frequencies can then be used to determine the magnetic field gradient more accurately than using the method described in Chapter 1. The magnetic field gradient was measured using this method to be 23.3(6) T/m.

Rabi flopping can also be performed between  $|0'\rangle$  and  $|-1\rangle$  or  $|+1\rangle$  using RF radiation.

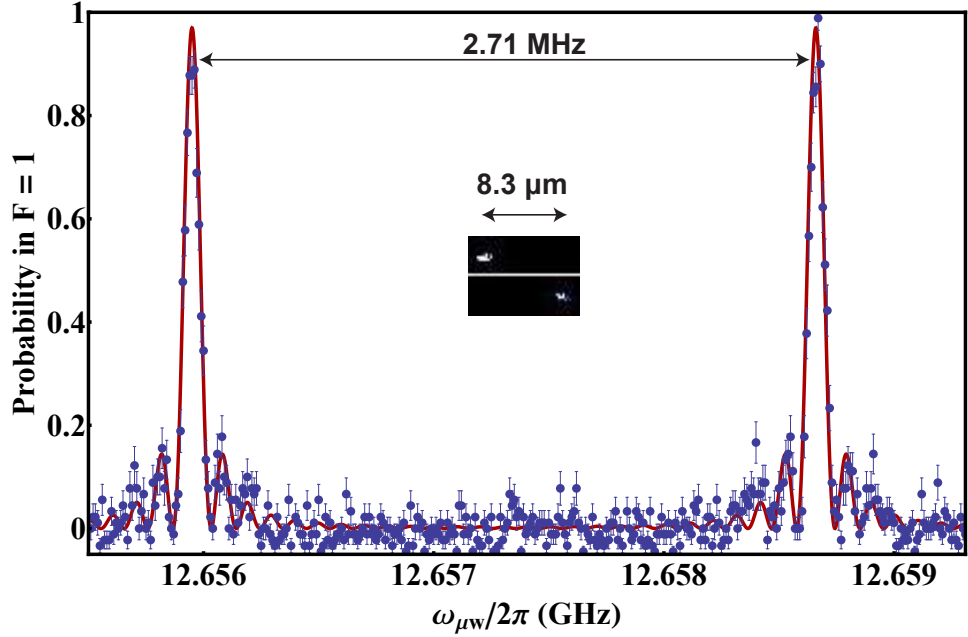


Figure 2.12: Individual addressing of each ion through the  $|0\rangle$  to  $|+1\rangle$  transition with a different splitting from  $|0'\rangle$  due to the static axial magnetic field gradient. The crosstalk of the probability distributions for the population transfer to  $F = 1$  for each ion is  $10^{-4}$  demonstrating near-perfect individual addressability [61]. The inset picture shows the individual illumination of each ion by closing the  $^2S_{1/2}$  portion of their cooling cycles using the two different microwave transition frequencies shown on the main graph. The left peak corresponds to the left ion and the right peak corresponds to the right ion. This figure is directly taken from the paper on spin-motion entanglement of which I am co-author [18].

This operation is used to measure the RF Rabi frequency which is important when it comes to characterising the dressed states which will be discussed later in this chapter. Since both of these states are in  $F = 1$ , this means that a more complex pulse sequence must be used in order to differentiate between what have only considered to be “light” states up to this point. This can be done by applying a  $\pi$ -pulse to transfer the ion from the initial state  $|0\rangle$  to  $|0'\rangle$ . This is then followed by an RF pulse, for example, resonant with the transition  $|0'\rangle$  to  $|+1\rangle$  with increasing pulse time for each step of the experiment. After this, one can apply a  $\pi$ -pulse resonant with  $|0\rangle$  to  $|0'\rangle$  which causes any population in  $|0'\rangle$  to be transferred back to  $|0\rangle$  and thus will be seen as “dark” by the detection pulse. As population is transferred to  $|+1\rangle$ , more population will remain in  $F = 1$  after the  $\pi$ -pulse, thus a “light” state will be detected by the final pulse. A frequency scan will also return the splitting of  $|+1\rangle$  and  $|-1\rangle$  from  $|0'\rangle$  using this method, which, as discussed in Chapter 1, will be different due to the non-linear Zeeman effect.



### 2.3.2 Resolving motional sidebands

As discussed in Chapter 1, the magnetic field gradient provides a coupling between the secular motion of the ion and its internal state. As with the effect demonstrated during a Stern-Gerlach experiment, a static magnetic field gradient exhibits a force on the magnetic dipole of particle which is dependent on the spin state. In our experiment, this corresponds to a “momentum kick” [17] [50] as the ion is transferred from  $|0\rangle$  or  $|0'\rangle$  to  $|-1\rangle$  or  $|+1\rangle$ . This force forms the basis of entanglement operations using trapped ions as it allows a change of the internal state of the ion to affect its motion. As previously discussed, for microwave operations, this force is directly proportional to the effective Lamb-Dicke parameter  $\eta_{\text{eff}}$ , which is proportional to the magnetic field gradient; a stronger motion to spin state coupling and therefore faster operations can be realised by implementing much larger magnetic field gradients. In addition to this, the faster a gate is performed, the smaller the error associated with decoherence and therefore the higher the operation fidelity. Methods of creating much larger gradients than realised in this experimental setup will be discussed in detail in Chapter 3.

This coupling of the ion motion to its internal states manifests itself as sidebands on the  $|0\rangle$  to  $|-1\rangle$  and  $|0\rangle$  to  $|+1\rangle$  transitions. If one applies microwave radiation to one of the sidebands then the ion’s state can be driven from  $|0\rangle$  to  $|-1\rangle$  or  $|+1\rangle$  as with driving the carrier. However, this also results in the addition (blue sideband) or subtraction (red sideband) of a motional quanta from the ion during this population transfer. The probability of population transfer from  $|0\rangle$  to  $|+1\rangle$  through resonantly driving a motional sideband is given by [62]:

$$P_{\pm}(t) = \sum_{n=0}^{\infty} p_n \frac{1}{2} (1 - \cos(\Omega_{n,n\pm 1} t)) \quad (2.16)$$

where the  $\pm$  sign is used for the red ( $-$ ) and blue ( $+$ ) sideband transition respectively;  $n$  is the (initial) motional state of the ion.  $p_n$  is the population in this motional state, and, to first order in  $\eta_{\text{eff}}$ ,  $\Omega_{n,n-1} = \eta_{\text{eff}}\Omega\sqrt{n}$  and  $\Omega_{n,n+1} = \eta_{\text{eff}}\Omega\sqrt{n+1}$  are the Rabi frequencies of the red and blue sideband transitions from  $|0, n\rangle$  to  $|+1, n \pm 1\rangle$  respectively, where  $\Omega$  is the carrier Rabi frequency. The population of these motional states is given by [62]

$$p_n = \frac{1}{\bar{n} + 1} \left( \frac{\bar{n}}{\bar{n} + 1} \right)^n$$

for an ion in a thermal distribution of motional states which can be described as having a mean phonon number  $\bar{n}$ . One can see from Equation 2.16 that that stronger the gradient,

the stronger the motional coupling, i.e. the faster the Rabi frequency, and the less time that microwave radiation needs to be applied in order to perform an operation. One can also see that the probability of producing population transfer by exciting the motional sidebands is also highly dependent on the temperature of the ion, i.e. the number and distribution of motional quanta that the ion has. This will be explored in more detail when I discuss ground state cooling using motional sidebands.

Since both the strongest gradient in this experimental setup is oriented along the axial direction and the axial secular frequency is the lowest, the axial secular motion is most highly coupled to the internal states. Due to this, we perform all operations that involve this coupling using sidebands on the axial mode. We can observe the axial sidebands by performing a scan in frequency space around one of the transitions from  $|0\rangle$ .

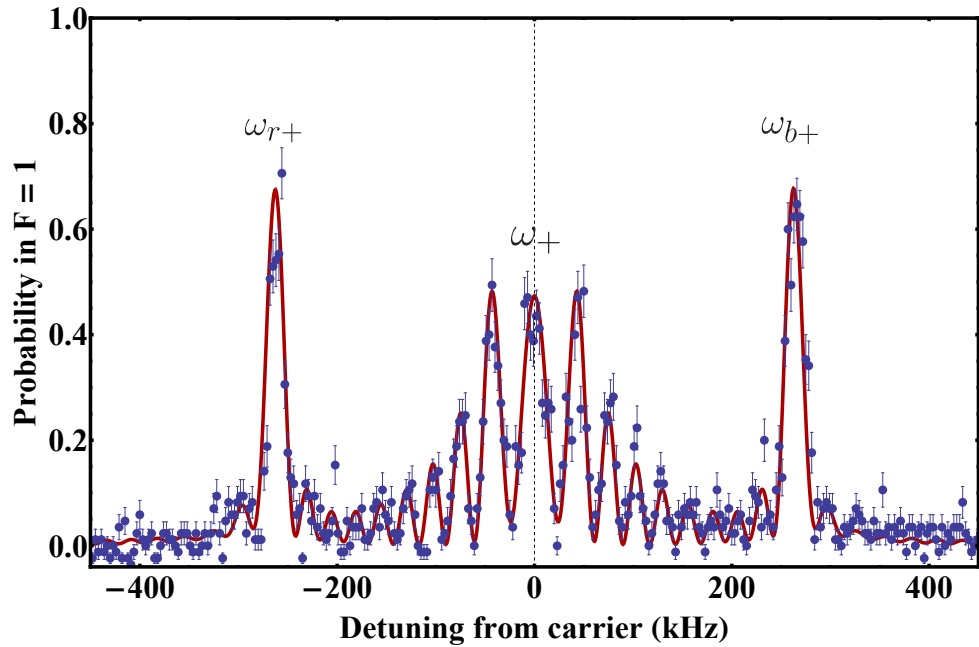


Figure 2.13: A frequency scan over the  $|0\rangle$  to  $|+1\rangle$  transition with both the carrier transition  $\omega_+$  and its red and blue motional sidebands resonant with  $\omega_{r+}$  and  $\omega_{b+}$  respectively and showing the probability of driving the population from  $|0\rangle$  to  $|+1\rangle$  using a  $40\ \mu\text{s}$  pulse time and 200 runs for each data point. The axial secular frequency is  $\frac{\nu_z}{2\pi} = 268\ \text{kHz}$  and the theory curve is fitted for a carrier Rabi frequency of  $2\pi \times 46\ \text{kHz}$ . By fitting the data to the theory curve the thermal distribution of phonon states (a measure of the motional temperature of the ion) is determined to be  $\bar{n} = 290(50)$ . This figure is directly taken from the paper on spin-motion entanglement of which I am co-author [18].

Such a frequency scan is shown in Figure 2.13 taken from [18]. In our experimental setup, a full scan over the red sideband, transition, and blue sideband results in two resolved peaks and a transition probability distribution with many side-lobes due to the pulse-time being set to much greater than the  $\pi$ -time of the carrier transition. This is due to the sideband Rabi frequency being much lower than the carrier Rabi frequency as it is

mediated by  $\eta_{\text{eff}}$  which is much less than 1. If several transitions and/or their sidebands are present in a small frequency band the microwave or RF power must be lowered so that the Rabi frequency and therefore the width of each probability distribution within a frequency band is small enough that all peaks can be resolved with minimal crosstalk. By using a sufficiently long microwave pulse, one can also drive harmonics of the sidebands at an integer multiple of the secular frequency if the ion is extremely hot.

Though we are able to observe the bare state sideband peaks, these transitions do not behave in the same way as the carrier transition when a time scan is performed. This is because the Rabi oscillation period of the sideband is dependent on the motional state, hence Rabi flopping is not observed because of the range of possible motional states of the ion.

These sidebands are observed for the axial secular motion of a single ion, however, for two ions there are two axial modes of motion, depending on whether the ions are oscillating in-phase or  $\pi$ -out-of-phase with each other along the axial direction. These are known as the “centre-of-mass” (COM) mode and “stretch” mode respectively, each with their own secular frequency and therefore their own motional sidebands. The COM mode secular frequency  $\nu_{\text{com}}$  is equal to that of a single ion. The stretch mode secular frequency  $\nu_{\text{str}}$  is higher,  $\nu_{\text{str}} = \sqrt{3}\nu_{\text{com}}$  [24]. An illustration of these two motions is shown in Figure 2.14.

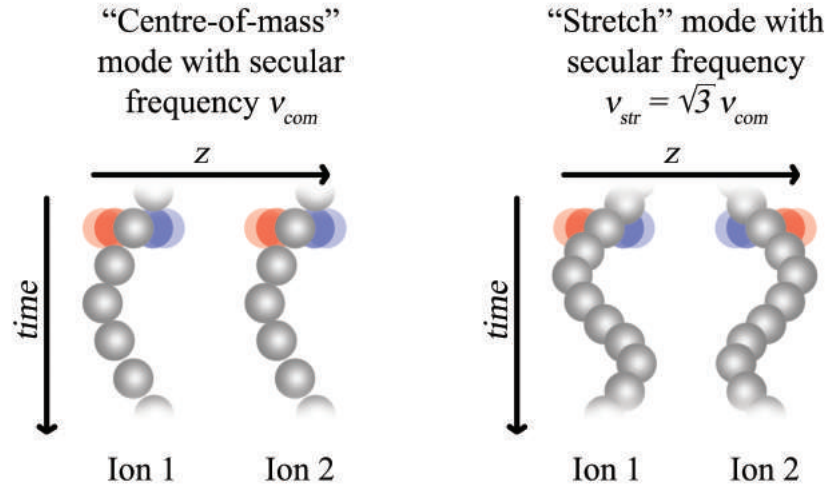


Figure 2.14: An illustration showing the COM and stretch modes of motion for two ions trapped along the  $z$ -axis. The ions are illustrated in grey and the spatial position of the ion due to the secular motion in the axial direction is shown for several snap-shots in time.

In our experiments, we only address the axial mode sidebands as the magnetic field gradient is largest in the axial direction and therefore the mode exhibits the strongest coupling to the internal states. Radial mode sidebands are also apparent on the magnetically field sensitive transitions, however, the radial gradient is approximately half the axial

gradient using this magnetic geometry so the coupling is weaker. Magnetic geometries designed to provide high radial gradients will be discussed in Chapter 3 and implemented with microfabricated planar traps in Chapter 4.

### 2.3.3 Spin-motional entangled states

By simultaneously driving the sidebands of a transition with a small equal but opposite detuning  $\delta$ , an entanglement between the motion of the ion and its internal state can be created. Since this is an entanglement of a “macroscopic” motion and quantum spin state, spin-motional entangled states are sometimes known as Schrödinger’s cat states due to the analogue with the macroscopic cat and quantum nature of whether it is alive or dead. On application of these fields, the ion’s motion undergoes a spin dependent displacement for the two eigenstates of the two-level system. These are given for  $|0\rangle$  to  $|+1\rangle$  by

$$|\rightarrow\rangle = \frac{1}{\sqrt{2}}(|0\rangle + |+1\rangle)$$

$$|\leftarrow\rangle = \frac{1}{\sqrt{2}}(|0\rangle - |+1\rangle)$$

for a microwave pulse with phase  $\varphi = 0$ . For an ion initially in  $|0\rangle = \frac{1}{\sqrt{2}}(|\rightarrow\rangle + |\leftarrow\rangle)|\alpha\rangle$ , where  $|\alpha\rangle$  is the initial motional state, after sufficient time applying the detuned sideband microwave fields the state evolves into  $\frac{1}{\sqrt{2}}(|\rightarrow\rangle|\alpha + \alpha'\rangle + |\leftarrow\rangle|\alpha - \alpha'\rangle)$ , where  $|\alpha \pm \alpha'\rangle$  are the displaced motional states. Since the spin states  $|\rightarrow\rangle$  and  $|\leftarrow\rangle$  undergo different motional displacements, this is an entanglement between the ion’s motion and its internal spin state [18]. An illustration of a spin-motional entanglement experiment is shown in Figure 2.15.

For an ion in a thermal state with mean phonon number  $\bar{n}$ , the probability of population transfer from  $|0\rangle$  to  $|+1\rangle$  through simultaneously driving the red and blue motional sidebands of  $|+1\rangle$  with an equal but opposite detuning  $\delta$  for a pulse time  $t$  is given by [18]:

$$P_{|+1\rangle} = \frac{1}{2} - \frac{1}{2} \exp \left( -2(2\bar{n} + 1) \left| \frac{\eta_{\text{eff}}\Omega}{2\delta} (1 - e^{-i\delta t}) \right|^2 \right) \quad (2.17)$$

where  $\Omega$  is the Rabi frequency of the sideband transitions and  $\eta_{\text{eff}}$  is the effective Lamb-Dicke parameter. For a pulse length of zero, the motional states are the same (the initial state) and  $|0\rangle$  can be written as a superposition of  $|\rightarrow\rangle$  and  $|\leftarrow\rangle$ . When both sidebands are driven at an equal but opposite detuning,  $|\rightarrow\rangle$  and  $|\leftarrow\rangle$  undergo different motional displacements which makes the states well separated from each other. This means the

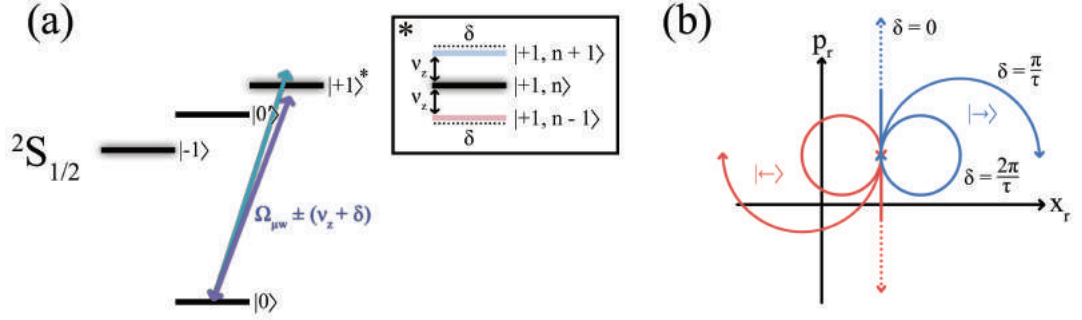


Figure 2.15: Diagrams detailing a spin motional entanglement experiment. **(a)** - Simultaneous driving of the red and blue motional sidebands of  $|+1\rangle$  in order to create a spin-motional entangled state. **(b)** - The evolution of the superposition states  $| \leftarrow \rangle$  and  $| \rightarrow \rangle$  in motional phase space. At  $\delta = \frac{\pi}{\tau}$  the states are well-separated in phase space indicating maximal entanglement of the spin and motional state. At  $\delta = \frac{2\pi}{\tau}$  the states have returned to their initial position in phase space and the level of entanglement is minimised.

state of the ion can no longer be written as a factor of  $|0\rangle$  because  $| \rightarrow \rangle$  and  $| \leftarrow \rangle$  are distinguishable. However, on measurement of the state, only one of the spin states can be detected because the ion can only be detected in one of the displaced motional states, hence, Schrödinger's Cat. Since  $| \rightarrow \rangle$  and  $| \leftarrow \rangle$  are equal superpositions of  $|0\rangle$  and  $|+1\rangle$ , the population in  $|+1\rangle$  is detected at 50 percent when  $| \rightarrow \rangle$  and  $| \leftarrow \rangle$  are distinguishable. For a completed loop in phase space the motional displacement goes back to zero,  $| \rightarrow \rangle$  and  $| \leftarrow \rangle$  are no longer well separated and  $|0\rangle$  is detected. If there is a small motional displacement,  $| \rightarrow \rangle$  and  $| \leftarrow \rangle$  are quite distinguishable but cannot always be distinguished, thus the state is sometimes detected as  $|0\rangle$  and the population in  $|+1\rangle$  is much lower than 50 percent. The  $\bar{n}$  term comes from  $| \rightarrow \rangle$  and  $| \leftarrow \rangle$  being more easily distinguished depending on the temperature of the ion. Experimentally, this means that for a hot ion it may be difficult to know when the states have completed a loop in phase space because the smallest motional displacement will make  $| \rightarrow \rangle$  and  $| \leftarrow \rangle$  distinguishable and the population in  $|+1\rangle$  detected at 50 percent. This means we wish to cool our ions down so that a larger motional displacement is required to distinguish  $| \rightarrow \rangle$  and  $| \leftarrow \rangle$  and we can easily determine the ion's completion of a loop in phase space.

This is important because spin-motional entangled states are the basis of multi-qubit gates using trapped ions. The states of a pair of ions may be expressed as a superposition of the four combinations of  $| \rightarrow \rangle$  and  $| \leftarrow \rangle$  for each ion. When the gate is performed, some of the spin states undergo a motional displacement and gain a phase as they complete a loop in phase space. However, this phase term on some of the two-ion spin states means that the pair of ions are no longer in their initial state but are in an entangled state which is dependent on what the original state of each ion was. The combined state of the pair

of ions cannot be factorised into the states of each individual ion so they are therefore entangled. This entanglement scheme for multiple ions is known as the Mølmer-Sørensen gate [19].

One can experimentally demonstrate the production of spin-motional entangled states in two ways; this can be done by looking at the population in  $|+1\rangle$  (or  $|-1\rangle$ ) either as a function of detuning for a fixed pulse time, or pulse time for a fixed detuning.

A scan of detuning is shown in Figure 2.16. Near to zero detuning, the orthogonal spin states  $|\leftarrow\rangle$  and  $|\rightarrow\rangle$  are well separated in phase space, which means that there is high level of entanglement between the internal spin and the motional degrees of freedom of the ion. At a detuning of  $\pm 5.5$  kHz (for the pulse time of  $180\ \mu\text{s}$ ) one can see that the probability in  $F = 1$  is near to zero indicating that the orthogonal spin states have completed a loop in phase space and reoccupy the start point with no residual entanglement.

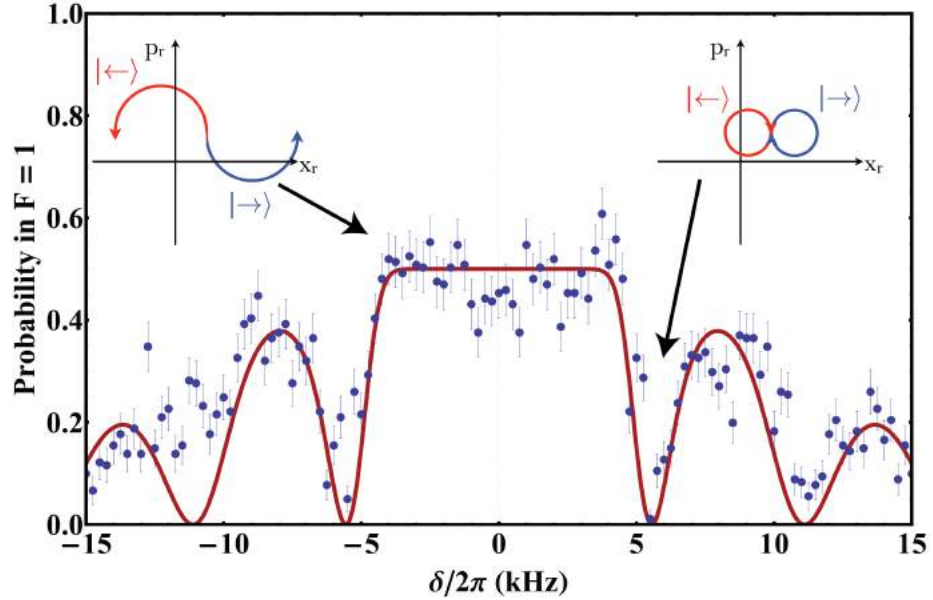


Figure 2.16: The probability of an ion initially in  $|0\rangle$  being in  $|+1\rangle$  after simultaneously driving the (single-ion) red and blue sidebands at a given detuning for  $180\ \mu\text{s}$ . Each point is the average of 200 runs. The theory line corresponds to Equation 2.17 and is shown for an initial thermal excitation of  $\bar{n} = 110$ . The deviation from the theory line at  $-11$  kHz is likely due to a drift in the magnetic field and therefore unequal detunings with the respect to the sidebands due to the Zeeman shift of  $|+1\rangle$  changing. The inset diagrams show the displacement of the orthogonal spin states in motional phase space. At small detuning, the states are far apart indicating that the spin state is entangled with the motion. The points where the probability goes to zero indicate that the microwave pulse has formed a complete loop in phase space and there is no residual entanglement between the motion and the internal state. This figure is directly taken from [18].

The time evolution of the spin-motional entanglement is shown in Figure 2.17 for a detuning of  $\sim 5$  kHz. One can see that with this detuning, the pulse time required to

complete a single loop in motional phase space is approximately  $180 \mu\text{s}$  thus one can see that the residual entanglement drops significantly at this time though some remains due to the decoherence of the state in this dataset. At around  $90 \mu\text{s}$  one can see that the level of entanglement between the spin and motional degrees of freedom has reached a maximum, as in the frequency scan at small detuning. At the time of this particular time scan, the coherence time was limited to around  $250 \mu\text{s}$ . Due to this low coherence time, the ion had significantly decohered by the second completion of a loop in phase space as shown by the drop in the probability of the ion being detected in  $F = 1$  at this time being small, rather than all the way to zero.

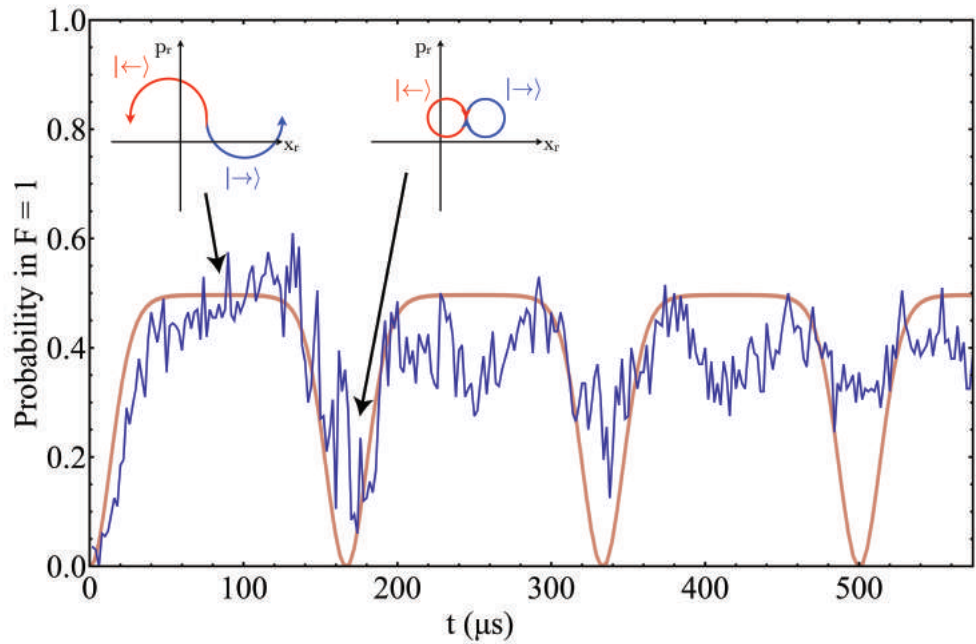


Figure 2.17: A spin motional entanglement time scan using the (single-ion) red and blue sidebands of  $|-1\rangle$  at a symmetric detuning of  $\frac{\delta}{2\pi} \approx 5 \text{ kHz}$ . The blue line shows the raw data graph as seen on the experimental program where each point is the average of 200 runs. The red line shows a very approximate theory curve given by Equation 2.17 for  $\bar{n} = 110$ . The inset pictures (adapted from our spin-motional entanglement paper diagram [18]) show the separation of the orthogonal spin states in motional phase space for the different features of the graph. Due to the low coherence time of this state (prior to the implementation of electrical noise minimisation methods), one can see that significant decoherence is present before the completion of a second loop in phase space making this basis unsuitable for performing high fidelity entanglement operations of this nature.

Although coherence times of  $\sim 2500 \mu\text{s}$  are now observed, this data illustrates the need for a more magnetically robust qubit. The finite coherence time of the magnetically sensitive bare states poses issues when considering the time it takes to entangle two ions. A much longer coherence time is realised through the use of a dressed state qubit which is much less sensitive to small magnetic field fluctuations.

## 2.4 Dressed state qubits

By applying microwave fields, it is possible to decouple magnetic field noise from the ion, increasing coherence times. The dressed states are the eigenstates of the Hamiltonian describing simultaneous driving of the  $|0\rangle$  to  $|-1\rangle$  and  $|0\rangle$  to  $|+1\rangle$  transitions with equal Rabi frequency  $\Omega_{\mu w}$  after applying the rotating wave approximation. This Hamiltonian can be written as [49]:

$$\hat{H}_{\mu w} = \frac{\hbar\Omega_{\mu w}}{2} \left( | +1\rangle\langle 0| + | -1\rangle\langle 0| + \text{H.c} \right) \quad (2.18)$$

where H.c is the Hermitian conjugate and for simplicity we take the phase of the microwave fields to be zero. The eigenstates of this Hamiltonian, i.e. the dressed states, can be written as follows [49]:

$$|D\rangle = \frac{1}{\sqrt{2}}(|+1\rangle - |-1\rangle) \quad (2.19)$$

$$|u\rangle = \frac{1}{2}|+1\rangle + \frac{1}{2}|-1\rangle + \frac{1}{\sqrt{2}}|0\rangle \quad (2.20)$$

$$|d\rangle = \frac{1}{2}|+1\rangle + \frac{1}{2}|-1\rangle - \frac{1}{\sqrt{2}}|0\rangle \quad (2.21)$$

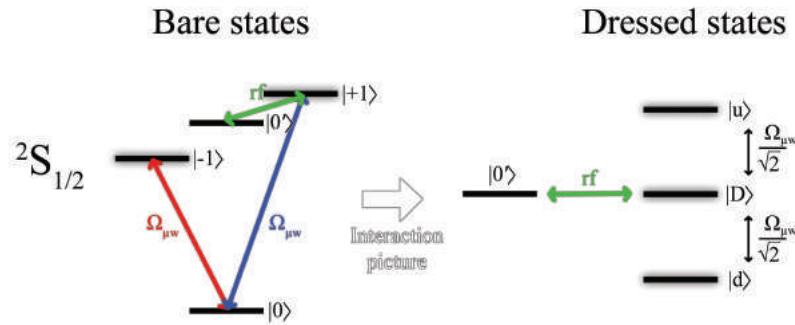


Figure 2.18: The change of basis from the bare states (left) to the dressed states (right). By driving the  $|0\rangle$  to  $|-1\rangle$  and  $|0\rangle$  to  $|+1\rangle$  transitions simultaneously with equal Rabi frequency  $\Omega_{\mu w}$ , one can create a dressed state basis using RF radiation to transfer the population between  $|0'\rangle$  and the dressed states  $|D\rangle$ ,  $|u\rangle$ , and  $|d\rangle$  where  $|u\rangle$  and  $|d\rangle$  are spaced from  $|D\rangle$  by  $\frac{\Omega_{\mu w}}{\sqrt{2}}$ . The dressed states are advantageous over the bare states as they are not first order sensitive to magnetic field fluctuations but still experience strong coupling to the secular motion of the ion.

The Hamiltonian can be written in the dressed basis as:

$$\hat{H}_{\mu w} = \frac{\hbar\Omega_{\mu w}}{\sqrt{2}} \left( |u\rangle\langle u| - |d\rangle\langle d| \right) \quad (2.22)$$

which shows the dressed states  $|u\rangle$  and  $|d\rangle$  are separated in energy from  $|D\rangle$  by  $\frac{\hbar\Omega_{\mu w}}{\sqrt{2}}$



and  $-\frac{\hbar\Omega_{\mu w}}{\sqrt{2}}$  respectively [49].

The perturbation to this Hamiltonian caused by magnetic field fluctuations can be written to first order [49]:

$$\hat{H}_p = \hbar\lambda_0(t) \left( | +1 \rangle \langle +1 | - | -1 \rangle \langle -1 | \right)$$

where  $\lambda_0(t) = \frac{\mu_B \Delta B(t)}{\hbar}$  and  $\Delta B(t)$  is an arbitrary time dependent magnetic field [24], i.e. magnetic field noise. By rewriting the perturbation Hamiltonian in the dressed state basis as [49]:

$$\hat{H}_p = \frac{\hbar\lambda_0(t)}{\sqrt{2}} \left( |D\rangle \langle u| + |D\rangle \langle d| + \text{H.c.} \right) \quad (2.23)$$

it can be shown that in the limit of the first-order Zeeman effect, only magnetic field fluctuations near to  $\frac{\Omega_{\mu w}}{\sqrt{2}}$  will drive population between the dressed states [49]. This dressed state basis is therefore robust against decoherence due to small magnetic field fluctuations. The change from the bare to the dressed state basis for our qubit subspace is illustrated in Figure 2.18.

We can use a single RF field to transfer the ion from  $|0'\rangle$  to one of the dressed states by using frequencies near to the  $|0'\rangle$  to  $|+1\rangle$  or  $|0'\rangle$  to  $|-1\rangle$  transition frequencies. The Hamiltonian of the RF field in the bare state basis (in the interaction picture and after applying the rotating wave approximation) is given by [49]

$$\hat{H}_{\text{RF}} = \frac{\hbar\Omega_{\text{RF}}}{2} \left( | +1 \rangle \langle 0' | e^{-i\Delta_+ t} + | -1 \rangle \langle 0' | e^{i\Delta_- t} + \text{H.c.} \right) \quad (2.24)$$

where the phase has been set to zero for clarity and  $\Delta_{\pm} = \omega_{\text{RF}} - \omega_B^{\pm}$  is the detuning of the RF field from the  $|0'\rangle$  to  $|\pm 1\rangle$  transition, and the difference between  $\Delta_+$  and  $\Delta_-$  is set by the static magnetic field that the ion sits in. This Hamiltonian can be written in the dressed basis as [49]

$$\begin{aligned} \hat{H}_{\text{RF}} = & \frac{\hbar\Omega_{\text{RF}}}{2\sqrt{2}} \left( |D\rangle \langle 0' | (e^{-i\Delta_+ t} - e^{i\Delta_- t}) + \text{H.c.} \right) \\ & + \frac{\hbar\Omega_{\text{RF}}}{4} \left( (|u\rangle + |d\rangle) \langle 0' | (e^{-i\Delta_+ t} + e^{i\Delta_- t}) + \text{H.c.} \right). \end{aligned} \quad (2.25)$$

This can then be transformed to the interaction picture with respect to Equation 2.22

to get [49]

$$\begin{aligned}\hat{H}'_{\text{RF}} = & \frac{\hbar\Omega_{\text{RF}}}{2\sqrt{2}} \left( |D\rangle\langle 0'| (e^{-i\Delta_+ t} - e^{i\Delta_- t}) + \text{H.c.} \right) \\ & + \frac{\hbar\Omega_{\text{RF}}}{4} \left( |u\rangle\langle 0'| (e^{-i(\Delta_+ - \frac{\Omega_{\mu\text{W}}}{\sqrt{2}})t} + e^{i(\Delta_- + \frac{\Omega_{\mu\text{W}}}{\sqrt{2}})t}) \right. \\ & \left. + |d\rangle\langle 0'| (e^{-i(\Delta_+ + \frac{\Omega_{\mu\text{W}}}{\sqrt{2}})t} + e^{i(\Delta_- - \frac{\Omega_{\mu\text{W}}}{\sqrt{2}})t}) + \text{H.c.} \right).\end{aligned}\quad (2.26)$$

This Hamiltonian contains six possible transitions from  $|0'\rangle$ :  $|0'\rangle$  to  $|D\rangle$ ,  $|u\rangle$ , and  $|d\rangle$  via  $|+1\rangle$  or  $|-1\rangle$  for each transition. For  $\Delta_+ = 0$  or  $\Delta_- = 0$  the ion is driven between  $|0'\rangle$  and  $|D\rangle$  with Rabi frequency  $\frac{\Omega_{\text{RF}}}{\sqrt{2}}$ . For  $\Delta_+ = \frac{\Omega_{\mu\text{W}}}{\sqrt{2}}$  or  $\Delta_- = -\frac{\Omega_{\mu\text{W}}}{\sqrt{2}}$  the ion is driven between  $|0'\rangle$  and  $|u\rangle$  and for  $\Delta_+ = -\frac{\Omega_{\mu\text{W}}}{\sqrt{2}}$  or  $\Delta_- = \frac{\Omega_{\mu\text{W}}}{\sqrt{2}}$  the ion is driven between  $|0'\rangle$  and  $|d\rangle$ , each with Rabi frequency  $\frac{\Omega_{\text{RF}}}{2}$  [49]. In this way, one can see that by applying an RF  $\pi$ -pulse resonant with one of these transitions, one can prepare the ion in one of the dressed states. The experimental procedure we use to do this will be discussed in Section 2.4.1.

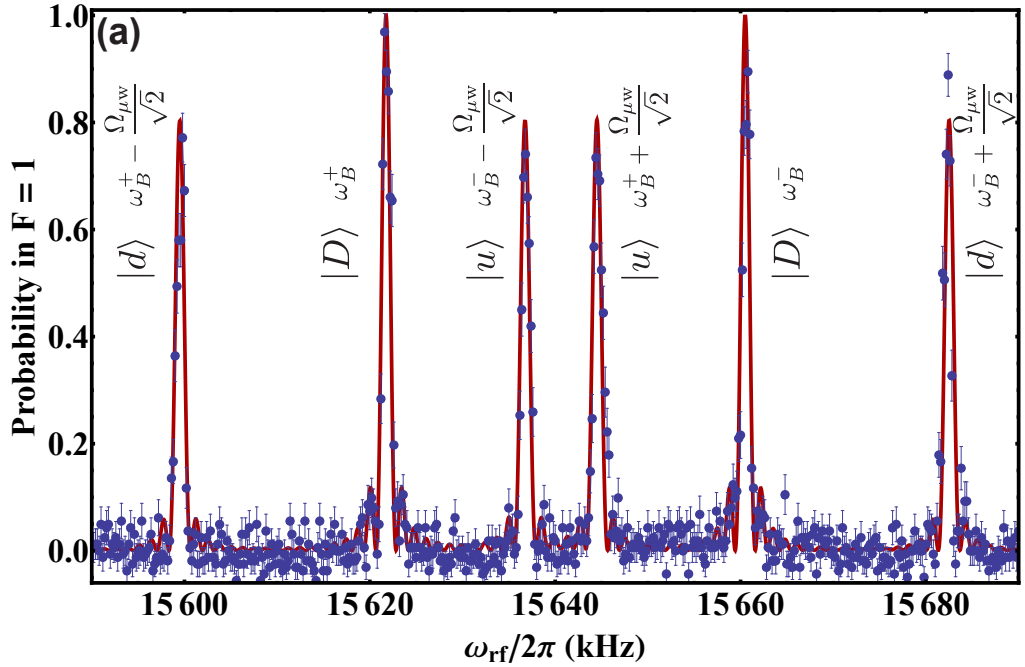


Figure 2.19: A frequency scan over the dressed state peaks using a single RF field applied for  $800 \mu\text{s}$  after the ion is initially prepared in  $|0'\rangle$  and the dressing fields are applied. After the RF pulse is applied, the dressing fields are turned off, then a  $\pi$ -pulse on the  $|0'\rangle$  to  $|0\rangle$  transition means that any population in  $|D\rangle$ ,  $|d\rangle$ , or  $|u\rangle$  is in  $F = 1$ , and population in  $|0'\rangle$  is in  $F = 0$  ready for detection. The different heights of the peaks are due to the different Rabi frequencies of each transition. The red line is a theory curve that describes the six expected transitions to the dressed states. This figure is directly taken from [49].

A frequency scan over the dressed state peaks is shown in Figure 2.19 which, shows the result of this effect on the previously discussed theory. Detailed preparation of these

dressed state peaks will be discussed in the next section of this chapter, however, for the purpose of this discussion, these are resolved in a frequency scan by applying the dressing fields and then scanning RF radiation over the frequencies resonant with  $|0'\rangle$  to  $|\pm 1\rangle$  plus or minus the microwave Rabi frequency of the dressing fields.

As one can see, there are actually six peaks in the dressed state basis which are pairs of three due to the slight difference in the energy gap between  $|0'\rangle$  to  $|-1\rangle$  and  $|0'\rangle$  to  $|+1\rangle$  due to the second-order Zeeman effect. The dressed transitions  $|D\rangle$  via  $|+1\rangle$  and  $|D\rangle$  via  $|-1\rangle$  are spaced based on the magnitude of the magnetic field that the ions sit in, resultant from the  $\sqrt{1 + \chi^2}$  term in the Zeeman splitting shown in Chapter 1. The  $|d\rangle$  and  $|u\rangle$  states associated with each  $|D\rangle$  are separated from this state by  $\frac{\Omega_{\mu w}}{\sqrt{2}}$  which is therefore proportional to the power of the microwave dressing fields.

### 2.4.1 Preparation of the dressed states

Experimentally, we prepare an ion in the dressed state basis by applying a  $\pi$ -pulse from  $|0\rangle$  to  $|0'\rangle$ . At this point one applies the dressing fields by simultaneously turning on the  $|0\rangle$  to  $|-1\rangle$  and  $|0\rangle$  to  $|+1\rangle$  microwave fields. RF pulses can be used to manipulate the dressed state basis. In order to characterise the dressed states, one can scan the frequency of an RF pulse to view the energy structure of the dressed states.

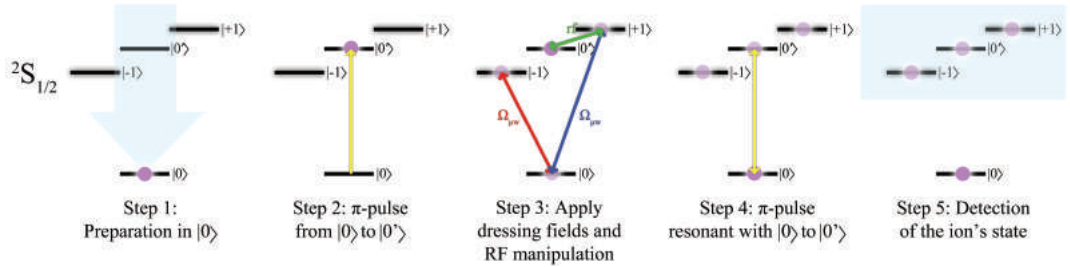


Figure 2.20: The experimental pulse sequence used to prepare an ion in the dressed state basis and detect the result. Any population that was not transferred to one of the dressed states ends up in  $|0\rangle$  and is detected as “dark”. Any population remaining in  $F = 1$  has previously been transferred to a dressed state during the operation and is detected as “light”.

After the manipulation of the dressed state qubit, a  $\pi$ -pulse resonant with  $|0\rangle$  to  $|0'\rangle$  brings any remaining population in  $|0'\rangle$  back to  $|0\rangle$ . This would register any population that has not been transferred to one of the dressed states as “dark” on detection. This pulse sequence for a single ion is shown in Figure 2.20.

### 2.4.2 Rabi flopping

Rabi flopping can be performed on the six dressed state transitions shown in Figure 2.19. This enables us to measure the coherence time of the states in the dressed basis. A Rabi flop between  $|0'\rangle$  and  $|D\rangle$  is shown in Figure 2.21 with a much longer coherence time (hundreds of milliseconds [49]) than the bare states  $|-1\rangle$  and  $|+1\rangle$ .

Though a qubit based on  $|0'\rangle$  and  $|D\rangle$  has a long coherence time, this is not the same as for the other dressed states. This is due to the energy of  $|u\rangle$  and  $|d\rangle$  being dependent on the microwave Rabi frequency of the dressing fields, which means that amplitude noise on the microwave dressing fields will cause decoherence during operations using these states. A single Rabi oscillation between  $|0'\rangle$  and each of the dressed states is shown in Figure 2.22. The lifetime of  $|d\rangle$  was measured to be 70 ms in comparison to 700 ms for  $|D\rangle$  [49].

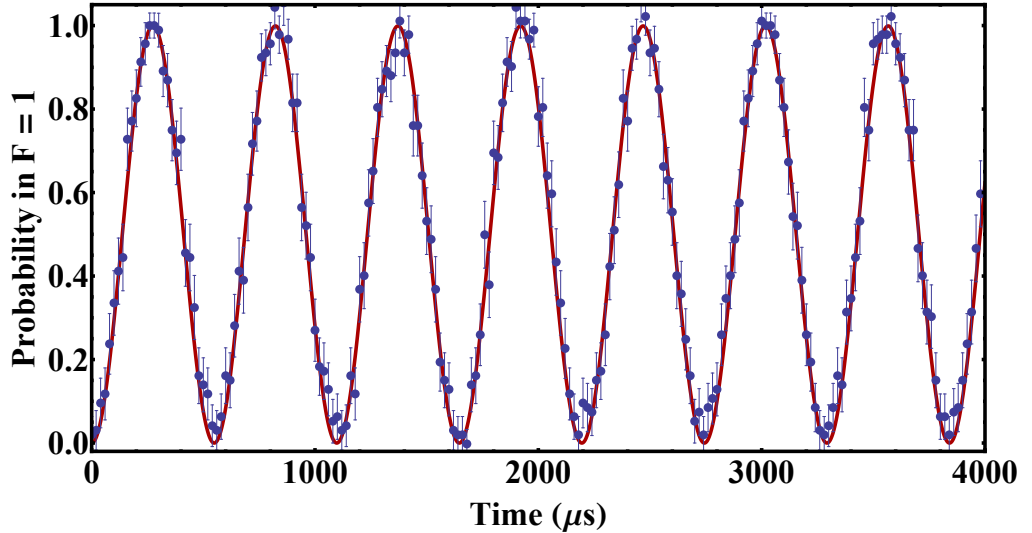


Figure 2.21: A Rabi flop between  $|0'\rangle$  and  $|D\rangle$  showing the extended coherence time (similar to Rabi flopping between  $|0\rangle$  and  $|0'\rangle$ ) in comparison to the magnetically sensitive bare states. This shows promise as  $|D\rangle$  exhibits an extremely long coherence time while still retaining the strong coupling to the ions' secular motion required for spin-motional state entanglement operations. This figure is directly taken from [49].

The dressed states  $|0'\rangle$  and  $|D\rangle$  form a two-level system which can be used to describe a qubit. It is this qubit that we use for many of our high fidelity operations due to the robustness to magnetic field noise, leading to the long coherence time. However, access to all three dressed states allows us to form a “qutrit” from the three-level dressed state system. This would be done using  $|0'\rangle$  as a via between  $|u\rangle$ ,  $|D\rangle$ , and  $|d\rangle$  and RF radiation to drive the population between these states [49]<sup>7</sup>.

<sup>7</sup>Though this may be useful for future experiments that one may propose, the dressed state qutrit does not play a part in further coherent manipulation operations discussed in this thesis.

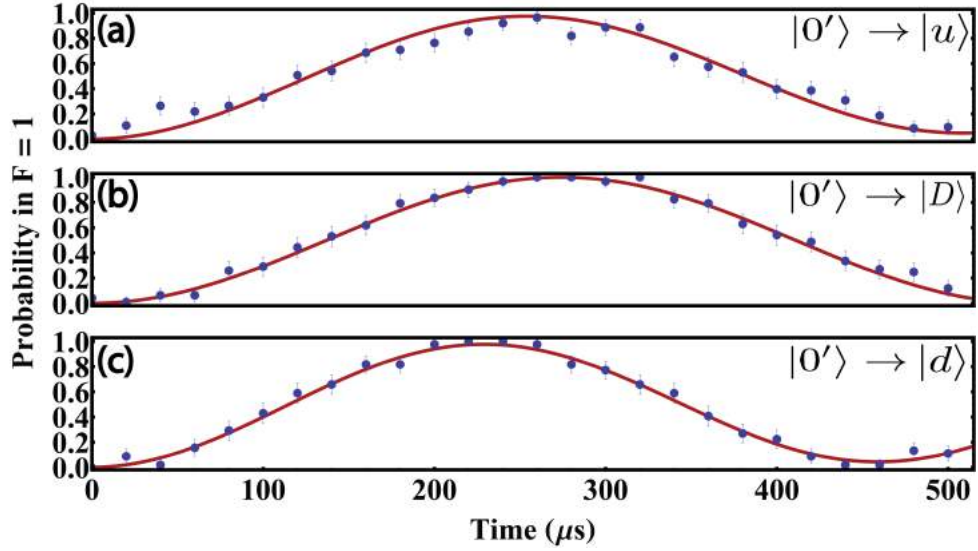


Figure 2.22: A single Rabi oscillation between  $|0'\rangle$  and each of the dressed states  $|u\rangle$ ,  $|D\rangle$ , and  $|d\rangle$  shown in (a), (b), and (c) respectively. This figure is directly taken from [49].

### 2.4.3 Spin-motional entangled states

While the dressed states are protected against magnetic field fluctuations, they are still affected by magnetic field gradients in the same way as the sensitive states in the bare states. We demonstrate this by creating spin-motional entangled states in the dressed state basis.

A frequency scan and time scan using the stretch mode sidebands of  $|D\rangle$  is shown in Figure 2.23 as taken from the thesis of Dr Joseph Randall. One can now see that a time scan with many completions of loops in motional phase space is possible due to the much longer coherence time of the dressed states, unlike the previous attempt shown in Figure 2.17. The long coherence time of the  $|0'\rangle$  to  $|D\rangle$  qubit enables us to perform two-ion entanglement using the Mølmer-Sørensen gate scheme, which, as previously mentioned, is performed by a generalisation of spin-motional entanglement to two ions. This would be extremely difficult to perform in the bare states at high fidelity using our gradient, since the coupling of the transitions to the secular motion is not strong enough for us to perform the entangling operation in the time it takes to overcome decoherence. Though the dressed state basis allows for high-fidelity performance of spin-motional entanglement operations, the fidelity can be further increased if the ion is cooled to the ground state of motion as this reduces the effects of small timing and detuning imperfections [62]. Ground state cooling can be achieved using sideband cooling techniques.

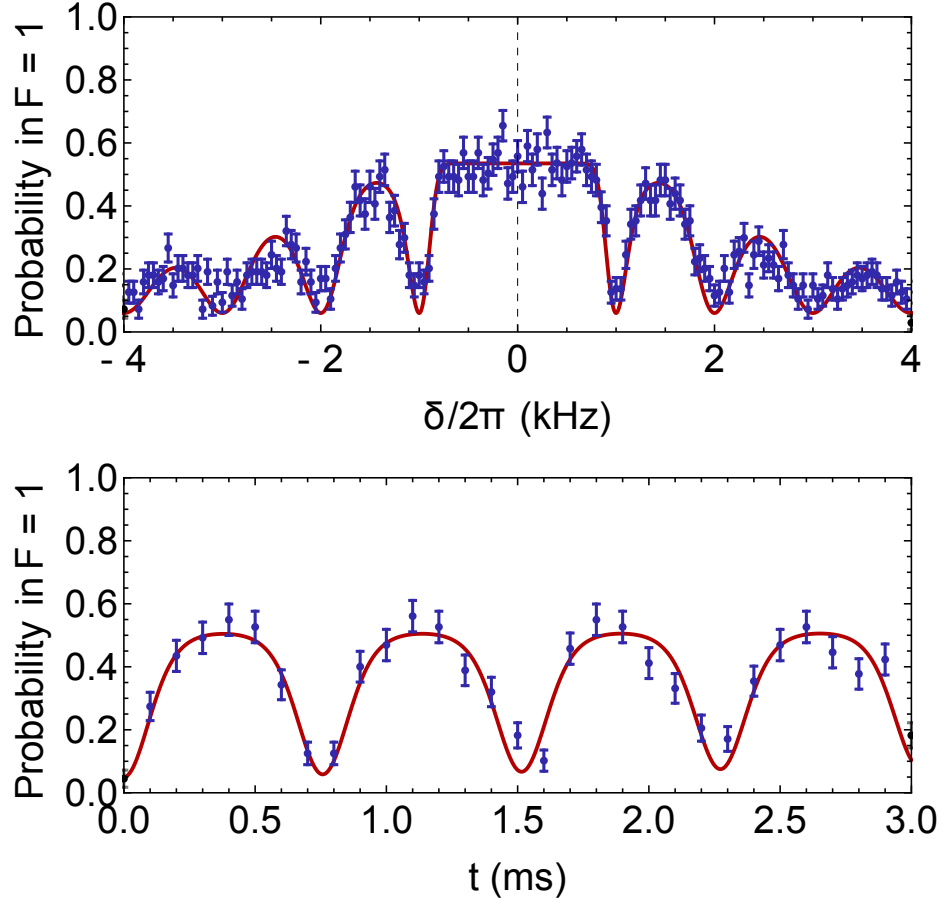


Figure 2.23: Spin-motional entanglement state probability in the dressed state as a function of symmetric detuning  $\delta$  for a pulse time of 1 ms (top) and pulse time  $t$  for a fixed symmetric detuning of  $\frac{\delta}{2\pi} = 1.32$  kHz (bottom). The second ion is prepared in  $|0\rangle$  and does not take part in the operation, though the combined motion due to its presence is used. The theory curves correspond to Equation 2.17 (scaled to account for off-resonant coupling to the carrier transition) and are fit for a dressed state Rabi frequency  $\frac{\Omega_D}{2\pi} = 41$  kHz and  $\bar{n} = 40$ , approximately twice the Doppler limit. This figure is altered from that shown in the thesis of Dr Joseph Randall [24]. Note that this is performed on the stretch mode of a two-ion crystal to reduce the heating rate.

## 2.5 Ground state cooling using motional sidebands

Sideband cooling allows us to cool the ion below the Doppler temperature which is limited by the natural linewidth of the transition used. This is useful for our spin-motional entanglement experiments because the lower the temperature of the ion, the harder it is to distinguish the two displaced spin states, and thus the easier it is to determine the time taken to perform a complete loop in phase space resulting in minimal residual entanglement; this is indicated by a wide dip in a spin-motional entanglement time scan.

Sideband cooling is the use of the red motional sideband of a transition to remove motional quanta from the ion. By repeatedly exciting the red sideband, which transfers the

ion to a higher energy state while removing a motional quantum, then using a dissipative process to prepare the ion in the initial lower energy state, and repeating this process many times, many motional quanta can be removed from the ion. This cools the ion beyond the Doppler limit because as many motional quanta are removed by the sideband cooling process (which is only limited by the coherence time), the ion gains much less motional quanta through anomalous heating, thus there is a net reduction in the ion temperature.

The initial temperature of the ion can be determined by the ratio of the heights of the red and blue sidebands. This is because the sideband Rabi frequencies are differently dependent on the motional temperature of the ion; to first order in  $\eta_{\text{eff}}$ , the red sideband Rabi frequency  $\Omega_{n,n-1} = \eta_{\text{eff}}\Omega\sqrt{n}$ , and the blue sideband Rabi frequency  $\Omega_{n,n+1} = \eta_{\text{eff}}\Omega\sqrt{n+1}$ , where  $\Omega$  is the carrier Rabi frequency as previously explained in Section 2.3.2. Also, the population transfer to a state by driving its motional sidebands is given by Equation 2.16 which is characterised by the temperature of the ion and the sideband Rabi frequency. For high  $n$ , i.e. high motional state of the ion, the sideband Rabi frequencies are very close to each other, thus the height of the sidebands are almost identical. However, when  $n$  is much smaller, there is a large difference in the sideband Rabi frequency and thus the height of each sideband for the same pulse length is very different; the red sideband will be much smaller than the blue sideband. By comparing the heights of the sidebands for a given probe pulse length, one can compare the sideband Rabi frequencies and therefore determine the temperature of the ion.

Experimentally, sideband cooling can be performed, for example, by preparing the ion in  $|0\rangle$ , applying a microwave pulse resonant with the red sideband of  $|+1\rangle$  for the length of time required to achieve maximum population transfer, then using a laser repump to prepare the ion in  $|0\rangle$  again, and repeating the process many times. However, as the ion cools down, the length of the sideband pulse required to achieve maximum population transfer increases as the red sideband Rabi frequency is proportional to  $\sqrt{n}$ . We therefore initially used a pulse sequence which performs several sets of different length cooling pulses in order to address this issue, for example, 200 cooling pulses of length 80  $\mu\text{s}$ , followed by 100 cooling pulses of length 160  $\mu\text{s}$  each with a laser repump to  $|0\rangle$  between each pulse [61]. These initial sequences were far from optimum and the procedure was later improved by using a calibrated program written by Andrea Rodriguez-Blanco in order to optimise the increase in pulse length as the ion is cooled. Nevertheless, in the bare states, the  $|0\rangle$  to  $|+1\rangle$  and  $|0\rangle$  to  $|-1\rangle$  coherence times are on the order of the pulse time required in order to drive the red sideband as it nears the ground state which therefore limits the temperature that

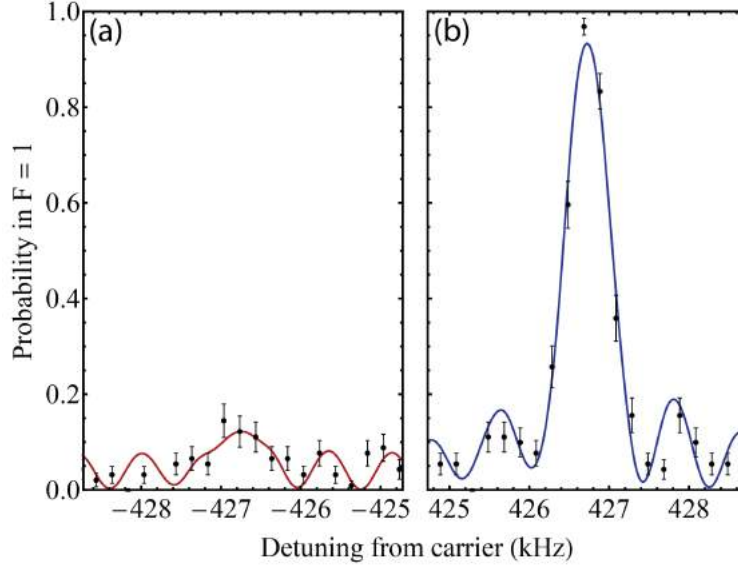


Figure 2.24: A post sideband cooling, dressed state frequency scan over (a) - the red sideband, and (b) - the blue sideband, of  $|D\rangle$ . The red and blue line correspond to numerical simulations of the system given an axial secular frequency of  $\frac{\nu_z}{2\pi} = 426.7$  kHz, a dressed state RF Rabi frequency of  $\frac{\Omega_{\text{dr}}}{2\pi} = 32$  kHz, a microwave Rabi frequency of  $\frac{\Omega_{\mu\text{w}}}{2\pi} = 61.2$  kHz, and a probe pulse length for the frequency scan of  $1270 \mu\text{s}$ , with the motional temperature,  $\bar{n}$  as the only free parameter. A least squares fit corresponds to  $\bar{n} = 0.13(4)$  corresponding to a ground state occupation probability of  $0.88(7)$ . This figure is directly taken from [62].

one can cool to using this method.

One can cool beyond this limit by performing dressed state sideband cooling using the red sideband of the  $|0'\rangle$  to  $|D\rangle$  transition; since the coherence time of this dressed state is much longer than the bare state, the cooling pulses can be applied for much longer when the ion gets to lower temperatures<sup>8</sup>. This is done by first preparing the ion in  $|0'\rangle$  then applying the microwave dressing fields with an RF pulse to the red sideband of  $|D\rangle$  for maximum population transfer to the state. This is followed by a  $\pi$ -pulse resonant with the  $|0\rangle$  to  $|0'\rangle$  transition in order to ensure that any population in  $|D\rangle$  remains in  $F = 1$  for the purposes of detection, after which the ion is re-prepared in  $|0\rangle$  by the laser repump. These steps are then repeated many times in order to remove motional quanta from the ion as previously described.

As previously mentioned, one is able to determine the motional temperature of the ion,  $\bar{n}$ , by fitting a scan over the red and blue sidebands to Equation 2.16. A scan over both sidebands after sideband cooling was applied is shown in Figure 2.24 taken from our

<sup>8</sup>At this point in the lifetime of the experiment, I personally worked on optimisation of the dressed states for spin-motional entanglement operations as other members of the group performed dressed state sideband cooling operations. This was done so that we could cover more experimental ground to prepare for two-ion entanglement gates. As such, these operations have not been personally performed by myself but are included here for completeness as taken from the paper of which I am co-author [62].



ground state cooling paper [62]. This ground state occupation can be improved upon by increasing the magnetic field gradient and therefore the coupling of the ion to its motion which enables this operation to be done faster as the microwave pulse required to drive the sideband could be much shorter. Using motional sideband cooling techniques the ion was able to be cooled down to  $\bar{n} = 0.13(4)$ , corresponding to 0.88(7) probability that the ion is in the ground state of motion. This therefore demonstrates the ability to perform ground state cooling using microwave and RF radiation with trapped ions in a magnetic field gradient [62].

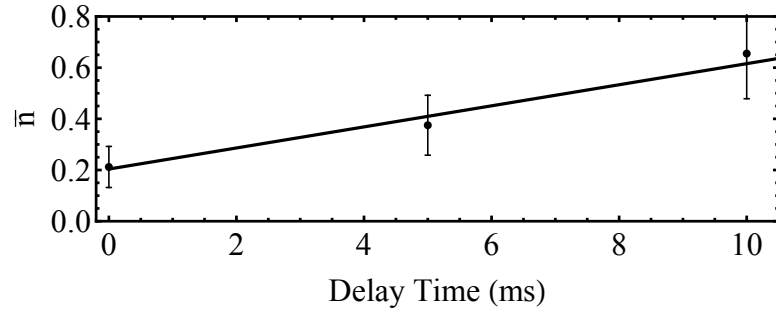


Figure 2.25: The ion motional temperature  $\bar{n}$  as a function of delay time in order to measure the heating rate. For each of the three data points, a scan over the red and blue sidebands is performed and a temperature is fit to a numerical simulation of the system as for Figure 2.24. The black line corresponds to a fit line to the data corresponding to a heating rate  $\dot{\bar{n}} = 41(7)$  quanta per second at an axial secular frequency of  $\frac{\nu_z}{2\pi} = 426.7$  kHz. This figure is directly taken from [62].

Now that ground state cooling has been demonstrated, we can also use this method to make a much better measurement of the heating rate of the ion in the trap. Previously, the heating rate of the ion was measured by first laser cooling the ion with 369 nm laser light, blocking the laser for a given delay time, and then measuring the fluorescence of the ion on detection and fitting this to a temperature. By performing this experiment with many delay times, one can build up a temperature profile for a given delay time and therefore achieve a measure of the heating rate of the ion. Similarly, one can do this by sideband cooling the ion to the ground state, applying a delay time, and then scanning over the red and blue sidebands and fitting them for a certain temperature. Again, after performing this experiment for many delay times, one will achieve a measurement of the heating rate of the trap. This heating rate will set the limit on the time with which we have to perform a high fidelity operation using a trapped ion as a hot ion becomes subject to motional decoherence in the magnetic field gradient. The ion temperature  $\bar{n}$  as a function of delay time is shown in Figure 2.25 resulting in a heating rate measurement of 41(7) phonons per second for the axial secular frequency  $\frac{\nu_z}{2\pi} = 426.7(1)$  kHz [62].

## 2.6 Subsequent achievements using the Blade trap microwave entanglement experimental setup

Subsequent to my departure from this experiment to work on those that will be detailed in the following chapters, the Blade trap experimental setup has produced other results worthy of note in this thesis. This is most notably the two-ion entangling gate using microwaves and RF radiation achieved at a fidelity of  $0.985(12)$  [19]. The entangling gate used was the Mølmer-Sørensen gate described previously in Section 2.3.3, which is a generalisation of spin-motional entanglement for multiple ions. The fidelity of this gate is limited by heating and decoherence and could be improved by performing the gate operation faster. However, the speed of the gate is determined by the coupling of the ions to their motional sidebands and therefore the larger the magnetic field gradient, the faster one can perform the gate.

This is the main motivator for the remainder of the work described in this thesis; generation of large magnetic field gradients to enable fault tolerant gates using long-wavelength radiation. For the Blade trap, simulations indicate that a gradient of  $150\text{ T/m}$  would enable the aforementioned two-ion gate to be performed well within the fault tolerant regime [19]. This can be achieved using a closer spacing of the same retrofitted magnets as shown in Figure 2.26 in comparison with the current setup. This would require a minimised Blade trap design in order to use this magnet separation.

That said, a scalable trapped ion quantum computer is envisioned to consist of many microfabricated planar x-junction traps [20]. This means that it is important to consider generation of high magnetic field gradients on planar traps rather than just symmetric traps. At present, this is likely to be done using on-chip current carrying wires buried underneath the electrode layers of the chip. Nevertheless, in-vacuum permanent magnets could be used to produce the magnetic field gradient in smaller chip trap experiments.

In Chapter 3, I will compare the current methods of magnetic field gradient production and design a new scheme that enables gradients of well over  $100\text{ T/m}$  with planar chip traps. This is the approximate threshold that should enable fault tolerant gates as indicated by simulations performed by other members of the group, but ideally, higher gradients will be measured in reality. In Chapter 4, these high gradient designs will be realised in order to create a new experimental setup that aims to perform the operations described in this chapter with the addition of a fault tolerant two-ion entanglement operation.

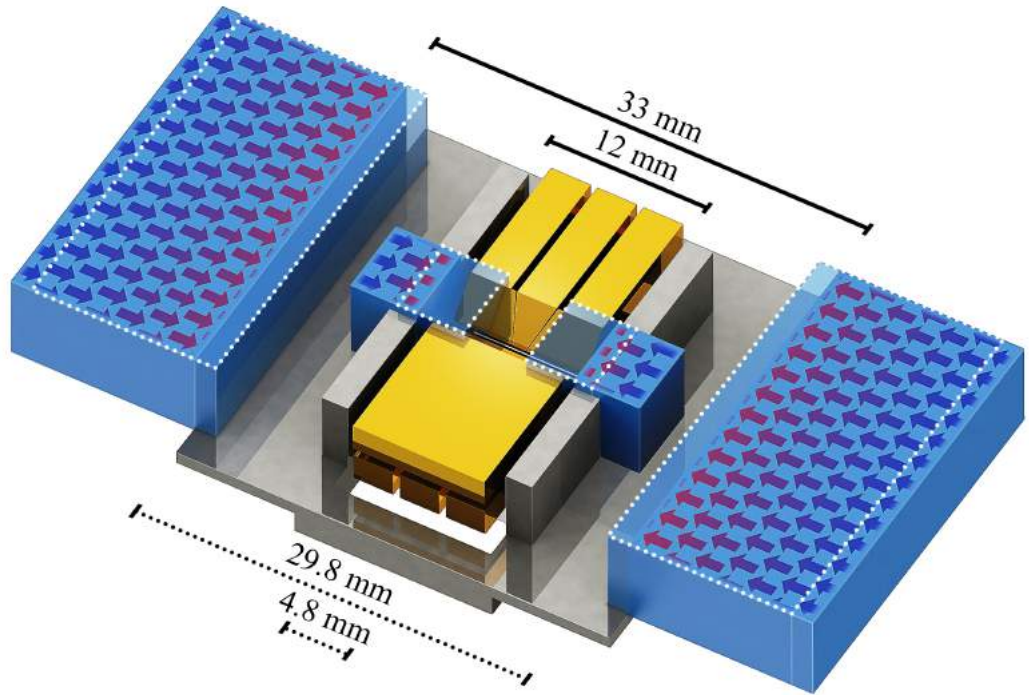


Figure 2.26: An illustration showing the current and minimised magnet spacings using a Blade trap geometry. The dotted lines show the separations of the two pairs of magnets which are simulated to create an axial gradient of  $\sim 150$  T/m. By minimising the endcap electrodes of the Blade trap design, this magnetic setup should allow us to achieve a two-ion gate well within the fault tolerant regime.

## Chapter 3

# In-vacuum high magnetic field gradients

As seen in the previous chapter, high magnetic field gradients are required in order to couple the external motion of trapped ions to their internal spin states when using our microwave based entanglement scheme. In addition to this, magnetic field gradients create individual addressability through the different hyperfine splitting for each ion of a string. In this chapter, I discuss the various methods available to produce high magnetic field gradients at the ion and produce designs for magnetic systems suitable for both traditional macroscopic Paul traps and for microfabricated surface traps that aim to create much higher gradients than previously demonstrated in this field, using both permanent magnets and current carrying wires.

This chapter has two parts. The first part of the chapter discusses some of the magnetic field terminology and practices which are used within the context of this thesis. I start by discussing “magnetic nilling” and how this can help us to create a high gradient at the ion position. Arrangements of multiple permanent magnets require the use of full computer simulations, and I continue by discussing the complexities involved in this. Also, the magnetic field gradients generated by the magnets integrated into the Blade trap, as described in the previous chapter, are simulated as a case study, which leads into a discussion of different magnetic materials, as well as the effect of magnetic coatings.

In the second part of the chapter, two different general configurations of permanent magnets for the generation of field gradients are discussed, one suitable for incorporation into macroscopic Paul traps, and a new method involving magnets placed underneath a planar chip trap to generate gradients at the position of the ions above the chip. I also discuss configurations of current carrying wires suitable for fabrication underneath the

surface of a chip trap.

### 3.1 Magnetic nilling

In the context of this thesis, magnetic field nilling, or simply “nilling”, means to apply a uniform global offset field in the direction of a field component  $B_x$ ,  $B_y$ ,  $B_z$ , or any combination of these. These can be provided by using external current coils or large external permanent magnets which have an extremely small spatial gradient within each component of the magnetic field. In the presence of a magnetic geometry, this offset field is used to reduce the total magnetic field to zero at a single point (or number of points with identical field components) within the setup, hence the field at the point is “nilled”. Since the absolute magnetic field is the vector summation of its components, a single component may dominate the total field. As the value of this single, dominant component is decreased to zero, the effect of the smaller field components become more dominant in the summation. This may result in a magnetic field profile that is vastly different to the original case. It will be later discussed in this chapter how the nilling of a single field component can reveal an extremely high gradient in another field component when in the presence of no nilling field there was minimal or zero gradient in the absolute value of the magnetic field. The nilling field may also be referred to as an external compensation field or bias field when it is produced from outside the magnetic system of interest.

Though I have described nilling in the context of large scale field shaping and manipulation by vector summation of the field components, nilling can also be used to describe the process of making small field compensations in order to reposition the nil point of the magnetic setup in order to bring the zero field point to the position of a trapped ion in an experiment. It will become apparent later in this chapter that alignments will be required between macroscopic magnetic systems and ion traps. These alignments are done mechanically “by hand” which leads to small offset fields due to the imperfect placement of magnets relative to the ion trap.

It is important for ions to sit in a relatively low magnetic field in order to perform high fidelity operations, however, the ions should not strictly sit at the nil position as there is no degeneracy of the Zeeman states at this point so one is not able to manipulate them separately with different frequencies of microwave field. Additionally, a string of ions should not sit over the nil point as this negates the benefits of high individual addressing fidelities as ions on opposite sides of the nil sit in the same or similar fields. This configuration is shown in Figure 3.1 (b); the green 3i, 2i, and 1i ions indicate the image

positions of ions 3, 2, and 1 respectively as they sit in frequency space with respect to ions 4, 5, and 6. Even if they sit equidistant in frequency space, the effective individual addressing gradient halves and the single-ion operation crosstalk increases. Additionally, this configuration is shown in Figure 3.1 (c). Ideally all ions should sit on one side of the nil for an axial gradient scheme as they will get the full benefit of the individual addressing gradient with minimal crosstalk between single-ion operations. This ideal configuration is shown in Figure 3.1 (a).

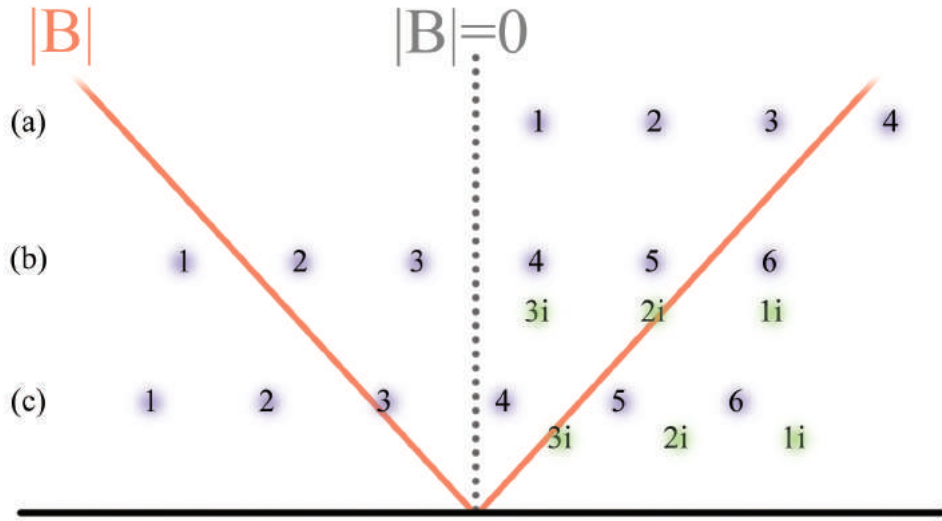


Figure 3.1: The real and effective positions of six ions sitting near to a magnetic nil point with high surrounding gradient. **(a)** - All ions sit on one side of the magnetic nil in different magnetic fields resulting in minimal crosstalk. **(b)** - The ions sit equally across the nil. Ions 3, 2, and 1 sit in the same field magnitude as 4, 5, and 6 respectively on opposite sides of the nil resulting in maximum crosstalk for each pair. **(c)** - The ions sit unequally across the nil such that the ion-ion spacing in the magnetic field results in an effective spacing of half that of configuration (a). Crosstalk is larger than (a) but less than (b).

This positioning of the ions in the magnetic field is slightly more difficult for globally addressed radial mode gates as the ions may be sat at the nil position preventing manipulation of the  $m_f = \pm 1$  Zeeman states. By applying a uniform global field in the direction of the field component responsible for the gradient, the ions can be shifted up the gradient slope to sit in sufficient magnetic field for good coherent manipulation. This is done using the same process as nilling but in the opposite sense. In this application it would be referred to as an offsetting or compensation field.

### 3.2 Simulating magnetic geometries

The magnetic fields (and field gradients) produced by magnetic systems are obtained using numerical modelling simulation software. For the simulations discussed in this thesis, this is primarily COMSOL.

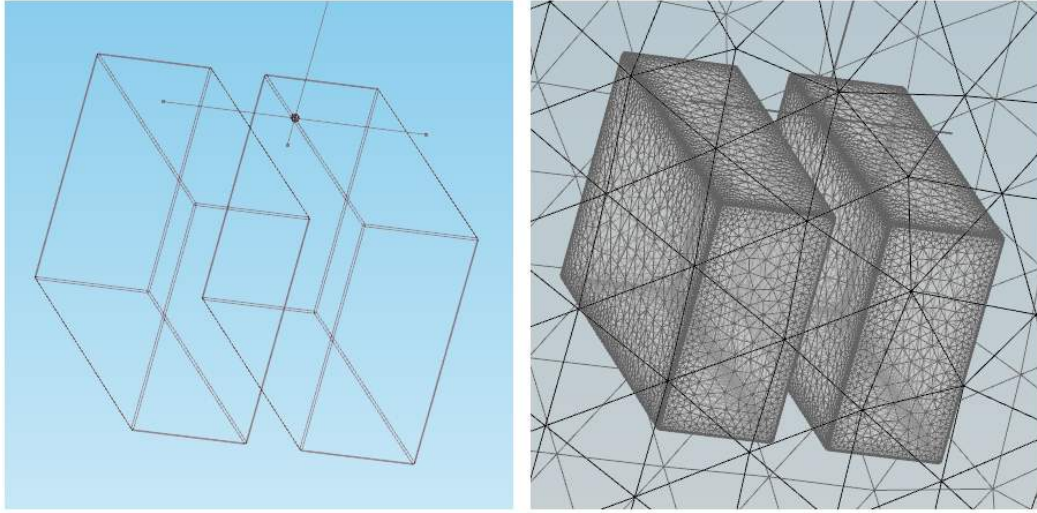


Figure 3.2: A diagram to show the meshing used in a simulation of a pair of magnets. Left - the original geometry as build in COMSOL. Right - the division of the component due to the mesh.

When a component of a model is created in the software, for example a cuboid magnet, in order to effectively map the properties of the component, it must be broken down into many pieces and each of these pieces must be simulated with their own properties and interactions with the rest of the simulation. The free space around a component must also be divided up in order to evaluate the magnetic field within this space. This process is known as “meshing”. An example of the meshing required to simulate a pair of magnets is shown in Figure 3.2. This allows for the reality that the magnetic properties of a component are not uniform throughout its body, for example, the magnetic field inside a permanent magnet is not of uniform strength throughout its volume. A high mesh density means that there are a lot of small mesh pieces within a given volume of the simulation. For most of the free space surrounding the component, the mesh is coarse as we are less interested in the field far from the magnet. The mesh gets finer nearer to the magnets as the free space mesh must interface with each vertex of the magnet mesh in order to be valid for the simulation. However in order to get an accurate simulation result at a point of interest in free space, there should be a high mesh density around that point. If not, there may be problems with the data at the region of interest leading to a false simulation result. Since we are mainly interested in the total magnetic field  $|B|$ , the results of the simulations

are given as a magnitude without indication of direction of the individual components  $B_x$ ,  $B_y$ , and  $B_z$ , and thus the value of magnetic field is always positive. That said, one can analyse individual components of the magnetic field in order to note which component the gradient originates from. In the magnetic designs mentioned in this thesis, the point of zero field is the main point of interest in a simulation because this is the position that I aim to coincide with the ion<sup>1</sup>. When reading off a graph generated from the simulation data, we expect to see a point where the field goes down to zero and instantly “reflects” off the graph axis and grows again. However, even with a very high mesh density, it is very unlikely that a value of zero field will ever occur in a simulation. This means that at the reflection point on the graph, it is much more common to see a data fit where two positive field values are connected on either side of where one would expect the nil to be.

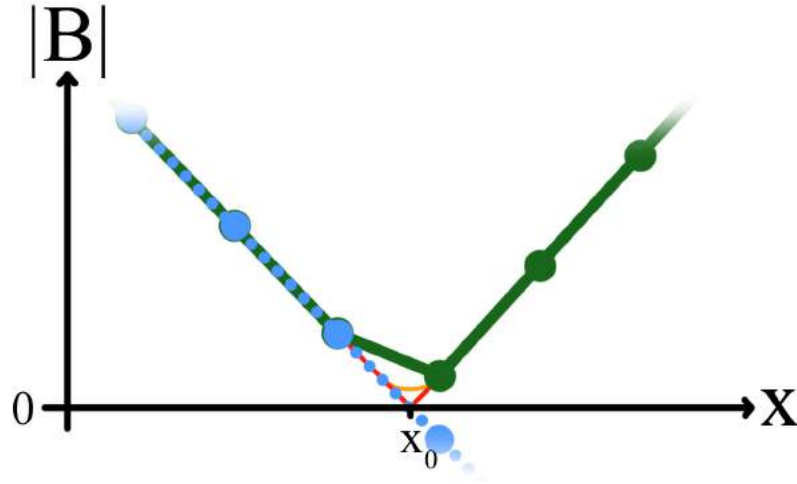


Figure 3.3: An example of aliasing in simulation data around a point  $x_0$  and how the true field can be determined. Green - Connected data points of the magnitude of the total field  $|B|$  near to the zero field point. Blue (dotted) - Connected data points for a single, unspecified component of the field  $B_\phi$  where  $B_\phi \approx B$  and  $|B(x_0)| = 0$ . The high gradient is defined by  $\frac{dB_\phi}{dx}$ . Red - The actual value of  $|B|$  which is masked by the aliasing of the simulation and uncovered by plotting  $B_\phi$ . Orange - Another possible  $|B|$  line which does not have a high gradient at  $x_0$  but results in the same aliased data. In this case  $B_\phi \approx B$  is not valid and there are other field components that are non-zero at  $x_0$  which dominate  $|B|$ .

This is known as aliasing and is a problem when the mesh density is not high enough around a point close to zero field. An example of aliasing is shown in Figure 3.3. Due to the quantisation of the green plot by the data points, it is impossible to tell whether the red or orange line is the real shape of the magnetic field. Only by using a finer mesh size, i.e.

<sup>1</sup>In reality, we do not want the ion at zero field for our experiments as this results in no splitting of our hyperfine manifold. However, aligning the magnetic nil to (near) the ion position allows us to choose our offset field using an adjustable magnetic field source. This can be produced by from a pair of coils or by moving the ion in the gradient.



more data points, can the red line be verified as being the real set of field values. With experience of simulations, one can become sufficient at inferring the actual field profile when aliasing is present, however, it is important to solve this issue for accurate data simulation. One can concentrate a mesh around a point of interest by placing a smaller air box around it which forces the mesh to become denser around said point and reduce the errors due to aliasing. By making intersecting measurement lines at the point that would seem most likely to have zero field, one can force the mesh to create a measurement point there to verify that there is a zero field inflection point and not a smooth bottom curve. Both of these solutions can be seen implemented in the left picture of Figure 3.2.

The position of the nil can also be verified by plotting the individual components  $B_x$ ,  $B_y$ , and  $B_z$  of the magnetic field. Since these are single components of the magnetic field, they have a direction associated with them represented by a shift from positive to negative values on a plot of the single component. Since the total field is a vector summation of the individual components, this direction is lost on a plot of  $|B|$  resulting in an inflection point at zero field. At the nil position, it is highly likely that one or more of these field components will cross the zero field point at some position along a measurement line that intersects the nil. This is illustrated by the blue line in Figure 3.3. A plot of a single field component responsible for the high gradient will intersect the zero field point as it crosses the graph axis. This results in a clear indication of the nil position and is a good way of checking that there is a high magnetic field gradient (or a high magnetic gradient that can be revealed by field nilling) near to the nil point as the field component responsible has a linear transition from positive to negative field values. From this linear region, an accurate gradient at the nil point can be evaluated.

Another possible issue in reviewing simulation data is that the mesh density may not be high enough far from the point of interest. This can lead to a simulation line that is not smooth, though since this is not in the region of interest it is not as much of an issue.

All magnetic fields and gradients in this chapter are simulated using COMSOL unless otherwise stated. The naming convention for magnetic field gradient directions are as follows: Axial is a gradient that is formed along a string of ions such that each ion sits in a different magnetic field. Radial is a gradient that is perpendicular to the ion string of which two subsets may be labelled for planar ion chip traps. Vertical radial is in the direction of height away from the chip surface. Planar or horizontal radial is at a constant height parallel to the chip surface. These definitions are illustrated in Figure 3.4. In Cartesian coordinate space, unless otherwise stated, all permanent magnetisations are along the  $x$ -

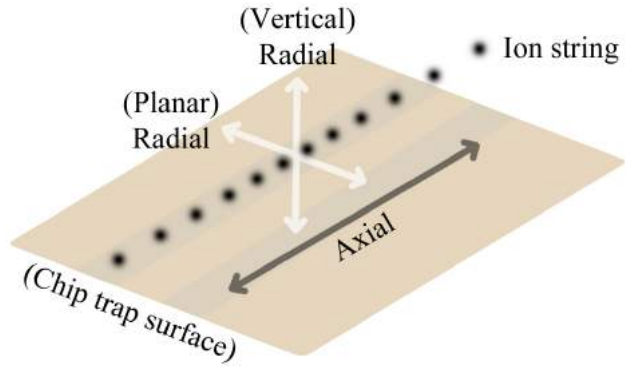


Figure 3.4: Diagram to define the axial and radial directions with respect to a string of trapped ions. In brackets denotes the modification to the naming convention in the presence of a chip trap.

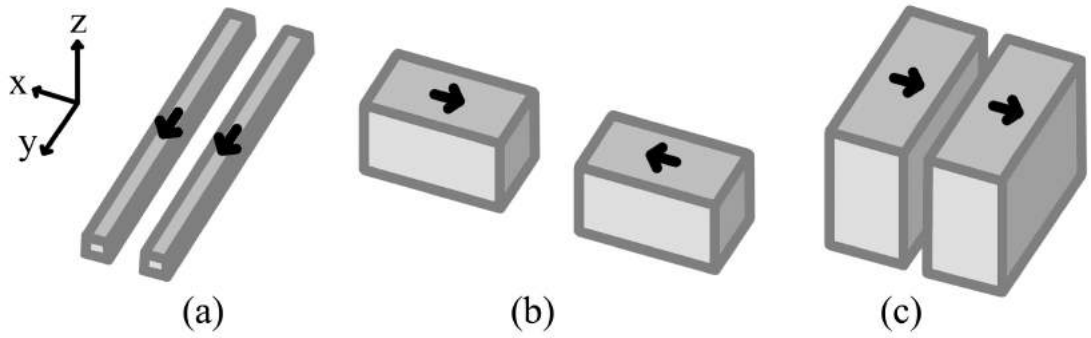


Figure 3.5: The coordinate orientation used in order to define gradients. (a) - A current wire geometry with currents flowing in the  $y$ -direction and separated in  $x$ . (b) - A symmetric magnet geometry with magnetisation and separation in the  $x$ -direction. (c) - An asymmetric magnet geometry with magnetisation and separation in the  $x$ -direction.

direction, symmetry, i.e. along an axis which the magnetic field profile remains nearly constant, is along the  $y$ -direction<sup>2</sup>, and height above or below the chip, wires, or magnet surface is in the  $z$ -direction as shown in Figure 3.5. I will use this coordinate system to illustrate the origins of each magnetic field gradient. One must also be aware that these axes differ from the axes previously used to describe the trapping potential in Chapter 1 for a symmetric trap geometry. This is because the alignment of these magnets with respect to an ion string can be changed depending on the gradient that one intends to use. One must therefore be careful to consider the orientation of the ion string in the magnetic field when assessing any gradients.

Now that I have covered all the relevant terminology required in order to understand the magnetic models and simulations used in this chapter, I will proceed to discussing the creation of magnetic field gradients for use in trapped ion coherent manipulation experiments using long wavelength radiation.

### 3.3 Magnetic materials and coatings

For any gradient production scheme which uses permanent magnets it is important to consider what materials should be used in order to produce the highest gradients and for the chip to operate safely. The Blade trap experimental setup used coated samarium cobalt magnets in order to provide the magnetic field gradient used for the experiments described in Chapter 2. In this section, I discuss the desired properties that must be exhibited by permanent magnets used in a high magnetic field gradient setup and use these criteria to re-evaluate the most suitable magnetic material that is available on the market for purchase.

#### 3.3.1 Selecting a permanent magnetic material

Concerning the material that the magnets are made of, it is desirable to have the following properties:

- A high remanence as this is proportional to the magnetic field produced and therefore the magnitude of the magnetic field gradient.
- A high coercivity so that we can be sure that the field of one magnet is not affecting the magnetisation of the other, thus lowering the gradient.

---

<sup>2</sup>The  $y$ -direction symmetry is not apparent for some of the magnetic geometries described in this chapter, in particular the symmetric magnet geometries discussed which only generate a single magnetic nil point. However, definitions of the  $x$  and  $z$ -directions still remain true.

- Be UHV compatible for our experimental setup.
- A Curie temperature much higher than that of the vacuum bake so the magnets are not demagnetised by this process.

If one desires the remanence of the magnets to be greater than 1 Tesla for high field/gradient strengths, this leaves three main options of magnetic material: samarium cobalt, AlNiCo, and neodymium<sup>3</sup>.

In terms of their physical properties, samarium cobalt and AlNiCo are both very inert whereas neodymium corrodes very easily and must therefore be coated with a protective layer. Neodymium also has a relatively low Curie temperature of approximately 320 °C and though it has the greatest remanence of the three, it is possible that the vacuum bake at 200 °C could drastically effect the magnetisation and reduce this remanence, a risk that was not deemed necessary given that samarium cobalt had worked well previously. One can therefore reduce our list of possible materials to samarium cobalt and AlNiCo which have much higher Curie temperatures of approximately 800 and 524 °C respectively.

AlNiCo is further dropped from the list as its relative permeability is likely to be much greater than unity in the presence of the external magnetic fields produced by the second magnet of the pair. We know this because simulations show that the field at a small distance from one of the magnets is of similar magnitude to the coercivity of the material. Therefore, the second magnet is likely to cause a shift in the magnetisation causing movement around the hysteresis loop. This means that the relative permeability is not near-unity for AlNiCo when used in our experimental setup, unlike samarium cobalt which has a relative permeability of around 1.05 in the region of its hysteresis loop that corresponds to the external field it is expected to be in the presence of. The properties of each of these magnetic materials is summarised in Table 3.1.

By having this discussion, we verify that samarium cobalt is the best choice of magnetic material for our experiment due to its inert nature, high Curie temperature, high remanence, and near-unity relative permeability. This allows us to create high gradients at a clearly defined magnetic nil position using a pair of magnets. The geometries for creating this nil will be the focus of this chapter.

---

<sup>3</sup>“Neodymium” or “neodymium magnet” is the usual shortened name given to NdFeB magnets. I will use the minimal naming convention in this thesis as I will only mention the element within a magnetic context. Additionally, the properties of these magnets are taken from the specifications dictated by manufacturers.

Table 3.1: The approximate values for some magnetic properties of material candidates for my scheme. Note that these properties are highly dependent on the manufacturing process and therefore may be very different between manufacturers. \* - There are many different grades of AlNiCo. \*\* - This relative permeability was used in simulations based on the  $B = \mu H$  law. Though  $\mu$  is not a constant as it follows hysteresis for ferromagnetic materials, I hypothesise that in the presence of an external magnetic field, AlNiCo does not have a high enough coercivity to ignore the effect that one magnet will have on the other since the simulated  $H$ -fields are in the order of the mid  $10^4$  A/m. Although this hypothesis could be valid for samarium cobalt and neodymium magnets, their coercivity is much greater and I believe that I can trust the rectangularity of their hysteresis curves at these auxiliary field strengths enough that a relative permeability of 1.05 is still valid despite  $H$ -fields present in the low  $10^5$  A/m.

Magnetic material	Remanence (T)	Coercivity (kA/m)	Intrinsic coercive force (kA/m)	Relative permeability (dimensionless)	Curie temperature (°C)
AlNiCo (V)*	1.25	50	54	20**	524
SmCo	0.82 - 1.16	493 - 1590	636 - 1990	1.05	800
NdFeB	1 - 1.3	875 - 1990	875 - 2785	1.05	320

### 3.3.2 Protective magnet coatings

Since samarium cobalt is a brittle material, it may be useful to coat the magnets in order to improve their durability. The standard coating used for custom magnets manufactured by Bunting magnetics, our supplier, is nickel-copper-nickel (Ni-Cu-Ni) at  $10\text{ }\mu\text{m}$  thick<sup>4</sup>. Figure 3.6 displays an illustration to show the nickel-copper-nickel coating finish available on the custom magnets. This is mandatory for neodymium magnets to prevent corrosion, but is available for most other magnets (eg. samarium cobalt and AlNiCo (both relatively inert)) for surface and edge protection against chipping and other forms of damage. The typical  $50\text{ }\mu\text{m}$  chamfer (to avoid potentially dangerous magnetic knife edges) has been omitted in this illustration so that scale can be more easily observed.

However, nickel may be a problematic material due to its high ferromagnetic nature. At zero external field, the relative permeability is near unity, however, in the presence of a magnetic field the relative permeability grows to values as large as 200 – 600 before limiting back to unity at saturation. The specific relative permeability is an unknown as the details of the fabrication method and measurements of the nickel plating hysteresis relationship is unknown to us.

<sup>4</sup>Though other coatings can be used, for example gold, these were not available on custom magnets at the time our magnets were ordered.

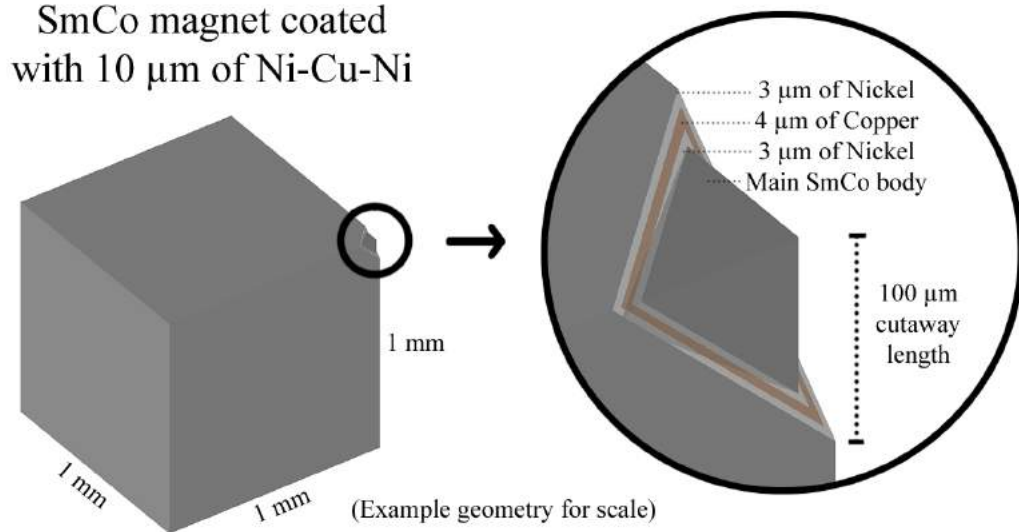


Figure 3.6: An illustration to show the nickel-copper-nickel coating finish available on the custom magnets. The standard chamfering on the magnet edges has been omitted in this illustration so that coating scale can be more easily observed.

It is important to see what effect this would have on the magnetic field profile produced by our magnets. This is particularly interesting to us because the magnets in the Blade trap experimental system are Ni-Cu-Ni coated, and the gradient that was measured experimentally was close to half that which was originally simulated. Though the presence of the trap electrodes could have caused this reduction in the gradient, this would only have been if they have a relative permeability that is far from unity and since they are specified as non-magnetic stainless steel this should not be the case. I therefore hypothesise that this is an effect of the coating and aim to verify this through simulation.

Due to issues with thin domain meshing we are only able to simulate a much thicker coating than expected in real life. However, simulations show that with a thicker, purely nickel plating of high relative permeability, the gradient formed between two magnets in symmetric configuration is more than halved.

Let us compare the simulated results for the uncoated and coated cases. Figure 3.8 shows the field plots for both an uncoated and coated simulation of the original Blade trap magnet setup shown in Figure 3.7. The coating is modelled as nickel at a thickness of 50  $\mu\text{m}$  achieving the same overall dimensions as the uncoated case. In order to match our real world results of the measured magnetic field gradient with the Ni-Cu-Ni coated magnets in Chapters 1 and 2, a scaled relative permeability value for the nickel was found to be 150 at this coating thickness, giving an axial gradient of 23.75 T/m, and radial gradients of 10.9 T/m and 11.5 T/m along the 6 mm and 6.5 mm lengths respectively.

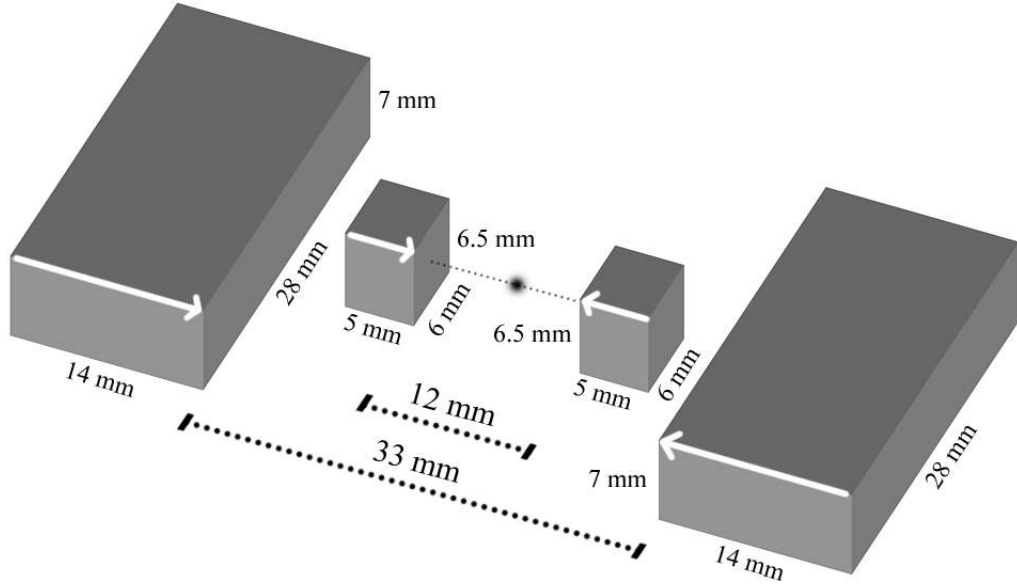


Figure 3.7: The magnetic geometry designed by Dr Joseph Randall as used in the Blade trap experimental setup.

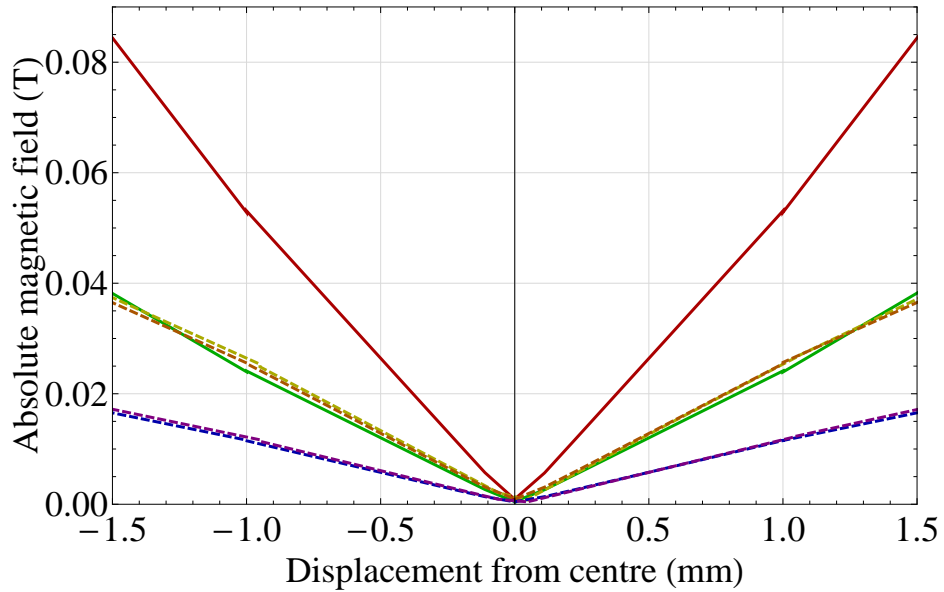


Figure 3.8: Field plots for both an uncoated and coated magnet setup as shown in Figure 3.7. For the original uncoated magnets; Red - Axial direction, Orange - Radial direction along the 6 mm length, Yellow (overlapping Orange) - Radial direction along the 6.5 mm length. For the magnets coated with  $50 \mu\text{m}$  of nickel with a relative permeability of 150; Green (overlapping Yellow and Orange) - Axial direction, Blue - Radial direction along the 6 mm length, Purple (overlapping Blue) - Radial direction along the 6.5 mm length.

Though I have shown that a purely nickel coating affects the intended magnetic field profile, using COMSOL it has not been possible to simulate the real Ni-Cu-Ni coating that could be put onto our magnets. However, the results of these coating simulations could still explain why the measured gradient was much less than that simulated for the magnets

used with the macroscopic Blade trap. For this reason, I will use uncoated magnets for any future permanent magnetic gradient setups. Since this means that there is no protection to the magnet edges, a large quantity would be ordered to ensure a good quality pair of specimens is available for use in an experiment.

Now that uncoated samarium cobalt has been determined to be the best candidate for magnetic material in order to produce the highest gradients at the ion position, I will continue by describing the simplest way that one can create a high gradient magnetic nil for an ion trap experiment. Unless otherwise stated, any permanent magnets for gradient production are simulated as samarium cobalt with  $B_r = 1.08$  T and  $\mu_r = 1.05$ .

### 3.4 Symmetric scheme in-vacuum permanent magnets

The magnetic field gradient setup in the Blade trap experiment consists of two pairs of magnets with opposing polarities. The ions sit along the line of separation of the two innermost pole faces. In a similar way to the surrounding electrode geometry of a symmetric trap, I call this a symmetric magnet geometry. This setup is a retrofit and the arrangement of magnets was heavily constrained by the existing trap. Symmetric scheme permanent magnets are a simple way to create a magnetic field gradient in an experimental setup; broadly, all that needs to be done is two magnets must point towards each other (in repulsion configuration) and an ion needs to sit directly between them. Given this simplicity, it is important to make sure that in future we have an optimised magnet configuration for the highest possible magnetic field gradients, which equates to higher fidelity multiple-ion gates. Here, I present a near-optimal magnetic arrangement as a function of the separation of the innermost pole faces of the magnets and find a simple relationship between the axial gradient and this separation, which is dictated by the trap size.

#### 3.4.1 Basic principles of a symmetric magnet setup

Before describing an optimised magnet geometry, I will outline the generalities of any symmetric magnet setup and the origins of the magnetic field gradients produced. This can be understood by looking at the magnetic field profile produced by a very simple symmetric magnet setup. Figure 3.9 shows an example of the magnetic field between two permanent magnets with a square pole face side length of 8 mm and a length along their magnetisation of 14 mm. The pole faces in this case are separated by 11 mm for use with one of our chip traps. One can see that the opposing magnetisations force the fields away



from the central position of the separated magnets creating a point of zero field and a region of high gradient in all directions around said point as indicated by the change in hue on the diagram.

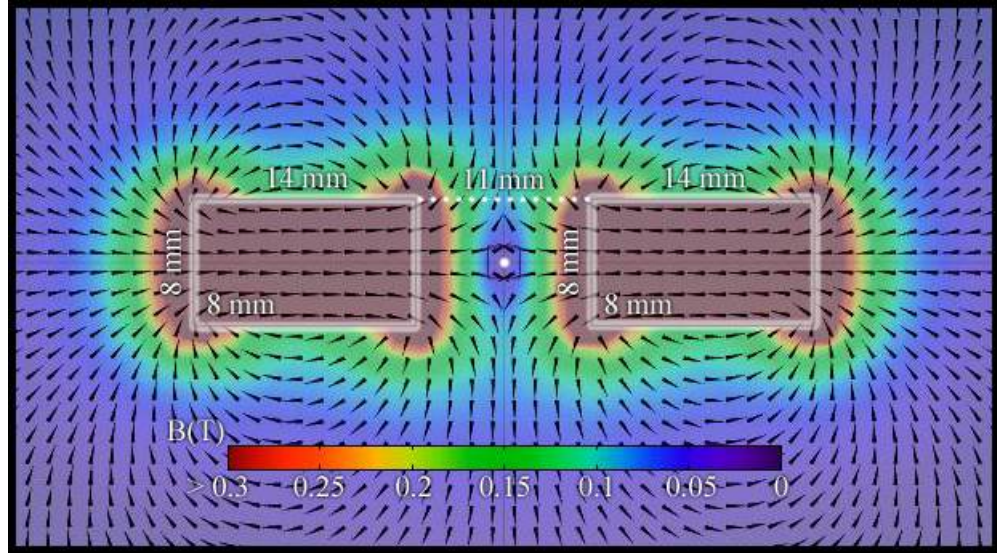


Figure 3.9: A typical symmetric magnet scheme geometry. Two magnets point towards each other creating a central nil (marked with a white dot) with a high magnetic field gradient between them. For the purpose of this chapter, red hues denote high fields relative to purple hues denoting low fields. These diagrams also contain arrowheads to show the direction of the field at regular points in the geometry. In this example, the magnets have a square pole face side length of 8 mm and a length of 14 mm along their magnetisation with central separation of 11 mm (marked by the dotted line), however the central nil position remains the important feature and would be seen similarly in any symmetric magnet scheme.

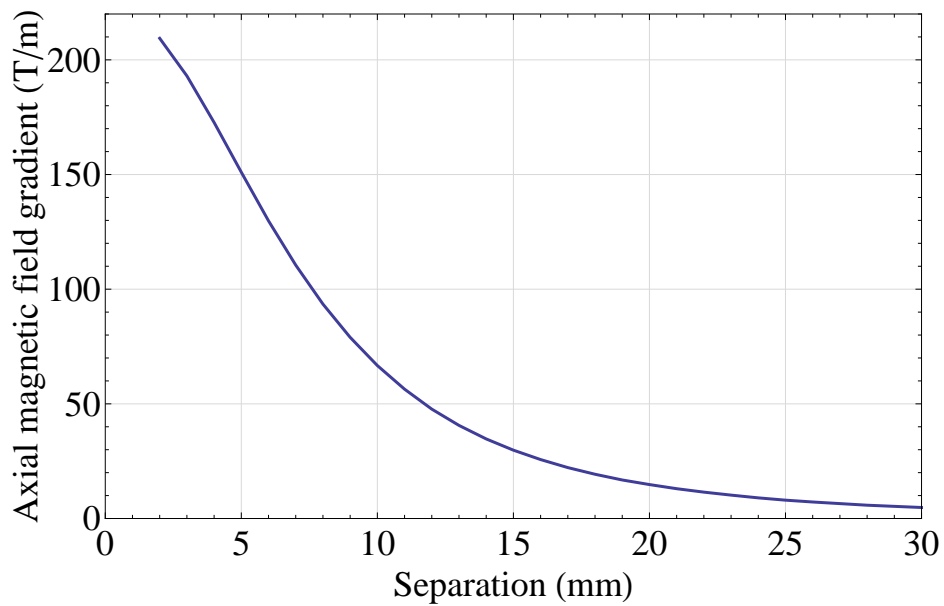


Figure 3.10: The axial gradient as a function of the inner separation distance of the magnets shown in Figure 3.9.

The magnetic field gradients produced by this configuration are highly dependent on the separation between the two magnets. Figure 3.10 shows the axial gradient between the magnets shown in Figure 3.9 as a function of their separation in order to illustrate this point explicitly. The roll-off in gradient for separations below 5 mm is because the magnet pole face size is far from optimum; I will discuss optimisation of the magnet dimensions for a given separation imminently. The separation of the magnets is determined by the size of the trap as the magnets will have to fit around it. Within the region between 5 mm and 10 mm separation there is a very large gain in gradient for even a millimetre size difference of the trap, therefore if attempting to design a linear trap with a symmetric magnet scheme in mind it is worth asking how long a linear section is required to be for a given experiment; a trap half the size would enable a much larger possible gradient. This is especially true if one aims to only use a small region of the trap with a small number of ions. The trap size is the ultimate limiting factor of the gradients produced by this scheme.

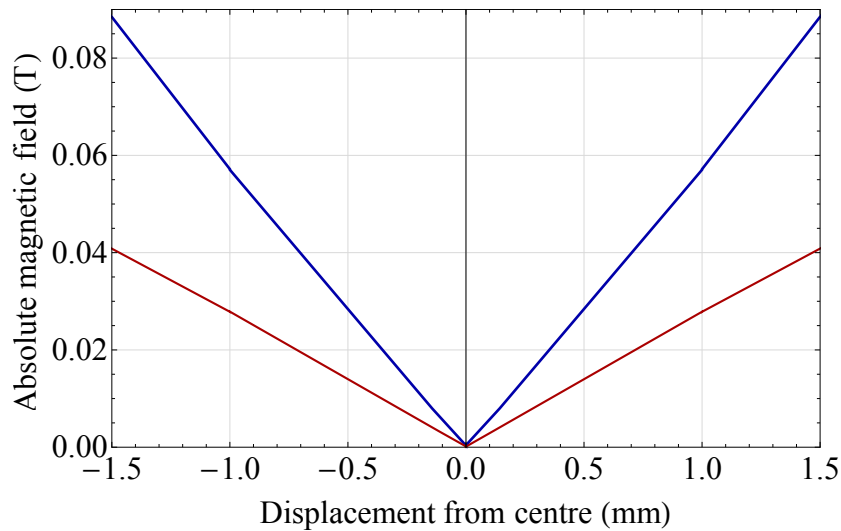


Figure 3.11: Line graphs showing the magnetic field at a given displacement from the centre of the magnetic setup shown in Figure 3.9. Blue - Axial direction, Red - Radial direction parallel to the edge of the magnets.

Figure 3.11 shows the magnetic fields simulated for the magnetic setup shown in Figure 3.9 in both the axial and radial directions. One can see that at the distances shown, both gradients are approximately constant. The radial gradient is approximately half the axial gradient (27.9 T/m and 56.6 T/m respectively for this geometry) and this is evident for all simple symmetric schemes that I have simulated where a near-square pole face has been used. The origin of the gradient in terms of the individual components of the magnetic field is also important to know so that one can understand how to compensate

the offset fields at the ion position for any misalignment with respect to the magnetic nil. For the symmetric magnet scheme, the high gradient originates from the growing field component parallel to the measurement direction. Close to the nil the axial gradient is given by  $\frac{dB_x}{dx}$ , and radial gradients are given by  $\frac{dB_y}{dy}$  and  $\frac{dB_z}{dz}$ .

### 3.4.2 Optimising the symmetric scheme permanent magnet setup

The symmetric magnet scheme is a relatively simple way to produce a high magnetic field gradient at the ion position. We have already seen that the gradients are highly dependent on the separation of the two magnet pole faces so I will now determine the optimum size of the other magnet dimensions, once we have fixed this separation.

The first thing to consider is the effect that the size of the pole faces have on the gradient that can be achieved for a given separation of the magnets. This is important as it links the size of the magnet to the separation in order to find an optimum magnet size in order to create the highest magnetic field gradient. For simplicity, I assume that the pole face of the magnet is square. This should produce the most confined nil position without being circular but also makes the magnets easier to mount. In order to determine the best magnetic pole face size, I simulated different pole face side lengths for five different separations that span the size of traps that we as a group would aim to operate. The axial gradient as a function of the side length of the pole faces of the magnets are shown in Figure 3.12 for a separation of 6 mm, 8 mm, 11 mm, 13 mm and 16 mm. The length of the magnets in this case was set to 14 mm as with the previous magnets shown in Figure 3.9.

These simulations show the gradient is maximised by using a pole face side length of slightly greater than the separation. This effect is greater for smaller separations but as the magnets get bigger, the separation and pole face side length become closer to equal for the highest axial gradient. Since the gain in gradient is relatively small, we can make the assumption that by using a pole face side length equal to the separation of the magnets, a high gradient will still be achieved. This simplifies the problem as we do not need to consider the pole face size adjust as a function of the separation. This simplification will become clearer later in the next stage of the optimisation process as this too does not result in an absolute maximum gradient.

The next dimension to consider in creating an ideal magnet size is the magnet length along the magnetisation direction. This will finalise the optimum size of magnet and allow us to simulate several optimally scaled magnets in order to determine a scaling law. In order to determine the magnet length for the best gradient, I simulated the axial gradient

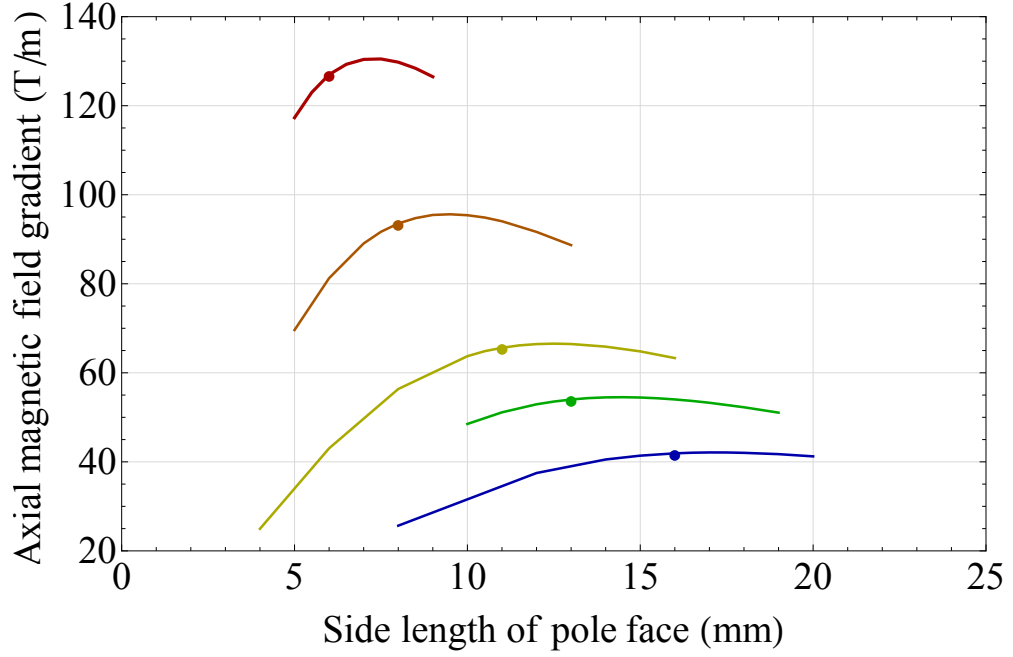


Figure 3.12: The simulated axial gradient as a function of the side length of the pole faces of two magnets in symmetric configuration for three separations of: Red - 6 mm, Orange - 8 mm, Yellow - 11 mm, Green - 13 mm, and Blue - 16 mm. To within 3 percent, the highest gradient occurs at a side length equal to the separation, denoted by an enlarged point.

as a function of the magnet length using a pole face side length equal to the separation of the magnets, the results of which are shown in Figure 3.13 for the same separations previously simulated.

The axial gradient increases with the magnet length but magnet lengths greater than two times the separation gain minimal additional gradient by increasing this dimension. Though higher gradients are possible with a slightly more optimised geometry for a specific separation and experimental setup, one can therefore determine that a high axial gradient can be formed by using a magnet with a square pole face of side length equal to the separation of the two magnets, and a magnet length equal to two times the separation.

Figure 3.14 shows the axial gradient produced by pairs of magnets sized using this rule, as a function of the magnet separation. We are able to fit these simulation results for the axial gradient to a curve given by  $B'_{ax} = \frac{756}{s}$ , where  $B'_{ax}$  is the axial magnetic field gradient measured in T/m and  $s$  is the separation of the magnetic pole faces measured in mm. This agrees with our simulation results to well within 1 percent. We now have a scaling law that can be used to create a near-ideal set of magnets for a given separation, i.e. trap size, and tell us the magnitude of axial gradient for said separation.

Throughout these simulations I have only considered a single magnet grade; this is

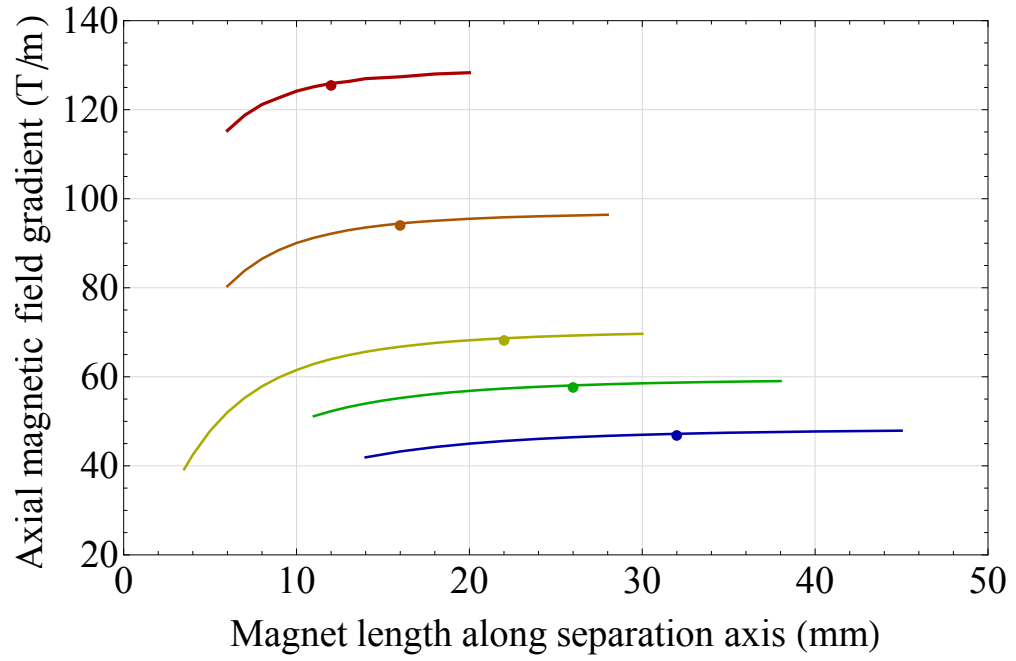


Figure 3.13: The simulated axial gradient as a function of the magnet length for two magnets in symmetric configuration with a pole face side length equal to their separation. This is simulated for three separations of: Red - 6 mm, Orange - 8 mm, Yellow - 11 mm, Green - 13 mm, and Blue - 16 mm. The enlarged point denotes the result for a magnet length that is twice the separation between the innermost pole faces. For lengths greater than this there is a minimal increase in gradient.

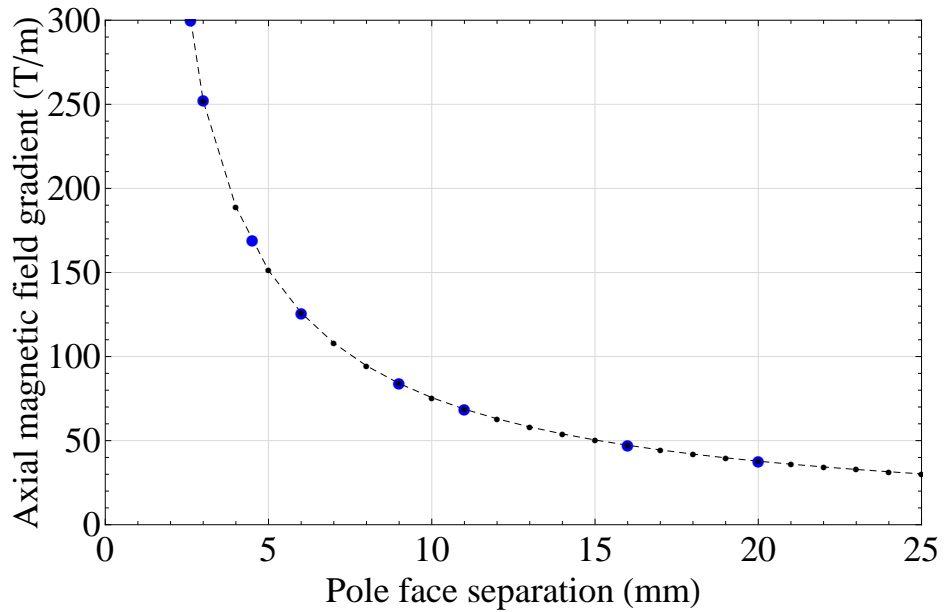


Figure 3.14: The axial magnetic field gradient produced by a pair of idealised magnets as a function of the separation between them. The blue dots indicate the results of a simulation. The black dots and dashed line indicate a scaling curve given by  $\frac{756}{s}$ , where  $s$  is the separation of the magnets.

samarium cobalt with  $B_r = 1.08$  T and  $\mu_r = 1.05$ . The strength of the magnetic field produced by a magnet is dictated by its remanence, thus it is likely that the magnetic field

gradient is directly proportional to this. By performing further simulations of the gradient for different values of  $B_r$  in several of our idealised simulations, it was determined that the axial gradient has a completely linear relationship with the remanence of the magnets. Assuming that the magnets used for this scheme are high-grade samarium cobalt and also have a relative permeability very close to unity, the scaling law can be modified to include the remanence  $B_r$  of the magnets measured in Tesla (T). We therefore arrive with our final scaling law for the axial magnetic field gradient produced by a pair of magnets of size (width (mm) by depth (mm) by length (mm))  $s \times s \times 2s$ . This axial magnetic field gradient in Telsas per metre (T/m) is given by

$$B'_{\text{ax}} = \frac{700B_r}{s} \quad (3.1)$$

I have kept the separation units in terms of millimetres in order to emphasise that this scaling law works best in the millimetre regime for separations between 3 and 25 mm, outside which, the magnet size will be close to the order of fabrication imperfections (which will be discussed later) or the magnets are dangerously large and smaller, less optimum magnets should be used in the interest of safety.

In this section I have discussed how one can construct a high magnetic field gradient setup in a relatively straight-forward manner using in-vacuum permanent magnets. However, I have also noted that this scheme does not lend itself well to a scalable quantum architecture. The solution lies in producing magnetic fields underneath the trapping electrodes of a planar surface trap, and the next two sections describe using either permanent magnets or current carrying wires to do this.

### 3.5 On-chip current carrying wires

The next scheme that I will discuss is on-chip magnetic field gradient production using current carrying wires. As it stands, this method of magnetic field gradient production is the main candidate for a scalable trapped ion quantum computing architecture using microwaves due to its ability to be fabricated as part of the chip [20]. By fabricating buried wires under the top electrode layer and applying currents through them it is possible to create very large tunable magnetic fields and gradients at the position of a trapped ion [33]. A typical on-chip current carrying wire setup may consist of two short sections of parallel wire underneath the trapping zone as shown in Figure 3.15.

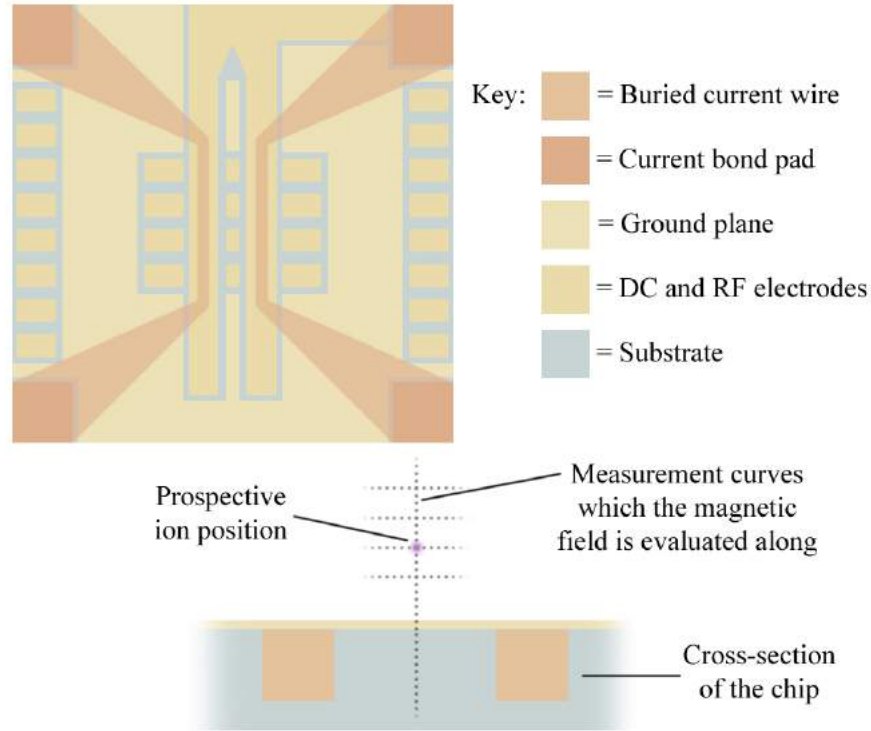


Figure 3.15: A conceptual illustration of a typical current carrying wire chip geometry with the wires oriented for radial gradients. The two sections of wire at the centre provide a high magnetic field gradient at the ion position and can be fed parallel or anti-parallel depending on the desired scheme. The lower diagram shows the position of an ion trapped above the chip (and current wires) and the orientations of the magnetic field measurements analysed in this chapter. This diagram is not to scale.

These in turn can be orientated to be parallel or perpendicular to the RF rails to create in-plane radial or axial magnetic field gradients respectively. The currents through these wires can additionally be run parallel or anti-parallel to each other. Though it may seem counter-intuitive to run the currents anti-parallel as this, like a current loop, would give a unidirectional field, it will be shown that high gradients can be revealed through the use of magnetic field nilling.

In comparison to in-vacuum permanent magnets on-chip current carrying wires have a lot more potential for integration into a scalable system due to their ease of manufacturing as part of a chip. This also means that they are automatically aligned to the trapping regions and therefore do not suffer from problems arising from having to align two or more macroscopic pieces to within tens of microns. A possible limitation of the current carrying wires is that there must always be a current in and current out port on the chip in order for it to operate, and that sufficient compensation magnetics are required in order to get the highest possible gradients. Additionally, since current wires must be an

unbroken line, there are limits to the possible geometries that can be implemented using a two-dimensional topology.

For ease of location, the simulated field and gradient values for some initial simulated wire geometries are summarised at the end of Appendix A rather than quoted throughout the explanation of the schemes and origins of each of their gradients. These results are tabulated for the reference of the reader and members of my experimental group but also serve as a source of the data used at the end of this thesis in order to compare all magnetic field gradient production methods that have been discussed.

### 3.5.1 Analytical calculation of the magnetic field produced by a pair of current carrying wires

In order to assess the gradients produced by a pair of current carrying wires, one will first need to calculate the absolute magnetic field they produce. In this thesis, I do not use any equations which directly state the magnetic field gradient produced by a pair of current carrying wires. This is because a simple calculation of the gradient gives no indication of the offset magnetic field at the position of the high gradient. This is problematic because a high offset field will affect laser cooling of the ion due to the large Zeeman splittings which will cause problems for running an experiment if not properly addressed. It is therefore important that one always considers the magnetic field profile first, highlights a suitable point for coherent manipulation, and then measures the gradient at that point in the magnetic field profile. This is particularly important for current carrying wires as we will soon see that alone they do not produce an explicit magnetic nil at the ion position.

Though I primarily used COMSOL in order to simulate the current carrying wires in this chapter, it is often useful to start by considering the problem analytically before using physical modelling software. A good approximation of the fields and gradients can be made by using analytically derived equations such as  $H = \frac{I}{2\pi r}$  [63], the magnetic field  $H$  produced by an infinitely long current line at a distance  $r$  from it. In this case let us apply  $B = \mu_0 H$  and give the wires a separation  $d$ . The equations describing the magnetic field value at a planar distance  $x$  with respect to wire 1 at a height of  $h$  above the two current carrying wires is given by:

$$B_{x\Rightarrow} = -\frac{\mu_0}{2\pi} \left( \frac{I_1 h}{x^2 + h^2} + \frac{I_2 h}{(d-x)^2 + h^2} \right) \quad (3.2)$$



$$B_{z\Rightarrow} = \frac{\mu_0}{2\pi} \left( \frac{I_1 x}{x^2 + h^2} - \frac{I_2 (d - x)}{(d - x)^2 + h^2} \right) \quad (3.3)$$

$$B_{x\Leftarrow} = \frac{\mu_0}{2\pi} \left( \frac{I_2 h}{(d - x)^2 + h^2} - \frac{I_1 h}{x^2 + h^2} \right) \quad (3.4)$$

$$B_{z\Leftarrow} = \frac{\mu_0}{2\pi} \left( \frac{I_1 x}{x^2 + h^2} + \frac{I_2 (d - x)}{(d - x)^2 + h^2} \right) \quad (3.5)$$

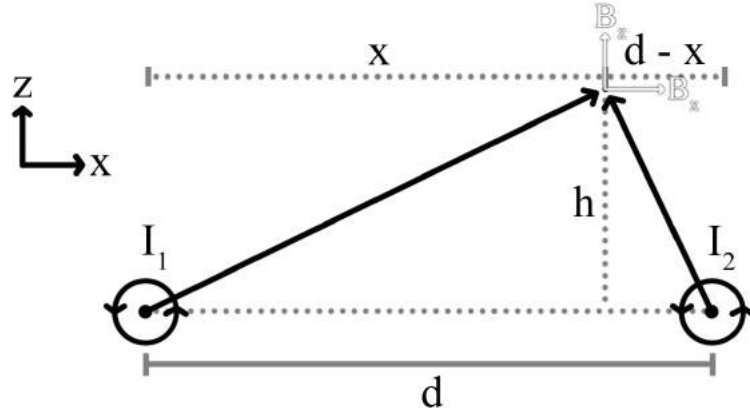


Figure 3.16: A diagram to show the correct orientation of variables in order to use Equations 3.2, 3.3, 3.4, and 3.5.

where  $I_1$  and  $I_2$  are the currents running in each of the infinitesimal wires 1 and 2 respectively, and  $\Rightarrow$  and  $\Leftarrow$  denote the parallel and anti-parallel current cases respectively for the field components  $B_x$  and  $B_z$ . The total magnetic field can be found by combining the components as usual using  $B = \sqrt{B_x^2 + B_z^2}$  where  $B_y$  in this case is set to zero due to the approximated infinite nature of the wires. Figure 3.16 illustrates the orientations of the variables for the correct usage of the equations above. For the anti-parallel case, the current in  $I_2$  is reversed in the diagram. A derivation of these equations is given in Appendix A.

These equations describe the current carrying wire schemes as infinitesimally small uniform current paths. This is unrealistic to the real world case as the wires have finite size. This chapter also only considers straight parallel current wires in order to create magnetic field gradients. Simulations show that in wires that have many sharp turns, it is inaccurate to simulate a current path at the geometric centre of the wire expecting the result to be the same for a wire at finite dimensions. This is because the current will

flow along the path of least resistance and therefore the sharp turns in the geometry will not be experienced by the bulk of the current flowing. This is more clearly illustrated in Figure 3.17 though this is only valid for the DC case. For this reason, I will only consider straight, parallel current wires in this chapter as effects of small bends in the wire are minimal at the ion position and do not appear to help to create a better field profile for higher magnetic field gradients at the ion position.

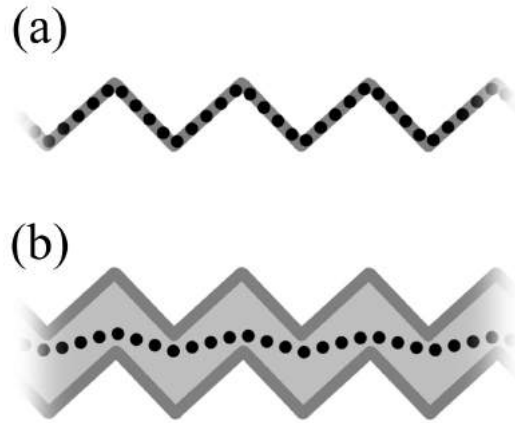


Figure 3.17: The bulk current flow (black dots) in **(a)** - an infinitesimal wire, and **(b)** - a real wire with many small kinks in it. In both cases the highest current density is along the path of least resistance. In the case of (b) a much more complex analytical model would be required in order to give results that reflect reality.

That said, these equations describe the straight wire scheme extremely well, even down to heights of  $20\ \mu\text{m}$  above the wires which is comparable to their dimensions where one would expect there to be effects from the square edges of the microfabricated wire. I am confident that these equations coincide with the simulated results for rectangular wires to within 10 G at the most important regions of interest in each plot. Saying this, there are still simulation errors from poor meshing in some areas so in these areas the analytical equations may be more accurate though these areas are usually far from the ion position where meshing is much finer. Arguably, a slightly more accurate model can be created by splitting each current wire into many small current wires and summing them. However, since the results from the previously mentioned equations are so close to the simulated values at the ion position it is unwarranted to further complicate the model at the height scales we are interested in<sup>5</sup>. COMSOL simulations have been used as a benchmark for all static magnetic field work in this thesis as it allows for easy simulation of much more complex permanent and electromagnet geometries which are difficult to

<sup>5</sup>Both the analytical and COMSOL simulations have shown agreement with other software packages that use different simulation methods which have achieved comparable results.

model with a simple analytical model. These simulations also serve as a starting point within the software for future members of our experimental group who will simulate more complex geometries which are optimised for microfabrication.

### 3.5.2 Analysis of gradient production using current carrying wires

Now that I have introduced the on-chip current carrying wires, I will proceed to discuss simulations of several geometries and characterise the magnetic field produced by each scheme. Each scheme uses a pair of current carrying wires underneath the electrode layer of the chip in order to create a magnetic field gradient at the ion position. However, an explicit nil is not created at the ion position using current carrying wires alone. For this reason, external (nilling) fields are used to cancel offset field components at the ion position in order to reveal a high gradient centred around a nil. In the following sections I will first discuss the field produced by wires alone and then proceed to discussing the field produced by the same wires in the presence of an external nilling field.

Before presenting my first simulation of a pair of current carrying wires, it is appropriate to clarify the geometry that was simulated, and why I chose to simulate it this way before discussing these simulations in detail. In all my COMSOL simulations the wires are modelled as 10 mm long unlike the geometry shown in Figure 3.15. This is because due to the nature of the simulation, current feeds in and out of each wire must be placed on a simulation boundary. If conforming directly to the fabricated wire geometry, one may be restricted in the amount of free space around the wires that can be simulated at reasonable time-scales due to required computing power. If there is insufficient free space surrounding the wires within the simulation geometry, the magnetic field becomes distorted due to the boundary conditions dictated by the simulation, namely  $B = 0$ . By simplifying the geometry to two 10 mm long wires, it does not affect the magnetic field at the region of interest, i.e. the prospective ion position, and makes it much easier to parametrise the wires for editing in order to optimise their separation and cross-section for a given ion height and maximum current. The cross-sectional dimensions of these wires come from chips previously fabricated by Dr Bjoern Lekitsch and discussions with him regarding new chip designs. The reasons for these dimensions will be discussed later in this chapter with regards optimisation of the anti-parallel current carrying wires scheme which has been determined to be the best scheme for producing on-chip gradients using current carrying wires. One must also remember that since these wires are buried underneath the electrode layer, zero height above the wires will correspond to the top surface of the wires.

### Parallel current carrying wires

Perhaps the simplest geometry to discuss is a pair of current wires with a small separation between them and equal currents flowing parallel to each other in both wires. A two-dimensional magnetic field plot for a pair of parallel current wires is shown in Figure 3.18 in order to illustrate the shape of the magnetic field around this set of wires. All out-of-plane components of the field are cancelled along the line stretching vertically from the centre of separation of the wires. This is due to the opposing direction of the magnetic field on opposite sides of each wire due to the current flowing in the same direction. The zero magnetic field region is directly between the two wires, which means that there is a large offset field at the height of the ion. This offset field is oriented in the direction parallel to the surface of the chip for typical geometries.

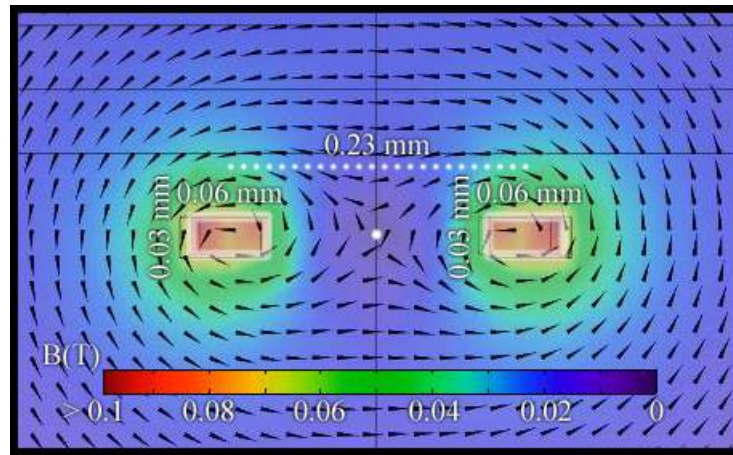


Figure 3.18: The field diagram for a pair of parallel current carrying wires. A single nil with high magnetic field gradient is created centrally between the two wires as no horizontal field is present and the opposing vertical fields of each wire cancel. As we extend vertically from the centre into the far-field solution, the field becomes that of a single current wire and a nil is no longer present. The simulated current in these wires is 10 A and their length is 10 mm. This standard will be used throughout this chapter unless stated otherwise.

The field profile produced by a pair of parallel current wires is therefore contrary to the symmetric permanent magnet scheme, which produces a well defined nil point at the ion position. This is simply a limitation of the current wires being confined to the plane of the trap; a well defined nil could be created at the ion position using current carrying wires if implemented with a symmetric trap geometry such that the ions sit directly between the wires. However, the ions would need to be suitably shielded from any electric field effects that may happen as a result of pulsing a current through the wires. An additional difference is that straight parallel current wire geometries exhibit a linear nil line along

the length of the geometry as opposed to a single point of zero field between two opposing magnets in the symmetric schemes I have discussed. This means that it is possible for a string of ions to exist in the same field if the wires are fabricated with a radial gradient in mind.

Figure 3.19 shows the magnetic field of two parallel current carrying wires 0.06 mm by 10 mm by 0.03 mm separated by 0.23 mm for a current of 10 A measured along the vertical radial direction. From this, one can see that the maximum field is at approximately 0.1 mm above the top surface of the wires. Above this, the field profile gradually becomes closer to that produced by a single wire with twice the current given by  $B = 2 \cdot \frac{\mu_0 I}{2\pi h}$  at a displacement from centre equal to zero. At approximately 1 mm above the wires, one can see no difference between the two-wire and single-wire field profiles as the near-field effects become less dominant and the far-field dominates.

This means that any gradients measured or uncovered using nilling at heights above this can be produced by using a single current wire. We therefore want to utilise near field effects of the two wires significantly below the maximum field height in order to achieve a high gradient. One can also see that the field cancels at the central position between the two wires as there is no  $B_x$  component (as the measurement is in the same plane as the wires) and the  $B_z$  components are equal and opposite as previously illustrated in Figure 3.18. In this case, the vertical radial gradient produced by two parallel current carrying wires is defined by  $\frac{dB_x}{dz}$ . For a height of 50  $\mu\text{m}$  above this set of wires, the gradient is 11.5 T/m/A at an offset field of 15.2 G/A. This is not optimal because of the high offset field that the ion sits in. However, it is still a significant gradient that is explicitly created by the two-wire solution, and is therefore worthy of note in our discussion.

Let us now consider the planar gradients produced by this scheme as this is the gradient that can be used for individual addressing. The field of these wires at various heights is shown in Figure 3.20. Simulations show that there is a large offset field at a displacement from centre of zero due to the  $B_x$  component dominating the total field at this point. The maxima at approximately  $\pm 0.14$  mm displacement from centre of the field profile measured 50  $\mu\text{m}$  above the wires are due to the in-plane component of the field above the individual wires which are at relatively close proximity when compared to their separation, hence the field is stronger. The central dip is due to the lack of this strong field at small distances from their centre of separation as this is relatively far from the wire when compared to the measurements at  $\pm 0.14$  mm.

For a single wire, the out-of-plane component of the field would be dominant for a small

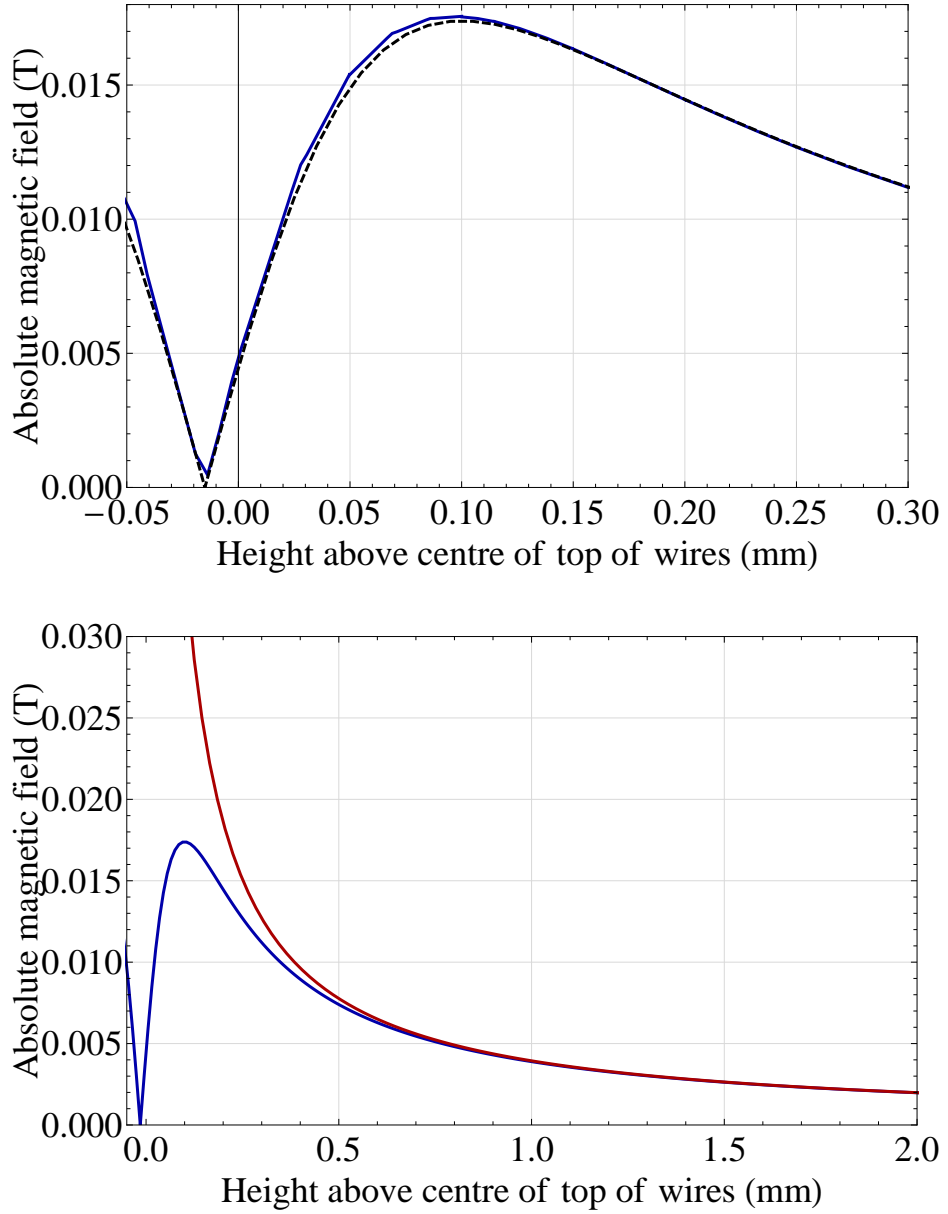


Figure 3.19: The magnetic field produced by two current carrying wires measured centrally along the vertical radial direction. These wires are 0.06 mm by 10 mm by 0.03 mm ( $x$  by  $y$  by  $z$ ) centre separated by 0.23 mm (along  $x$ ) and carrying 10 A of current each flowing parallel to each other. The zero nil point is shown at -0.015 mm as the wires are 0.03 mm thick and the height is shown relative to the top surface of the rectangular wires for better comparison with the ion height above the chip surface. The top graph shows the results of a simulation performed in COMSOL (blue line) and the results using our analytical equations (dashed line). The bottom graph shows the results from the analytical equations for two wires (blue) and for the single-wire far-field solution (red) given by  $B = 2 \cdot \frac{\mu_0 I}{2\pi h}$  at a displacement from centre equal to zero.

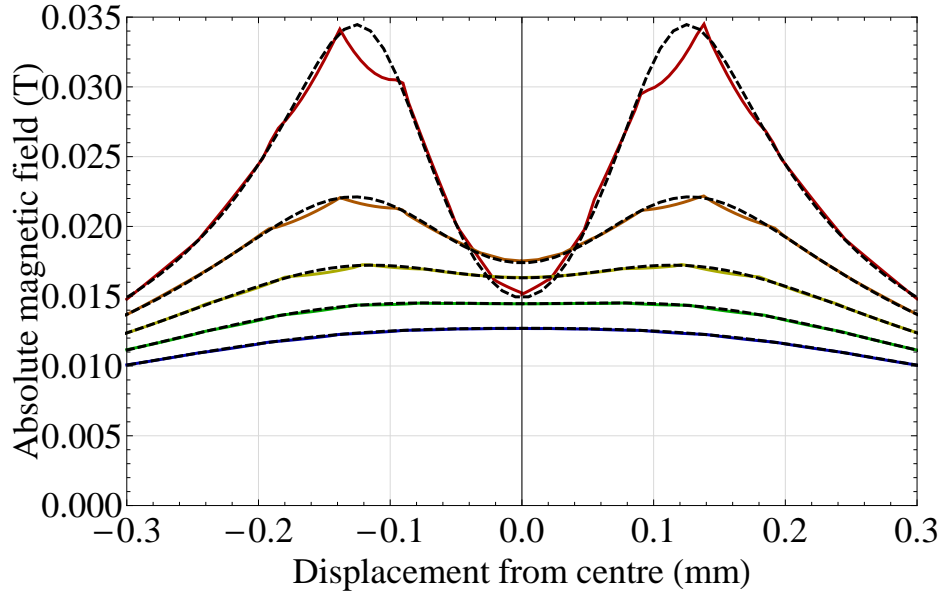


Figure 3.20: The magnetic field produced by two current carrying wires measured at several heights above them along the planar direction. These wires are 0.06 mm by 10 mm by 0.03 mm ( $x$  by  $y$  by  $z$ ) centre separated by 0.23 mm (along  $x$ ) and carrying 10 A of current each flowing parallel to each other. Red - 50  $\mu\text{m}$ , Orange - 100  $\mu\text{m}$ , Yellow - 150  $\mu\text{m}$ , Green - 200  $\mu\text{m}$ , and Blue - 250  $\mu\text{m}$ . The slight quantisation of each line is due to a relatively coarse simulation mesh. The analytical results for each height are shown by the dashed curves.

height but large planar displacement from it, assuming the wire is confined to a plane as is the case with on-chip current carrying wires. However, since there are two parallel current wires in this application, the out-of-plane component of the field is cancelled at an equal distance from the centre of each wire, i.e. a “displacement from centre” equal to zero. This means that only the in-plane component of the field remains at this central position. This is the cause of the dip seen at the centre of the field profile.

For heights below the maximum field point at  $\sim 100 \mu\text{m}$  above the wires, as shown in Figure 3.19, a moderate planar magnetic field gradient is apparent slightly off-centre from the field minimum which can be seen in the 50  $\mu\text{m}$  and 100  $\mu\text{m}$  high measurement lines. This is defined by  $\frac{d|B|}{dx}$  where  $|B|$  is dominated by  $B_x$ . For this set of wires, a planar gradient of 22.22 T/m/A at an offset field of 22.5 G/A can be found for a height of 50  $\mu\text{m}$  above the wires and a displacement of approximately 60  $\mu\text{m}$  from centre. If the offset field were to be nilled at the centre using a uniform field parallel to  $B_x$ , a moderate gradient would be formed from the  $B_z$  and remaining  $B_x$  components at heights below and above the maximum field point. At the maximum, there is no strong change in either component of the field so the gradient is relatively small regardless of field nilling. Above this, the gradient is comparable to that formed by a single wire.

One can see that magnetic field gradients are apparent with parallel current carrying wires, however, they are not competitive with those created by the symmetric magnet scheme for the simple reason that the ion is not aligned to a high gradient magnetic nil; the gradients only occur at high offset fields within the scope of possible ion positions. Nevertheless, the gradients produced by the parallel current scheme are much better than the anti-parallel current scheme which will be discussed next.

### Anti-parallel current carrying wires

Unlike the parallel current carrying wire case, anti-parallel current carrying wires create a large out-of-plane magnetic field with zero in-plane magnetic field above the centre of separation of the wires. This is shown in Figure 3.21 which displays the two-dimensional magnetic field diagram for a pair of current carrying wires with currents flowing anti-parallel to each other. One can also see from this that there is no nil created. That said, there will still be a magnetic field gradient due to the fact that the field decays as a function of distance from the wires.

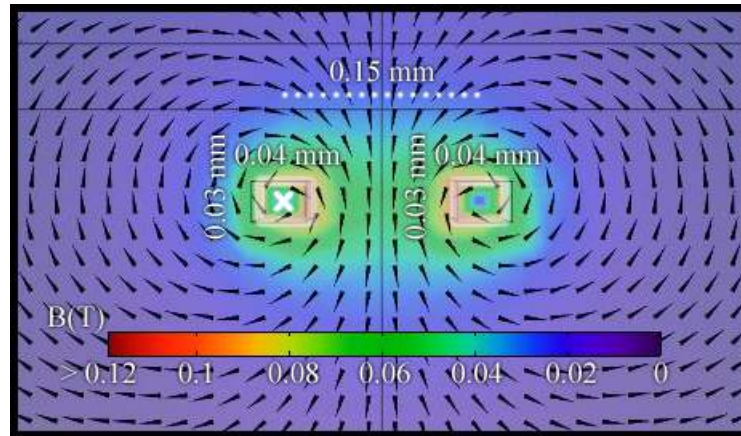


Figure 3.21: The field diagram for a pair of anti-parallel current carrying wires. No nil is present as no fields are directly opposing at any point. Additionally no explicit gradient is formed. The far-field solution still recognises the scheme as the magnetic field produced by two anti-parallel current wires. A uniform vertical field is created between the two wires giving it the field profile of a single permanent magnet with an out-of-plane magnetisation.

Figure 3.22 shows the magnetic field of two anti-parallel current carrying wires measured centrally along the vertical radial direction. This field profile is for a pair of wires 0.04 mm by 10 mm by 0.03 mm separated by 0.15 mm for a current of 10 A. We see that the maximum field along this line occurs centrally between the wires to within simulation error. The vertical radial gradient at this central position is defined by  $\frac{dB_z}{dz}$  and is merely the gradient of a dying field from a singular source, very similar to a single permanent



magnet. For this geometry, the gradient at a height of  $55\ \mu\text{m}$  above the wires is  $37.5\ \text{T/m/A}$  for an offset field of  $28.7\ \text{G/A}$  at a displacement from centre equal to zero. These gradients are still competitive with that of the parallel current scheme, however, there is a much larger offset field than the previous case.

When we consider the planar gradients produced by this scheme, it is clear that it is not viable for our application. Figure 3.23 shows the magnetic field produced by the same pair of wires measured at several heights above them along the planar direction. This simulation confirms that there are no explicit gradient characteristics apart from that defined by the change in field at increased distance from a single magnetic field source. The spiking at the tops of the graphs are merely simulation errors possibly from meshing or boundary condition issues.

However, at a heights low relative to the wire separation, the field profile becomes similar to that of the parallel current scheme. An approximately flat top is achieved to the field profile above the wires at slightly lower than the  $55\ \mu\text{m}$  measurement height shown in Figure 3.23. Below this height, the field is dipped in the centre with larger peaks on either side of the central point, much like the parallel current case. Again, this is due to the low height and the relative proximity of the desired field measurement position to the individual wires generating them. For anti-parallel current wires, this can be considered to be the near-field, though this is not typically observed at our ion heights.

In the anti-parallel configuration the wires provide a high uniform offset field dominated by  $B_z$ . However, by examining the individual components of the field, one can produce extremely high gradients using this scheme. This will be discussed immanently. However, without the use of nilling fields, the anti-parallel current scheme is most useful for creating large offset fields which are non-uniform in its individual components. In the next section I will discuss how nilling works before proceeding to describe the aforementioned wire setups in the present of a nilling field and how with the use of a single uniform offset field, the field profile can be changed dramatically in order to reveal high magnetic field gradients centred around a nil.

However, without the use of nilling fields, the anti-parallel current scheme is most useful for creating large offset fields which are non-uniform in its individual components. In the next section I will discuss how nilling works before proceeding to describe the aforementioned wire setups in the present of a nilling field and how with the use of a single uniform offset field, the field profile can be changed dramatically in order to reveal high magnetic field gradients centred around a nil.

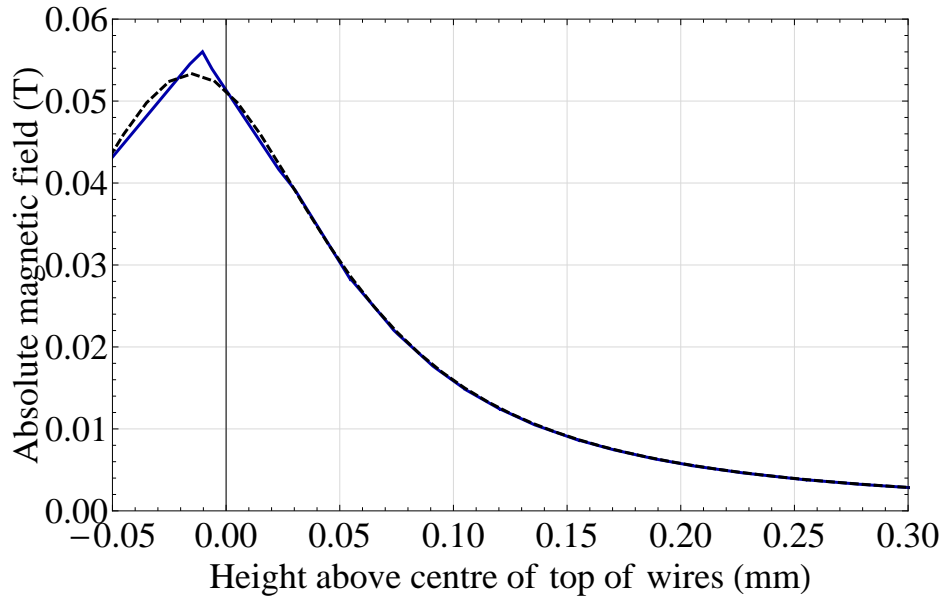


Figure 3.22: The magnetic field produced by two current carrying wires measured centrally along the vertical radial direction. These wires are 0.04 mm by 10 mm by 0.03 mm ( $x$  by  $y$  by  $z$ ) centre separated by 0.15 mm (along  $x$ ) and carrying 10 A of current each flowing anti-parallel to each other. The results of the analytical equations are shown by the dashed curve.

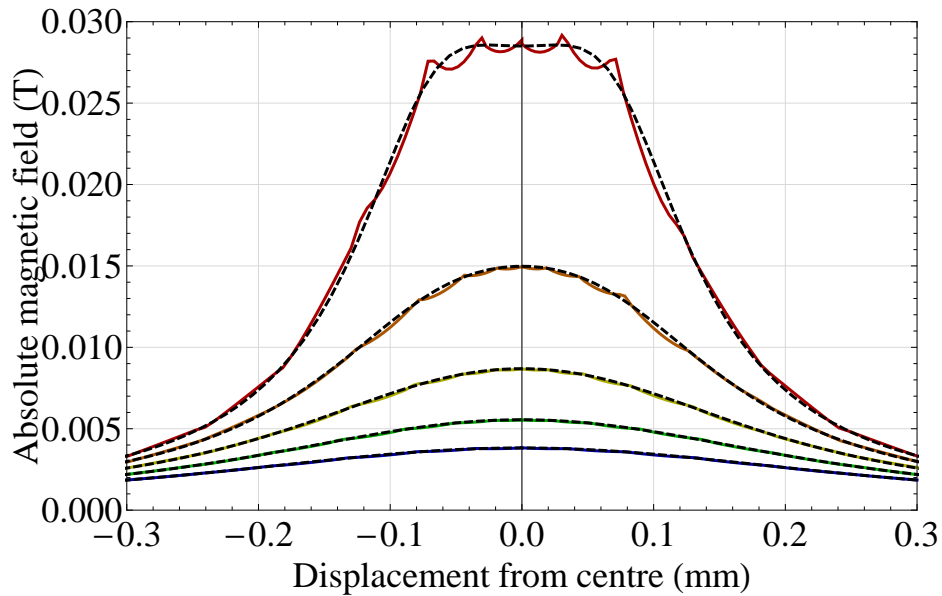


Figure 3.23: The magnetic field produced by two current carrying wires measured at several heights above them along the planar direction. These wires are 0.04 mm by 10 mm by 0.03 mm ( $x$  by  $y$  by  $z$ ) centre separated by 0.15 mm (along  $x$ ) and carrying 10 A of current each flowing anti-parallel to each other. Red - 55  $\mu\text{m}$ , Orange - 105  $\mu\text{m}$ , Yellow - 155  $\mu\text{m}$ , Green - 205  $\mu\text{m}$ , and Blue - 255  $\mu\text{m}$ . The bumps at the top of each curve are likely to be a result of boundary or meshing conditions within the simulation and are unlikely to be a real feature of the magnetic field produced by the wires. The results of the analytical equations are shown by the dashed curves where these bumps are not present.

### Nilling the offset field produced by current carrying wires

In order to get the most out of current carrying wires, one can nil the component of the magnetic field that is creating a high offset field in order to maximise or reveal the gradient. This also allows for higher gradients to be created at an offset field that is experimentally viable for coherent manipulation, i.e. close to zero. If one breaks down the components of the magnetic field into in-plane and out-of-plane components, it is clear how a very strong gradient can be created using this scheme.

Figure 3.24 shows the breakdown of the magnetic field components above a single current wire to indicate how a strong gradient can be revealed<sup>6</sup>. Directly above the wire the  $B_x$  component of the field dominates the total field as the  $B_z$  component is equal to zero. However, at a small distance in  $x$ , this  $B_z$  component grows linearly. At the same time the  $B_x$  component of the field diminishes but much more gradually. One can infer this from the parametric equation for a circle defined in terms of sine and cosine for each component. If one applies a uniform offset field in the vicinity of the wire of  $B_x' = -B_x(0)$ , where  $B_x(0)$  is the field directly above the wire at our region of interest, there is a strong cancellation of the  $B_x$  component of the field. This creates a total field profile  $|B| = 0$  directly above the wire with a high surrounding gradient created by an increase in both components of the field when moving along the  $x$ -direction that is much more rapid than in the uncompensated case. One can therefore see how it is possible to create a high gradient magnetic nil by compensating a single component of the field at a single point if there is a rapid change in field components perpendicular to the one that is nilled. This explanation is also valid at large distances from a pair of parallel current carrying wires, however, in the case of a single wire it is quite easy to see that a magnetic field gradient is present even without nilling because the field produced by a single wire is visibly non-uniform.

Let us now discuss a situation where the magnetic field appears to be uniform but in reality there is a very rapid change in one component of the field which is masked by a perpendicular component which dominates the total field magnitude. For two anti-parallel current wires, the out-of-plane components of the field from each wire constructively add to create the large offset field that may appear to be much more uniform than the field produced by a single wire. However, the in-plane components from each wire point in opposite directions and thus cancel along the vertical line extending out of the plane from

---

<sup>6</sup>A high magnetic field gradient can be realised by nilling the  $B_x$  of the field of a single current wire, however, for a scalable system one would aim to produce all magnetic fields for gradient and offset production on the chip. We therefore use a two-wire scheme as this gives us greater control of the field components at the ion position than a single wire.

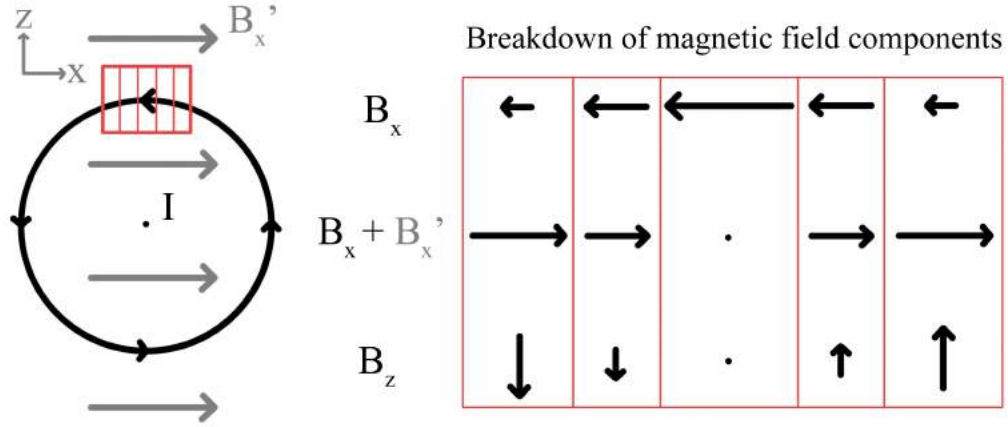


Figure 3.24: An illustrated breakdown of the magnetic field components produced by a single current wire with current  $I$  and the effect that a uniform offset field  $B_x'$  has on one component in shaping the total field. The red box indicates the region above the wire where the field it produces is cancelled by the uniform offset field. This box is divided into five sections so that I may illustrate the change in magnetic field components across this region. The absolute magnetic field of the wire, given by  $|B| = \sqrt{B_x^2 + B_z^2}$  results in a large field dominated by  $B_x$  directly above the wire, i.e. a prospective position of a trapped ion above a planar trap with current carrying wires. When  $B_x$  is cancelled by a uniform offset field  $B_x'$ ,  $|B| = 0$  directly above the wire but grows quickly in  $B_x$  and  $B_z$  as one moves along  $x$ . One can therefore see that by nilling the field at this point, a magnetic field nil with a high gradient is created above the wire.

the centre of separation of the wires.

Figure 3.25 graphically describes how a high planar magnetic field gradient  $\frac{dB_x}{dx}$  near to the centre of separation of the wires can be revealed by nilling the out-of-plane field component  $B_z$  for the anti-parallel current carrying wire case. Since the in-plane components of the field are very small compared to the out-of-plane components they have very little weight on the Pythagorean summation and thus contribute very little to the total field. This means there is very little change in the total field for a small planar displacement at a given height above the wires.

When the out-of-plane components of the field are cancelled by an external unidirectional offset field, the in-plane components dominate the summation and an extremely high gradient is realised from a seemingly zero gradient starting point. In fact, this scheme provides a better magnetic field gradient than the parallel current case as long as one is able to cancel the high out-of-plane offset field. This is interesting when one considers that without nilling there is almost no planar gradient at a displacement from centre equal to zero as shown in Figure 3.22.

In the following sections, I discuss the magnetic field gradient that is revealed in the presence of a uniform offset field that creates a magnetic field nil at the ion position. It will

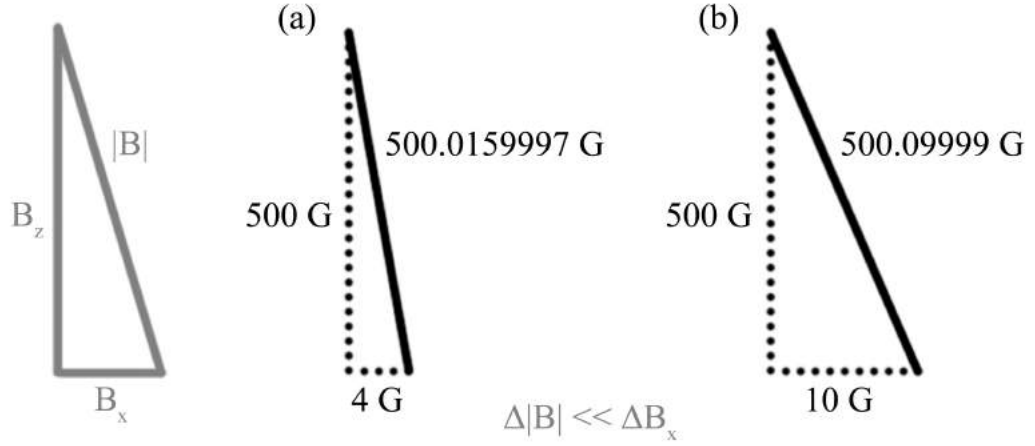


Figure 3.25: A two-dimensional field cancellation example applicable to anti-parallel current carrying wires. (a) and (b) are two points close to each other in the magnetic field near to the centre of the geometry at a given height above the wires. By globally cancelling the  $B_z$  component of both points using external field compensation, the difference between the remaining field at these points is much greater. This results in a magnetic field gradient a few orders of magnitude greater than that without nilling. These magnetic field components are switched for the parallel case. In both of these cases the wires are oriented parallel to the  $y$ -axis and separated in the  $x$ -direction.

be shown that the gradients produced in this case are much larger than those produced by the wires alone. In addition to this, the gradient is centred around a point of zero field, which brings the ion back into a similar field profile as that produced by the symmetric scheme permanent magnets. Given the gradients produced, it is unlikely that one would choose to use on-chip current carrying wires of this geometry without the use of nilling.

### Nilled parallel current carrying wires

Let us first begin by discussing the same pair of parallel current wires that were previously analysed, but this time in the presence of a nilling field oriented parallel to the plane of the chip.

The field diagram for a pair of parallel current carrying wires in the presence of a uniform offset field is shown in Figure 3.26. This offset field is applied horizontally flowing left to right in reference to Figure 3.18. One can see in this case that two nils are formed above the current wires at a displacement from centre equal to zero at the points of equal  $B_x$  to the uniform offset field above and below the maximum field point that is shown in Figure 3.19. Conversely, the field produced below the wires is strengthened by the uniform offset field as they flow in the same direction.

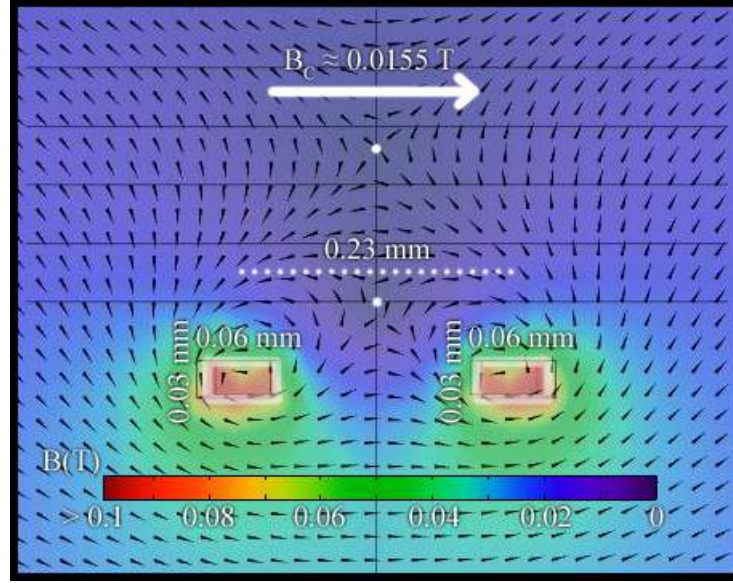


Figure 3.26: The field diagram for a pair of parallel current carrying wires compensated by a global magnetic field applied horizontally flowing left to right. The field below the wires is strengthened but the field above is strongly cancelled. Two nills are formed with a moderate gradient above the central position between the two wires. One is created from the cancelled field in the growing with height field region of the two wire near-field solution, and another from the cancelled field in the decaying with height field region as the field tends towards the one wire far-field solution. The position of the nills is dependent on the compensation field strength. A single nil with smallest relative gradient is formed when the field of the two wires is compensated at its maximum value.

The minimum gradient occurs at the height of maximum field strength, i.e. at the point where the two wire solution starts to switch to the single wire solution. Any gradients produced at distances greater than this are merely formed from the cancellation of a single wire type geometry with a compensation field. This means that for nilled parallel current carrying wires, the separation is extremely important in order to get the best gradients at a given ion height as one wants the height of maximum field to be much greater than the ion height so that the gradient at the ion is a two-wire phenomenon and not the single-wire phenomenon. The single-wire gradients are relatively weak when compared to the two-wire gradients as the change in the  $B_z$  component of the field is small for a given planar distance. Gradients formed below the height of maximum field are substantial and much greater than their non-compensated counterparts, which makes them useful for coherent manipulation experiments. The maximum gradient can be found directly between the centre of the wires where nilling is not required. This means that any field nilling undermines the natural gradient that this scheme produces and an optimum gradient at our ion position does not explicitly exist.

Let us now examine the field profiles in detail to see how they have changed in the

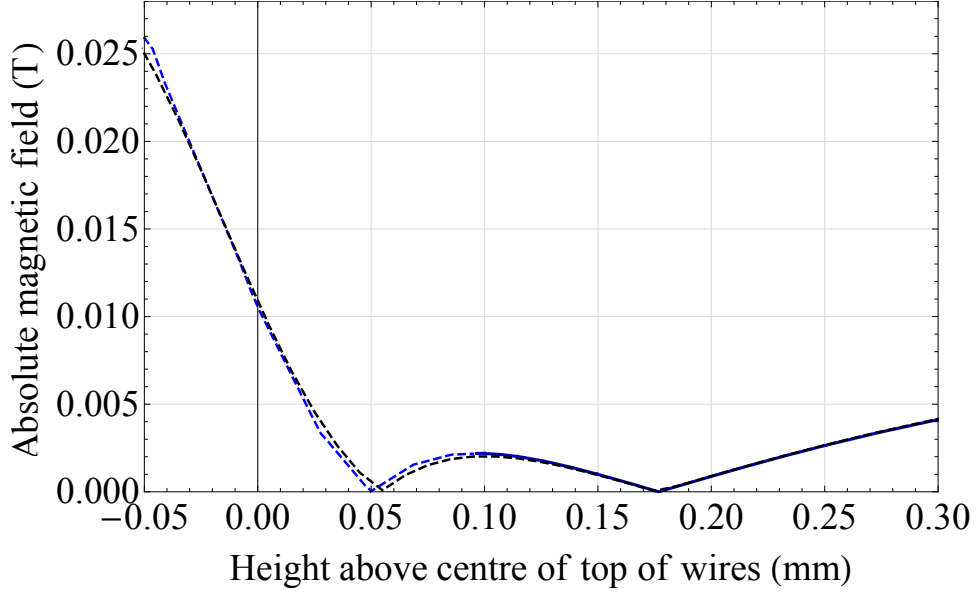


Figure 3.27: The magnetic field produced by two current carrying wires with a compensation field of  $\sim 155$  G in the  $B_x$ -direction applied measured centrally along the vertical radial direction. These wires are 0.06 mm by 10 mm by 0.03 mm ( $x$  by  $y$  by  $z$ ) centre separated by 0.23 mm (along  $x$ ) and carrying 10 A of current each flowing parallel to each other. The dashed portion of the simulated blue curve indicates the relatively high gradient near-field regime beneath the field maximum. The results of the analytical equations are shown by the dashed black curve.

presence of a nilling field. Figure 3.27 shows the magnetic field of two parallel current carrying wires with a uniform offset field applied measured along the vertical radial direction. The wires are 0.06 mm by 10 mm by 0.03 mm separated by 0.23 mm carrying 10 A of current and the nilling field is oriented in  $B_x$  compensating the offset field produced by the wires for a height of  $50\ \mu\text{m}$  above them. One can see the two explicit nil points due to the field cancellation at both points of equal field above and below the maximum field value. In this case these nils occur at  $50\ \mu\text{m}$  (as aimed) and approximately  $175\ \mu\text{m}$  above the wires (consequential). An explicit vertical radial gradient centred around each nil is defined by  $\frac{dB_x}{dz}$  where  $B_x = B_{x_w} + B_{x_c}$ . From this point onwards,  $B_{\phi_w}$  and  $B_{\phi_c}$  will denote the  $\phi$  components of the magnetic field produced by the wires and compensation magnets respectively. The vertical gradient around the  $50\ \mu\text{m}$  high nil for this wire geometry is 80 T/m at 10 A. This is much larger than that in the non-compensated scheme and is now centred around a nil, however this assumes that one can compensate an offset field of this magnitude. In my experience, it is possible to create an offset field of approximately 100 G at the ion position using external compensation coils in order to produce a uniform offset field at the ion position<sup>7</sup>. For the scalable architecture, it is proposed that additional

<sup>7</sup>This is dependent on the size of the vacuum chamber that the experiment operates in. Designing compensation coils are discussed in Chapter 4, however, due to the size of the vacuum systems in these

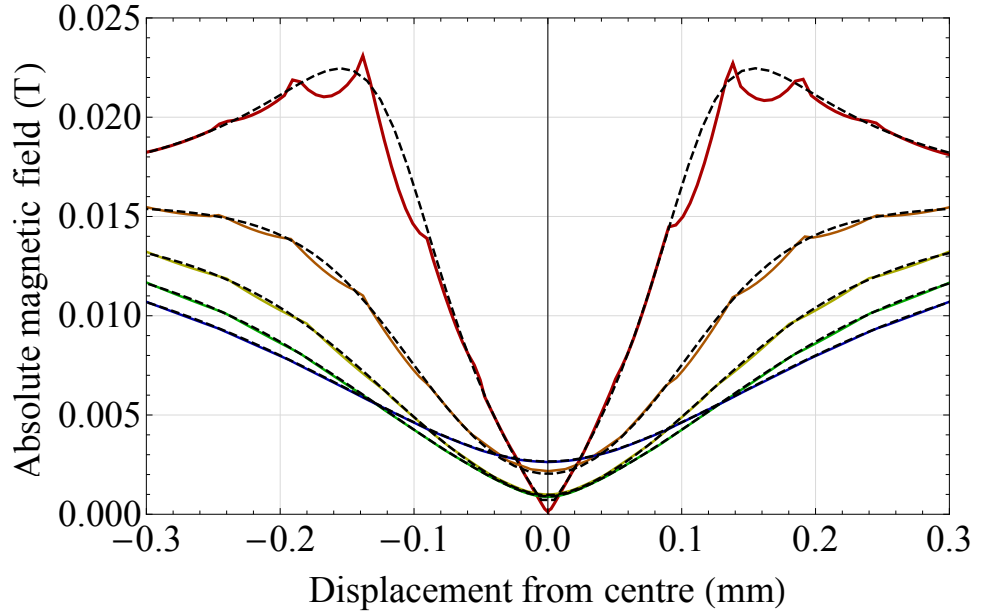


Figure 3.28: The magnetic field produced by two current carrying wires with a compensation field of  $\sim 155$  G in the  $B_x$ -direction applied measured at several heights above them along the planar direction. These wires are 0.06 mm by 10 mm by 0.03 mm ( $x$  by  $y$  by  $z$ ) centre separated by 0.23 mm (along  $x$ ) and carrying 10 A of current each flowing parallel to each other. Red - 50  $\mu\text{m}$  (nilled at this height), Orange - 100  $\mu\text{m}$ , Yellow - 150  $\mu\text{m}$ , Green - 200  $\mu\text{m}$ , and Blue - 250  $\mu\text{m}$ . As before, the kinks at the top of the red curve are unlikely to be a real feature of the magnetic field and is likely to be caused by the simulation boundary conditions as previously explained. The results of the analytical equations are shown by the dashed curves. The slight deviation between the sets of results for higher ion heights is due to the slight non-uniformity in the offset field within the COMSOL simulation due to its origin from a physical magnetic field source within the model.

on-chip wires will be used to provide this offset field, though this in itself is difficult to do with a uniform profile at that magnitude at such a small size. Solutions to this problem will be discussed later in this thesis. Nevertheless, If we apply the 100 G, 10 A limit to the gradient then a smaller gradient of 52.6 T/m for 100 G compensated is achieved, still very promising when compared to the uncompensated parallel current carrying wires.

Let us now consider the change in field profile along a certain height above the wires in order to observe the change in axial gradient which arises from applying this compensation field. Figure 3.28 shows the magnetic field produced by the same current wires measured at several heights above them along the planar direction. As with Figure 3.27 the field component  $B_x$  is centrally nilled at 50  $\mu\text{m}$  above the chip creating a sharp gradient and nil point in that region. Since the offset is uniform, the  $B_x$  component is only nilled at one point at this height meaning that extremely close to the nil the gradient can be

---

experiments, the coils we use produce significantly less compensation field than this within their operating range. Nevertheless, designs in previous experiments such as the Blade trap experimental setup show offset fields at around 100 G to be possible.



approximated by  $\frac{dB_z}{dx}$ . At a larger distance from the nil this quickly becomes  $\frac{d|B|}{dx}$  where  $|B| = \sqrt{(B_{x_w} + B_{x_c})^2 + B_z^2}$  due to the growing  $B_x$  component. At this nil point, the planar gradient is 76.05 T/m for a 100 G nilling field, again a vast improvement when compared to the non-nilled case.

Though the gradients at the ion position have definitely been improved by the use of a nilling field, for parallel current wires this is improving on a case where explicit vertical and planar gradients were still present. It is therefore much more interesting to consider nilled anti-parallel current carrying wires as these do not have explicit axial gradients in the uncompensated scheme.

### Nilled anti-parallel current carrying wires

For nilled field anti-parallel current carrying wires, the geometry is less important in order to achieve high gradients, but is still worth optimising for the best gradients at the intended ion height.

Let us observe how the magnetic field around these two wires changes in the presence of an out-of-plane offset field in order to see where explicit high gradient nils are created and how the magnetic field lines change close to this nil. The field diagram for two anti-parallel current carrying wires in the presence of a uniform offset field is shown in Figure 3.29. Here, the offset field is oriented flowing bottom to top relative to Figure 3.21. One can see that two nils are formed at the points where  $B_z$  is equal in magnitude but in the opposite direction to the offset field at equal heights above and below the central position of the current wires. Though this geometry creates a large field out of the plane of the chip with near zero gradient when not compensated, the gradient formed is not that of the cancellation of a single field component source by an external field, but that of the revelation of the in-plane field components masked by the out-of-plane offset field. At this nil position one can explicitly see that the field arrows above and below it point in opposite directions, and the field arrows either side of it point in opposite directions, signifying that there is a strong change in each field component in all directions which is characteristic of a high gradient nil.

Similarly to other cases, I will now discuss the field profile in order to show how and where the high gradient nil is formed. Figure 3.30 shows the magnetic field produced by two current carrying wires in the presence of a uniform offset field measured centrally along the vertical radial direction. These wires are 0.04 mm by 10 mm by 0.03 mm separated by 0.15 mm carrying a current of 10 A and the nilling field is oriented in

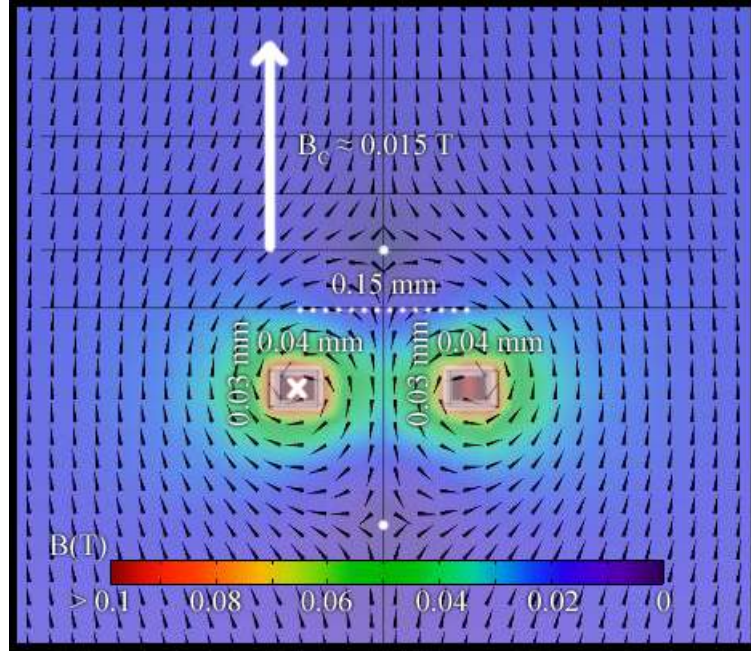


Figure 3.29: The field diagram for a pair of anti-parallel current carrying wires compensated by a global magnetic field applied vertically flowing bottom to top. The field stretching vertically outside the wires is strengthened and the field stretching vertically between them is strongly cancelled. Two nils with high gradients are formed equally and symmetrically from the centre of separation of the wires as the vertical component of the field is cancelled. The stronger the cancelling field, the closer the two nils are to the central position between the two wires until a single nil is formed at this position with maximum gradient.

$B_z$  and cancelled the field of the wires at a height of  $105 \mu\text{m}$  above them. One can see that the field minimum occurs at a single height above (and below) the current carrying wires. The vertical radial gradient here is still defined by  $\frac{dB_z}{dz}$  but is now centred around a nil. This gradient should in theory be the same as for the non-compensated field as the field from the wires along this line is only dependent on  $B_z$ . Since the offset field is uniform in  $B_z$  and is therefore a constant it should have no weight on the gradient value and merely shift the field profile. For a height of  $55 \mu\text{m}$  above the wires, the vertical radial gradient for 100 G nilled is  $130.7 \text{ T/m}$ , much larger than that of the nilled field parallel wire example at a similar nil height at the previously agreed limit of field compensation<sup>8</sup>.

I will now show that a large planar gradient is created at the nil height in the remaining components of the magnetic field. Figure 3.31 shows the magnetic field produced by the same wires and nilling field measured at several heights above them along the planar direction. It is clear now that there is an explicit gradient formed which originates from the

<sup>8</sup>Though the parallel current wires are spaced further apart, this is requirement of that scheme in order to experience the two-wire near-field effect which produces the gradient. This means that the separation is not so comparable between the parallel and anti-parallel schemes because of the different demand of the field profile. These general examples illustrate non-optimised gradients which may be typically tried in the early stages of these current wire investigations.

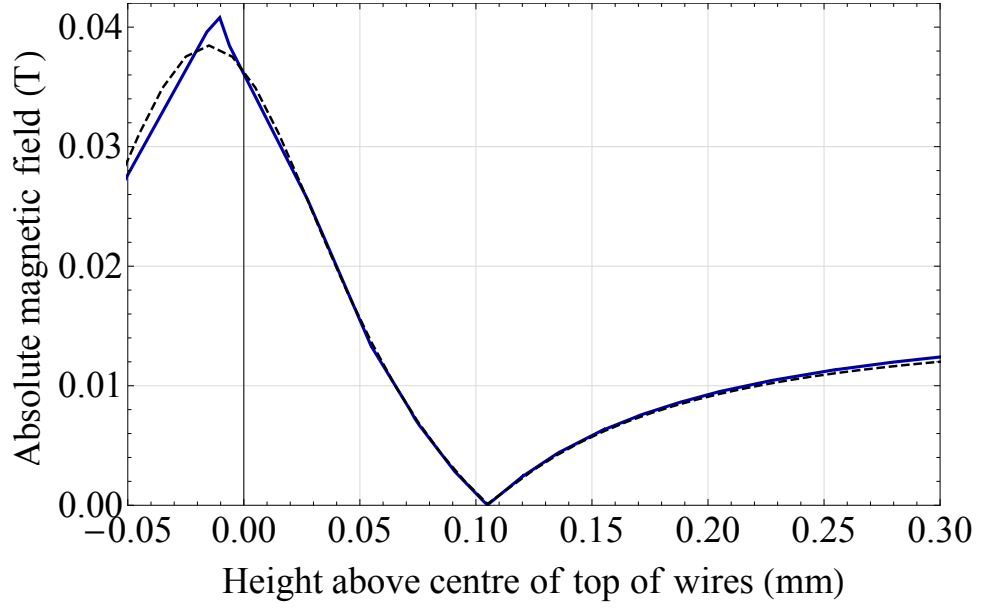


Figure 3.30: The magnetic field produced by two current carrying wires with a compensation field of  $\sim 150$  G in the  $B_z$ -direction applied measured centrally along the vertical radial direction. These wires are 0.04 mm by 10 mm by 0.03 mm ( $x$  by  $y$  by  $z$ ) centre separated by 0.15 mm (along  $x$ ) and carrying 10 A of current each flowing anti-parallel to each other. The results of the analytical equations are shown by the dashed curve.

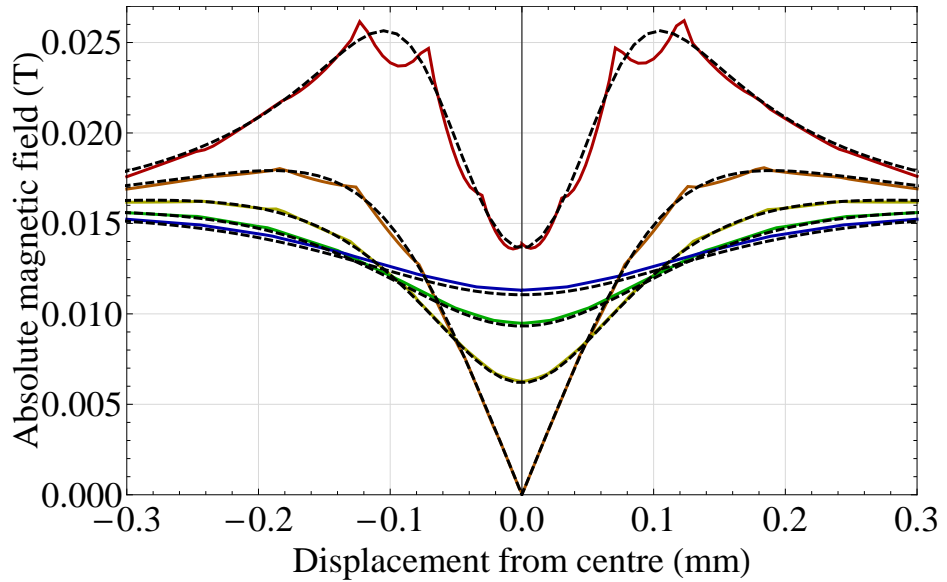


Figure 3.31: The magnetic field produced by two current carrying wires with a compensation field of  $\sim 150$  G in the  $B_z$ -direction applied measured at several heights above them along the planar direction. These wires are 0.04 mm by 10 mm by 0.03 mm ( $x$  by  $y$  by  $z$ ) centre separated by 0.15 mm (along  $x$ ) and carrying 10 A of current each flowing anti-parallel to each other. Red - 55  $\mu\text{m}$ , Orange - 105  $\mu\text{m}$  (nilled at this height), Yellow - 155  $\mu\text{m}$ , Green - 205  $\mu\text{m}$ , and Blue - 255  $\mu\text{m}$ . The results of the analytical equations are shown by the dashed curves.

$B_x$  component of the field which grows with off-centre distance above the wires. Similarly to the parallel current case, since the offset is uniform, the  $B_z$  component is only nilled at one point meaning that extremely close to the nil the gradient can be approximated by  $\frac{dB_x}{dx}$ . Away from the nil this quickly becomes  $\frac{d|B|}{dx}$  where  $|B| = \sqrt{(B_{zw} + B_{zc})^2 + B_x^2}$  due to the growing  $B_z$  component. The planar gradient for 100 G nilled at  $55 \mu\text{m}$  above the wires is 134 T/m. One must note that both of these gradients are significantly higher than those simulated with regards parallel currents. This is mainly because the parallel current scheme relies on high gradient within near-field regime above the wires. For the anti-parallel current scheme, the near field profile is much closer to the wires, and therefore, within our range of ion heights, the field profile is essentially the same, thus the gradients are always relatively high. If the offset field were to be nilled within this near-field regime, the planar gradient is very small because the in-plane component of the magnetic field by the side of a wire is very small.

Though an out-of-plane offset field creates a very high gradient for the nilled field anti-parallel current wires, this is not the only way that a high gradient nil can be created at a prospective ion position. An additional high gradient nil point can be revealed by applying a uniform offset field oriented in  $B_x$  as hinted from discussions of the non-compensated anti-parallel wires.

Let us observe this less obvious gradient production method by looking at the field diagram for a pair of anti-parallel current carrying wires in the presence of this in-plane nilling field as shown in Figure 3.32. This uniform offset field flows right to left with respect to Figure 3.21. One can see now that two nils are formed at the points where  $B_z = 0$  at a large distance from the central position. At these points,  $B_x$  is equal in magnitude but in opposite direction to the offset field. If we go look back to Figure 3.21, we can clearly see where these nil points come from. Since there is a diagonal line of zero  $B_z$  component, a nil point can be created by applying a  $B_x$  component to nil the remaining field at that point. However, as this line of zero  $B_z$  component increases in distance from the centre of separation of the wires, there is a very sharp drop-off in gradient at higher nil heights as they occur further from the centre of the wires. Nevertheless, this still creates a relatively strong gradient at low heights above the wires.

Figure 3.33 shows the magnetic fields measured along the planar directions at a constant height above the wires for this magnetic setup. The field is nilled at a height of  $55 \mu\text{m}$  above the wire but also at a displacement of  $103.4 \mu\text{m}$  from the central position of the wires. At this position, a high planar and vertical radial gradient of 149.19 T/m

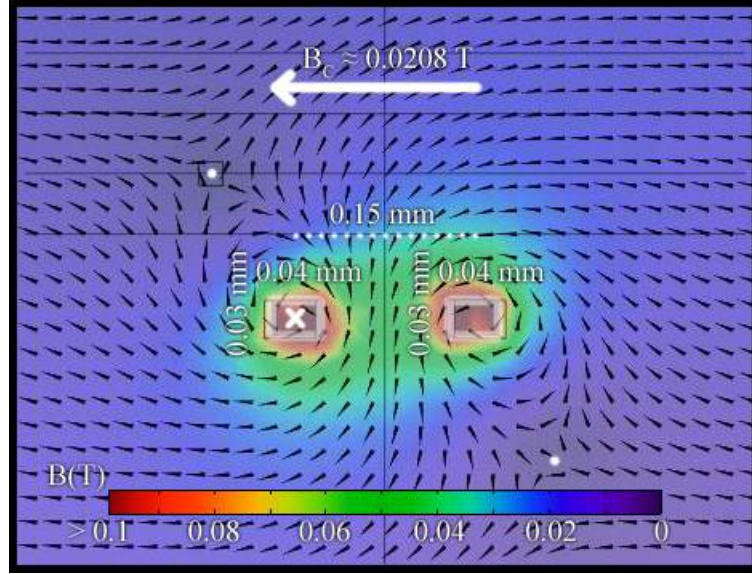


Figure 3.32: The field diagram for a pair of anti-parallel current carrying wires compensated by a global magnetic field applied horizontally flowing right to left. The field on the top right and bottom left of the wires is strengthened and the field on the top left and bottom right is strongly cancelled. Two nils with high gradients are formed equally and rotationally symmetrically from the centre of separation of the wires as the horizontal component of the field is cancelled. The stronger the cancelling field the closer the two nils are to just above (or below) each single wire.

and 212.1 T/m respectively are still observed at this position for the 100 G, 10 A limit. One may notice that these are greater than the gradients produced at the centre. This is mainly valid for lower ion heights simply because the nil position is much closer to one of the wires. In this case the planar and vertical gradients are defined by  $\frac{d|B|}{dx}$  and  $\frac{d|B|}{dz}$  where  $|B| = \sqrt{(B_{x_w} + B_{x_c})^2 + B_{z_w}^2}$  respectively. The revelation of a gradient using both in-plane and out-of-plane nilling fields for the anti-parallel current carrying wire scheme indicates that a high gradient nil can be mapped above the wires using a combination of two compensation fields.

For arguments sake let us consider applying an in-plane nilling field to a pair of anti-parallel current wires which have already been nilled using an out-of-plane nilling field, i.e. the field shown in Figure 3.29. One can see from this field profile that once an out-of-plane nilling field has been applied, the only points where  $B_z = 0$  but  $B_x > 0$  is below the nil and closer to each of the wires. If one were to combine two nilling fields, for heights below the centrally  $B_z$  nilled height, two high gradient points can be formed rotationally symmetrical about the centre of separation of the wires by applying an additional  $B_x$  offset field. The planar and vertical gradient at these points is defined by  $\frac{d|B|}{dx}$  and  $\frac{d|B|}{dz}$  respectively where  $|B| = \sqrt{(B_{x_w} + B_{x_c})^2 + (B_{z_w} + B_{z_c})^2}$ .

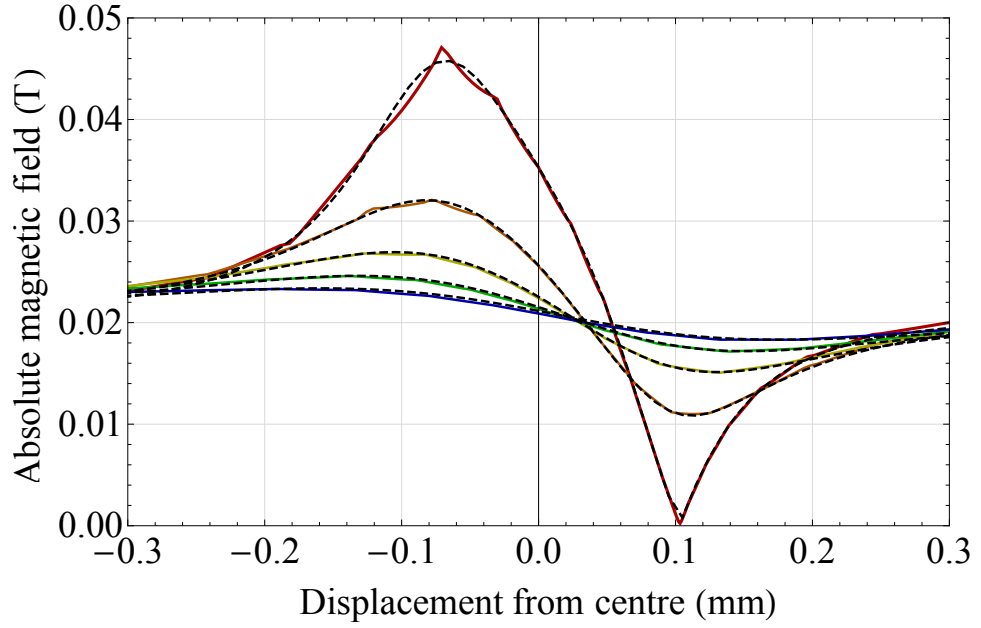


Figure 3.33: The magnetic field produced by two current carrying wires with a compensation field of  $\sim 208$  G in the  $B_x$ -direction applied measured at several heights above them along the planar direction. These wires are 0.04 mm by 10 mm by 0.03 mm ( $x$  by  $y$  by  $z$ ) centre separated by 0.15 mm (along  $x$ ) and carrying 10 A of current each flowing anti-parallel to each other. Red - 55  $\mu\text{m}$  (nilled at this height), Orange - 105  $\mu\text{m}$ , Yellow - 155  $\mu\text{m}$ , Green - 205  $\mu\text{m}$ , and Blue - 255  $\mu\text{m}$ . The results of the analytical equations are shown by the dashed curves.

This demonstrates an ability to map a nil with an accompanying high gradient using multiple offset fields. Aside from the higher gradients possible, this ability to map to different points and still maintain a high gradient gives the anti-parallel current carrying wires a distinct advantage over the parallel case.

### Summary of magnetic field gradient production methods using a pair of current carrying wires

The previous discussion gave an in-depth look into the origins of the shape of the magnetic field and the gradients produced by a pair of current carrying wires both on their own and in the presence of an offset field. I have shown how by manipulation of single component of the magnetic field, one is able to uncover gradients much larger than those naturally produced by the scheme and have discussed the origins of each gradient in terms of the individual components of the magnetic field, as essential piece of knowledge when designing any magnetic field compensation apparatus.

Now that these schemes have been discussed, I can simply summarise the main points and reaffirm the best candidate for high magnetic field gradient for use in our ion trap experiments:

- Parallel currents wires create moderate planar and vertical gradients when a current is run through them.
- These operate within two regimes; the near field, two-wire regime with a higher gradient, and the far-field, single wire regime with much lower gradients.
- Anti-parallel wires create a large offset field oriented out of the plane with no explicit planar gradient and a large vertical gradient due to proximity from the field source.
- For both schemes, nilling fields can be used to reveal larger gradients in a single component of the magnetic field.
- The nilled field anti-parallel current wires exhibit much higher gradients than the nilled field parallel current wires. This nil is mappable using a combination out-of-plane and in-plane nilling fields while retaining a very high magnetic field gradient.
- The magnetic field gradients of the nilled field schemes are dictated by the offset field that one can compensate.

From these discussions, we conclude that the nilled field anti-parallel current carrying wires scheme produces the highest magnetic field gradients within the heights above the wires that we are interested in. It is therefore important that the optimum dimensions of these wires can be determined for the largest possible gradients using this scheme.

### 3.5.3 Optimisation of the nilled anti-parallel current carrying wire scheme

In this section I will attempt to create a series of steps by which one can determine the optimum separation of a pair of anti-parallel current wires in order to achieve the highest gradients in a given experimental setup.

Since the parallel current scheme produces a natural point of highest gradient at the centre of separation, optimisation of the wire separation is a trade-off for a given ion height as the ion position needs to be suitably far from the field maximum in order to achieve a high gradient. This is therefore a futile effort.

Conversely, for the anti-parallel case, an optimisation protocol can be created by determining the wire separation required to create the maximum offset field that one is able to compensate using in-vacuum or external compensation sources. This offset field is dictated by the current that can be run through wires of a certain cross section at a given height above them. This results in a limit to the gradient that one can produce; too much offset field means we cannot compensate it and can therefore not apply as higher current

or vice versa, thus lowering the gradient. The gradient is therefore maximised when the wire separation for the highest applicable current creates the highest compensable offset field at the ion position.

In order to perform this optimisation, we start with Equation 3.5 for the  $B_z$  component of the field produced by a pair of anti-parallel current carrying wires. We then set  $x = \frac{d}{2}$  for an ion above the centre of separation of the wires, and  $I_1 = I_2 = I$  for equal current in each wire, which gives

$$B_{z\rightleftharpoons} = \frac{\mu_0}{2\pi} \left( \frac{Id}{\left(\frac{d}{2}\right)^2 + h^2} \right)$$

which can be rearranged to get

$$\frac{d^2}{4} - \frac{\mu_0 I}{2\pi B_{z\rightleftharpoons}} d + h^2 = 0$$

We now have a quadratic in  $d$  related to the height above the wires that we want to create our maximum offset field. We can solve this for the separation  $d$  using

$$d = \frac{-b \pm \sqrt{b^2 - 4ac}}{2a}$$

setting  $a = \frac{1}{4}$ ,  $b = -\frac{\mu_0 I}{2\pi B_{z\rightleftharpoons}}$ , and  $c = h^2$ . Since this is quadratic function, there are typically two solutions for the separation. The smaller of these two values is the high gradient solution above two close wires (closer to the wires means a greater change in the field components, thus a higher revealed gradient) and the other is the low gradient solution from the summation of the peripheral fields of two wires that are approximately in-plane with the point of measurement, previously described as the near-field for this scheme. We therefore solve for the smaller value of  $d$  and get our final relationship:

$$d = 2(\gamma - \sqrt{\gamma^2 - h^2}) \quad (3.6)$$

where

$$\gamma = \frac{\mu_0 I_{\max}}{2\pi B_{zC}}.$$

Here,  $I_{\max}$  is the maximum current that can be applied through the wires, and  $B_{zC}$  is the maximum (uniform in  $x$ ) offset field that can be generated in the  $B_z$  direction to cancel the field of the anti-parallel current wires. We now have an equation which, given the maximum current in the wires, the maximum  $B_z$  offset field we can compensate, and a height above the wires, we can determine the optimum separation of the wires for the highest gradients. Given this separation, we can then plot or simulate  $B_{x\rightleftharpoons}$  (given by Equation 3.4) for our



chosen ion height in order to find the maximum planar magnetic field gradient that can be produced given these constraints. However, there is another constraint to Equation 3.6. The maximum field can only be created for a certain current up to a height of  $h = \gamma$ . Above this, the solutions of the separation  $d$  become complex because it is not possible to create this offset field at a greater height from the wires without increasing  $I_{\max}$ . This optimisation process therefore also gives the range of heights for which the current and offset field constraints are valid.

Equation 3.6 presents a useful way to design a pair of nilled field anti-parallel current wires for the highest magnetic field gradients. However, this equation assumes that the wires are infinitesimal in nature. It is therefore a good and simple starting point when designing a set of on-chip current carrying wires, but simulation of the gradients produced by wires with a defined size is best done using a program such as COMSOL. Let us use this optimisation method in order to determine an example optimum separation for a pair of current carrying wires within an experimental setup.

### Example use of the optimisation process

For the current wires we have discussed in this section, we have assumed a maximum current of 10 A can be applied to the wires<sup>9</sup> and that a maximum compensation field of 100 G can be used to nil the offset field at the ion position in order to create a high planar gradient. This 100 G nilling field is based on the offset field that was compensated using external compensation coils after initial trapping following the retrofit of the symmetric scheme magnets in the Blade trap setup. This means that we know it is possible to create such a field using external coils. In the scalable system, it is intended that this nilling field would be produced on-chip, however, working designs in order to do this have not yet been verified, though they are in development. For this optimisation example, I will consider the 100 G nilling field to be produced using external or in-vacuum coils to produce a uniform offset field in  $B_z$ . The current limit of 10 A is determined by the dimensions of the wires that have been previously fabricated. The reason for this limit will be discussed later in this section.

If we set  $B_{zC} = 0.01$  T and  $I_{\max} = 10$  A, Equation 3.6 becomes

$$d = 2(0.0002 - \sqrt{0.0002^2 - h^2})$$

---

<sup>9</sup>This is the limit chosen due to current supply stability and the previously optimised wire cross section. The latter and its implications for current wire operation will be discussed imminently.

which we can now use to determine the optimum separation given our limits and the range of heights which these constraints are valid.

The maximum height that these limits apply is  $h = 0.0002$  m, i.e.  $200\text{ }\mu\text{m}$  above the centre of the wires, where 100 G offset for 10 A applied current is achieved using a separation of  $400\text{ }\mu\text{m}$ . The lower limit of nil heights is determined by the width of the wires, which from chips previously fabricated by Dr Bjoern Lekitsch is  $40\text{ }\mu\text{m}$  (by  $30\text{ }\mu\text{m}$  thick). This means that the minimum separation must be greater than  $40\text{ }\mu\text{m}$  which is achieved for an approximate height of  $88\text{ }\mu\text{m}$  above the centre of the wires. In order to achieve a separation in which the wires are relatively far from each other when compared to their width, I will state that the range of heights for which these separations are valid is  $120 - 200\text{ }\mu\text{m}$ . Closer than this, the wires are separated by less than their width, which may be difficult to fabricate given the aspect ratio of the wires. We can now determine the separation of the wires for our range of valid nil heights. In order to convert to ion height, one must remember that this equation approximates the wires as being infinitesimally thin, thus the ion height is  $h - (\frac{t_w}{2} + t_e)$  where  $t_w$  and  $t_e$  are the thicknesses of the current carrying wires and electrode layers respectively.

In order to see what gradients could be achieved using these constraints, I simulated four sets of current wires with the optimally determined separation for a set of target heights above the top surface of the wires. Table 3.2 shows the gradients for the heights that were simulated. These gradients are all greater than those in the non-optimised geometries shown at the end of Appendix A, which indicates that the optimisation protocol used here is at least valid for this range of heights, however, different protocols will have to be used in order to design the “best” wire geometries for heights higher than this. The simplest way to do this is to use a separation of  $0.4\text{ mm}$  and merely apply less compensation field or, if possible, up the current in the wires, though one would re-optimize the wire separation given this new constraint.

### **Investigation into the optimum cross section of the wires**

Ideally, one would desire an infinitesimal current line for each of these separations in order to achieve the highest magnetic field gradients as this is the ideal analytical case. For real current wires one can maximise the gradients by making the wires have the smallest cross section possible that can take 10 A of current. However, this would cause them to melt if there was insufficient cooling due to ohmic heating and eventually electromigration.

Electromigration is a phenomenon whereby the atoms in the metal begin to move due to

Table 3.2: Optimum wire separations and the resulting vertical and planar gradients for the compensated anti-parallel current carrying wire scheme. The range of heights is limited by the optimisation constraints of 100 G at the specified height for a current of 10 A in each wire of dimensions  $0.04 \times 10 \times 0.03$  mm (width  $\times$  length  $\times$  depth). The separation is parallel to the width and the depth is parallel to the height above the wires. \* - These separations are rounded for ease of simulation.

Height above top of wires ( $\mu\text{m}$ )	*Optimum centre-centre separation (mm)	Vertical gradient at 10 A (T/m)	Nilled planar gradient at 10 A (T/m)
105	0.08	173.9	146.2
130	0.124	123.5	114.2
155	0.19	86.7	88.6
180	0.311	66.7	62.5

the collisions of the electrons with crystal defects at extremely high current densities [64]. This would essentially destroy our current wires as the metal atoms are pushed along the chip by the electron flow. If I assume that one uses a cooling system to bring the chip down to  $\sim 160$  Kelvin, the current density resulting in electromigration in copper is  $10 \text{ MA}/\text{cm}^2$  [64]. Assuming a square cross section<sup>10</sup> with sufficient cooling power, the smallest wires one would be able to use on-chip with a current of 10 A would be  $10 \mu\text{m}$  by  $10 \mu\text{m}$ . This produces gradients around 15 percent greater than those shown in Table 3.2.

Conversely, the  $40 \mu\text{m}$  by  $30 \mu\text{m}$  wires have a current density of  $0.83 \text{ MA}/\text{cm}^2$  when 10 A is applied to them, much closer to the  $2 \text{ MA}/\text{cm}^2$  limit at 350 Kelvin [64]. This would allow the original wires to operate at up to 24 A at this temperature<sup>11</sup>, which is why they were previously optimised for fabrication at this size. Additionally, since the surface area is greater, this will help in thermal conduction of heat away from the wires with the aide of a cooling system and allow for a larger current in the event that higher uniform offset fields can be generated, though this may be difficult to do. By fabricating the wires at larger than the optimum size determined by the current density which produces electromigration, we allow ourselves some leeway with regards mistakes during experimental operation.

### Summary of optimisation findings

I have now discussed optimisation of nilled field anti-parallel current carrying wire geometries in significant detail. The main conclusions of this investigation are summarised below:

<sup>10</sup>This shape is due to the microfabrication process. Rectangular wires can also be used to enhance thermal conduction to the substrate, however, previous investigations have shown that wire widths of  $20 - 60 \mu\text{m}$  (and a thickness of  $30 \mu\text{m}$ ) reduce the gradient by up to 5 percent when compared to square wires.

<sup>11</sup>The currents would be pulsed during operation to stop the wires from melting though the time limit that the pulse could be applied would be dictated by the ohmic heating rate.

- The gradient produced by a pair of nilled field anti-parallel current carrying wires is limited by the offset field  $B_{zC}$  that can be compensated, the largest current  $I_{\max}$  that can be applied, and the separation  $d$  of the current wires.
- By rearranging the equation for the  $B_z$  component of the magnetic field produced by a set of anti-parallel wires, we arrive at a quadratic equation that can be solved for the smallest wire separation for a given current in order to produce the offset compensation limit at a given height  $h$  above the wires.
- This separation is given by  $d = 2(\gamma - \sqrt{\gamma^2 - h^2})$  where  $\gamma = \frac{\mu_0 I_{\max}}{2\pi B_{zC}}$ . When this separation was rounded to the nearest micrometre, the achieved offset field was equal to  $B_{zC}$  to within 0.1 G/A for our optimised wire cross section.
- One can then plot/simulate the  $B_x$  component of the magnetic field produced by the same wires for the chosen height and required separation in order to find the gradient.
- The range of heights for which the chosen limits are valid is given by the minimum separation dictated by the physical wire size and the upper limit  $h = \gamma$  above which the offset field cannot be produced for the current limit.
- The cross section of the wires dictates the largest current that can be applied before melting or electromigration.
- The highest gradients are created using wires with a square cross-section with minimal side length.

We now have the necessary tools in order to design an optimum nilled field anti-parallel current wire geometry given our fabrication, compensation, and current limits using an optimisation process determined from the analytical equations for a pair of current carrying wires.

Though it would be most logical to run a pair of current carrying wires in series from the same power supply, the effect of unequal currents in the wires was investigated in case a separate current supply needed to be used for each current wire. This is particularly important to consider when selecting current supplies for purchase as one needs to know what stability is suitable for the current carrying wires to be independently operated effectively.

### Unequal currents in a pair of current carrying wires

An unreasonably large difference of 1 percent in specified current was chosen to see the effect it would have on the central position of the gradient. For this, I simulated the anti-parallel wire scheme shown in Figure 3.31 with 10 A in one wire and 10.1 A in the other wire with the region of interest at the nilled 100  $\mu\text{m}$  height above the wires. For this extreme exaggeration of the current difference, the change in central position of the nil point was only 0.3  $\mu\text{m}$  towards the lower current wire, with less than 1 G change in the offset field of the uncompensated wires (149.25 G to 148.6 G) and a gradient shift from 178 T/m to 175 T/m. Though these changes would cause a shift in the sideband Rabi frequency and hyperfine splitting, so long as these effects are small, it has been shown that reasonable levels of current supply noise do not prevent high fidelity operation<sup>12</sup>. It was therefore deemed that any reasonable current supply output uncertainty would not have a large enough effect on the ion over other sources of experimental noise giving us peace of mind when deciding on what current supplies would be appropriate.

One can also use independent control of the current wires to alter the position of the nil in the presence of a uniform offset field. This is useful for selecting the field that the ion sits in if one is unable to shuttle the ion to a different position. This is of particular importance for current wires aligned in order to produce planar radial gradients as it would be ill advised to shift the ion string radially as this would create excess micromotion due to its displacement from the RF nil position.

I have now thoroughly examined on-chip current carrying wire gradient production methods and indicated a procedure by which the highest possible gradients can be determined for an experimental setup.

#### 3.5.4 Closing thoughts on gradient production using on-chip current carrying wires

In this section, I have described magnetic field gradient production using current carrying wires in great detail. I will briefly compare the gradient production methods discussed thus far before moving onto a new under-chip magnet scheme which is the main focus of the work described in this thesis.

For the chip trap size that we use (10 mm by 10 mm) the symmetric magnet scheme will give an approximate axial gradient of 70 T/m with a radial gradient of 35 T/m for

---

<sup>12</sup>We know this because compensation fields created by currents were used when obtaining the data discussed in Chapter 2. The current supplies used when obtaining the results had 10 mA peak to peak ripple at 20 MHz, much smaller than the effects discussed in this section.

the idealised magnet size. Since this gradient is only determined by the chip size, it is independent of the ion height, contrary to gradients produced by on-chip current carrying wires which create much higher gradients at low ion heights when compared to higher ion heights. However, in general, the gradients produced by the optimised nilled anti-parallel current wires have been shown to be much better than the symmetric scheme for ion heights up to  $\sim 180 \mu\text{m}$ . One would therefore only benefit from using the symmetric magnet scheme for high ion heights on smaller chips. The only advantage of symmetric magnets in this case is that they are much easier to operate and implement, but are not a worthy candidate for a scalable system because of their off-chip nature. This therefore places on-chip current carrying wires as the best candidate for magnetic field gradient production for a scalable quantum computing architecture with trapped ions using long-wavelength radiation. That said, it may be initially difficult to perform high fidelity experiments using current carrying wires due to the nuances in experimental control of a variable magnetic field gradient and cooling the wires during these operations. Gradient production for initial high fidelity experiments using a planar trap can be simplified by using an under-chip magnetic spacer.

### 3.6 In-vacuum under-chip magnetic spacer

So far in this chapter I have described two methods by which one can create a high magnetic field gradient at the ion position. The first method uses a pair of magnets in a symmetric configuration about the ion with opposing polarities in order to create a single point of zero magnetic field between the two magnets which is surrounded by a high magnetic field gradient. While this type of geometry has been successfully used with the macroscopic Blade trap setup discussed in Chapters 1 and 2, this scheme has several limitations when paired with a planar chip trap. For a high magnetic field gradient, the two magnets should be as close together as possible, however, the size of the chip limits this as the ions, and therefore the chip, must sit directly between the faces of the two magnets. In addition to this, a significant portion of the magnets sit above the surface of the chip, and though this scheme works well for a macroscopic symmetric trap, complications arise when moving to planar chip trap geometries, mainly due to the possibility of magnets blocking laser access and atomic oven beam paths. That is to say that creating a high magnetic field gradient using a similar scheme is not impossible, but merely that many more geometric aspects must be taken into account when designing an appropriate geometry.

The second method that is discussed uses on-chip current carrying wires in the presence

of a uniform offset field. While this is envisioned as a long term solution for creating gradients on a scalable architecture, construction and operation of a chip with buried current carrying wires is challenging. In this eventuality, it would be useful to devise a method of magnetic field gradient production that could be used with chip traps without the use of current carrying wires. However, this would have to be more suited to planar geometries than the symmetric magnet scheme in order to get higher gradients than those limited by the size of the chip. This magnetic structure would need to sit close to the chip trap but not cause problems to laser or atomic beam path access to the ion position. It must also be compatible with the in-vacuum chip carrier so that the planar trap is still able to be installed into the vacuum system with minimal concerns to the effects that installing a new magnetic system may have on the successful operation of said trap.

Atom traps use a high magnetic field gradient in order to trap atoms. For planar atom traps, this gradient can be produced by a magnetic structure confined to the plane of the chip in a similar way to the electrodes on a planar ion trap. Given this, it is perhaps useful to look to atom trapping for inspiration when starting to design a planar magnetic field gradient setup for use with a planar ion trap.

### **3.6.1 An asymmetric approach to creating high magnetic field gradients using permanent magnets**

Surface traps for atom trapping have been shown to employ asymmetric magnet geometries in order to create the high magnetic field gradients required for trapping atoms. By analysing this approach to creating a magnetic field gradient, we can better understand how a set of permanent magnets can be designed to create a high gradient nil at a small height above them. When translating this gradient production approach to our ion traps, this may give us the information required to use under-chip magnets in order to create a high gradient nil at the ion position above them.

Such a magnetic geometry for the application of high magnetic field gradients on planar atom traps was proposed and constructed by Dr Iuliana Barb in 2010 [65]. In her thesis, Barb proposes methods by which one can create a high magnetic field gradient using on-chip magnetics confined to a planar geometry. Directly taken from her thesis, Figure 3.34 shows three ways that permanent magnets (or equivalent current carrying wire geometries) can be used to create a high gradient nil above a magnetic geometry using an asymmetric field approach. Important to note is that this figure is plotted with lines of equal magnetic potential rather than the field or flux lines of previous figures in this thesis.

Scheme (a) shows a single permanent magnet with out-of-plane magnetisation in the presence of an external bias (nilling) field oriented opposite to that produced by the magnet. When considering the equivalent wire geometry, one can see that I have already discussed this scheme in Figure 3.29 regarding nilled anti-parallel current carrying wires. In this case, all field and gradient definitions remain the same and a moderate gradient nil is formed above the magnet in this case. Since this scheme has effectively been discussed in detail earlier in this chapter, I am most interested in schemes (b) and (c) for our application as these do not require an external field in order to create a magnetic nil above the magnets.

Schemes (b) and (c) both show that a planar magnetic waveguide can be formed by a pair of magnets separated by a small distance. For (b) the magnetisation of both magnets is oriented out of the plane and for (c) the magnetisation is parallel through the direction of the separation of the magnets. A magnetic nil with high surrounding gradient is formed above (and symmetrically below) these pairs of magnetic strips at the point where the field lines of the system begin to change from a two magnet system (the near-field solution) to a one magnet system (the far-field solution). This is similar to the parallel current carrying wire scheme except that a high-gradient minimum is created rather than a point of maximum field. Assuming the waveguide is of infinite length, the thickness, width, and separation of the magnetic strips determine the position of the magnetic nil above the waveguide.

For geometry (c) in Figure 3.34, Barb states a set of equations for the magnetic field gradient  $B'$  for two infinite strips of magnetised material, and the height  $z_0$  that the waveguide (or nil line) is formed above them. These equations are defined by the physical parameters of the strips:  $w$  - the width of the magnetic strips,  $s$  - the separation of the magnetic strips along their widths,  $d$  - the thickness of the strips, and  $M$  - the magnetisation (in A/m) of the strips aligned in the plane and through their separation [65].

$$z_0 = \frac{1}{2} \sqrt{d^2 + s^2 + 2sw} \quad (3.7)$$

$$B' = \frac{\mu_0 M}{4\pi} \frac{16dw \sqrt{d^2 + s(s+2w)}}{s(s+2w)(d^2 + (s+w)^2)} \quad (3.8)$$

For the atom trap geometries in Barb's thesis, assumptions were suggested by Barb in order to simplify the equations which led to optimum geometries for the highest possible gradient. For thin films where  $d \ll w, s$ , and  $z_0$ ,  $z_0$  can be approximated by [65]:



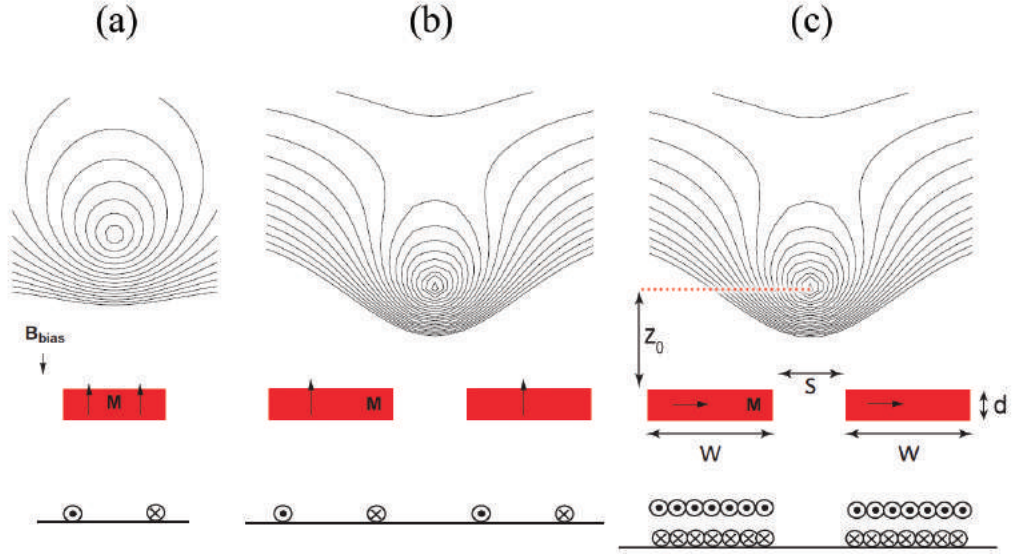


Figure 3.34: This diagram was directly taken from Barb's thesis [65] with additional labels in order to clarify dimensions. Although intended for atom traps, these magnetic configurations are the key inspiration for the under-chip magnetic spacer scheme. The figure presents three ways that permanent magnets can be used to create a high gradient above a magnetic geometry by using an asymmetric field approach. The graphs are plotted as lines of equal magnetic potential rather than as magnetic field or flux lines. Below each magnetic geometry shown in red, there is an equivalent wire geometry. **(a)** - A single magnet with magnetisation vertically upwards nulled by an external compensating (bias) field pointing downwards. A moderate gradient nil is formed above the magnet. **(b)** - Two magnets with magnetisations vertical and parallel. A nil is formed with a much higher gradient above and between the magnets. **(c)** - Two magnets with magnetisations oriented horizontally and parallel through each other. A similarly high gradient nil point is formed when compared to (b), however, Barb now provides an equation which can be used to determine the height of the nil position above the magnets when using this magnetisation direction.

$$z_0 \sim \frac{1}{2} \sqrt{s(s+2w)} \quad (3.9)$$

For a target height  $z_0$ , the magnet width  $w$  is given by  $s = -w + \sqrt{w^2 + 4z_0^2}$  which gives a maximum gradient at  $z_0$  of approximately [65]

$$B' = \frac{\mu_0 M}{4\pi} \frac{2d}{z_0^2}$$

for  $s = 2(-1 + \sqrt{2})z_0$  and  $w = 2z_0$ .

Equation 3.7 gives us our main concern if choosing to place a macroscopic magnetic geometry under the chip. The alignment of the height of this magnetic nil to the RF nil will be the main challenge of implementing an off-chip gradient scheme, however, this will

be discussed later in this chapter and with regards the experimental setups described in Chapter 4. One can see that the height of the nil is dominated by the separation of the magnetic strips when the thickness, separation, and width are at a similar scale, as well as in the thin film approximation. Though Equation 3.7 implies that the height of the magnetic nil is determined solely by the geometry of the infinitely long magnetic strips, this is shown to not necessarily hold true outside of this approximation and that the magnetic properties of the strips will affect this nil height. Unfortunately, these thin film approximations would only apply in the event one was microfabricating the magnets or making them out of a thin foil which would have to be done using methods that would not be used by a typical custom magnet company. It is likely that these equations function best when making calculations in a certain regime of nil height and magnet dimensions. Nevertheless, since this regime is not explicitly stated and does not appear to agree with simulations at the nil heights and magnet dimensions that I am interested in, all further designs in this thesis will be evaluated using COMSOL simulations.

Barb has described an interesting approach for creating a high magnetic field gradient above a set of two magnets confined to a plane. In the next section I discuss how we can use a similar gradient production approach in our own experiments.

### **3.6.2 Re-purposing this approach for our ion traps using macroscopic magnets**

Integration of on-chip magnetic strips onto our chips would be challenging due to the new microfabrication techniques that would have to be introduced and be compatible with the process that we currently use. This means that it may be easier to create an off-chip magnetic structure that is inspired by the geometry used by Barb but that we can construct using macroscopic magnets. That said, microfabricated on-chip magnetic structures will be discussed in Chapter 5.

Let us now see how we can use what we have learned from Barb's thesis in order to create our own asymmetric magnetic geometry which can be integrated with our ion chips without the use of microfabrication. We can obtain a similar magnetic field profile to those shown in Figure 3.34 (b) and (c) by placing a pair of macroscopic magnets with a small separation between them below a planar chip trap as depicted in Figure 3.35. The magnetic structure that I have designed is large enough for a high magnetic field gradient, but small enough that it can fit underneath the chip. This replaces part of the standard copper block/plinth that our chips would usually be glued to when in-vacuum and thus

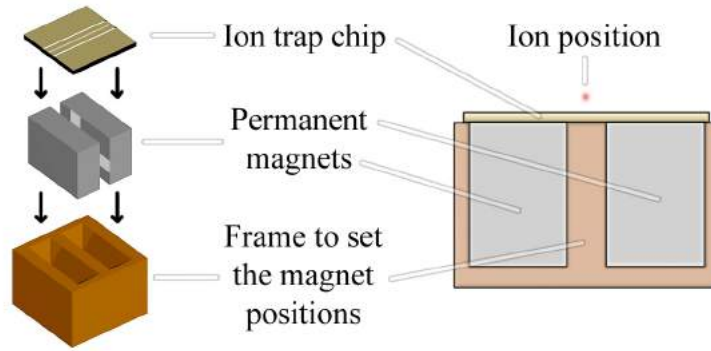


Figure 3.35: The magnetic structure which is placed under an ion trap chip in order to implement the magnetic field gradient production method used on Barb’s atom traps. This uses a pair of macroscopic magnets as an alternative to the microfabricated on-chip magnetic rails used by Barb [65]. These are held in place by a frame which determines the separation between the magnets and therefore the height of the magnetic nil above them. This separation is selected so that the magnetic nil coincides with the ion position.

does not block any optical access or atomic oven beam paths to the trapping position.

### Initial simulations of under-chip magnets

If we are to construct an under-chip asymmetric gradient scheme, let us assess which of the magnetisation configurations discussed in Barb’s thesis is best suited for our desired magnetic nil height that will coincide with an ion trapped above a chip surface. In order to do this, I have adjusted the magnet size to be suitably macroscopic so that we would be able to handle them when constructing an experiment. I have also set a separation that results in a nil height that is valid for our application.

Since Barb has shown that a high magnetic field gradient can be created using an in-plane or out-of-plane magnetisation of a pair of magnets, it is important that we ascertain which would work better for an under-chip magnet scheme. Figure 3.36 shows examples of the magnetisation direction’s effect on the height of the magnetic nil for a magnetic setup size that should be able to fit under the chip in our current setup. As with the previously simulated magnets of the symmetric scheme, I will use samarium cobalt as the magnetic material for the following simulations.

Let us discuss the first example which uses an in-plane magnetisation scheme. Figure 3.36 (a) shows a pair of magnets with in-plane magnetisation in the direction of the magnet separation which achieves a nil height of  $760\ \mu\text{m}$ . This is analogous to the gradient scheme in Figure 3.34 (c) but using macroscopic magnets. These nil heights are significantly larger than a typical ion height in order to account for the substrate thickness of the chip on top of the magnetic spacer. The required magnetic nil height for a given

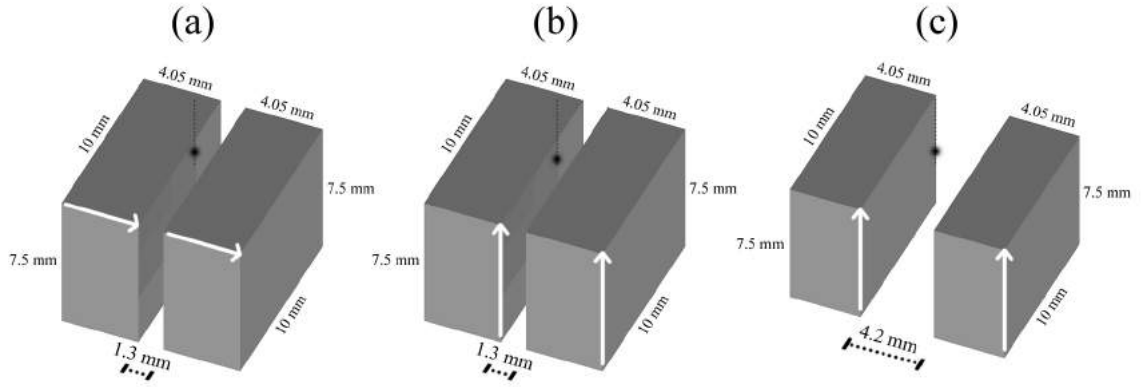


Figure 3.36: Examples of the magnetisation direction's effect on the height of the magnetic nil: **(a)** - In-plane magnetisation in the direction of the magnet separation with a nil height of  $760 \mu\text{m}$ . **(b)** - The same geometry as (a) but now with an out-of-plane magnetisation. A magnetic nil is still created but at a height of approximately  $195 \mu\text{m}$ . **(c)** - The same sized magnets with an out-of-plane magnetisation and a larger separation in order to achieve the same magnetic nil height as (a).

chip will be explained in more detail later in this chapter when I discuss how one would implement this scheme. This magnet size is reasonable to handle for construction of a real experiment and the nil height is appropriate for the ion heights and chip substrate thickness that we use.

As with the symmetric magnets and current carrying wire cases, I will now discuss how the the gradient is formed with regards a field diagram. Figure 3.37 shows the field diagram for the same pair of permanent magnets previously shown in Figure 3.36 (a). In this view, a nil with high magnetic field gradient is formed above and below the magnets at the distance where the two-magnet near-field becomes the single-magnet far-field. In reality, for the three-dimensional geometry, the nil is a rectangular loop around the whole geometry due to the symmetry of the magnetisation in the scheme. The magnet geometry and separation between the two magnets determines the height of this nil. The linear nature of the nil makes it useful for creating a radial gradient for a string of ions. For this geometry, the vertical radial gradient is  $149.4 \text{ T/m}$  and the planar radial gradient in the direction of the magnetisation is  $159.3 \text{ T/m}$ . The gradient along the separation is extremely small at the centre but grows towards the magnet edges because the magnetic nil line curves towards the magnet as it approaches the edge of the magnets. For the ion, this corresponds to a growing in-plane offset field as it moves from the centre of the geometry. Using this magnetisation scheme, it is clear that high gradients competitive with all previously discussed schemes can be created at the ion position.

Let us now see how the field profile changes if one were to use a set of magnets with an out-of-plane magnetisation. Figure 3.36 (b) shows the same geometry as (a) but now with

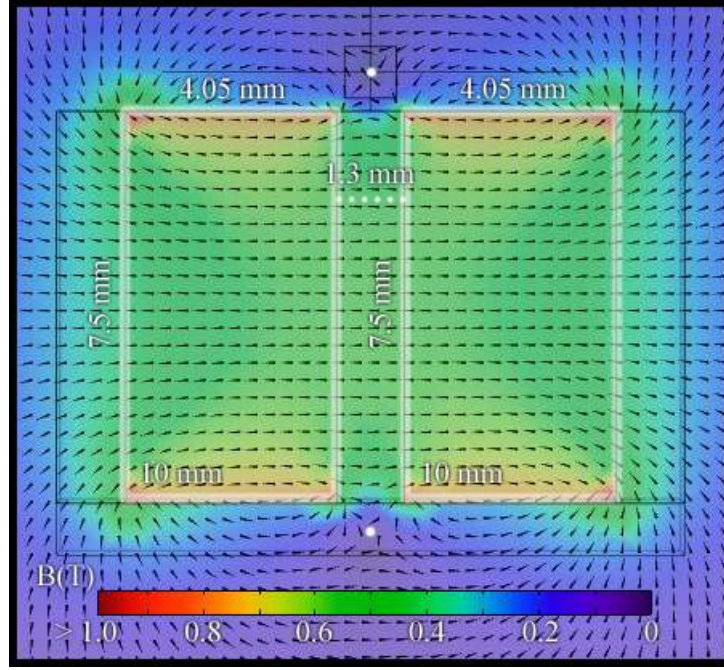


Figure 3.37: The field diagram for a pair of permanent magnets separated by a small distance with magnetisations parallel through their separation as shown in Figure 3.36 (a).

an out-of-plane magnetisation, analogous to Figure 3.34 (b). A magnetic nil is still created with high surrounding gradient but at a height of approximately  $195 \mu\text{m}$ , much lower than for (a). Figure 3.38 shows the field diagram for this pair of permanent magnets. Though the nil is formed much closer to the magnets than for the geometry of Figure 3.36 (a), it is still created at the distance where the two-magnet near-field becomes the single-magnet far-field. However, unlike Figure 3.36 (a), there is less symmetry in this setup and thus two linear moderate gradient sections are formed on the “north” and “south” side of the geometry rather than all the way around it.

In order to make a direct comparison with the in-plane magnetised magnets, we should increase the separation of the out-of-plane magnetised case until the nil heights are the same. By doing this we can compare the overall size of the geometry, the gradients they produce at the same nil height, and therefore identify which magnetisation would work best for our under-chip scheme. Figure 3.36 (c) shows the same sized magnets as before with an out-of-plane magnetisation but given a larger separation in order to achieve the same magnetic nil height as (a). The field diagram for this configuration is shown in Figure 3.39 for comparison to the previous cases. We can see that the separation required to match the nil height of the in-plane magnetised scheme is much larger for the out-of-plane magnets. This diagram therefore illustrates that for the purpose of our experiment, the parallel through separation magnetisation scheme, i.e. that shown in Figure 3.34 (c),



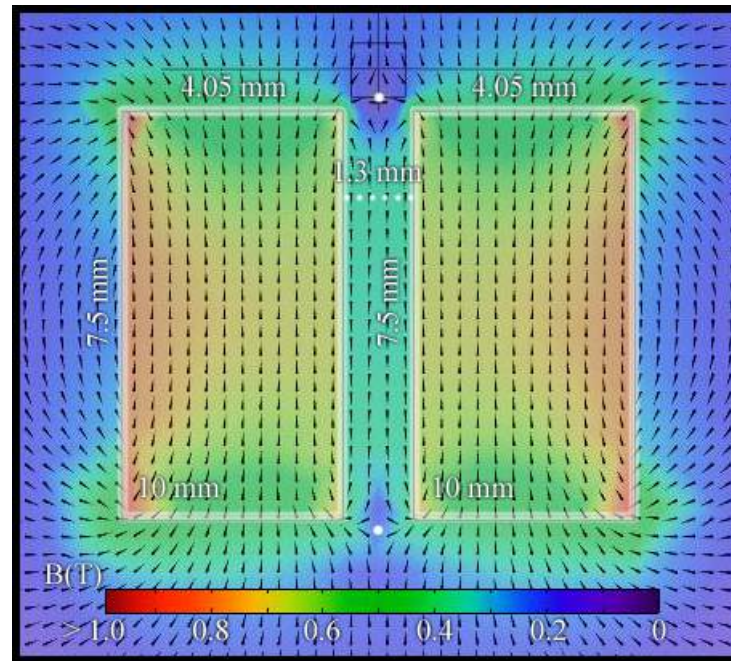


Figure 3.38: The field diagram for a pair of permanent magnets separated by a small distance with magnetisations parallel but perpendicular to their separation as shown in Figure 3.36 (b).

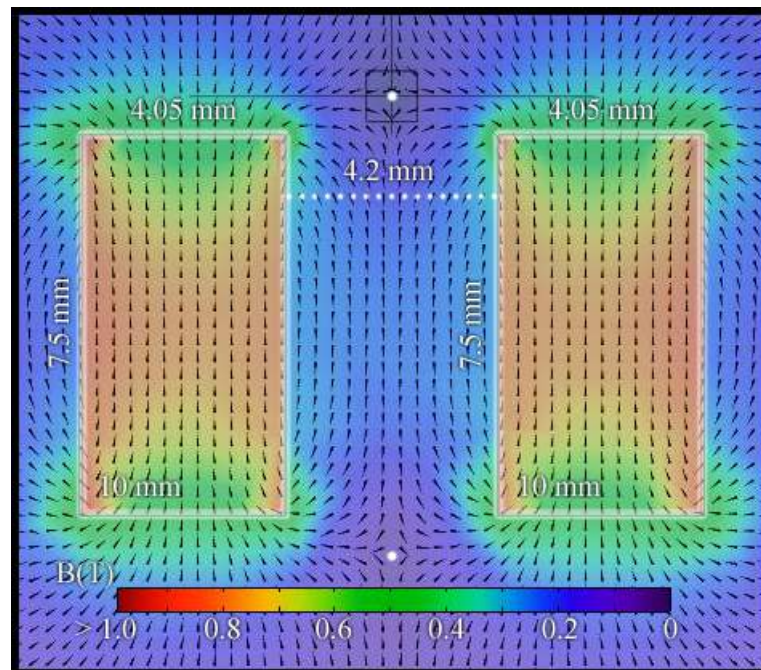


Figure 3.39: The field diagram for a pair of permanent magnets separated by a larger distance with magnetisations parallel but perpendicular to their separation as shown in Figure 3.36 (c) so that the height of the magnetic nil is that of Figure 3.36 (a).

is a more viable option for space saving at our desired nil height. In addition to this, the gradients for Figure 3.36 (c) are lower than that of (a) and are now vertical radially 69.7 T/m and planar radially across the separation 97.4 T/m. This is likely because the magnets are much further from the nil position. However, along the separation (let's say axially), there is a near-linear gradient of 19.7 T/m. This is interesting to note as this field profile is not present in Figure 3.36 (a) and by using the out-of-plane magnetisation scheme we get three explicit gradients rather than two perpendicular to a nil line for the in-plane magnetised scheme. This is because the nil line does not extend around the geometry and is a feature of the symmetry of the magnetisations with regards their separation. It would seem that this would be a very useful scheme for implementing radial gradients with a small axial gradient for radial mode entanglement schemes, however, I will later discuss a method using the same magnetisation scheme as Figure 3.36 (a) which gives a similar magnitude of all gradients with all the benefits of the in-plane through separation magnetisation scheme. These benefits are mainly that a higher gradient can be produced in a smaller package, but we will also see later that the in-plane magnetised scheme is much more structurally sound than the out-of-plane magnetised scheme.

As with the previously discussed schemes, it is important to know the origin of the gradients in terms of the individual magnetic field components and the expected field profile produced around the nil for a good gradient so that one knows how any offset fields should be compensated for a misalignment of the magnetic nil to the ion position. If the field profile does not match a similar shape to those shown here, it is likely that one is not in the same regime which produces the high gradient effects discussed in this thesis. By discussing the field plots here, one can use this information as a check on one's own simulations of such a scheme.

I will start by discussing the field at the centre of each geometry as a function of height above it. In each of these plots one can see where the nil height occurs above the magnets and is thus one of the most useful plots to make when designing a magnetic geometry which produces a nil at a given height above it.

Figure 3.40 shows the magnetic field measured along the vertical radial direction at the centre of each of the geometries in Figure 3.36. For (a), the high gradient originates from the change in the component of the magnetic field parallel to the magnetisation as the two-magnet near-field solution becomes the one-magnet far-field solution. This gradient is defined by  $\frac{dB_x}{dz}$ . Since the magnetisation is in the  $z$ -direction for (b) and (c) the gradient is defined by  $\frac{dB_z}{dz}$  but the reason for the gradient remains the same. The key feature on each

of these graphs is the explicit magnetic field nil at a defined height above the geometry which means that a plot of this field profile is the first point of call in determining the height of a magnetic nil above the magnets.

We are obviously also very interested in planar gradients as these can be used to individually address the ions as well as perform axial and radial mode gate operations. These gradients can be found by evaluating the field across or along the geometry at the height of the magnetic nil.

Let us first consider the in-plane magnetisation case. Figure 3.41 shows the magnetic fields measured along the planar directions at  $760\text{ }\mu\text{m}$  above the magnet surface for the same geometries. For Figure 3.36 (a), the gradient originates from the magnetic field loops between the pole faces of each magnet and the switching direction of the field as it is being sent by one of the magnets and returning to the other. Near the nil this gradient is defined by  $\frac{dB_z}{dx}$ . The gradient for geometry (a) along the separation of the magnets is created by the curvature of the magnetic nil line as it reaches the end of the magnet. Since this is line of near-zero magnetic field, this does not have a high explicit gradient. This can be defined at the extremes to be  $\frac{dB_x}{dy}$ .

For the out-of-plane magnetisation in Figure 3.36 (c), the origins of the gradient are similar but rotated with respect to the magnetisation. The gradient in both planar directions is a result of the requirement that the magnetic flux lines must loop from one pole face to another. The way that this creates two explicit gradients in both planar directions is explained below.

Imagine that this scheme is a single magnet with a cylindrical hole in the centre running from pole to pole. The flux lines can either flow from pole face to pole face through the central hole or around the outside edge. However, at a large distance from the magnet, the flux lines point straight out of the pole face. The nil is formed at the point where the flux lines stop looping through the central hole and start pointing directly away from the pole face. This creates a single point nil with equal planar gradients. For the pair of magnets, the gradient in  $y$  is less than in  $x$  as the magnetic “hole” is longer along the  $y$  direction, thus the nil is stretched and the gradient is lower. Across the separation, near to the nil, the magnetic gradient is defined by  $\frac{dB_x}{dx}$ . Similarly, along the separation, near to the nil, the magnetic gradient is defined by  $\frac{dB_y}{dy}$ . One can now see that the vertical magnetisation scheme is similar to the symmetric magnet scheme in terms of the origins of its gradients with respect to the magnetisation and its orientation in this coordinate basis, thus field compensation works in the same way. If the ion is displaced from the nil,



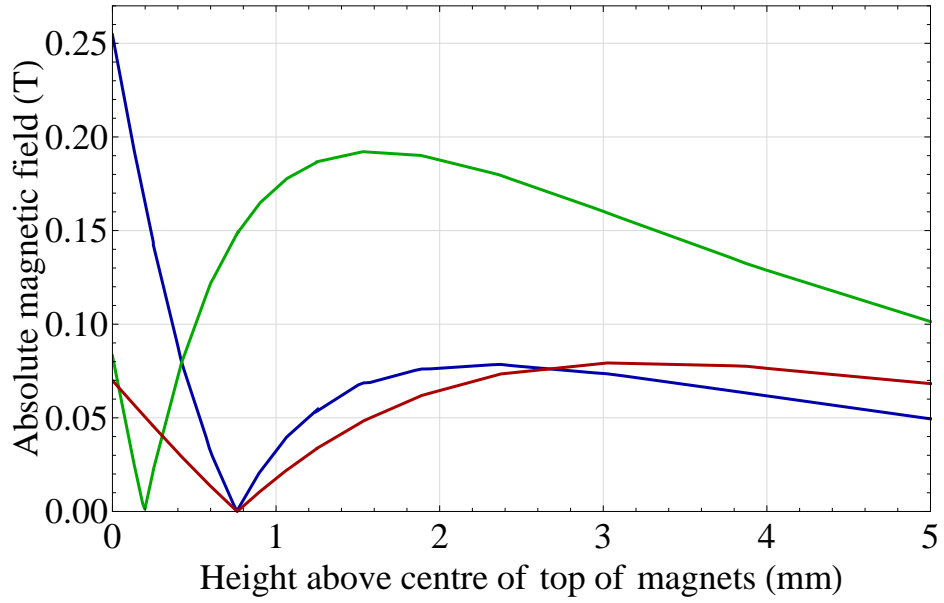


Figure 3.40: The vertical radial fields at the centre of the geometries in Figure 3.36. Blue - (a), Green - (b), and Red - (c).

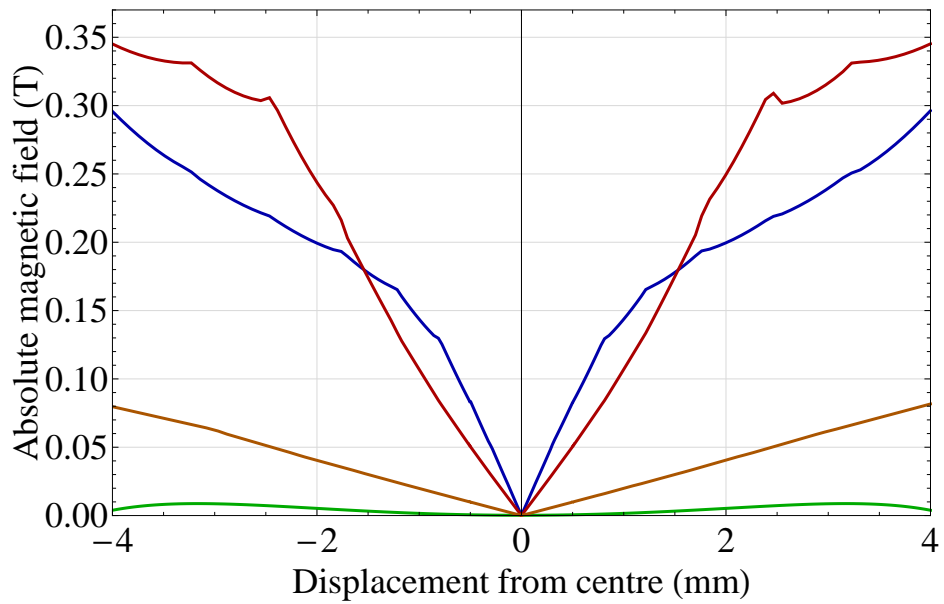


Figure 3.41: The magnetic field measured along the planar direction at  $760 \mu\text{m}$  above the magnet surface for the geometries in Figure 3.36. Blue - (a) across the separation ( $x$ ), Green - (a) along the separation ( $y$ ), Red - (c) across the separation, Orange - (c) along the separation.

then a compensation field in the direction of the displacement should be used to bring the ion back to zero field. This is contrary to the in-plane magnetised scheme where the gradients are defined by perpendicular components of the magnetic field with respect to the direction of displacement.

### **Summary of the effect of different magnetisation directions for a pair of under-chip permanent magnets**

I have now shown some initial simulations in order to compare the effects of using an in-plane or out-of-plane magnetisation of permanent magnets to create high magnetic field gradients. The findings from this investigation are summarised below:

- The in-plane magnetised scheme, i.e. the scheme inspired by Figure 3.34 (c), allows for much higher gradients at the nil heights we are interested in when compared to the out-of-plane magnetised scheme.
- The in-plane magnetised scheme produces high gradients at a large nil height for a much smaller total magnetic size.
- The in-plane magnetised scheme produces high vertical and planar gradients across the magnet separation with near-zero gradient in the direction along the separation. A smaller axial gradient is formed when the ions sit off-centre close to the edge of the magnets.
- The out-of-plane magnetised scheme produces high explicit gradients in all three directions.

Given these findings, we can determine that the in-plane magnetised scheme is the best candidate for our under-chip application due to the higher gradients and more confined geometry for nil heights that correspond to an ion above a chip. With the correct geometry and alignment with respect to a chip trap, this combination of gradient directions should allow for high radial and/or axial motional coupling with the ability to individually address each ion using different frequency microwave fields.

Using Barb's scheme, a magnetic geometry can be placed under the chip to replace part of the normal copper block. When aligned correctly, this should yield a high magnetic field gradient for use with planar ion traps which will enable such trap geometries to perform microwave based entanglement experiments with high operation fidelity. Such a geometry solves the problem that symmetric magnets in the vacuum system may cause by blocking

laser access to the trap since the magnets replace a spacer that would usually be present anyway.

I aim to demonstrate that a planar trap and an under-chip magnetic spacer can be combined successfully in order to provide planar trap geometries with the same capabilities as our main entanglement experiment and better. In order to do this I will start with the simplest geometry; this will be a linear ion trap with a linear magnetic structure.

### 3.6.3 Designing an under-chip high magnetic field gradient structure

In this section I will discuss the design aspects of creating an under-chip magnetic spacer for use with a planar ion trap. In order to do this, I will need to consider our current in-vacuum setup and how it can be minimally modified in order to accommodate a set of under-chip magnets<sup>13</sup>. Given the constraints that this may create, I will then explain how one can create large magnetic field gradients at the ion position.

As previously discussed, the chip is mounted on top of the magnetic structure so that the ions can sit much closer to the magnets and thus experience a magnetic field gradient that is much higher than when using a symmetric magnet scheme. Since the chip is likely to get hot when the trapping RF is applied to it, the frame which holds the magnets should have a high thermal conductivity in order to conduct heat away from the chip. In addition to this, the frame material needs to be near-non-magnetic in order to prevent yoking of the magnetic field as this will have an adverse effect on the gradient<sup>14</sup>. High thermal conductivity is also required for an even distribution of heat on the magnets both during operation and when vacuum baking as temperature changes will affect the magnetisation of the magnets. Concerning these properties, the most obvious choice of material is copper with aluminium as another option due to a better ease of machining.

Given the magnetic strength of samarium cobalt, one can be confident that the attractive force between the two magnets is sufficient to hold them in place when put into the copper frame. This is the structural advantage of the in-plane magnetised scheme over the out-of-plane magnetised scheme. The chip will later be glued on top of these magnets which should mean that the magnets will be unable to move and therefore give us a stable magnetic field and gradient for our experiment.

For our in-vacuum setups, the chip is mounted atop a copper block which conducts

---

<sup>13</sup>In order to ensure that the magnetic field profile created by the under-chip spacer is representative of the simulations, magnetic materials close to the spacer inside the vacuum system should be kept to a minimum in order to prevent yoking of the field.

<sup>14</sup>This would also be required for current carrying wire chips in order to prevent complications due to hysteresis when applying the required compensation fields to create a magnetic nil near to the ion position.

heat away from the chip. Around this, an in-vacuum PCB houses all connections to the chip and this PCB is bolted to the same copper block which the chip sits upon. This is the in-vacuum setup prior to modification for installation of an under-chip magnetic spacer. In order for the under-chip magnets to be installed, this copper block will have to be replaced or modified.

When starting to design a magnetic structure in place of the normal copper block, several constraints must be taken into account. The spatial limits of the setup are dictated by the type of chip carrier we use which gives the maximum footprint of the under-chip magnetic structure. Using our chip carrier PCB, this was set to be 12 mm by 12 mm in our experimental setup<sup>15</sup>. The maximum possible wire bonding length of approximately 10 mm sets the thickness limit of anything that is placed under the chip<sup>16</sup>, however, this can be extended if we choose to have the magnetic structure recessed in the main copper block. These modifications are shown in Figure 3.42. One can see that by recessing the magnetic spacer in the normal copper block, the wire bonding length can be optimised for the best connectivity as specified for the wire and bond type. This results in less constraints on the depth of the magnets.

In addition to the spatial constraints for installing an under-chip magnetic spacer, one must also take note of what height the magnetic nil should be above the top surface of the magnets as this needs to coincide with the ion position.

The height of the nil position above a pair of magnets is determined by the magnet size and the separation between them<sup>17</sup>. In a general sense, once the spatial constraints have been dictated (this is given for our setup by the top cross-section of the copper block that the chip would usually sit atop), the overall size of the two magnets and the separation between them is set. One can then simulate many widths of magnet and separation between them until the magnetic nil height coincides with the ion position. This can be easily ascertained by evaluating the magnetic field as a function of distance from the centre of separation of the magnets; an explicit zero field point will always be apparent with this geometry. The larger the separation between the two magnets, the higher the nil height above them.

---

<sup>15</sup>I will discuss the size of the magnets within this spatial limit at a later point in this chapter when I discuss the gradients that can be produced. For now I will concentrate on integrating under-chip magnets with the in-vacuum setup.

<sup>16</sup>This wire bond length has been demonstrated by members of our group but results in extremely delicate bonds and is an uncomfortable top limit. It is recommended that the wire bond length be less than 5 mm for a durable setup.

<sup>17</sup>Previous investigations have also found that the relative permeability of the magnets has a drastic effect on this nil height. This reaffirms our use of non-coated samarium cobalt magnets due to their near-unity relative permeability.

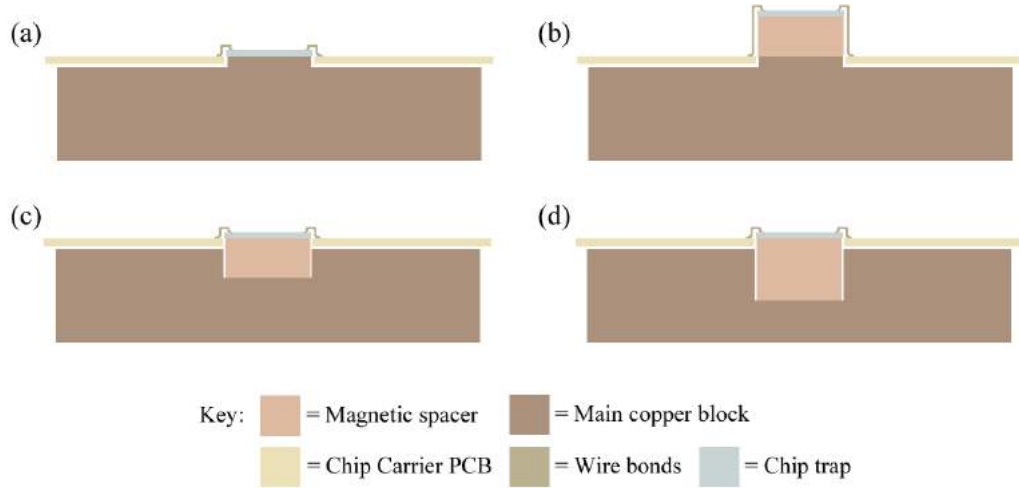


Figure 3.42: Illustrations of the advantages of recessing a magnetic spacer in the under-chip copper block. **(a)** - Our standard mount structure for use with a planar chip trap. **(b)** - The same mount as (a) but with a magnetic spacer under the chip. The wire bond length sets a maximum thickness of the magnetic spacer. **(c)** - The same magnetic spacer as (b) now recessed in the main copper block resulting in the same (safe) wire bonding length as (a). **(d)** - A thicker optimised magnetic spacer further recessed into the main copper block producing no change to the wire bonding length.

Though this may seem trivial, complications can arise very quickly if thorough checks are not made before manufacturing. Firstly, since we are pairing the magnetic structure with a microfabricated chip, one must consider the substrate thickness and simulated (or known) ion height for that chip. For higher gradients, a thinner substrate is better as the ions themselves are closer to the magnets regardless of the ion height above the chip. Figure 3.43 shows the thicknesses of material between the magnet surface and the ion that should be considered in order to accurately align the RF and magnetic nls in the ion height direction. These distances are as follows:

- (a) - The ion height from the electrode surface.
- (b) - The electrode thickness.
- (c) - The substrate thickness.
- (d) - Any amount of bowing of the substrate that is expected to occur.
- (e) - The glue or other adhesive thickness.

In our design (b) and (c) are treated as one measurement and (d) is determined to be negligible. This also means, for example, that a  $240\ \mu\text{m}$  ion height on a  $500\ \mu\text{m}$  substrate will have the same ion-magnet distance (and therefore gradient) as a  $60\ \mu\text{m}$  ion height on

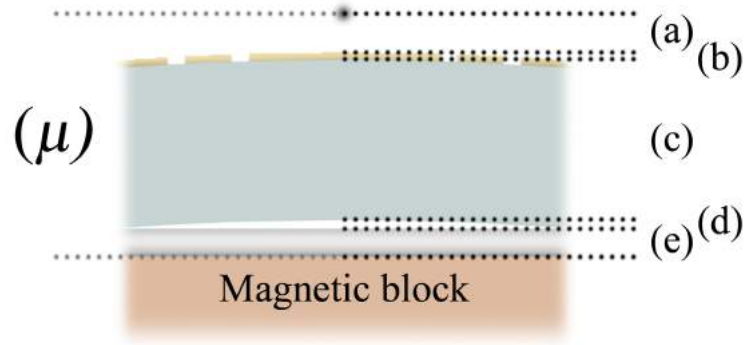


Figure 3.43: One must take into account all thicknesses of material between the magnet surface and the ion in order to accurately align the RF and magnetic nil in the ion height direction. **(a)** - The ion height from the electrode surface. **(b)** - The electrode thickness. **(c)** - The substrate thickness. **(d)** - Any amount of bowing of the substrate that is expected to occur. **(e)** - The glue or other adhesive thickness.  $(\mu)$  - The total magnetic nil height required  $(a) + (b) + (c) + (d) + (e)$ .

a  $680\ \mu\text{m}$  substrate. Since the ion-electrode distance is a primary dictator for the heating rate of a trapped ion, this comparison is an eye-opener for creating a chip-spacer pairing which can achieve the highest fidelities. To first approximation, it is favourable to have a high ion height trap fabricated on a relatively thin substrate as the ions will be further from the electrodes but still close to the magnets. This means that anomalous heating is reduced and the gradient is increased, which translates to less decoherence over faster gate operations resulting in higher fidelities.

In addition to these three heights, one must also account for the distance between the magnet and the bottom of the chip due to adhesion, mounting structure, or substrate bowing. The last of those points is assumed to be minimal for any high-grade substrate, however, adhesion and mounting structure thicknesses should be kept to a minimum in order to achieve the highest gradients. I will discuss determination of glue thickness for our attachment process in further detail in Chapter 4.

I have now discussed the minimal modification to our in-vacuum experimental setup in order to install a magnetic spacer designed to achieve a high gradient magnetic nil which coincides with the ion position. However, for the in-plane magnetised scheme that we use, there are two high magnetic field gradients, one across the separation of the magnets, and another out of the plane of the chip. This means that the chip and spacer can be aligned for a high axial gradient, or a high planar radial gradient.

### Axial versus radial alignment of the chip

For the under-chip magnetic geometries previously discussed in this section, one can create a high axial or high planar radial gradient at the ion position by aligning the magnetic and RF nil lines perpendicular or parallel to each other respectively. In addition to these gradients, there is also a strong vertical radial gradient for both of these alignments.

We aim to perform axial mode gates with our trapping setup and thus we wish to have the highest axial gradient possible. For this magnetic setup it is possible to perform both axial and radial mode gates with a large coupling to the ions' motion. However, due to the large axial gradient, we are limited to two or three ions before the ions in a chain get into extremely large fields. This can be troublesome when it comes to laser cooling if the linewidth of the laser is not sufficient to cover the increased splitting of the magnetically sensitive transitions for multiple ions.

If we wish to mainly perform radial mode operations with a larger group of ions in much lower fields, then one can align the magnetic and trapping nils on top of each other. Since these magnets are based on a waveguide approximation, the axial gradient is approximately zero at the central position of the nil in this radial alignment, but due to its finite nature, the gradient grows as one moves to the extremities of the magnets as shown in Figure 3.41 (green line). If global operations on ions are desired, then this small axial gradient can be approximately nulled by increasing the length of the magnets or decreasing their width giving them a longer aspect ratio. If individual operations are desired, this near-zero gradient poses a problem as it means that ions along the string will have a very similar splitting and will be very difficult to individually address without crosstalk. In order to minimise this, the Rabi frequency would have to be lowered so much that one would not be able to perform any high-fidelity operations because of decoherence and heating.

If desired, it is possible to create a small axial gradient for individual addressability using a radially aligned scheme by making a small rotational misalignment between the trapping axis and the magnetic nil line. Within the limit of a small angle such that the maximum wire bonding length is still reasonable ( $< 20$  degrees), this rotational misalignment linearly adds a small amount of axial gradient at the centre of the trap. This can be easily calculated by simple trigonometry, i.e. if  $B'_0$  is the planar gradient and  $\theta$  is the angular displacement of the ion string off the magnetic nil line, then the radial and axial gradients are given by  $B'_{\text{rad}} = B'_0 \cos \theta$  and  $B'_{\text{ax}} = B'_0 \sin \theta$  respectively. That in mind, this rotation may present difficulties when it comes to micron-level alignment because the

centre of rotation is dictated by the apparatus used to align the chip to the magnets. This means that the axis of rotation may not necessarily be about the magnetic nil point or centre of the magnetic geometry, which makes creating an axial gradient using this method challenging in practice. Later in this chapter I will show that an offset magnetic design can be used to provide a small axial gradient with high radial gradients which does not require this angular misalignment. The alignment of the chip to the magnets and the equipment used to do so will be discussed in detail in Chapter 4.

Now that I have discussed ways to create the desired gradient orientation for an ion chip trap experiment, I will now discuss the specific processes by which one can design an under-chip magnetic spacer.

### **Designing an under-chip magnetic spacer**

I have already briefly mentioned the processes by which one can design a magnetic spacer in order to create a nil height which coincides with the ion position. In this section I will go into much more detail as to how one can specifically alter the magnet geometry in order to perform fine adjustments to the nil position and show the potential gradients as a function of ion height for a small set of magnets that are designed to fit under a 10 mm by 10 mm ion chip trap.

In general, coarse adjustment of the nil height can be achieved by altering the separation of the two magnets. This separation is adjusted in steps of 100  $\mu\text{m}$  as the manufacturing tolerances on the magnets are specified at 50  $\mu\text{m}$ <sup>18</sup>. Within 10  $\mu\text{m}$  of the desired nil height, fine adjustment can be made by adjusting the thickness of the magnets. These adjustments can be done using a step size of 100  $\mu\text{m}$  which is a large enough increment that a change of this size in the overall dimensions will not become masked by the expected manufacturing tolerances on the magnets or the frame that keeps them in place.

Due to the size of the chip carrier PCB, the width and length of the magnetic spacer was set to be 12 mm by 12 mm in order for the chip to be connected to the in-vacuum electronics without additional difficulties. Additionally, it was decided that the mounting structure for the magnets would be recessed in order to allow for larger magnet thicknesses and for ease of wire bonding. This thickness limit was chosen to be 8 – 9 mm so that there was a sufficient amount of material left on the copper block after milling a recess for the magnetic spacer to fit into. Given the 12 mm by 12 mm by 9 mm total dimensions of the magnetic spacer, the total size of the magnets, including the separation between

---

<sup>18</sup>The magnets we use for our experiments are typically ordered from Bunting magnetics.



them was set to 10 mm by 10 mm by 8 mm giving a frame that was at least 1 mm thick on all sides; the top is uncovered as the chip will be affixed here. In the eventuality of mis-manufacturing or if any unforeseen problems arose, it was also decided that a small amount of leeway would be given to the width of the magnets in the direction of their magnetisation, as the separation of the magnets is also in this direction.

The length of this leeway is measured from the edge of the magnet to the edge of the 10 mm by 10 mm box that I have decided is the maximum magnet and separation top face dimensions, for example, a 1 mm leeway would mean that the dimensions of the top face of the magnets and separation is 8 mm by 10 mm as there is 1 mm taken from the maximum width of both magnets. Having this leeway also allows us to use magnets that are not necessarily optimised for a certain chip because the separation can be greater than intended without the magnets breaching the 10 mm by 10 mm maximum profile set by the frame and chip carrier PCB.

The thicknesses of the magnets were optimised using COMSOL simulations for leeways of 0.7 mm and 0.3 mm along the maximum widths of each magnet at nil heights of 770, 865, and 950  $\mu\text{m}$ , corresponding to ion heights of 70, 165, and 250  $\mu\text{m}$  on a 700  $\mu\text{m}$  thick substrate as used by our group. These simulations indicated that the gain in planar gradient was around 5 T/m for all ion heights for the 0.3 mm leeway in comparison to magnets that had 0.7 mm leeway which was expected since the magnets were larger. The results of these simulations with the overall magnet size and separation used are shown in Table 3.3. Though it is desirable to have the highest gradients for a greater coupling of the ion to its motion, which occur when using a leeway of 0.3 mm, it was decided that due to the small scale of the magnets used, any miscalculation might mean that the magnets would have to be slightly further apart. Thus, the 0.7 mm leeway magnets were chosen to ensure that they would fit in the designated spacer footprint.

By optimising the magnet thickness for a certain leeway, we have gained our first set of simulations which really exhibit the high gradients that can be created using this scheme. These gradients are much larger than those produced by the idealised symmetric magnet configuration for a similar chip trap ( $\sim 70$  T/m for 11 mm separation). In addition to this, there are high, near equal gradients in both the planar and vertical directions and between ion heights of 70 – 250  $\mu\text{m}$  (nil height minus the substrate thickness), the change in gradient as a function of nil height is relatively small when compared to the on-chip current carrying wires. Additionally, the high gradient nils are explicit and do not require nilling fields to be created. Given these preliminary simulation results, the under-chip

Table 3.3: Simulated results of the magnetic field gradient at a given nil height above the magnets for width leeways of 0.3 mm (top) and 0.7 mm (bottom) from a 10 mm by 10 mm magnetic footprint. The magnetic material is modelled as samarium cobalt with a remanence of 1.08 T and a relative permeability of 1.05. The separation and magnetisation are in the direction of width,  $w$ , for magnets of width ( $w$ ) by length ( $l$ ) by thickness ( $d$ ).

Nil height above magnets ( $\mu\text{m}$ )	Magnet size ( $w \times l \times d$ in mm)	Spacing (mm)	Planar gradient (T/m)	Vertical gradient (T/m)
770	$4.05 \times 10 \times 7.4$	1.3	172.2	199.1
865	$3.95 \times 10 \times 7.6$	1.5	145.9	165.9
950	$3.85 \times 10 \times 8$	1.7	127.2	137.5
770	$3.6 \times 10 \times 6.8$	1.4	167.8	182.2
865	$3.5 \times 10 \times 6.9$	1.6	140.9	159.7
950	$3.4 \times 10 \times 7.1$	1.8	121.8	130.9

magnet scheme looks very promising.

We have now determined the highest gradients that can be produced on our own trap designs given the spatial limits of our experimental setup. However, it would be interesting to see how much our potential gradients are limited by constricting the magnetic footprint, i.e. the size of the magnets and the separation between them. A set of simulations were performed in order to ascertain the nil height to gradient relationship with a constant magnetic footprint size of  $8.6 \times 10 \times 7$  mm (similar to that decided previously<sup>19</sup>), and conversely using a constant magnet size of  $3.5 \times 10 \times 7$  mm<sup>20</sup>. The range of nil heights simulated was approximately 400 – 1250  $\mu\text{m}$  which covers a large range of ion heights and substrate thicknesses.

The results of these simulations are shown in Table 3.4. From this investigation, it has been determined that within the reasonable scope of nil heights, there is very little difference (approximately  $\pm 10$  T/m for all simulated heights) in achievable gradient between these two schemes. This means that in this regime, one does not miss out much by limiting the magnetic footprint to this extent. This also means that in general, though a different magnet size should be optimised for each setup, it does not affect the end result dramatically if changes should have to be made to the design and a non-optimum magnet geometry is used.

Within the 8.6 mm by 10 mm by 7 mm magnets plus separation size constraints of our experiment, and the selected material (SmCo with  $B_r = 1.08$  T and  $\mu_r = 1.05$ ) the nil height  $h$  produced by a magnet separation  $s$ , with both  $h$  and  $s$  measured in mm, can

<sup>19</sup>The magnets will change size with the separation in order to have a constant footprint size.

<sup>20</sup>For this magnet size it is reasonable to assume that regardless of the separation required to create an applicable nil height above the magnets, they will still be able to fit underneath the chip trap.

Table 3.4: Simulated results to compare the gradients produced by a constant magnet size ( $3.5 \times 10 \times 7$  mm)(top) and a constant footprint size ( $8.6 \times 10 \times 7$  mm) (bottom). This table additionally shows the nil height to gradient relationship for the magnetic spacer scheme. \* denotes an unreliable result where the gradient is likely to be slightly higher than stated due to explicit simulation uncertainty due to issues with meshing. This has been determined by observing the trend in the gradients for a given ion height.

Separation (mm)	Nil height above magnets ( $\mu\text{m}$ )	Planar gradient (T/m)	Vertical gradient (T/m)
0.8	404	349.6	386.3
1.0	513	265.4	225
1.2	628	214.8	247
1.4	740	165.5	154.1
1.6	855	132.8	143.5
1.8	977	116.3	117.6
2.0	1097	97.5	102.9
2.2	1224	85.4	89.1
0.8	451	311.2	321.7
1.0	554	230*	355.8
1.2	659	187.4*	203.3
1.4	760	160.3	171.4
1.6	855	132.8	143.5
1.8	955	121	122.1
2.0	1050	104.3	106.7
2.2	1142	92.4	99.2
2.4	1235	80.8	87.2

be approximated to within  $10 \mu\text{m}$  by

$$h = 0.57s^{0.9} - 0.015 \quad (3.10)$$

within the  $0.8 - 2.4$  mm scope of separations that I have investigated. The planar and vertical gradients  $B'_p$  and  $B'_v$  at a given height above the magnets can then be approximated to within  $\pm 7$  and  $\pm 4$  T/m respectively by

$$B'_p = \frac{162}{h} - 50 \quad (3.11)$$

and

$$B'_v = \frac{168}{h} - 50 \quad (3.12)$$

where  $h$  is measured in mm. Though these equations are only valid for a magnetic spacer size defined by this specific set of constraints they are useful for evaluating the possible gradients that can be used with a chip trap in our experimental setup, as well as giving a rough separation from which one can start to optimise the magnetic geometry using (say) COMSOL. This set of equations obviously does not apply to all geometries and sig-

nificant further investigation would be required in order to create an analytical equation for the magnetic field gradient produced for any magnet size and separation using a similar scheme. However, due to other geometric factors of manufactured magnets, general equations may not be sufficient for simulating true to life pairs of magnets in order to determine the nil position and gradient for a real magnetic spacer.

### **Edge chamfering on the magnets**

Though I have simulated perfectly cuboid magnets so far, this is often not the case in reality. For commercially manufactured magnets, a chamfer is usually applied in order to avoid magnetic knife edges that are likely to cause severe injury. Since these chamfers will be present at the closest point between the magnet and the ion, it is important to know if the height of the nil is affected. The standard chamfer from our chosen magnet manufacturer was  $50\text{ }\mu\text{m}$  at 45 degrees, and given this specification, we can simulate the effect that this might have using COMSOL. Though simulations showed a small effect on the gradient, the nil height at our standard range ( $750 - 1000\text{ }\mu\text{m}$ ) was unaffected down to the micron level in our simulations. The effect on the gradient was not defined as a definite loss or gain, it was merely slightly changed within  $\pm 5\text{ T/m}$  depending on the simulation. A chamfer of  $100\text{ }\mu\text{m}$  had the same minimal effect. Therefore, at these scales, this magnetic scheme can be designed and simulated without a chamfer for a correct nil height, though it should be included for a more accurate prediction of the gradient.

### **Mismatched magnets due to manufacturing tolerances**

So far, I have only considered pairs of magnets that are exactly the same size. However, since real magnets have a manufacturing tolerance associated with their size, it is extremely important to assess the effect that a mismatched pair of magnets will have on the nil position and the gradient; if there is a large change in the nil height for a slightly mismatched pair of magnets then the scheme may not be viable.

The manufacturing tolerance of the magnets from our supplier is  $50\text{ }\mu\text{m}$  as previously stated, thus an extreme case was modelled in order to magnify any effects that a size mismatch would result in. The same pair of magnets from Figure 3.36 (a) were simulated with the modification that one magnet of the pair was  $100\text{ }\mu\text{m}$  smaller on all sides. This magnet was positioned with the same separation as the perfect case and aligned to be matched flat on the top faces and on one of the side faces with regards the other magnet. With this mismatch, the magnetic nil height at the centre of the geometry shifted from

760 to 757  $\mu\text{m}$  above the magnets and magnetic nil line shifted 15  $\mu\text{m}$  towards the smaller magnet. This resulted in an offset field of 35 G at the centre of the geometry with a larger planar gradient of 170.6 T/m after this field was nilled; the vertical gradient at nilled field was 174.5 T/m at this central position. This is compared to planar and vertical gradients of 159.3 T/m and 149.4 T/m for the matched pair case respectively.

The offset field and position of the nil created by this mismatch is well within the margin of error dictated by what we are able to compensate (which will be described in Chapter 4) meaning that it should not be a problem if the magnets are slightly mismatched as they inevitably will be. That said, the interesting thing to notice here is the larger gradient than the “perfect” case. Though I would hypothesise that this is due to the change in certain field components being greater in the high field region, this result strongly illustrates the fact that designing these magnetic spacers comes from optimisation over many simulations rather than a simple calculation, and that the slightest alteration to the geometry can have surprising consequences. Nevertheless, initial calculations are useful for predicting a gradient for a given ion chip in order to assess the fidelity of possible gate operations that may be performed using a prospective chip-spacer combination.

### **Summary of under-chip magnetic spacer design aspects**

In this section I have discussed many design aspects which should be considered when designing an under-chip magnetic spacer for an ion chip trap experimental setup. The main conclusions from each discussion are summarised below:

- The magnets sit underneath the chip and by recessing the spacer in the original structure that the chip is mounted onto, one can allow the magnets to be thicker than dictated by the maximum wire bonding length.
- For our experimental setup, the magnet size is limited by the surface area of the chip and the recess distance that can be machined into the under-chip copper block. I have set the size limit of the magnets and the separation between them to be 10 mm by 10 mm by 8 mm in our setup with a 1 mm thick copper frame on all sides bar the top face of the magnets.
- The separation of the pair of magnets must be optimised for a nil height which coincides with the position of an ion trapped on a chip affixed to the top face of the spacer.

- This nil height must consider; the ion height above the electrode surface, the electrode thickness, the substrate thickness, any gap created by bowing of the substrate, and the glue or adhesive thickness between the chip and the top surface of the magnets.
- This spacer can be aligned with high axial or high radial gradients in mind by aligning the RF nil perpendicular or on top of the magnetic nil line respectively.
- For coarse adjustment of the nil height for magnets at this scale, the separation of the magnets should be adjusted in steps of  $100\text{ }\mu\text{m}$ . Once close to the target height, the magnet thickness can be changed using the same step size to optimise the thickness for the target nil height given this separation. These adjustments are dictated by the magnet manufacturing tolerance of  $50\text{ }\mu\text{m}$ .
- A leeway of  $0.7\text{ mm}$  is applied to the length of each magnet along its magnetisation direction so that the separation between the magnets can be larger without breaching the size limits previously dictated. This changes our maximum magnets plus separation size to  $8.6\text{ mm}$  by  $10\text{ mm}$  by  $8\text{ mm}$ .
- For a size constraint of  $8.6\text{ mm}$  by  $10\text{ mm}$  by  $7\text{ mm}$ , the nil height  $h$  (mm) produced by a magnet separation  $s$  (mm) can be approximated to within  $10\text{ }\mu\text{m}$  by  $h = 0.57s^{0.9} - 0.015$  for  $s$  in the range  $0.8 - 2.4\text{ mm}$ .
- Given this, the planar and vertical gradients  $B'_p$  and  $B'_v$  can then be approximated to within  $\pm 7$  and  $\pm 4\text{ T/m}$  respectively by  $B'_p = \frac{162}{h} - 50$  and  $B'_v = \frac{168}{h} - 50$ . These equations are only valid for our specific constraints and choice of magnetic material.
- A standard  $50\text{ }\mu\text{m}$  chamfer on the magnet edges is applied by the manufacturer. This does not affect the nil height but slightly affects the gradient and should be accounted for in simulations for more accurate gradient predictions.
- Though magnets should be chosen as same sized pairs, within manufacturing tolerances this has minimal effect on the ability to perform an experiment, however, the accurate dimensions should be simulated to determine the shift in the magnetic nil position from optimum.

I have now thoroughly discussed the design aspects of creating an under-chip magnetic spacer gradient production method to be paired with a linear chip trap. Though these points should be noted in order to help one in designing such a scheme, ultimately,

simulations using an appropriate software package are highly recommended in finalising a design. This is important for simulating real magnets due to the subtleties of real magnet geometries and the importance of accurate determination of gradients and nil positions, which may require compensation once a chip is affixed to the spacer and an ion has been successfully trapped.

Though this design of magnetic spacer is useful for a linear trap for both high axial and high radial gradient experiments, slightly more novel spacer designs can be used to create different gradient schemes. In the following sections I will describe some such novel designs starting with an offset design which provides a small axial gradient and high radial gradient without the need for angular misalignment before moving onto some junction trap designs.

#### **3.6.4 An offset magnetic spacer design for a high radial, low axial gradient scheme**

Due to the difficulty of centring an angular misalignment of the chip and magnetic spacer, one can also create a small axial gradient and larger radial gradient by using an offset magnet design and vertically offsetting the magnetic nil above the RF nil. An offset magnet design consists of two magnets that do not cover the whole length of the spacer. By doing this the ions sit closer to the edge of the magnet where the magnetic nil line begins to curve around the geometry. By designing the magnets so that above the centre of their geometry the nil height is higher than the ion height, at the edge of the magnet, the RF and magnetic nil lines will cross each other at angle. This creates a small axial gradient which can be used to individually address the ions.

An example of an offset magnet design that was simulated is shown in Figure 3.44. Though offsetting the RF nil with respect to the magnetic nil puts the ions in a slightly higher magnetic field, it also creates two high axial gradient regions on the line of symmetry from the centre of the trapping nil due to the zero field zone being curved for a finite waveguide. The field intensity diagram in Figure 3.44 shows the curving of the magnetic nil on approach to the edge of the magnet meaning that there is a sufficient gradient in the direction of an ion string for individual addressing as the magnetic and RF nil meet at only one point but at a significant angle to each other. By shortening and offsetting the magnets in their frame, one can move the low field region to a more central position above the chip. This presents a simple solution to individually addressing ions in a radial gradient entanglement scheme when using a finite magnetic waveguide structure to pro-

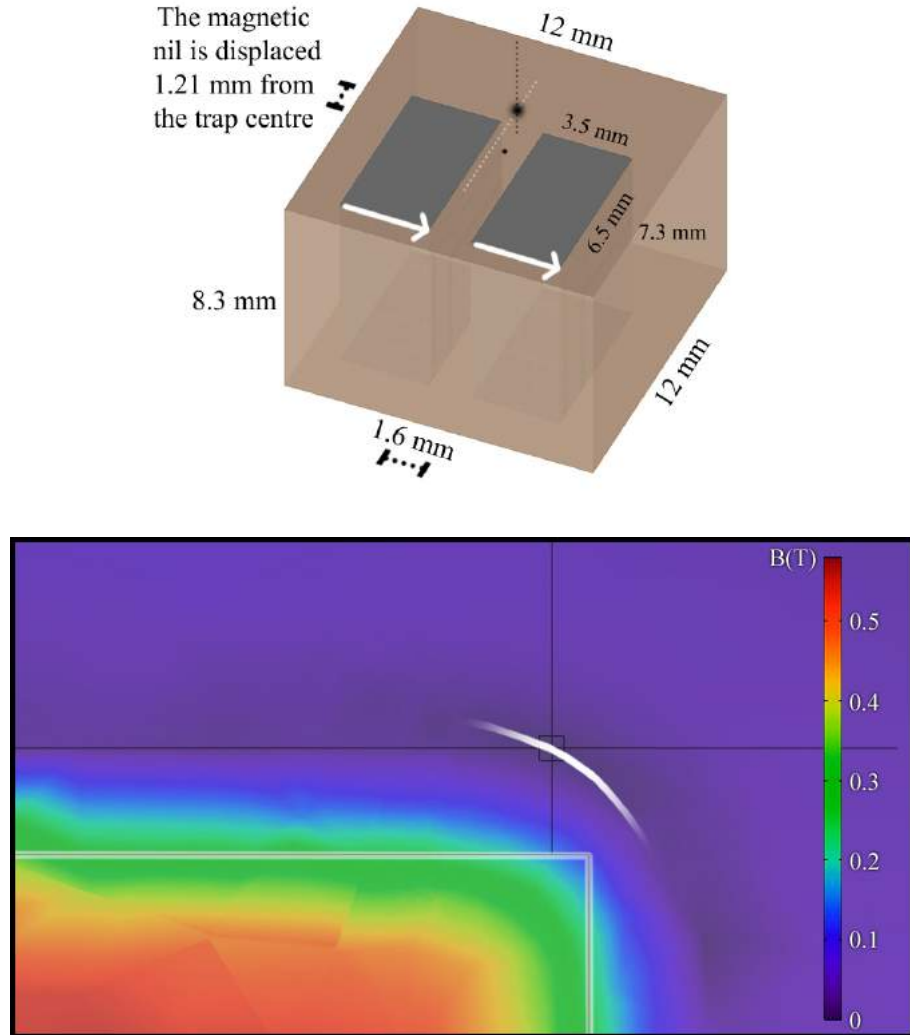


Figure 3.44: An offset magnetic spacer geometry in order to create a small axial gradient in addition to a large radial gradient. The white dotted line at a constant height above the spacer corresponds to the RF nil. The field intensity diagram is also displayed, the orientation as viewed if looking down the labelled 3.5 mm edge of the magnets. The edges of the magnets are highlighted in white and the field profile shown is a slice through the centre of the geometry in the  $z - y$  plane. The magnetic nil line (marked in white) curves on approach to the edge of the magnets. When this intersects the RF nil (shown by the horizontal black line) at an angle it creates an axial magnetic field gradient along the RF nil line near to the edge of the magnet.



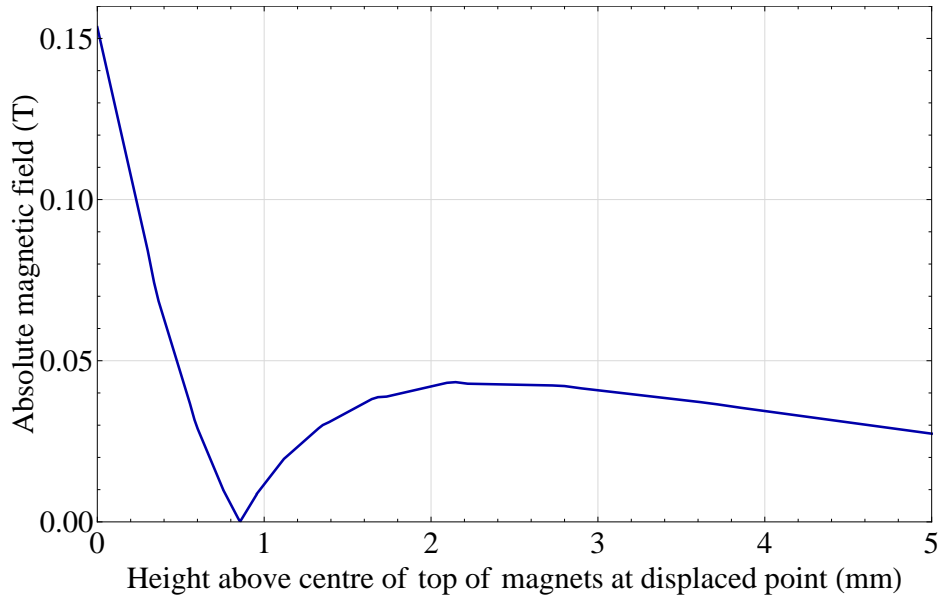


Figure 3.45: The magnetic field produced by the magnetic geometry shown in Figure 3.44 measured 1.21 mm off-centre along the vertical radial direction. For this offset spacer design, the magnetic nil still corresponds to the ion height but only for a single point in the ion string. This results in a small axial gradient that can be used to individually address the ions.

duce the gradients. For this geometry, a vertical radial gradient of 91.7 T/m, a planar radial gradient of 95.4 T/m, and an axial gradient of 30.4 T/m are achieved. This offset magnetic spacer scheme is extremely competitive with the gradients produced by the vertical magnetisation scheme in Figure 3.36 (c). Additionally, for the magnetic nil heights we desire, the offset scheme produces these gradients using a much smaller magnetic geometry with the added structural advantages of the magnetisations of the magnets being parallel through their separation.

Now we have discussed how this offset scheme works, let us clarify the field profiles that are produced about the nil position. Figure 3.45 shows the vertical radial field of the magnet geometry shown in Figure 3.44. The nil sits at a height of 855  $\mu\text{m}$  at this point which is displaced 1.21 mm from the centre of the geometry. Using a linear chip trap, this places the best ion position for coherent manipulation slightly off-centre from the middle of the linear trapping region, though this is not a problem as long as we are able to centre our trapping potential around that point.

Figure 3.46 shows the planar radial field simulated for the same magnetic geometry. Though the resulting gradient is not as strong as it could be for the non-offset scheme, the gain in axial gradient from the offset design is beneficial to the operation of experiments using radial modes because it allows us to individually address the ions.

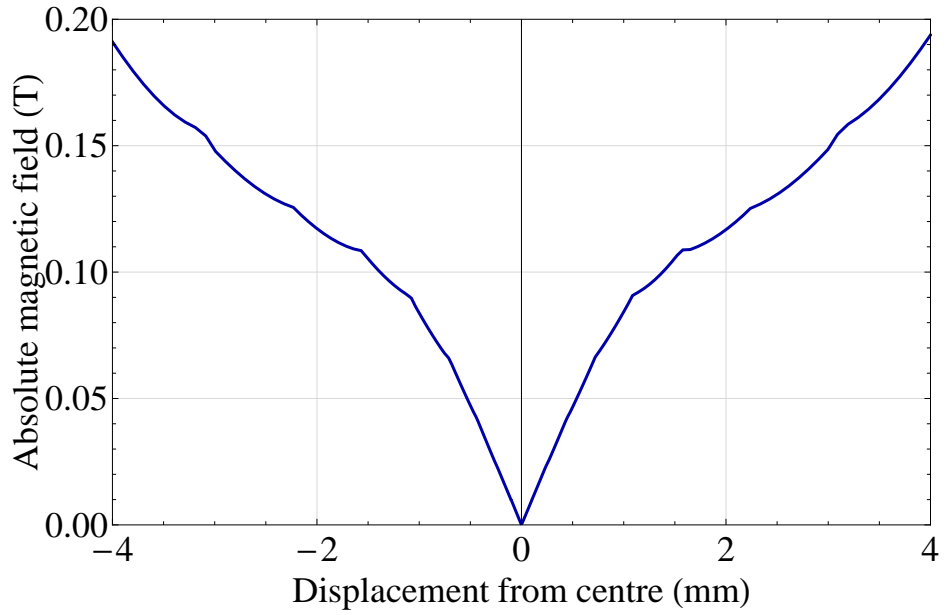


Figure 3.46: The magnetic field produced by the magnetic geometry shown in Figure 3.44 measured along the planar radial direction (across the separation of the magnets) at a height of  $855 \mu\text{m}$  above the magnets.

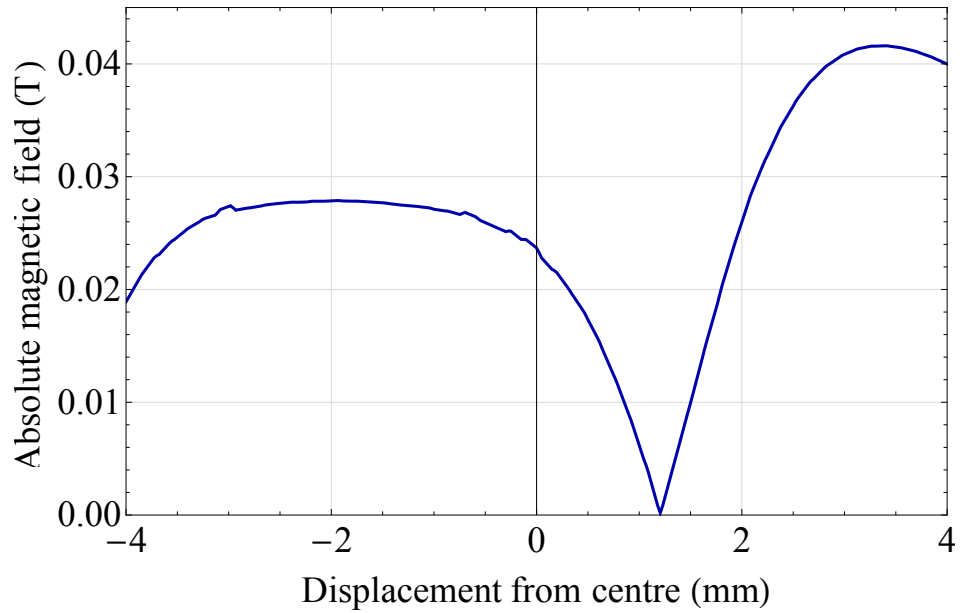


Figure 3.47: The magnetic field produced by the magnetic geometry shown in Figure 3.44 measured along the axial direction (along the white dotted line) at a height of  $855 \mu\text{m}$  above the magnets. The ions sit at a displacement of  $\sim 1.2 \text{ mm}$  from centre in order to access the small axial gradient used for individual addressing.

Lastly, Figure 3.47 shows the axial field of this magnetic geometry. There is now a significantly smaller gradient than the desired axial gradient in the previously discussed under-chip magnetic setups. However, this means that this setup can fit many more ions before the offset field is too high for the outermost ions to be effectively cooled. This would allow us to perform quantum simulation experiments using a large number of ions with the radial modes rather than a small amount of ions with the axial modes. Though this would seem to be a different shape than the field along the separation as shown in Figure 3.41 (green line), the only difference is that the field in this geometry is at an lower offset height resulting in a near-linear change in the direction of the  $B_x$  field component and thus a high gradient. As before, this gradient is defined by  $\frac{dB_x}{dy}$ .

The offset magnet scheme is therefore a useful geometry to use if one desires a large number of ions with high radial gradients in addition to individual addressability. However, since this design requires offsetting the magnetic and RF nil lines from each other, it is not as simple to design as the previously described under-chip magnetic spacer. In this case one should evaluate both the axial field profile along the centre of separation of the magnets at the RF nil height and, in addition to this, the vertical radial field in order to ascertain the height of the magnetic nil line. This is to make sure that above the centre of the magnetic portion of the spacer, the nil height is not lower than the RF nil height as this means that they will not cross each other in order to create the axial gradient zone. One can then adjust the separation of the magnets until a suitably high axial gradient is created, after which the displacement from the centre of the geometry should be noted and one can evaluate all gradients at the offset magnetic nil position.

### 3.6.5 Advanced designs for x-junction traps

Though the magnetic spacer scheme lends itself nicely to linear ion traps, a scalable quantum computer will require more than a single linear trap. Our proposed architecture would use an array of x-junctions where ions are shuttled between zones in order to perform algorithmic computations [20]. In this case it may be useful to see the sorts of gradient schemes that could be implemented for x-junction traps. By implementing the under-chip magnetic spacer with a junction trap, it allows us to perform smaller scale investigations and practice some algorithm operation procedures required for a scalable architecture, but limited to one x-junction without worrying about the possible difficulties of using current carrying wires. Having shown by the work described in Chapter 2 that a permanent magnetic field gradient is very useful for performing high fidelity entanglement operations,

it stands that in combination with an x-junction, a similar proof of principle experiment involving entanglement and shuttling using a permanent magnetic field gradient is a logical step towards the scalable architecture.

The most obvious expansion of the under-chip magnetic spacer scheme in order for it to be used with a junction trap is by using three or more magnets to create high axial gradient zones in two opposite arms of an x-junction. Let us start by discussing a set of three magnets that creates a high axial gradient in two opposite arms of the junction and a region of high magnetic field in the arms of the junction perpendicular to these.

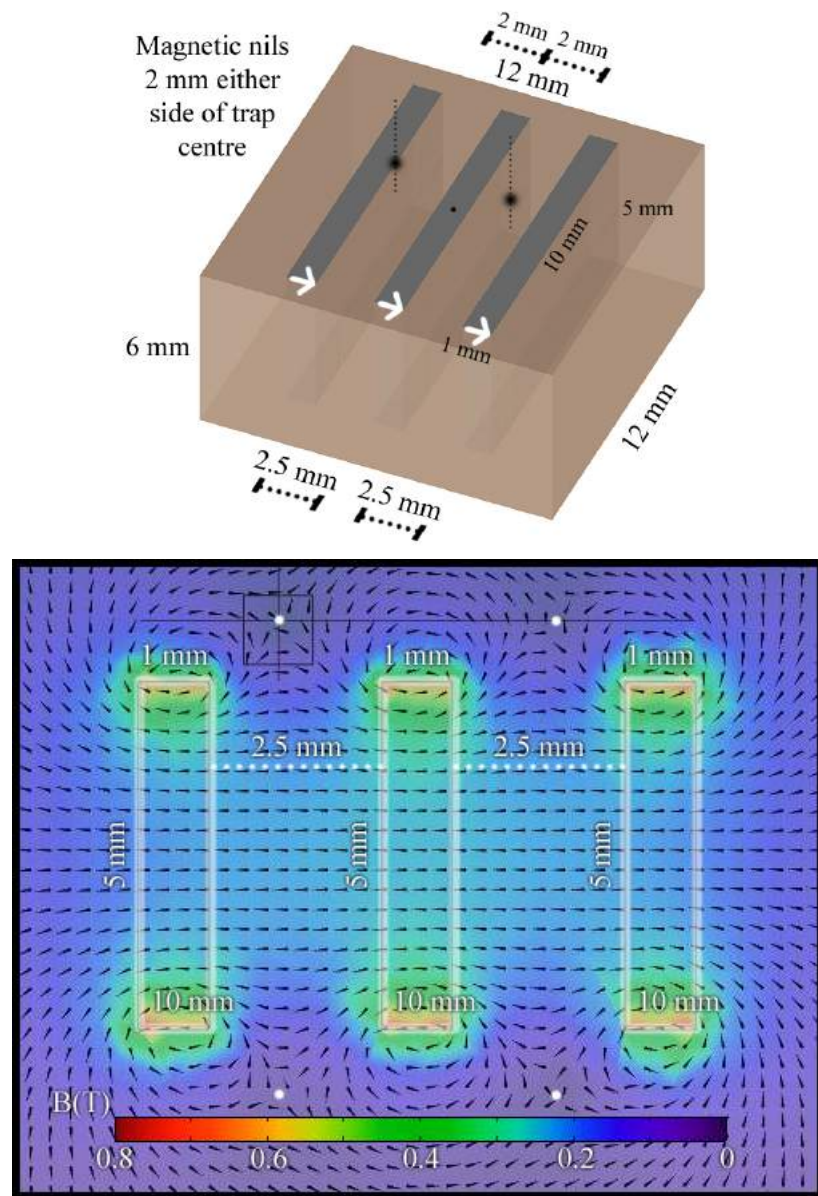


Figure 3.48: A three-magnet design for axial gradients in opposite arms of an x-junction and a high field in arms perpendicular to those using the same spatial constraints as previously discussed.

The example magnet geometry that was simulated is shown in Figure 3.48 which creates two high gradient nils at a height of  $890\text{ }\mu\text{m}$  above the magnets at positions off-centre from the middle of the magnetic spacer. I have set the same spacing constraints for the size of the magnets and set the nil distance to be greater than  $100\text{ }\mu\text{m}$  away from the junction. This should ensure a homogeneous RF potential at the nil position such that the conditions are suitable for coherent manipulation operations to be performed with high fidelity<sup>21</sup>. My designs are also set by the realistic size of manufacturable magnets; since there are now three magnets in the same space, they are much thinner along their width, which means that since samarium cobalt is a brittle material, if they were any thinner they would likely break when inserted into the spacer. The field diagram shows the positions of the nils which are, as explained in Figure 3.37, actually two nilled loops around the geometry. The vertical radial gradient at each of the two marked nils is  $49.3\text{ T/m}$  and the planar axial gradient across the magnets at the nil height is  $60.7\text{ T/m}$  at each nil with an offset field of around  $1000\text{ G}$  running over the central magnet.

Though it would seem that it is possible to generate a large gradient using the triple magnet scheme, when compared to the gradient expected for the same ion height given a linear ion chip, it is slightly disappointing as simulations of the previously discussed two-magnet scheme predict gradients of  $136\text{ T/m}$  and  $125.1\text{ T/m}$  in the vertical and planar directions respectively. This is due to the need for the magnets to be much thinner along the direction of magnetisation in order to fit within the copper block structure. Additionally, installation problems would almost certainly occur due to the high aspect ratio and brittle nature of the magnets.

Another problem when using this type of design is that the offset field of  $1000\text{ G}$  at the centre of the geometry is extremely large and unlikely to be compensate-able using external magnetics. This means that if we were to attempt to shuttle through this magnetic field, it would have to be done extremely slowly as the Lorentz force on the ion could be very large. In addition to this, laser cooling of the ion would become very difficult due to the increased Zeeman splitting resulting from the magnetic field. This means that the transition energy gap between the states we use for Doppler cooling will be altered to such an extent that the line-width of the laser is no longer sufficient to cover the transition. This can be remedied by applying sidebands to said laser.

Given these complications, the three magnet design is not suitable for our experimental requirements as it does not create a simple enough solution to not using current carrying

---

<sup>21</sup>This measurement is as discussed with members of the group who have designed and simulated similar traps.

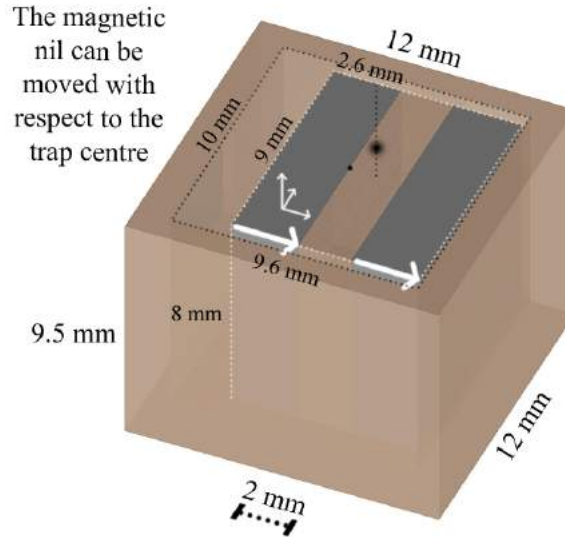


Figure 3.49: An abstract geometry proposed by Anton Grounds in which the magnets are able to be moved underneath the x-junction allowing for high axial gradients in opposite arms and a low field region with high radial gradients in the perpendicular arms subject to engineering solutions.

wires. We should therefore re-evaluate the possible under-chip magnetic spacer designs if we would want to use such a gradient production scheme for small scale experiments using junction traps.

Another way of creating a permanent magnetic gradient for a junction trap (proposed by Anton Grounds of our experimental group) is to have a pair of magnets suspended on a micro-translation stage underneath the chip. This would mean that one could move the nil to be in one arm, across the junction into the perpendicular arms, or in the opposite arm. An example of such a geometry is shown in Figure 3.49 and is very similar to the originally discussed magnetic spacer with the exception of the magnet translation stage. This uses a smaller magnetic footprint so that the magnets can be moved under the chip within the greater magnetic footprint of the original spacer design.

The vertical radial gradient achieved in simulations for this scheme is 104.4 T/m with a planar axial gradient of 109.2 T/m. This is much more competitive with the standard discussed geometry than with the three-magnet scheme in Figure 3.48. The lower gradient is to be expected due to the smaller magnets but since this scheme allows us to move the magnets, and therefore the nil point and gradient as the ions are shuttled, this scheme is a much better way of creating a magnetic field gradient scheme for an experimental setup involving an x-junction ion chip trap. The added bonus that the offset field is much less than 1000 G in the arms without an axial gradient means that we are able to easily store ions in these arms when we are not using them for coherent manipulation.

Using this spacer, the chip would not be able to be glued on top of the magnets as they would need to be able to move freely beneath it. However, the chip could be clamped in place with a slightly larger mounting structure above the chip carrier. Additionally, movement of the magnets underneath the chip would need to be performed with micron-level parallelism in order to effectively cool the ions while they are shuttled around the junction. Though very demanding in terms of mechanical engineering, this would allow for a much larger field gradient as the magnets could be much larger than the three-magnet scheme.

### 3.6.6 Comparison of gradients produced by an under-chip magnetic spacer with other schemes

In this chapter, I have discussed the possible magnetic field gradients that can be produced by symmetric scheme permanent magnets, on-chip current carrying wires, and now, a newly developed under-chip magnetic spacer. Now that I have an approximate ion height to gradient relationship for the under-chip magnets, I can compare this new scheme with those that have been discussed previously.

When compared to the idealised symmetric scheme magnets, a higher gradient in both the axial and radial directions can be produced using the under-chip magnetic spacer for any 10 mm by 10 mm chip that we would be likely to use in the range of magnetic nil heights that I have simulated. This is simply due to the size of the chip limiting the closeness of the symmetric magnets. Another distinct advantage of the under-chip magnetic spacer is the ease by which it can be mounted when compared to a symmetric geometry. Additionally, once installed, the under-chip magnetic spacer is effectively invisible and does not cause any complications with laser or atomic beam access to the ion.

The disadvantages of the under-chip magnetic spacer is that if the under-chip mounting structure cannot be modified to install it, it is much more difficult to implement. It also prevents backside loading if that is the loading method used by an experimental setup. Nevertheless, this scheme should produce gradients over 100 T/m using our magnet size constraints for any experiment that can cater for it, so long as the nil height remains below  $\sim 1$  mm above the magnets.

When compared with the optimised nilled field anti-parallel current carrying wires, the advantages of the under-chip magnetic spacer become a lot more dependent on the thickness of substrate used and what the current limit on the wires needs to be. For our substrate thickness, gradients produced for ion heights below 150  $\mu\text{m}$  are extremely

competitive with the nilled anti-parallel current carrying wires. However, at higher ion heights the magnetic spacer scheme wins outright. These comparisons demonstrate that the magnetic spacer scheme is definitely competitive with current technologies though it is not necessarily easy or appropriate to implement in a scalable system since the magnets are not microfabricated. In addition to this, under-chip magnets do not require cooling to function well and macroscopic samarium cobalt magnets have a good temperature coefficient at -0.03 percent of the remanance per Kelvin<sup>22</sup>. This means that since the remanence of the magnets does not affect the nil height so long as they are the same, and the magnets are in close proximity to each other in a highly thermally conductive copper block and can thus be assumed to be at the same temperature, there will be very minimal effect on the gradient for reasonable temperature fluctuations in the experiment.

The under-chip magnetic spacer is therefore a very useful way of creating a high magnetic field gradient on planar ion chips and is competitive, if not dominant over other gradient production methods that have been discussed in this thesis thus far. Though this is not thought to be a scalable solution to gradient production, it is nevertheless a useful stepping stone in the route towards producing fault tolerant gates using the long-wavelength radiation entanglement scheme.

In this chapter, I have thoroughly examined and compared the current technology used for creating a high magnetic field gradient in order to couple the motion of a trapped ion to its internal state. I have also devised a new method of doing so which has certain advantages over former methods that have been used with a planar trap geometry. Simulated results show that with careful consideration of our choice of material and geometry, this under-chip magnetic spacer should give us competitive gradients when compared to the other schemes.

In the next chapter, I describe the construction and installation of an under-chip magnetic spacer into a vacuum system and, paired with a trap, aim to verify the magnetic field gradients simulated for such a scheme. In order to do this, I also devise a method by which one can align a chip so the ion position coincides with the magnetic nil produced by under-chip magnets and have constructed the apparatus required to do so.

---

<sup>22</sup>As specified by our manufacturer.



## Chapter 4

# Installation of a high magnetic field gradient under-chip spacer into a vacuum system

Having discussed the generation of magnetic field gradients using an under-chip magnetic spacer, here I describe the installation of such a scheme into two vacuum systems. These will each use a different under-chip magnetic spacer design, ion trap chip, and alignment of the two in order to provide our group with two very different sets of gradients in which to perform entanglement operations.

One system will employ a high axial gradient and high out-of-plane radial gradient for a chip chosen with near-optimum ion height (where the possible secular frequencies and heating rate will be in competition with each other) in order to maximise the possible fidelity of a two-ion gate. The ultimate aim for this setup will be to demonstrate fault tolerant two-ion gate operations using the microwave entanglement scheme discussed in Chapter 2. These operations would aim to be performed using the axial modes of motion, hence why the chip is aligned to the magnetic spacer in such a way that the ions experience a high axial gradient. The high out-of-plane radial gradient is merely resultant from the magnetic geometry and it is not aimed that radial mode entanglement operations would be the focus of operations with this setup. The high axial gradient limits the number of ions that we would be able to perform operations with due to the high offset magnetic field for a third or fourth ion likely having an effect on laser cooling efficiency due to a shift in energy levels bridged using 369 nm laser light.

The second system will allow us to perform operations using many more ions by employing an axial gradient lower than that of the Blade trap experimental setup, but paired

with in-plane and out-of-plane radial gradients of  $\sim 100$  T/m. This axial gradient would be primarily used for individual addressing and should allow us to perform radial mode entanglement operations with as many as twenty ions as the offset field at the twentieth ion will be similar to that of the second ion in the high axial gradient configuration. The ion trap to be paired with this gradient would have a higher ion height in order to minimise heating, which will improve fidelities, though this setup would not be aiming for fault tolerant operations. This gradient configuration should, however, allow us to perform multiple-ion radial mode operations that have not yet been demonstrated in this group with the ultimate aim of producing quantum simulations using a linear chain of ions.

## 4.1 Vacuum systems and experimental setup

Each of the two vacuum systems have been previously used within the group, and the modifications and improvements to the original design and overall setup were led by two different PhD students. The “axial” gradient system, overseen by David Murgia, originally housed a two-dimensional ion trap array, while the “radial” gradient system, overseen by Tomas Navickas, housed a ring trap. As such, the main body of each vacuum system remains the same but the internal setup has changed dramatically in order to cater to our experiments.

### 4.1.1 Axial gradient system

This vacuum system was modified from the Two-Dimensional Ion Trap Array experimental setup, originally set up by Dr Robin Sterling and described in detail in his thesis [36]. The main external difference is the addition of a nitrogen cooling system that provides a significant reduction in the chip surface temperature and aims to drastically improve the heating rate of trapped ions and cool the chip in the event that current carrying wires are being used. In addition to this, the HV feedthrough used to apply the trap RF was changed to a single SMA feedthrough and some parts of the system were rearranged using different cross pieces to connect the chamber together. This system is shown in Figure 4.1.

### 4.1.2 Radial gradient system

This vacuum system was modified from the Ring Trap experimental setup, originally set up by Dr Marcus D. Hughes and described in detail in his thesis [42] with the main external addition of an argon sputter gun which aims to be used to clean the chip surface in order to improve the heating rate of the trapped ions [33]. In addition to this, a

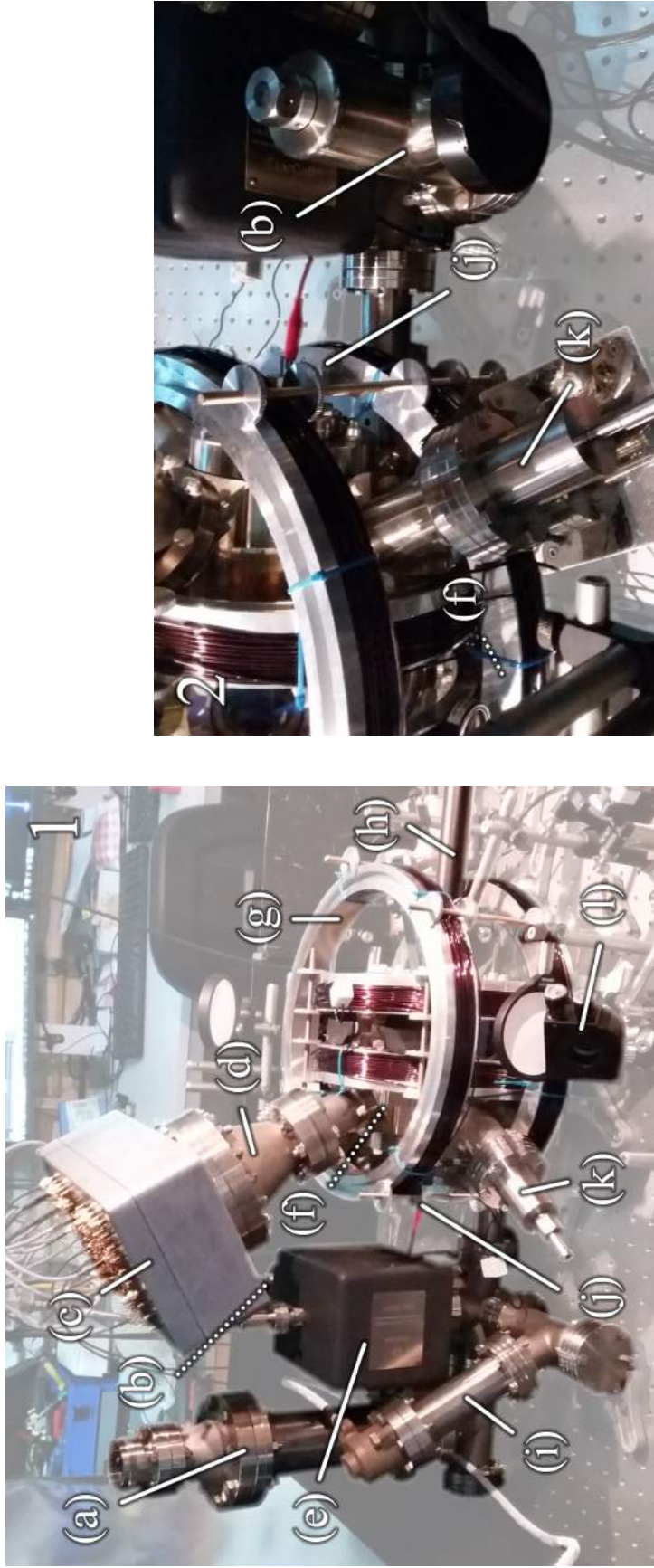


Figure 4.1: The exterior of the axial gradient system. View 1: (a) - Titanium sublimation pump (Varian 9160050), (b) - All-metal valve (shown in view 2), (c) - DC filter box, (d) - 100 pin DC feedthrough with reducer, (e) - Ion pump (Varian Starcell 9191145), (f) - Single SMA RF feedthrough (view obscured by the compensation coils), (g) - Compensation coils, (h) - Imaging tube, (i) - Ion gauge (Agilent UHV-24p which is fitted with a thorium coated iridium filament), (j) - Atomic oven voltage feedthrough, (k) - Nitrogen cooling feedthroughs (in/out), (l) - Final imaging mirror which allows the beam to enter the system at 45 degrees to the experimental table surface.



Figure 4.2: The exterior of the radial gradient system. View 1: (a) - All-metal valve, (b) - Titanium sublimation pump, (c) - Ion pump, (d) - Ion gauge, (e) - Custom elbow, (f) - Atomic oven voltage feedthrough, (g) - Hemisphere and octagon with front window, (h) - Sputter gun, (i) - 100 pin DC feedthrough with reducer, (j) - Four SMA microwave and RF feedthrough (shown in view 2).

four SMA feedthrough replaced the HV feedthrough and the front window was repaired and coated for 493 nm laser light so that the system could be used with barium ions in addition to the usual ytterbium ions. A nitrogen cooling system (not shown in Figure 4.2) was proposed to be added to this system in order to have the same benefits of the axial gradient system during experiments. However, this was an afterthought following the design and fabrication of all magnetic components of the experiment, thus it was aimed to be added to the system subject to the timing of completion of other aspects of the experimental design. The titanium sublimation pump, ion pump, and ion gauge are the same models as used on the axial gradient system. This system is shown in Figure 4.2.

## 4.2 Offset field compensation using current coils and large external permanent magnets

Since the ion chip trap is glued on top of the magnetic spacer it is important to align them with very high precision; any slight error could cause a large magnetic field offset at the trapping position of the ions due to the high spatial gradient. A misalignment in the ion height direction would result in an offset field in the direction parallel (or anti-parallel) to that of the magnetisation direction. If the ion sits closer to one magnet than the other at a given height then an offset field will be oriented in the vertical radial direction, i.e.  $B_z$ ; this is the basis of our individual addressability using the axial gradient. Additionally, any rotational misalignment of the magnets, edge effects, or external magnetic fields could create a small offset field in the direction perpendicular to those previously mentioned. As with the Blade trap setup, we therefore would typically require a triple-axis compensation coil setup to nil and offset all components of the magnetic field near to the ion position. This would allow us to place the ions in an appropriate magnetic field for trapping and coherent manipulation.

### 4.2.1 Designing a compensation coil setup

With our compensation coils, we aim to be able to compensate fields of up to 100 G at the ion position resulting from a misalignment between the magnetic and RF nil positions when the under-chip magnetic spacer is glued to the chip. This field value is taken from experience during initial trapping using the Blade trap setup after the magnetic field gradient retrofit, and has thus been set as general benchmark for a desirable compensation limit throughout this thesis.

However, the vacuum hemisphere used for our vacuum systems is much larger than that of the Blade trap experimental setup, which means that it is likely that the magnetic field that we can compensate using these coils will be smaller due to their larger radius. This means that I designed the compensation setup prior to alignment of the chip to the magnetic spacer, so that we can ascertain what misalignment we can compensate for before attempting any chip-spacer alignments.

The compensation coils were originally designed by Tom Crane (one of our summer students) using an equation previously used in order to design coils for the Blade trap system. The equation used is given by [66]:

$$B = \frac{\mu_0 N I R^2}{2} \left( \frac{1}{(R^2 + (x - \frac{d}{2})^2)^{\frac{3}{2}}} + \frac{1}{(R^2 + (x + \frac{d}{2})^2)^{\frac{3}{2}}} \right) \quad (4.1)$$

which approximates the turns of the coil as being confined to two infinitesimal loops separated in space. Here,  $B$  is the combined field of the coils separated by  $d$  along the  $x$ -axis symmetrically from the origin,  $I$  is the current flowing through a single turn,  $N$  is the number of turns, and  $R$  is the radius of the coils. Though this equation has been shown to be a very good starting point when designing a coil, it does not account for the actual size of the coil profile used and the positions of each wire in this profile. It also does not allow for coils of different radii to be used and only gives an on-axis field value. The final coil simulations were performed in COMSOL in order to get a better idea of off-axis values resulting from a misalignment of the coils from the ion position. For the coil profile that we use, which will be discussed later in this chapter, Equation 4.1 produced central field values of around 7 percent more than those simulated in COMSOL. This equation is therefore a useful starting point in coil design but one must also account for the coil winding profile in order to make a more accurate calculation of the field produced.

Ideally, we would want a triple-axis compensation coil setup in order to compensate any direction of offset field that we may encounter in the experiment, however, when applied to our vacuum system, it was found that in order to achieve a target offset field of around 100 G at 10 A the coils would have to be so large that the vacuum system would have to be raised from the surface of the experimental table. This was mainly due to the additional modules on the hemisphere, namely the sputter gun, nitrogen cooling system, and the DC reducer. This would cause problems for the running of the experiment as a large amount of special mounting would be required to secure the raised vacuum system, which may make it more difficult to set up the required optics for shaping the beam at the ion position.

After weighing up the pros and cons, it was decided that the system should not be raised. This involved cutting the number of turns on the coils which would compensate the field in the ion height direction. For the purpose of this discussion, I will refer to each pair of coils as the  $B_z$ , “in-plane”, and “out-of-plane” coils<sup>1</sup>. The  $B_z$  coils compensate the field in the ion height direction, the “in-plane” coils compensate the field in the direction that is parallel to the plane of the experimental table but perpendicular to the ion height direction, and the “out-of-plane” coils compensate the field in the direction that is out of the plane of the experimental table.

It was investigated as to whether the in-plane set of coils would be able to fit with the limitation of not raising the vacuum system. Simulations showed that at the closest, the coils could only produce a small compensation field of 17.3 G for 10 A of current using an appropriate winding profile. It was decided that these in-plane coils would not be fitted and the out-of-plane coils would be made stronger. This was decided as the in-plane coils would be compensating fields in the direction of ion height to magnetic nil misalignment for the high axial gradient alignment scheme, or along the separation in the radially aligned scheme. The ion height to magnetic nil misalignment will later be shown to have the smallest possible error associated with it due to its sole dependence on the adhesive thickness which has been heavily investigated. Additionally, in the radially aligned setup, there is ideally no component of the field in this direction, so large compensation fields are not as strictly required.

In this eventuality, the in-plane coils would be replaced with a large permanent magnetic compensation setup in the case of a large required compensation field or by using small hand-wound coil loops for the trimming of a small offset component. The out-of-plane coils remained unchanged aside from a small reduction in radius allowing for a greater compensation field in the direction out of the plane of the experimental table.

For the coils used for the new vacuum systems, I used a relatively thick enamel coated wire with a smaller amount of turns than the compensation coils used in the entanglement setup shown in Chapter 1 and 2. This lowers the total resistance of the coils and therefore reduces the power required for a given magnetic field and minimises the resistive heating associated with it. Using a wire diameter of 2 mm, the  $B_z$  coils have 69 turns on each coil and produce a 6.5 G/A offset field using a centred coil radius and separation of 121 mm and 50 mm respectively. The out-of-plane coils, have 120 turns on each coil

---

<sup>1</sup>Though it may be more appropriate to label all these coils in correspondence with the field component that they compensate, this is problematic because this depends on whether the chip is aligned with the magnetic spacer for a radial or axial gradient entanglement scheme.

producing a 7.5 G/A offset field using a centred coil radius and separation of 153 mm and 120 mm respectively. The compensation field from these coils is obviously less than the previously stated target of 100 G for 10 A, however, the magnetic field can be additionally compensated using large external permanent magnets which will be discussed later. Since we have eliminated one of the coils, I will now refer to them as the primary (smaller,  $B_z$ ) and secondary (larger, “out-of-plane”) coils from now on.

#### 4.2.2 Compensation coil setups for each vacuum system

In this section I discuss the construction of the real sets of coils for each vacuum system. The primary and secondary coil formers for each system were made from aluminium with channels on the side in case a water cooling retrofit is later required. When applying high currents to the coils used in the Blade trap setup, it was found that water cooling was required in order to prevent damage to the wires and their coating. Though this issue has been addressed by using thicker wires (larger cross section means less resistance means less ohmic heating), it is still possible that high currents will heat up the coils to a high temperature. By accounting for the possibility that retrofitted cooling may be required in future, this makes it easier to make the required modifications to the coil formers should we require them.

The winding and diameters for each system are slightly different due to differences in each vacuum system so I will describe them separately from each other.

For the axial gradient system, the inner diameter of the primary coil formers was 224 mm with an aim for 69 turns of 2 mm diameter wire to be wrapped around. The inner diameter of the secondary coil formers was 280 mm with an aim for 120 turns of the same wire. The wire used was a 200 °C rated enamel coated 1.8 mm diameter wire (TX1800D) purchased from Scientific Wire Company. The average enamel coating thickness was estimated to be 100  $\mu\text{m}$  bringing the total wire diameter to 2 mm. I aimed to use the closest packing method in order to maximise the amount of turns on each coil as shown in Figure 4.3 which also details the cross-sectional dimensions of each of the coil types. Though one would usually wind similar coils using a lathe or coil turner, the rigidity of such thick copper wire made this almost impossible. The coils were hand-wound by myself and Weikang Fan. The final winding of each coil is shown in Table 4.1.

Due to the relative size of the coils and the vacuum system hemisphere with all peripherals attached, one of the coils has to be fitted around the vacuum system as it is assembled, meaning that it also has to be baked with the system in order to get the system down to



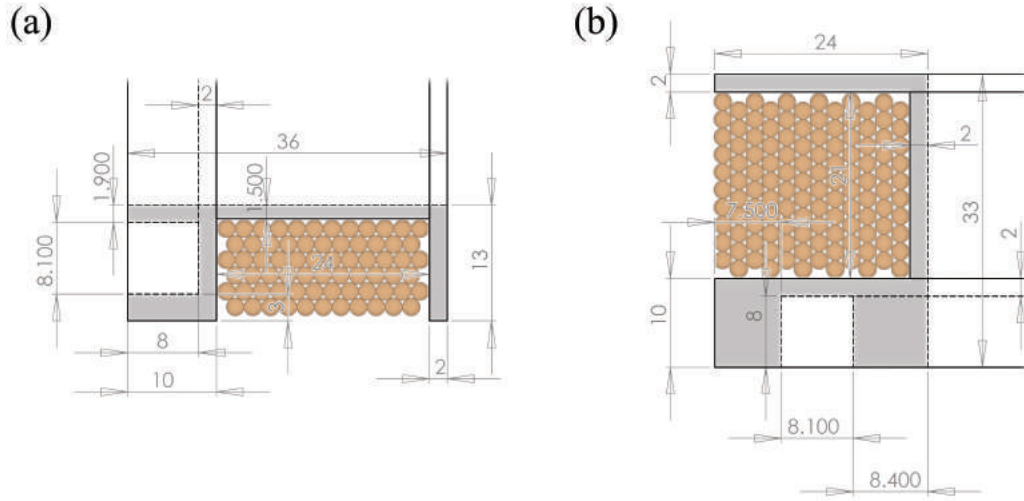


Figure 4.3: The cross-sectional profiles of each of the coil types and the perfect winding order for the maximum number of turns of wire. **(a)** - The primary-type coil profile with a maximum of 69 turns. **(b)** - The secondary-type coil profile with a maximum of 120 turns. The profile of each coil is highlighted in grey and the turns of copper wire are shown in orange. The 8.1 mm gap on the side of each former enables the retrofit of an 8 mm diameter copper pipe for water cooling if required for safe operation of the experiment.

Table 4.1: A summary table showing the general properties of the coils for the axial gradient system. \* denotes that there are slight imperfections in the coil winding process which do not affect the final number of turns. \*\* denotes larger imperfections in the coil winding process that have prevented the intended full number of turns from being wound.

Coil name	Former inner diameter (mm)	Number of turns	Approximate single-coil resistance (Ohms)
Primary 1a	224	65**	0.35
Primary 1b	224	65**	0.35
Secondary 4a	280	120*	0.8
Secondary 4b	280	120*	0.8

UHV pressures. Primary coil “a” was pre-baked in order to make sure it would not short out due to heat damage to the enamel coating. Although there was a slight bonding of the enamel, the coil seemed otherwise to be electrically sound. The resistance value was within measurement error to the pre-bake measurement and the measured magnetic field for a given current was identical for the baked Primary “a” and non-baked Primary “b” coil.

The primary coil formers for the radial gradient system are identical to the previous, however the spacing is slightly further apart due to the position of the sputter gun. The secondary coil formers have the same profile but are slightly larger with an inner diameter of 290 mm so that they could sit closer to each other around the hemisphere in the event that an additional nitrogen cooling system was not used. The final winding of each coil is

Table 4.2: A summary table showing the general properties of the coils for the radial gradient system. \* denotes that there are slight imperfections in the coil winding process which do not affect the final number of turns.

Coil name	Former inner diameter (mm)	Number of turns	Approximate single-coil resistance (Ohms)
Primary 2a	224	69	0.35
Primary 2b	224	69	0.35
Secondary 3a	290	120	0.8
Secondary 3b	290	120*	0.8

shown in Table 4.2.

The coils were constructed with passive provision for water cooling. To determine if water cooling should be added, the current temperature profile of the coils was measured. The coils were tested as series connected pairs and the temperature was measured using a thermocouple secured on the outside edge of the winding under aluminium foil. Temperature measurements were taken for 0 - 10 A in steps of 1 A with 15 - 20 minutes stabilisation time between measurements. As shown in Table 4.3, the temperature of the primary coils remained relatively cool until around 7 A but was still within a normal operational temperature region up to the 10 A mark. At 10 A, the temperature reached 82 °C after a 20 minute stabilisation period. The temperature was still slowly increasing at this point, reaching 87 °C after an additional 40 minutes<sup>2</sup>.

The current-temperature profile of the larger coils is shown in Table 4.4. The secondary coils reached higher temperatures than the primary ones due to the longer length of wire and thus a higher resistance. At 10 A, the temperature reached 119 °C after a 20 minute stabilisation period with an increase to 133 °C after an additional 40 minutes. However, when the temperature was remeasured outside of the foil, it was found to be 107 °C. Insulation due to this foil is therefore likely to have impeded any dissipation of heat to the surrounding air, therefore the temperature profiles for both of these coils are very likely to be much worse than when integrated with an experiment.

The primary coils operated within safe/normal temperatures up to 7 A which allows for 45.5 G compensation without additional cooling. For the secondary coils, the current is smaller at 5 A which allows for 32.5 - 37.5 G compensation (depending on the system) without additional cooling. It was decided that water cooling was not necessary for the expected initial trapping runs and daily operations.

---

<sup>2</sup>Note that during these tests the coils were poorly connected thermally to their mounts. It is likely that when mounted in place during the experiment the additional thermal anchoring would reduce the temperatures reached.

Table 4.3: The current-temperature profile for a pair of the primary 2a-2b coils. \* - After an additional 40 minutes, the temperature had risen to 87 °C.

Current (A)	Voltage (V)	Power (W)	Temperature (°C)
1	0.7	0.7	25-26
2	1.5	3	27
3	2.2	6.6	29-30
4	3	12	33
5	3.9	19.5	37
6	4.7	28.2	43
7	5.7	39.9	50
8	6.7	53.6	58
9	7.8	70.2	67
10	9.1	91	82*

Table 4.4: The current-temperature profile for a pair of the secondary 4a-4b coils. \* - After an additional 40 minutes, the temperature had risen to 133 °C.

Current (A)	Voltage (V)	Power (W)	Temperature (°C)
1	1.6	1.6	26
2	3.3	6.6	28
3	5	15	31
4	6.8	27.2	38
5	8.8	44	45
6	10.9	65.4	55
7	13.2	92.4	66-67
8	16	128	81
9	18.9	170.1	101
10	22.1	221	119*

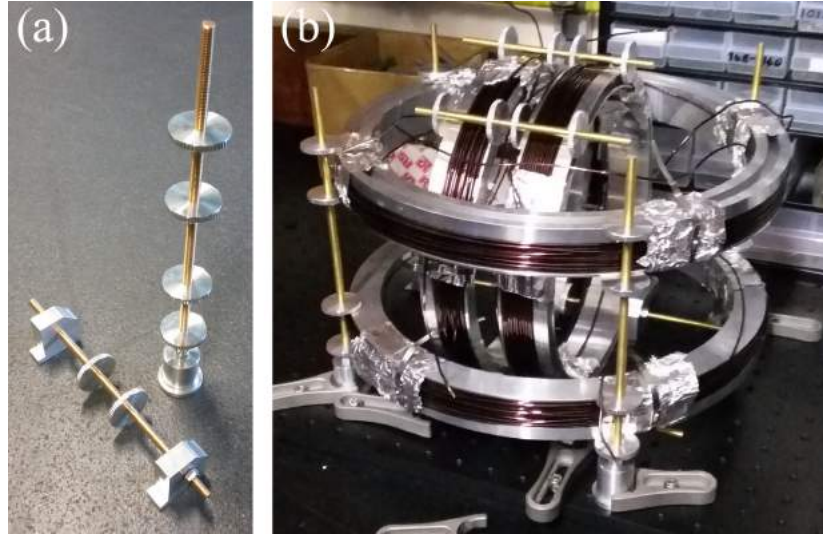


Figure 4.4: The mounts constructed in order to secure the coils in place around the hemisphere of the vacuum system. **(a)** - One of each type of mount constructed. The lower mount secures the primary coils to the optical table, the mount to the right secures a “corner” of the secondary coils at a pair of specified heights off the surface of the optical table. **(b)** - The coils and mounts combined on an optical breadboard. Additional mounts maintain the separation at the top of the primary coils.

When it comes to integrating the coils with the experimental setup they must be securely mounted in place with a defined separation so that the field they generate can be accurately predicted for a given current. Several mounts were made to suspend these coils around our vacuum hemispheres which ensure their structure remains rigid during the course of the experiment. These mounts consisted of M6 brass studding with several knurled disks each with an M6 hole in the centre. With additional aluminium optical post type mounts, the coils were clamped between the disks at the optimum spacing in four places per pair and in turn clamped to the table as shown in Figure 4.4. When reasonably hand tightened the coils remain extremely sturdy to vibration and steady force with this very minimal additional structure. This design also creates minimal additional crowding around the vacuum hemisphere making it ideal for our experimental setup.

During the initial trapping process, it is useful to have a large easily adjustable field compensation setup in order to minimise the offset magnetic field at the ion position. Compensation coils lend themselves very well to this application. However, once the offset field is known one can use large external permanent magnets to compensate most of this field. The compensation coils can thereon be used for fine tuning of the offset field in order to get a good Zeeman splitting for the ion. The current in the coils can then be much smaller which allows us to swap out powerful but noisy current supplies for more stable low power ones. We should therefore assess how much offset field can be provided using

external permanent magnetic compensation methods and determine suitable designs that can be implemented with the experimental setup.

### 4.2.3 Designing an external permanent magnet setup

Permanent magnetic field compensation can be achieved by using large external neodymium magnets on all axes that may require them. By using cylindrical magnets which have a hole through them, these can be mounted securely in stacks suited to the required compensation field. We use 32 mm diameter cylindrical magnets that are 25 mm long with a 6 mm diameter hole through the centre in order to compensate offset fields. Stacks of these magnets would be configured as shown in Figure 4.5, a single stack of four magnets, Figure 4.6, a double stack with sufficient spacing in order to fit imaging optics or other apparatus between them, and Figure 4.7; this quadruple stack aims to provide a similar magnitude of field compensation to a Helmholtz pair and does not have to be “fully loaded” if not required. The fields produced by these configurations are shown in Figure 4.8 and Figure 4.9. Figure 4.8 shows the field as a function of distance from the compensation magnets. These magnets have been simulated using  $B_r = 1.1$  T which is a mid-range remanence for the possible grades of neodymium that are available from manufacturers. One can see that each configuration has its own advantages for positioning around the vacuum system but that as more stacks are added, the field at a distance further than 80 mm is greater in magnitude. The lower field in the double and quadruple stacks is only due to the near-field observation that the measurement starts from between the magnet stacks, hence the single stack has a greater field as it is measured in direct line with a pole face<sup>3</sup>. Figure 4.9 shows the field across the compensation magnets at a distance of 100 mm from the pole faces. 100 mm is approximately the closest distance to the ion that the magnets can sit due to the vacuum chamber walls. The spread of this field will tell us how far off the intended compensation field will be if we are unable to get the magnets in the optimum position. For the single stack, the field is  $\sim 50$  G, the double stack is  $\sim 65$  G, and the quadruple stack is  $\sim 143$  G for a distance of 100 mm from the magnets, which is our expected distance to the ion position. Within 20 mm off-centre displacement this compensation field is not reduced by any notable amount meaning that there is minimal gradient which may have a negative effect on that produced by the under-chip magnetic spacer.

---

<sup>3</sup>The small dip at the short distance is due to the magnets having a hole in the centre. This is a another near-field effect the same as shown for configurations (b) and (c) of Figure 3.36 and in Figure 3.40 of Chapter 3.

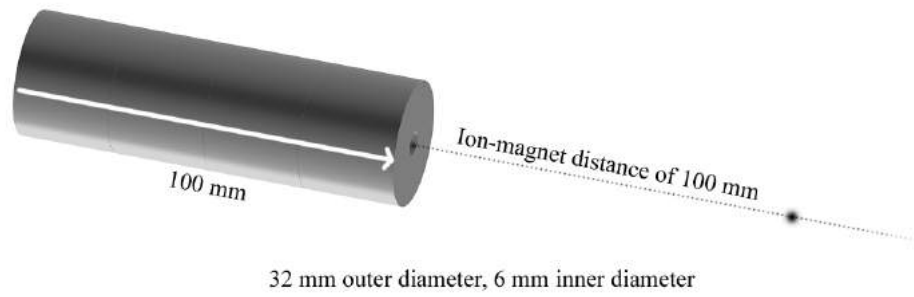


Figure 4.5: A single stack of four neodymium magnets for external compensation of offset magnetic fields at the ion position resultant from misalignments between the chip and the magnetic spacer. At 100 mm away, the offset field created is  $\sim 50$  G.

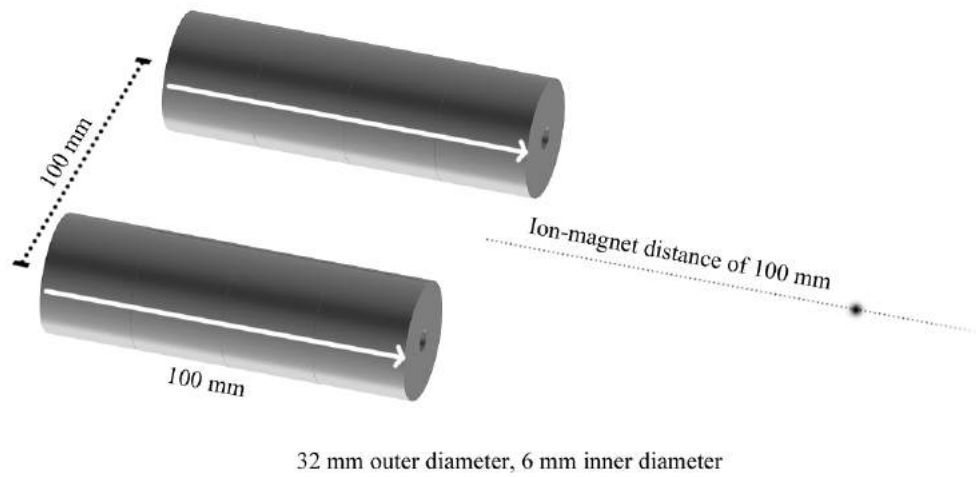


Figure 4.6: A double stack of neodymium magnets for external compensation which allows for an imaging tube or feedthrough to sit between the stacks. At 100 mm away, the offset field created is  $\sim 65$  G.

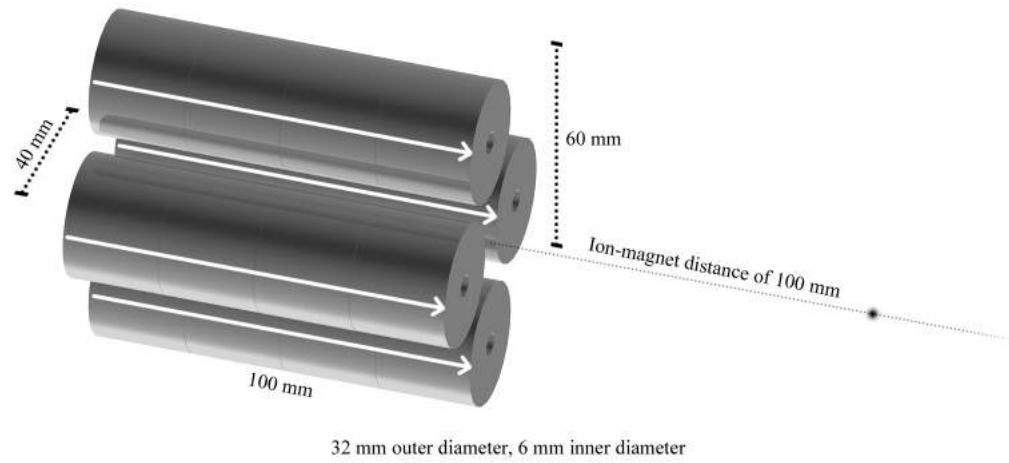


Figure 4.7: A quadruple stack of neodymium magnets for external compensation on the axis where offset field components are not covered by the compensation coils. At 100 mm away, the offset field created is  $\sim 143$  G.

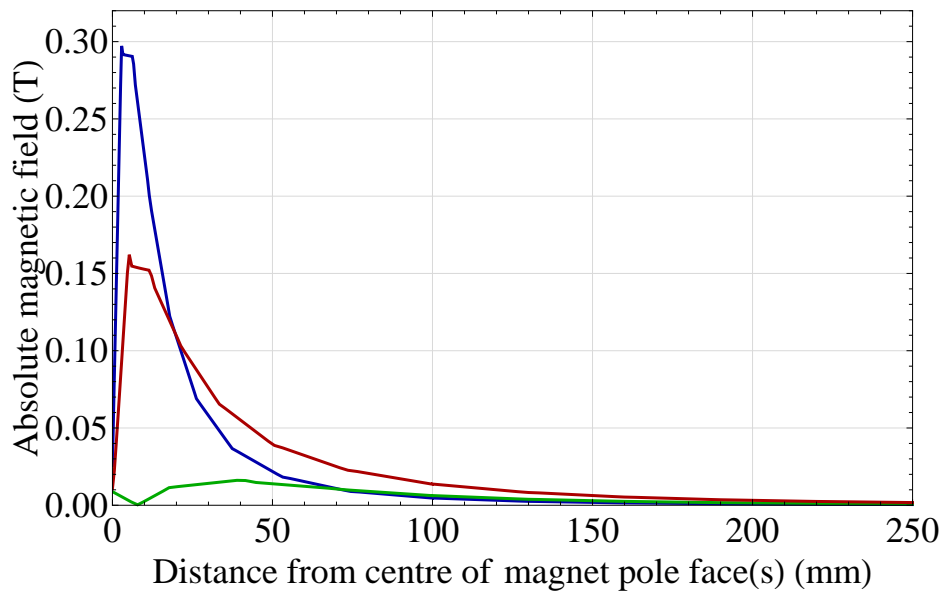


Figure 4.8: The field at a distance (along the dotted line shown in Figures 4.5, 4.6, and 4.7) from the compensation magnets. Blue - The single stack shown in Figure 4.5, Green - The double stack shown in Figure 4.6, and Red - The quadruple stack shown in Figure 4.7.

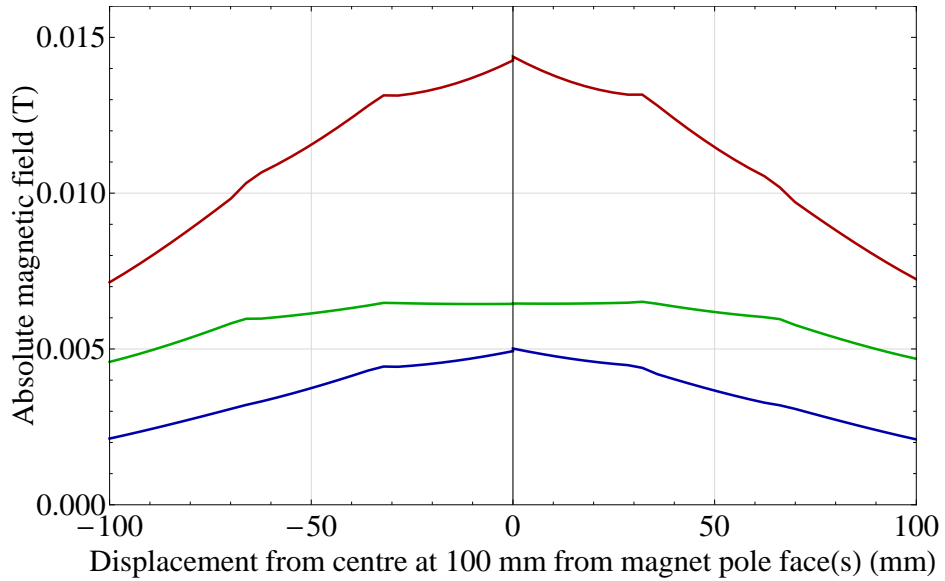


Figure 4.9: The field across the compensation magnets at a distance of 100 mm from the pole faces. Blue - The single stack shown in Figure 4.5, Green - The double stack shown in Figure 4.6 along the 100 mm separation, and Red - The quadruple stack shown in Figure 4.7 along the 40 mm separation. The meshing in each of these simulations is very coarse so the simulation line is not a smooth curve, however, one can still determine an approximate offset field given that the 100 mm distance will also have an error associated with it when integrated with the experiment. The main point illustrated in these graphs is that there is not a sharp drop in magnetic field for a small misalignment along this axis.

#### 4.2.4 Finalised magnetic field compensation setups

For the experiment, the magnets used to provide these compensation fields are cylindrical Ni-Cu-Ni coated neodymium magnets (Bunting Magnetics N50M)<sup>4</sup> at the same dimensions to the simulations. The mount for the axis not addressed by compensation coils was constructed with M6 brass studding and an aluminium frame attached to a standard ThorLabs single-directional translation stage (PT1/M) which will allow for small adjustments of the field magnitude. This mount was designed to house a maximum of sixteen magnets for approximately 180 G of field compensation, however, it was intended to use typically between four and eight magnets during normal use. Additional aluminium blanks were constructed in order to bring the magnets to the minimum protrusion from the ThorLabs stage so that they could fit in between the secondary coils. Since magnets at this size are extremely strong and would be unlikely to be safely separable in the event of direct surface attraction, small brass jackets were machined to sit around each magnet. These jackets include a tab on the side that can be used to separate them more safely using a

<sup>4</sup>The magnetic material “N50M” is actually specified to have a remanence of 1.4 T meaning that the compensatable field will be significantly larger than in previous simulations.



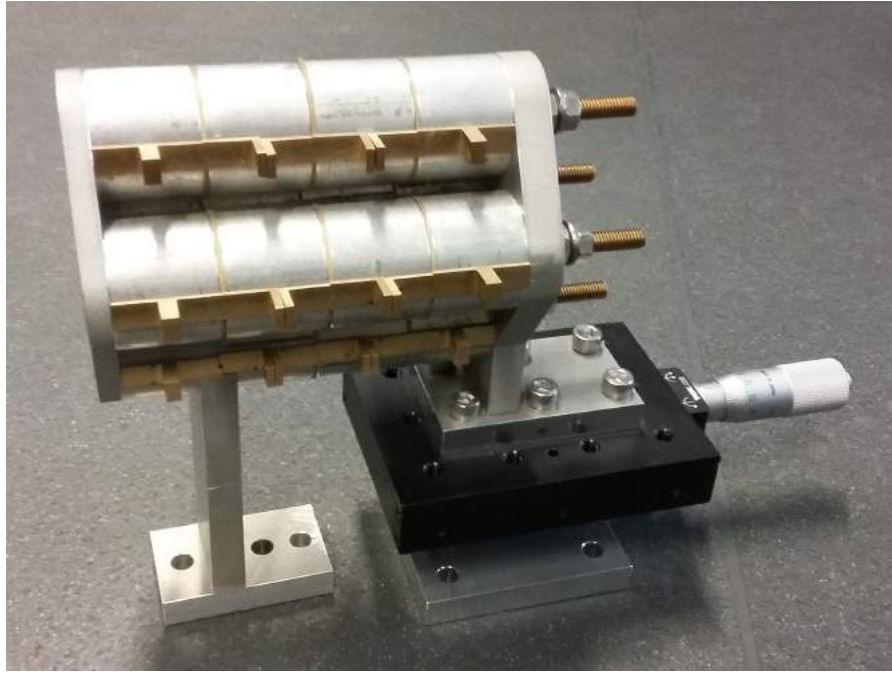


Figure 4.10: The missing coil axis permanent magnet compensation setup fully loaded with sixteen aluminium magnet blanks and combined with a standard ThorLabs PT1/M single-axis translation stage.

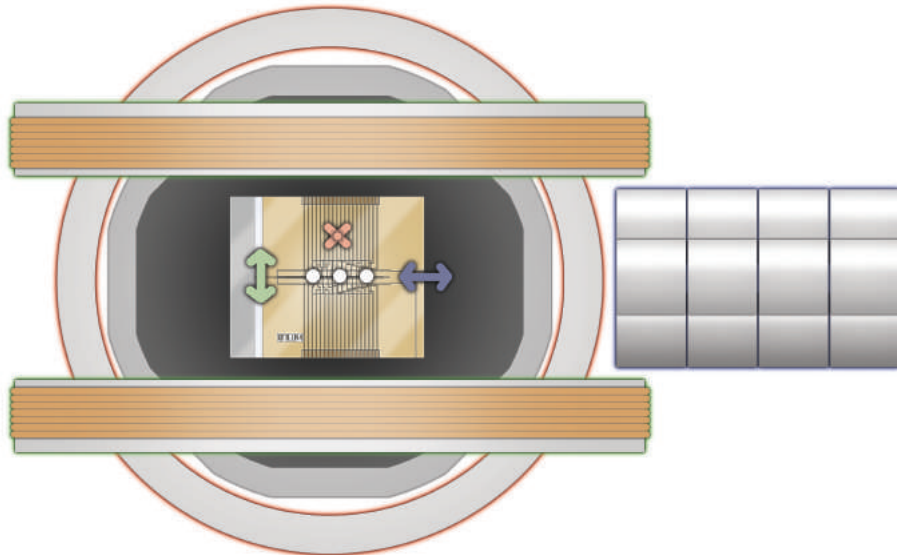


Figure 4.11: The final orientation of the field compensation apparatus with respect to the ion trap (oversized for clarity). The primary and secondary coils are highlighted in red and green respectively and the external permanent magnets are highlighted in blue. The direction of field compensation provided by each of these is shown in the same colour as their highlights and the orientation of the ion string is shown by the three white dots.

linear jacking method<sup>5</sup>. This magnetic mount is shown in Figure 4.10 while fully loaded with the aluminium blanks.

The configuration of the final compensation assembly is illustrated in Figure 4.11. This orientation is shared for both axial and radial magnetic alignments and additional permanent magnets can be used to aid compensation in the directions addressed by the coil axes.

### 4.3 Alignment of the under-chip magnetic spacer with an ion chip trap

The magnetic spacer and ion chip trap must be aligned with maximum accuracy to our simulations in order to realise the high magnetic field gradients at the ion position but also so that the ion position coincides with the predicted magnetic nil position as this is where coherent operations will be performed. In order to perform this alignment I needed to construct an apparatus that could do so to near micron precision. The precision required is dictated by the magnetic field gradient predicted to be at the position of the trapped ions, and given this, the maximum possible offset field that we can compensate using the previously discussed methods.

In this section I will begin by describing the construction of an alignment stage with an integrated microscope which can be used to align the chip and magnetic spacer to the required precision. The ion chips are also fragile and must be held by this alignment stage firmly but without causing damage to them. I describe two methods by which this can be done, one using a specialist adhesive-less tape, and another using pump-activated suction.

Once the chip is successfully aligned to the magnetic spacer, it has to be permanently attached using vacuum compatible epoxy. The heating apparatus required to control the curing process was constructed and integrated with the main alignment stage, and the thickness of the epoxy after curing was characterised so that it could be accounted for in the determination of the required magnetic nil height above the under-chip spacer.

After describing the fully assembled alignment stage, this section finishes with two step-by-step guides to the pre-alignment and alignment procedures, which will allow other members of the group to perform alignments of chips and magnetic spacers in future.

Now that this section has been outlined, I will begin by describing the construction of

---

<sup>5</sup>From experience it is best to place additional non-magnetic objects between the magnets as they are pulled apart. Magnets of this size are extremely dangerous and can cause loss of fingers if not used with the correct respect and precaution.

a high precision alignment stage.

#### 4.3.1 Designing and building a high precision alignment system

The first part to consider in this apparatus is the viewing optics, which one would confidently need to be able to resolve down to the micron level. I chose to use a hobbyist digital USB microscope with  $600\times$  magnification and a continuously adjustable level of LED illumination. This microscope works very well in resolving down to the features I require to observe in order to perform a micron-level alignment. In order to attach this microscope to a micrometer controlled translation stage, a small aluminium adapter was designed to work with the plastic mount that came with the microscope. I now had a very accurately translatable microscope with the ability to record its position in the  $x - y$  plane down to a micron. Due to the polished chip surface, one has to be careful with the level of illumination in order to best see the chip features.

The alignment scheme that I intended to use would require the ability to suspend the chip under the microscope and move the magnetic spacer into alignment below it knowing both the on-chip features and the features of the spacer and subsequently overlaying them prior to adhesion. The first obstacle to overcome in this scheme is how one would be able to suspend a chip in space temporarily while being able to see its topside features and leaving its underside completely bare. The solution to this problem was found in the form of nano-suction-cup tape, a zero-adhesive tape that uses microscopic suction cups to grip to non-porous surfaces. This was stuck to the underside of an aluminium piece, known as the “chip tongue”, and is able to suspend the chip for weeks using the micro-vacuum of the suction cups while leaving it very easy to remove without leaving any residue. This chip tongue is shown in Figure 4.12 (a) and (b). Figure 4.13 shows a picture taken by the USB microscope of the nano-suction-cup tape after being removed from a gold coated chip. Since one can clearly see that there is a material on the tape that is unquestionably gold in colour, it is clear from this picture that although the tape does not leave a residue, there should be significant concerns about electrode surface lift-off. In this eventuality, the aluminium piece was constructed so that the suction-cup tape only attached itself to points on the chip that were electrically inactive or on the edge of large ground planes far from the trapping region. This also gives us full optical access to the complete electrode structure of the chip for finding reference points during the alignment process.

It was intended that future chips would be fabricated with as little space between them as possible meaning that chips would no longer have dead space on them which the

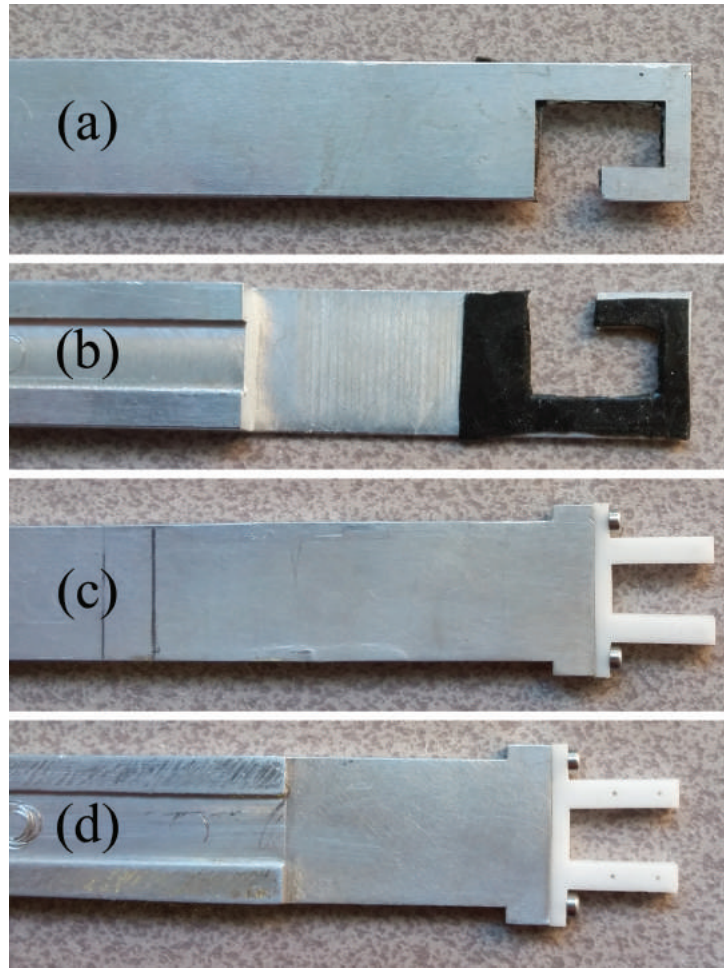


Figure 4.12: Chip tongues in order to hold the chip during the alignment procedure. **(a)** - Suction-cup tape tongue top (camera) side. **(b)** - Suction-cup tape tongue bottom (chip) side. **(c)** - Pump-activated tongue top side. **(d)** - Pump-activated tongue bottom side.

nano-suction-cup tape could safely attach to instead of the electrodes. In this eventuality, an alternative chip tongue was constructed which would be safe to use on all chips. This piece was largely concept designed by Dr Bjoern Lekitsch (who designed the masks for the chips we intended to pair with the magnets) with technical drawings and finalising done by myself and the workshop. The bulk of this piece is constructed out of aluminium identically to the original chip tongue but with a PTFE component attached to the end. This PTFE piece would be in contact with the chip surface and consists of two prongs each with two small holes leading to an internal channel. These channels match to ones within the aluminium piece which are then connected to a small pump via a custom gas nipple and PVC hose tube in order to create enough suction to hold the chip in place. This pump-activated chip tongue is shown in Figure 4.12 (c) and (d), where one is able to see the small holes through which air is sucked in order to create the negative pressure to suspend the chip during the alignment procedure. For both chip tongues, the inner

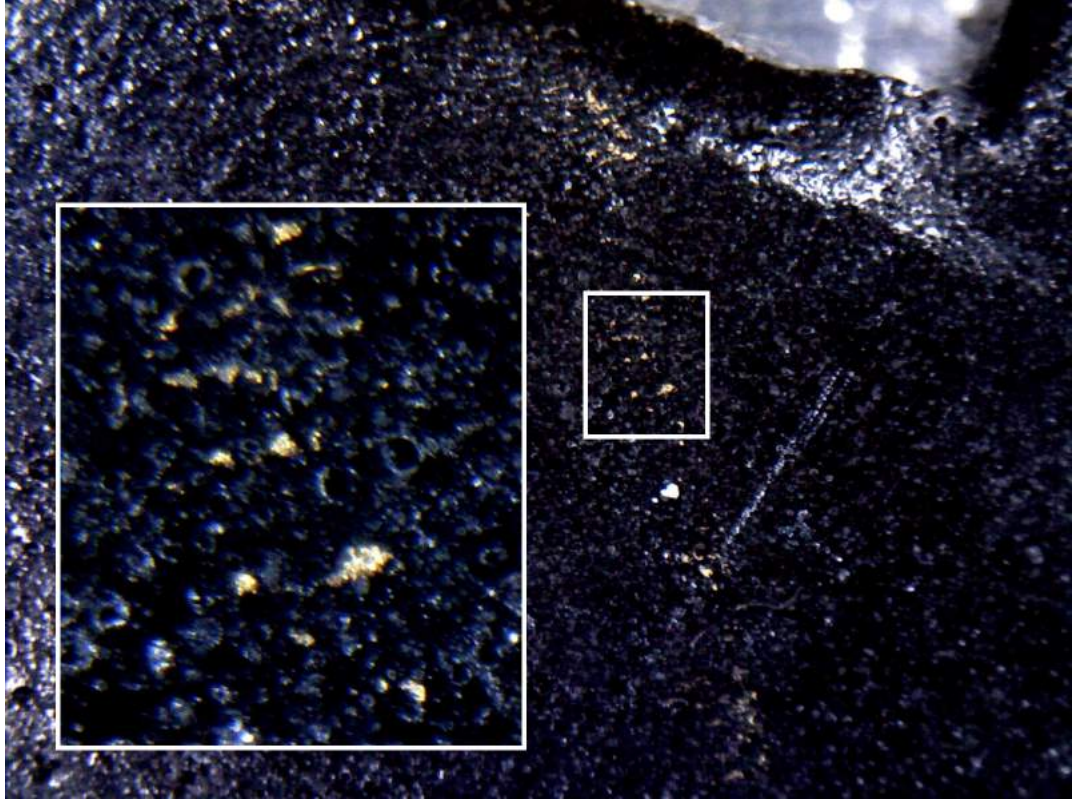


Figure 4.13: A picture taken by the USB microscope of the nano-suction-cup tape after being removed from a gold coated chip. A gold streak is visible due to electrode surface lift-off on the nano-suction-cup tape. The inset picture shows the same streak at a higher magnification.

channel shown in (b) and (d) was to make sure the chip tongue did not get stuck in its mount due to surface damage of the metal as a result of over-tightening the securing bolts. This damage can be seen on the very edge of image (d).

The next stage was to decide what alignment processes would be required in order to align the magnetic spacer to the chip. Other degrees of translation required for alignment would be translation along the  $x$ ,  $y$ , and  $z$ -axes as well as rotation about the  $z$ -axis. A combination of two ThorLabs stages were chosen to cater to these alignment requirements. These stages are shown in Figure 4.14. The  $z$ -axis stage was a standard part with a mechanically read micrometer and a travel of approximately 13 mm. This stage has an extremely precise parallelism specified to be less than  $10\ \mu\text{m}$  over the course of the whole 13 mm travel, very sufficient for our alignment requirements. The  $x - y$  rotational stage was a custom model with digital micrometers instead of mechanical ones. These are able to resolve down to a single micron and have the ability to be locked and zeroed. The rotational stage was Allen key lockable with marked increments down to a single degree. This combination of stages is capable of performing translation of the magnetic spacer to the micron-level accuracy we require.



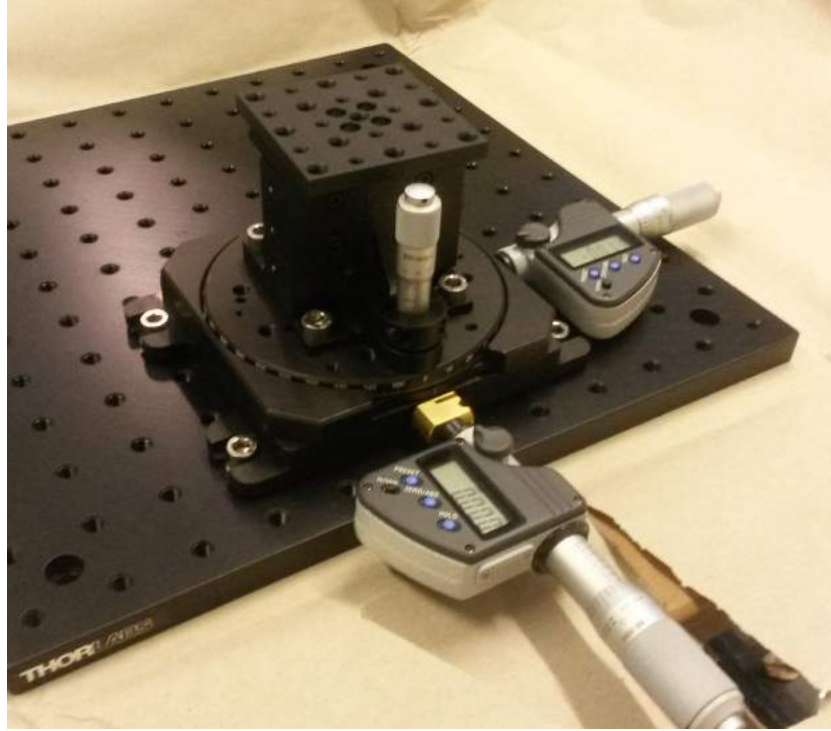


Figure 4.14: The combined lower alignment stages which should allow for precise translation of the chip and magnets in  $x$ ,  $y$ ,  $z$ , and  $r$ , the angle around the  $z$ -axis. The upper stage is a ThorLabs MVS005/M and the lower stage is a ThorLabs custom XYR1/M with the standard micrometers replaced with DM713 “Digimatic” micrometers. These stages in turn sit upon a ThorLabs MB3030/M optical breadboard.

Finally, several extra mounts were created in order to combine the stages into one solid unit. This included a stage which houses the removable chip tongue and raises the microscope stage up to above the lower alignment stages so that a chip can be held in place over the magnetic spacer. A small holding jig was also created to hold the magnetic spacer securely in place during the alignment procedure. This jig is shown in Figure 4.15 (a) as part of the heating plate which will be discussed immanently<sup>6</sup>. The cable for the microscope and tubing for the suction pump were clamped in two places each so that any movement of the stages, pump vibration, or adjustment to the brightness of the illumination LEDs would not interfere with the pointing direction of the microscope. Now that the optical and translational components of the alignment stage have been outlined I will discuss the additional heating plate that is used to cure the epoxy which secures the chip to the magnetic spacer.

---

<sup>6</sup>These parts were made of aluminium so that they would not interfere with the magnets at any point whilst performing the alignment.

### 4.3.2 Heating plate and determination of glue thickness

Due to the unpredictable nature of glue thickness, the chip is glued to the magnetic spacer using a small amount of adhesive on the outer edges rather than a uniform layer covering the bottom of the chip. The aligned magnetic spacer is then raised into contact with the chip underside prior to gluing by using the vertical aspect of the combined translation stages. This drastically reduces the expected error in the alignment in the ion height direction, which is particularly crucial for an offset magnetic spacer design since the axial gradient is determined by the vertical offset between the RF and magnetic nil lines. For an axially aligned magnetic spacer, this results in an offset field that must be compensated using the large external permanent magnets. We must therefore ascertain the expected effective glue thickness in order to clarify what misalignments may be expected.

The glue used is a two-part silver epoxy (EPO-TEK H21D 1OZ) which requires a curing temperature of around 100 °C. Since there were concerns as to whether this temperature would cause thermal expansion in parts of the alignment apparatus, a gluing test procedure was attempted without the use of high temperature curing. However, after a week, two small aluminium test pieces had not become suitably adhered to each other. A heating plate was therefore created which could be mounted on top of the vertical translation platform in order to cure the epoxy. This would additionally need to be suitably thermally isolated from the vertical stage, as well as have the appropriate mounting holes so that the previously mentioned jig could be mounted onto it in order to hold the magnetic setup. This heating plate was realised by mounting a small electric heating element to the underside of a square aluminium plate as shown in Figure 4.15. The mounting holes at each corner have additional channels cut so that they are significantly thermally isolated from the main body of the plate through reducing the material cross-section for thermal conduction. Additionally, these corners sit on small PTFE feet (with through holes) when mounted onto the top plate of the vertical translation stage as shown in Figure 4.15 (c) which provides good thermal isolation between stages.

Though an accurate measurement of the temperature of the heating plate was not investigated, by applying 20 W to the electric heating element, a glue curing time of around 15 – 20 minutes was achieved depending on the ratios of the two-part epoxy used. This corresponds to a temperature of over slightly 100 °C when compared to the specified curing time of the epoxy mixed at the correct ratio.

An investigation into the effective thickness of the epoxy using this procedure was

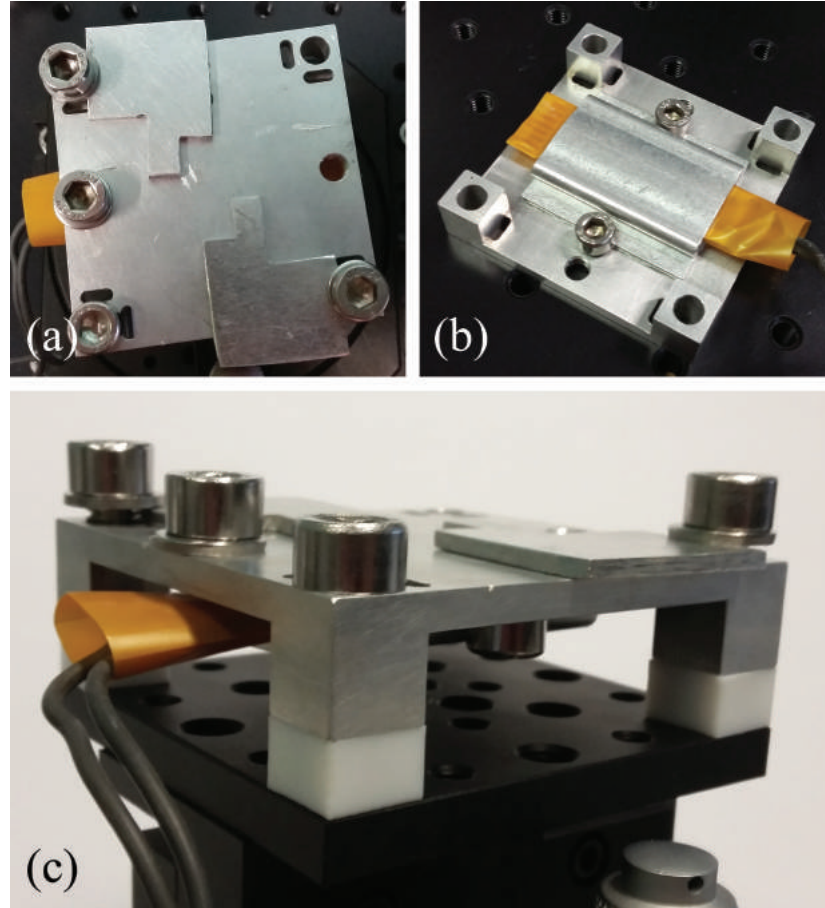


Figure 4.15: The heating plate created in order to cure the silver epoxy. **(a)** - Top view showing the jig used to hold the magnetic spacer during an alignment. **(b)** - Bottom view showing the DBK HP05-1/14-24 heating element of the plate. **(c)** - Side view showing the PTFE feet when the plate is mounted onto the vertical translation platform.

required in order to assess the possible vertical misalignment due to the glue. Since we would want to take the chip off if the alignment was not satisfactory, it was important that the chip could be glued securely to the spacer but be removed without damaging either of them if they needed to be realigned. This was realised by placing a small portion of epoxy on one edge of the chip lying flat in direct contact with the spacer which was found to be very secure but breakable using a scalpel or small, directed knock. Though it would seem that there should be no additional space between the magnetic spacer and chip after gluing, possible slips, dust, or any curvature to either material could lead to deviations from the zero-thickness case.

Using a set of chip fragments ( $680\text{ }\mu\text{m}$  thick) and mock spacers made from aluminium, the glue thickness was determined to be  $\sim 10\text{ }\mu\text{m}$ , determined from a mean of four test pieces measured<sup>7</sup> at  $8.9\text{ }\mu\text{m}$  with a standard deviation of  $9.5\text{ }\mu\text{m}$ . Though this is arguably a null result due to the standard deviation being larger than the mean, it is likely this is

<sup>7</sup>Each measurement was an average of three made at several points over the chip fragment.



due to the loss of parallelism between the top and bottom faces of the mock spacers when they were cleaned of excess epoxy after previous glue tests, which were shown to be untrustworthy as they used guillotined metal pieces in place of chip fragments. Additionally, since the distances are extremely close to the precision limit of the measuring device it is likely that the change in zeroing position of the device may be causing errors, though this was calibrated prior to the measurement. Thermal expansion and contraction may also play a part in this error as the parts may not have fully cooled down after curing on the heating plate at the time that some of the measurements were taken.

I concluded from this investigation that one could use a chip thickness accounting for glue measurement of  $690\text{ }\mu\text{m}$  plus the ion height in order to get our desired magnetic nil height for the chips used in our setup. We are now in a position where we have all the necessary tools to design an under-chip magnetic spacer with high magnetic field gradients for use with a planar ion chip trap. We also have the ability to align it to the on-chip features to micron-level accuracy and to design all peripheral magnetics that will be used for compensation of any tolerable misalignment or unknown offset field that we may encounter during an experiment.

### 4.3.3 Finalised alignment stage

I will now describe the finalised alignment stage which is shown in Figure 4.16. From bottom to top, the 3-axis stage from Figure 4.14 sits on top of a standard optical bread-board. Atop this sits the heating plate from Figure 4.15 with the mounting jig holding a copper spacer prior to the insertion of the magnets. In the inset picture, one can also see the pump-activated chip tongue as shown in Figure 4.12 with the custom gas nipple and PVC hose tube which goes to the pump. The chip tongue has been recessed in this picture in order to get a better view of the system. Above this stage, one can see the USB microscope (with the lens cap still on) mounted using the aforementioned mount onto a three-axis translation stage combination. This sits on a specially constructed aluminium stage that brings it to the required height above the lower alignment apparatus. This stage also holds the chip tongue in place as previously mentioned. Two nuts can be seen clamping down the cabling for the USB microscope so that translation of the camera stage does not interfere with the imaging axes due to tension in the cable.

Prior to use for alignment purposes, the stages are cleaned on the mating surfaces (faces that are in contact) using isopropanol on optical tissue in order to remove any fibres or dust that may angle the stage. The  $x - y$  stages are then calibrated so that

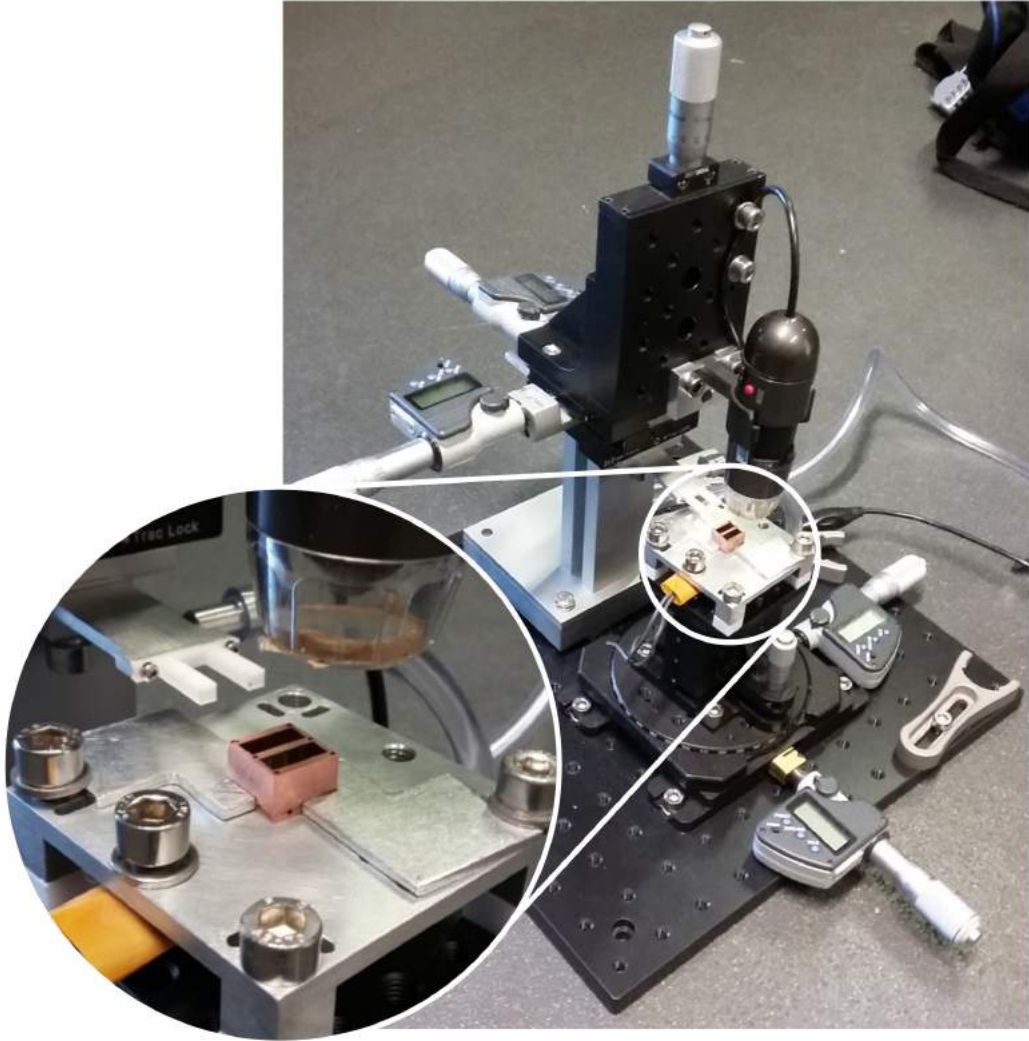


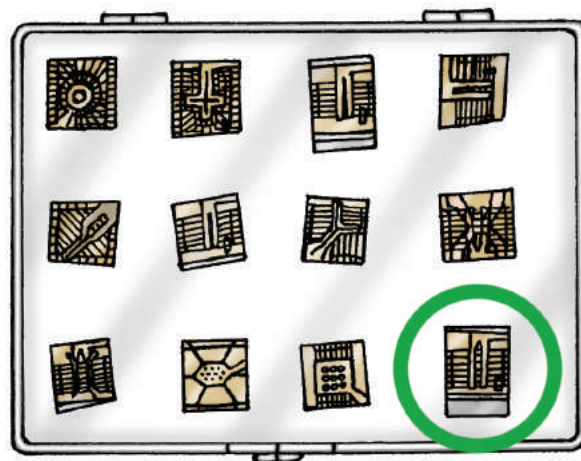
Figure 4.16: The finalised alignment stage used in order to glue the chip and magnetic spacer to each other with high precision. The inset picture shows a copper spacer prior to magnet installation in order to show the details around the heating plate.

the axes of each stage are parallel and perpendicular to each other and to those of the other stages. This parallelism is calibrated to within the resolution of the microscope (confidently within  $2\ \mu\text{m}$ ) along the whole translation of the stage, approximately 13 mm. This gives a maximum angular misalignment in the stages of less than  $10^{-2}$  degrees. A similar calibration is done on the vertical stages by checking that a reference point such as a metal defect remains to within  $2\ \mu\text{m}$  of the reference point on the camera as the metal piece is moved upwards in-line with the focus of the camera, achieving a similar angular deviation to the  $x - y$  stages. These calibrations are repeated if insufficient. Additionally, before each alignment, the heating plate is cleaned as previously described and the stage is covered when not in use. If it has been a while since the stage has been used, it is recalibrated or dismantled and re-cleaned to be assembled again from scratch.

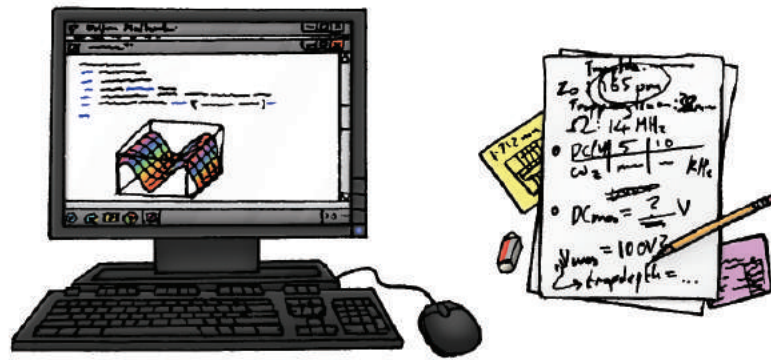
#### 4.3.4 Pre-alignment preparation procedure

Now that I have discussed the relevant components in order to create a micron-level alignment stage, I will discuss the process by which the chip and magnetic spacer will be aligned from first principals. I begin by discussing the pre-alignment procedure, which includes selection of the chip, designing and ordering the magnets, and finalising the copper frame that holds the magnets in the under-chip magnet spacer. This is presented as an in-depth how-to guide for future students in our group to ensure that the correct steps are taken when fabricating a magnetic spacer for a chosen chip. Additionally, the main alignment procedure is extensively detailed so that future users of the alignment stage should be able to successfully perform the alignment procedure.

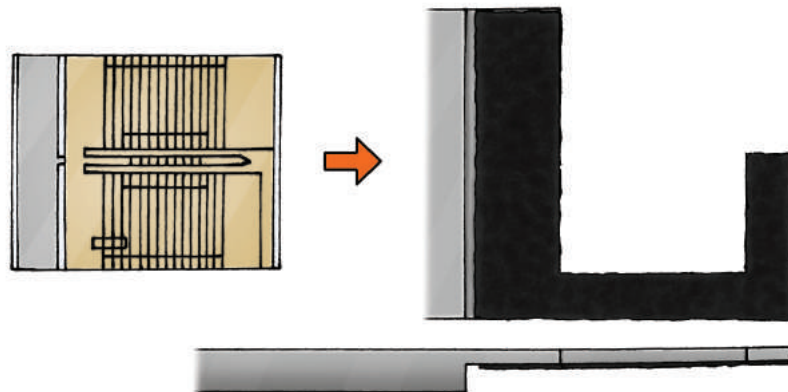
1. Firstly, once a particular ion chip is selected for use, the substrate thickness, the ion height above the surface of the chip, and the general geometric layout of the chip all need to be examined, noting electrode-free zones which will be gripped by the nano-suction-cup tape if using the original chip tongue design.



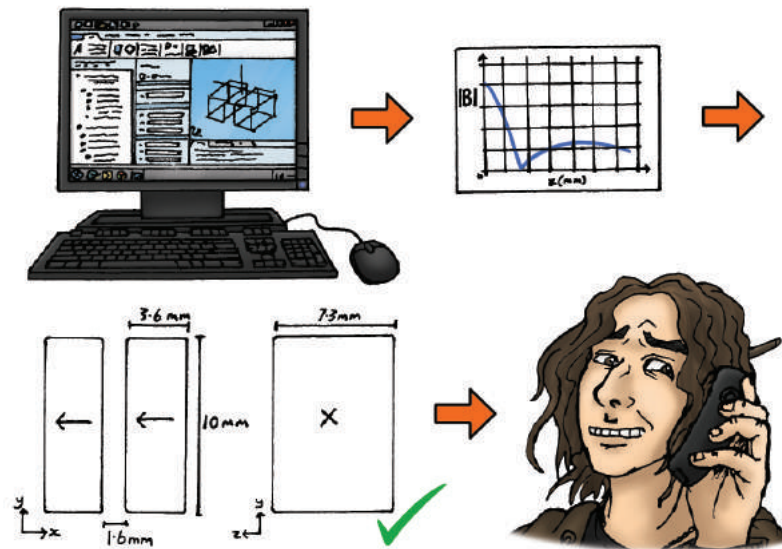
2. If necessary, the chip is simulated and the position of the trapping nil relative to the geometric features of the chip is noted down.



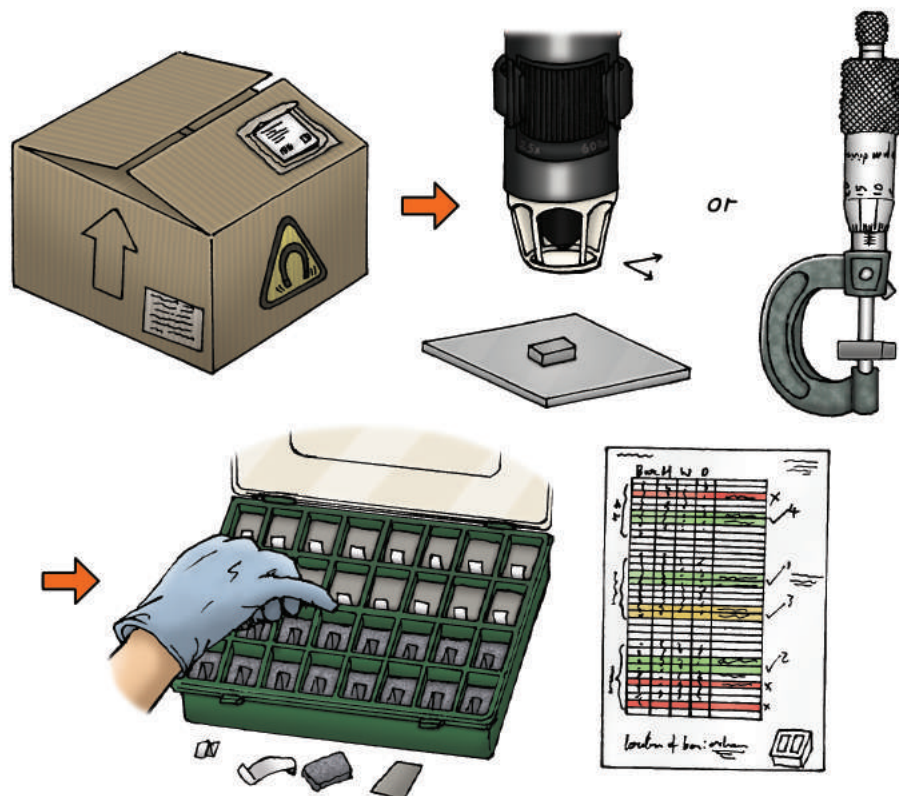
3. The chip tongue can then be designed for the specific chip and sent to the workshop for fabrication. This is mostly required if using the suction-cup tape chip tongue rather than the pump-activated chip tongue.



4. The magnetic structure must then be designed (using COMSOL for example) within the hemisphere of the vacuum system accounting for any expected chamfers or features that may be added to the magnets during the manufacturing process. Due to the crucial alignment required to get the best results, any yoking of the magnetic field from the surrounding objects must be taken into account. This can be significantly simplified in the event that one has no magnetic objects within the hemisphere. Once an optimised and agreed upon design has been created, one can then order a large quantity of magnets.

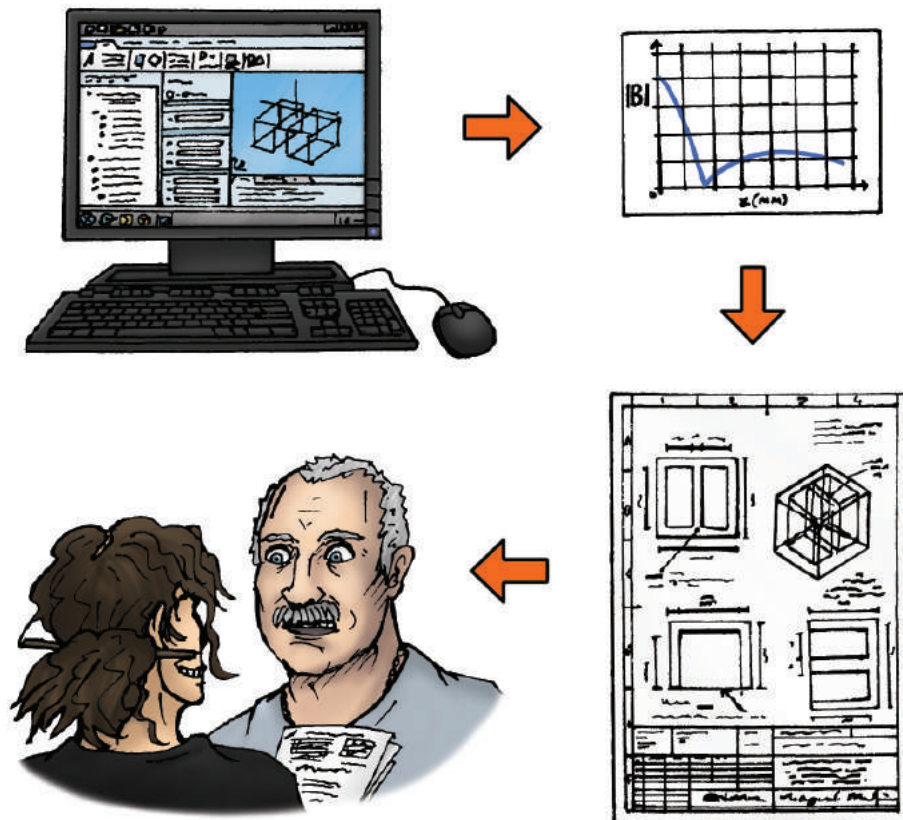


5. Due to manufacturing tolerances, there will be variations in the size of nominally identical magnets. For Bunting Magnetics UK, the manufacturing tolerance is stated to be within  $50 \mu\text{m}$  of the desired size, therefore, the magnets must be measured (preferably with the microscope and translations stages), labelled, and sorted into best matched pairs.

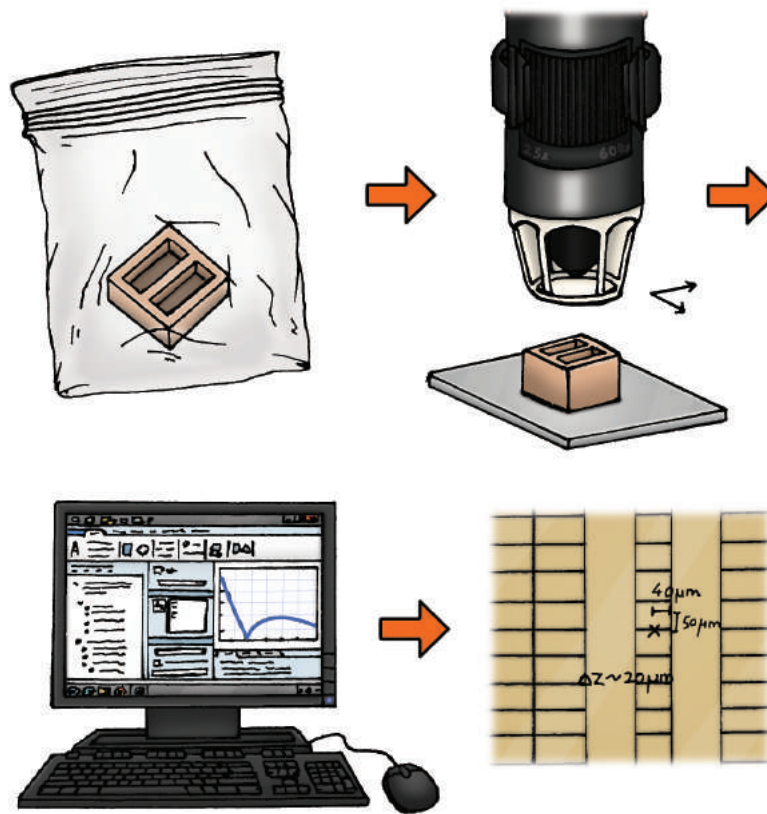




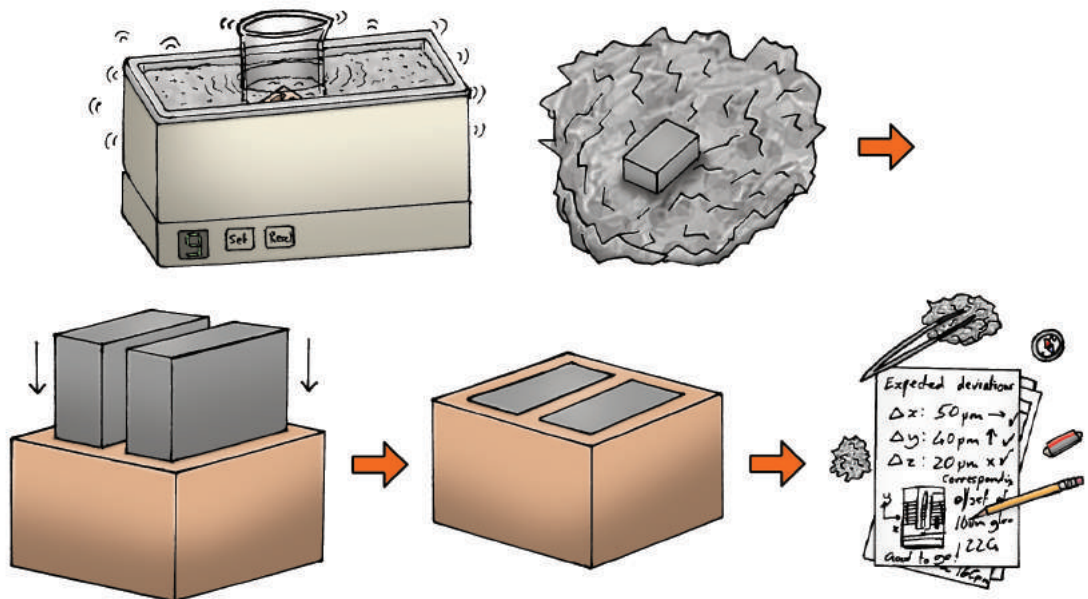
6. Once the best pair of magnets has been selected, the design of the ideal mount may need to be redone in order to re-optimize the possible gradients and field for these magnets at the desired nil height. One must then design an appropriate frame taking into account venting for trapped air voids and give this design to the workshop to be manufactured.



7. Once the mount has been received from the workshop, one should measure it (again using the microscope and translation stages) and re-simulate the physical system. One can then make notes of the simulated location of the nil which is likely to be slightly different from the perfect case. These shifts can then be accounted for during the final stages of alignment of the chip. If the displacement from the optimum nil position is at an unacceptable level based on what one is able to compensate for, the mount must be remade.



8. The mount and magnets must then be thoroughly cleaned before combining them and step 7 should be repeated for this final assembly.

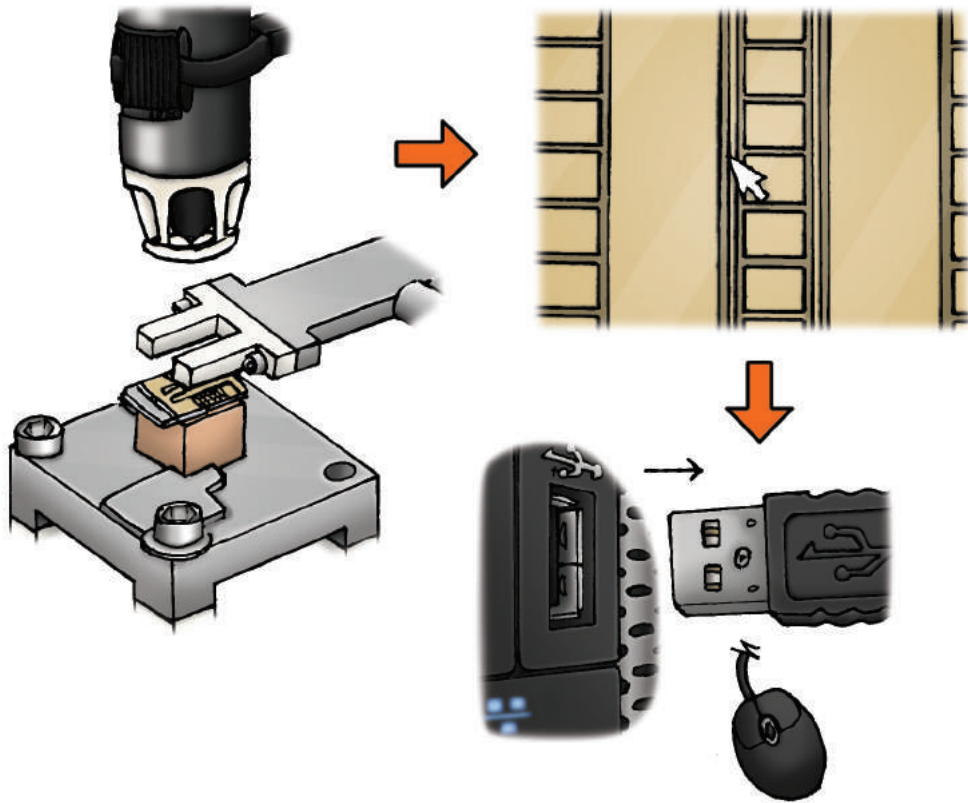


Once there is an accurate simulation of the physical, real magnetic spacer one is able to start the alignment procedure.

#### 4.3.5 Alignment procedure

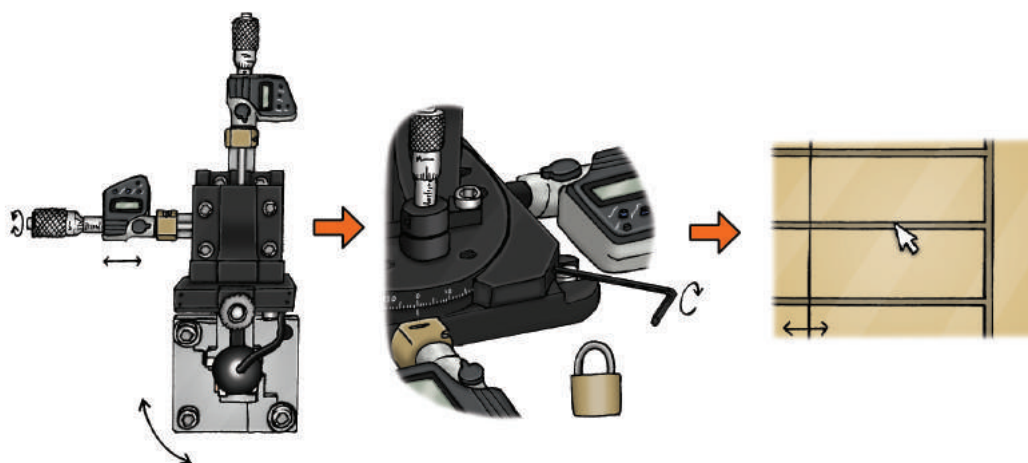
The process I used is limited by the technology we have but follows similar techniques to those described in A.R. Mirza's "One micron precision" paper of 2000 [67], which discusses various methods of wafer alignment. After evaluating our ability to use these methods, I devised my own based on the new method described in said paper, however, this is in the limit of using one camera objective and without the use of explicit alignment keys as these could affect the trapping potential and are not present on the available chips. The following procedure is used in order to align our chip with the magnetic spacer.

1. The microscope is set up in order to see the chip and magnetic spacer in best illumination to see the on-chip features clearly before creating a reference point on the camera image. This is most easily done by placing the mouse pointer in the middle of the screen and then unplugging the mouse.

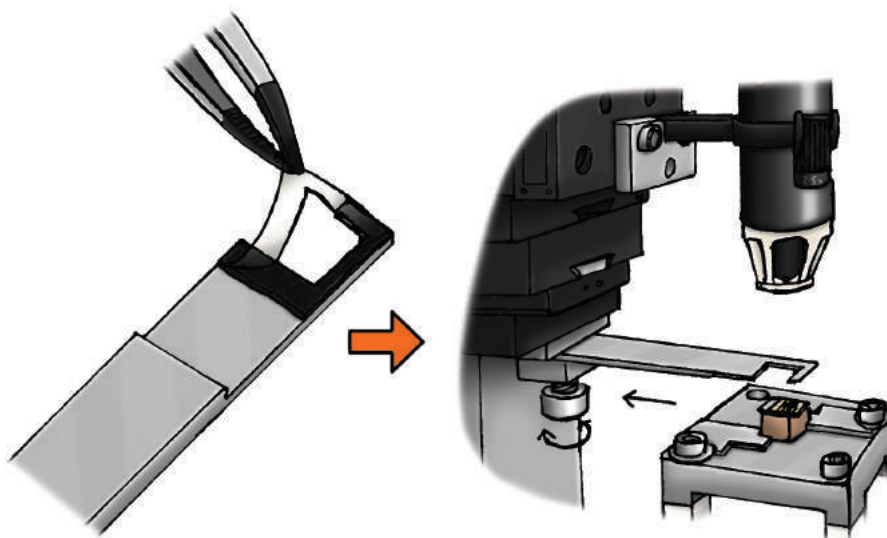




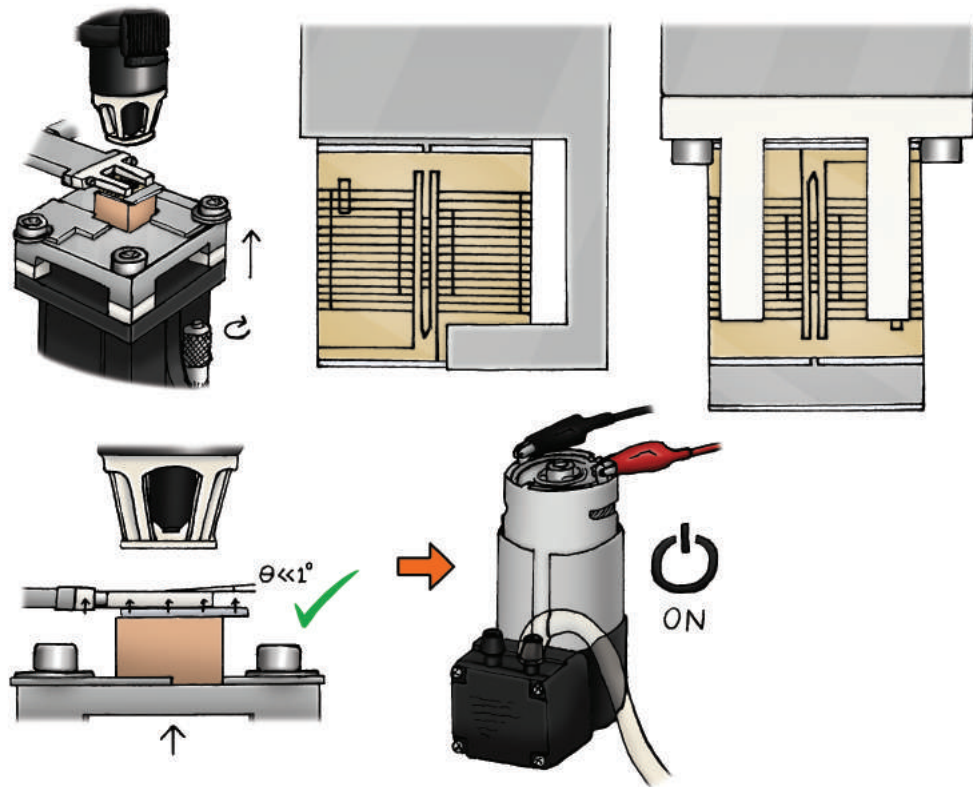
2. The chip can then be repositioned on the heating plate vertical stage on top of the clamped magnetic spacer and aligned with the camera axes by using the rotation stage and then scanning across the linear sections of the chip using the horizontal translation of the microscope stage. The rotation stage should be locked using an Allen key if no more rotational adjustment is required.



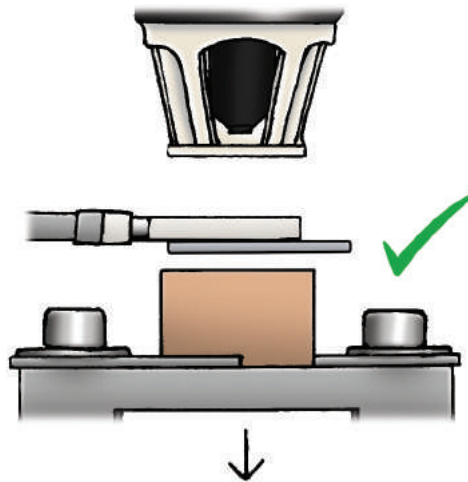
3. If a nano-suction-cup tape tongue is used, fresh tape should be applied to the tongue before putting it into the mount. The length of the tongue protruding from the stage is predetermined by the travel of the XY/R stage in the parallel direction to the length of the tongue and should be calibrated and marked in previous alignment trials. An example of this mark is seen in Figure 4.12 (c) on page 195.



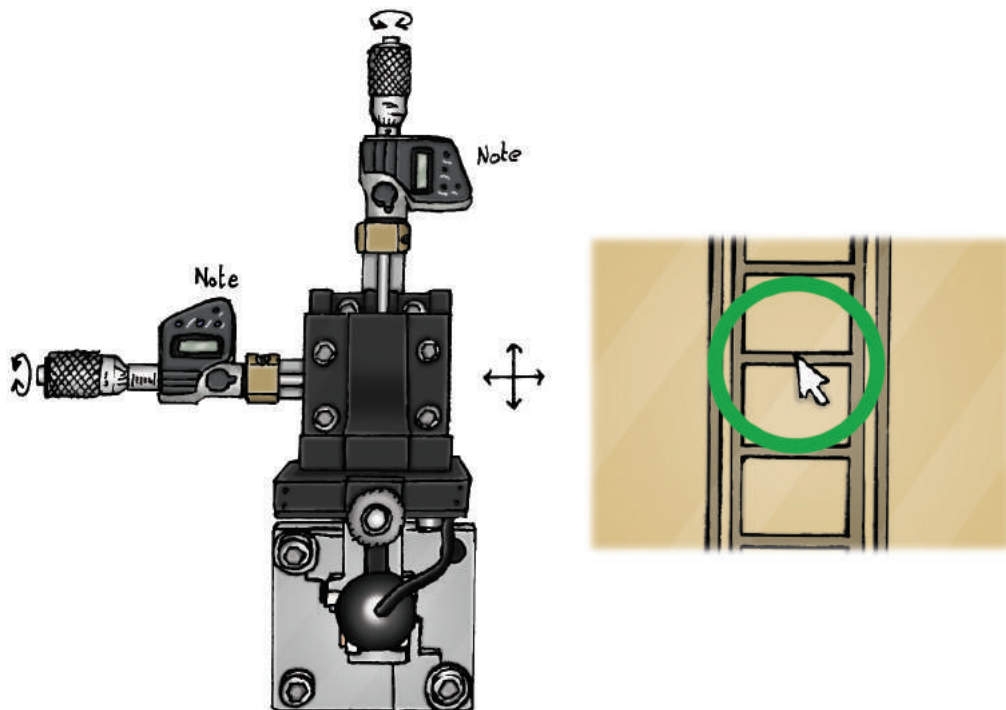
4. The chip is then aligned with the tongue by using the bottom stages and raising it into contact with the chip using pressure from the vertical stage and making sure that only the non-electrode surfaces come into contact with the nano-suction-cup tape. If using the pump-activated chip tongue, the pump is turned on only after the chip is in contact with the suction forks. If the chip moves as the pump is turned on, the alignment process should be restarted. If need be, one should use the  $x - y$  translation of the rotation stage in order to make sure that the chip is in the correct orientation for the mount. During this stage of the procedure, constant checks are made using the camera translation stage in order to assure the rotational alignment remains true. It is important that the tongue is not permanently bent while applying vertical pressure as this will affect future alignments.



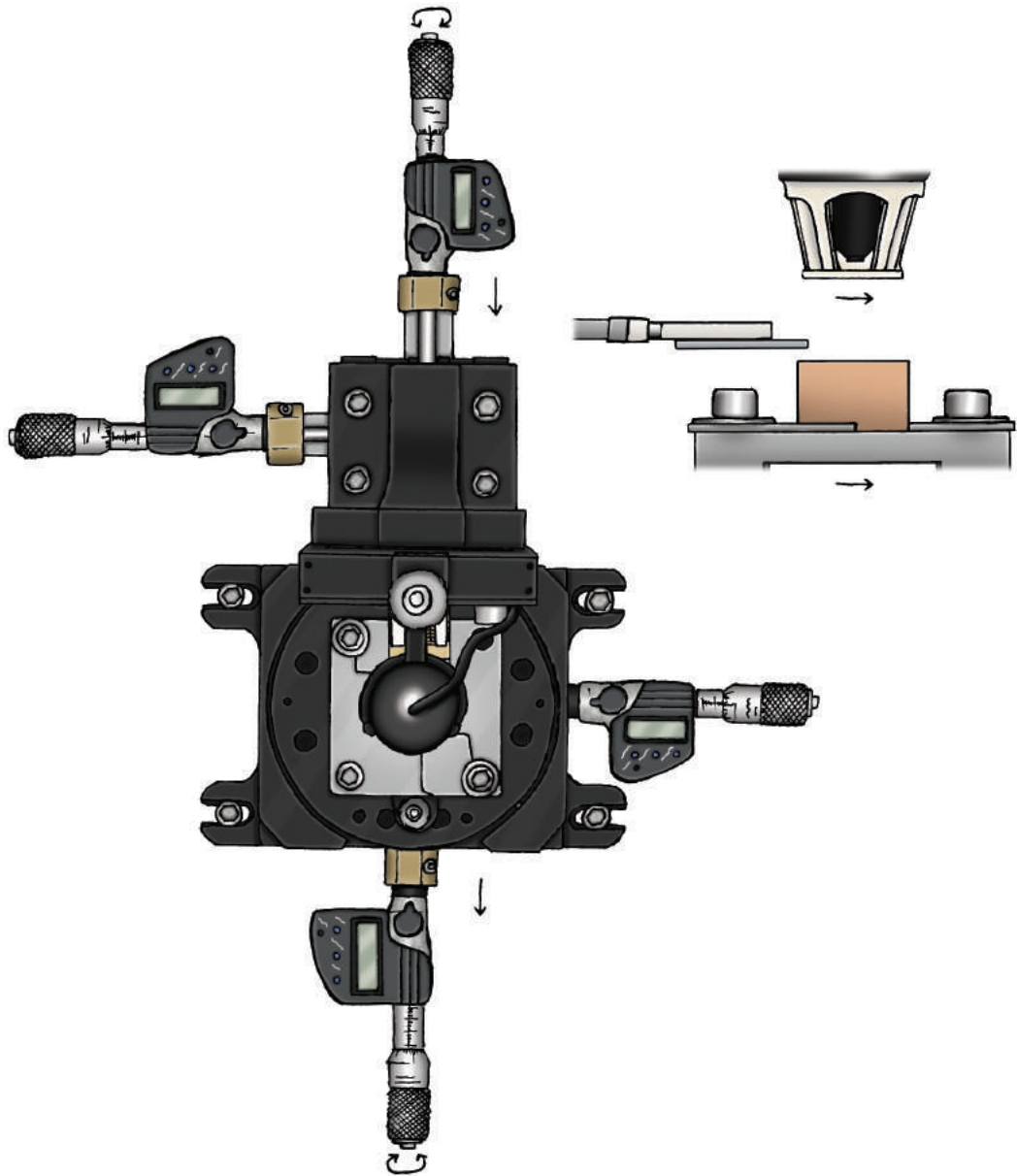
5. The vertical stage is then lowered and the chip is checked to make sure it is secure on the tongue. This is generally not a problem with a clean chip if moderate pressure was previously applied with either fresh nano-suction-cup tape or sufficient pressure from the suction pump.



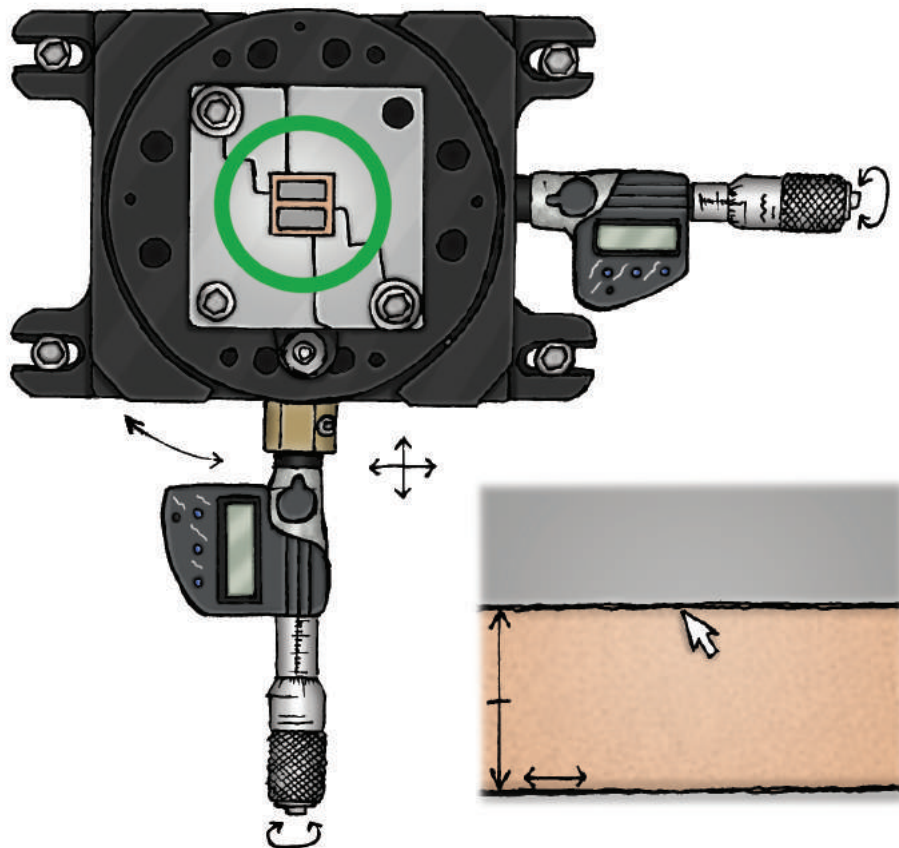
6. The values of key points on the chip are then noted using the camera by taking numbers from the camera translation stages. Using these points, the camera position corresponding to the trapping position on the chip that we wish the magnetic gradient to be aligned with can be calculated. This camera value should be clearly noted so that it can be returned to later in the procedure.



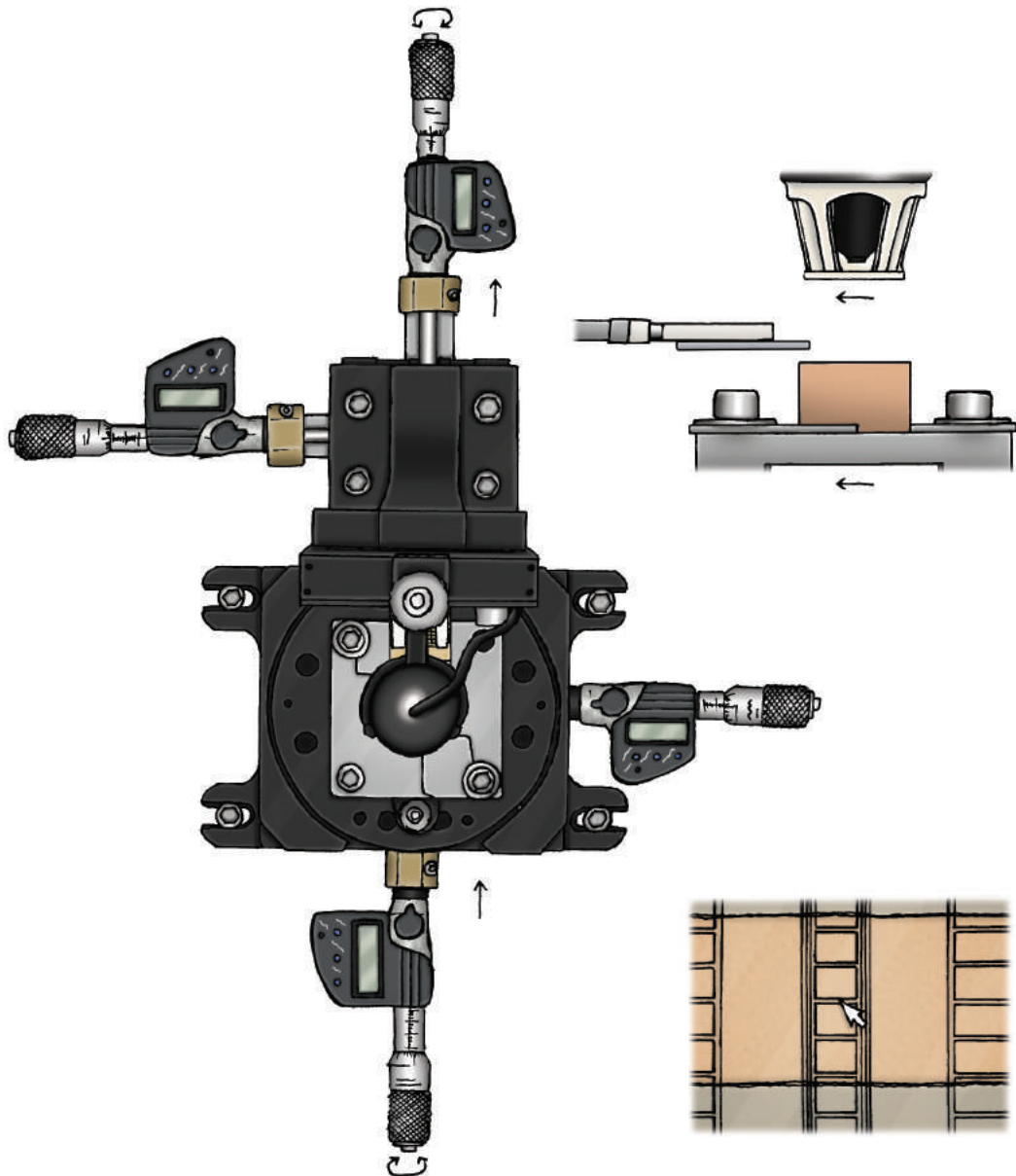
7. The camera and XY/R translation stage are then displaced from the chip so that the features of the magnetic spacer can be seen clearly in order to align it to the centre of the camera image at this translation value. Again, this camera value should be clearly noted so that it can be returned to later in the procedure.



8. The magnets are subsequently aligned perfectly centred and geometrically to the translation axes in the same manner as with the chip but using the XY/R stage taking into account the position along the magnetic nil line that will correspond with the desired zone for ion trapping. The central spacing of the magnets is aligned parallel for radial gradients and perpendicular for axial gradients with regards the linear section of the ion chip trap. Rotational alignment of the chip can be verified by horizontally scanning along the edges of the spacer using the camera to assure a common axis with the chip. Once this is traced, the camera is positioned back at the position noted in step 7. The optimised parallelism of the travel for these stages should be obtained while constructing the alignment apparatus.

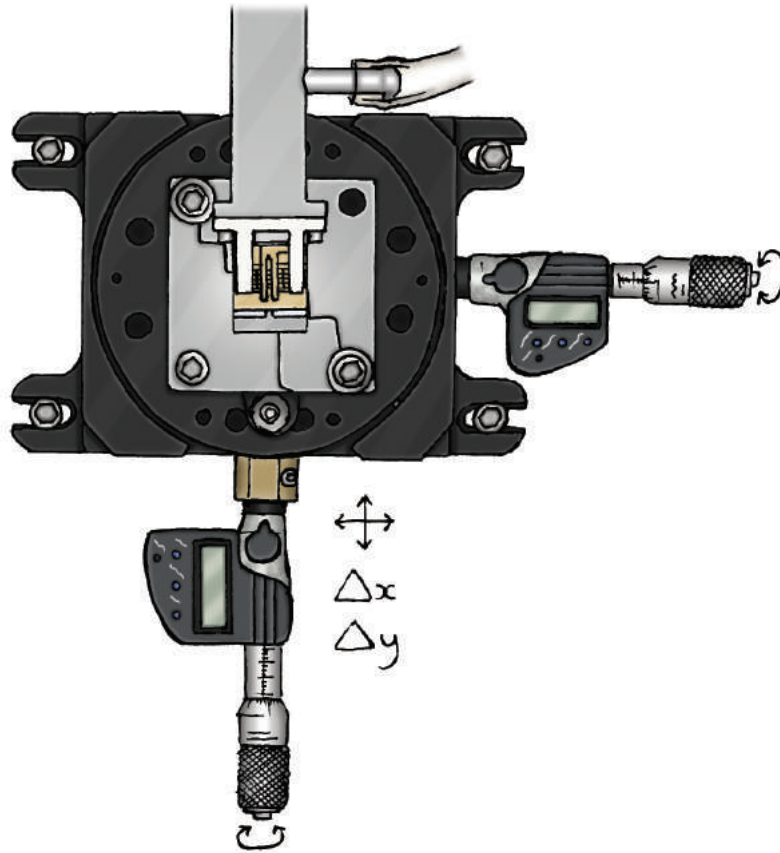


9. The magnetic spacer and camera are then simultaneously brought back into alignment with the chip using the value noted in step 6. The stages should move in perfect synchronicity and the optimum distance of displacement should be calibrated during practice alignment procedures.

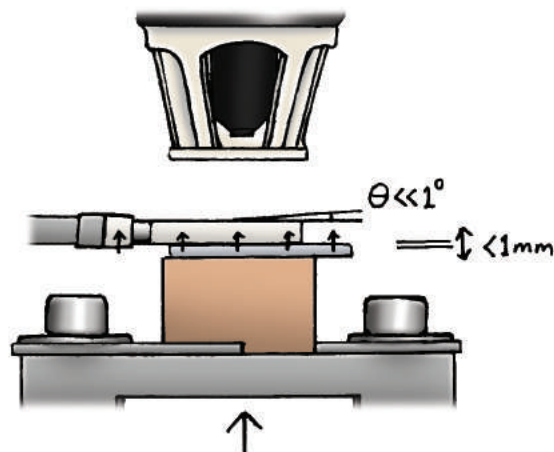




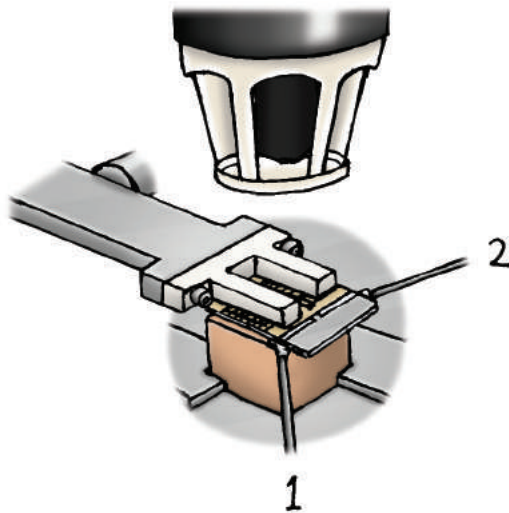
10. Any deviations from the ideal nil position as noted from simulations are then applied to the spacer alignment.



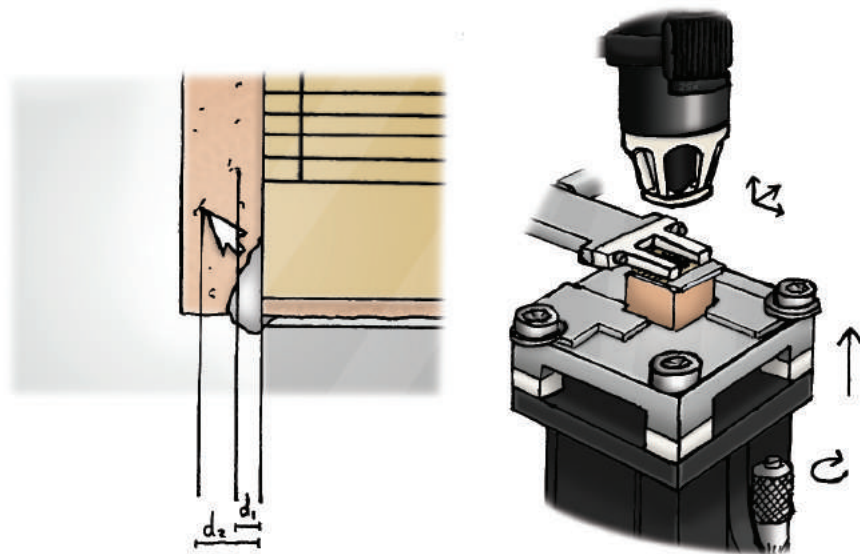
11. The magnets are then raised into contact with the chip. This distance is less than a millimetre so that there is a minimum possible displacement caused by any slight angle of the vertical stage.



12. Epoxy is then spot dropped onto the edges of the chip that are exposed where it is safe to do so while making sure that the alignment is not compromised at any point during this process. The magnetic structure should be placed under sufficient pressure in contact with the chip so that this should not be a problem. If the chip moves, the alignment procedure must be started again.

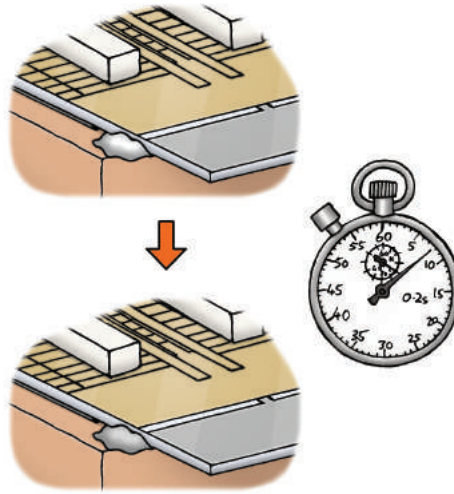


13. The camera is then used to make note of several reference defects in the metal of the magnetic spacer in order to assess any misalignment that may occur as a result of the glue drying.

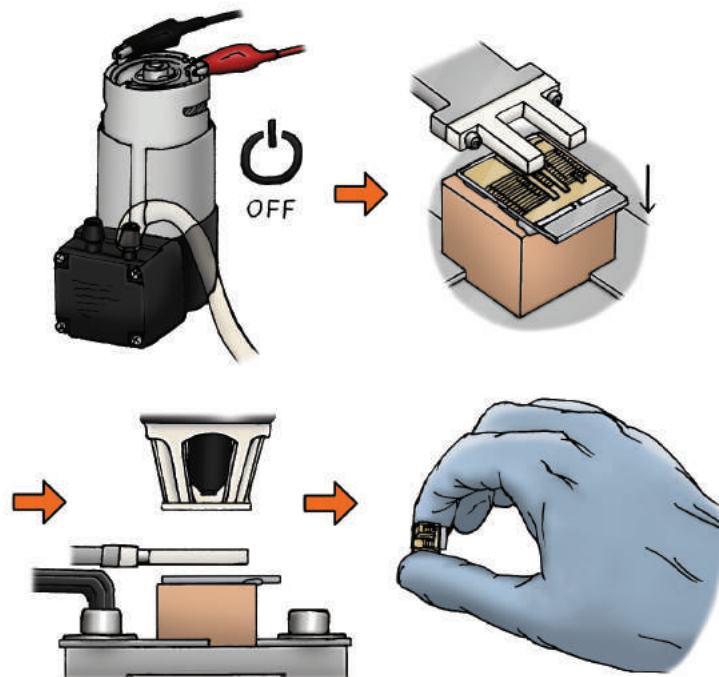




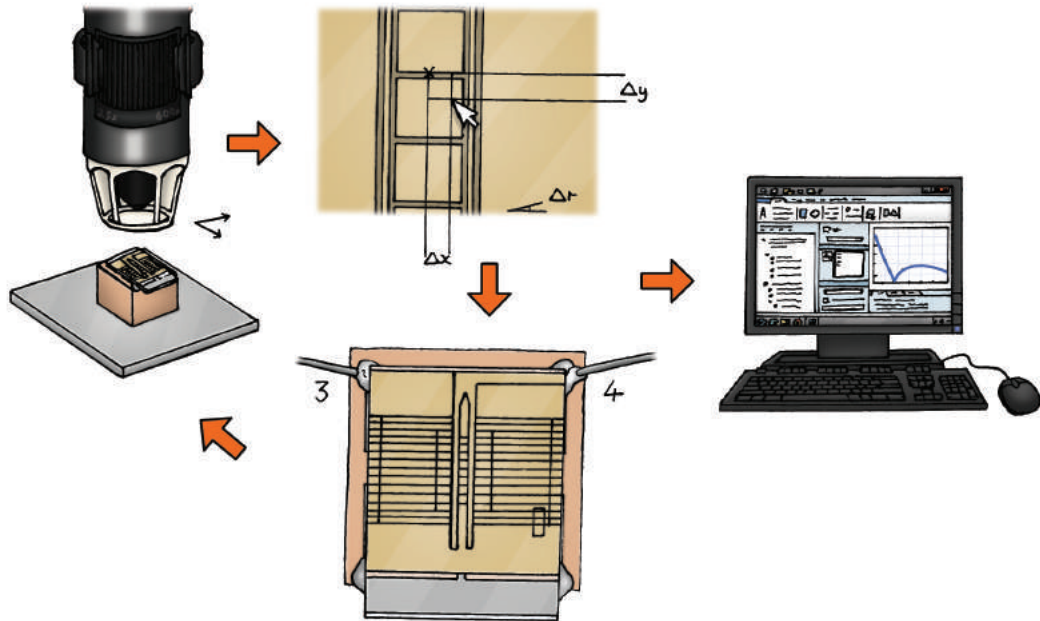
14. The curing procedure for the epoxy (or other adhesive) is then commenced keeping continuous pressure between the magnetic spacer and chip.



15. Once the epoxy is cured, the assembled chip and magnetic spacer are removed from the nano-suction-cup tape or the suction pump is turned off. This should be done by loosening the jig holding the magnetic structure and lowering the vertical stage. If using the nano-suction-cup tape chip tongue, the assembled piece will likely be stuck to it. The tongue should be carefully taken out of the camera raising stage and the chip-spacer combination should be gently removed from the tape.



16. If the alignment looks good (to within 30 percent of the offset fields one is able to compensate), more secure gluing points are made on edges that were inaccessible with the chip tongue in place. The alignment is checked again using the metal defects for reference and the predicted level of the offset magnetic field component in each direction is reviewed by adjusting the simulations for the real chip position. These values may become useful later during initial trapping experiments.



The performance of the alignment stage using these procedures is detailed later in this chapter for the real chip to magnetic spacer alignments for installation into the vacuum systems. During initial alignment attempts several things have been noted in addition to the explicit alignment steps which aid in the alignment process. These are documented below.

For real alignment runs, the silver epoxy is cured for 30 minutes to be sure it has cured and inspected under the microscope to ensure that this is the case. One must also make sure that a constant power is applied to the heating plate in order to make sure the temperature remains stable for the duration of the curing process. If this power is not kept constant, this can lead one to believe that the epoxy is cured when it has not.

The magnetic spacer can be cleaned in the event that an alignment has gone wrong, however, this can effect the straightness of the edges of the spacer and therefore one has to be very careful when finding parallel and perpendicular references on the structure during the next alignment.

We have also found that cured epoxy is much easier to remove from a surface than “wet” epoxy; it is actually better to finish curing small epoxy spots than to stop in the middle of the process. However, if the chip moves while the spot is being applied, then the alignment process should be stopped and both the chip and spacer should be cleaned immediately. It is also extremely helpful to have another person to hand to spot you during this stage as one is unable to simultaneously look at the screen and spot glue in the correct position by eye.

Now that we have devised how we can implement an under-chip magnetic spacer and quantified the glue thickness and compensation limits for our particular experimental setups, we are able to order a set of magnets to construct this spacer and install it into a vacuum system. The following sections will detail this installation process and additional concerns in setting up a planar chip trap experimental setup for performing microwave based entanglement operations.

#### 4.4 Preliminary external measurement of the magnetic field gradient

The magnets of the under-chip magnetic spacer are made from samarium cobalt (Bunting Magnetics SmCo2:17) with a manufacturing tolerance of 50  $\mu\text{m}$ . We therefore ordered a large quantity in order make sure that a best matched pair could be selected for each system<sup>8</sup>. This would also mean that there were a lot of magnets left over, which allowed us to perform an external magnetic field gradient measurement prior to installing an under-chip magnetic spacer into a vacuum system.

Given the precision required for such a small geometry, it was originally presumed that one would be unable to measure the magnetic field gradient of this scheme until ions had been trapped on a chip mounted atop them. However, in order to make detailed magnetic profiles of superconducting tape, John Lacy (of the group of Dr Jose Verdu Galiana) was using an AREPOC HHP-VA Hall probe mounted on a CNC machine to make many measurements of the out-of-plane component of the magnetic field above his tape geometries<sup>9</sup>. This probe had a spatial resolution of 50  $\mu\text{m}$  by 50  $\mu\text{m}$ , well within the requirements of measuring the magnetic field profile of our test geometry. Additionally, since the gradient originates from a linear change in the out-of-plane ( $B_z$ ) component of

---

<sup>8</sup>The steps that should be taken prior to ordering the magnets and sorting them on arrival are outlined in Section 4.3.4.

<sup>9</sup>The CNC machine is capable of making movements to sub-micron precision and could be programmed to follow a path in order to take a measurement.

the magnetic field at the centre of the geometry, any spatial averaging by the probe should not affect the gradient measurement. This experimental setup is shown in Figure 4.17.

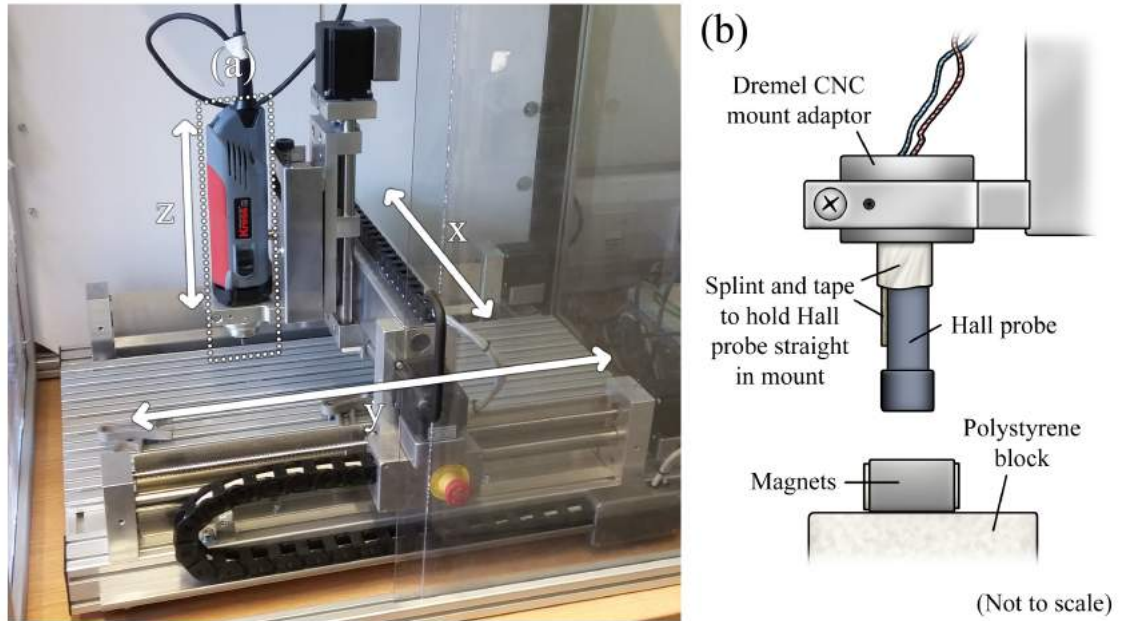


Figure 4.17: A CNC machine similar to the one used in order to make the magnetic measurements. (a) - A dremel attachment used for cutting/milling. (b) - Replacing the dremel, the hall probe clamp setup created by John Lacy so that the CNC machine could be used to map magnetic fields above an object.

There are two disadvantages of this setup. Firstly, since the Hall probe only measures one component of the magnetic field, one is unable to know whether the simulated nil height is correct. This is because the out-of-plane component of the magnetic field in this geometry crosses zero at the centre position regardless of height. That said, the geometric change in the out-of-plane component of the field is where the gradient for our scheme comes from, therefore if the absolute field was non-zero, as long as the in-plane component of the field could be compensated, the gradient measured is still an accurate representation of the gradient expected for the scheme. Secondly since the Hall probe was attached to the CNC machine as a retrofit rather than a part designed especially for the machine, there were small concerns of the angle of the probe to the perfect upright position, i.e. the true out-of-plane component of the magnetic field. Additionally, the macroscopic nature of this setup made it difficult to ascertain when the probe was zeroed for a reference by which the height above the magnets could be determined in order to make a measurement of the field that could be accurately compared to COMSOL simulations. The general procedure for creating a zero position was to lower the probe until it was touching the object to be sampled. The probe would then be moved in the in-plane direction to see whether the

probe would drag the sample. The height at which the sample was only just starting to be dragged would be marked as the zero height. This means that the real measurement height is likely to be slightly higher than our proposed measurement height as this zero can only be positively offset. The error on this height is also very hard to ascertain, however, all I desire from this measurement is a readout comparable to the simulation data, thus a height error of  $\pm 50 \mu\text{m}$  is unlikely to take us far from the desired order of magnitude of the gradient. It will become apparent later that this error is unlikely to be the greatest threat to a perfect dataset.

A very basic setup was put together and measured up for simulation shortly prior to the measurement<sup>10</sup>. Two medium condition, very non-optimum<sup>11</sup>, magnets were selected and a small separator was fashioned out of some plastic packaging. The force of attraction between the magnets was sufficient to keep them together, though small deviations in the simulated measurement could have occurred while transferring the pair from the measurement apparatus (the microscopic alignment stage) to the CNC machine. The magnetic setup used for this test is shown in Figure 4.18.

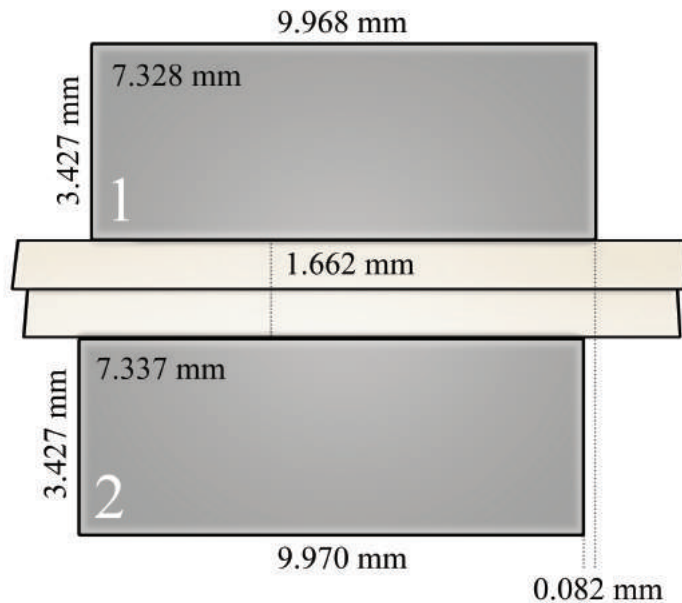


Figure 4.18: A schematic of the set of magnets measured using the Hall probe mounted on a CNC machine. In this chapter, the thickness of the magnets is labelled on its body and displacements of parts relative to each other will be labelled by a dotted line for clarity.

<sup>10</sup>Due to the time window that results could be taken using this apparatus, a copper spacer was not made for these magnets.

<sup>11</sup>These magnets had the largest manufacturing error associated with them and would be the last choice for use as a backup for the experimental setup. This means that in the event they got damaged or destroyed in the machinery it would not impact our stock of magnets that could potentially be used in future experiments.

For the given geometry, COMSOL simulations indicate that the magnets create a central minimum point at  $865\text{ }\mu\text{m}$  above the top surface of the magnets with a magnitude of 8 G. This offset is most likely due to the horizontal shift in the magnets relative to each other. Assuming the magnets have a remanence of 1.08 Tesla, the gradient is simulated to be 130 - 137 T/m. With the out-of-plane component of the magnetic field alone, the simulated gradient is 138 T/m<sup>12</sup>. Using a step size of  $100\text{ }\mu\text{m}$ , a 10 mm scan across the magnets at approximately 1 mm off the true centre (due to the zeroing of the setup) achieved a measured gradient of approximately 74 T/m, much lower than the gradients previously simulated. A detailed look into the specification of the Hall probe revealed that the main sensing portion of the device was in fact  $350\text{ }\mu\text{m}$  from its front surface. This meant that although we had brought the Hall probe to a height of approximately  $865\text{ }\mu\text{m}$  above the magnets, we were in fact measuring the field at a height of  $1215\text{ }\mu\text{m}$ . After correcting for the sensor position another measurement at the intended height yielded a measured gradient of 113 T/m (18 percent less than simulated)<sup>13</sup>.

Figure 4.19 shows this particular dataset against values simulated using COMSOL. On the left side of the measurement graph a small “kink” can be found at a displacement of  $-1.6 - -1.4$ . This is unlikely to be a real feature of the magnetic field as this measurement is far above the magnets; this is most likely due to the CNC machine or magnets being jogged during the measurement. Based on the symmetry of the field profile for positive displacements from centre, one can infer that the measurements at the displacements between  $-2.5$  and  $-1.6$  are shifted relative to the centre of the separation of the magnets and can therefore be ignored.

The deviation from the simulated value could be from a number of factors, most notably the uncertainty of the height of the Hall probe during sensing. The green line in Figure 4.19 corresponds to a simulated measurement at a height of  $985\text{ }\mu\text{m}$  above the magnets which was found to fit the measured result well at central values where the effect of any angular misalignment would be minimal. Assuming the probe height was accurately zeroed, this corresponds to an angular misalignment of  $< 2$  degrees of the probe from vertical which is more than likely given the nature of the mounting method. With the accidental measurement at  $1215\text{ }\mu\text{m}$  I also had results that could be used to check the simulated model. A simulation of the out-of-plane component of the magnetic

---

<sup>12</sup>As previously discussed in Chapter 3, the gradient can be maximised through compensation of offset field components.

<sup>13</sup>After recalibrating the probe height above the magnets a second time, a repeat measurement yielded a gradient value of 108 T/m (22 percent less than simulated). Given this, I will state the measured gradient to be  $\sim 110\text{ T/m}$  when referenced elsewhere in this thesis.

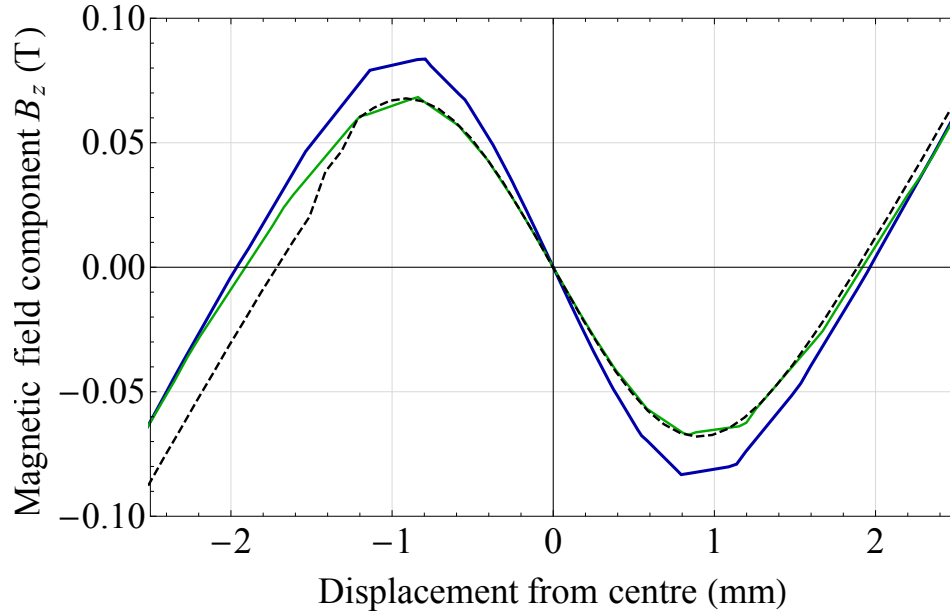


Figure 4.19: The magnetic field component  $B_z$  at  $865 \mu\text{m}$  above the geometry shown in Figure 4.18. Blue line - The results simulated in COMSOL using the standard magnetic material properties of SmCo as discussed in Chapter 3. Dashed black line - The results measured using the Hall probe mounted on a CNC machine. Green line - The results simulated in COMSOL to fit the Hall probe data corresponding to a measurement at  $985 \mu\text{m}$  above the geometry.

field at that height gave a magnetic gradient of  $74.8 \text{ T/m}$ , extremely close to the measured value (1 percent less than simulated). Though the measurements made at  $865 \mu\text{m}$  have quite a reduction in gradient when compared to the simulated value (assuming that an angular misalignment from vertical was not the cause of this difference), it must be noted that the sensitivity to distance at lower heights is much greater than for the  $1215 \mu\text{m}$  measurement. Additionally, a reduction of 20 percent is still extremely promising when the reduction in gradient in the macroscopic trap setup mentioned in Chapters 1 and 2 was around 50 percent from the simulated value. As explained in Chapter 3, this is proposed to be due to an ill advised Ni-Cu-Ni coating. Nevertheless, the results yielded from the preliminary measurement of the magnetic field gradient show extreme promise for the under-chip magnetic spacer scheme as a viable component of a fault tolerant setup.

## 4.5 Installation of the under-chip magnetic spacers

For each system, an under-chip magnetic spacer was designed in order to produce the desired gradients. Several aspects of these designs changed slightly when compared to the ideal simulated cases discussed in Chapter 3 due to real world complications and insight. I



will first discuss in detail the construction of the magnetic spacers for both systems before moving onto the results of aligning them with each of the ion chip traps. I will then discuss installation of the chip-magnet combinations into the vacuum systems.

#### 4.5.1 Magnetic spacer for the axial gradient system

This section details the construction of the magnetic spacer for the axial gradient vacuum system. The copper frame for the under-chip magnets has several small but significant changes from the theoretical simulation when compared to the real world construction of the pieces. The first major difference is that in order to avoid trapped air voids that could cause explosions and unwanted sudden out-gassing in the UHV environment, venting flutes were incorporated into the design of the copper spacer. An example of this kind of structure is shown in Figure 4.20. Full details of these designs can be found in Appendix B with the technical drawings of the magnetic spacers for both systems.

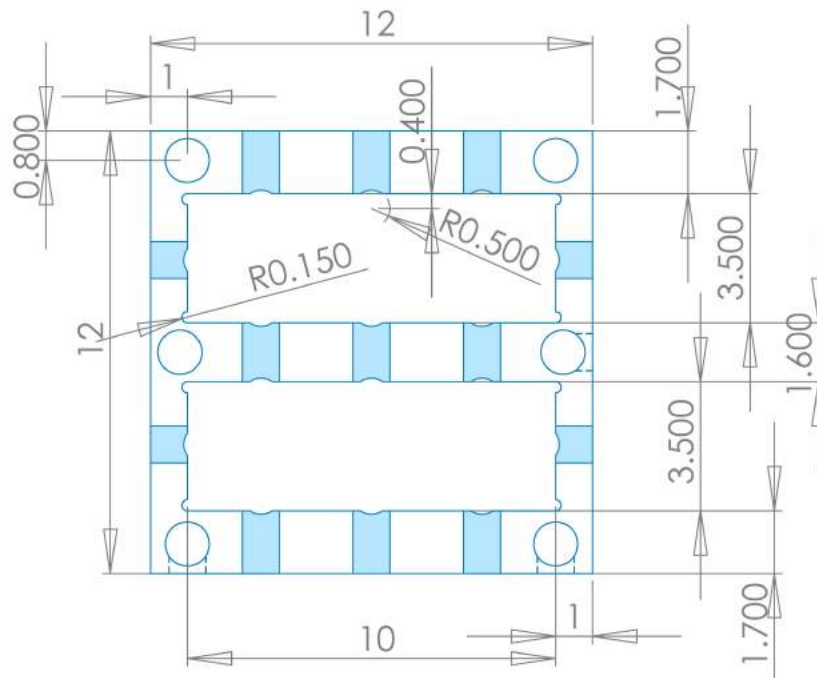


Figure 4.20: An example of the venting flute arrangement (marked in solid blue) as seen from the bottom face of the copper structure that holds the magnets in place for the axial gradient system. Dimensions are in mm. The 0.5 mm radius offset holes provide a small gap for air to escape on the sides of the magnet without compromising the structural integrity of the piece or present a possible edge that might damage the magnets. The 0.15 mm radius holes over-cut the corners of each pocket in order to make sure that the magnet corners are able to fit into the copper frame.



In addition to these venting holes, there were also holes at the bottom of each magnet pocket so that the magnets could be more easily removed from the spacer. Though these inevitably change the geometry of the spacer, it is not required that these be simulated as copper has a near unity magnetic permeability and the percentage difference in magnetic nil position is much smaller than the error associated with the alignment or manufacturing tolerances for the scales we are dealing with.

The second major difference is that the real spacer is made up of two main copper parts with additional A2 stainless steel screws to secure them together<sup>14</sup>. These parts are the main “figure-eight” that the magnets sit in and a lid/bottom that would be attached using non-magnetic screws and set a secure base for the magnets<sup>15</sup>.

This change to the design has some advantages. Since the block is in two parts, the “figure-eight” can be modified easily if the magnets do not slide in easily, this is easily done using a needle file being careful not to alter the central separation distance as this will affect the nil position. With the ability to remove the bottom of the structure, one is also able to make measurements of the magnets on their underside to check the parallelism of the structure. These magnet mounts were constructed using oxygen free copper and A2 stainless steel screws<sup>16</sup> to ensure both UHV compatibility, good thermal conductivity when using the cooling system, and the lowest possibly magnetic nil misalignment due to yoking of the surrounding materials.

For this system we will be using a high axial gradient full spacer design with an ideal magnet size of  $10 \times 7.1 \times 3.5(a)$  mm<sup>17</sup> and a separation of  $0 \times 0 \times 1.6$  mm for a magnetic nil position of 855  $\mu$ m above the surface of the magnets and a magnetic gradient of around 140 T/m. This configuration was determined given the size constraints outlined in Chapter 3.

On receipt from the workshop, the copper frame and magnet combination was measured and an appropriate simulation was done to better represent the real positions of the magnets relative to each other and the magnetic field this would give. These simulations were well within the limits of any offset fields that would need to be compensated for an acceptable misalignment and a chip was selected to be paired with this piece<sup>18</sup>. Figure 4.21

<sup>14</sup>This was a decision for ease of manufacturing discussed and suggested by the workshop with main credit for the adaptation of the design going to Alan Mayers.

<sup>15</sup>It was decided not to braze/solder/weld the lid on due to the high probability that this would distort the spacer which would be unacceptable for such a high precision piece.

<sup>16</sup>A2 steel screws was chosen as they easily sourced at the time of fabrication. The screw holes are top vented to prevent trapped voids.

<sup>17</sup>The “(a)” denotes the dimension parallel to the remanence of the permanent magnet.

<sup>18</sup>Since a final remeasurement and simulation is required as part of the alignment process, the appropriate geometric layout, simulated gradient, and offset field values can be found as part of the chip to magnet alignment section.

shows the real two-part spacer prior to the insertion of the magnets. (a) clearly shows the large venting flutes on the mating faces of the lid/bottom and “figure-eight” of the spacer. (b) and (c) illustrate how compact this design is by using a twenty pence coin for scale. It is very obvious now how small an addition this would be to a vacuum system in order to produce the high magnetic field gradients required for high fidelity microwave based quantum computing with trapped ions.

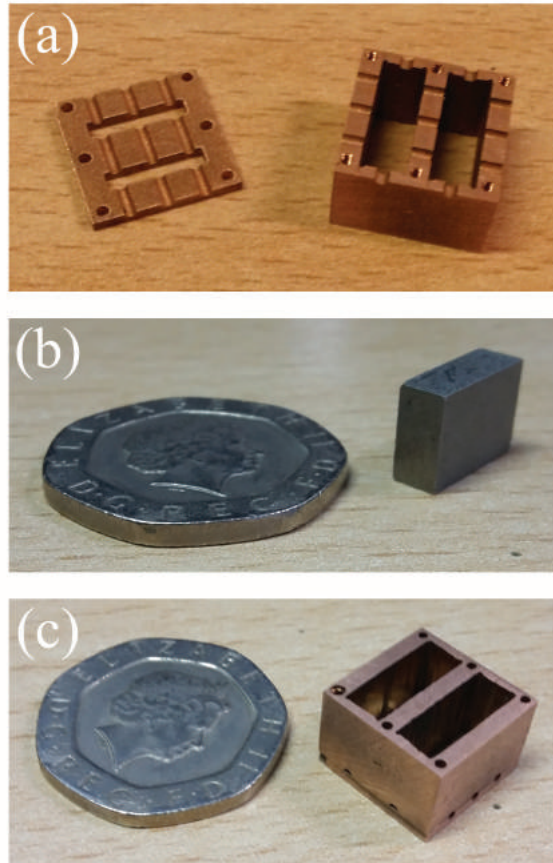


Figure 4.21: The copper spacer that holds the under-chip magnets installed in the axial gradient system. **(a)** - The mating faces of the lid/bottom and the “figure-eight”. **(b)** - A single SmCo magnet that fits into the spacer next to a twenty pence coin for scale. **(c)** - The assembled spacer prior to the insertion of the magnets, again, next to a twenty pence coin for scale.

Although the magnets were securely held in their spacer, it was discovered that the attractive force was enough to slightly distort the copper region that defines their central separation. Measurements made using the microscope indicate that the compression of the copper separator was around  $25\ \mu\text{m}$  with a measurement error of  $15\ \mu\text{m}$  due to the chamfer and lighting conditions on the magnets. This unfortunately leads to a reduction in the magnetic nil height on the order of  $5 - 15\ \mu\text{m}$  depending on other geometric anomalies

but since this is very compensatable with external fields this was deemed to be acceptable. Additionally, this would allow for a better alignment in the unlikely case that the magnet to chip underside distance is less than the predicted glue thickness.

In order to test the structural integrity of the magnets' attractive force in the mount, a mock spacer fully aligned with a broken chip was put into a vacuum system and baked for two weeks as per standard procedure to achieve our desired UHV pressure. This process is generally understood to have a lot of inherent vibration and motion that could shift the position of objects involved, however, it was found that the chip had not moved relative to the magnets, nor the magnets relative to each other (including the central spacer thickness) to within the measurement error of our apparatus. Another single magnet was put through the same process and appeared to not suffer any degradation in the internal magnetisation.

#### 4.5.2 Magnetic spacer for the radial gradient system

This section details the construction of the magnetic spacer for the radial gradient vacuum system. For this system, I aim to use the slightly more novel offset magnet design which provides a large radial gradient for spin-motional coupling and a small axial gradient for individual addressability. This should allow us to have significantly longer ion strings than for the previously explained system while maintaining the spin-motional coupling albeit to the radial modes of motion. The ideal magnet size for this design<sup>19</sup> was  $7.3 \times 10 \times 3.4(a)$  mm separated by  $0 \times 0 \times 1.8$  mm giving a nil height of  $940 \mu\text{m}$  above the magnets at a position of  $1.5$  mm from the centre of the copper block, an in-plane radial gradient of approximately  $100 \text{ T/m}$  and an axial gradient of approximately  $15 \text{ T/m}$ . On receiving the real piece from the workshop, the offset “figure-eight” was slightly thicker than the magnets so this was carefully sanded down so that the thickness was slightly less than the magnets to ensure that additional unwanted space would not be created between the chip and magnets after adhesion. Due to the larger thickness of the piece in two directions the compression of the central spacer was significantly less than the normal design at around  $5 \mu\text{m}$ . This magnetic spacer is shown in Figure 4.22 after insertion of the magnets .

---

<sup>19</sup>The order of sixty magnets originally considered only the optimised magnet geometries for the full length axial scheme at the previously quoted ion heights. However, by rotating the magnets by  $90$  degrees in the spacer, the offset design could be achieved with little change to the experimental setup and minimal deviation from an optimised magnetic geometry.

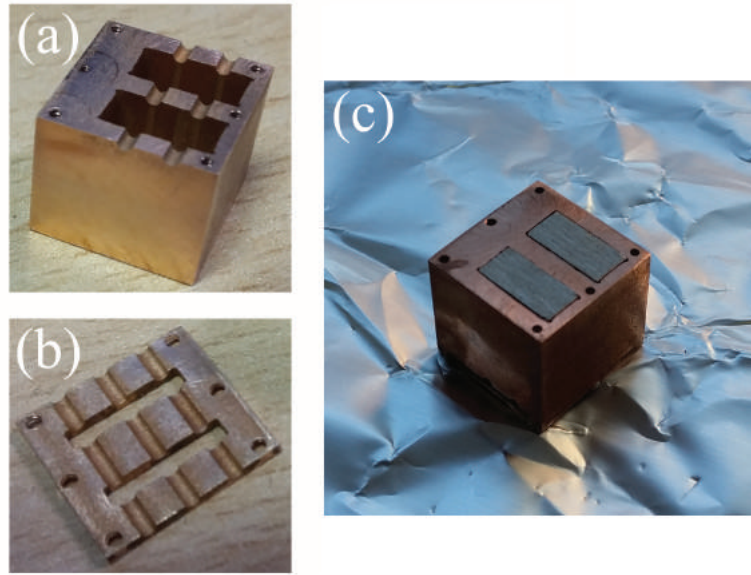


Figure 4.22: The offset copper spacer that holds the under-chip magnets installed in the radial gradient system. **(a)** - The “figure-eight” part of the spacer with the mating face shown. **(b)** - The lid/bottom part of the spacer identical to that of the set used in the axial gradient system. **(c)** - The assembled spacer after the insertion of the magnets after the pre-alignment cleaning.

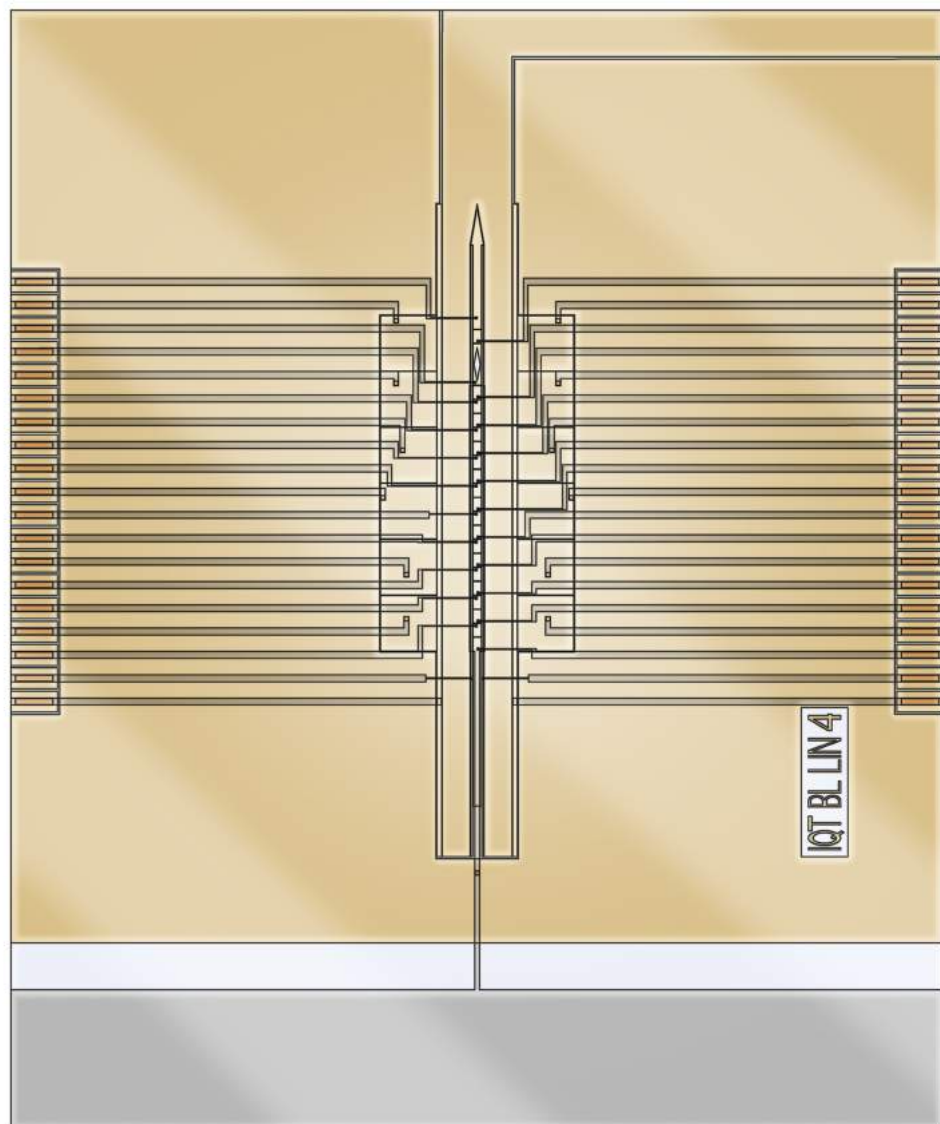
### 4.5.3 Alignment of the chip and magnetic spacer

We now come to the alignment of the chips with their respective magnetic spacers for each vacuum system. These alignments were performed with minimal change to the previously described process and for the purpose of these alignments I used the pump-activated chip tongue for suspension of the chip during the alignment process.

#### Axial gradient system magnetic alignment

This section documents the final alignment attempt for the chip and spacer installed into the axial gradient system. Prior to this, two other alignment attempts were performed, of which both, though very well aligned, resulted in the chip being removed from the spacer for a variety of reasons.

The chip selected for the axial gradient system was a  $165\ \mu\text{m}$  ion height linear chip (code *IQT BL LIN 4*) which is shown in Figure 4.23. This picture is a more realistically coloured representation of the mask design in the thesis of Dr Bjoern Lekitsch [33]. The exposed buried ground plane is the tab that one would hold when moving the chip and overhangs the magnetic spacer on the bottom side. The position corresponding to the best working electrodes and therefore the desired trapping position must also be noted in order to align it to the magnetic nil point. If this is not thoroughly checked then one can find





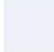



Key:	 = Exposed buried ground plane	 = Buried ground plane
	 = Exposed substrate	 = Buried DC wires
	 = Surface electrode layer	 = Surface to buried layer vias

Figure 4.23: The linear  $165\ \mu\text{m}$  ion height chip, *IQT BL LIN<sub>4</sub>* to be paired with the high axial gradient magnetic spacer for the axial gradient system. This diagram is oriented to the desired alignment with the magnetic spacer shown in Figure 4.25.

that the magnetic nil corresponds with a region of the trap that may or may not work, which is obviously very problematic. The electrode resistances and best working region for this trap are shown in Figure 4.24.

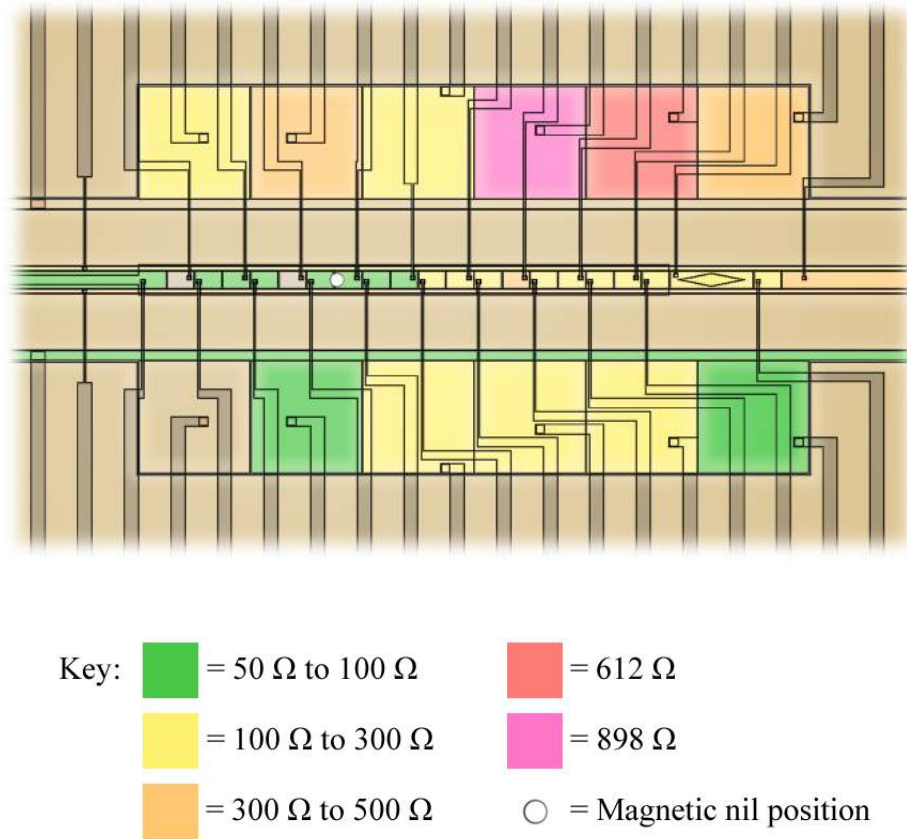


Figure 4.24: The inner electrode structure of the *IQT BL LIN4* chip with certain electrodes marked with the resistances to the relevant bond pads. The unmarked electrodes have a much lower resistance relative to those that are highlighted.

In actuality, the final alignment was done almost five months after the second attempt, significantly after that of the chip and magnetic spacer for the radial gradient system. This meant that the alignment stage needed to be cleaned and recalibrated. However, serious problems were encountered during this process and optimisation was not possible. The XY/R stage had become significantly out of calibration in such a way that a translation of, for example, 4 mm on the micrometer stage did not correspond to that shown on a metal ruler in agreement with the camera translation stage distances. Since the alignment was axial in nature and the electrodes of the new chip mostly showed promise of working extremely well, the alignment in  $x$  and  $y$  was not too crucial. This is because a misalignment in  $x$  is along the ion string and therefore can be compensated by shuttling,

and a misalignment in  $y$  is along the magnetic “nil” line and therefore does not add any significant offset field at the ion provided that the angular misalignment is less than 1 degree. The alignment process was altered to use the camera axis for all angular alignments and any measurements of the chip or magnetic spacer geometry. I decided that since the alignment was extremely crucial for the timing of the experiment, I would perform it with the semi-calibrated stage and adjust the procedure to fit the noted problems.

As with every alignment attempt, the magnetic spacer was measured and simulations were performed in order to assess the possible gradients and the position of the magnetic nil for the physical geometry. This spacer was the same as that used for the first and second alignment attempts and was cleaned of silver epoxy before each alignment. This third measurement of the spacer is shown in Figure 4.25.

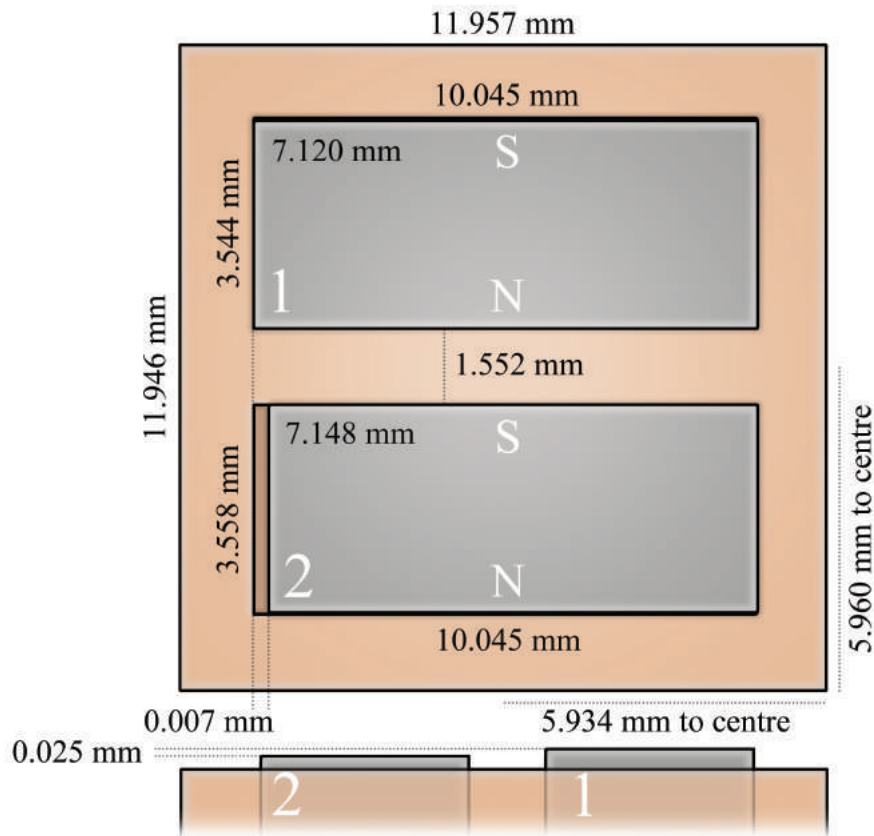


Figure 4.25: A schematic of the magnetic spacer to be paired with the chip to be installed in the axial gradient system as measured during the third alignment attempt. The distance from the centre of the simulated magnetic geometry is noted in order to help with alignment in light of the calibration issues.

On measuring and simulating the magnetic spacer, it was found that the magnetic nil height had dropped to approximately  $817 \mu\text{m}$  above the surface of the magnets meaning

that there would be a 53 G offset field in the direction compensateable by the external compensation permanent magnets for the predicted glue thickness of 10  $\mu\text{m}$ . This would be very impractical, however, this field could be reduced to 38 G in the same direction if at least one of the magnets was in direct contact with the bottom of the chip. Since the magnets protruded from the spacer by around 130  $\mu\text{m}$ , this seemed very possible, and given that another magnetic spacer would not be available for a long time, it was decided to go ahead with the alignment.

Though the worst alignment in  $x$  and  $y$  to date, the key value of 0  $\mu\text{m}$  between the bottom of the chip and the top surface of the Magnet 1 was achieved. The misalignment along the ion string was 173  $\mu\text{m}$  towards Magnet 1 after accounting for the shift in the magnetic nil position due to its vertical separation from Magnet 2. The misalignment along the magnetic “nil” was 113  $\mu\text{m}$  left of the magnetic centre shown in Figure 4.25 and the angular displacement was less than 1 degree<sup>20</sup>. This achieved the previously simulated 38 G offset field compensateable by the large external magnets with trace components (less than 2 G) in the directions addressed by the coils. Additionally, the magnetic field gradient realised once the offset field is compensated is simulated to be 140 T/m in the axial direction and 139 T/m in the vertical radial direction, thus we should not have lost any gradient by reusing this magnetic spacer<sup>21</sup>. This alignment also indicates that the axially aligned scheme is very robust to reasonable misalignments with minimal deviation from the predicted magnetic field gradients as long as the trap has a good linear trapping region in which to operate in.

It is important to realise that one should note the magnetisation direction of the magnet pair with respect to the chip. This is vital for knowing which direction one might need to apply a compensation field caused by a misalignment in the ion height direction; compensation for a *smaller* than predicted glue thickness is in the *opposite* polarity to the magnets in order to cancel the field going between their closest faces, and compensation for a *greater* than predicted glue thickness is in the *same* polarity as the magnets in order to cancel the returning external field of the single-magnet far-field frame of reference.

---

<sup>20</sup>These shifts are caused by expansion of the silver epoxy during the curing process which pushes the chip out of alignment. Initial alignment can be achieved to within 2  $\mu\text{m}$  before the epoxy is applied.

<sup>21</sup>Due to the degradation after each adhesion of a chip and the subsequent cleaning processes required to re-prepare it for an alignment, I would not suggest using the same spacer more than five times as parallelism checks and measurements of the spacer dimensions gain a significant error.



### Radial gradient system magnetic alignment

This section documents the first alignment attempt for the radial gradient system. At the time that this thesis was written, this spacer had not yet been installed, thus this may not be the final alignment that will be used in the experiment. The magnetic spacer for the radial gradient system used the offset design described in Chapter 3; the geometry measured and simulated during the alignment procedure is shown in Figure 4.26.

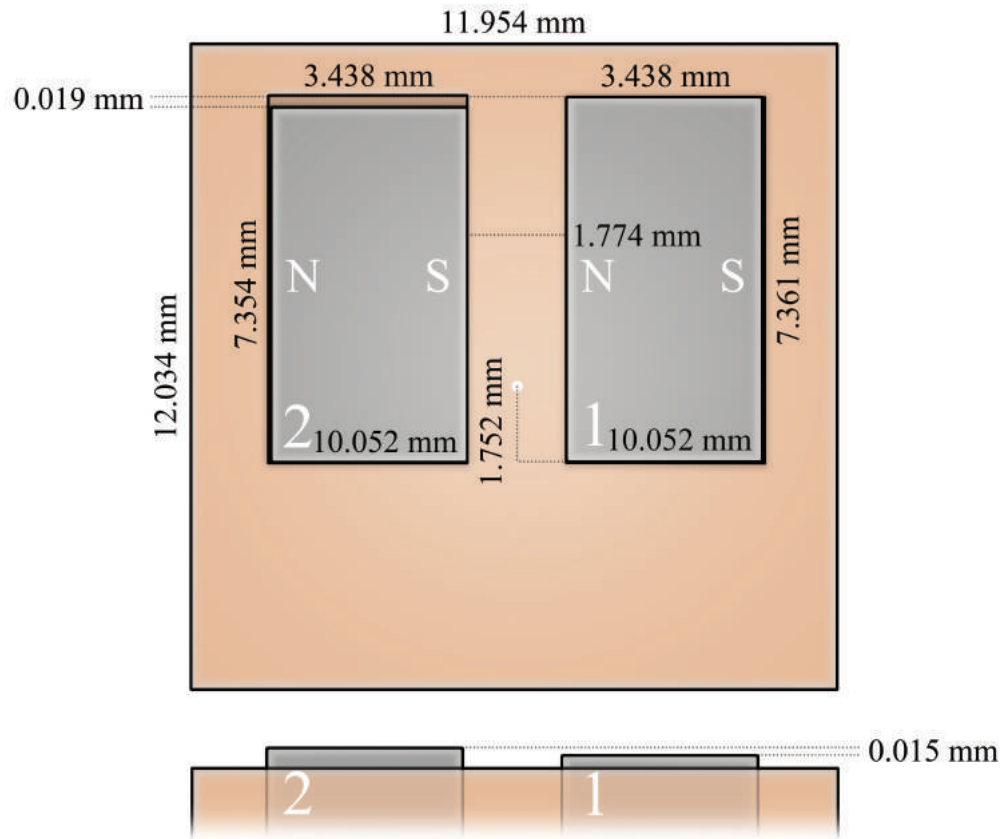
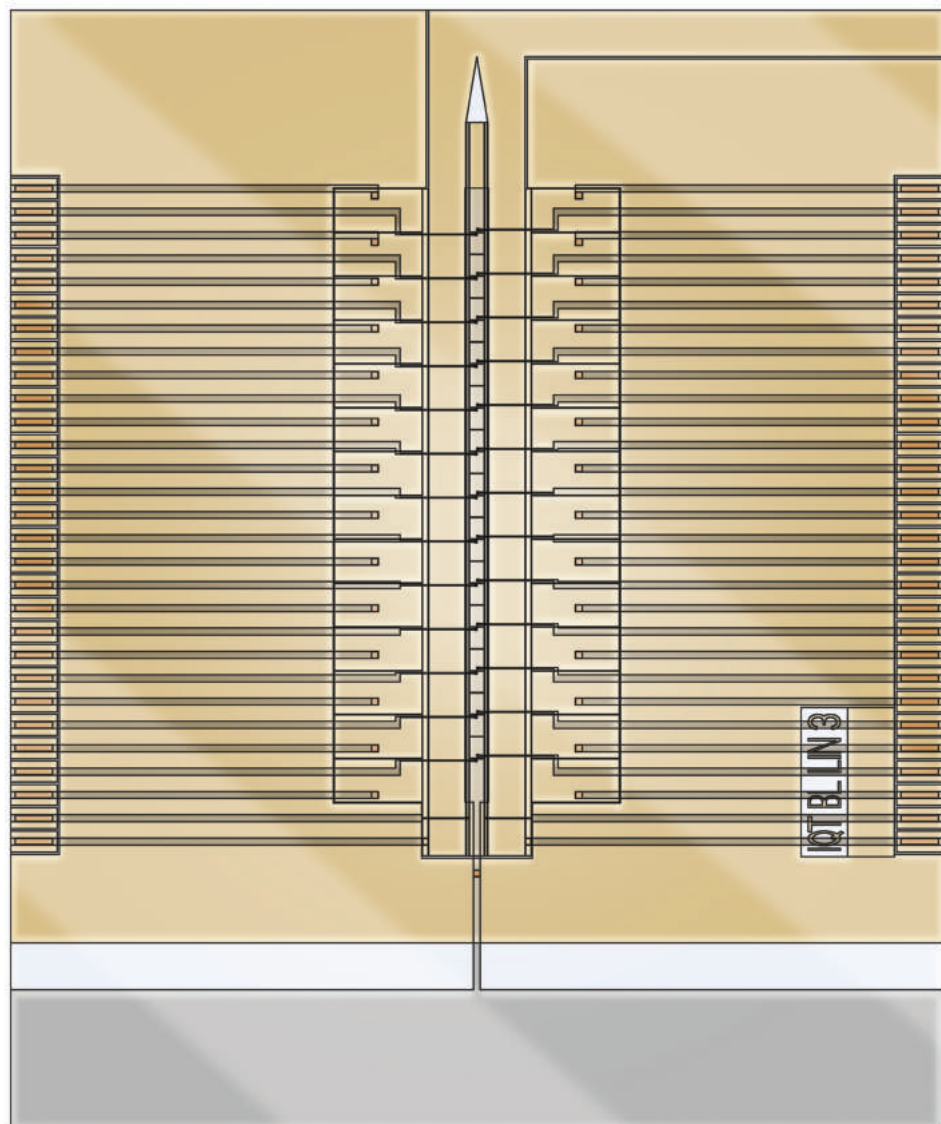


Figure 4.26: A schematic of the magnetic spacer to be paired with the chip to be installed in the radial gradient system as measured during the alignment procedure. The nil point at the desired height of  $940\text{ }\mu\text{m}$  is found  $1.752\text{ mm}$  from the bottom edge of Magnet 1 approximately at the centre of separation.

After careful measurements using the alignment stage microscope, a simulation was run with the real geometry yielding a nil height of  $940\text{ }\mu\text{m}$  above the magnets with a  $14\text{ }\mu\text{m}$  shift towards Magnet 1, as referred to in Figure 4.26. This shift from centre was due to the magnet being slightly lower in height than the other in relation to the copper block surface. This did not affect the predicted gradient to any significant degree and it was decided that since an alignment for high radial gradients was intended, the noted shift for the alignment procedure would be  $14\text{ }\mu\text{m}$  from centre in order to overlap the magnetic



Key:







	= Exposed buried ground plane		= Buried ground plane
	= Exposed substrate		= Buried DC wires
	= Surface electrode layer		= Surface to buried layer vias

Figure 4.27: The linear 250  $\mu\text{m}$  ion height chip, *IQT BL LIN3* to be paired with the high radial, low axial gradient magnetic spacer for the radial gradient system. This diagram is oriented to the desired alignment with the magnetic spacer shown in Figure 4.26.

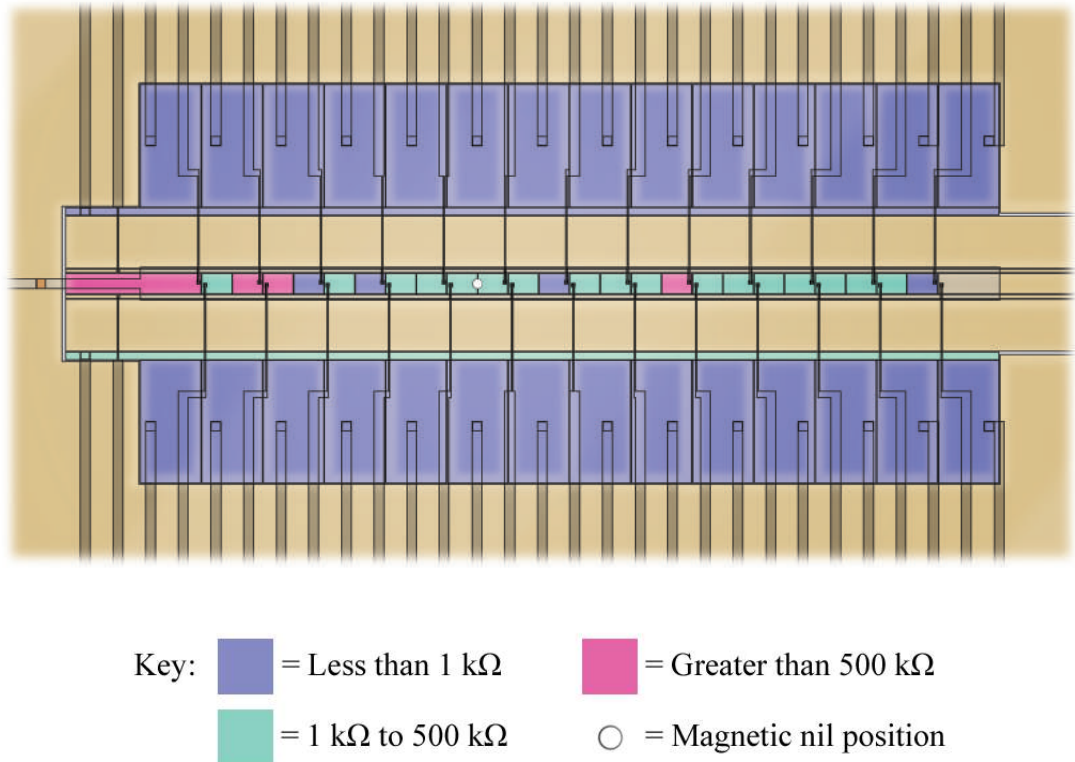


Figure 4.28: The inner electrode structure of the chip shown in Figure 4.27 with certain electrodes marked with the resistances to the relevant bond pads. The unmarked electrodes have a much lower resistance relative to those that are highlighted.

and RF nil lines.

The chip selected for the real alignment was a 250  $\mu\text{m}$  ion height linear chip (code *IQT BL LIN 3*) which is shown in Figure 4.27 with similar notes regarding the surface electrode layer and the exposed buried ground plane as applicable for the chip shown in Figure 4.23.

The central trapping region desired for a small axial gradient was decided from the electrode checks performed by Tomas Navickas and was agreed to be between the 5th and 6th buried electrode access lines from the end of the RF rails furthest from the feed-in. The via to electrode resistances and magnetic nil alignment position that was agreed upon are shown in Figure 4.28.

After curing, the final misalignment of the chip was 34  $\mu\text{m}$  to the right, 154  $\mu\text{m}$  down (which was still very much within the fully functional electrode region), with much less than 1 degree misalignment. This gave an offset field of 32 G in the out of the plane direction, a simulated axial gradient of 17.9 T/m, a planar radial gradient of 104.3 T/m, and a vertical radial gradient of 102.4 T/m once the field has been compensated.

The last intended alignment for both of these systems went extremely well and should provide the trapped ions with a very interesting gradient set due to the small axial gradient for individually addressing and the much larger radial gradients. This combination of gradients should enable us to do experiments that we have not been able to perform using our previous experimental setups such as radial-mode multiple-ion entanglement or quantum simulation experiments with a large number of ions.

#### 4.5.4 Installing the aligned spacer into the vacuum system

In the time scale of the work described in this thesis, only the axial gradient system was fully constructed thus only the high axial gradient chip-spacer combination was installed and put to use.

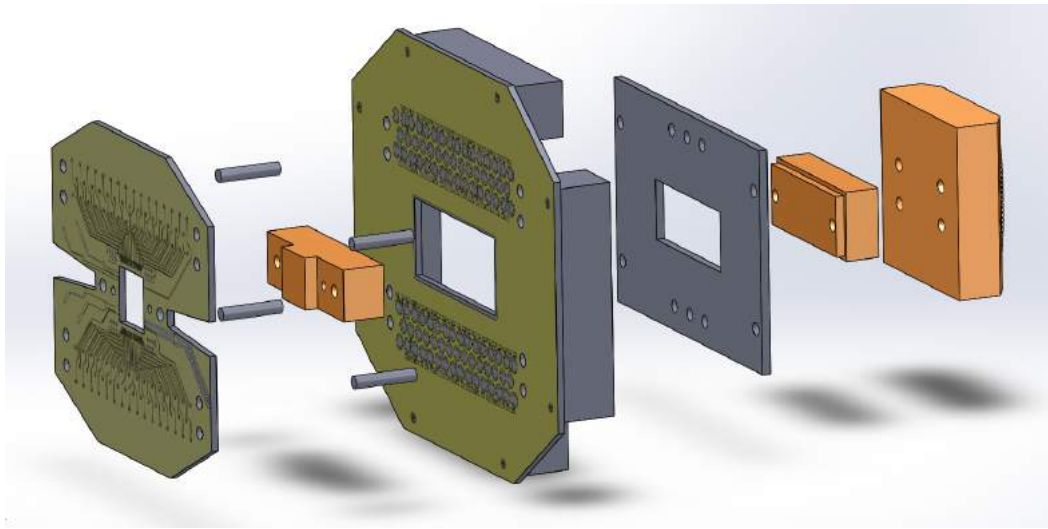


Figure 4.29: The internal structure of the vacuum system connecting the chip to the trapping voltages as designed by David Murgia. From left to right: The front PCB which routes the voltages to the relevant wire bonding pads, the copper block/plinth discussed in Chapter 3 which is recessed when using the under-chip magnetic spacer scheme, the back PCB which houses the connections and filtering of the voltages to be applied to the chip, a support plate, and two copper heatsink blocks which are in direct contact with the cooling system. This figure was drawn by David Murgia.

As part of the cooling system, several copper blocks provide a direct path to conduct heat away from the chip which protrudes through the centre of an in-vacuum set of PCBs which house the atomic ovens, RF connections, and DC connections with filtering. A breakdown of each of these components is shown in Figure 4.29. When used with current carrying wire chips, the chip is glued to a central copper block/plinth, however, when using the magnetic spacer setup, this plinth is machined away and the magnetic spacer is glued in the recess bringing the chip to the same relative height as previously discussed in

Chapter 3. The vertical alignment of the chip with regards the top surface of the PCB is crucial in order for the atomic beams to reach the ion. Additionally, this height has been designed in order to make wire-bonding from the chip to the PCB more manageable than with the previous chip carrier which could be at a much steeper angle depending on the chip and plinth structure used. The wire-bonded chip atop the magnetic spacer which has been glued into the recessed copper block is shown in Figure 4.30.

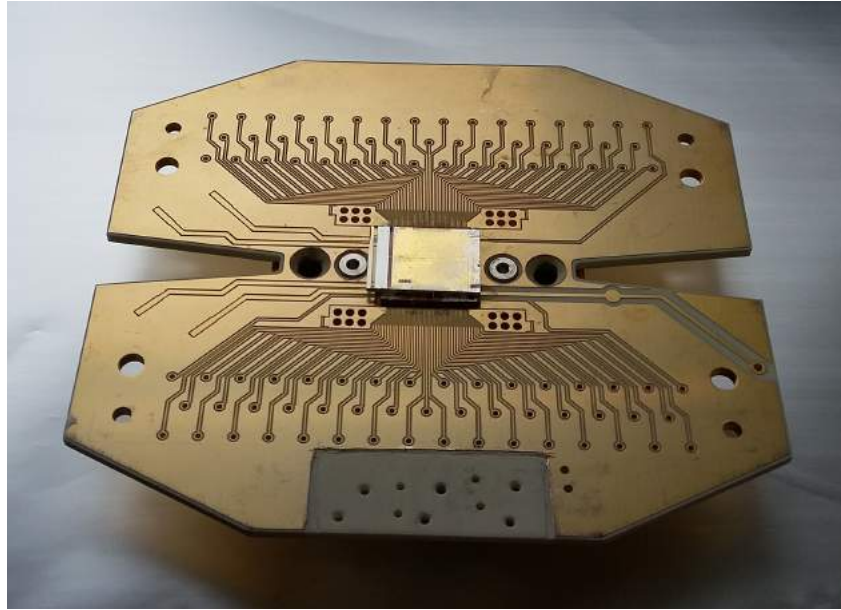


Figure 4.30: The front in-vacuum PCB with a wirebonded chip in place as assembled and bonded by David Murgia. The chip sits atop the magnetic spacer which is subsequently glued into a recessed copper block as discussed in Chapter 3.

As previously intended, the under-chip magnet design is effectively invisible after installation and laser access due to surrounding symmetric scheme magnets is not longer an issue when creating a magnetic field gradient in a similar experimental setup. Now that I have discussed the installation of the magnetic spacer, we can move onto the components of the experiment that are outside of vacuum.

## 4.6 Experimental table setup

As with the main entanglement experiment discussed in Chapters 1 and 2, the vacuum system sits atop an optical table and requires an ion imaging system, laser setup, microwave and RF setup for coherent manipulation, and a helical resonator for the application of the trapping RF to the trap. In this section I will detail some of the main differences for the new experiments to that which houses the macroscopic Blade trap.

#### 4.6.1 Ion imaging and camera setup

In order to see the ions and readout from them, we require a specialist camera and optical setup. Though the principals of operation remain the same, the setups differ slightly for each experiment.

The axial gradient system uses an Andor Xion Ultra888 EMCCD camera and a doublet triplet lens setup in order to image the ions. Figure 4.31 shows the imaging setup used for this vacuum system. The iris in the centre of the imaging tube allows one to reduce photon counts due to scatter or background counts in the rest of the imaging, which is extremely useful for data taking using a PMT; this may be installed at a later date.

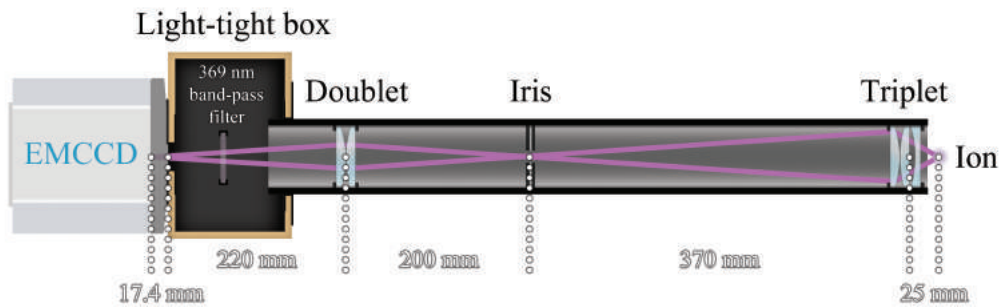


Figure 4.31: The imaging tube lens setup used for the axial gradient system. The fluorescence from an ion first travels through the triplet lens group which focuses the image in the region of an adjustable iris. The light then travels through the doublet lens group which focusses the image on the focal point of the EMCCD after passing through a 369 nm band-pass filter in order to remove unwanted light at the other laser wavelengths. The imaging tube is clamped using a three-axis translation stage so that the image centre and focus plane can be adjusted and recorded with micron-level precision.

#### 4.6.2 Laser setup

As with our other ytterbium experiments, a dedicated laser system was arranged using 935 nm, 399 nm, and 369 nm light as shown in Figure 4.32<sup>22</sup>. Each of these laser beams is divided and fibre coupled from master laser sources elsewhere in the lab. An iris at each fibre coupler allows us to block certain beams when beam imaging the traps. In addition to this, the 399 nm beam is blocked immediately after the desired number of ions are trapped in order to prevent the trapping of unwanted additional ions as this will change the secular frequencies of certain modes of motion.

The 935 nm laser is often blocked in order to verify the presence of an ion or take a

<sup>22</sup>The 638 nm laser was omitted in these setups as it is not heavily required for the purpose of trapping experiments. Should transition to the dark  $^2F_{7/2}$  state become a large issue during coherent manipulation experiments, this can easily be added at a later date.



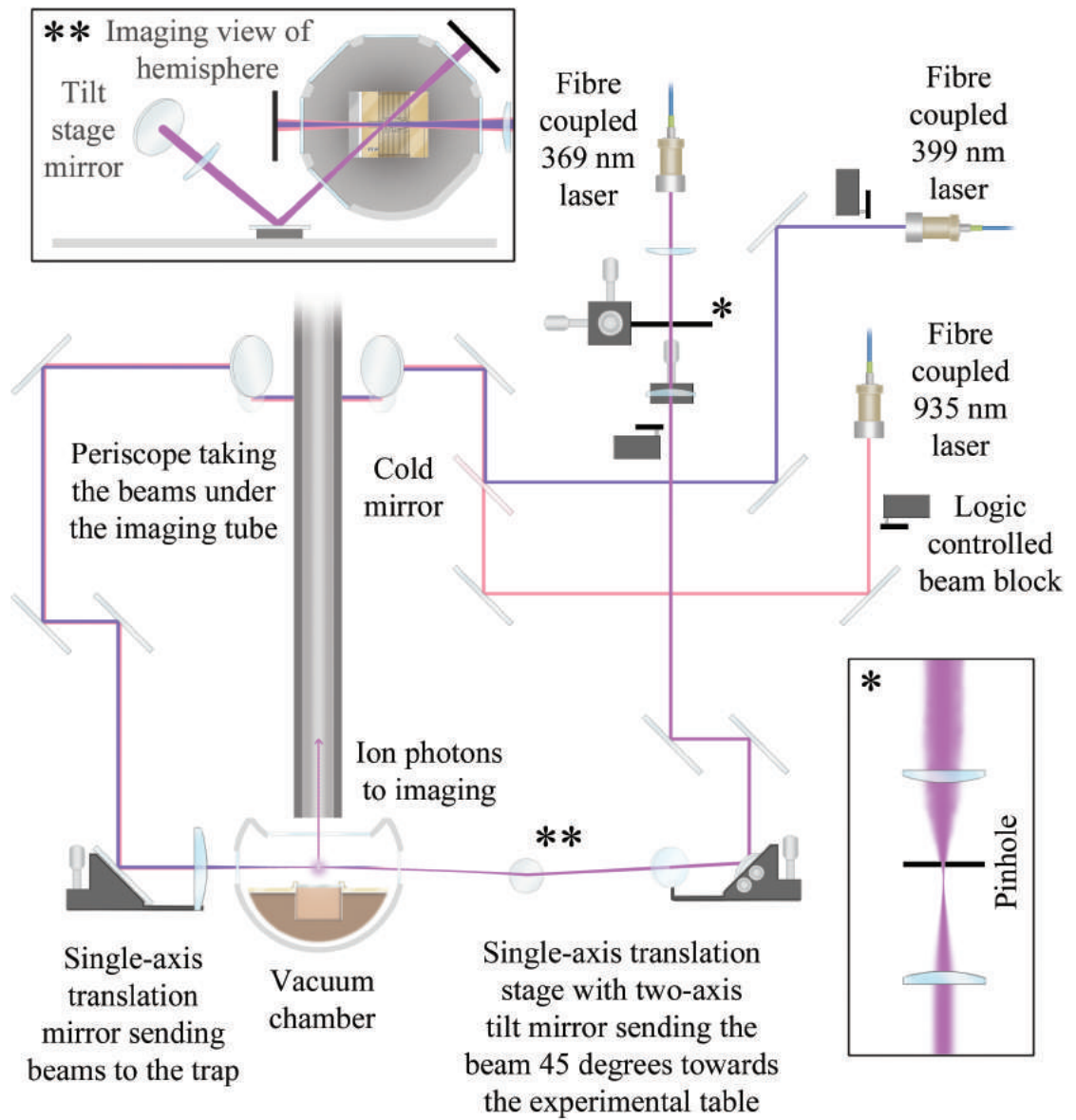


Figure 4.32: The laser setup used for the axial gradient system. A similar layout is intended for the radial gradient system. \* - A beam profile cleaning telescope setup. This is placed as required after the irises at the laser feed-in from the fibres. \*\* - The beam angles as they enter the vacuum hemisphere. The 369 nm beam is reflected off a mirror parallel to the experimental table surface in order to orient it 45 degrees to the atomic oven beams which are directed upwards. This gives a larger component of the laser beam direction in the direction of the atomic beam to provide better Doppler cooling. The 399 nm and 935 nm beams enter parallel to the plane of the experimental table as atomic fluorescence was tested at this angle relative to the ovens.

background count reading; by blocking the 935 nm laser, the cooling cycle of the ion is broken and it will therefore appear as dark on the imaging as the photons are no longer spontaneously emitted.

The beam profile of any of these beams can be “cleaned” by using a telescope setup as shown in Figure 4.32\*. The “dirty” beam is focussed by a convex lens and is passed through a pinhole at a small distance from the focal point. This pinhole removes optical amplitude noise at the edge of the beam profile after which the “cleaner” beam can be re-collimated by a second convex lens. This can be used to reduce scatter off the trap electrodes which will become background counts in any coherent manipulation experiments and thus reduce the fidelity of operations. Alternatively, in the case of trapping experiments, scatter may make it more difficult to see the a ion and verify that one has trapped. This method works best when the beam profile starts near to Gaussian.

### 4.6.3 Microwave and RF setup

Since we aim to perform microwave and RF driven coherent manipulation operations, these new experimental setups will understandably require their own microwave and RF setups. These fields will likely be produced by radio frequency Arbitrary Waveform Generators (AWGs), similar to those used to perform the two-ion entangling gate discussed in [19], mixed with a 12.6 GHz microwave generator for the microwave fields. The emitters of each of these fields and their position must be carefully considered in order to maximise the capability of this setup when using planar chip traps.

As part of the vacuum system design a wire mesh is located behind the front window, between the window and the chip trap. The mesh is there to shield trapped ions from the effect of any charge that may build up on the window which may distort the trapping potential. However, the mesh would also act to attenuate RF and microwave radiation sent in through the front window for coherent manipulation of the ion. For this reason the effect of the mesh was simulated, to observe its effect on the magnetic fields of the radiation as this is the field that drives our qubit rotations.

### Microwave and RF simulations in EMPro

We needed to make sure that the amplitude of coherent manipulation fields would still be sufficient in the presence of a front window mesh in order to be useful for coherent manipulation of trapped ions. Simulations were performed using EMPro, a software program that is specialised for RF and microwave simulations, so that we could ascertain the



best way to feed the microwaves and RF to the ion given the expected attenuation by the mesh. Several scenarios were considered, most notably using:

- A standard microwave horn and RF coil at the front window.
- A recessed side viewport with a microwave-guide or horn and an in-vacuum RF emitter.
- An in-vacuum RF or microwave emitter near to the chip.

It was also important at this point to ascertain the polarisation of each of the fields to make sure that we would be able to address all three transitions in the  $^2S_{\frac{1}{2}}$  manifold [47]. The magnetic field per Watt of the microwaves present at the ion in the macroscopic Blade trap experimental setup was determined for the  $|0\rangle$  to  $|0'\rangle$  transition in order to make a comparison with those indicated by the EMPro simulations.

For a Rabi frequency  $\Omega_\pi = 20$  kHz given a direct microwave output power of  $\sim 2$  Watts, ignoring phase terms, one can find the  $H$ -field at the ion using  $\Omega_\pi = \frac{\mu_B \mu_0}{\hbar} H_z$  where  $\mu_B$  is the Bohr magneton,  $\mu_0$  is the permeability of free space, and  $H_z$  is the microwave magnetic field amplitude parallel to the quantisation axis of the qubit [47]. This gives an approximate field strength per unit power of  $\sim 0.09$  A/m/W which will serve as our benchmark. Understandably, this is only a small component of the net polarisation of the  $H$ -field of the microwaves, which means that the absolute value of the field is likely to be much larger than this as different polarisations drive different transitions. This means that in each simulation the absolute field at the ion position will need to be greater than this so that there is sufficient power in all polarisations; any  $H$ -field significantly less than this should be considered to be insufficient for our experiment.

In each of the simulations I consider, the microwaves will be set at a fixed frequency of 12.6 GHz, the RF will be set to 20 MHz, 50 MHz, and 100 MHz, and all emitters will be considered as a 1 Watt modal source. The simulated mesh was required to be significantly bigger than the real mesh due to (simulation) meshing issues with the small domain geometry. The mesh simulated had a square wire of side length  $100\ \mu\text{m}$  and a grid spacing of 2 mm and a central hole diameter of 16 mm; this was determined from a trade-off between the transmitted radiation (inferred from initial simulations made in COMSOL), the imaging photon collection, and the expected portion of the window above the trap that may effect the trapping potential in the event of charge build-up. The vacuum hemisphere was modelled with all the octagon flanges open and as either aluminium or stainless steel depending on the simulation and the coil was for the most part modelled as a single 38

mm diameter turn of 2 mm diameter copper wire. A large copper block was placed 10 mm behind the front window to approximate the inside of the vacuum system without creating further meshing issues. The total simulated structure with example emitters is shown in Figure 4.33.

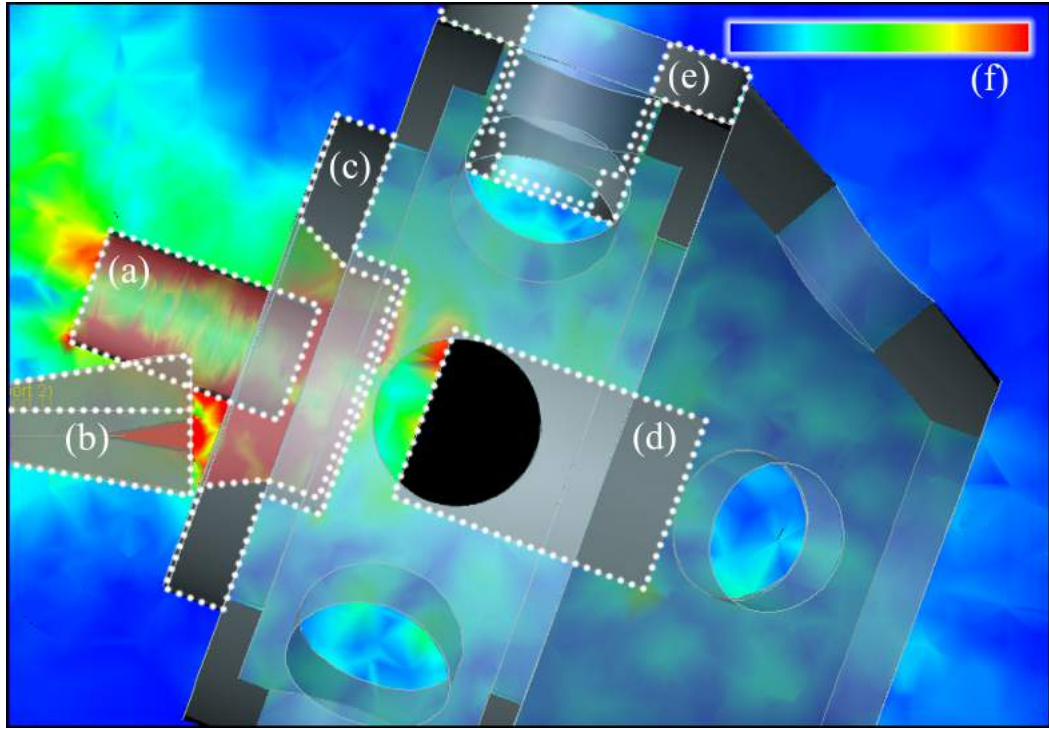


Figure 4.33: The simulation geometry with important components highlighted by a dotted white outline. **(a)** - An imaging tube at the front window. **(b)** - An emitter, in this case a microwave horn. **(c)** - The front window where the mesh is put in place. **(d)** - The internal copper block in place of the far more complex internal structure of the cooling system. **(e)** - The recessed side viewport for side injection of microwave and RF if we decide to go with that option. **(f)** - The minimum (blue) and maximum (red) field range values and the linear colour-field relationship between these extremes. Any field lower than the value at blue will also be displayed as blue and any value higher than than set for red will also be displayed as red. The remainder of the vacuum hemisphere can be seen in the background of this diagram. The holes in the geometry, such as the circle central to this diagram, are the flanges of the octagon and back of the main hemisphere of the vacuum system.

### Microwave emission at the front window of the system using a horn

The first setup that I will consider is the case where the microwaves are emitted from a horn at an angle to the front window as this is the setup used on the Blade trap experimental setup which has been shown to produce good experimental results. For this scenario I will consider three variations; a  $\sim 1$  inch,  $\sim 1.5$  inch, and  $\sim 2$  inch imaging tube, each simulated as aluminium as per the specification of the manufacturers. These sizes have

been considered due to the possibility that the ion imaging optics will use larger diameter objectives in future with a lower magnification. This will allow for the entire chip to be imaged and simultaneous individual fluorescence readout for each ion using the photon counts on set regions of the EMCCD image instead of using a PMT for global photon detection. The horn in all of these simulations is modelled as a 12.6 GHz standard gain horn (Model 18240-10) by Flann Microwave made of silver for the best conductivity. This is placed at an angle of 20 degrees between the imaging tube and the emitting direction in order to get the best line of sight to the ion.

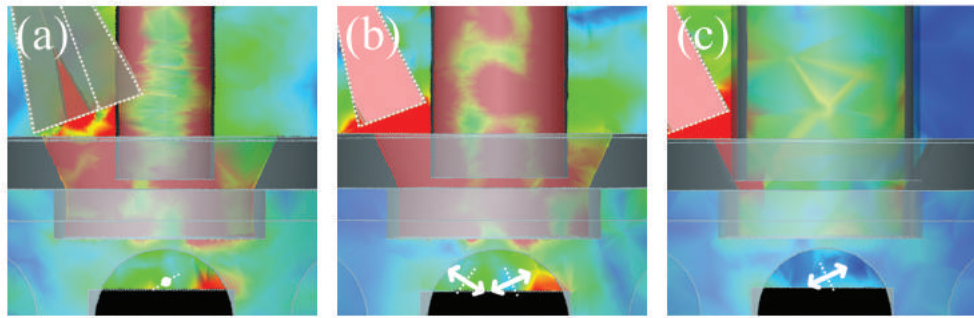


Figure 4.34: The absolute field plot for microwaves injected into the system via a horn (highlighted with a white dotted outline) at the front window with a mesh with a central hole in place for: **(a)** -  $A \sim 1$  inch diameter imaging tube with the horn at 45 degrees rotation with respect to the axis parallel to the imaging tube. **(b)** -  $A \sim 1.5$  inch diameter imaging tube. **(c)** -  $A \sim 2$  inch diameter imaging tube. Red denotes fields over 2 A/m/W and blue denotes zero field. The white arrows denote the polarisation of the field near to the ion position which inverts about the axis denoted by the dotted line with the oscillation of the wave. For (a) the polarisation is in/out-of-plane. The second arrow in (b) illustrates a high position dependence on the polarisation seen by the ion.

Figure 4.34 shows the magnitude of the  $H$ -field for each of these imaging tube diameters where red indicates any field over 2 A/m/W and blue denotes zero field. One can see that the microwaves are significantly attenuated by the mesh but the central hole allows for some power transmission to the ion. For the 1 and 1.5 inch diameter imaging tubes, this method of microwave injection into the system gives a satisfactory 1 A/m/W. However, when using the 2 inch diameter imaging tube, this is greatly reduced to 0.4 – 0.5 A/m/W as there is significant blocking of the line of sight to the ion<sup>23</sup>.

In each of these cases, the polarisation indicates sufficient components of the  $H$ -field in all principle axes of the chip at the ion position with a strong dependence on the position

<sup>23</sup>It is possible that one could use an imaging tube that is non-conductive and ungrounded which may allow for transmission of the microwaves but this does not follow the specifications of the imaging systems that we usually use or intend to have custom made.

of the horn. As with the macroscopic Blade trap experimental setup, it is very likely that we will have to adjust the angle of the horn in order to get the best Rabi frequencies for the ion. This is mainly due to the diffraction and reflection of the microwaves due to the mesh and surrounding metal objects.

It must be also noted that the lower the ion height, the more parallel the polarisation is to the plane of the chip, which may limit Rabi frequencies dependent on an out-of-plane component of the  $H$ -field for future experiments if using this method of microwave injection. It should be reiterated at this point that the magnetic field and therefore the quantisation axis of the qubit is out-of-plane for the axially aligned magnetic spacer (axial gradient system) and in-plane but perpendicular to the ion string for the radially aligned magnetic spacer (radial gradient system). This is extremely important when determining whether a scheme is suitable for high Rabi frequencies on each of the three microwave transitions from  $|0\rangle$  to the  $F = 1$  states of  $^2S_{\frac{1}{2}}$ .

### **RF emission at the front window of the system using a coil**

I will now consider RF fields externally emitted by a single turn coil at the front window, which again is the method of RF injection used for the Blade trap experimental setup that has been shown to work. For this setup, I found there to be minimal difference in transmission with the presence of the mesh with a central hole for each of the three previously discussed frequencies. I will therefore discuss all RF simulations from this point for a 50 MHz emitter<sup>24</sup>.

The field plots are shown for two scales in Figure 4.35; this has been done to illustrate the field transmission drop-off at the mesh. By directly radiating RF at a metal sheet, a minimum is created due to the boundary condition that the  $H$ -field is parallel to the surface of the boundary at zero distance. This effect changes the expected polarisation of the field which one would expect to be straight along the axis from the coil if we consider the free-space solution. Diffraction due to the mesh offsets this minimum from the ion position meaning that there are still positions close to the ion where sufficient fields for coherent manipulation are realised. Offsetting this minimum so that sufficient fields are created at the ion position will be explained at the end of this section.

---

<sup>24</sup>Marginally more power appeared to get through the mesh for lower frequencies, possibly due to the higher skin depth and longer wavelength.

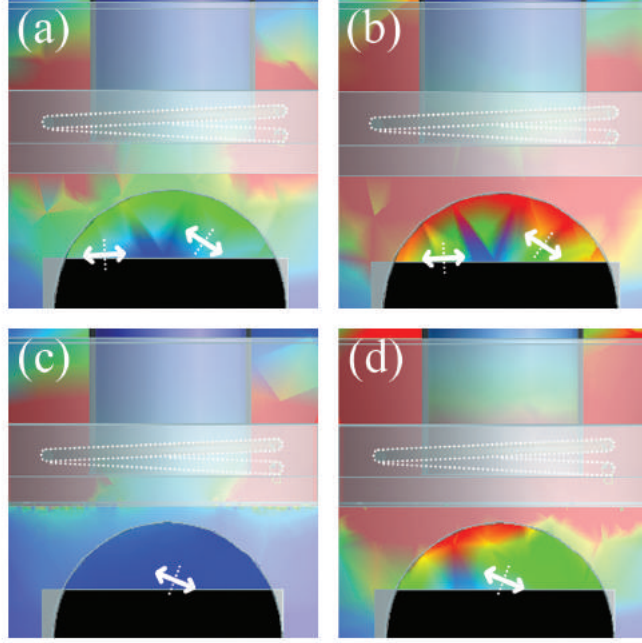


Figure 4.35: Several simulations of the absolute field plot for 50 MHz RF injected into the system via a single turn coil (highlighted with a white dotted outline) at the front window. For all simulations blue denotes zero field. **(a)** - No mesh and red denoting fields over 0.1 A/m/W. **(b)** - No mesh and red denoting fields over 0.04 A/m/W. **(c)** - A mesh with a central hole and red denoting fields over 0.1 A/m/W. **(d)** - A mesh with a central hole and red denoting fields over 0.01 A/m/W. The white arrows denote the polarisation of the field near to the ion position which inverts about the axis denoted by the dotted line with the oscillation of the wave. One can see that a minimum forms at the centre of the surface of the copper block when no mesh is in place due to the RF boundary conditions.

Since the polarisation is closer to plane-parallel with the chip surface at a distance from the field minimum, this scheme should work well for the axially aligned scheme as it is perpendicular to the quantisation axis and therefore allows population transfer between  $|0'\rangle$  and  $|\pm 1\rangle$ <sup>25</sup>. However, this may not be suitable for a radially aligned scheme as the offset of the minimum will have to be carefully engineered in order to get the correct in-plane polarisation components at the ion position.

In terms of field, the RF is at a significantly lower amplitude than the microwaves, however, this is not a problem as it should still be sufficient to perform coherent manipulation experiments. In the presence of a mesh with a central hole, the  $H$ -field at the ion is 0.001 – 0.005 A/m/W and is highly dependent on position due to the minimum formed. This is in contrast to 0.02 – 0.03 A/m/W off-centre from the minimum and 0.005 – 0.01 A/m/W near to the minimum when there is no mesh in place. This attenuation reflects the results of initial investigations made using COMSOL. Careful positioning of

<sup>25</sup>This has been explicitly inferred from experience of performing RF driven qubit manipulation on the Blade trap experimental setup.

the minimum will be required in order to get a high field strength at the ion position due to the RF boundary conditions of the setup.

### **Microwave injection through a recessed side viewport of the vacuum hemisphere**

Since the front window mesh has an attenuating effect, it might be advantageous to apply the microwave fields through a recessed side viewport of the vacuum hemisphere which may provide stronger fields at the ion position. This scenario is considered in the following simulations; in this case the microwaves are injected through a recessed side viewport where three window sizes of 24.13 mm, 19 mm, and 15 mm diameter have been considered<sup>26</sup>. I will first consider simulations using the previously simulated horn before moving onto simulations using a rectangular waveguide both with a rotation of 45 degrees with respect to the copper block surface in order to maximise the possibility of polarisations with components in all directions relative to the quantisation axis. Though in reality the horn could not fit inside the recessed portion of the viewport structure, for the purpose of these simulations, it was modified so that it could sit directly at the window.

The field plots of these simulations are shown in Figure 4.36 all of which have the mesh with a central hole in place. The main phenomenon worth noting in these simulations was that a cavity of sorts was formed between the copper block and the front window mesh which appeared to cause only partial transmission of the radiation to the ion. However, the wavefront, particularly for the horn, was unable to pass the mid-point in this cavity causing a substantially higher field on the side closer to the horn. In addition to this, the polarisation of the field was essentially the same for all of these simulations with equal components of both in-plane directions with minimal out-of-plane components.

In general, for the larger window, a higher field was simulated at the ion position when compared to the smaller window, however this was subject to the reflection of the microwaves off the internal structure of the vacuum system. The field at the ion was found to be 1 A/m/W (with a large node of 1.6 A/m/W slightly off the ion position), 1 – 1.8 A/m/W, and 0.75 – 1.1 A/m/W for the 24.13 mm, 19 mm, and 15 mm windows respectively. A later simulation showed that the window structure sufficiently guides the microwaves if the horn sits external to the recessed structure with a field at the ion of  $\sim 1$  A/m/W. Conversely, the waveguide simulations do not appear to be so affected by

---

<sup>26</sup>These three sizes were considered due to the lead times and prices of each window size for a given flange diameter and to ascertain whether this would affect the transmission of the microwaves through the window.

wave propagation problems through the cavity area. The field at the ion was found to be  $1 - 1.4$  A/m/W,  $1$  A/m/W, and  $0.7 - 1$  A/m/W for the 24.13 mm, 19 mm, and 15 mm windows respectively.

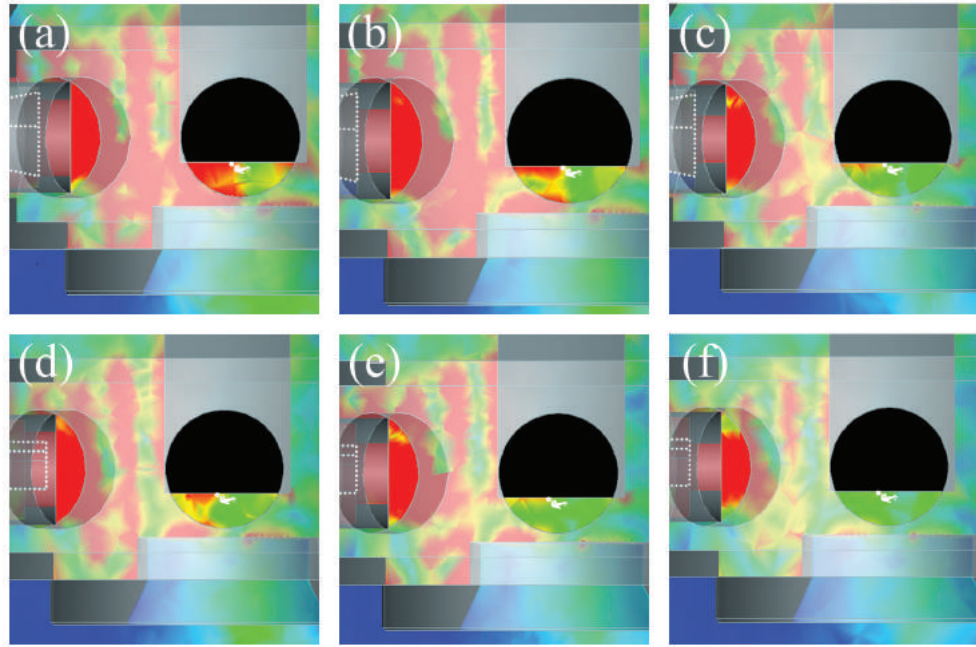


Figure 4.36: Several simulations of the absolute field plot for microwaves injected through a recessed side window using a horn (top) and a rectangular waveguide (bottom) (highlighted with a white dotted outline). For all simulations, a mesh with a central hole is in place over the front window and red denotes field over 2 A/m/W with blue denoting zero field. **(a)** - The horn in the 24.13 mm window diameter recessed viewport. **(b)** - The horn in the 19 mm window diameter recessed viewport. **(c)** - The horn in the 15 mm window diameter recessed viewport. **(d)** - The waveguide in the 24.13 mm window diameter recessed viewport. **(e)** - The waveguide in the 19 mm window diameter recessed viewport. **(f)** - The waveguide in the 15 mm window diameter recessed viewport. The white arrows denote the polarisation of the field near to the ion position which inverts about the axis denoted by the dotted line with the oscillation of the wave.

Both these side window microwave sources seem very promising for the axial and radial alignment types, however, since there is a large dependence on the internal structure of the vacuum system as to where nodes and anti-nodes form, a more detailed structure is recommended for final sanity checks. Ordinarily, we would be tempted to create a small angular displacement of the waveguide (this cannot be done with the horn as it is wedged in the recessed window), however, one must not forget that there are compensation coils around the system which will severely restrict this displacement.

All in all, these methods look promising for future experimental setups but require more simulations and experimental trials before I can confidently say they are the best



option, though the preliminary polarisations and  $H$ -field magnitude at the ion look very promising.

### In-vacuum RF and microwave emitters

Finally, since the mesh attenuates fields generated outside the front window, the best solution may be to produce the radiation inside the vacuum system. I will now discuss our first simulations involving in-vacuum emitters of the coherent manipulation fields. As with the recessed viewport, in-vacuum emitters mean that the coherent manipulation fields will not be attenuated by the front window mesh, which again may allow for larger fields at the ion position. It also allows the emitters to be much closer to the ion, the only downside being that one cannot adjust them externally to change the polarisation of the radiation.

I will start by simulating an RF coil wrapped around the inside of the recessed window as shown in Figure 4.37 (a) and (b), as it would be relatively easy to install. This was found to have a much greater field than a coil wrapped inside the recessed viewport on the outside, which gave fields of the order  $2 \times 10^{-5}$  A/m/W. The inside coil is simulated to generate fields of  $0.002 - 0.004$  A/m/W at the ion position, slightly weaker without the mesh due to the mesh keeping the RF inside the vacuum system. The polarisation is almost completely parallel to the chip surface.

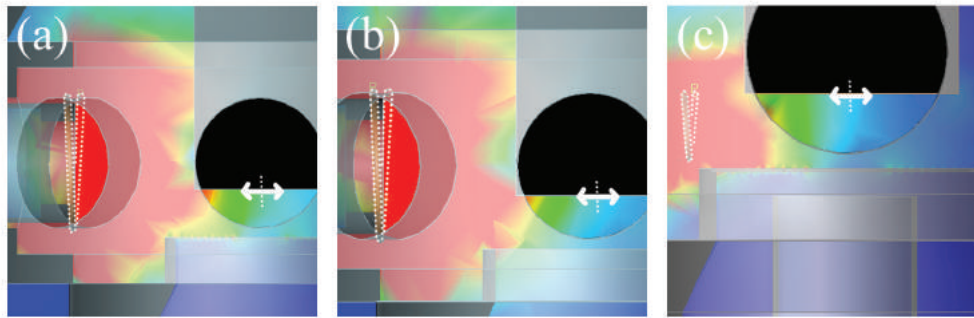


Figure 4.37: Several simulations of the absolute field plot for in-vacuum 50 MHz RF coils (each highlighted with a white dotted outline). For all simulations blue denotes zero field. **(a)** - A coil wrapped around the recessed viewport on the vacuum side with the mesh with a central hole in place over the front window. Red denotes a field over  $0.01$  A/m/W. **(b)** - A coil wrapped around the recessed viewport on the vacuum side without the mesh with red denoting a field over  $0.01$  A/m/W. **(c)** - A  $1$  cm diameter coil near to the edge of the front window with the same mesh with a central hole in place. Red denotes a field over  $0.1$  A/m/W. The white arrows denote the polarisation of the field near to the ion position which inverts about the axis denoted by the dotted line with the oscillation of the wave.

Depending on the position of the viewport around the octagon of the vacuum hemisphere, this polarisation and field magnitude is useful for either alignment type and is



therefore worth noting for future experimental setups. A greater field magnitude of  $0.01 - 0.025 \text{ A/m/W}$  can be created using a  $1 \text{ cm}$  diameter coil close to the chip at the edge of the front window resulting in a polarisation similar to the previous simulation. This setup, shown in Figure 4.37 (c), is very promising, however, it would also require mounting to the front PCB in order to be positioned correctly which may involve modification to the current setup. Nevertheless, this is still a nice idea that may become useful in future.

The last simulations I will discuss are those pertaining to in-vacuum microwave emitters all of which create generally weaker fields than the external emitters despite the much smaller distance to the ion.

First, I will discuss two small coils of  $1 \text{ cm}$  and  $2.1 \text{ cm}$  diameter at the same position as the aforementioned RF coil near to the front window. These create fields of  $\sim 0.1 \text{ A/m/W}$  and  $0.01 - 0.02 \text{ A/m/W}$  respectively. These results are shown in Figure 4.38 (a) and (b). Oddly, the polarisation is perpendicular to the previous in-vacuum RF coil, most likely due to the relative wavelength and scattering around the previously discussed cavity and the gap due to central hole in the mesh. This means that although the field magnitude is a lot smaller than external emitters, these coils are not to be ruled out as they can be localised for each entanglement zone in a larger experimental setup. However, if the quantisation axis is out-of-plane, qubit rotations will not be driven and these coils will no longer be suitable.

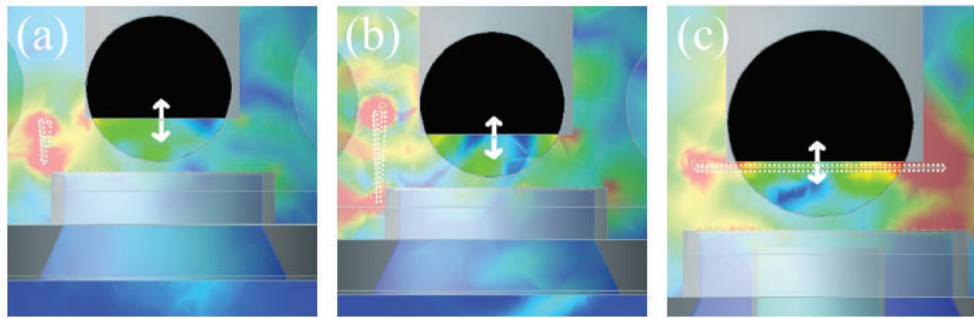


Figure 4.38: Several simulations of the absolute field plot for in-vacuum microwave emitters (each highlighted with a white dotted outline). For all simulations the mesh with a central hole is in place and blue denotes zero field. (a) - A  $1 \text{ cm}$  diameter coil near to the edge of the front window with red denoting a field over  $0.2 \text{ A/m/W}$ . (b) - A  $2.1 \text{ cm}$  diameter coil near to the edge of the front window with red denoting a field over  $0.1 \text{ A/m/W}$ . (c) - A set of two balanced line emitters each  $1 \text{ mm}$  in diameter separated by  $10 \text{ mm}$  which allows for adjustable polarisation. Red denotes a field over  $0.1 \text{ A/m/W}$ . The white arrows denote the polarisation of the field near to the ion position which inverts about the axis denoted by the dotted line (or central dot if rotating around the axis “out-of-page”) with the oscillation of the wave.

Proposed by Anton Grounds (of our experimental group), a balanced line consisting of two 1 mm diameter wires suspended  $250\text{ }\mu\text{m}$  above the ion position 10 mm apart could allow for controllable polarisation of the microwaves extremely close to the ion position. This is shown in Figure 4.38 (c). For this particular geometry, the field is quite small;  $\sim 0.02\text{ A/m/W}$  at the ion position. However, for a smaller separation of around  $250\text{ }\mu\text{m}$  separation and a wire diameter around  $30\text{ }\mu\text{m}$ , fields close to  $50\text{ A/m/W}$  have been simulated. Though extremely challenging, this system could in principle be assembled given that I have shown alignments to tens of microns previously in this thesis. This would require a high precision piece in order to hold the wires in place at the correct separation. The main limit to this scheme is likely to be the power that can be applied to such thin wire and the maximum duration of microwave pulses that can be used. Such a system would be useful in order to perform fast gate operations and is likely to be implemented in future experiments.

### Conclusions given these results

The conclusion of these simulations was that for the axial gradient system, the first of the two new systems to be put to use, we would use the previously verified methods of microwave and RF injection to the ion, i.e. both emitters would be external and located at the front window. Since the horn and coil are external, this minimises any problems we may face with an untested in-vacuum design and does not require the ordering or positioning of any new feedthroughs on the vacuum hemisphere.

The only change to the previously simulated emitters is that the RF coil would now be offset from the centre of the front window so that it was asymmetric to the central hole in the mesh. Simulations verified that this would allow us to adjust the polarisation at the ion by moving the coil and subsequently change the position of the central minimum due to the different diffraction/reflection off the mesh and copper block or chip surface.

For the radial gradient system, it was decided that there is sufficient time in order to perform real world investigations into using in-vacuum emitters for this experimental setup, however, these will not be discussed in this thesis.

Understandably, the simulated values may not perfectly reflect reality due to the different mesh size and simplified internal structure of the vacuum system. Nonetheless, these simulations help us to understand the general effects that the mesh will have and the polarisation of the field at the ion position for a given emitter. From these results we can still expect the emitters chosen for this experimental setup to work well<sup>27</sup>.

---

<sup>27</sup>Further experiments using a real mesh in conjunction with qubit rotations on the Blade trap system

### Installing the front window mesh

Now that we have some results that can clarify that using the mesh will still enable us to perform the intended coherent manipulation experiments, we are able to discuss how the real mesh is secured in place.

For installation into the axial gradient system, the mesh was cut achieving an oval hole of perpendicular diameters 16 mm and 17 mm. After a standard acetone and isopropanol clean, this mesh was secured in place using two stainless steel cable ties around the vacuum-side frame of the front window of the vacuum system. This could be pulled tight until the mesh sat near to flat on the window surface. In doing this, the diameters of the central hole increased to 17 mm and 18 mm. This assembly is shown in Figure 4.39.



Figure 4.39: The front window with the vacuum-side mesh in place. Stainless steel cable ties hold the mesh tight and flat on the window surface and a central hole allows for better transmission of microwave and RF radiation required for coherent manipulation of the ion qubit.

#### 4.6.4 Trapping RF and helical resonator

As with the Blade trap experiment, a helical resonator is required in order to couple the RF trapping voltage to the trap. The helical resonator for each system was primarily

---

verified that the real mesh does not prevent the transmission of RF and microwave radiation, however since the length scales and in-vacuum setup are very different to the new experimental setup, the exact transmission values should be taken with caution.

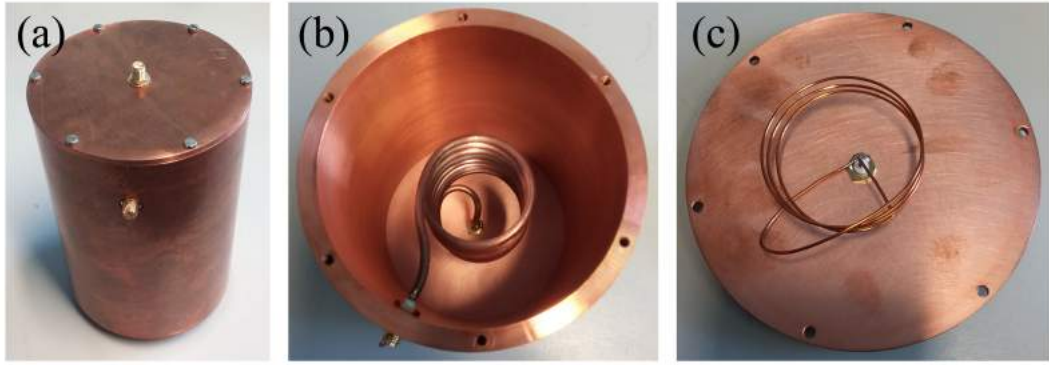


Figure 4.40: One of the resonators designed and built by Nikolaus Lorenz. **(a)** - The resonator exterior. **(b)** - The resonator interior. The larger coupler coil at high voltage is held in place by an SMA connector on the bottom of the can and anchored to ground at a shorted SMA on the side of the can. **(c)** - The interior of the resonator lid. The smaller injector coil is attached to an SMA connector at the top of the resonator.

constructed by Nikolaus Lorenz and is slightly modified when compared to the original resonator for the experimental setup in Chapters 1 and 2. One of these resonators is shown in Figure 4.40. Though the principle of using a small injector and larger coupler coil in order to impedance match an external RF source so that one can apply the radial trapping voltage to the chip is the same, the HV and BNC connections have both been replaced with SMA connectors. This means that the RF is effectively shielded from external noise or coupling all the way to the in-vacuum PCB. In addition to this, the SMA connection to the vacuum system allows for a much less delicate connection method than the barrel connection to the HV feedthrough, which have been known to crack on occasion when the original style connection was made in the past. This also means that the internal connections of the vacuum system can be made using fully shielded in-vacuum SMA to SMP cables, and the resonator can sit more remotely from the vacuum system if desired. Consequently, the need for an additional shielding modification to the resonator, as discussed in Chapter 2, is no longer required as the coaxial cable performs this action. Finally, the can of the resonator has been redesigned in order to minimise the cost of materials and manufacturing, and to save space around the experimental setup.

#### 4.6.5 DC voltages

As previously mentioned, each vacuum system is equipped with a 100 pin DC feedthrough for insertion of the DC electrode voltages that provide axial confinement of the ion. Though the back in-vacuum PCB provides filtering of the voltage that is applied to the trap electrodes, the D-sub connector of this feedthrough is connected to an external filter box which

in addition to filtering of each voltage line, allows for each connection of external voltages using SMA connectors. For the initial trapping runs, these DC voltages were provided by a Digital to Analogue Converter (DAC) card from one of the older previous experimental computers. However, these will be expected to be quite unstable and although they may be suitable for the initial trapping runs, for high fidelity operations we will undoubtedly switch these out for some low noise DC power supplies similar to those designed by Dr Bjoern Lekitsch for the macroscopic Blade trap experimental setup.

## 4.7 Initial trapping of $^{174}\text{Yb}^+$ ions

Within the time-scale of submitting this thesis, only the axial gradient system was fully set up for trapping experiments. Successful trapping of  $^{174}\text{Yb}^+$  ions was achieved using this experimental setup, however,  $^{171}\text{Yb}^+$  had not yet been trapped though the appropriate polarisation optics had been added to the optical setup and a 12.6 GHz microwave emitter is in place. This means that the magnetic field gradient produced by the under-chip magnetic spacer has not yet been measured with an ion or pair of ions. Nevertheless, the initial measurement of the magnetic field gradient using John Lacy's CNC mounted Hall probe setup is a promising result which shows that the magnitude of magnetic field gradient that was simulated is a positive physical result. We have shown that the under-chip magnetic spacer gradient production scheme has not prevented successful, stable trapping of ions of which trapping lifetimes of over 30 minutes have been observed with our initial setup.

In addition to trapping, the alignment procedures between each chip and magnetic spacer were very successful. I believe the expansion of the silver epoxy was the ultimate limiting factor of any alignment attempt, but the process was repeatable and with the use of a different adhesive could provide even better initial alignment. The alignment stage that I designed and built may in future be replaced by a much higher standard of apparatus with finer control of spacer and chip translation and better imaging optics. These improvements would only be required when using a thinner substrate as the magnetic field gradients can be much larger at the ion position. This would mean that there is significantly less room for error in the alignment before the desired trapping position sits in an offset field which is too high to reasonably compensate. In this case, silver epoxy would have to be replaced with a low expansion alternative. A new set of chips with a substrate thickness of  $430 \pm 20 \mu\text{m}$  are envisioned as a possible next set of chip traps to be used by our group for similar experiments. This would enable magnetic field gradients

well over 200 T/m for ion heights below 200  $\mu\text{m}$  using the same size constraints on the under-chip magnets that were laid out in Chapter 3. This would require much less error in alignment, particularly for a radially aligned scheme due to the required overlap of two nil lines but ultimately provide even faster, high fidelity operations than the setups described in this chapter.

For now, all trapping attempts have been made without compensation of the simulated offset field at the ion position as this is simulated to be much less than the 100 G offset that was originally trapped at on the macroscopic Blade trap experimental setup. This would also require the use of the large external permanent magnets which would require rearrangement of the optical setup as they need to sit at the window of the vacuum system which currently serves as the entry point for the 399 nm and 935 nm laser beams. We therefore aim to put these magnets in place after trapping  $^{171}\text{Yb}^+$  as the lasers would be in a known correct position in order to trap. Only, once  $^{171}\text{Yb}^+$  ions have been stably trapped will we be able to determine the magnetic field gradient produced by our under-chip magnetic spacer and verify that this experimental setup contains the resources by which a fault tolerant two-ion gate can be realised using long-wavelength radiation.

## Chapter 5

# On-chip production of gradients using microfabricated magnets, yoking, and hybrid systems

The previous chapter detailed the implementation of a macroscopic under-chip magnetic spacer in order to provide a magnetic field gradient for a planar chip trap suitable for performing fault tolerant two-ion gate operations using long wavelength radiation. This is, however, not an easily scalable method of magnetic field gradient production and on-chip magnetics are the next logical step in the fabrication of ion trap chips for use in a scalable architecture. In Chapter 3, I discussed on-chip current carrying wires which are the proposed method at present for providing the required magnetic field gradients for microwave and radio frequency based quantum computing with trapped ytterbium ions [20]. However, this may not be the best gradient production method for all geometries; more novel ion trap designs, for example a ring, may require more abstract gradient production methods in order to perform experiments which involve long-wavelength radiation entanglement methods. In addition to this, it would be interesting to consider other methods by which one can create a magnetic field gradient at the ion position using methods which have not yet been discussed in this field.

In this chapter, I discuss some alternative methods by which one may want to produce magnetic field gradients on-chip. These discussions include microfabricated permanent magnets, remotely activated on-chip high permeability yokes, and hybrid schemes. The latter uses a combination of current carrying wires and yokes for on-chip yoke activation resulting in self-compensation of the offset field components produced by the current carrying wires. These discussions are structured around examples of conceptual designs

of magnetic geometries that simulations show are able to produce high gradients for more abstract purposes. I will finish by reflecting on all magnetic field gradient production methods discussed in this thesis in order to directly compare them and assess their best applications.

This chapter does not serve as a conclusive document on the described subjects but is an introduction to concepts and principles of magnetic field gradient production that have not yet been successfully implemented in this field, and which I believe deserve further investigation. I will start my discussion with on-chip permanent magnets before moving onto more abstract gradient production methods.

## 5.1 On-chip permanent magnetic materials

Chapters 3 and 4 demonstrated that macroscopic magnets can create high magnetic field gradients that are ideal for integration with simple linear traps, and should allow high fidelity quantum gates to be performed in such traps. As we move to more complicated trap architectures however, a simple arrangement of a small number of regularly sized magnets may no longer be able to provide the complex gradient structures we might require. If we could microfabricate on-chip permanent magnetic structures then we open ourselves to the possibility of magnetic field profiles which may not be possible using on-chip current carrying wires. Contrary to macroscopic magnets, in the ideal case, on-chip magnetism should not have any misalignment so no external compensation coils should be necessary; any shift in the ion's magnetic coordinate should be able to be provided by complimentary current carrying wires. This would allow for magnetic geometries that are too complex to align at the macroscopic scale in larger scalable systems. The question is, would current fabrication methods allow us to manufacture such magnetic structures?

For on-chip applications, we require the following properties of the permanent magnetic material in order to ensure the highest possible gradients. These requirements are common to many MEMS (Micro-Electro-Mechanical-Systems) and are documented in a review article written by Tsung-Shune Chin [68]:

1. The magnets should have a high coercivity, remanence, energy products ( $BH$ ), and Curie temperature, while having a small temperature coefficient for each of the previously mentioned properties.
2. They must be adaptable to the processing and fabrication of other materials that may be previously or later deposited around them and be able to withstand any



possible annealing processes that may happen to the substrate subsequent to their deposition.

3. They must be environmentally stable, mechanically well bonded to their surroundings, corrosion resistant, and structurally resistant to any processes that they may unintentionally take part in.

In addition to this, one would also desire a magnet thickness of several microns in order to produce sufficient gradients at the desired ion heights of  $50 - 250 \mu\text{m}$  using a reasonable width and separation of the magnets<sup>1</sup>.

SmCo has been shown to be able to be fabricated at a thickness of  $5 \mu\text{m}$  though the remanence of these samples is not clearly documented [69]. Many other fabrication methods that exist are limited to thicknesses of  $\sim 150 \text{ nm}$  which we would not be able to simulate to evaluate. However, the remanence of these films has been shown to be lower but comparable to the macroscopic case. Since we are unsure of the remanence for microfabricated SmCo, it is hard to quantify what the gradients would be for any magnetic geometries. This can be remedied by using implanted magnets that have been made using macroscopic or foil based methods.

A similar process has been demonstrated by Bleiker et al. through the implantation of gold coated nickel “Through Silicon Vias” (TSVs) into a chip in order to create high aspect ratio interconnects that go through the chip to the back of the substrate to create transmission lines for MEMS [70]. These vias were fabricated in the range of  $5 - 150 \mu\text{m}$  diameter and  $20 - 200 \mu\text{m}$  thick [70]. It stands to reason that a similar technique may be possible in order to create larger magnetic geometries than those deposited via sputtering or electroplating. This would also allow for macroscopic fabrication techniques which would ensure greater remanences regardless of the magnetisation direction at thicknesses that would create a reasonable gradient at the ion position. Though a promising idea, this fabrication technique would have to be suitably characterised for our application before implementation with a wider range of chips.

For the permanent magnet simulations discussed hereon, I will use a normalised remanent field of  $1 \text{ T}$  so that the gradients are close to scalable via the remanence to first approximation, a near unity relative permeability typical of SmCo or FePt, and assume a thickness of  $5 \mu\text{m}$  (so that we are able to simulate the problem) which could be created

---

<sup>1</sup>These dimensions have been determined from initial simulations of such schemes but are also required in order to simulate the film in COMSOL as a sub-micron film thickness for ion heights of hundreds of microns would very likely not be able to mesh and therefore not solve.

by developments of the fabrication processes discussed above or via implantation using Bleiker's methods [70].

We can therefore say that though development of the fabrication techniques is required, it should be possible to create on-chip permanent magnets for magnetic field gradient applications. This means that I can continue by discussing some geometries which could be fabricated as part of our chips and see what magnitude of gradients can be achieved using on-chip permanent magnets in order to compare them to the other magnetic field gradient production methods documented in this thesis.

### 5.1.1 Linear magnetic high gradient regions

As with Barb's microfabricated scheme discussed in Chapter 3, which was elaborated to become the under-chip magnetic spacer, in order to create a permanent magnetic field gradient using microfabricated magnets, the simplest geometry would be two magnetic strips with a small separation through their magnetisation direction. Again, with the correct dimensions, this should create a high gradient nil at the ion position. This geometry is shown in Figure 5.1.

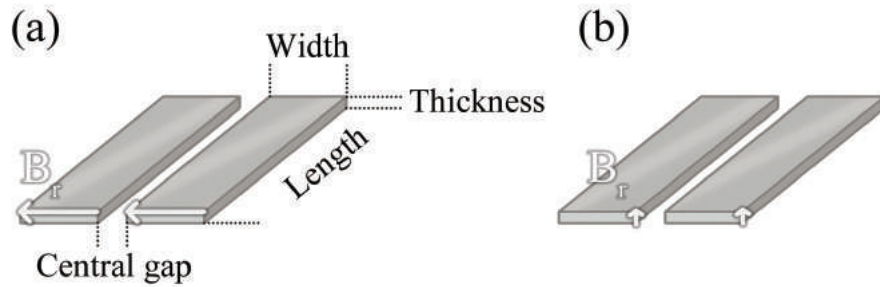


Figure 5.1: The linear gradient geometry of the on-chip magnets that would be situated under the main electrode layer. **(a)** - The in-plane magnetisation scheme with all relevant geometric features labelled as they are referred to in this chapter. **(b)** - The same geometry with an out-of-plane magnetisation for the alternate scheme.

A two-dimensional field diagram for such a geometry is shown in Figure 5.2. For my simulations I have chosen to use a thickness of  $5\ \mu\text{m}$  and a normalised remanence of 1 T by which the gradient will scale as previously discussed. For films thinner than this, simulations indicate it is unlikely that a high gradient would be possible at ion heights above  $120\ \mu\text{m}$ . These gradients are displayed in Table 5.1 but are understandably very optimistic for this scheme using the aforementioned fabrication techniques.

As with the macroscopic under-chip magnetic spacer with in-plane magnetisation, the vertical radial gradient is defined as  $\frac{dB_x}{dz}$  with  $\frac{dB_z}{dz}$  for the out-of-plane magnetisation

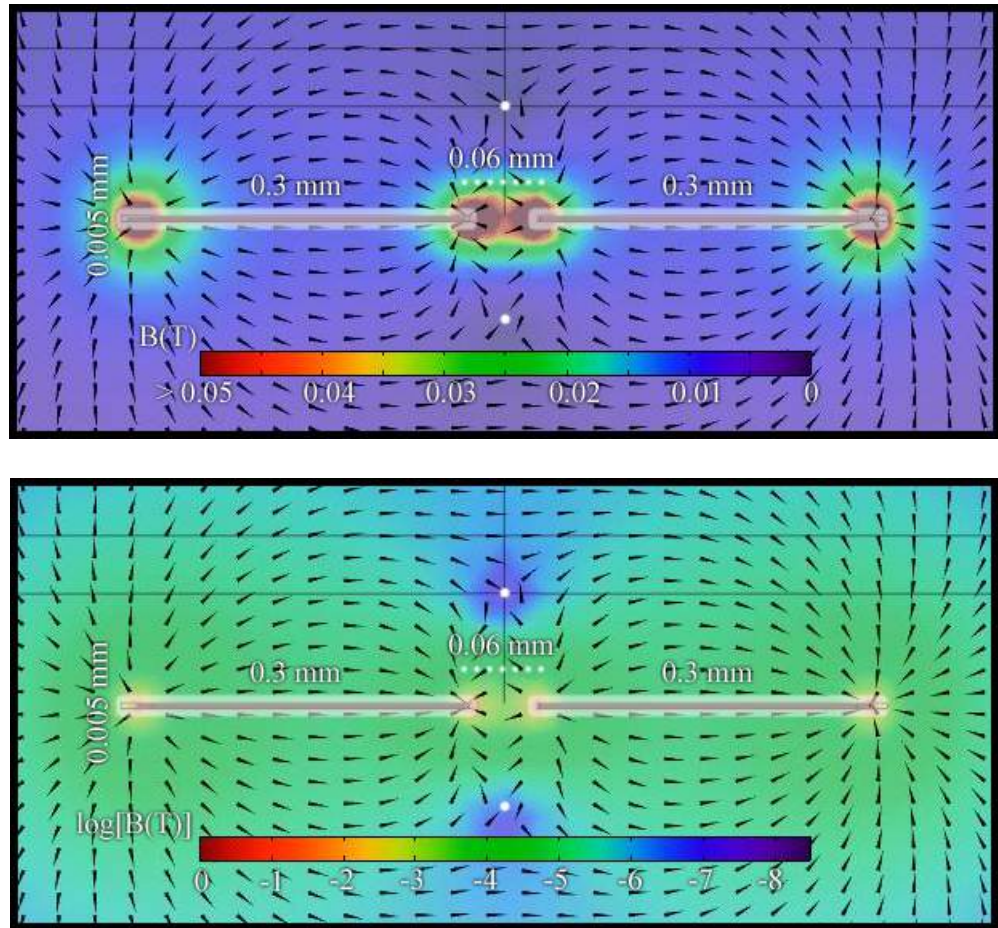


Figure 5.2: The field diagram for a pair of on-chip permanent magnets with an in-plane magnetisation through their separation. As with the under-chip magnets discussed in Chapter 3, a magnetic field nil line with high surrounding gradient is created above and below the central gap. The top diagram shows the field magnitude using a linear scale with colour. The bottom diagram uses a logarithmic scale in order to accentuate the position of the nil points above and below the geometry. The length of the magnets in this simulation is 6 mm.

Table 5.1: The simulated gradients for two different pairs of on-chip magnets of size width  $\times$  length  $\times$  thickness each magnetised in the plane of the chip for a variety of separations parallel to their width. Each magnet was modelled with a relative permeability of 1.05 and a remanence of 1 T in order to normalise the gradient about the remanence. Similar gradients and nil heights are achieved for the out-of-plane magnetised scheme.

Magnet dimensions (mm)	Central gap ( $\mu\text{m}$ )	Nil height above top of magnets ( $\mu\text{m}$ )	Vertical gradient (T/m)	Planar gradient (T/m)
$0.3 \times 6 \times 0.005$	20	55	221.3	141.8
	60	98	94.5	74.4
	140	151	39.9	34.7
	200	195	23.3	19.9
	300	250	12.0	10.9
$0.9 \times 6 \times 0.005$	10	66	63.5	40.4
	20	91	42.7	33.7
	40	130	31.3	24.3
	60	161	24.3	18.7
	80	188	18.8	14.6
	140	250	13.1	10.2

case. However, the planar radial gradient does not follow the simple single magnetic field component relationship to the macroscopic magnet case as the structure that creates the gradient is much smaller, thus  $B_x$  grows at a similar rate to  $B_z$  at these length scales. The planar radial gradient is therefore defined as  $\frac{d|B|}{dx}$  for both magnetisations.

In comparison to the under-chip magnetic spacer which this thesis focusses on, the on-chip magnets produce a gradient that is relatively small. The gradients produced by the under-chip magnetic spacer may be much smaller for a particularly thick chip substrate, however, for ion heights over 120  $\mu\text{m}$ , the gradients produced by on-chip magnets are much smaller than one would get for most reasonable chip thicknesses. This is merely a result of the magnet size; the thickness of a microfabricated magnet will nearly always be less than the nil height above them for ion trapping applications thus the gradient will drop off faster with height above the magnets when compared to the macroscopic case. The main advantage of on-chip permanent magnets is that it gives one the opportunity to create geometries that would be extremely difficult to align macroscopically or are nearly impossible using current carrying wires, such as on a ring trap, which will be discussed momentarily. That said, for radial gradient schemes, on-chip magnets could work very well for an x-junction trap which may desire a field profile more complex than that of a simple linear trapping region. This can be done by altering the normal two-strip linear design in order to tailor the gradient to one's own specifications.

### 5.1.2 Radial gradients on a ring shaped trap

The main advantage of using on-chip permanent magnets over other gradient production methods is the ability to fabricate them using patterned masks in order to achieve geometries near impossible using aligned macroscopic magnets or current carrying wires. The most obvious application of on-chip permanent magnets would be for creating a radial gradient on a ring trap. Ring traps are particularly interesting to the field of quantum simulation as they allow for periodic boundary conditions, i.e. an equal ion-ion spacing throughout a chain of ions [30]. In order to do this, one would need to be able to entangle all the ions in the ring. If using a microwave based entanglement scheme, this inevitably means that only radial gradients can be used for entanglement of the ion ring through the use of global microwave fields as an axial gradient would not be periodic and would require many different frequencies in order to address each ion individually. For a large ring this would be very impractical.

Due to the required topology, creation of such gradients for a ring shaped ion crystal is not possible using simple current carrying wires as there must be a feed in and out of the circle of each the concentric wires. Additionally, the alignment of two centres of symmetry makes this scheme nearly impossible using under-chip magnets as any planar misalignment would mean that the offset field created would not be uniform at all ion positions and therefore extremely difficult to compensate. This means that on-chip microfabricated permanent magnets are the most logical option in order to create this gradient profile. The out-of-plane magnetisation scheme is the obvious choice for the microfabricated magnets as an in-plane magnetisation would have to be applied radially from the centre of the ring; an out-of-plane magnetisation would be just as simple as for the linear case.

An example of the type of magnetic geometry that could be used to create such a gradient is discussed here and is very similar to the RF electrode geometry used to create a ring shaped ion crystal. By fabricating two circular rails of width of  $200\ \mu\text{m}$  and thickness  $5\ \mu\text{m}$  such that there is a central gap of  $80\ \mu\text{m}$  at a radius of  $960\ \mu\text{m}$ , one can create a nil at a height of approximately  $100\ \mu\text{m}$  above the magnet surface with vertical and planar radial gradients of  $80.0\ \text{T/m}$  and  $72.8\ \text{T/m}$  respectively for an out-of-plane remanence of  $1\ \text{T}$  and a relative permeability of  $1.05$ . This geometry is illustrated in Figure 5.3. The field across such a ring is shown at this nil height in Figure 5.4. Using a design similar to the one described here, the magnetic field gradients required to achieve global entanglement of a ring-shaped crystal of trapped ions when using the microwave or RF radiation based entanglement scheme should now be possible.

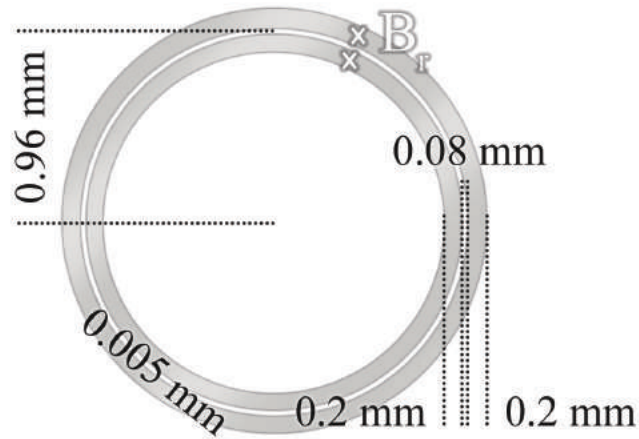


Figure 5.3: The on-chip magnet geometry resulting in the magnetic field profile shown in Figure 5.4. The magnetisation is out-of-plane and the thickness of the magnet is marked as 0.005 mm on the main body of the magnet in a similar manner to the macroscopic magnets shown in Chapter 4. This convention will remain throughout this chapter.

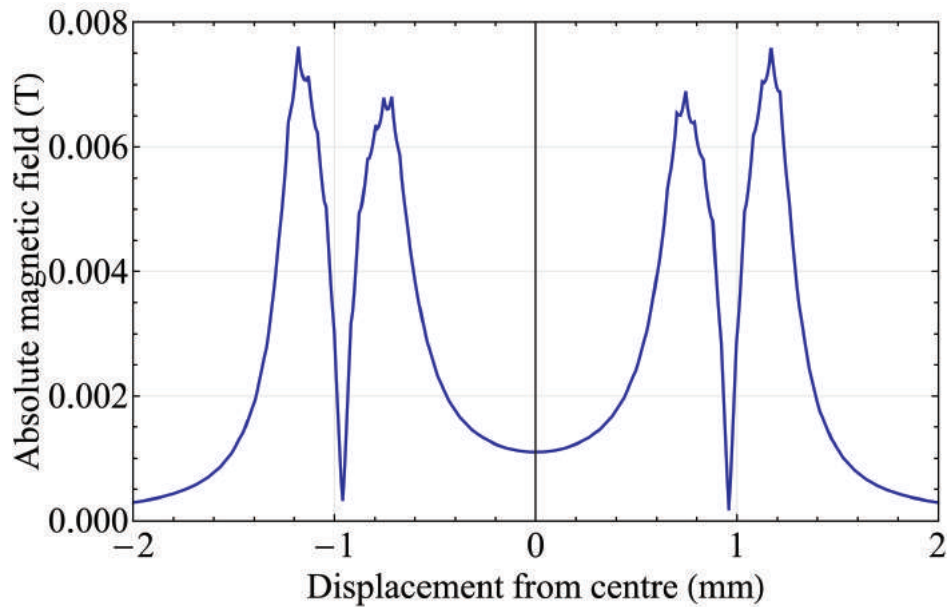


Figure 5.4: The magnetic field for a set of two circular magnets of radial width  $200\ \mu\text{m}$  and thickness  $5\ \mu\text{m}$  such that there is a central gap between them of  $80\ \mu\text{m}$  at a radius of  $960\ \mu\text{m}$ . These magnets have an out-of-plane remanence of 1 T and a relative permeability of 1.05. The blue line shows the field at  $100\ \mu\text{m}$  above the geometry across the ring through its centre. This creates a ring of zero magnetic field with a radius of  $960\ \mu\text{m}$  above the magnet surface.

### 5.1.3 Magnetisation of on-chip magnets for a scalable system.

Magnetisation of on-chip permanent magnets is obviously required in order to complete the successful fabrication of a chip equipped with these technologies. A single chip cut from a larger fabrication wafer can be magnetised individually by subjecting it to the magnetic field from a coil with a high current running through it. A scalable system which may

use up to a whole wafer as the chip structure would consist of much larger pieces, which makes placement of the entire structure into a large solenoid or Helmholtz pair difficult when trying to achieve the required magnetic fields for the best magnetic properties. Since the field diminishes with larger diameter of coil, the larger the sample that one needs to magnetise, the larger the required current to produce a sufficient  $H$ -field.

Given this difficulty, one could create a dedicated table which has many parallel wires under its surface with a high current running through them. When activated, this would create a large uniform magnetic field parallel to the table surface. By placing the wafer on top of it, all on-chip magnets would be magnetised, nevertheless, this only accounts for a single magnetisation direction which may not be suitable for certain architectures.

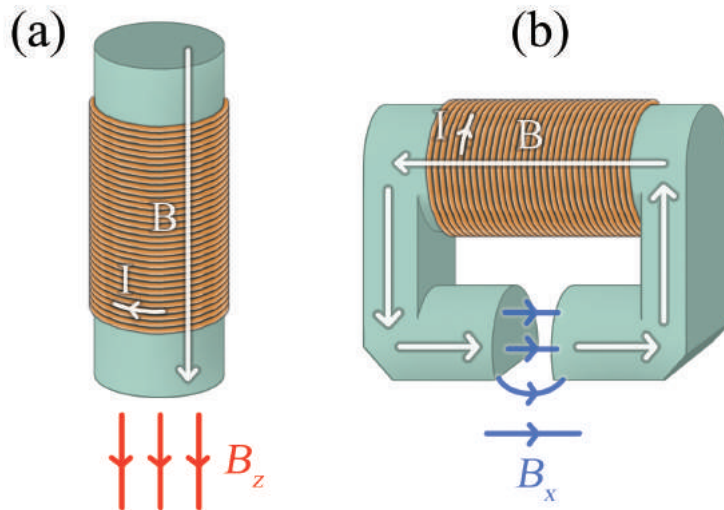


Figure 5.5: Magnetic writing head designs used for imprinting a magnetisation into a magnetic film. **(a)** - An out-of-plane magnetisation writing head. The field from the solenoid is channelled by the yoke to the end of the writing head which moves across the magnetic film in order to imprint a remanent magnetisation onto it. **(b)** - An in-plane magnetisation writing head similar to those used for audio cassette reading and recording. The field from the solenoid is channelled by the yoke which has a split on the writing side. This causes the field to no longer be contained within the yoke and bow outwards so that it can write an in-plane magnetisation onto a magnetic film that runs across it. In this way a magnetic film can be magnetised using a moving writing head without having to be placed in a large uniform field generator.

Alternatively, the required external fields could be produced by a large magnetic writing head not unlike those used to write information onto cassette tapes. These use a soft magnetic core to channel the field produced by a small coil in order to produce a certain field profile at the tip of the writing head. Typical geometries for an out-of-plane and in-plane magnetic field writing head are shown in Figure 5.5. These could be designed to operate on a servo motor cradle and go to each point of the chip and “write” in the

magnetisation to each thin film section on the substrate with independent magnetisation directions for each region.

#### 5.1.4 Reflections on gradients produced by on-chip permanent magnets

I have now discussed the concept of on-chip magnets in some detail outlining the potential benefits that they may have as a method by which gradients can be produced in future. The main points of this discussion are summarised below:

- The best material to use for on-chip magnets is SmCo or FePt though fabrication techniques require significant investigation and development in order create high gradients at our desired ion heights, with particular emphasis on magnet thickness as well as their hard-magnetic properties.
- Initial simulations show that on-chip permanent magnets are moderately competitive with non-optimised current wire schemes but do not produce gradients competitive with the under-chip magnetic spacer or optimised, nilled anti-parallel current wires.
- The main advantage of on-chip permanent magnets is that novel geometries are possible, most notably radial gradients on a ring trap, which can be realised much simpler than if using any other scheme discussed thus far.
- Magnetisation of on-chip magnets for a scalable system should be relatively easy using a specialised magnetic writing setup.

On-chip permanent magnets indeed have their merits, though until fabrication techniques are developed and verified, the results discussed in this section are merely theoretical. Significant further investigation into the practical realisation of on-chip permanent magnets for ion chip traps will be required in order to bring these designs to fruition.

From devising a way in which permanent magnetic sections on a scalable architecture can be magnetised, an interesting point has been illustrated in the use of magnetic writing heads. The possibility of using a high permeability material to channel the magnetic field has not yet been discussed with regards to the advantages it may have for production of on-chip gradients. Moreover, this brings into question whether one could activate an on-chip gradient using an off-chip field source to drive on-chip high permeability plates. This will be discussed in the following section which introduces the concept of on-chip yoking in order to create remotely activated magnetic field gradients.



## 5.2 On-chip magnetic field gradients using locally excited yokes

Magnetic yoking is the name given to the phenomenon by which the magnetic field produced by a permanent or electromagnetic source is redirected or channelled using a piece of material with a high relative permeability. A magnetic yoke is any high permeability piece of material that may be used to channel a magnetic field; typically, a horseshoe magnet will often be seen with a small iron yoke connecting its poles when not in use in order to better contain the magnetic field within the structure. Magnetic yokes may also be known as “cores” when used to strengthen an electromagnetic application such as a solenoid or a transformer, or alternatively a “pole piece”, such as in the context of an electromagnetic pickup used in an electric guitar. Yoking is also responsible for low frequency magnetic shielding by forcing a magnetic field to be contained within the high permeability medium by guiding the flux lines in a closed loop. By utilising this effect, I propose that switchable magnetic field gradients can be activated using remote field sources in order to create high gradients at the ion position. This would be done by using high permeability plates embedded under the chip electrodes to shape the field produced by driving magnetics situated in the vacuum system. However, I will first explain the principles of magnetic yoking using an easy to understand real-world scenario to clarify how it works and demonstrate its capabilities.

### 5.2.1 Macroscopic demonstration of electromagnetic yoking

Magnetic yoking can easily be demonstrated in macroscopic systems. By passing  $\sim 3\text{A}$  through  $\sim 250$  turns of copper wire wound around a chrome-vanadium steel spanner, I was able to stack three one penny coins edge to edge, both near to the solenoid and on the opposite end of the spanner. This shows that by using the principle of magnetic yoking, even the tiny surface contact area of the penny circumference was enough to channel enough magnetic flux for the coins to be stacked. Additionally, the high permeability of the steel spanner means that it is able to channel the magnetic field induced in the wound section throughout its length as well as through the additional pennies, which can be considered remote from the driving magnetic field. The magnetic field strength in each of these components is illustrated in Figure 5.6 in order to show the propagation of the magnetic field produced by the coil. The field strength is lower further along the spanner as alignment is no longer aided by the current wires and is mainly a result of the

other internal spins within the high permeability materials. When the current was turned off, the spanner and coins had little to no residual magnetisation. This shows that soft magnetic materials can be used to create switchable magnetic systems with the use of a driving magnetic field created by a remote source.

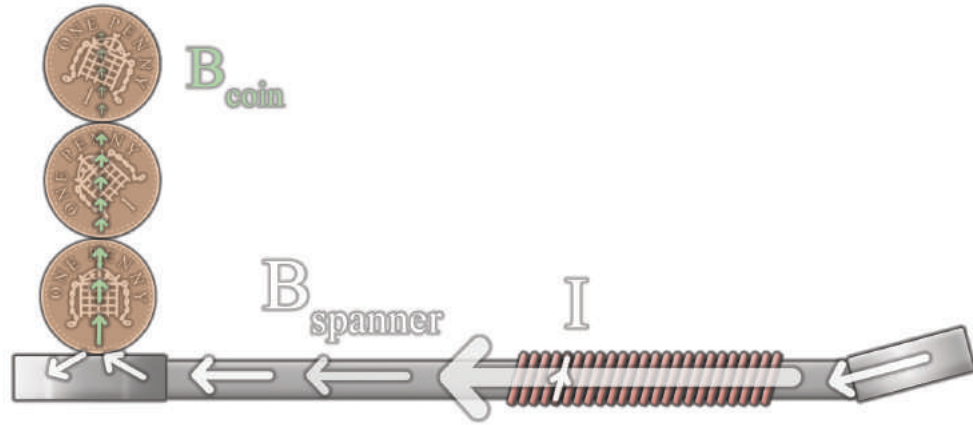


Figure 5.6: An illustration of the internal magnetic field propagation due to magnetic yoking in the electromagnetic coin stacking demonstration. The current in the turns of wire around the spanner produces a large internal field which propagates with diminishing magnitude along the length of the spanner. This internal magnetisation is shown in white. The coins redirect the field upwards and out of the spanner due to their high permeability as this is the lowest energy state for the alignment of their internal spins. However, due to the small contact area with the spanner due to the circular geometry, only a very small portion of the magnetic field is diverted in the internal magnetisation of the spanner and thus only a small field (shown in green) perpendicular to the length of the spanner is induced in the coin.

Similarly, on-chip yoking structures could be activated using a switchable electromagnet and any field created at the ion position would not remain after the driving field is removed. Any residual magnetisation in the yokes can be removed by running a de-gaussing pulse through the driving electromagnet, as the yokes have much lower  $H$ -field requirements to exhibit permanent magnetisation by definition.

### 5.2.2 Redirection of magnetic fields using on-chip yokes in order to create high magnetic field gradients

For many singular magnetic field sources the natural shape of the field that is created does not have the high gradient field profile that is useful for our experiments. By using yokes in the vicinity of the ion in addition to other magnetic field sources, it is reasonable to infer that one could accentuate and redirect the driving magnetic field into a shape that creates a higher gradient or more useful field profile for a given experiment.

By fabricating a ferromagnetic structure onto a chip using similar methods to those

used to create current carrying wires, one can guide the magnetic field of a delocalised magnet such that a high magnetic field gradient is present in the vicinity of the ion. This works on the same principle as magnetic shielding; by fabricating a narrow, high permeability plate under the electrode layer of a planar trap, a magnetic field gradient is created near to the plate boundary when in the presence of an external magnetic field. This can be accentuated by having two plates with a small separation between them. This will be illustrated later in this chapter when I discuss specific on-chip geometries.

The main disadvantage of on-chip yokes is that since the magnetic field in the yokes is dependent on the applied magnetic field, the gradient and absolute field are proportional to each other<sup>2</sup>. This means that unlike the under-chip magnetic spacer, the geometry of the magnetic yokes do not determine the position of a magnetic nil at the ion position, but rather the proportionality between the applied magnetic field and the gradient within the geometry size that I am considering. We also find that for many geometries the magnetic field grows with ion height meaning that this scheme works best for lower ion heights where the heating rate may become a problem. This means that the strongest driving magnetic fields are not necessarily the best choice for operation of the experiment.

If one were to use a permanent magnet as the source of the driving field for the yokes, a low remanence is required to obtain a low offset field at the ion since we cannot compensate this offset field without affecting the field redirected by the yokes. Sintered ceramic magnets are the main candidate for this application due to their relatively low remanence of 0.2 – 0.5 T.<sup>3</sup> However, their maximum operating temperature lies around 200 °C which is our standard baking temperature. This would mean that they could become demagnetised due to the bake, thus rendering the setup useless for the intended experiment. Using adjustable electromagnetic field sources solves this issue.

An advantage of this scheme over permanent magnetic schemes is that since the required magnetic field is very small, the driving magnetics can be glued to the back of the chip carrier. This means that the chip can be wire bonded once and trapped on without the magnet in place to test that it is working and then the magnet can be retrofitted once a trap is working well. Since the magnetic field that creates the gradient is not on-chip, this also means there is a less stringent requirement for under-chip cooling as the heat on the chip is not caused by high currents running through wires in order to create the gradient.

---

<sup>2</sup>This also means that magnetic nilling does not work as the driving field which creates the gradient becomes negated.

<sup>3</sup>These properties are taken from the specification of ceramic magnets sold by Bunting Magnetics.

The greatest possible advantage of yokes over current carrying wires, under chip magnets, or microfabricated permanent magnets is simply due to their relative ease of fabrication, alignment, and operation. On-chip yokes would not require cooling in order to work effectively and also could be aligned with electrodes as part of the fabrication process. In general, the fabrication processes for high permeability magnetic materials are more straight forward and well documented than for permanent magnetic materials within our required dimensions. The introduction of high permeability yokes in combination with electromagnetic field sources also paves the way for more complex, switchable magnetic field gradients with less requirement for external compensation of offset field components.

### 5.2.3 Microfabrication of high-permeability yokes

Microfabrication of high permeability magnetic materials is essential for the realisation of on-chip yoking and hybrid gradient production methods which use a combination of yokes and on-chip current wires. We now need to consider what material our yokes should be made from and how they can be fabricated onto our ion chip traps. The chosen material should have the following properties:

- A high relative permeability that is (near) constant and much greater than 100 and preferably in the thousands so that minimal field is required to activate the yokes.
- A very low remanence and coercivity so that when all driving fields are removed there is no residual magnetisation, or, if there is, it can be easily removed using degaussing techniques.
- A high saturation which allows for a large operating range of magnetic fields where the relative permeability can be approximated as linear. This is so that the field profile shaped by the yokes stays near-proportional to the magnitude of the driving fields.

These properties will ensure that the yokes behave as close as possible to our simulations, though investigation with physical samples will be the ultimate determining factor as to whether these conceptual designs have good real-world applications.

For the most part, soft magnetic materials have been fabricated for MEMS applications such as micro-inductor cores [71] or micro-actuators and motors [72]. These have been realised with extremely complex geometries such as a copper wire wrapped around a high-permeability core for a transformer style inductor [73].

For my on-chip yoke designs, I am mainly interested in fabricating rectangular plates of high permeability material at a thickness of  $5 - 50 \mu\text{m}$ . Thanks to the expertise of Dr Bjoern Lekitsch in fabricating nickel films using electro-plating, the bulk of designs will use nickel yokes at a thickness of  $10 - 20 \mu\text{m}$ . For the purpose of these simulations, the relative permeability of the yokes is assumed to be that of bulk nickel at a value of 200, though the effect of higher and lower permeability materials will also be discussed.

This means the obvious choice for a proof of concept design for any of the yoking or hybrid gradient production methods would be nickel, simply because the fabrication expertise is already present within our group. However, permalloy ( $\text{Ni}_{80}\text{Fe}_{20}$ ) and supermalloy ( $\text{NiFeMo}$ ) are the prime candidates for a higher permeability material than nickel [71] with a relative permeability in the hundreds to several thousand respectively, which is likely to enhance any effects that occur in the presence of nickel yokes.

A good fabrication method in order to create (su)permalloy plates is the electroplating scheme used by Park and Allen as they allow for a large range of thicknesses with very good magnetic properties for our application [71] [74]. Using the LIGA technique, nickel plates at high thickness should also be possible depending on their magnetic properties [75], thus I consider plate thicknesses of  $10 - 200 \mu\text{m}$  for my simulations.

#### 5.2.4 Linear magnetic high gradient regions

Much like the under-chip magnetic spacer, a high gradient can be created between two long magnetic plates with a small separation between them, these of course being driven by a small field produced by a magnet below them. Such a geometry is shown in Figure 5.7. Since this gradient is created by the shielding effects near to the edge of the magnetic plate, a large magnetic field gradient can be created using a single plate, however, the gradient created between two plates is greater due to the larger emphasis of the activation field near to the central yoke edges where the magnetic field is no longer confined. This effect is shown in Figure 5.8 which displays the two-dimensional field plot for such a geometry.

Several designs have been simulated using this yoking scheme to produce gradients for a linear trap geometry. As with permanent magnets, one should consider both out of plane magnetisations and in-plane magnetisation through the separation of the yokes.

#### Initial simulations

For out-of-plane driving fields, simulations indicate that there is insufficient shielding caused by the on-chip yokes in order to shape the driving field to create a high gradient.

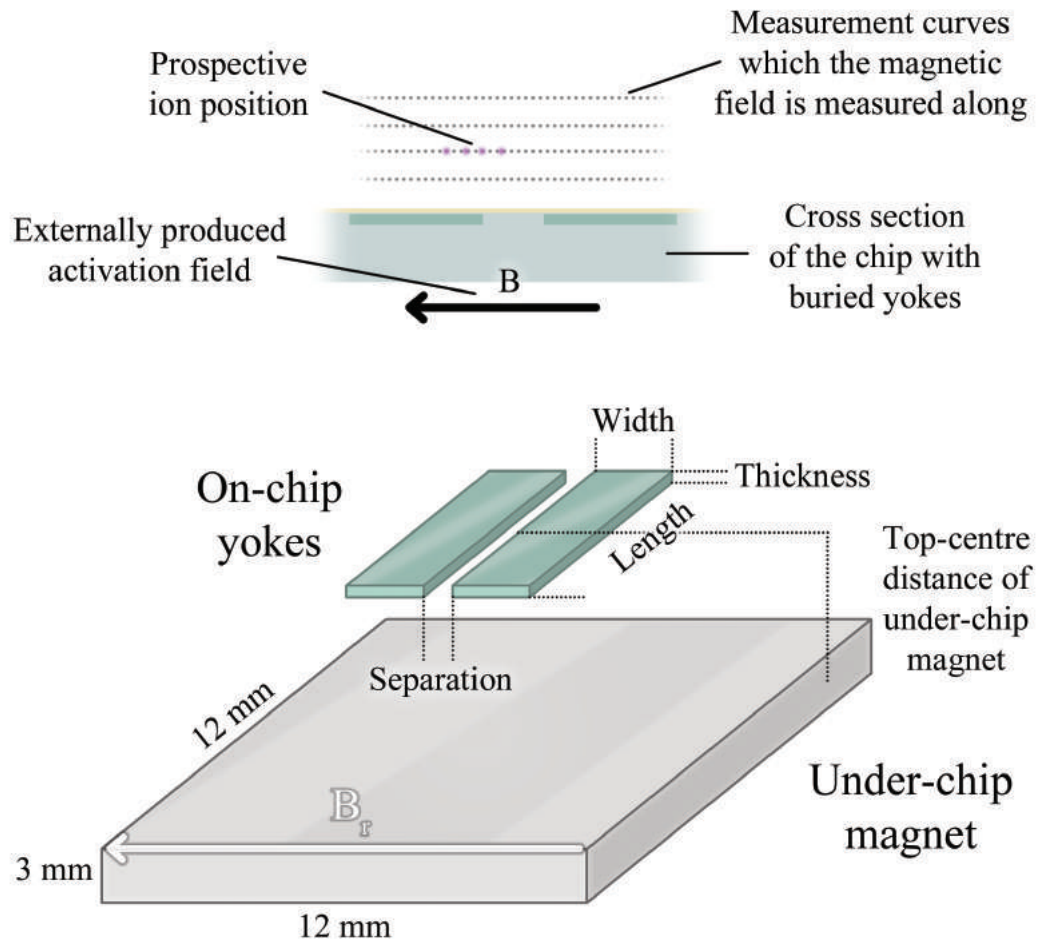


Figure 5.7: The geometric configuration for two on-chip yokes with a small separation between them driven by an under-chip magnet. The upper diagram shows the position of the yokes underneath the electrode layer, within the substrate of the chip. The off-centre orientation of trapped ions with respect to the yokes is also shown. The yokes shape the externally produced magnetic field in order to create a magnetic field gradient. This diagram is not shown to scale. The lower diagram shows the simulation geometry used in order to evaluate the magnetic fields produced using on-chip yoking of an under-chip magnetic field source. All features are labelled as they appear in any tables concerning this scheme. The magnet size is constant for all simulations discussed in this chapter.

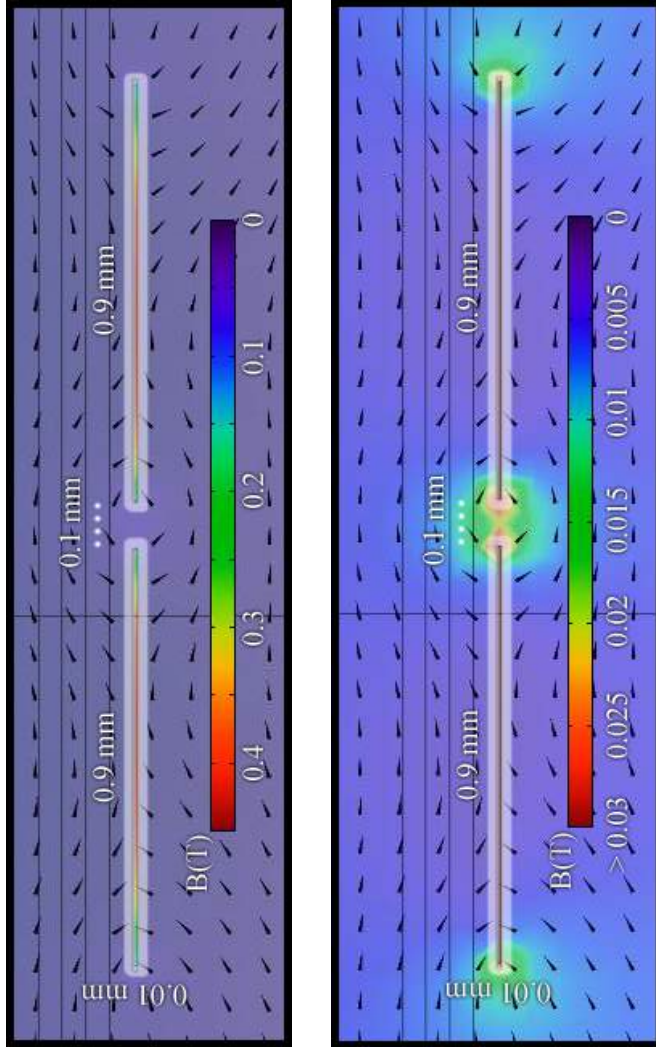


Figure 5.8: The field diagram for a pair of on-chip permanent magnet of size  $12\text{ mm} \times 3\text{ mm} \times 3\text{ mm}$  at a (centre) distance of 8 mm below the top of the yokes (not shown in this diagram) with a remanence parallel to the plane of the chip across the yoke separation. The top diagram shows the internal field of the yokes which is greatest at their centre. The bottom diagram sets the internal field of the yokes off the scale in order to show the relative field magnitude around them. The field produced by the under-chip magnet is significantly attenuated near to the main body of each yoke and accentuated near to their boundaries in the direction parallel to their magnetisation creating a high magnetic field gradient at these positions. The lengths of the yokes in this simulation is 6 mm.

A simulation using an out-of-plane field to activate the yokes is shown in Figure 5.9. Note that the scale on the  $y$ -axis has an extremely small range. This results in a maximum planar gradient of less than 3 T/m and a vertical gradient even smaller than this. Significantly thicker yokes of the order 100  $\mu\text{m}$  showed little improvement in the gradient so I can therefore say that an out-of-plane driving field produced insufficient results for our application. This also means that one is currently unable to produce high gradients on a ring or two-dimensional array ion trap using such a scheme.

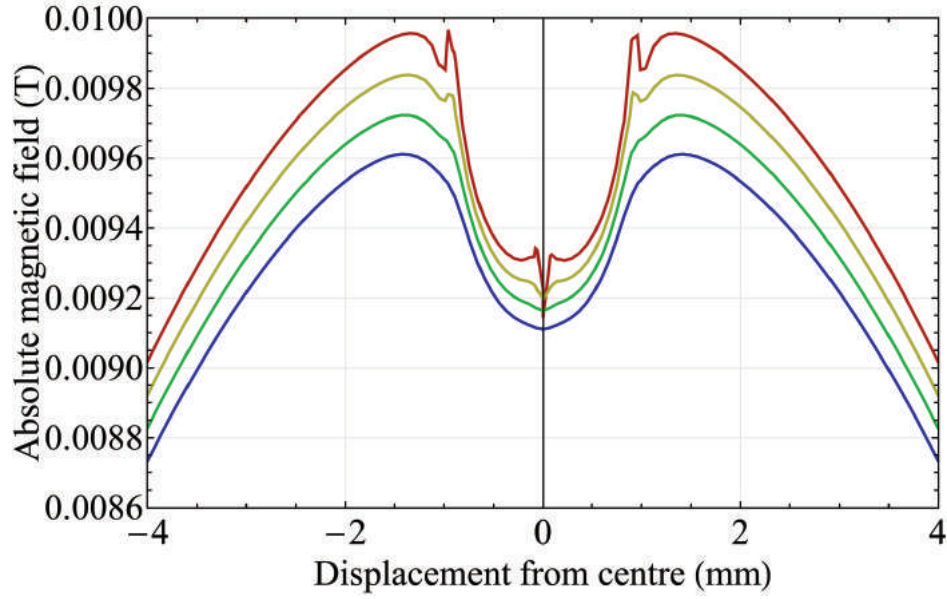


Figure 5.9: The magnetic field measured along the planar direction for a pair of yokes  $0.9 \times 6 \times 0.01$  mm with a separation of 100  $\mu\text{m}$  and a relative permeability of 200. These are driven by a  $12 \times 12 \times 3$  mm magnet with an out-of-plane remanence of 0.2 T and relative permeability 1.28 at a distance of 8 mm under the yokes from their top surface to the centre of the driving magnet, similar to the geometry shown in Figure 5.7. The field is shown for several heights measured across the geometry. Red - 50  $\mu\text{m}$ , Yellow - 100  $\mu\text{m}$ , Green - 150  $\mu\text{m}$ , and Blue - 200  $\mu\text{m}$ . Note that the range of the magnetic field is extremely small, therefore this scheme produces insufficient gradients for our applications.

This means that the driving magnetics must have a magnetisation in  $B_x$  for all yoking simulations shown in this chapter. In addition to this, there is a minimal vertical radial gradient,  $\frac{d|B|}{dz}$ , of 10 – 1 T/m over the 50 – 200  $\mu\text{m}$  ion height range for all geometries discussed in this chapter regarding the on-chip yoking scheme. I will therefore concentrate only on the planar gradient, which is defined as  $\frac{d|B|}{dx}$  with significant contribution from the  $B_x$  and  $B_z$  components. The highest reasonable gradients will be measured and the absolute field at this measurement point will be noted. This field and the relationship between the gradient and the height above the yokes at which it is measured, is highly dependent on the proximity, size, and remanence of the driving magnet. The closer the



magnet, the higher the gradient but this also results in a higher offset field. Understandably, the remanence is directly proportional to both the gradient and the offset field as previously noted.

I will now discuss several simulations of this yoking scheme with an in-plane driving field in order to show how the field is shaped by the on-chip plates in order to create a magnetic field gradient. The magnetic field in the presence two yokes of dimensions  $0.9 \times 6 \times 0.01$  mm with a separation of  $100 \mu\text{m}$  and relative permeability 200 is shown in Figure 5.10 for several heights above the yokes going across their separation.

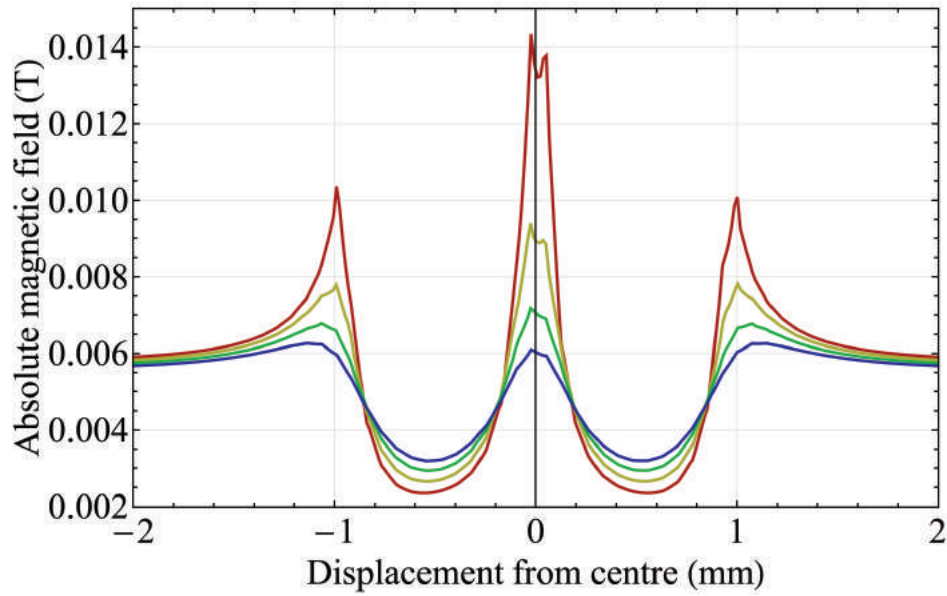


Figure 5.10: The magnetic field measured along the planar direction for a pair of yokes  $0.9 \times 6 \times 0.01$  mm with a separation of  $100 \mu\text{m}$  and a relative permeability of 200. These are driven by a  $12 \times 12 \times 3$  mm magnet with an in-plane remanence of 0.2 T parallel to the width of the yokes and relative permeability 1.28, similar to the geometry shown in Figure 5.7. This sits at a distance of 8 mm under the yokes from their top surface to the centre of the driving magnet. The field is shown for several heights measured across the geometry. Red -  $50 \mu\text{m}$ , Yellow -  $100 \mu\text{m}$ , Green -  $150 \mu\text{m}$ , and Blue -  $200 \mu\text{m}$ .

For this simulation, the yokes are driven by a  $12 \times 12 \times 3$  mm magnet of remanence 0.2 T at a distance of 8 mm under the yokes. One can see that above each yoke there is a significant drop in the magnetic field due to the effective shielding provided by the high permeability material. Near to the edges of the yokes, the field spikes as there is a contribution from the driving magnet and the accentuated field is no longer contained within the high permeability medium. This change in the field over this region creates the high magnetic field gradient that is of interest to us which, as with most other schemes discussed in this thesis, diminishes with ion height. The gradients at several heights above two yoke configurations are shown in Tables 5.2 and 5.3 for a variety of under-chip magnet

distances. For all these cases, a ceramic magnet of relative permeability 1.28, remanence of 0.2 T, and size  $12 \times 12 \times 3$  mm is used. The locations of the field values and gradients taken at specific features of the field profile are labelled in Figure 5.11.

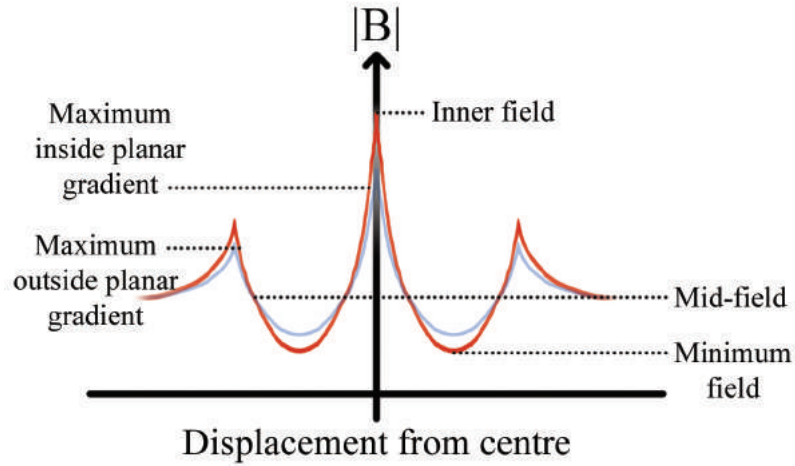


Figure 5.11: An illustration of a typical field profile across a pair of activated yokes at two different heights above them, the red being the lower of the two where I have labelled the important regions. The labels correspond to the position on each curve of the relevant field and gradient values that are documented in the tables featured in this chapter. Unless otherwise state, these are the points that will be used to compare the gradients produced by this scheme.

The mid-field is the field value which is approximately the same regardless of the height above the yoke that the field is measured. This field value within the central curve of the field profile typically has a high gradient over half the maximum gradient indicated in the simulation but at a much lower field. This explicit value is difficult to ascertain due to the meshing of the simulation but one can see from the field plots that this gradient is still significant when compared to the maximum gradient as the field approaches the central maximum above the separation between the yokes. Below this field value, the gradient tends to zero as one approaches the minimum field due to the shielding over the main body of the yokes. This is an important point to consider because it is the absolute field that an ion would sit at for entanglement operations using this scheme.

One can see that the gradients produced are not very competitive with permanent magnets or nilled field current carrying wire schemes, especially at higher ion heights. However, the shape of the field profile is interesting as it is very wide when compared to the field profiles produced by the aforementioned schemes. The benefits of this field profile will be discussed with regards junction traps later in this chapter. For now, I will

Table 5.2: Simulation results for a set of yokes  $0.5 \times 6 \times 0.01$  mm separated by  $100 \mu\text{m}$  with a relative permeability of 200 driven by a  $12 \times 12 \times 3$  mm magnet of remanence 0.2 T and relative permeability 1.28 for a variety of under-chip distances.

Top-centre distance of under-chip magnet (mm)	Mid-field (G)	Height above the yokes ( $\mu\text{m}$ )	Inner field (G)	Minimum field (G)	Maximum inside planar gradient (T/m)	Maximum outside planar gradient (T/m)
10	28.5	50	70	13.2	48	30
		100	47	17.5	17	15
		150	37.7	21	8.5	8.5
		200	33	23.5	5	5.5
8	45	50	111.5	21	73.3	49.7
		100	74	27.5	27.7	23.6
		150	59	33	13	13.7
		200	52	37	7.6	8.8
6	71.5	50	180	33	133	81
		100	118	44	45	38
		150	94	52.4	21	22
		200	82.8	58.7	12	13.5
4	112	50	275.5	51.5	178.5	128.5
		100	183	68.1	66	58
		150	146	81.7	33	33.5
		200	128.7	91.7	19.5	21.5

Table 5.3: Simulation results for a set of yokes  $0.9 \times 6 \times 0.01$  mm separated by  $100 \mu\text{m}$  with a relative permeability of 200 driven by a  $12 \times 12 \times 3$  mm magnet of remanence 0.2 T and relative permeability 1.28 for a variety of under-chip distances.

Top-centre distance of under-chip magnet (mm)	Mid-field (G)	Height above the yokes ( $\mu\text{m}$ )	Inner field (G)	Minimum field (G)	Maximum inside planar gradient (T/m)	Maximum outside planar gradient (T/m)
10	29.5	50	97	15	40.8	42.3
		100	61	17	22.6	15.7
		150	46	18.7	10.7	9.1
		200	39	20.3	6.4	6.4
8	47	50	153	23.5	64	67
		100	96.4	26.5	35.5	24.9
		150	73	29.3	16.8	14.3
		200	61	31.9	10	10.1
6	74	50	242.5	37.4	114.5	108
		100	153	42.2	56.8	37.7
		150	115.5	46.7	27.3	21.6
		200	97	50.8	15.8	16
4	114	50	381.5	58.4	171.8	165
		100	238	66	85.5	60.3
		150	178.5	73	41	34.5
		200	151.5	79.5	23.8	25.7

concentrate on investigating how this field profile can be changed to be more beneficial for our experiments.

Closer driving magnets create a larger gradient but also a larger offset field which therefore creates a trade-off between the field that one would use for coherent manipulation operations and the gradient that can be used for entanglement experiments. If the contrast between the minimum field and maximum field were to be increased, then it is possible that the ion could sit at a lower field for the same gradient or access higher gradients for the same field.

### **Improving the field profile produced by a set of yokes**

We can improve the trade-off between offset field and gradient by using a higher permeability yoke material; the contrast between the minimum and maximum fields is increased thereby increasing the gradient. This can also be viewed as having the same gradient for a smaller offset field. Table 5.4 shows the simulation results for several different relative permeabilities for the final geometry of Table 5.3. These simulated fields at 50  $\mu\text{m}$  above the yokes are also displayed in Figure 5.12 illustrating the dramatic dependence of the field profile on relative permeability. One can see that this scheme produces much better results for higher permeabilities and the gradient increase is significant over this range of values, however, the mid-field does not scale as well as the field or gradient values. This indicates that optimisation of this scheme should begin by choosing a geometry with a small value of this offset field and optimising the gradient from there.

Lastly, one would want to consider the effect that the thickness of the yoke has on the field and gradient to see if this improves the trade-off. This also addresses concerns on what the best way to fabricate the yokes might be, i.e. deposition or implantation. The simulation results for three thickness of the same yoke topology are shown in Table 5.5 and displayed in Figure 5.13 for a height of 50  $\mu\text{m}$  above the yokes. One can see that the minimum fields have dropped significantly for thicker yokes, however, the gradients remain very similar.

Though this may seem promising, the gradient at the mid-field value of the inner field profile is much smaller than half the maximum gradient for the thicker yokes and operating at a higher field becomes a better option in order to access the higher gradient region. From these results, it therefore means that one does not necessarily want thicker yokes and that the thickness of 10  $\mu\text{m}$  that was used previously, is probably a better way forward.

Since the under-chip magnet can be aimed to be used as a retrofit following verification

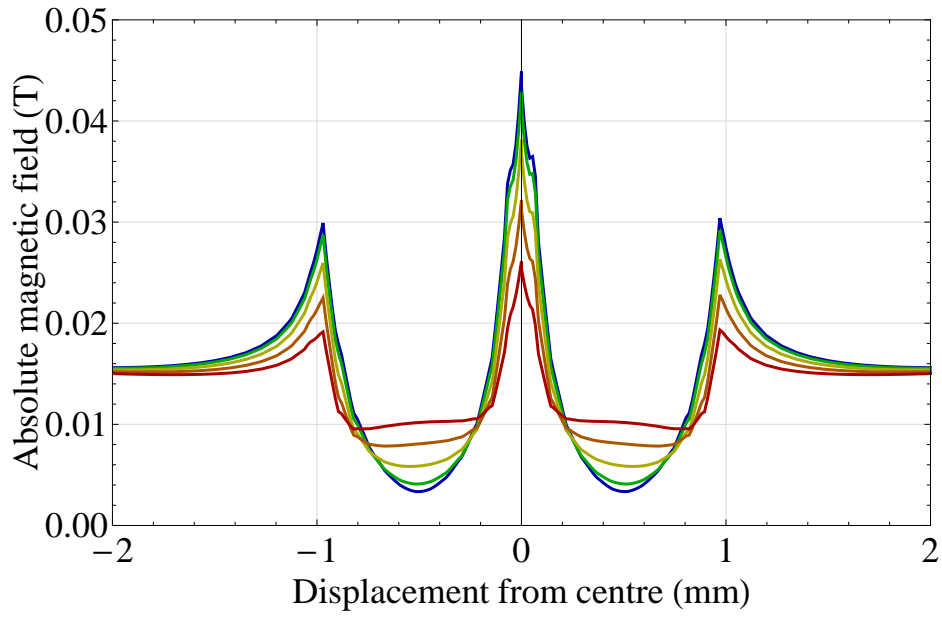


Figure 5.12: The magnetic field for a pair of yokes  $0.9 \times 6 \times 0.01$  mm with a separation of  $100 \mu\text{m}$  driven by a  $12 \times 12 \times 3$  mm magnet of remanence 0.2 T and relative permeability 1.28 at a distance of 4 mm under the yokes from their top surface to the centre of the driving magnet. The field is shown for several different relative permeabilities of the yoke material measured at a height of  $50 \mu\text{m}$  across the geometry. Red - 50, Orange - 100, Yellow - 200, Green - 400, and Blue - 600.

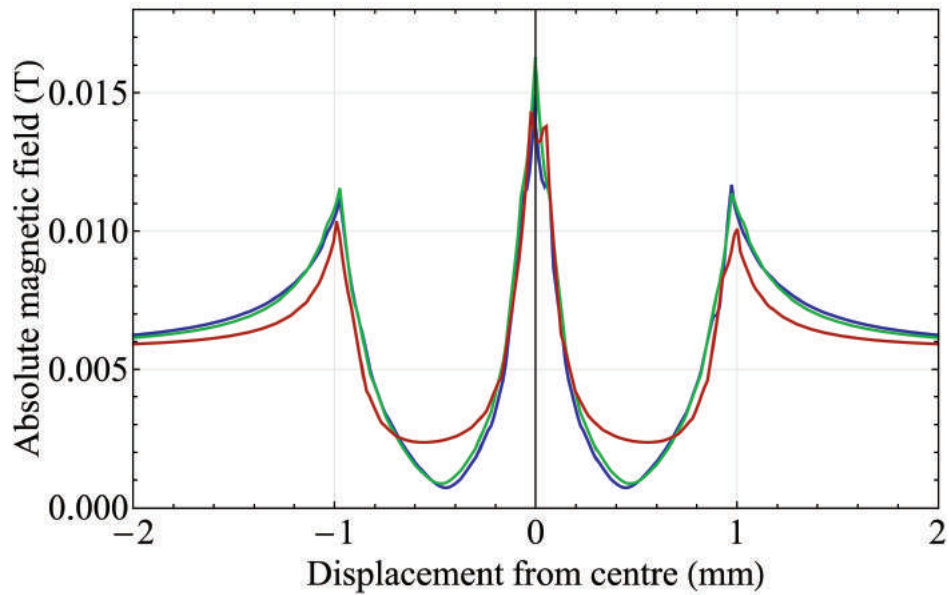


Figure 5.13: The magnetic field measured along the planar direction for a pair of yokes with a planar topology of  $0.9 \times 6$  mm with a separation of  $100 \mu\text{m}$  and a relative permeability of 200. These are driven by a  $12 \times 12 \times 3$  mm magnet of remanence 0.2 T and relative permeability 1.28 at a distance of 8 mm under the yokes from their top surface to the centre of the driving magnet. The field across the geometry at a height of  $50 \mu\text{m}$  is shown for three different thicknesses of yoke. Red -  $10 \mu\text{m}$ , Green -  $100 \mu\text{m}$ , and Blue -  $200 \mu\text{m}$ .

Table 5.4: Simulation results for a set of yokes  $0.9 \times 6 \times 0.01$  mm separated by  $100 \mu\text{m}$  for several relative permeabilities. The yokes are driven by a  $12 \times 12 \times 3$  mm magnet of remanence 0.2 T and relative permeability 1.28 at a top-centre distance of 4 mm under the top surface of the yokes.

Relative permeability of yokes	Mid-field (G)	Height above the yokes ( $\mu\text{m}$ )	Inner field (G)	Minimum field (G)	Maximum inside planar gradient (T/m)	Maximum outside planar gradient (T/m)
50	129	50	261	95.3	91.9	107.3
		100	185	101.6	45.2	42.3
		150	154	104.8	21.6	20.5
		200	140	107	12.4	13.9
100	125	50	322	78.5	134.5	139.7
		100	211.5	84.5	66.5	53.3
		150	166.5	89.2	31.8	27
		200	145.5	93.3	18.4	19.3
200	114	50	381.5	58.4	171.8	165
		100	238	66	85.5	60.3
		150	178.5	73	41	34.5
		200	151.5	79.5	23.8	25.7
400	112.5	50	430	41	199	182.5
		100	259	51	99.4	65.6
		150	189	60	47.8	40
		200	156	68.5	28.3	30.3
600	108	50	449	33.5	210.3	189.3
		100	268	44.5	105	68.9
		150	193	54.8	50.5	42
		200	158	63.8	30.2	32.1

of trapping, one might argue that the alignment required to produce these gradients is too difficult to make this scheme possible without complete dismantling of the in-vacuum apparatus. Fortunately, due to the dynamics of the lowest energy state of a magnetic yoke, the scheme is resilient to a small angular misalignment ( $< 20$  degrees) of the driving magnet. If one did not aim to perform the attachment as a retrofit, trapping in the low field region above one of the yokes would be the best option for initial operations after which shuttling to the higher field region would be used to access the high gradient assuming an axial alignment. This principal also presents an interesting comparison of the yoking scheme with permanent magnetic and current based gradient production methods for an x-junction trap as a flat bottom curve allows for two high gradient regions significantly far from the middle of a junction. Though this on-chip yoking scheme may not hold any great advantage for a linear trap, the field profile it produces may lend itself well to creating magnetic field gradients for more novel geometries.

Table 5.5: Simulation results for a set of yokes of width and length of  $0.9 \times 6$  mm separated by  $100 \mu\text{m}$  for different thicknesses. The yokes have a relative permeability of 200 and are driven by a  $12 \times 12 \times 3$  mm magnet of remanence 0.2 T and relative permeability 1.28 at a top-centre distance of 8 mm under the top surface of the yokes.

Yoke thickness (mm)	Mid-field (G)	Height above the yokes ( $\mu\text{m}$ )	Inner field (G)	Minimum field (G)	Maximum inside planar gradient (T/m)	Maximum outside planar gradient (T/m)
0.01	47	50	153	23.5	64	67
		100	96.4	26.5	35.5	24.9
		150	73	29.3	16.8	14.3
		200	61	31.9	10	10.1
0.1	37.5	50	163	8.6	65.5	64
		100	97.8	13.3	38.6	26.8
		150	69.3	17.6	19	17
		200	56.2	21.4	12.9	12.9
0.2	35	50	149.3	7	61	72.4
		100	87.3	11.7	35.6	23.9
		150	62.4	15.8	17.3	16.4
		200	50.8	19.5	10.8	12.7

### 5.2.5 High gradient regions on a junction

In this section I aim to discuss how on-chip yoking may be especially beneficial for creating axial gradients on x-junction traps due to the very different field profile when compared to other magnetic field gradient production methods. Though I will not discuss different schemes in detail, by using a one or three yoke scheme, one can create a high axial gradient in two opposite arms of an x-junction with a uniform low offset field region in arms perpendicular to these as illustrated in Figure 5.14. This allows ions to be shuttled through a near-constant magnetic field but also to perform entanglement operations, using the magnetic field gradients, at a sufficient distance from the junction for a uniform trapping potential.

The simulated magnetic field for a three yoke scheme is shown in Figure 5.15 both across and along the centre of the geometry. Given this field profile, such a scheme is perhaps advantageous for an x-junction trap as the high gradient region is suitably far from the centre of the junction. Contrary to other permanent magnet schemes using an axial gradient in one arm of a junction, this has a relatively flat bottom minimum at the junction position but does not require shuttling through a high field maximum in order to get to a high gradient region. Though not ideal, as there is no magnetic field nil in which a sharp, defined gradient is created, this well-shaped field profile may have its advantages for initial experiments involving quantum algorithms involving shuttling as there is no

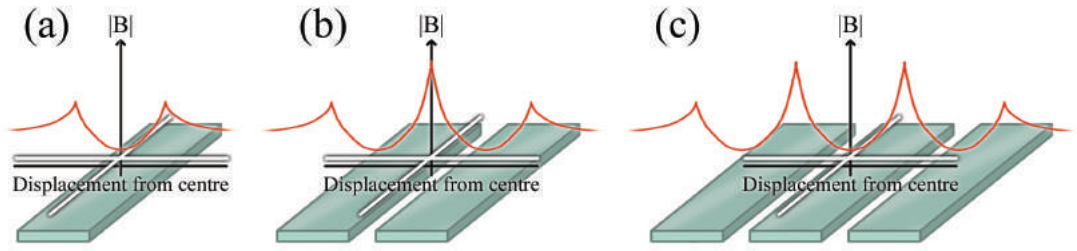


Figure 5.14: An illustration of the field profiles (red) for several different sets of yokes that may be used with an x-junction. The RF nil of the junction is shown in white. **(a)** - A single yoke with a single curved minimum that provides a low field region in the two arms parallel to the yoke length and a moderate axial gradient further into the arms across the yoke width. **(b)** - The normal two-yoke scheme which could sit displaced so that the junction sat directly over one of the yokes providing similar gradients to (a) but with a larger gradient in the arm going across the yoke separation. **(c)** - A three yoke scheme with the best features of (a) and (b), a high gradient in the two arms across the yoke separations and a low field in the arms parallel to the yoke length when centred over the central yoke. Notably, these yoke geometries do not require the ion to be shuttled through a region of high magnetic field at the junction position.

need for synchronous operation of current wires and compensation in order to produce a large gradient. Furthermore, there is no need to shuttle through high magnetic field regions during the algorithm operation.

These different scenarios for each field profile are illustrated in Figure 5.16. A graph which compares the field seen by an ion at an ion height of approximately  $100\text{ }\mu\text{m}$  on an x-junction is shown in Figure 5.17. Though dependent on the electrode geometry of the trap design, I have assumed that  $200\text{ }\mu\text{m}$  from the junction position (at a displacement of  $0\text{ mm}$ ) that the RF potential seen by a chain of ions will be uniform<sup>4</sup>. One can see that the offset field produced by the yoking scheme (red line) is less than half of that produced by the on-chip permanent magnets that are offset from the junction (green dashed line) though the gradient at the nil position is much greater than that produced by the yokes at  $50\text{ G}$  offset field. Alternatively, at  $200\text{ }\mu\text{m}$  from the junction, the centred on-chip permanent magnets (blue line) is sufficiently displaced from the magnetic nil that the gradient has significantly diminished and the gradient of the yokes for the same offset field is actually greater.

Given this, it is obvious that the centred on-chip permanent magnets are not the best scheme for this application, however, off-centre permanent magnets and yokes are very competitive in order to do fast shuttling operations. I have already stated that the on-chip permanent magnet simulations are quite optimistic, which means that with

<sup>4</sup>This has been ascertained from simulations of traps performed by other members of the group and discussions with those who have designed said traps.



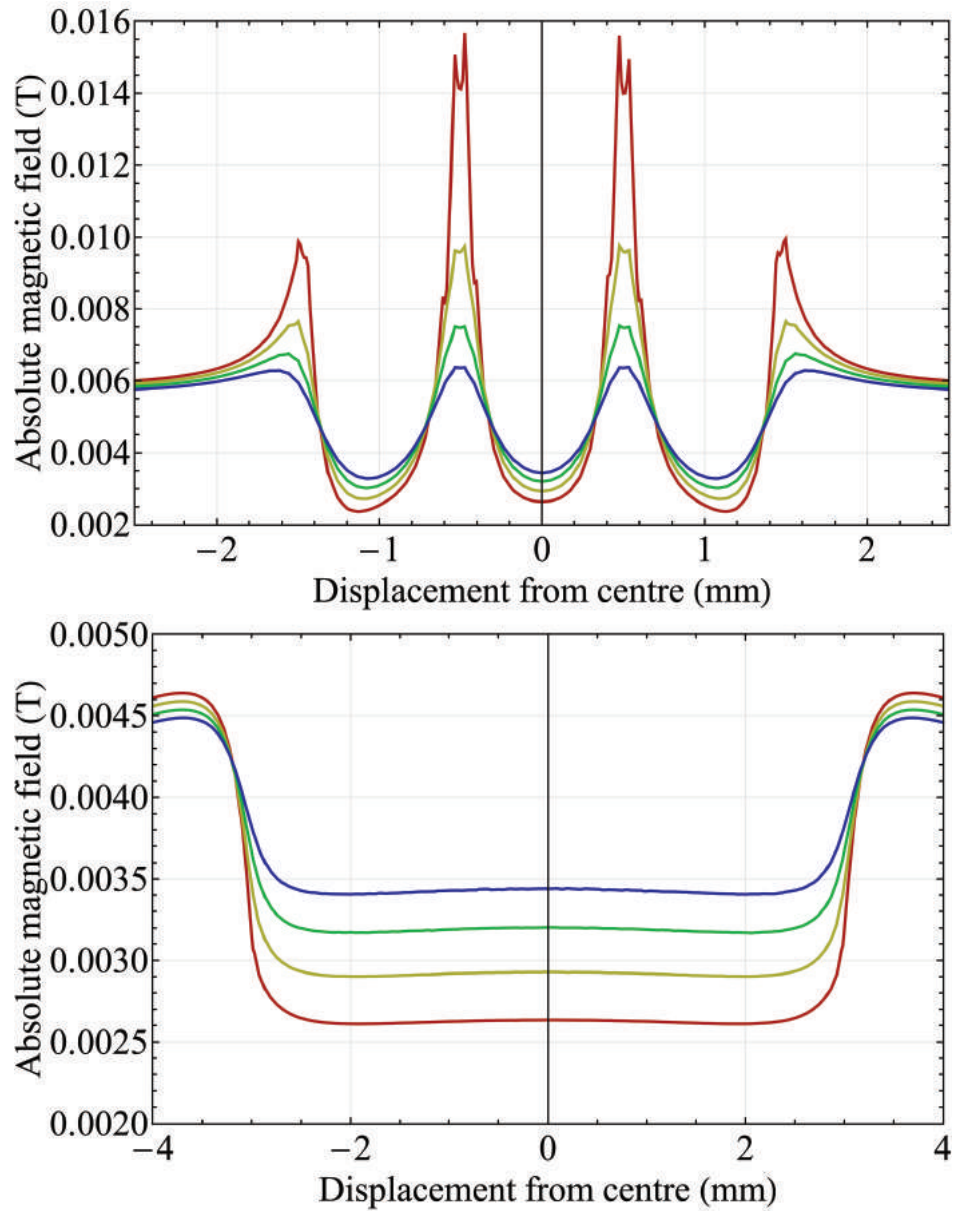


Figure 5.15: The magnetic field measured along the planar direction for a set of three yokes  $0.9 \times 6 \times 0.01$  mm with separations of  $100 \mu\text{m}$  from the central yoke and a relative permeability of 200. These are driven by a  $12 \times 12 \times 3$  mm magnet of remanence 0.2 T and relative permeability 1.28 at a distance of 8 mm under the yokes from their top surface to the centre of the driving magnet. The field is shown for several heights measured across (top) and along (bottom) the centre of the geometry. Red -  $50 \mu\text{m}$ , Yellow -  $100 \mu\text{m}$ , Green -  $150 \mu\text{m}$ , and Blue -  $200 \mu\text{m}$ .

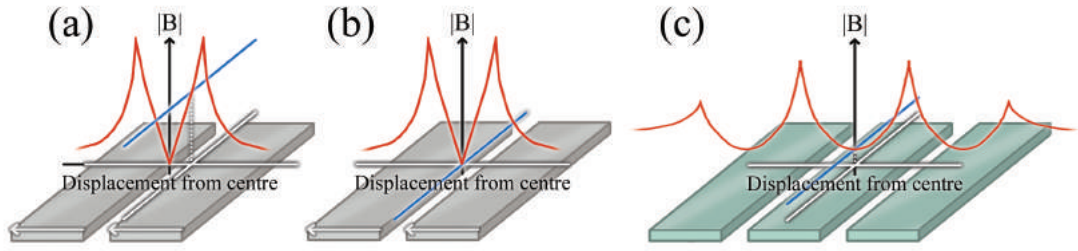


Figure 5.16: An illustrated comparison of the field profiles on an x-junction for on-chip permanent magnet and yoking schemes when an axial gradient is used. The field in the axial gradient arms and constant field arms are shown in red and blue respectively and the RF nil of the junction is shown in white. **(a)** - A high axial gradient with a magnetic nil point in one arm of the junction using on-chip permanent magnets. Though a high axial gradient is formed in one arm, the junction and arms perpendicular to this are in a very high offset field which will limit the speed of shuttling operations and make it difficult to cool the ion effectively during the operation. **(b)** - A high axial gradient on the junction using on-chip magnets aligned perfectly on the junction. Two arms of the junction are at near-zero field and there is no large offset to shuttle through at the junction. However, the axial gradient on the perpendicular arms is extremely high and the ion will sit at an extremely high field or outside of the optimum gradient region when shuttled at a sufficiently far displacement from the junction such that the RF potential is uniform. **(c)** - The three-yoke scheme aligned central to the junction. Two arms are at low non-zero field and the axial gradient gradually ramps as the ion is shuttled into the perpendicular arms. Though operations are done at slightly higher field than (a) or (b), the field near to the junction is relatively low and near constant allowing the ion to be with moderate gradient and in a stable RF potential for all operations without having to shuttle through a high magnetic field.

a higher permeability material, the three-yoke scheme is likely to be the best scheme, as the gradient would be higher with a lower offset field at the junction position. Since the field is near-constant at the junction, this also means that one would need to vary less parameters such as microwave frequency or compensation field if attempting to lower the offset magnetic field during the already complex shuttling operation in order to keep the ion suitably cooled. It will also be shown that these yokes can be switched off by using an electromagnet to drive them instead of a permanent magnetic field source. This makes the three-yoke scheme promising for an initial demonstrator experimental setup for entanglement operations on two opposite arms of the junction.

In addition to this, the three-yoke scheme provides an offset field that is very uniform along the low field arms meaning that many ions can be stored there using global microwave fields to aid laser cooling techniques when not being shuttled or coherently manipulated. The gradients produced by this three yoke scheme are displayed in Table 5.6.

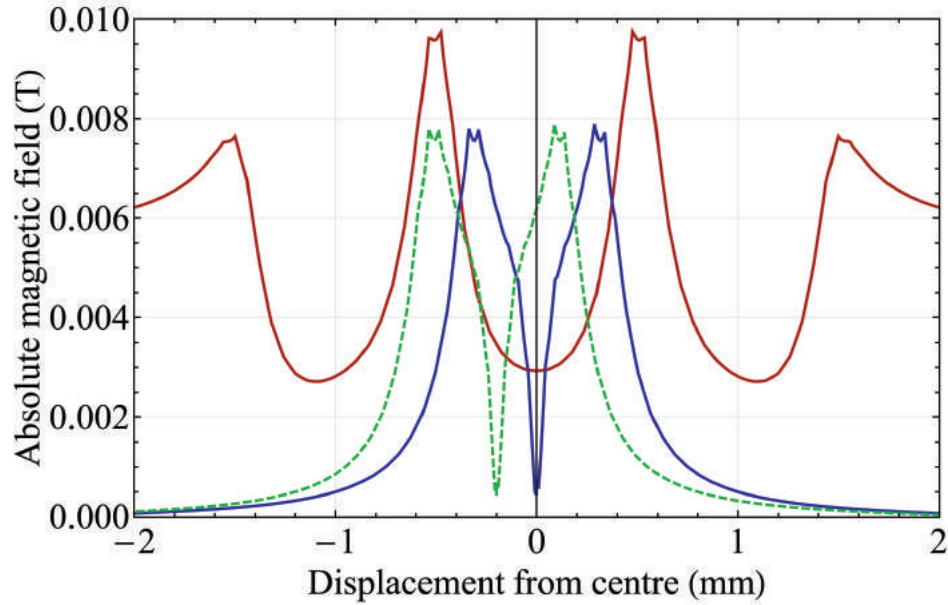


Figure 5.17: A comparison of the high axial gradient schemes that can be implemented with an x-junction trap using on-chip permanent magnets or yokes. Dashed Green - The field for a pair of on-chip magnets with in-plane magnetisation that create a nil point at  $98 \mu\text{m}$  above them (as previously described in this chapter) displaced  $200 \mu\text{m}$  off-centre, i.e. the field illustrated in Figure 5.16 (a), Blue - The same field as the green line but centred on the junction, i.e. the field illustrated in Figure 5.16 (b), and Red - The three yoke scheme displayed in Figure 5.15 for a height of  $100 \mu\text{m}$  above the yokes, i.e. the field illustrated in Figure 5.16 (c).

Table 5.6: Simulation results for a set of three yokes  $0.9 \times 6 \times 0.01 \text{ mm}$  separated by  $100 \mu\text{m}$  for an x-junction trap design. The yokes have a relative permeability of 200 and are driven by a  $12 \times 12 \times 3 \text{ mm}$  magnet of remanence  $0.2 \text{ T}$  and relative permeability 1.28 at a top-centre distance of  $8 \text{ mm}$  under the top surface of the yokes.

Height above the yokes ( $\mu\text{m}$ )	Maximum			
	Maximum	Minimum	inside	Gradient
	field	field	planar	at $48 \text{ G}$
	(G)	(G)	gradient	(T/m)
			(T/m)	
50	156.8	26.4	157.4	28.6
100	97.4	29.3	24.9	21.9
150	75	32	18.9	15.3
200	63.7	34.3	10.9	10.1

Though the gradients produced using this scheme do not surpass those of other methods discussed in this thesis, the effect is still interesting to note due to the ease of fabrication and operation. The ease of fabrication and activation of a gradient for an x-junction trap

using this scheme serves as a design of a proof of principal shuttling and quantum algorithm experimental setup. It is unlikely that this scheme would be used for high fidelity operation using the simulated geometries as the gradients are too low for sufficient coupling based on previous experience. However, the scaling of this scheme in terms of the gradient for a given offset field is arguably better than non-nilled parallel current carrying wires, and is thus worth noting. It will later become much more apparent why I am interested in on-chip yoking when I discuss on-chip hybrid systems using a combination of yokes and current carrying wires. However, the aforementioned scheme is the first stepping stone towards the design of a hybrid system and must therefore be explained in detail.

### 5.2.6 Remote yoke excitation using electromagnets

The inability to compensate the magnetic field while retaining the gradient potentially poses a large hindrance to experimental control of the ion as one is unable to choose the desired splitting of the  $^2S_{1/2}$ ,  $F = 1$  states which is particularly important in the manipulation of the microwave qubit. This can be solved by using an externally controllable yoked electromagnet in order to activate the on-chip yokes as and when required, instead of an under-chip permanent magnet. This electromagnet would be constructed underneath the chip in the vicinity of the copper spacer and for the purpose of my simulations has been designed to have a nickel core of radius 3.5 mm with 100 turns of thin wires around it for a length of 12 mm. When sitting 5 mm below the chip, simulations indicate a much better scaling than the permanent magnet case though the gradients at lower heights are lower. This geometry is shown in Figure 5.18 with the yoke dimensions for the simulation results displayed in Table 5.7, which shows the simulated gradients measured at the 45 G/A mark for two yokes  $0.9 \times 6 \times 0.01$  mm with a central gap of 200  $\mu\text{m}$  and a relative permeability of 200. The simulated fields at several heights above the yokes are shown in Figure 5.19 in order to see if there is a significant difference with the field profiles of yokes activated using a permanent magnet.

One can see that within this range of ion heights the gradient appears to only halve every additional 100  $\mu\text{m}$  above the yokes, much better than the scaling for any other on-chip gradient production method where a limit, be that the offset field that can be compensated or the current that can applied, was not put in place. The main problem is that we are limited by the 45 G/A field that the gradient is measured at, however, improvement of the yoke dimensions should help to make this lower.

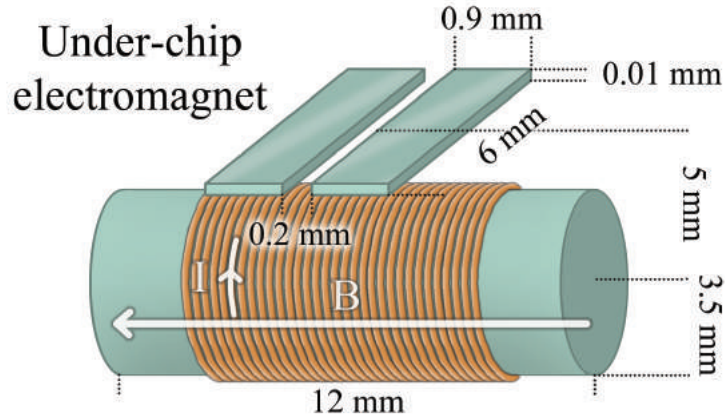


Figure 5.18: The geometric configuration for the pair of yokes driven by an under-chip electromagnet which is simulated in this section. The electromagnet replaces the under-chip permanent magnet so that one can have switchable or adjustable gradients.

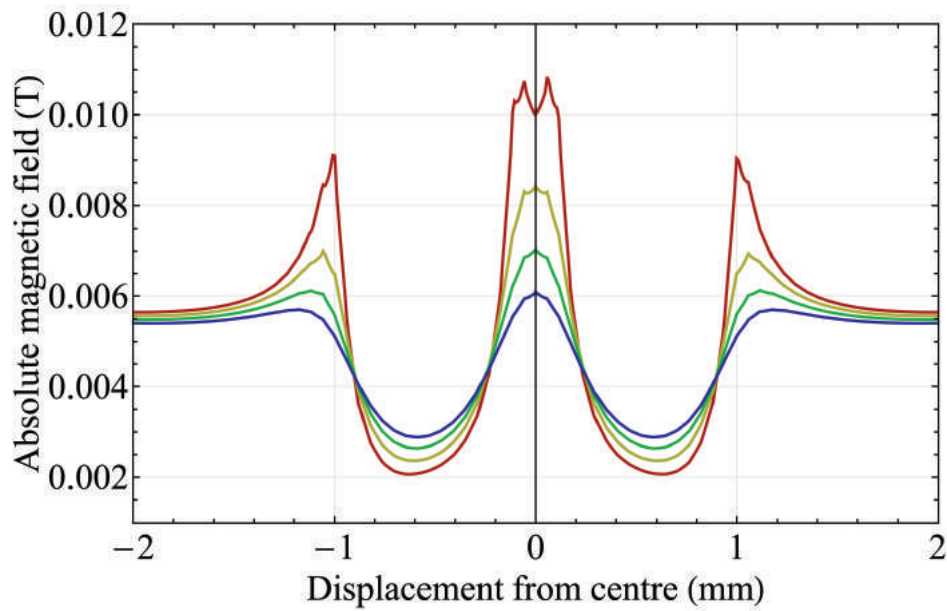


Figure 5.19: The magnetic field for a pair of yokes  $0.9 \times 6 \times 0.01$  mm with a separation of  $200 \mu\text{m}$  and a relative permeability of 200. These are driven by a nickel core electromagnet of radius 3.5 mm with 100 turns of wire for a length of 12 mm at a distance of 5 mm under the yokes from their top surface to the centre of the electromagnet. The field for 1 A of applied current is shown for several heights measured across the geometry. Red -  $50 \mu\text{m}$ , Yellow -  $100 \mu\text{m}$ , Green -  $150 \mu\text{m}$ , and Blue -  $200 \mu\text{m}$ .

Activation of the yokes using a remote electromagnet shows one effect that has not yet been discussed in this thesis, namely that one can have significant switchable magnetic field gradients without the use of on-chip currents. This therefore means that the time that a gradient can be activated is much longer than with current carrying wires as there is very little risk that the current wires would melt. This also means that the magnetic profile created by the yokes can be thoroughly investigated at room temperature using a

Table 5.7: Simulated gradients measured at the 45 G/A mark for a pair of yokes of relative permeability of 200 activated using a 3.5 mm diameter, 100 turn electromagnet 5 mm below them.

Yoke dimensions (mm)	Separation ( $\mu\text{m}$ )	Height above the yokes ( $\mu\text{m}$ )	Planar gradient (T/m/A)
$0.9 \times 6 \times 0.01$	200	50	30.6
		100	20.6
		150	15.3
		200	10.3

similar CNC setup as discussed in Chapter 4. One could also experiment with different profiles of electromagnet in order to drive the yokes. Due to complications when trying to simulate square coils in COMSOL, I have only managed to simulate one that is round for the results shown in this thesis. Nevertheless, since this design is made independently from the on-chip yokes, by using a similar magnetic field profile measurement method as that documented in Chapter 4, one could build several different activation electromagnets outside of vacuum and measure the resultant magnetic field profile in conjunction with on-chip yokes. The design of this activation electromagnet can then be developed in order to improve the gradients produced using this scheme.

Of course, since this is not fully self contained on the chip, this is not the best candidate for a scalable system as it requires peripheral activation of the yokes, but this is no different to the compensation coils required in order to nil the field of the anti-parallel current carrying wire scheme. The obvious adjustment to this scheme to improve scalability would be to activate the yokes using on-chip current carrying wires underneath them. This should allow for a similar switchable magnetic field gradient as the above scheme. However, complications arise as the current wires have a much more complex near-field in the region of the yokes resulting in a slightly different field profile and gradient scaling with regards the remotely activated yoking scheme. This will be discussed in the next section which serves as the next stepping stone towards our final result.

### 5.2.7 On-chip yoke excitation using current carrying wires

The next logical step in order to move towards a scalable system is for yokes to be activated using on-chip current carrying wires. This would mean that the scheme is fully self contained with no peripheral magnetics. As it stands, there are two possible options for the fabrication of current carrying wires under the yokes using this scheme. These are; direct deposition on a layer fabricated underneath the yokes, or by fabricating them on

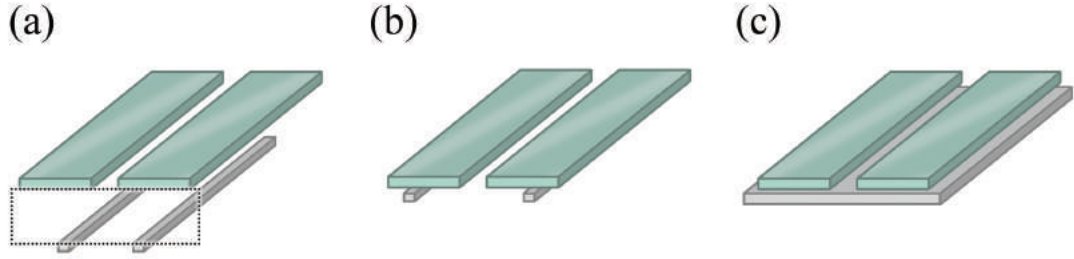


Figure 5.20: Three configurations of under-yoke current wires that could be used in order to activate them using solely on-chip field sources. **(a)** - Current wires fabricated on the underside of the substrate. Though easier to fabricate, the current required to drive the yokes is greater and individual adjustment of the yoke magnetisation is difficult due to their distance from the yokes. **(b)** - Directly under-yoke current wires fabricated on the top side of the substrate. These allow for minimal activation current and very good individual control of each yoke's magnetisation provided they have a sufficient separation. **(c)** - A single large current wire fabricated on the top side of the substrate directly under the yokes. Though individual control is no longer possible, the field is uniform through both yokes resulting in a field profile slightly closer to the under-chip magnetic yoking schemes.

the under-side of the chip substrate as shown in Figure 5.20.

I will first consider a two wire case as this allows for individual adjustment of the activation field for each yoke when using the under-yoke set of wires and therefore should give us better control of the gradient and offset field at the ion. The results from simulations of scenarios (a) and (b) of Figure 5.20 are shown in Table 5.8 with one set of wires on the backside of a  $550\ \mu\text{m}$  thick substrate and another set buried  $65\ \mu\text{m}$  under the electrode layer. The magnetic fields of both these cases are shown in Figures 5.21 and 5.22 respectively.

One can see that both cases produce similar gradients for a given offset field, however, more field/gradient per current is produced by the closer wires, namely due to the close proximity to the yokes. That said, if the wires are fabricated directly under the yokes, they must be sufficiently far apart in order to achieve a uniform field distribution across the geometry. This is most likely due to the near field effects of the two-wire geometry that is closer to the yokes (Figure 5.20 (b)). So long as this separation is sufficient, the inner and outer gradients are approximately the same. Understandably, this would imply that a single yoke is sufficient for creating the gradient, however, by using two independently activated yokes, one has greater control over the field at the ion position. However, this independent control is only applicable to wires fabricated directly under each yoke (Figure 5.20 (b)) as the field above wires fabricated on the underside of the chip (Figure 5.20 (a)) will be almost uniform at both yokes. This assumes that the wires



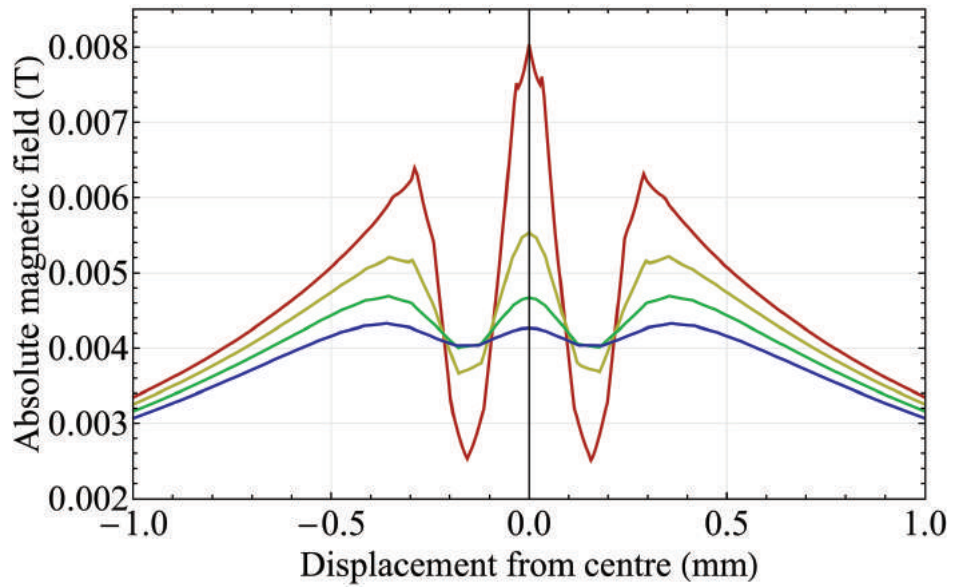


Figure 5.21: The magnetic field for a pair of yokes  $0.2 \times 6 \times 0.02$  mm with a separation of  $80 \mu\text{m}$  and a relative permeability of 200. These are driven by a pair of current carrying wires  $0.2 \times 6 \times 0.03$  mm with a centre-centre separation of  $240 \mu\text{m}$  at a distance of  $0.565$  mm under the yokes from their top surface to the centre of the wires. The field for  $10$  A of applied current is shown for several heights measured across the geometry. Red -  $50 \mu\text{m}$ , Yellow -  $100 \mu\text{m}$ , Green -  $150 \mu\text{m}$ , and Blue -  $200 \mu\text{m}$ .

are quite close together under the centre of the yoke separation as one would expect that there would be a significant out-of-plane field component at the yoke position if only one of the wires had a current flowing through it. The advantage of having two wires on the underside of the substrate (Figure 5.20 (a)) is therefore that one would be able to create a more uniform field at the yoke position which may improve the field profile produced.

Logically, these effects are not observed when using a single activation wire (Figure 5.20 (c)) so long as it is wider than the yokes so that they have a more uniform magnetisation. The magnetic fields for two yoke sizes using a single current wire to drive them are shown in Figure 5.23. Again, the fields/gradients produced for a given current are very similar in this case to the two-wire scenario, however, for the wider yokes, the field is significantly less uniform, hence I have documented both the inner and outer fields and gradients (with the same definitions as Figure 5.11) in Table 5.9. This is because the internal magnetisation of the larger yokes is non-uniform due to the current wire being a similar size to the yoke geometry.

On-chip current carrying wires are therefore sufficient for producing the activation field for yokes fabricated above them if desired for the experimental application whether driven by a single wire or by a pair of wires, with gradients that are quite competitive with those of the off-chip driving sources, especially at lower ion heights.



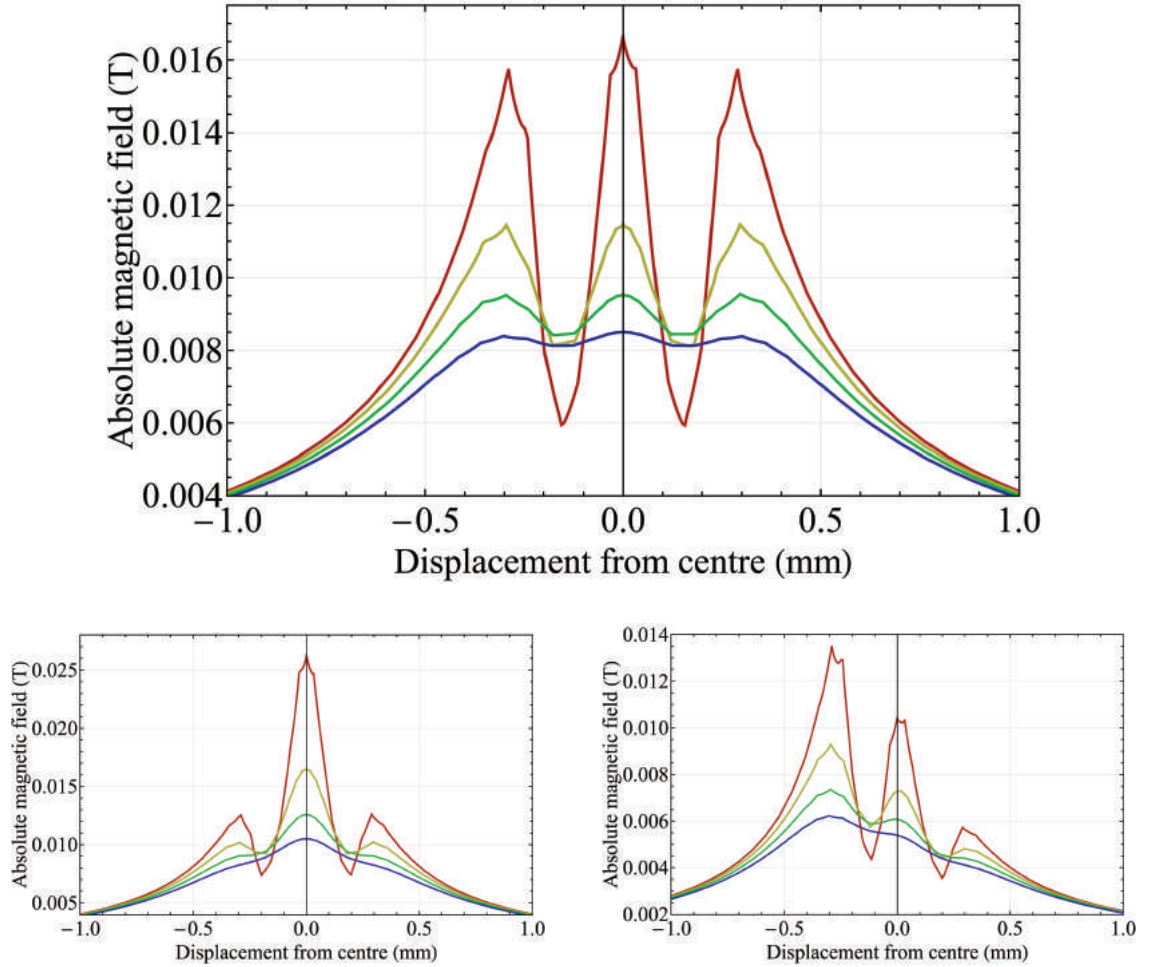


Figure 5.22: The magnetic field for a pair of yokes  $0.2 \times 6 \times 0.02$  mm with a separation of  $80 \mu\text{m}$  and a relative permeability of 200. These are driven by a pair of current carrying wires  $0.1 \times 6 \times 0.03$  mm with a centre-centre separation of  $360 \mu\text{m}$  (top) and  $220 \mu\text{m}$  (bottom left) at a distance of  $65 \mu\text{m}$  under the yokes from their top surface to the centre of the wires. The top geometry was also simulated with  $\frac{1}{5}$  the current in the right wire as shown in the bottom right graph. This shows that there is significant independent control of each yoke's activation which can be used to tailor the field and gradient at the ion position. The field for 10 A of applied current is shown for several heights measured across each geometry. Red -  $50 \mu\text{m}$ , Yellow -  $100 \mu\text{m}$ , Green -  $150 \mu\text{m}$ , and Blue -  $200 \mu\text{m}$ . One can see that the closer and less centrally located under each yoke the wires are, the less uniform the field profile becomes which produces lower gradients at high ion heights and a greater offset field at the minima.

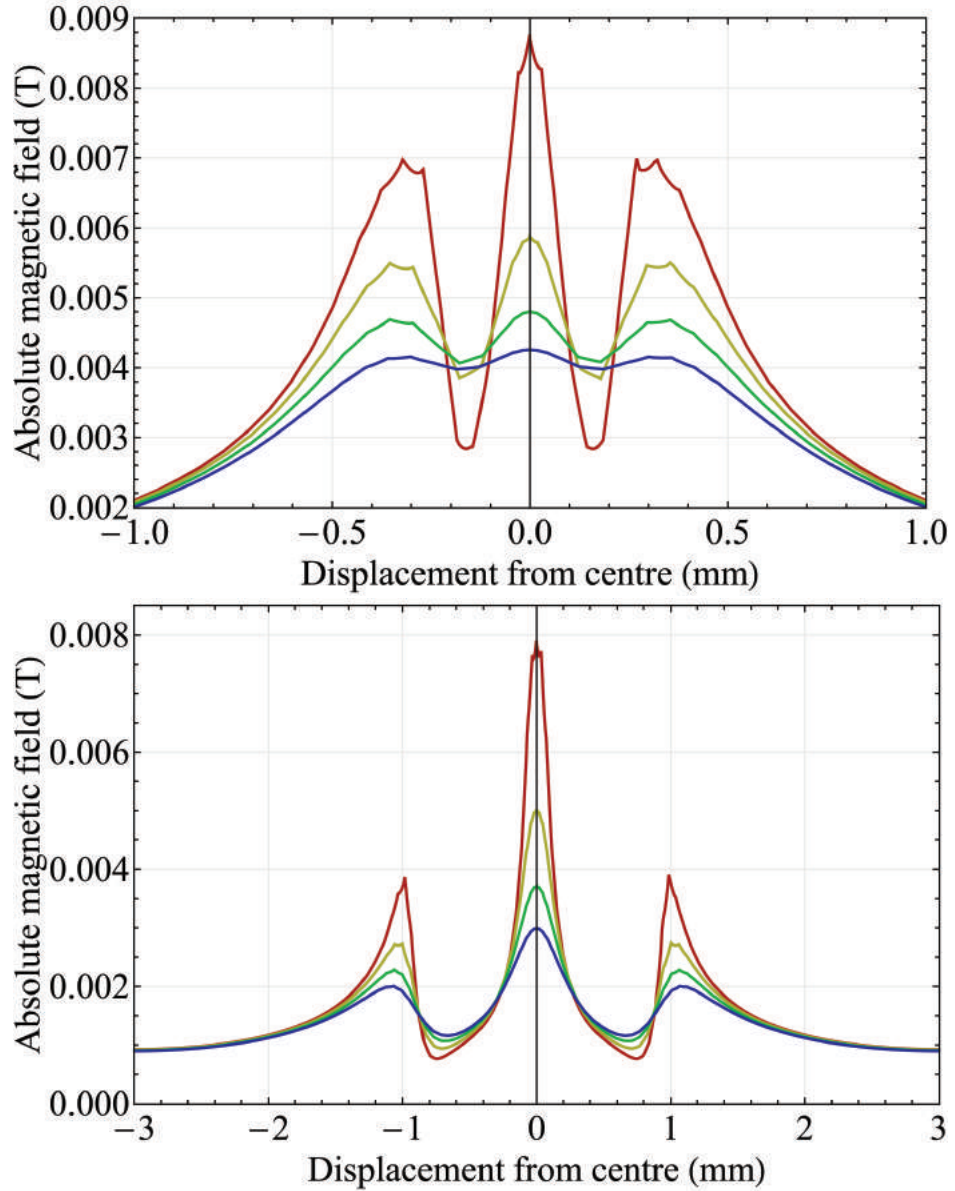


Figure 5.23: The magnetic field for a pair of yokes  $0.2 \times 6 \times 0.02$  mm with a separation of  $80 \mu\text{m}$  (top) and  $0.9 \times 6 \times 0.02$  mm with a separation of  $100 \mu\text{m}$  (bottom) each with a relative permeability of 200. These are driven by a single current carrying wire  $0.8 \times 6 \times 0.03$  mm (top) and  $2 \times 6 \times 0.03$  mm (bottom) at a distance of  $65 \mu\text{m}$  under their respective yokes from their top surface to the centre of the wires. The field for 10 A of applied current is shown for several heights measured across each geometry. Red -  $50 \mu\text{m}$ , Yellow -  $100 \mu\text{m}$ , Green -  $150 \mu\text{m}$ , and Blue -  $200 \mu\text{m}$ .

Table 5.8: Simulation results for a pair of yokes  $0.2 \times 6 \times 0.02$  mm separated by  $80 \mu\text{m}$  with a relative permeability of 200 driven by a pair of parallel current carrying wires fabricated on the chip.

Wire size (mm)	Wire separation (mm)	Centre distance under top of yokes (mm)	Height above the yokes ( $\mu\text{m}$ )	Inner field (G/A)	Minimum field (G/A)	Inside planar gradient (T/m/A)	Inner field at which the gradient is measured (G/A)
$0.2 \times 6 \times 0.03$	0.24	0.565	50	8.04	2.53	4.83	4.2
			100	5.53	3.66	1.83	4.1
			150	4.67	4	0.64	4.3
			200	4.27	4.03	0.22	4.15
$0.1 \times 6 \times 0.03$	0.36	0.065	50	16.68	5.95	9.05	9.5
			100	11.45	8.13	3.16	9.2
			150	9.52	8.42	1.03	8.8
			200	8.5	8.13	0.36	8.3

Table 5.9: Simulation results for a pair of yokes with a relative permeability of 200 driven by a single current carrying wire fabricated on the chip at a central separation of 0.065 mm from the top surface of the yokes.

Yoke size (mm)	Yoke separation (mm)	Wire size (mm)	Height above the yokes ( $\mu\text{m}$ )	Inner field (G/A)	Minimum field (G/A)	Inside planar gradient (T/m/A)	Inner field at which the gradient is measured (G/A)	Outside planar gradient (T/m/A)	Outer field at which the gradient is measured (G/A)
$0.9 \times 6 \times 0.02$	0.1	$2 \times 6 \times 0.03$	50	7.9	0.77	4.4	4.5	2.47	1.8
			100	5.02	0.94	1.89	3.8	1.18	1.8
			150	3.7	1.07	0.84	2.6	0.61	1.7
			200	2.99	1.16	0.52	2.4	0.35	1.6
$0.2 \times 6 \times 0.02$	0.08	$0.8 \times 6 \times 0.03$	50	8.77	2.84	5	4.5		
			100	5.87	3.85	1.82	4.5		
			150	4.8	4.07	0.67	4.4		
			200	4.25	3.98	0.24	4.15		

### 5.2.8 Reflections on gradients produced by on-chip yoking

In a general sense, on-chip yokes do not necessarily hold any advantages over other methods of on-chip gradient production in terms of the magnitude of gradient. Nevertheless, investigation of this gradient production method has given a good insight into hybrid gradient productions which have not been documented previously. A summary of findings from my investigations is detailed below:

- Initial simulation results for nickel yokes using electroplating have a distinct advantage due to the simplicity of implementation as they do not require large offset fields (current carrying wires) or much deeper investigation into fabrication techniques (on-chip magnets).
- Field profiles can be improved by using higher permeability yokes but do not necessarily require yokes that are thicker than those that can be easily electroplated.
- Highest gradients are best produced at low ion heights, however, those at higher positions could be improved through advances in material fabrication techniques.
- The curved shape of the field profile may be advantageous over a sharp nil point for x-junction axial gradients and could be a simple way of creating an on-chip gradient for a proof of principle shuttling algorithm experiment with entanglement capabilities.
- Using yokes with on-chip activation improves the scaling of the gradients with respect to the offset fields though in-vacuum activation using an electromagnet is also very promising. Additionally, alignment of in-vacuum driving magnetics is not as stringent due to the magnetic axes of the yokes and thus a high precision alignment procedure is not strictly required.

The ability to activate an on-chip gradient using an off-chip source is still an exciting prospect, however, the use of yokes in general paves the way for hybrid geometries exhibiting the best features of a permanent magnetic scheme using currents as a mediator for the field at the ion position.

Due to the nature of the gradients being not what is typically desired for an entanglement setup it is perhaps best to use this form of on-chip yoking outside of the scalable architecture for more novel experiments such as those described in conjunction with an x-junction trap. However, if the gradients producing this method can be significantly improved, on-chip yoking may find its place in the scalable quantum computer.

### 5.3 Self-compensation of current carrying wires using simultaneously driven yoked electromagnets

We now arrive at the final result for this chapter which would only have been possible through the investigation of on-chip yoking and the integration of said yokes with current carrying wires. I will now discuss a hybrid scheme which utilises electromagnetic yoking in combination with current carrying wires in order to produce a current-controllable, high magnetic field gradient which is centred on a point of zero magnetic field which can be aligned to the ion position. This scheme exhibits the best qualities of all the schemes discussed in this thesis thus far by having the high magnetic field gradient profiles exhibited by permanent magnetic and nilled current wire schemes with the ability to adjust the gradient without having to worry about synchronous field nilling.

While attempting to optimise the gradient for the under-yoke two-wire activation scheme, I noticed that the natural magnetic field nil between the current wires appeared to be displaced downwards from the expected central position. By flipping the magnetic layers of the chip and re-evaluating the simulation to make sure this was not a boundary effect, I realised that the natural gradient produced at the central nil point between two parallel currents could be significantly displaced such that a high gradient nil could be created at the ion position.

#### 5.3.1 How self-compensation works

Broken down into the individual components, self-compensation of current carrying wires works as follows. An illustration of each effect is shown in Figure 5.24 to aid in describing this phenomenon.

A pair of current carrying wires with parallel currents running through them creates a high gradient nil at the centre of their separation as shown in Figure 5.24 (a).

When a high magnetic permeability material sits in the presence of a current, a strong electromagnet is created and the magnetic field propagates through the yoke material as this is the minimum energy state. If a thin plate of this magnetic magnet material has a current wire running on top of it, the magnetisation will be in-plane as shown in Figure 5.24 (b).

Additionally, two magnetic plates with a small separation between them in the their magnetisation direction will cause the field between them to bow upwards and outwards as it is no longer confined to the volume of the material as shown in Figure 5.24 (c).

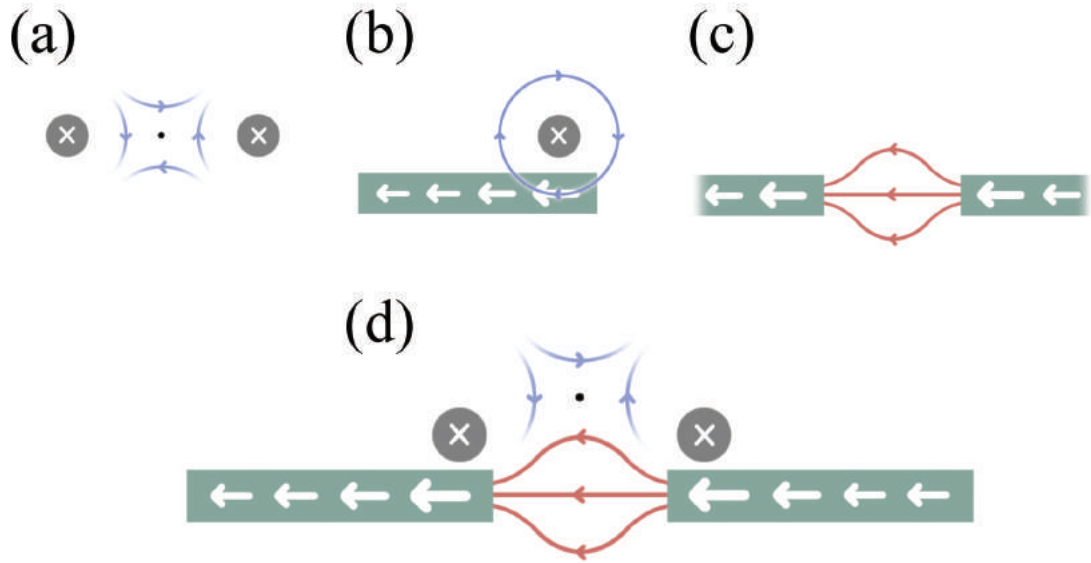


Figure 5.24: An illustration of the method by which the natural nil position of two parallel current carrying wires can be displaced from their centre of separation using yokes. **(a)** - Two parallel current carrying wires (grey) with currents directed into the page resulting in a central nil point between them. The field of the wires near to this nil is shown in blue. **(b)** - A single current wire activating a yoke (green) underneath it. The field from the wire is amplified due to the high relative permeability and propagates along the length of the yoke. **(c)** - The external near-fields between two separated yokes (red). The fields bow outwards as they are no longer guided by the high permeability material. **(d)** - The sum of these phenomena. The yokes are activated by the current wires and their external field forces the high gradient nil of the current wires upwards as the field from the separated yokes opposes that of the wires above the natural nil position.

Combining all these points, two current wires can be used to drive two yoked electromagnets simultaneously creating a high magnetic field gradient about a nil whilst increasing the internal magnetisation of the yokes. As the magnetisation increases, so does the gradient, but the field produced from the separation of the yokes opposes the field above the natural high gradient nil between the parallel currents. This results in a shift in the natural nil position upwards, but the position is constant for a given geometry. This is because the opposing field from the yokes is created at the same rate of growth as the gradient around the nil as they are both mediated by the current. This combined effect is shown in Figure 5.24 (d).

This means that a nil will be created at a set height above the wires as the compensation field from the yokes is generated by the same field that creates the high gradient and therefore moves in perfect synchronicity throughout the ramping process of the current in the wires. In this case, the height of the nil is determined by the separation of the wires and associated yokes, their thickness, and the permeability of the yoke material. This provides a solution to the problem of having to compensate the large offset fields in

the current carrying wire schemes discussed in Chapter 3, both in the sense of generating the compensation field and the synchronous ramping during the gradient activation pulse. Not only this, but this solution is compact and on-chip meaning that it should be scalable to large systems.

### 5.3.2 Initial simulation results

The two-dimensional magnetic field diagram for a self-compensating wire setup is shown in Figure 5.25 for the first entry of Table 5.10 at the end of this section. Table 5.10 displays the simulated gradients produced from various geometries using this scheme. The field measured along the vertical radial direction and across the geometry at a height of  $55\ \mu\text{m}$  above the top surface of the current wires are additionally shown in Figure 5.26 indicating a vertical gradient of  $15.9\ \text{T/m/A}$  and a planar gradient of  $19.9\ \text{T/m/A}$ . These are extremely promising given the extremely raw nature of this scheme at present

The magnetic field gradients created using this scheme are defined similarly to the gradient created by the nilled two parallel current wires or the under-chip magnet scheme discussed in Chapter 3. The vertical radial gradient is defined as  $\frac{dB_x}{dz}$  and the planar radial gradient can be approximated as  $\frac{dB_z}{dx}$  near to the nil position but becomes  $\frac{d|B|}{dx}$  as one moves away from this point due to the growing  $B_x$  term.

### 5.3.3 Design and fabrication factors for the self-compensating scheme

Now that we have seen an initial simulation, it is important to consider how the scheme can be further improved and how changing certain parameters affects the nil height for a given separation of the wires, and the gradient at said nil position.

The permeability of the yokes is the primary matter of importance in the alignment of the magnetic nil to the RF nil, i.e. the ion position. Trivially, the lower the relative permeability, the lower the nil position as yokes with a relative permeability of 1 (non-magnetic) would result in no shift of the nil position from between the wires. With high relative permeability (greater than 2000), the nil position approaches a limit set by the dimensions and separation of the current wires and associated yokes. In this case, one would ideally want the yokes to be constructed from a high permeability material such as permalloy. As previously discussed, this has been shown by Park and Allen [71] to be able to be fabricated at a thickness in the realm of tens of microns, however, simulations show that nickel works suitably well for this application with a relative permeability of 200. That said, this permeability is only an approximate value based on the properties of



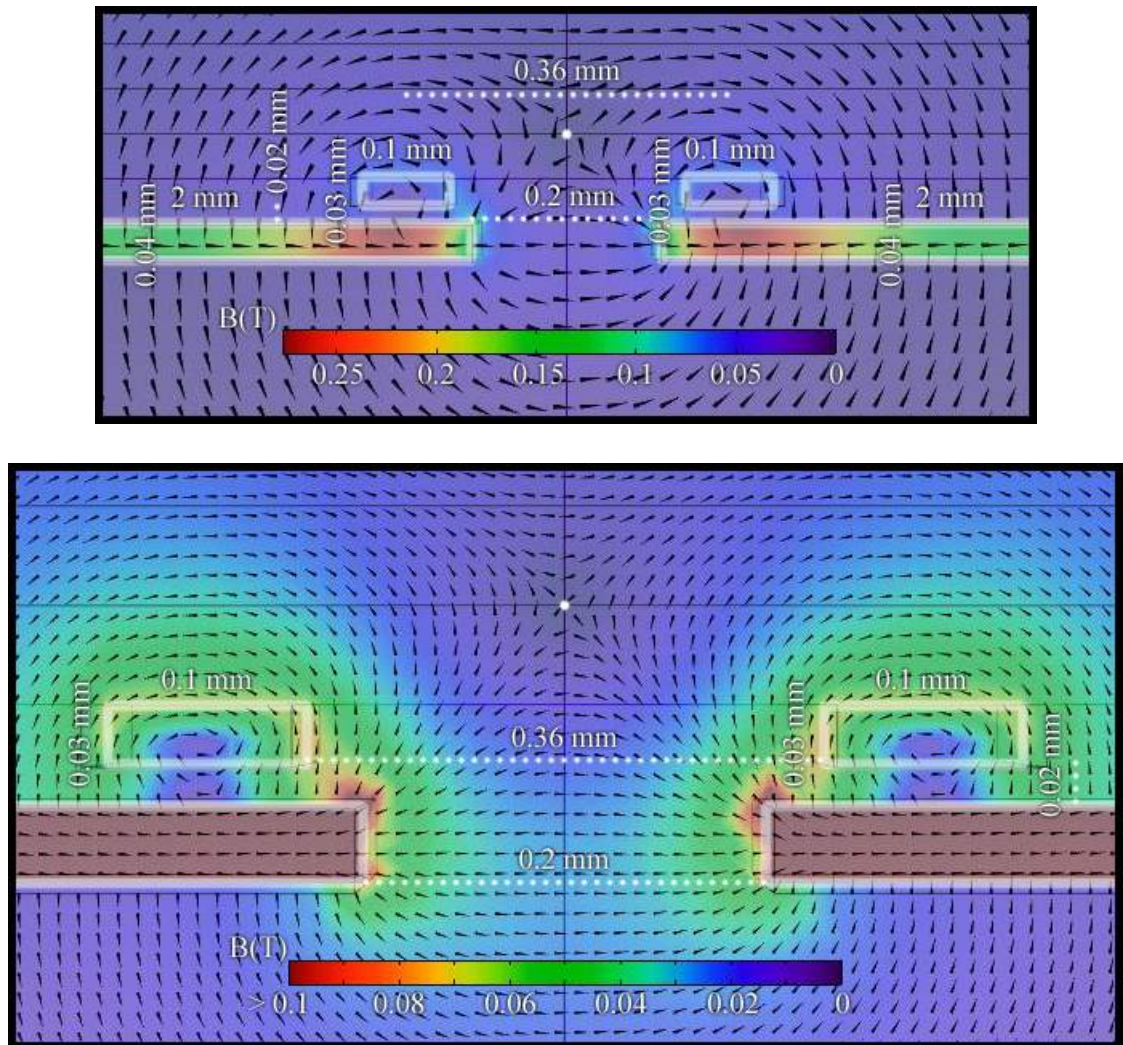


Figure 5.25: The field diagram for a set of self-compensating buried current carrying wires using simultaneously activated yokes. The natural nil position is shifted by the fields from the yokes to 55  $\mu\text{m}$  above the top of the current wires. The top image shows the internal magnetisation of the wide yokes underneath the current carrying wires. The internal magnetisation is strongest at the point just under the current wire but propagates at high field strength along the length of the yoke. The bottom image shows the field closer to the nil scaled so that one is able to see the relative field strength external to the yokes. The simulated length of the wires and yokes is 6 mm.

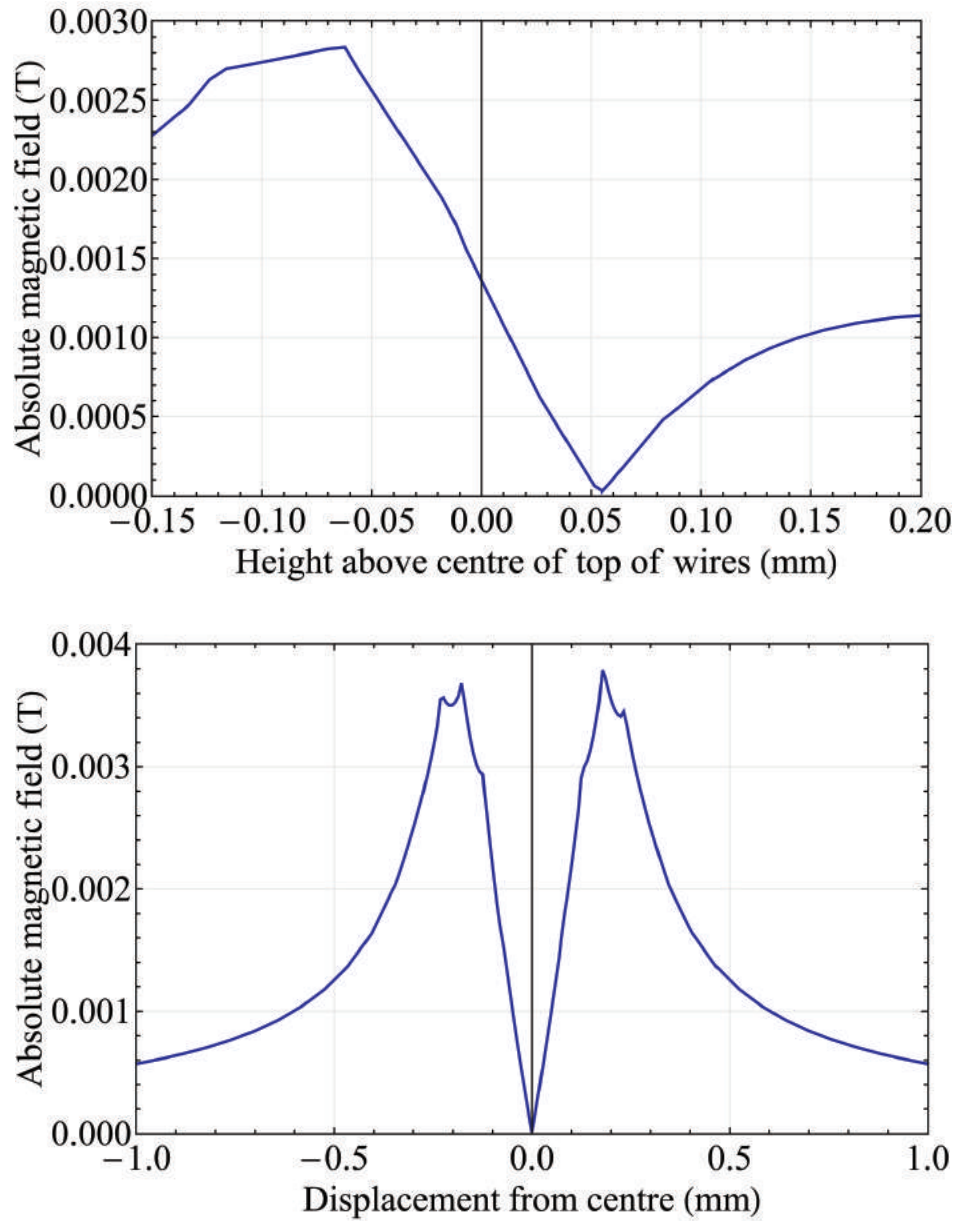


Figure 5.26: The field measured along the vertical radial direction (top) and along the planar direction at a height of  $55\ \mu\text{m}$  (bottom) across two current wires  $0.1\ \text{mm}$  by  $6\ \text{mm}$  by  $0.03\ \text{mm}$  ( $x$  by  $y$  by  $z$ ) centre separated by  $0.36\ \text{mm}$  (along  $x$ ) and carrying  $1\ \text{A}$  of current each flowing parallel to each other.  $20\ \mu\text{m}$  underneath these wires are two  $40\ \mu\text{m}$  thick yokes with a relative permeability of 2000 overhanging the wires by  $30\ \mu\text{m}$  as shown in Figure 5.25.

bulk nickel and may not be representative of the relative permeability of a fabricated film. This means that in order to determine the nil height for a chip that is fabricated above it, one would need to fabricate test samples of the yokes and determine their permeability experimentally for the given fabrication process. This is much less of an issue for permalloy as the permeability is high enough to be near enough to the maximum nil height that the alignment error is minimal and can be corrected using methods which will be described later in this section.

The yokes have been simulated as 2 mm wide as this allows the effective length of the electromagnet to increase with the current as the propagation of the internal magnetisation is strengthened. This phenomenon is identical to the effect shown in Figure 5.6 on page 265 using a spanner as the electromagnetic yoke. In a similar way to the relationship between the nil height and the relative permeability, this yoke length was determined to be such that a further increase would have little to no increase in the nil height. This therefore provides the highest nil height for a given current wire separation and therefore the highest gradient for a set yoke and wire thickness and the out-of-plane distance between them.

In general, the thicker the yoke, the larger the compensation field produced and therefore the higher the nil height for a given separation of current wires. Since the current wires are the component of this scheme that creates the high gradient, this means that for thicker yokes there is a stronger gradient produced for a given ion height. Understandably, this means that a thick, high permeability yoke is the ideal structure under each wire, but in practice one is limited by the material that one can fabricate and the possible thickness achievable using this method of deposition. Moreover, depending on the relationship between thickness and relative permeability, there will inevitably be a trade-off if there is a strong inverse proportionality. This thickness is also limited by the initial etch into the substrate in order to deposit the material if this is the preferred fabrication method. These limits and properties would have to be determined before designing the electrode structure of the chip as the yoke thickness in combination with the wire dimensions and the associated separation will determine the height of the magnetic nil to be matched to the ion height.

Though the wire size in the current carrying wire scheme was required to be minimal in order to get the highest current density in the wires, this is less of an issue in this scheme as we are mainly interested in the gradient created in-between the wires rather than the gradient created above them. This is because the gradient in the current carrying wire scheme is determined by the ability to nil the field at a certain point for a given

magnitude of magnetic field that can be externally compensated. This is contrary to the self-compensating wires scheme as it is mainly the yoke geometry that determines the relationship between the separation of the wires and the height above them where a nil is formed. Therefore, the separation of the wires is the main determining factor for the high gradient. Additionally, by making the wires flatter and wider (within reason for fabrication ease), one can apply more current to them as there is a greater thermal contact with the substrate in order to cool them and a greater amount of in-plane field in order to activate the yoke. In this case, flatter wires allow for a closer positioning of the yoke to the possible ion positions and therefore the field can be compensated at a greater height above them.

From a fabrication standpoint, the main difficulty in making this scheme a reality would be that the wires have to be fabricated on top of the yokes and subsequently the electrodes have to be fabricated on top of these. Since the yokes are buried but very large, an insulating layer at least as thick as the current carrying wires has to be fabricated smoothly without voids on top of them before the electrode layers can be fabricated. In theory, the closer the yokes to the wires in the out-of-plane direction, the higher the height of the compensated nil and therefore the better the gradient defined by the separation of the current wires. However, the nickel yokes should also be electrically isolated from the wires so that they do not redirect any of the current. This means there must be a good insulating layer between them, however, since the current wires are above the yokes, this could mean that there is poor thermal conductivity away from the wires, thus limiting the current that can be applied to them and therefore the gradients that can be achieved. By fabricating an extremely thin (100 nm) insulating layer of silicon nitride on top of the yoke before depositing the current wire, this should enable adequate electrical isolation but still retain the benefits of good thermal conductivity for heat sinking. However, one concern would be that this temperature would negatively impact the internal magnetisation of the yoke but since an external field is in place, this should not create enough thermal excitation of the magnetic spins to disable magnetisation. Instead of providing a similar effect to increasing the temperature over the Curie temperature for a permanent magnet, this may put the yoke in a similar situation to a high temperature anneal, changing the properties of the yoke material such that it holds a significant remanent field. In this eventuality, the yoke would require degaussing after each activation in order to remove this remanence.

### 5.3.4 Additional offset field compensation using the self-compensating scheme

Though there is not likely to be any misalignment in the nil position due to the fact that this is a microfabricated scheme, one still may need to compensate offset fields produced externally from the experiment. Due to the use of yokes in this scheme, external compensation is not recommended as they will affect the gradient production method. However, field compensation can be addressed using additional current wires further from the centre of the geometry serving to boost the compensation power or allow for higher nil heights. This aids the alignment of the internal spins further along the yoke, thus allowing for adjustment of the in-plane magnetic field component at the ion position. Similarly, by applying a slightly different current in each of the wires, minor adjustments to the out-of-plane magnetic field component can be made at the ion position. These compensation methods are illustrated in Figure 5.27.

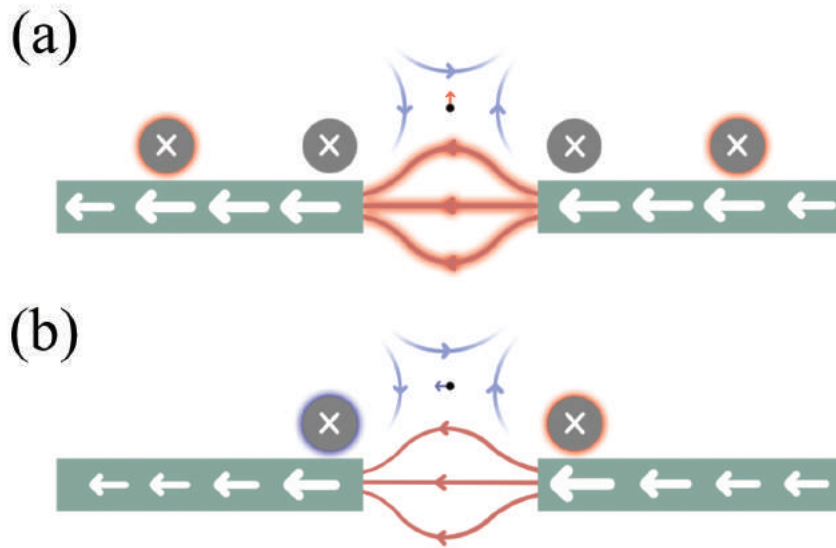


Figure 5.27: Two methods by which one can compensate or make small adjustments to the in-plane and out-of-plane components of the magnetic field at the ion position. **(a)** - Additional parallel current wires further down the yoke can strengthen the internal field of the yokes and therefore adjust the in-plane nilling field they provide. By applying a small anti-parallel current one can lower this field as this shortens the effective length of the yoke. This compensation will move the nil point in the direction perpendicular to the plane. **(b)** - By applying a different current on each of the wires, an out-of-plane offset field can be created where the direction is dependent on the larger of the two currents. This moves the nil closer to the wire with less current in the direction parallel to the plane. For extreme differences in currents this will likely also affect the height of the nil created.

One possible complication that I have not yet mentioned is that, within COMSOL simulations, the relative permeability of a material is considered to be constant. This

means that hysteresis effects such as magnetic saturation cannot be accounted for; as far as the simulation is concerned, I can have infinite gradient for infinite current as the internal magnetisation of the material will always increase with auxiliary field. In reality this is not the case.

At a certain high current, the magnetisation of the yoke will reach saturation and therefore be unable to compensate the field produced by the current wires if more than this current is applied. Not only that, but the relationship between the field produced by the currents and the compensation field produced by the activated yokes will become non-linear meaning that as we approach the high current operating limit for the yokes, the compensation will lag causing an increase in the in-plane field component at the ion position. Again, these properties are nearly impossible to know without testing the fabricated material and defining its hysteresis loop, however, I am confident that with the use of a good high permeability layer, that these currents will be outside of the range that we would operate at before damaging the wires.

In general, simulations show that the internal  $B$ -field of the yoke in the portion just under the current wire is around 0.04 T/A. Assuming a quite normal saturation of 1 T, it is reasonable to assume that in the agreed current operation range of 0 – 15 Amps this will be well within the linear regime for a normal yoke hysteresis loop. That said, this only considers saturation in a small section of the yoke, thus further propagation of the internal  $B$ -field may allow for the compensation to still increase past this limit until the whole yoke reaches saturation. This would need to be tested in order to determine the possible operating range of activation currents for the scheme, which could produce gradients much higher than previously seen in other schemes by pushing the current wires past the 15 A mark to 20 A and beyond. This would obviously be subject to sufficient cooling of the current wires.

### 5.3.5 Advantages of the self-compensating scheme

It is important to highlight why the concept of a self-compensating scheme marks a big leap forward in the production of magnetic field gradients in our experiments. The self-compensating current carrying wire scheme solves the main issue that may impede operation of a switchable magnetic field gradient in the currently proposed ion-state scalable quantum computer. In addition to the discussions in comparison with the current carrying wire scheme previously mentioned in Chapter 3 for single chip experiments, the use of yokes solves other issues envisioned in the scalable quantum architecture documented in

Dr Bjoern Lekitsch's paper [20].

Firstly, the use of self-compensation replaces additional current-based field compensation methods which therefore reduces the number of additional resources required in the proposed scalable system. In order to provide compensation of the large out-of-plane component of the magnetic field when using the anti-parallel current carrying wire scheme, it was proposed by Dr Bjoern Lekitsch that a loop of wire could be fabricated on the underside of the chip through which a current could be passed in order to address this offset. Though this would work to compensate the offset field, it creates an additional heat source on the underside of the chip, lowering the temperature gradient between the buried current wires and the under-chip heat sink or cooling system. This could limit the current that can be applied to the buried current carrying wires as heat transfer would become less efficient. By having all compensation methods on the top side of the chip, the temperature gradient is still present and this is no longer a concern provided thermal conductivity to the wires is sufficient given the additional yokes and thin electrical insulation layer. In addition to this, larger flatter current wires have little effect on the achievable gradients but provide much higher thermal transfer to the under-chip heat sink due to their larger surface area in contact with the substrate. This enables the wires to operate at higher currents and thus provide higher gradients.

Contrary to the original parallel current carrying wire scheme, by using yoked electromagnets we do not undermine the natural high gradient nil produced between two parallel current wires. Since the original scheme requires manipulation of the field far from this point, the gradient produced will never be as high when using uniform offset fields. By using activated yokes, the gradient created is much more similar to the permanent magnetic scheme demonstrated by Barb [65] but using a yoke to direct the field of a current wire as opposed to having to microfabricate an equivalent solenoid type wire geometry as shown in Chapter 3.

From comparisons between the natural high gradient between the wires and that produced at the nil position, one can consider the addition of the yokes as moving the nil rather than revealing a nil through compensation of an offset field component. This is due to the fact that the gradient produced at the nil position is actually greater than the natural gradient, as noted in Table 5.10. This is obviously not the case for the original parallel current carrying wire scheme as the gradients of the self-compensating scheme far surpass gradients under the explicit minimum gradient point above the wires. This scheme therefore has the potential for much higher gradients in the same way as the mi-



crofabricated permanent magnets but has the benefit that the gradient can be turned off and that fabrication processes should be simpler as there is no need for high temperature annealing of the magnetic material.

If thicker yokes can be fabricated, the nil position for a given wire separation can be raised further and the highest on-chip magnetic field gradients may become dominated by this scheme. That said, until these issues are addressed, though more difficult to operate, the anti-parallel nilled field current carrying wire scheme will remain the strongest candidate for the highest switchable gradients at ion heights over  $100\text{ }\mu\text{m}$ . However, below this height, the self-compensating scheme wins as the possible gradients of the anti-parallel scheme is limited by the offset field that can be compensated. The only disadvantage of this scheme over the permanent magnet scheme is that one is still limited by the topologies that current carrying wires can be fabricated in. However, this is a problem faced by any on-chip current carrying wire based magnetic field gradient generation method and is not specific to this scheme.

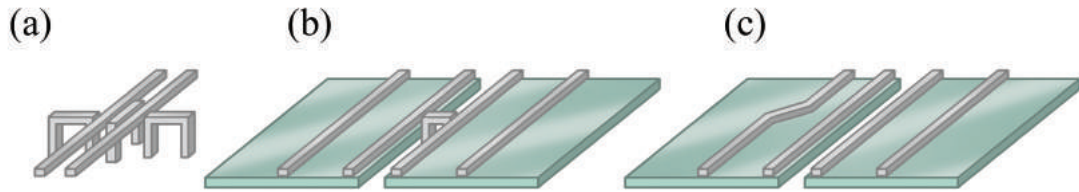


Figure 5.28: Three methods of field adjustment proposed for magnetic field gradient schemes involving current carrying wires. **(a)** - A current carrying wire scheme using three isolated additional compensation wires as proposed in Dr Bjoern Lekitsch's paper on a blueprint for a scalable trapped ion quantum computer [20]. **(b)** - An extended compensation scheme for the self-compensating current carrying wires scheme with an additional isolated wire between the two driving wires. **(c)** - An alternative compensation scheme for the self-compensating current carrying wire scheme using an angled wire to remove parallelism between the yoke magnetisations in order to create a magnetic field component parallel to the wire length.

Lastly, designs for on-chip adjustment of small magnetic field imperfections for all components of a global offset field becomes trivial as there is no longer a requirement for current wires to be isolated in a two-dimensional topology, i.e. with feeds that are not at the edge of the chip. In Dr Bjoern Lekitsch's paper, the two parallel current wires are accompanied by three smaller current wires used in order to make small adjustments to the magnetic field at the ion position [20] as shown in Figure 5.28 (a). However, since these are short wires that do not go to the edge of the chip, the current is fed through the back of the chip using vias instead of the more standard method of having all connections at the chip's outer edge. This should not necessarily be a problem for fabrication as



a similar connection through the substrate would not be unsuitable for the connections at the edge of the chip, but creating these vias for the current wires would inevitably require a complex fabrication process at the point where coherent manipulation and other entanglement operations would occur. This therefore means that the fabrication process is extremely complex at the most important region of the trap which increases the chances of problems during operation if the fabrication process encounters issues.

Since two-dimensional compensation of the self-compensating current carrying wires only requires the fabrication of additional surface wires further down the yoke, this would be much safer to fabricate than the three wire scheme. In terms of offset field in the direction parallel to the yoke symmetry, this may be more difficult to implement. That said, since the current wires in the self-compensating scheme are typically spaced further apart than the original scheme, a single wire from the three wire scheme may be able to be fabricated between the wires as shown in Figure 5.28 (b). This should be able to operate without affecting the yoke magnetisation as the current would be much smaller than the yoke driving wires and the field produced is parallel to the stronger axis of magnetisation. Alternatively, by having a single straight additional excitation wire further down only one of the yokes and a curved or angled wire further along the other, one may be able to generate this extra compensation field component by removing parallelism from the yoke magnetisations as shown in Figure 5.28 (c). This would require no additional fabrication of structures near to the region of interest and so long as a sufficient offset field can be generated, this will invariably be the best option. By making the currents in the main yoke driving wires asymmetric at the same time as running a current through the straight compensation wire, one should be able to make adjustments to the in-plane magnetic field component without affecting the out-of-plane component using this scheme.

### **5.3.6 Summary of discussions regarding the self-compensating current carrying wire scheme**

In this section, I have introduced a new method by which magnetic field gradients can be produced on-chip using a hybrid electromagnetic yoking scheme. A summary of this discussion is presented below:

- On-chip current wires with parallel applied currents can self-compensate by using said wires to simultaneously drive a high permeability yoke fabricated beneath each wire. This reduces the experimental resources when compared to on-chip current carrying wires which require a nilling field in order to access high gradients and is a

good on-chip solution to this issue.

- The wires can be larger than normal current carrying wires while still producing a high gradient allowing them to have better thermal conductivity to their surroundings and carry a higher current than the previously discussed wire schemes.
- The gradient produced is stronger than that naturally produced at the centre of separation of the two parallel current wires, thus this scheme does not undermine the natural gradient production of a non-yoked scheme.
- The gradients at ion heights below  $\sim 100 \mu\text{m}$  are extremely competitive with all other schemes discussed in this thesis with the possible exception of the under-chip magnetic spacer depending on the substrate thickness of the chip.
- Thicker, higher permeability yokes allows for a higher displacement of the nil position for a given wire separation and thus a higher gradient. Once fabrication methods can verify the thickness and permeability of yokes, this scheme could be improved for higher ion heights.
- Adjustment of the offset field components around the nil position should be realised relatively easily using this scheme with just two additional current carrying wires placed further down each yoke using the same fabrication process as the main wires.

Given the extremely promising simulation results when compared to other schemes, it is clear that self-compensating current carrying wires show great promise for implementation in future experiments involving on-chip magnetic field gradient production methods. Furthermore, all results shown here are extremely raw and could be significantly improved by optimisation of the wire and yoke geometries. Additional developments in the fabrication processes to create thicker yokes with a higher relative permeability would allow for higher possible gradients at higher ion heights. Further work may also uncover new possibilities using the same principles of this scheme with additional wires and/or yokes for use with more specialised trap geometries. Nevertheless, magnetic characterisation of yoke fabrication samples will be essential in making this scheme a reality in a scalable quantum computing architecture and though the preliminary results show great promise, a lot of work will be required in order to bring this scheme to fruition.

Table 5.10: The simulated results for two self-compensating current carrying wire schemes with different wire dimensions and yoke proximities. The bottom scheme shows results for dimensions that have been discussed with Dr Bjoern Lekitsch which should be fabricateable and provide sufficient thermal dissipation from the wires in the 0 – 15 A operating range in order to function as part of the chip. \* - Several extra simulation results shown in brackets which indicate that more study is required in order to optimise this scheme though the results at present are very promising.

Wire dimensions $w \times l \times d$ (mm)	Yoke dimensions $w \times l \times d$ (mm)	Yoke relative permeability	Wire-yoke face-face out-of-plane separation ( $\mu\text{m}$ )	Yoke overhang ( $\mu\text{m}$ )	Wire centre separation ( $\mu\text{m}$ )	Vertical gradient without yokes (T/m/A)	Planar gradient without yokes (T/m/A)	Nil height above wires ( $\mu\text{m}$ )	Vertical gradient at nil (T/m/A)	Planar gradient at nil (T/m/A)
$0.1 \times 6 \times 0.03$	$2 \times 6 \times 0.04$	2000	20	30	360	13.1	13.6	55	15.9	19.9
				50	500	6.09	6.87	80	10.7	9.9
				60	620	4.23	4.28	100	6.56	6.17
				50	800	2.49	2.56	120	3.61	3.41
$0.15 \times 6 \times 0.02$	$2 \times 6 \times 0.02$	200	0	15	340	16.6	17.6	54	20.2	26.3
				15	440	8.5	9.7	71	11.9	13.2
				15 (25)*	500	6.9	7.3	79 (85)	8.99 (10.5)	9.84 (10.1)
				15	740	2.97	3.09	100	4.04	3.93
				15	1340	0.87	0.93	130	1.03	1.11

## 5.4 Reflections on the production of magnetic field gradients for implementation with trapped ions using long-wavelength coherent manipulation techniques

In this thesis I have discussed many gradient production methods both on-chip and in-vacuum, using permanent, soft, and electromagnetic generation methods. Though I have directly compared several of these schemes at the point in this thesis where I first explained them, by directly comparing all the schemes I have discussed, one can get a feeling of which methods of magnetic field gradient production give the best results for the intended applications. For the purpose of simplicity, I will keep this discussion for linear trap geometries as other trap geometries such as an x-junction have already been thoroughly discussed. Moreover, these gradients will be discussed in terms of ion height above a planar chip trap as gradients on symmetric traps are directly influenced by their size which was discussed in detail in Chapter 3. That in mind, the use of a symmetric magnet geometry with planar traps is still a possibility, though since this is a function of chip size rather than ion height, I will take the benchmark figure (from the idealised magnet scaling law stated in Chapter 3) of approximately 70 T/m axial gradient and 35 T/m radial gradient for a magnet separation of 11 mm corresponding to a  $10 \times 10$  mm chip footprint.

### 5.4.1 Pros and cons of each gradient production method

First of all, let us reiterate the pros and cons of the schemes regardless of the ion height or gradient that they produce. This will allow us to ascertain what may be advantageous or problematic for the implementation of a scheme without any direct correlation to a specific experimental setup. I will start with permanent magnetic field gradient production methods.

#### Permanent magnetic gradient production methods

Of the gradient production methods discussed in this thesis, permanent magnets come under two main categories; the under-chip magnetic spacer and microfabricated on-chip magnets.

Under-chip permanent magnets produce a very strong gradient and though this is dependent on the substrate thickness, the gradients far surpass most on-chip schemes for all, especially high, ion heights. These magnets are also easy and inexpensive to obtain and have little limit on cuboid designs due to their macroscopic nature. They are also relatively

easy to install into a vacuum system as they only take the place of the mount under the chip. The downside is that they have to be aligned to extremely high precision on the order of  $10 - 50 \mu\text{m}$  in the direction of the gradient. This is a particularly stringent requirement for low axial, high radially aligned gradients. They are also difficult to retrofit as they are glued to the back of the chip rather than mounted around it like the symmetric magnet scheme. Finally, as these magnets are not microfabricated, both schemes are inappropriate for scalable systems.

Microfabricated on-chip permanent magnets allow for much more complex gradients on trap geometries that are extremely difficult to do via other means, such as on a ring, and are relatively easy to design. Specialised geometries can also be designed since they are patterned by a mask rather than by casting or other macroscopic techniques and are well aligned to other on-chip features as they are microfabricated. However, their magnetic properties are extremely dependent on the fabrication process which is very difficult when compared to plating of current wires or yokes and the remanences are typically not as good as the macroscopic case. Due in part to the thickness limit at which they can be fabricated, the gradients produced are far smaller than macroscopic magnets and the designs are essentially two-dimensional at a given thickness which limits the gradient that can be produced.

In general, permanent magnets have the advantage that they do not require an in/out feed for current and have fewer limitations on the field geometries that can be created. This is at the cost of being permanently “on” which results in high offset fields at certain regions of the trap. There is also an attraction of ferromagnetic filings when assembling any system involving permanent magnets. Though not a major problem, this is very tedious to clean as each filing has to be taken off individually using tweezers under a microscope. Permanent magnets are also susceptible to losing their magnetisation if the baking conditions are not correct due to reordering of the magnetic spins as they are heated over the Curie temperature. That said, they do not require cooling in order to operate efficiently, unlike on-chip current carrying wires. They also have a small drift in magnetisation due to temperature<sup>5</sup>, though this is only an issue if they are not aligned correctly to begin with or a single magnet gets significantly hotter than the other, which is unlikely in a well thermally characterised system.

---

<sup>5</sup>For our samarium cobalt magnets manufactured by Bunting Magnetics, this is -0.03 percent of the remanence per Kelvin.

### **Current based magnetic gradient production methods**

The next production method that I will discuss is on-chip current carrying wires. Since this utilises near-field effects, a macroscopic equivalent does not provide a gradient worthy of note.

On-chip current carrying wires are relatively easy to fabricate when compared to on-chip permanent magnets and can be turned on and off, removing the gradient at the will of the user. A pair of wires also has a lot of control over the field at the ion position by applying different currents to each wire.

However, the best gradients are only realised when a uniform offset field is applied to cancel the large field at the ion position as the zero field point is directly between the wires for the parallel current case and is non-existent for the anti-parallel current case. This limits the current that one would want to apply to the wires due to the necessity to null the offset field, which in itself is a difficult task as the field needs to be relatively uniform. These therefore may require larger macroscopic field sources in order to create this uniform nulling field unless more complex or multi-layer current carrying wire geometries can be shown to be fabricated. Nevertheless, the gradient around a null point created using offset fields can be manipulated with ease while retaining a high gradient when using anti-parallel currents.

On-chip current carrying wires also require in-vacuum cooling in order to access the higher currents required to achieve a high gradient at the ion position and require an in/out feed which limits the geometries that one can create on a chip if limiting fabrication to a two-dimensional topology. This is contrary to on-chip permanent magnets.

As a final point, in general, the stability of field for any current driven scheme will be dictated directly by the current supply noise. Moreover, for most supplies the higher the current, the higher the noise which must be considered for the practical application of any design involving currents.

### **Yoke based magnetic gradient production methods**

On-chip yokes are a much more novel method of gradient production that is very much in its infancy. They are also untested at this point but are also not described by clear theoretical models in the same way as current carrying wires thus it is difficult to truly quantify their potential. Nevertheless, my investigations arrive at the following advantages and disadvantages.

On-chip yokes suffer a similar predicament to on-chip current carrying wires in that

the gradients are produced at a high offset fields. However, through optimisation of the yoke geometry and material, of which fabrication is very well documented and only slightly more complex than the techniques used to produce current carrying wires, one can lower this offset field while enhancing the gradient.

That said, though current carrying wires are able to have the field nilled at the ion position, this does not work for on-chip yokes as it cancels their internal magnetisation, thus destroying the gradient.

On the other hand, since on-chip yokes can be activated using a remote field source, they are extremely suitable for testing a chip and subsequently retrofitting driving magnetics once the chip has been trapped on.

Though the yokes can be activated by on-chip wires with good control of the field profile at the ion position for two-wires fabricated directly underneath the yokes, they can also operate with a switchable magnetic field gradient without the requirement of an in-vacuum cooling system by using an under-chip electromagnet. This is the only scheme so far that exhibits switchable gradients without the use of in-vacuum cooling.

Yokes still suffer from some limitations to the gradient shapes produced as only an in-plane magnetisation has been shown to produce usefully high gradients. However, this method creates a good novel axial gradient scheme for an x-junction trap as previously discussed in this chapter.

### **Hybrid, self-compensating magnetic gradient production methods**

Self-compensating current carrying wires are another concept that is still in its infancy though it shows much more promise than the yoking scheme that it is developed from.

On-chip self-compensating current carrying wires using yokes have the massive advantage that they have all the benefits of current carrying wires without the requirement for an external compensation field.

They also produce higher gradients at lower ion heights but are limited by the currently agreed fabrication techniques as fabrication of this scheme is particularly difficult. That said, this is about as difficult as with on-chip permanent magnets but has the benefit that the field can be switched off.

The currents in the wires can also be larger than that in the normal current carrying wire scheme as their cross-section has less of an impact on the gradient produced. That said, this is still subject to in-vacuum cooling as to what currents can be achieved, though this is no longer limited by the uniform nilling field one can produce with supplementary

magnetics.

Manipulation of the field at the ion position is also relatively simple using additional on-chip current wires which do not significantly undermine the gradient at the ion position.

This is the only current carrying wire scheme where the gradient is truly limited by the current one can produce within the linear relative permeability operating range of the yokes.

#### 5.4.2 Direct comparison of gradients discussed in this thesis

Now that the general pros and cons have been discussed, let us directly compare the simulated gradients for the best schemes discussed in this thesis. This will allow us to ascertain in which regimes each gradient production scheme produces the best gradients.

When compared to the symmetric magnets at 70 T/m axial and 35 T/m radial, most on-chip schemes are better at ion heights under 100  $\mu\text{m}$  for axial gradients, with the exception of the nilled parallel current wires. Above this height only nilled anti-parallel current wires optimised or not remain better than the symmetric magnets. The under-chip magnets obviously remain better for all heights for reasonable substrate thicknesses of 700  $\mu\text{m}$  or less. In terms of vertical radial gradient, any scheme has better gradients than the symmetric schemes other than the nilled parallel current carrying wires and microfabricated magnets at heights higher than approximately 170  $\mu\text{m}$ .

In summary, for on-chip production of magnetic field gradients with a nil at the ion position in a linear non-specialised geometry:

- Nilled field parallel current wires are a no go for any realistic ion height.
- Below 75  $\mu\text{m}$  nil height the preliminary designs for self-compensating current carrying wires perform better than any other scheme.
- Over 75  $\mu\text{m}$  nil height one should use as close to optimal nilled anti-parallel current carrying wires so long as one is able to operate them.
- If on-chip gradient production methods are not a necessity, under-chip magnets win all out unless one has an ion height under 60  $\mu\text{m}$  in which the self-compensating current wires perform better.

Of the methods discussed, on-chip permanent magnets, at present, do not hold any particular advantages with the exception of gradient production on novel trap geometries. Thus, for a scalable system, they are unlikely to be implemented unless complications



with current carrying wire operation arise, though these remain the key candidate for a scalable system given my investigations. However, if self-compensation at higher ion heights can be achieved, this will become the dominant method as it would remove the main experimental complications of nilled-field anti-parallel current carrying wires. This would of course require further development of such a gradient production method and experimental demonstration of the self-compensating scheme.

Experimental implementation and verification of these gradient production methods is essential in creating a true comparison between each scheme discussed in this thesis. As with any technological development, it is unclear from the starting point with what form a scalable quantum computing architecture will eventually take. The work in this chapter serves as a starting point in opening these discussions for future work for new magnetic field gradient production methods for microwave entanglement schemes in the field of ion-trap quantum computing.

# Conclusion

In this thesis, I have discussed several different types of ion trap geometry and how a long-wavelength radiation entanglement scheme in the presence of a magnetic field gradient can be created using trapped ytterbium ions. I have demonstrated single-ion coherent manipulation operations using this scheme and discussed and implemented ways in which the fidelity of operations using this scheme can be improved by using a dressed state qubit, ground state cooling techniques, and minimisation of electromagnetic noise on electrical supplies and from outside the experimental setup.

Following experiments using a magnetic field gradient of  $23.3(6)$  T/m, I have discussed magnetic field gradient production methods for various trap and magnetic geometry combinations that have been proposed in the field thus far and defined a separation to gradient scaling law for an idealised set of symmetric scheme permanent magnets. In addition, I have thoroughly analysed gradient production methods using a pair of on-chip current carrying wires in the presence of an external compensation field and formulated the optimum wire geometry for a given ion height in order to achieve the highest possible magnetic field gradients with 10 A of anti-parallel applied current and 100 G compensated offset field.

I have also created a new method by which magnetic field gradients in excess of 100 T/m can be created by using a pair of magnets underneath a planar chip trap with the ultimate goal of reaching the fault tolerant regime using this entanglement scheme. I have discussed several variations of this design for high axial, high radial and small axial, high radial gradient requirements as well as designs for junction traps. Throughout this design process I have re-evaluated the best magnetic materials and shown that Ni-Cu-Ni coating on the magnets is detrimental to creating a high gradient.

To aid in the experimental implementation of these magnetic spacers, I have analysed compensation coil and external permanent magnetic compensation field sources and discussed the best ways to implement them for our vacuum system. A micron-precision alignment procedure has also been outlined in order to combine a chip with the magnetic spacer such that there are minimal offset fields at the trapping position. A custom

alignment stage was built in order to perform this process.

A preliminary external measurement of the magnetic field gradient produced using this scheme was made yielding  $\frac{dB_z}{dx} \approx 110$  T/m. Of two magnetic spacer designs, one has been installed into a vacuum system and I have verified the alignment procedure to be sufficient for our needs. The microwave and RF setups best suited to provide sufficient Rabi frequencies for our experimental setup have also been investigated and simulations have shown that a front window mesh will not prevent microwave and RF radiation from getting to the ion. Using one of the under-chip magnetic spacer experimental setups, we have successfully trapped  $^{174}\text{Yb}^+$  ions and verified that the presence of such a large magnetic field gradient has not had an adverse effect on trapping or ion lifetime that we have observed thus far. Nevertheless, we have yet to reliably trap  $^{171}\text{Yb}^+$  ions, thus an in situ measurement of the magnetic field gradient has not yet been achieved.

In the final chapter, I discussed the possible magnetic field gradients that may be produced using on-chip magnets focussing on the freedom of geometry that is evident with microfabricated magnets when compared to macroscopic magnets. I subsequently introduced a new gradient production method which utilises magnetic yoking in order to activate switchable on-chip gradients using on-chip or off-chip driving fields. For this scheme, I focussed on the advantages it brings over permanent magnetic field gradients or uncompensated on-chip current carrying wires in particular when creating gradients for an x-junction trap. I have also shown that by combining yoking and current carrying wire technology it may be possible to create a self-compensating current carrying wire scheme which produces a switchable magnetic field gradient oriented around a defined nil. Simulations of this scheme have shown that for low ion heights the possible magnetic field gradients surpass all other methods discussed in this thesis with the possible exception of the under-chip magnetic spacer, which would suffer greatly from any misalignment to the chip at these gradients. To finish, I have compared all of the magnetic field gradient production methods discussed in this thesis and evaluated the best situations when each method is the clear choice for implementation of said gradient.

For the work described in this thesis, I set out to develop methods of magnetic field gradient production in order to create faster, higher fidelity gate operations using the long-wavelength radiation entanglement scheme with trapped  $^{171}\text{Yb}^+$  ions. I have shown that it is possible to create much larger gradients than previously seen in this field, and produced a thorough, comprehensive overview of many schemes which can create high enough gradients to bring this entanglement scheme to the fault tolerant regime. I have

also implicitly indicated that magnetic field gradients of this level do not appear to have an adverse effect on trapping  $^{174}\text{Yb}^+$  ions though this gradient has yet to be confirmed with  $^{171}\text{Yb}^+$  ions. Verification of this gradient is the logical next step in continuing the work discussed in this thesis. Following this, execution of the same experiments discussed in Chapter 2 using the experimental setups discussed in Chapter 4 should outline any further complications towards bringing this entanglement scheme to fault tolerance. After a fault tolerant gate has been achieved using the under-chip magnetic spacer, more scalable methods such as current carrying wires or the microfabricated magnetics described in Chapter 5 should be implemented and the experiments repeated using these gradient production methods. This would be the next step towards a fault tolerant, scalable quantum computing architecture before creating a large array of junctions in order to perform complex quantum algorithms with many trapped ions.

To conclude, though they may be difficult to fabricate, sufficiently high magnetic field gradients should be possible to produce in order to create a scalable trapped ion quantum computer with  $^{171}\text{Yb}^+$  ions using long-wavelength coherent manipulation fields.

# Bibliography

- [1] L. K. Grover. A Fast Quantum Mechanical Algorithm for Database Search. In *Proceedings of the Twenty-eighth Annual ACM Symposium on Theory of Computing*, STOC '96, pages 212–219, 1996.
- [2] P. W. Shor. Polynomial-Time Algorithms for Prime Factorization and Discrete Logarithms on a Quantum Computer. *SIAM J. Comput.*, 26(5):1484–1509, October 1997.
- [3] D. P. DiVincenzo. The Physical Implementation of Quantum Computation. *Fort. Phys.*, 48(11):771–783, 2000.
- [4] T. P. Harty, M. A. Sepiol, D. T. C. Allcock, C. J. Ballance, J. E. Tarlton, and D. M. Lucas. High-fidelity trapped-ion quantum logic using near-field microwaves. *arXiv:1606.08409*, June 2016.
- [5] N. Akerman, N. Navon, S. Kotler, Y. Glickman, and R. Ozeri. Universal gate-set for trapped-ion qubits using a narrow linewidth diode laser. *New J. Phys.*, 17(113060), November 2015.
- [6] J. Zhou. *Building A Magnesium Ion Trap For Quantum Computation*. MSc thesis, McMaster University, August 2007.
- [7] M. Dietrich. *Barium Ions for Quantum Computation*. PhD thesis, University of Washington, 2009.
- [8] H.-J Briegel, T. Calarco, D. Jaksch, J. I. Cirac, and P. Zoller. Quantum computing with neutral atoms. *J. Mod. Opt.*, 47:415–451, 2000.
- [9] M. Fuechsle, J. A. Miwa, S. Mahapatra, H. Ryu, S. Lee, O. Warschkow, L. C. L. Hollenberg, G. Klimeck, and M. Y. Simmons. A single-atom transistor. *Nat. Nano.*, 7:242–246, April 2012.
- [10] J. M. Gambetta, J. M. Chow, and M. Steffen. Building logical qubits in a superconducting quantum computing system. *npj Quantum Inf.*, 3(2), January 2017.

- [11] S. Stanisic, N. Linden, A. Montanaro, and P. S. Turner. Generating entanglement with linear optics. *arXiv:1702.05209*, February 2017.
- [12] W. D. Phillips. Laser cooling and trapping of neutral atoms. *Rev. Mod. Phys.*, 70(3):721–741, July 1998.
- [13] J. Mizrahi, B. Neyenhuis, K. G. Johnson, W. C. Campbell, C. Senko, D. Hayes, and C. Monroe. Quantum control of qubits and atomic motion using ultrafast laser pulses. *Appl. Phys. B*, 114(1):45–61, 2014.
- [14] C. J. Ballance, T. P. Harty, N. M. Linke, M. A. Sepiol, and D. M. Lucas. High-fidelity quantum logic gates using trapped-ion hyperfine qubits. *Phys. Rev. Lett.*, 117:060504, August 2016.
- [15] D. P. L. Aude Craik, N. M. Linke, M. A. Sepiol, T. P. Harty, C. J. Ballance, D. N. Stacey, A. M. Steane, D. M. Lucas, and D. T. C. Allcock. High-fidelity spatial addressing of  $^{43}\text{Ca}^+$  qubits using near-field microwave control. *arXiv:1601.02696*, January 2016.
- [16] A. Sørensen and K. Mølmer. Entanglement and quantum computation with ions in thermal motion. *Phys. Rev. A*, 62:022311, July 2000.
- [17] F. Mintert and Ch. Wunderlich. Ion-trap quantum logic using long-wavelength radiation. *Phys. Rev. Lett.*, 87:257904, November 2001.
- [18] K. Lake, S. Weidt, J. Randall, E. D. Standing, S. C. Webster, and W. K. Hensinger. Generation of spin-motion entanglement in a trapped ion using long-wavelength radiation. *Phys. Rev. A*, 91:012319, January 2015.
- [19] S. Weidt, J. Randall, S. C. Webster, K. Lake, A. E. Webb, I. Cohen, T. Navickas, B. Lekitsch, A. Retzker, and W. K. Hensinger. Trapped-ion quantum logic with global radiation fields. *Phys. Rev. Lett.*, 117:220501, November 2016.
- [20] B. Lekitsch, S. Weidt, A. G. Fowler, K. Mølmer, S. J. Devitt, Ch. Wunderlich, and W. K. Hensinger. Blueprint for a microwave ion trap quantum computer. *arXiv:1508.00420*, August 2015.
- [21] P. J. Kunert, D. Georgen, L. Bogunia, M. T. Baig, M. A. Baggash, M. Johanning, and Ch. Wunderlich. A planar ion trap chip with integrated structures for an adjustable magnetic field gradient. *Appl. Phys. B*, 114(1):27–36, 2013.

- [22] S. Earnshaw. On the nature of the molecular forces which regulate the constitution of the luminiferous ether. *Trans. Camb. Phil. Soc.*, 7:97–112, 1842.
- [23] I. S. Grant and W. R. Phillips. *Electromagnetism*. John Wiley and Sons, 2<sup>nd</sup> edition, 2008.
- [24] J. A. D. Randall. *High-Fidelity Entanglement of Trapped Ions using Long-Wavelength Radiation*. PhD thesis, Imperial College London, February 2016.
- [25] K. Lake. *Towards high fidelity entanglement with dressed state qubits*. PhD thesis, University of Sussex, April 2014.
- [26] M. D. Hughes, B. Lekitsch, J. A. Broersma, and W. K. Hensinger. Microfabricated ion traps. *Cont. Phys.*, 52(6):505–529, September 2011.
- [27] W. Paul and H. Steinwedel. Ein neues Massenspektrometer ohne Magnetfeld. *Z. Naturforsch. A*, 8:448–450, 1953.
- [28] W. K. Hensinger, S. Olmschenk, D. Stick, D. Hucul, M. Yeo, M. Acton, L. Deslauriers, C. Monroe, and J. Rabchuk. T-junction ion trap array for two-dimensional ion shuttling, storage, and manipulation. *Appl. Phys. Lett.*, 88:034101, 2006.
- [29] H. Takahashi, A. Wilson, A. Riley-Watson, F. Oručević, N. Seymour-Smith, M. Keller, and W. Lange. An integrated fiber trap for single-ion photonics. *New J. Phys.*, 15(5):053011, 2013.
- [30] B. Tabakov, F. Benito, M. Blain, C. R. Clark, S. Clark, R. A. Haltli, P. Maunz, J. D. Sterk, C. Tigges, and D. Stick. Assembling a Ring- Shaped Crystal in a Microfabricated Surface Ion Trap. *Phys. Rev. Appl.*, 4:031001, September 2015.
- [31] J. D. Siversn, S. Weidt, K. Lake, B. Lekitsch, M. D. Hughes, and W. K. Hensinger. Optimization of two-dimensional ion trap arrays for quantum simulation. *New J. Phys.*, 14(8):085009, 2012.
- [32] R. C. Sterling, H. Rattanasonti, S. Weidt, K. Lake, P. Srinivasan, S. C. Webster, M. Kraft, and W. K. Hensinger. Fabrication and operation of a two-dimensional ion-trap lattice on a high-voltage microchip. *Nat. Commun.*, 5(3637), April 2013.
- [33] B. Lekitsch. *Development of Microfabricated Ion Traps for Scalable Microwave Quantum Technology*. PhD thesis, University of Sussex, November 2013.

- [34] D. T. C. Allcock, T. P. Harty, C. J. Ballance, B.C. Keitch, N. M. Linke, D. N. Stacey, and D. M. Lucas. A microfabricated ion trap with integrated microwave circuitry. *Appl. Phys. Lett.*, 102(4), 2013.
- [35] S. Weidt. *Towards microwave based ion trap quantum technology*. PhD thesis, University of Sussex, August 2013.
- [36] R. C. Sterling. *Ytterbium ion trapping and microfabrication of ion trap arrays*. PhD thesis, University of Sussex, May 2011.
- [37] J. D. Siverns, L. R. Simkins, S. Weidt, and W. K. Hensinger. On the application of radio frequency voltages to ion traps via helical resonators. *Appl. Phys. B*, 107:921–934, 2012.
- [38] T. Christensen. *Kinetic Theory of Gasses*. University of Colorado, March 2000.
- [39] A. H. Nizamani. *Yb<sup>+</sup> ion trapping and optimum planar trap geometries for scalable quantum technology*. PhD thesis, University of Sussex, February 2011.
- [40] J. McLoughlin. *Development and Implementation of an Yb<sup>+</sup> Ion Trap Experiment Towards Coherent Manipulation and Entanglement*. PhD thesis, University of Sussex, May 2011.
- [41] J. D. Siverns. *Yb ion trap experimental set-up and two-dimensional ion trap surface array design towards analogue quantum simulations*. PhD thesis, University of Sussex, June 2011.
- [42] M. D. Hughes. *The development of microfabricated ion traps towards quantum information and simulation*. PhD thesis, University of Sussex, November 2012.
- [43] Laser Interferometer Gravitational Wave Observatory. *LIGO Vacuum Compatible Materials List*. Web Database, December 2011.
- [44] W. A. Bell and J. G. Tracy. *Stable isotope inventory requirements and enrichment capabilities*. Oak Ridge National Laboratory, 1985.
- [45] G. Audi, O. Bersillon, J. Blachot, and A.H. Wapstra. The Nubase evaluation of nuclear and decay properties. *Nucl. Phys. A*, 729(1):3 – 128, 2003.
- [46] R. Chang, A. L. Hoendervanger, Q. Bouton, Y. Fang, T. Klafka, K. Audo, A. Aspect, C. I. Westbrook, and D. Clément. Three-dimensional laser cooling at the Doppler limit. *Phys. Rev. A*, 90:063407, December 2014.



- [47] A. Khromova. *Quantum Gates with Trapped Ions using Magnetic Gradient Induced Coupling*. PhD thesis, Universität Siegen, August 2012.
- [48] M. Johanning, A. Braun, N. Timoney, V. Elman, W. Neuhauser, and Chr. Wunderlich. Individual Addressing of Trapped Ions and Coupling of Motional and Spin States Using rf Radiation. *Phys. Rev. Lett.*, 102:073004, February 2009.
- [49] J. Randall, S. Weidt, E. D. Standing, K. Lake, S. C. Webster, D. F. Murgia, T. Navickas, K. Roth, and W. K. Hensinger. Efficient preparation and detection of microwave dressed-state qubits and qutrits with trapped ions. *Phys. Rev. A*, 91:012322, January 2015.
- [50] D. Murgia. *A scalable approach to quantum logic operations*. MRes thesis, Imperial College London, September 2013.
- [51] N. Daniilidis, S. Gerber, G. Bolloten, M. Ramm, A. Ransford, E. Ulin-Avila, I. Talukdar, and H. Häffner. Surface noise analysis using a single-ion sensor. *Phys. Rev. B*, 89:245435, June 2014.
- [52] E. C. Jordan. *Electromagnetic Waves and Radiating Systems*. Prentice Hall, 1968.
- [53] Carpenter. *Magnetic properties of Stainless Steels*. Web Database, June 2006.
- [54] The M $\mu$ Shield Company. *M $\mu$ Metal Specifications*. Web Database, 1998-2016.
- [55] R. A. Serway. *Principals of Physics*. London: Saunders College Publishing, 2nd edition, 1998.
- [56] G. Elert. *Resistivity of steel*. Web Database, 2006.
- [57] EngineeringToolBox.com. *metal-alloys-densities*. Web Database, Retrieved April 2016.
- [58] F. J. García de Abajo. Light transmission through a single cylindrical hole in a metallic film. *Opt. Express*, 10(25):1475–1484, 2002.
- [59] K. D. Skeldon, L. M. Reid, V. McNally, B. Dougan, and C. Fulton. Physics of the Theremin. *Am. J. Phys.*, 66:945955, 1998.
- [60] Mini-Circuits. *Understanding Mixers = Terms Defined, and Measuring Performance*. Manufacturer’s reference document, 2008.

- [61] S. Weidt, K. Lake, J. Randall, E. D. Standing, T. Navickas, D. F. Murgia, S. C. Webster, and W. K. Hensinger. *Towards Microwave Entanglement Generation For Quantum Computing And Simulation*. Poster, University of Sussex, September 2014.
- [62] S. Weidt, J. Randall, S. C. Webster, E. D. Standing, A. Rodriguez, A. E. Webb, B. Lekitsch, and W. K. Hensinger. Ground-state cooling of a trapped ion using long-wavelength radiation. *Phys. Rev. Lett.*, 115:013002, June 2015.
- [63] B. M. Moskowitz. *Hitchhiker's Guide to Magnetism*. Environmental Magnetism Workshop, June 1991.
- [64] J. R. Lloyd. *Reliability of copper metallization*. Lloyd Technology Associates, Inc, 1998.
- [65] I. Barb. *Permanent magnetic atom chips*. PhD thesis, Universiteit van Agnietenkapel, April 2010.
- [66] J. Randall. *Quantum Logic In Trapped Ions Using Microwaves and Dressed States*. MRes thesis, Imperial College London, September 2012.
- [67] A. R. Mirza. *One Micron Precision, Wafer-Level Aligned Bonding for Interconnect, MEMS and Packaging Applications*. 2000 Electronic Components and Technology Conference, pages 676 – 680, 2000.
- [68] T.-S. Chin. Permanent magnet films for applications in microelectromechanical systems. *J. Magn. Magn. Mater.*, 209:75–79, February 2000.
- [69] L. Allocca, C. Bonavolont, A. Giardini, T. Lopizzo, A. Morone, M. Valentino, M. F. Verrastro, and V. Viggiano. Laser deposition of SmCo thin film and coating on different substrates. *Phys. Scripta*, 78(5):058114, 2008.
- [70] S. J. Bleiker, A. C. Fischer, U. Shah, N. Somjit, T. Haraldsson, N. Roxhed, J. Oberhammer, G. Stemme, and F. Niklaus. High-Aspect-Ratio Through Silicon Vias (TSVs) for High-Frequency Application Fabricated by Magnetic Assembly of Gold-Coated Nickel Wire. *IEEE Trans. Compon. Packag. Manuf. Technol.*, 5, 2015.
- [71] J. Y. Park and M. G. Allen. Development of magnetic materials and processing techniques applicable to integrated micromagnetic devices. *J. Micromech. Microeng.*, 8(4):307, 1998.

- [72] M. Föhse and H.H. Gatzert. *Optimizing the Magnetic Properties of Electroplated Permalloy for Flux Guides in Micromotors*. Institute for Microtechnology, Hanover University, 2002.
- [73] Z. Li, X. Sun, Y. Zheng, and H. Zhang. Microstructure and magnetic properties of micro NiFe alloy arrays for MEMS application. *Journal of Micromechanics and Microengineering*, 23(8):085013, June 2013.
- [74] J. Y. Park, S. H. Han, and M. G. Allen. Batch-fabricated Microinductors with Electroplated Magnetically Anisotropic and Laminated Alloy Cores. *IEEE Trans. Magn.*, 35(5):4291–4300, 1999.
- [75] T. E Buchheit, T. R. Christenson, D. T. Schmale, and D. A. Lavan. Understanding and Tailoring the Mechanical Properties of Liga Fabricated Materials. In *Symposium AA - Materials Science of Microelectromechanical Systems (MEMS)*, volume 546 of *MRS Proceedings*, pages 121–126, 1998.

## Appendix A

# Supplementary information for the current carrying wires gradient production scheme

This appendix contains supplementary information about the current carrying wires scheme discussed in Chapter 3, beginning with a derivation of the analytical equations used to model the current carrying wires. In addition to this, several tables which show the gradients and offset magnetic fields produced by the example current carrying wire schemes discussed in Chapter 3 prior to optimisation are displayed for reference. This will help one to understand the gradient drop-off as a function of ion height and also verify that the optimised scheme described in the aforementioned chapter results in the highest gradients to date.

### A.1 Derivation of the equation for the magnetic field above two infinite straight current wires

Displayed here is the derivation of the equations used in Chapter 3 in order to analytically model the magnetic field above a pair of infinite straight current wires. I will do this explicitly for both the parallel and anti-parallel wire cases. Though these can be summarised as one set of equations, by creating two sets, it is much more difficult to make a mistake when evaluating the equations due to the direction conventions of the geometry that must be followed in order for them to be valid.

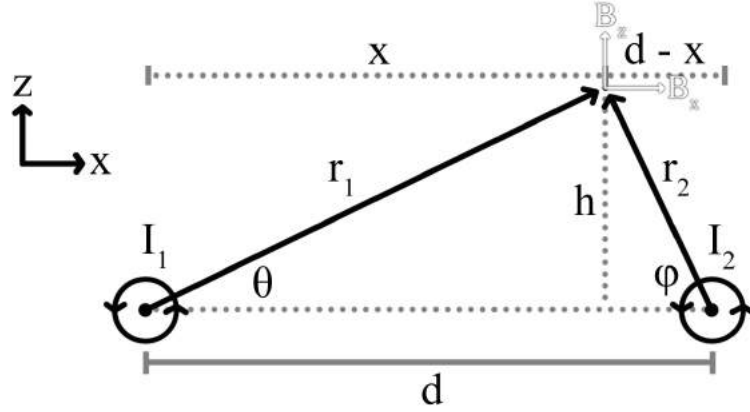


Figure A.1: The labelled geometry of the two-wire setup with both currents parallel to each other and coming out of the page.

The geometry of the problem is shown in Figure A.1 where  $I_1$ ,  $r_1$ ,  $\theta$ , and  $I_2$ ,  $r_2$ ,  $\varphi$  are the current passing through, distance from the field measurement point, and angle of this distance to the  $x$ -axis for wires 1 and 2 respectively. Additionally,  $d$  is the separation of the wires, and  $x$  and  $h$  are the horizontal distance from wire 1 and the height above the wires respectively. From this geometry, one can make a list of equations in order to convert between different variables for later use in the derivation of the final equations.

$$d = r_1 \cos \theta + r_2 \cos \varphi$$

$$= x + (d - x)$$

$$h = r_1 \sin \theta = r_2 \sin \varphi$$

$$x = r_1 \cos \theta \rightarrow \frac{x}{r_1} = \cos \theta \quad (\text{A.1})$$

$$d - x = r_2 \cos \varphi \rightarrow \frac{d - x}{r_2} = \cos \varphi \quad (\text{A.2})$$

$$\frac{h}{r_1} = \sin \theta \quad (\text{A.3})$$

$$\frac{h}{r_2} = \sin \varphi \quad (\text{A.4})$$

$$r_1^2 = x^2 + h^2 \quad (\text{A.5})$$

$$r_2^2 = (d - x)^2 + h^2 \quad (\text{A.6})$$

I will now re-state a couple of magnetic equations that will also be useful in this derivation, namely the magnetic field at a distance  $r$  from a single wire, and the total

magnetic field assuming  $B_y = 0$ .

$$B = \frac{\mu_0 I}{2\pi r} \quad (\text{A.7})$$

$$B = \sqrt{B_x^2 + B_z^2} \quad (\text{A.8})$$

Since the magnetic field is a vector field, it is most useful to break the field of each of the wires into the  $B_x$  and  $B_z$  components including an indication of the field direction for each of these components relative to the chosen coordinate axes. In the parallel currents case, for current flowing out of the page:

$$B_{x_1} = -\frac{\mu_0 I_1}{2\pi r_1} \sin \theta \quad (\text{A.9})$$

$$B_{z_1} = \frac{\mu_0 I_1}{2\pi r_1} \cos \theta \quad (\text{A.10})$$

$$B_{x_2} = -\frac{\mu_0 I_2}{2\pi r_2} \sin \varphi \quad (\text{A.11})$$

$$B_{z_2} = -\frac{\mu_0 I_2}{2\pi r_2} \cos \varphi \quad (\text{A.12})$$

Let us first perform the vector summation of the  $B_x$  components of each wire which I will call  $B_{x\Rightarrow}$ .

$$\begin{aligned} B_{x\Rightarrow} &= -\left(\frac{\mu_0 I_1}{2\pi r_1} \sin \theta + \frac{\mu_0 I_2}{2\pi r_2} \sin \varphi\right) \\ &= -\frac{\mu_0}{2\pi} \left(\frac{I_1}{r_1} \sin \theta + \frac{I_2}{r_2} \sin \varphi\right) \end{aligned}$$

substituting Equations A.3 and A.4 followed by Equations A.5 and A.6 gives,

$$= -\frac{\mu_0}{2\pi} \left(\frac{I_1 h}{r_1^2} + \frac{I_2 h}{r_2^2}\right)$$

resulting in,

$$B_{x\Rightarrow} = -\frac{\mu_0}{2\pi} \left(\frac{I_1 h}{x^2 + h^2} + \frac{I_2 h}{(d-x)^2 + h^2}\right) \quad (\text{A.13})$$

where this is the total value of  $B_x$  for the two wires separated by  $d$  at a height  $h$  above them and a distance  $x$  from wire 1 as previously defined. This is understandably easier than dealing with the angles from each wire.

Similarly, the derivation can be made for the total  $B_z$  component for the two wires which I will call  $B_{z\Rightarrow}$ .

$$\begin{aligned} B_{z\Rightarrow} &= \frac{\mu_0 I_1}{2\pi r_1} \cos \theta - \frac{\mu_0 I_2}{2\pi r_2} \cos \varphi \\ &= \frac{\mu_0}{2\pi} \left( \frac{I_1}{r_1} \cos \theta - \frac{I_2}{r_2} \cos \varphi \right) \end{aligned}$$

substituting Equations A.1 and A.2 followed by Equations A.5 and A.6 gives,

$$= \frac{\mu_0}{2\pi} \left( \frac{I_1 x}{r_1^2} - \frac{I_2 (d-x)}{r_2^2} \right)$$

resulting in,

$$B_{z\Rightarrow} = \frac{\mu_0}{2\pi} \left( \frac{I_1 x}{x^2 + h^2} - \frac{I_2 (d-x)}{(d-x)^2 + h^2} \right) \quad (\text{A.14})$$

where similarly this is the total value of  $B_z$  for the two wires using the same coordinate conventions. These two components can be summed using Equation A.8 in order to get the total field at any point in the geometry.

Though these equations should work implicitly for the anti-parallel case by merely putting a negative current in one of the wires, I will explicitly show here that this also works by reconsidering the geometry of the problem and going through the derivation as before.

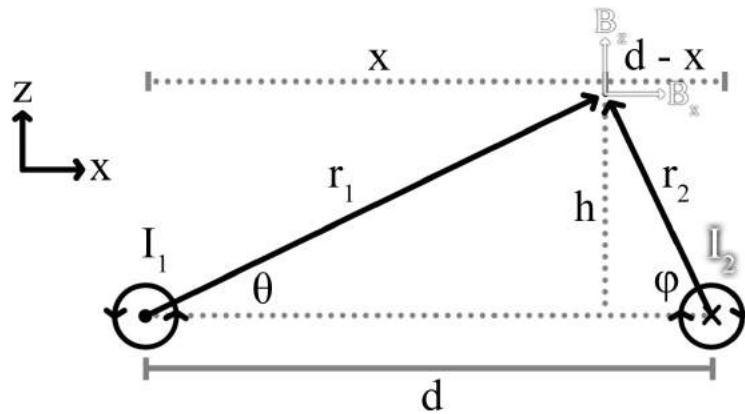


Figure A.2: The labelled geometry of the two-wire setup shown in Figure A.1 with the current in wire 2 now reversed for the explicitly anti-parallel case.

Figure A.2 shows the same geometric labels as Figure A.1 but with the current in wire 2 reversed. In this case, the  $B_x$  and  $B_z$  components for this wire are in the opposite direction (sign) and the field components of wire 1 remain the same. This gives the following equations for the field components of wire 2.

$$B_{x_2} = \frac{\mu_0 I_2}{2\pi r_2} \sin \varphi \quad (\text{A.15})$$

$$B_{z_2} = \frac{\mu_0 I_2}{2\pi r_2} \cos \varphi \quad (\text{A.16})$$

If we go through the same substitutions as for the parallel case we eventually get to the anti-parallel current field components,

$$B_{x\rightleftharpoons} = \frac{\mu_0}{2\pi} \left( \frac{I_2 h}{(d-x)^2 + h^2} - \frac{I_1 h}{x^2 + h^2} \right) \quad (\text{A.17})$$

$$B_{z\rightleftharpoons} = \frac{\mu_0}{2\pi} \left( \frac{I_1 x}{x^2 + h^2} + \frac{I_2 (d-x)}{(d-x)^2 + h^2} \right) \quad (\text{A.18})$$

It is clear that these do indeed obey a simple reversal of sign in the current term for the parallel case, however, since the geometry is quite complex in its definition, is it sometimes useful to consider the two cases as two different equation sets. As previously stated in Chapter 3, these equations are accurate to the COMSOL simulations for three-dimensional wires to within 1 G/A in the most important regions of interest.

By using these equations in conjunction with the gradient schemes described in Chapter 3, magnetic field simulations of current carrying wire geometries can be achieved extremely quickly producing high accuracy results using solely analytical methods ignoring the true geometry of the fabricated wires. Though these equations serve as a very applicable starting point in the design of a pair of current carrying wires, in regimes where near-field effects may start to dominate, verification through a COMSOL simulation is recommended.

## A.2 Reference data for current carrying wire schemes

As explained in Chapter 3, a summary of the reasonable capabilities for some current carrying wire schemes can be found in Tables A.1, A.2, A.3, A.4, and A.5. It is explicit in these results that compensated anti-parallel current carrying wires provide a much higher planar gradient than any gradient at an ion position in the parallel scheme. In addition to the bare gradient relations, a comparison has been done which limits the compensated field



to 100 G and/or 10 A. 100 G is a high but reasonable field to compensate using external field sources that can be built around the experiment. Similarly, 10 A is a suggested comfortable top limit current to run through the wires based on discussions with the rest of the group. My simulations show that the compensated anti-parallel scheme wins all out when using reasonable operation parameters when compared to the parallel case. In these tables, “tailored” gradients refer to gradients realised after nilling the anti-parallel set of current wires using an offset field oriented in  $B_x$  rather than  $B_z$ .

Table A.1: Summary of current wire planar gradient results for two parallel current carrying wire schemes. Dimensions of wires are given as width (w) by length (l) by depth (d). The separation is the centre separation in the width direction. \* denotes a high approximation, \*\* denotes a low approximation. \*\*\* - The offset field at the central position can be found in Table A.2.

Wire dimensions $w \times l \times d$ (mm)	Separation (mm)	Maximum field height above top of wires ( $\mu\text{m}$ )	Maximum field value at 10 A (G)	Height above top of wires ( $\mu\text{m}$ )	Planar gradient (T/m/A)	Offset field at which the planar gradient is measured (G/A)	Approximate gradient at 10 A with milled field (T/m)	Gradient at 10 A at 20 G mark at maximum point (T/m)	Approximate gradient for 100 G milled or 10 A limit (T/m)***
$0.06 \times 10 \times 0.03$	0.23	100	175.5	50	22.22	22.5	115.6		76.05
				75	10.72	21.5	45.1		26.34
				100	5.1	19.5	8	80	4.57
				150	1.02	16.8	36.9		22.58
				200	0.05*	14.45	38.5		26.63
				250	0.025**	12.68	32.8		25.85
$0.06 \times 10 \times 0.03$	0.35	158	114.7	50	13.64	13.5	88.7		88.7
				100	6.02	13.2	37		34.97
				150	2.87	13.1	5	40	4.37
				200	1.1	11.7	20		17.86
				250	0.34	10.65	15.63		14.87

Table A.2: Summary of current wire vertical gradient results for two parallel current carrying wire schemes. Dimensions of wires are given as width (w) by length (l) by depth (d). The separation is the centre separation in the width direction. \* denotes an effective value.

Wire dimensions $w \times l \times d$ (mm)	Separation (mm)	Maximum field height above top of wires ( $\mu\text{m}$ )	Maximum field value at 10 A (G)	Height above top of wires ( $\mu\text{m}$ )	Vertical gradient (T/m/A)	Offset field (G/A)	Approximate gradient at 10 A with milled field (T/m)	Approximate gradient for 100 G milled or 10 A limit (T/m)
$0.06 \times 10 \times 0.03$	0.23	100	175.5	50	11.5	15.2	80	52.6
				75	3.39	17.12	30	17.5
				100	0.3	17.52	0*	0*
				150	3.52	16.34	34	20.8
				200	3.75	14.46	38	26.3
				250	3.25	12.69	31.4	24.7
$0.06 \times 10 \times 0.03$	0.35	158	114.7	50	8.8	7.56	77.4	77.4
				100	3.6	10.58	31.7	30.0
				150	0.4	11.45	0*	0*
				200	1.05	11.2	7.8	7.0
				250	1.55	10.51	16	15.2

Table A.3: Summary of current wire planar gradient results for two anti-parallel current carrying wire schemes. Dimensions of wires are given as width (w) by length (l) by depth (d). The separation is the centre separation in the width direction. \* denotes an effective value accounting for simulation quantisation and mesh errors. \*\* - This gradient was simulated to be 170.67 T/m using an under-chip magnet in order to nil the field.

Wire dimensions $w \times l \times d$ (mm)	Separation (mm)	Maximum field height above top of wires ( $\mu\text{m}$ )	Maximum field value at 10 A (G)	Height above top of wires ( $\mu\text{m}$ )	Planar gradient (T/m/A)	Offset field at which the planar gradient is measured (G/A)	Approximate gradient at 10 A with nilled field (T/m)	Approximate gradient for 100 G nilled or 10 A limit (T/m)
$0.04 \times 10 \times 0.03$	0.15	-15	560	55	0*	28.7	385	134
				105	0*	14.95	175**	117
				155	0*	8.67	83.75	83.75
				205	0*	5.54	45.5	45.5
				255	0*	3.82	26.25	26.25
$0.04 \times 10 \times 0.03$	0.25	-15	327.5	55	0*	24.35	172	70.6
				105	0*	16.63	131.25	78.9
				155	0*	11.2	85.5	76.3
				205	0*	7.8	54.5	54.5
				255	0*	5.65	33.75	33.75

Table A.4: Summary of current wire vertical and “vertical tailored” gradient results for two anti-parallel current carrying wire schemes. Dimensions of wires are given as width (w) by length (l) by depth (d). The separation is the centre separation in the width direction. The high field and nilled vertical gradients should be the same in theory due to the nature of its origin.

Wire dimensions $w \times l \times d$ (mm)	Separation (mm)	Height above top of wires ( $\mu\text{m}$ )	Offset field at which the vertical gradient is measured (G/A)	Vertical gradient (T/m/A)	Approximate gradient for 100 G nilled or 10 A limit (T/m)	Off-centre position of tailored gradient ( $\mu\text{m}$ )	Offset field at which the tailored gradient is measured (G/A)	Approximate gradient at 10 A with nilled field (T/m)	Approximate gradient for 100 G nilled or 10 A limit (T/m)
$0.04 \times 10 \times 0.03$	0.15	55	28.7	37.5	130.7	103.4	19.15	406.1	212.1
		105	14.95	18.0	120.4	142.5	8.71	123.5	123.5
		155	8.67	8.5	85	185.9	4.7	52.8	52.8
		205	5.54	4.6	46	232.5	2.75	22.4	22.4
		255	3.82	2.53	25.3	279	1.96	14.8	14.8
$0.04 \times 10 \times 0.03$	0.25	55	24.35	16.6	68.2	143.9	23.03	418.8	181.8
		105	16.63	13.3	80	173.6	12.07	161	133.4
		155	11.2	8.55	76.3	211.1	6.7	65.5	65.5
		205	7.8	5.45	54.5	252.6	4.18	34.6	34.6
		255	5.65	3.2	32	296.6	2.82	15.8	15.8

Table A.5: Summary of current wire “planar tailored” gradient results for two anti-parallel current carrying wire schemes. Dimensions of wires are given as width (w) by length (l) by depth (d). The separation is the centre separation in the width direction. \* denotes a high approximation.

Wire dimensions $w \times l \times d$ (mm)	Separation (mm)	Height above top of wires ( $\mu\text{m}$ )	Off-centre position of tailored gradient ( $\mu\text{m}$ )	Offset field at which the tailored gradient is measured (G/A)	Approximate gradient at 10 A with nilled field (T/m)	Approximate gradient for 100 G nilled or 10 A limit (T/m)
$0.04 \times 10 \times 0.03$	0.15	55	103.4	19.15	285.7	149.19
		105	142.5	8.71	82	82
		155	185.9	4.7	30.8	30.8
		205	232.5	2.75	11.1	11.1
		255	279	1.96	9.5*	9.5*
$0.04 \times 10 \times 0.03$	0.25	55	143.9	23.03	345	149.8
		105	173.6	12.07	104.8	86.8
		155	211.1	6.7	46.7	46.7
		205	252.6	4.18	16.7	16.7
		255	296.6	2.82	8.5	8.5

## Appendix B

# Technical drawings

In this appendix, I display the technical drawings for some of the equipment I have designed and implemented over the course of my study in order to further the experimental setups discussed in this thesis. These are primarily displayed for reference purposes for other members of the experimental group but may also serve as inspiration to others intending to build a similar Faraday cage design or implement the under-chip magnet spacer scheme in their own experimental setups.

For these technical drawings, all dimensions are in millimetres unless otherwise stated. The tolerances, finish, and scale ratio have not been explicitly stated, however, all dimensions are clearly marked. This may mean that multiple technical drawings are used for certain parts due to their complexity. Additional information is provided in the captions regarding adjustments to these drawings that were made during manufacturing. Some terminology is not strictly correct from an engineering standpoint but is sufficient in order to describe the technical drawings, for example, an “M10 through hole”, may refer to a hole that is 10 mm in diameter in this thesis, the correct terminology being an R5 hole. This is contrary to an “M6 though hole” which is a hole drilled so that an M6 thread can fit through the hole, which is acceptable terminology for a drawing.

### B.1 The Faraday cage

The technical drawings for the Faraday cage discussed in Chapter 2 are detailed below. As previously detailed, this Faraday cage is made of 4 mm thick aluminium and fits over the vacuum system and a large portion of the optical setup on the experimental table. Figures B.1 – B.3 show the assembly of the cage, its exterior panels, and internal frame, which are labelled in order to correspond to the technical drawings in Figures B.4 – B.30.

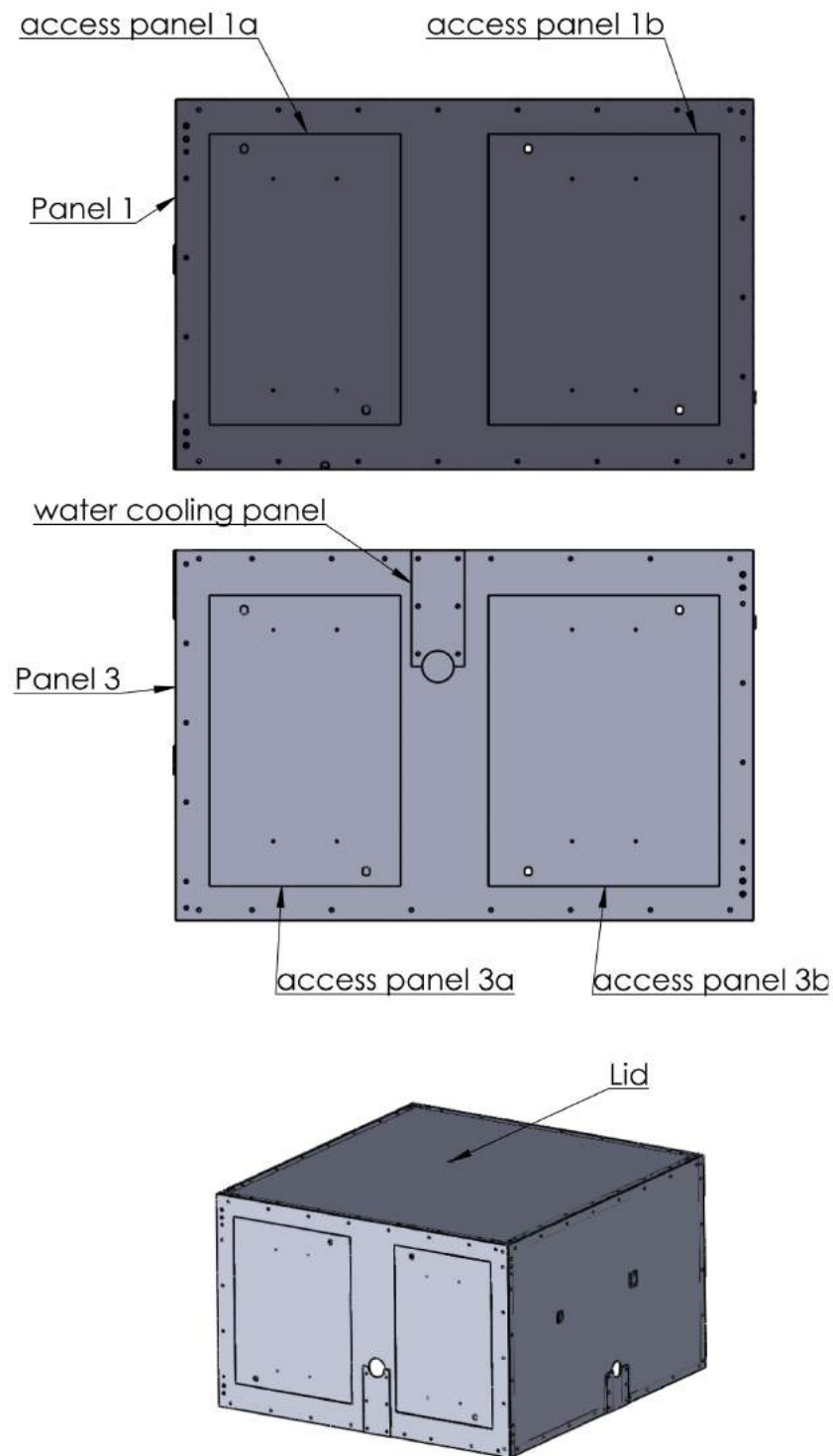


Figure B.1: An assembly diagram of the Faraday cage showing the two sides which have access panels, and the lid of the system. The technical drawings for Panel 1 are shown in Figures B.4 and B.5. Panel 3 is shown in Figures B.13 and B.14 and the water cooling panel attached to it is shown in Figure B.15. The “a-type” and “b-type” access panels are the same for each main panel. The a-type access panel technical drawing is shown in Figure B.6 and the b-type is shown in Figure B.7. The lid is shown in Figures B.29 and B.30.



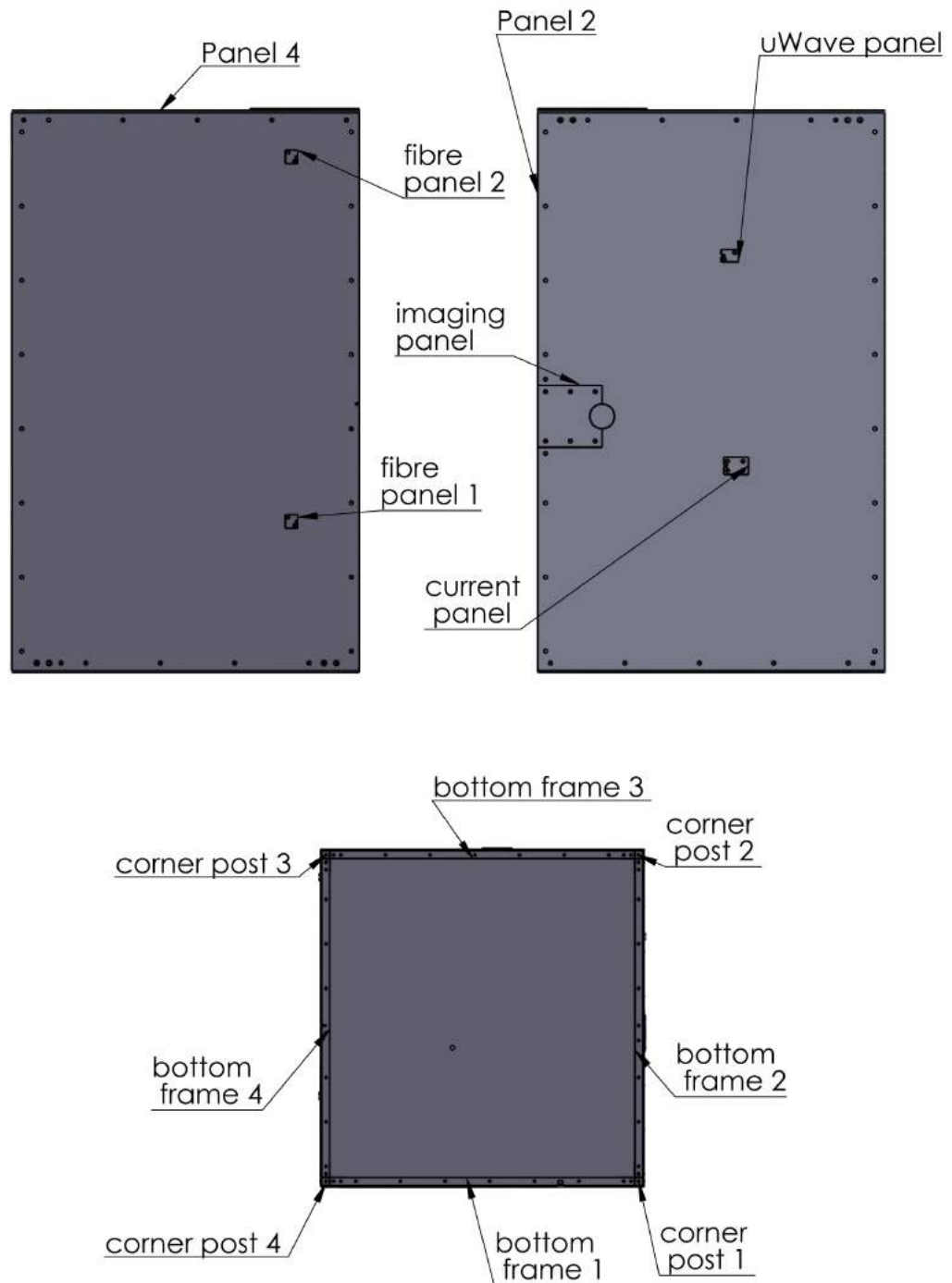


Figure B.2: Another assembly diagram of the Faraday cage showing the two sides which do not have access panels, and the bottom frame of the system. The technical drawings for Panel 2 are shown in Figures B.8 and B.9 with the current, microwave (uWave), and imaging panels shown in Figures B.10, B.11, and B.12 respectively. Panel 4 is shown in Figures B.16 and B.17 and the fibre panels attached to it are shown in Figure B.18. Bottom frames 1 – 4 are shown in Figures B.19 – B.22 and the corner posts are shown in Figure B.23.

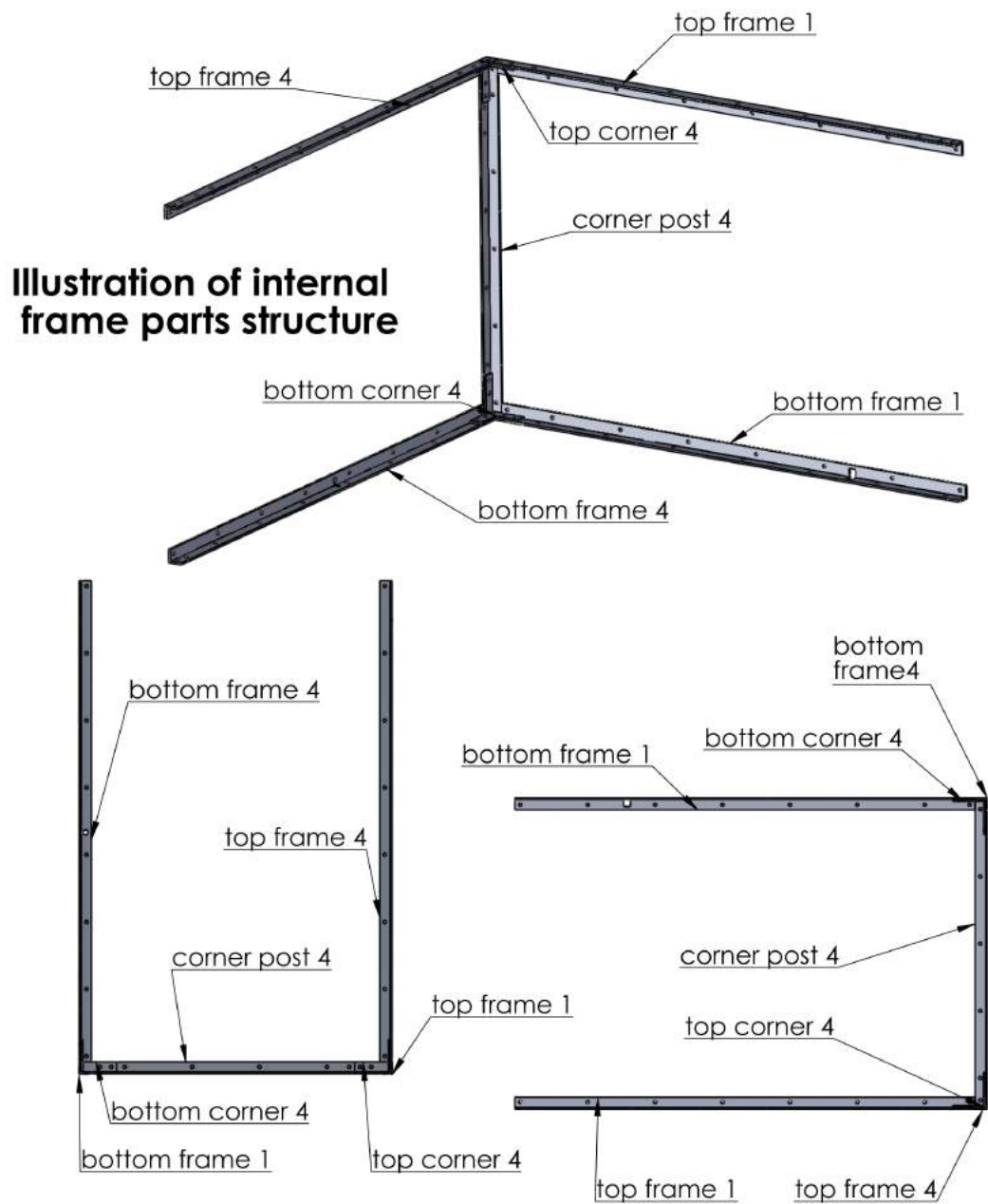


Figure B.3: The final assembly diagram of the Faraday cage showing part of the internal frame structure of the system. The technical drawings for the bottom frames are shown in Figures B.19 – B.22, the top frames are shown in Figures B.26 – B.28 where top frames 2 and 4 are identical, and the bottom corners, corner posts, and top corners are shown in Figures B.24, B.23, and B.25 respectively.

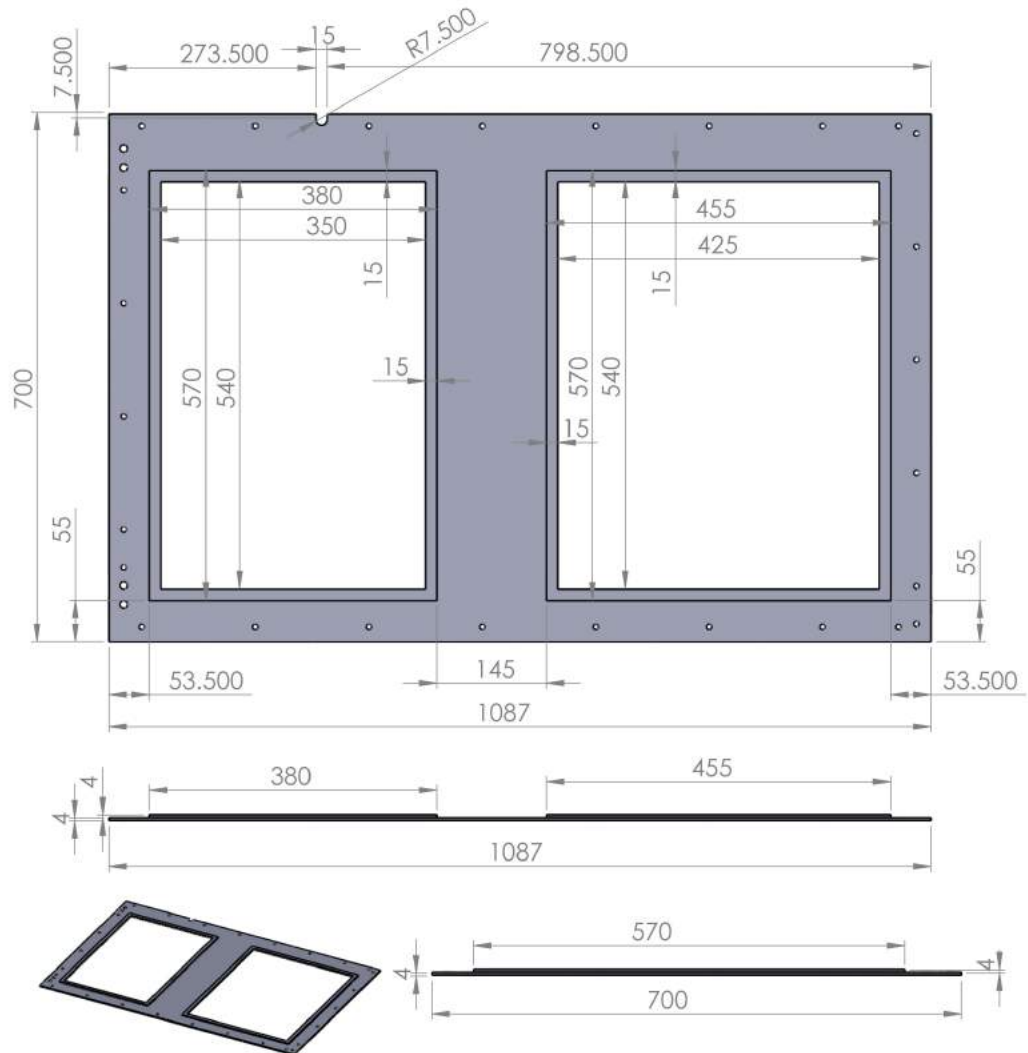


Figure B.4: Inside view of Panel 1 which shows the frames on the inside of the windows into which the access panels shown in Figures B.6 and B.7 fit in order to complete the cage without falling through in addition to providing a point at which the latches can grab onto the main panel. It is best to attach these inner frames using rivets as welding was shown to warp the panel to such a degree that the access panels would no longer fit. One can also see a small R7.500 slot cut into the side of the panel which allows DC cables to enter the cage.

Figure B.5: Outside view of Panel 1 showing the outer window dimensions and the hole placement in order to secure the panel to the inner frame structure of the Faraday cage.

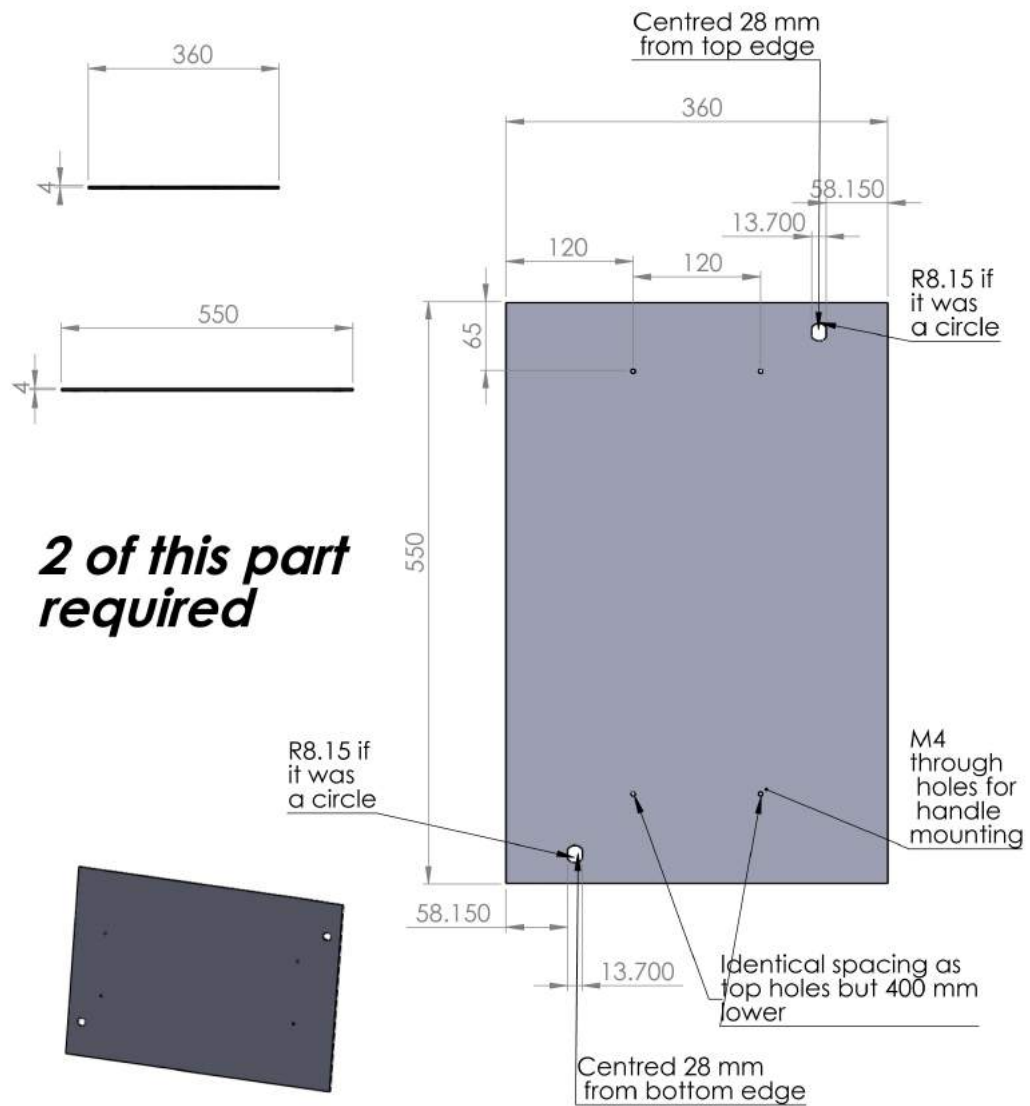


Figure B.6: The smaller a-type access panels which enable access to the inside of the Faraday cage via Panels 1 and 3. The through holes for M4 screws are for a set of aluminium handles purchased from RS Components which enable the panel to be held when being removed from the window. The large holes are machined to fit a set of compression locks, also from RS Components, which hold the access panels in place by grabbing the inner frame of the main panel.

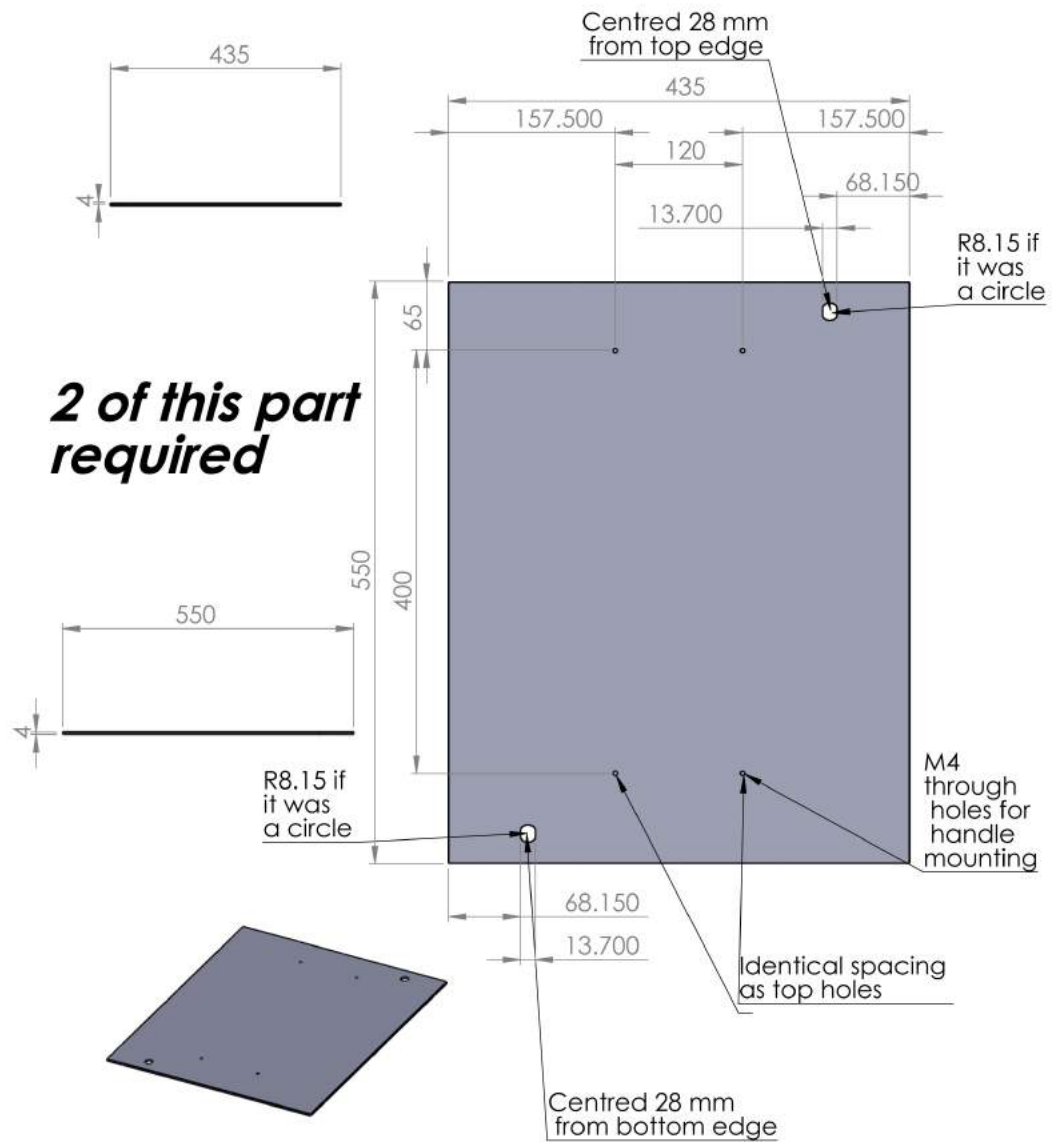


Figure B.7: The larger b-type access panels which enable access to the inside of the Faraday cage via Panels 1 and 3. The holes serve the same purpose as for the a-type access panels shown in Figure B.6.

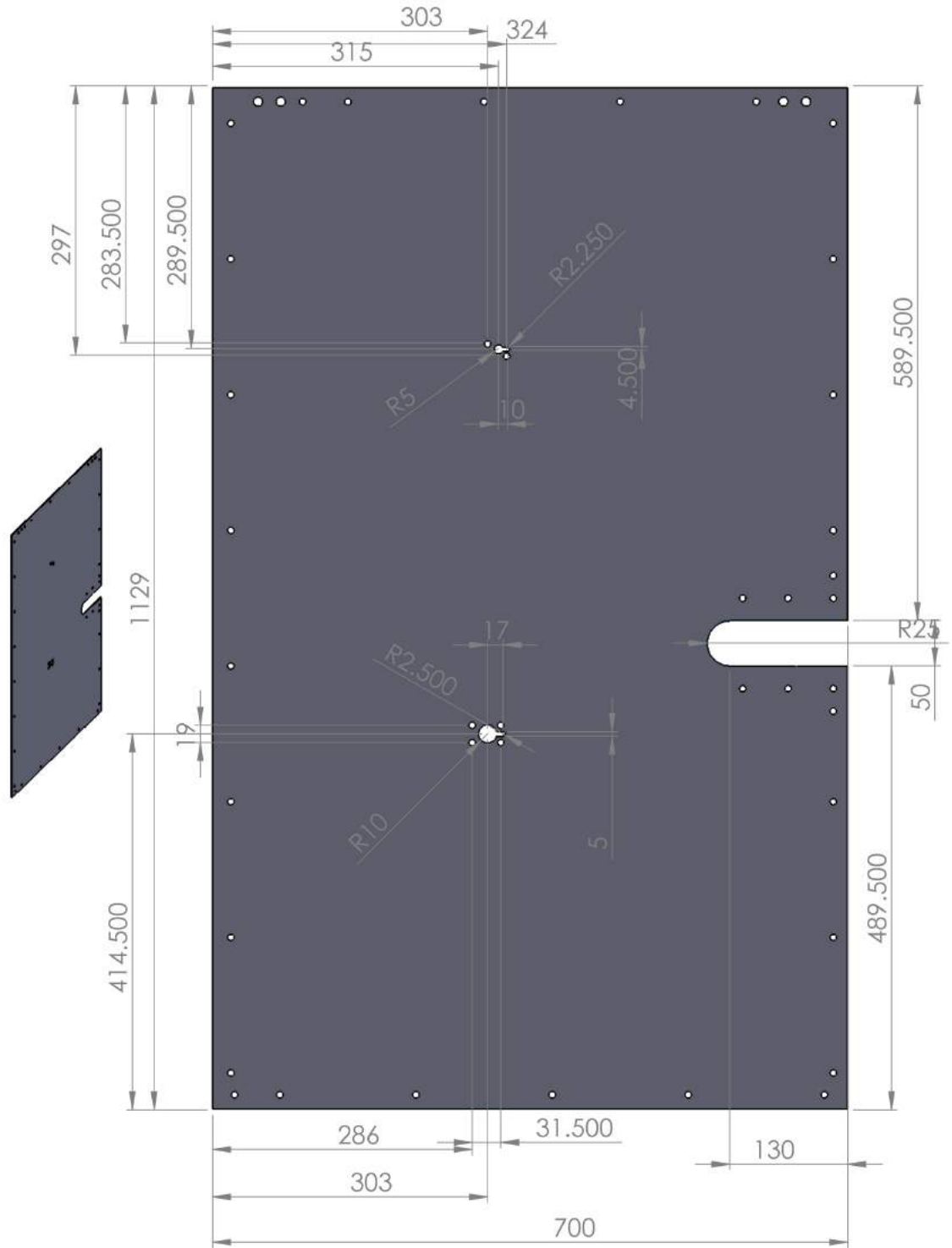


Figure B.8: Inside view of Panel 2 which shows the holes so that the connectors for the compensation coils and microwave cables for coherent manipulation can enter the system. In addition to this, one can see a large R25 slot cut into the side of the panel for the imaging tube. These are covered by their respective panels shown in Figures B.10, B.11, and B.12. The imaging tube hole structure allows this panel to be installed without taking the imaging setup apart. A radius of 25 mm was chosen so that there would be enough movement on the imaging translation stages in order to see the major points on the trap. The hole structure for the current and microwave wiring/cables allows the connector to be inserted into the cage. The cable itself then sits in the smaller section of the hole and the connector hole is covered by the respective panel in order to minimise gaps in the cage.

Figure B.9: Outside view of Panel 2 showing the hole placement in order to secure the panel to the inner frame structure of the Faraday cage.



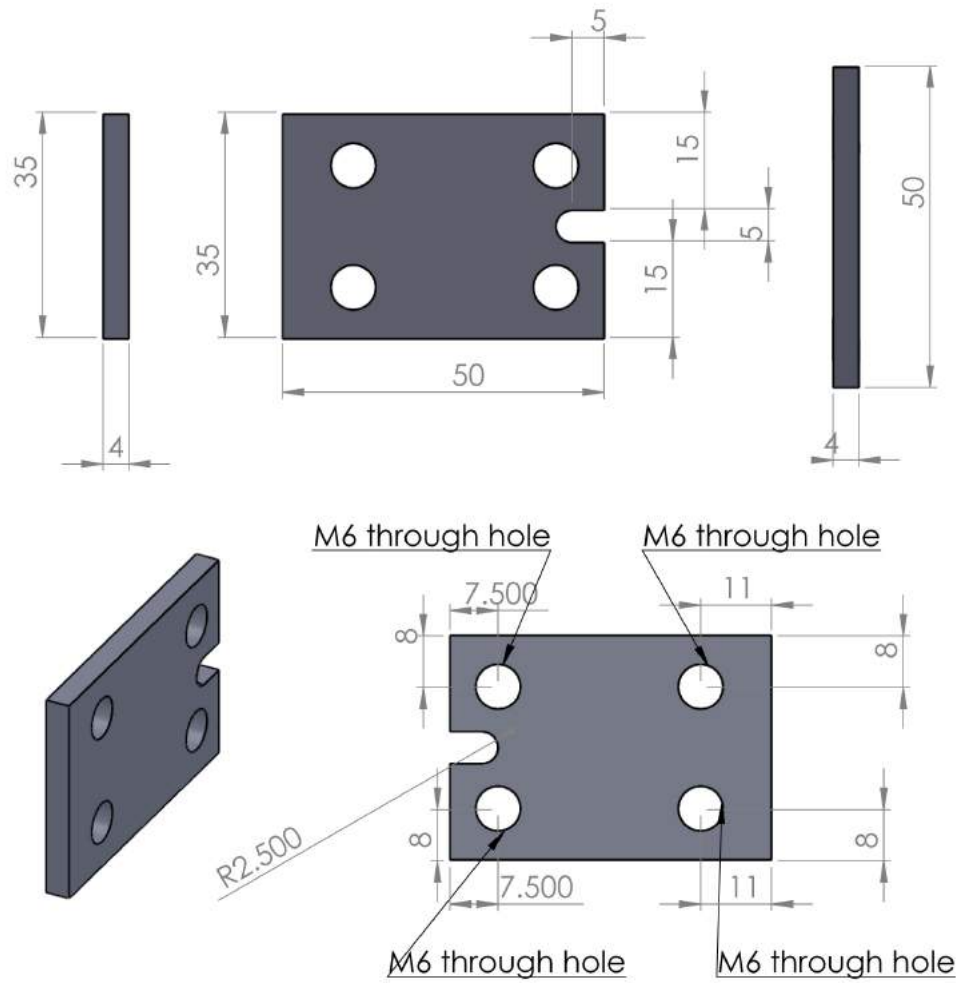


Figure B.10: The current panel that covers the larger (banana) connector hole in Panel 2.

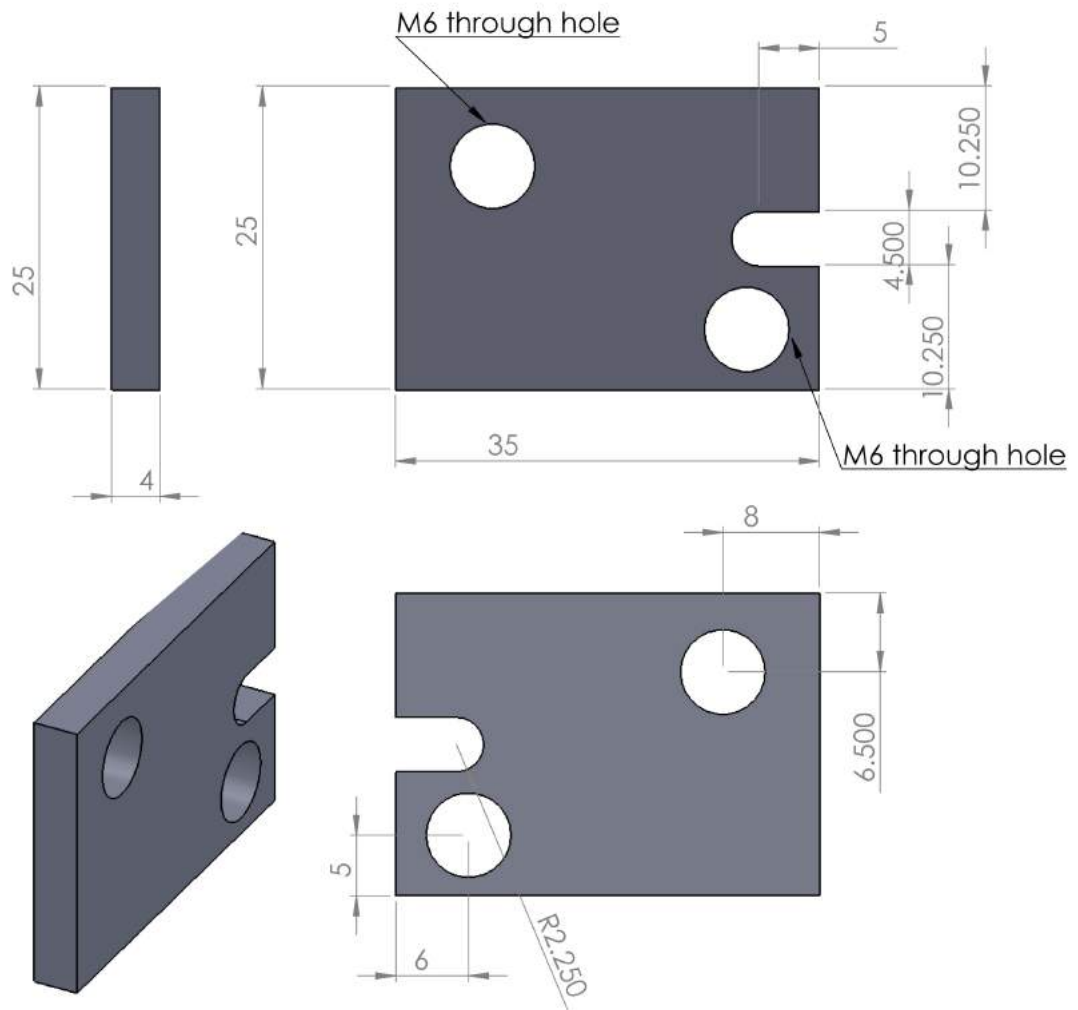


Figure B.11: The microwave (uWave) panel that covers the smaller (SMA) connector hole in Panel 2.

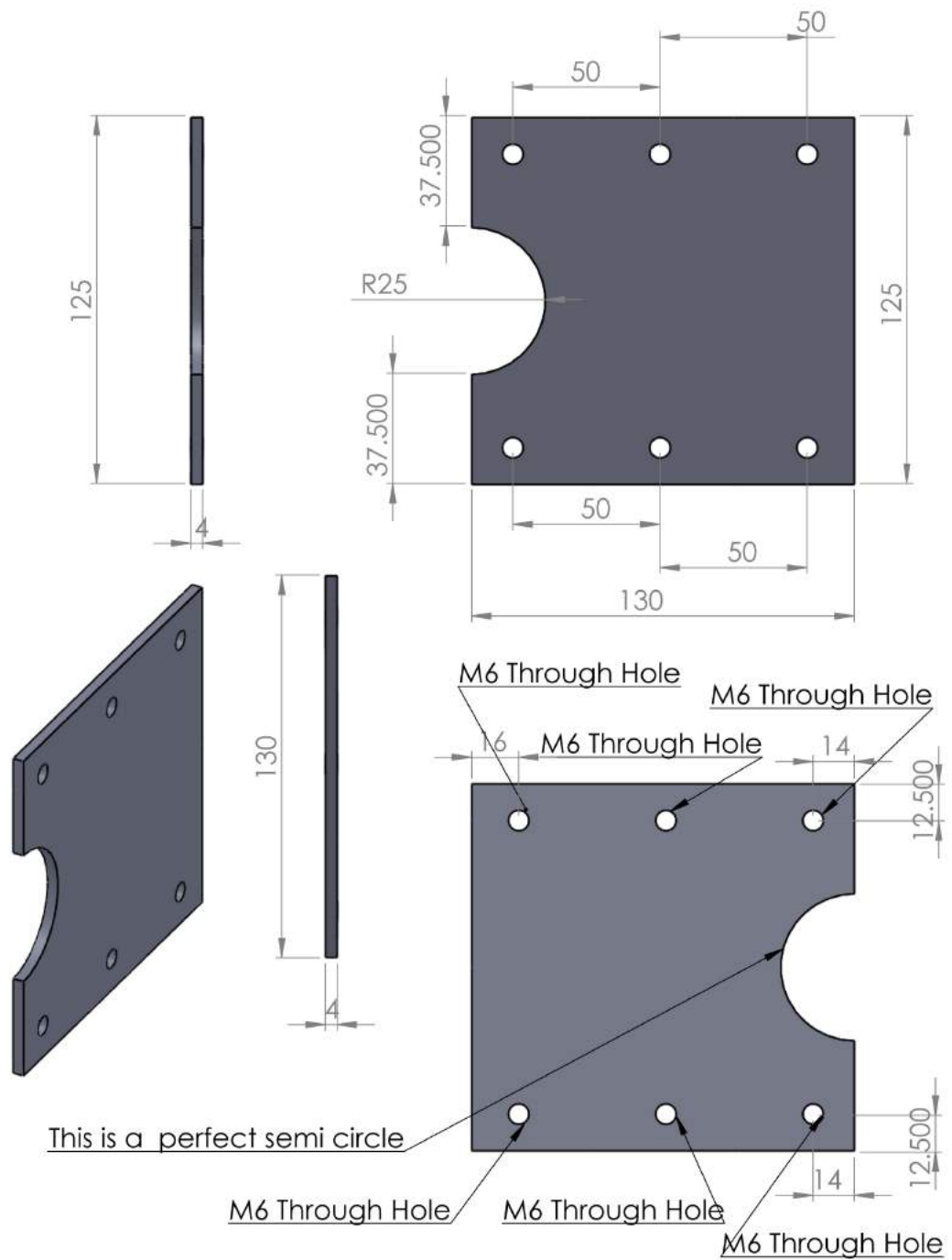


Figure B.12: The imaging panel that completes the cage under the slot in Panel 2 which allows it to be installed without removing the imaging tube.

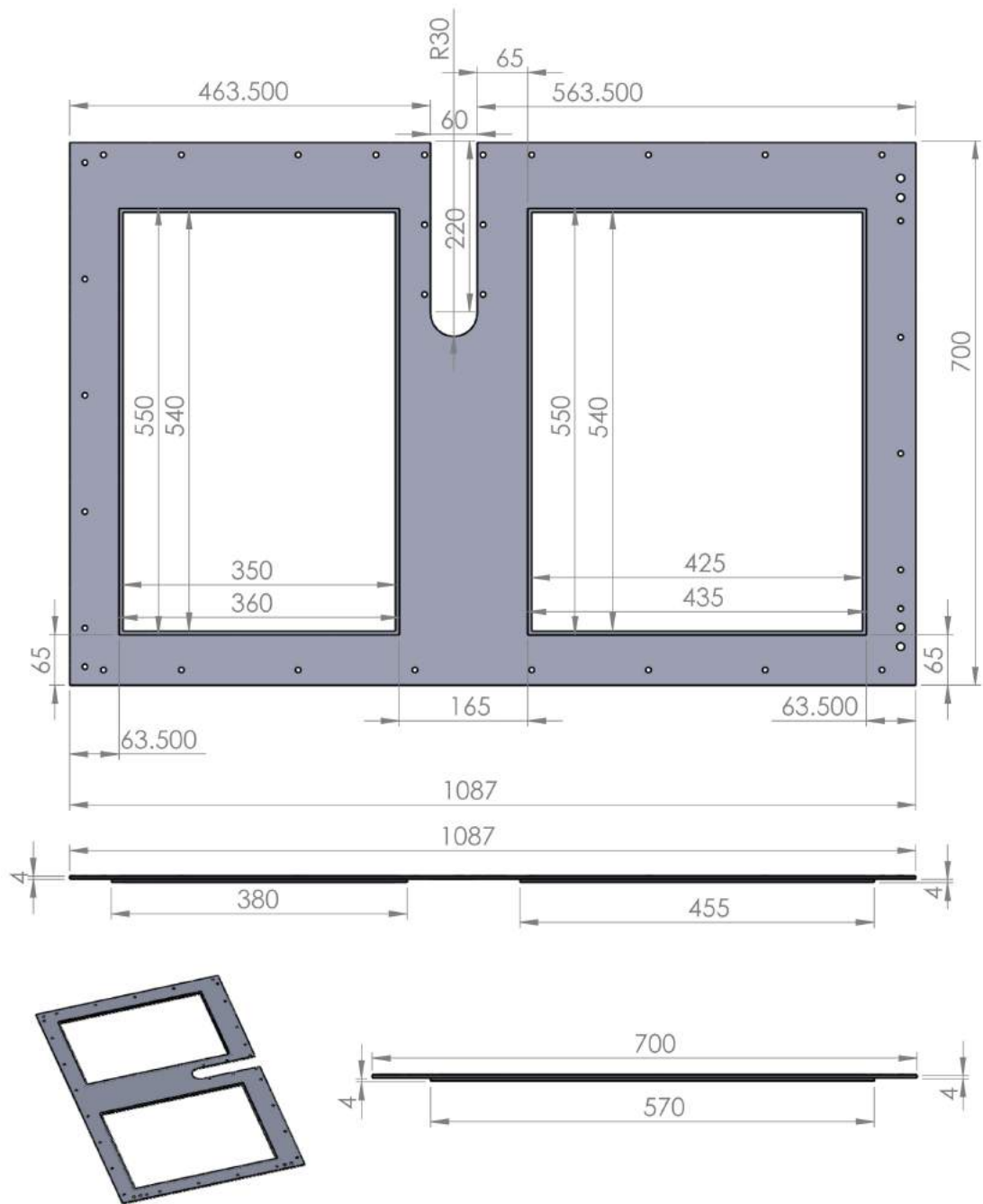


Figure B.13: Outside view of Panel 3 which shows the windows in order to fit the access panels and an R30 slot which allows the compensation coil water cooling pipes to exit the system. In a similar way to Panel 2, this slot allows Panel 3 to be installed without removing these pipes; this is covered by the water cooling panel shown in Figure B.15.

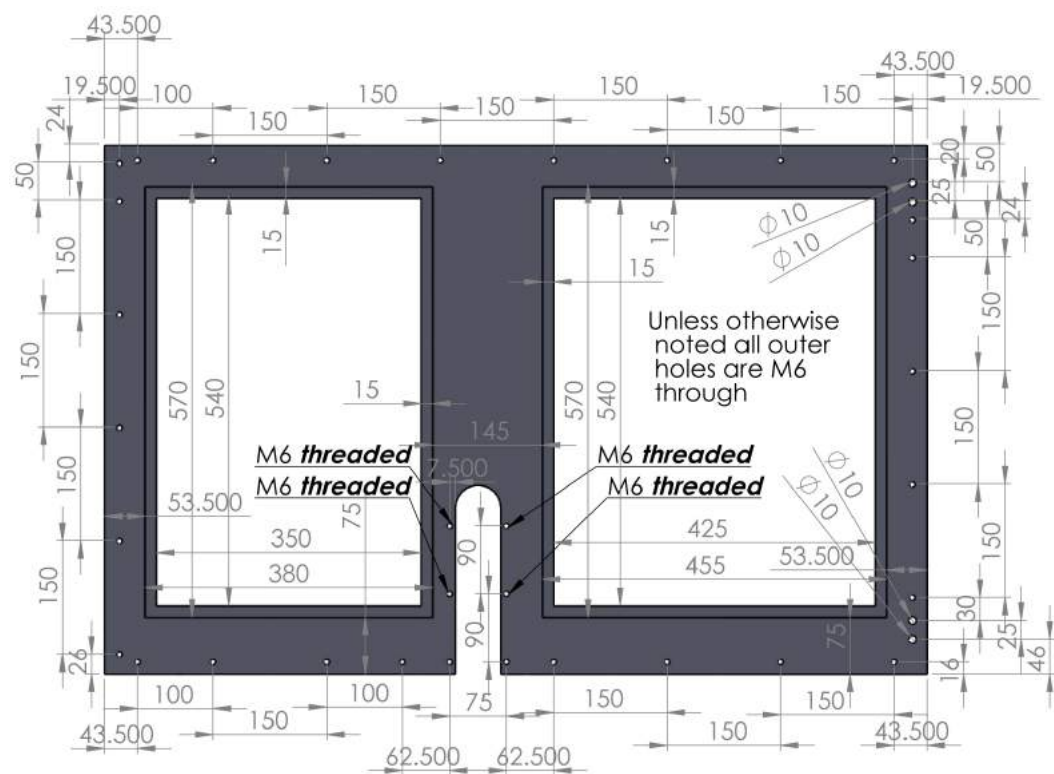


Figure B.14: Inside view of Panel 3 showing the inner frame measurements for the access panels and the hole placement in order to secure the panel to the inner frame structure of the Faraday cage.

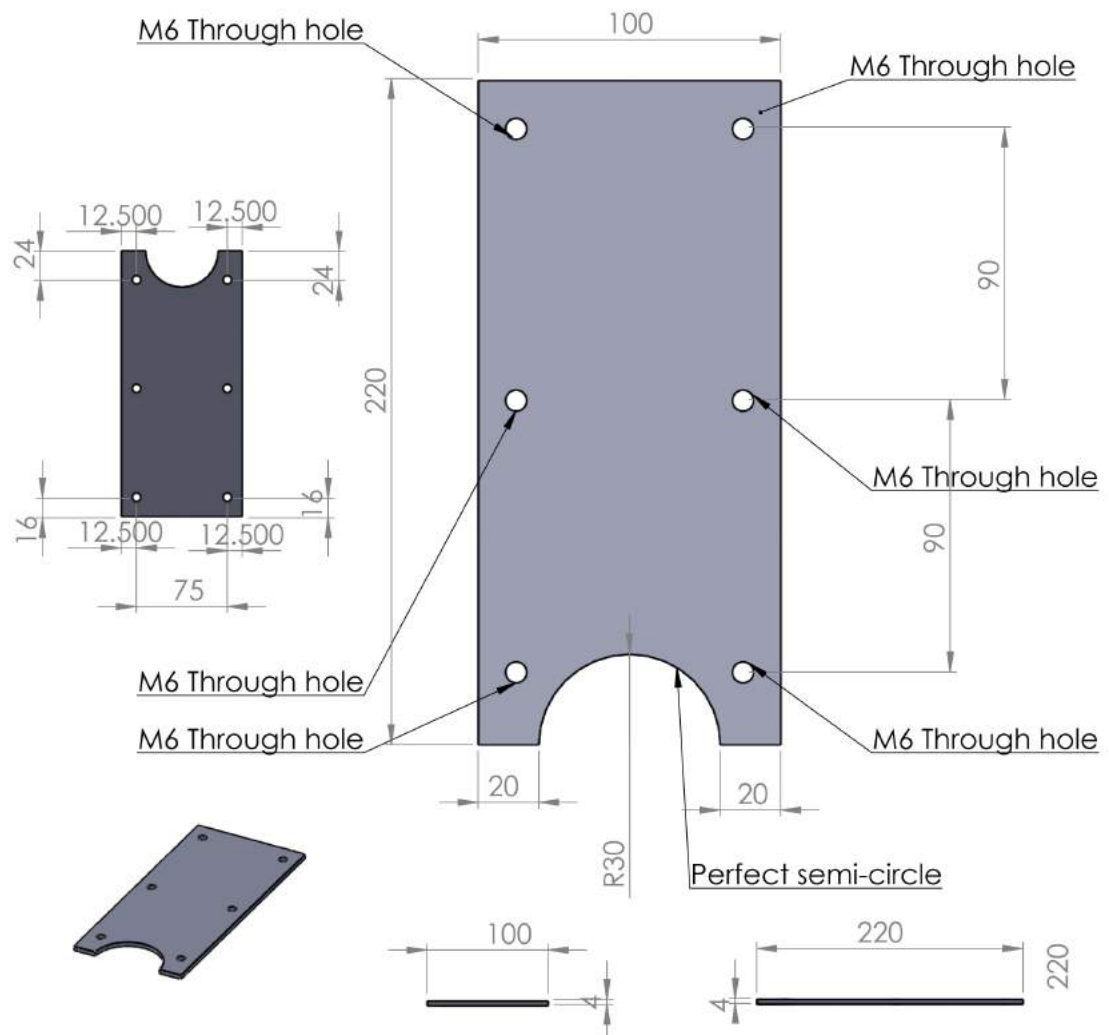


Figure B.15: The water cooling panel that completes the cage under the slot in Panel 3 which allows it to be installed without removing the water cooling piping.

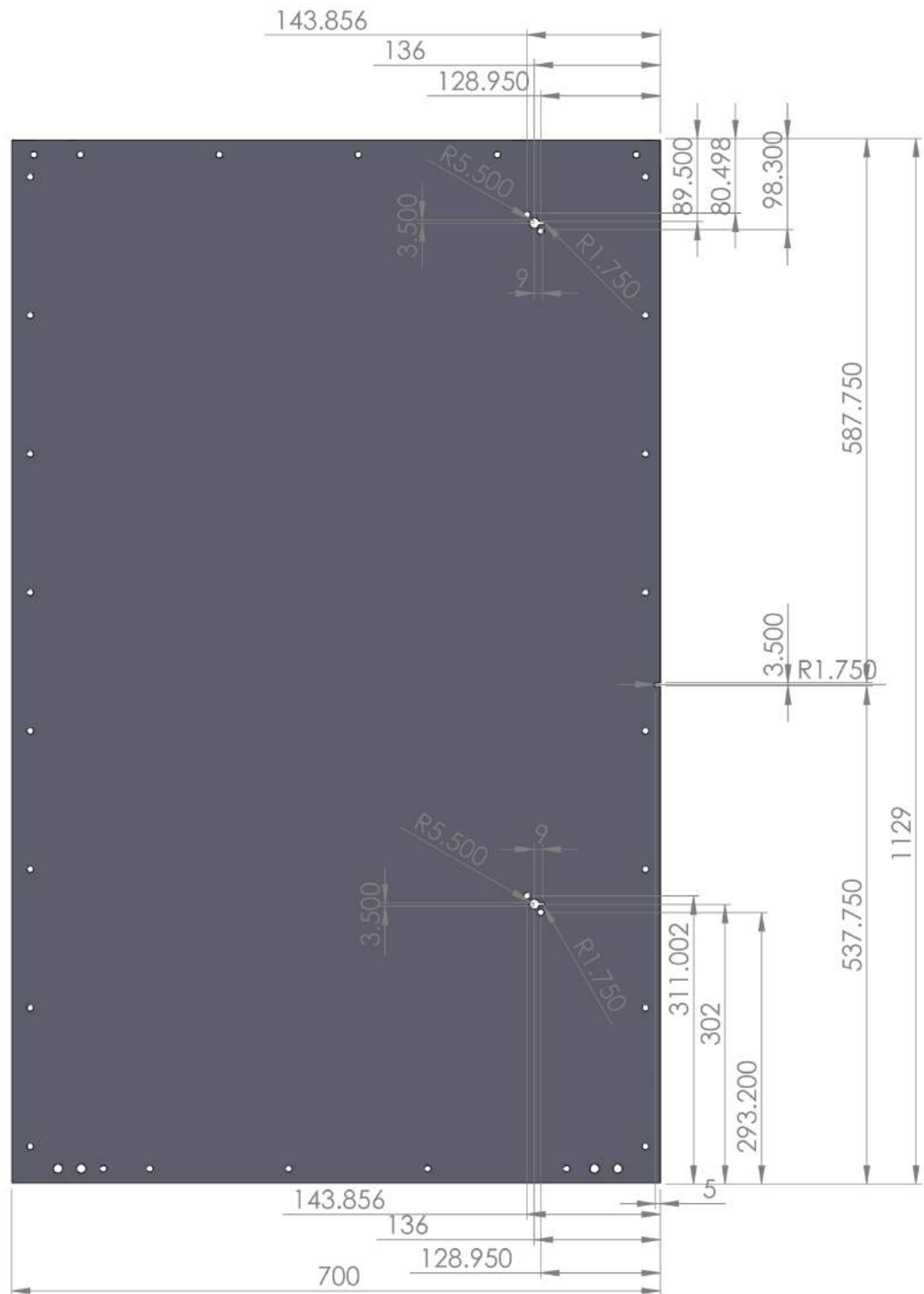


Figure B.16: Outside view of Panel 4 which shows the small connector holes that allow optical fibres to enter the cage for the post-fibre laser optical setup. An additional fibre can enter the cage through the small  $R1.750$  slot in the bottom on the frame.

Figure B.17: Inside view of Panel 4 showing the hole placement in order to secure the panel to the inner frame structure of the Faraday cage.



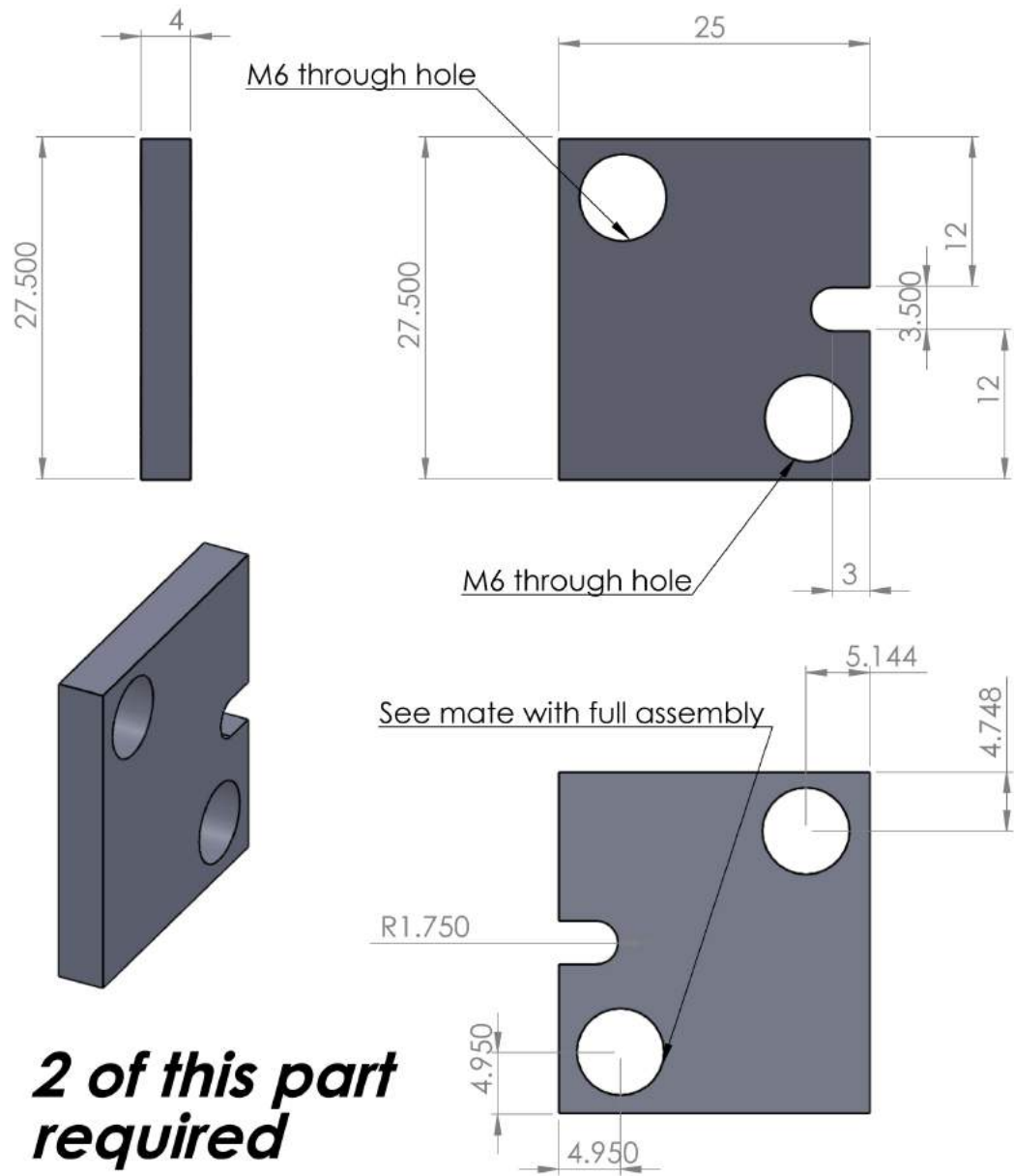


Figure B.18: The fibre panels that cover the optical fibre connector holes in Panel 4.



Holes along this orientation are M6 through

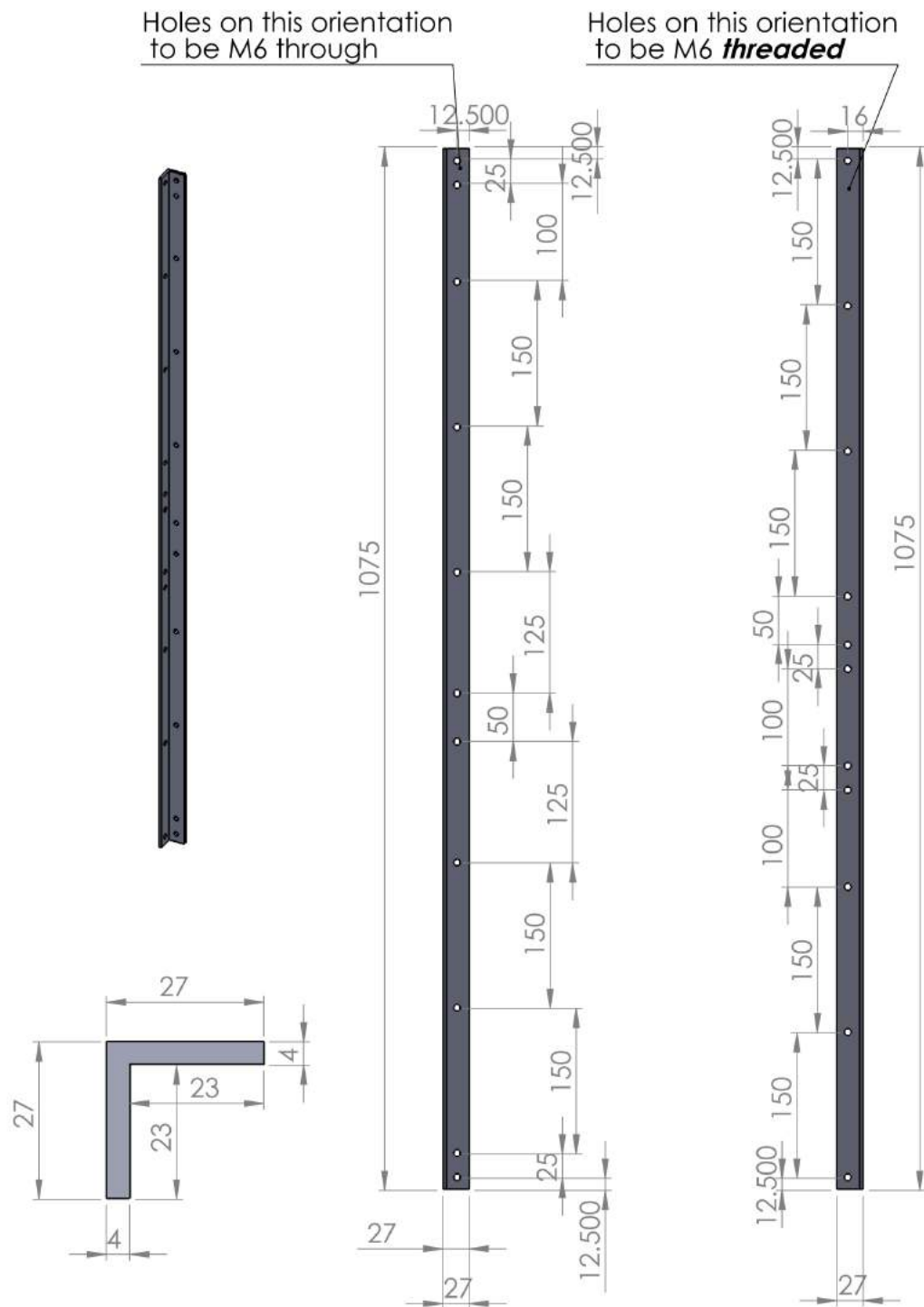


Figure B.20: Bottom frame 2 with extra holes associated with the position of the imaging panel on Panel 2.

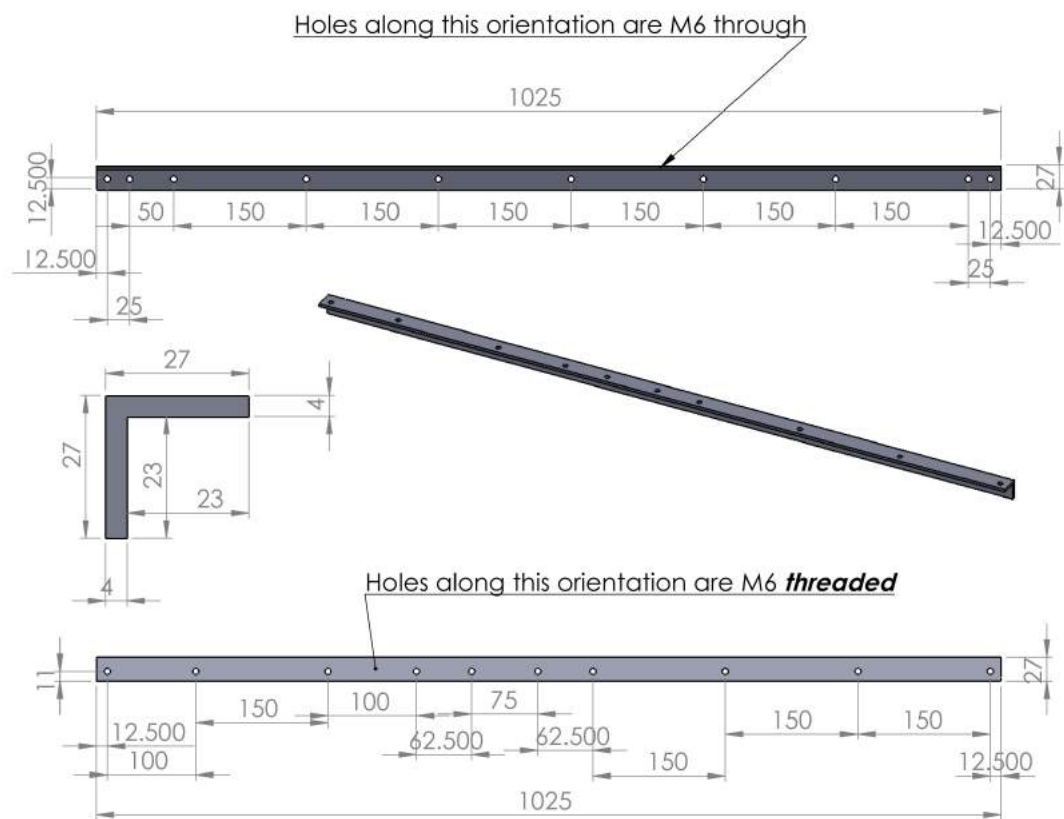


Figure B.21: Bottom frame 3 with extra holes associated with the position of the water cooling panel on Panel 3.



Holes along this orientation are M6 ***threaded***

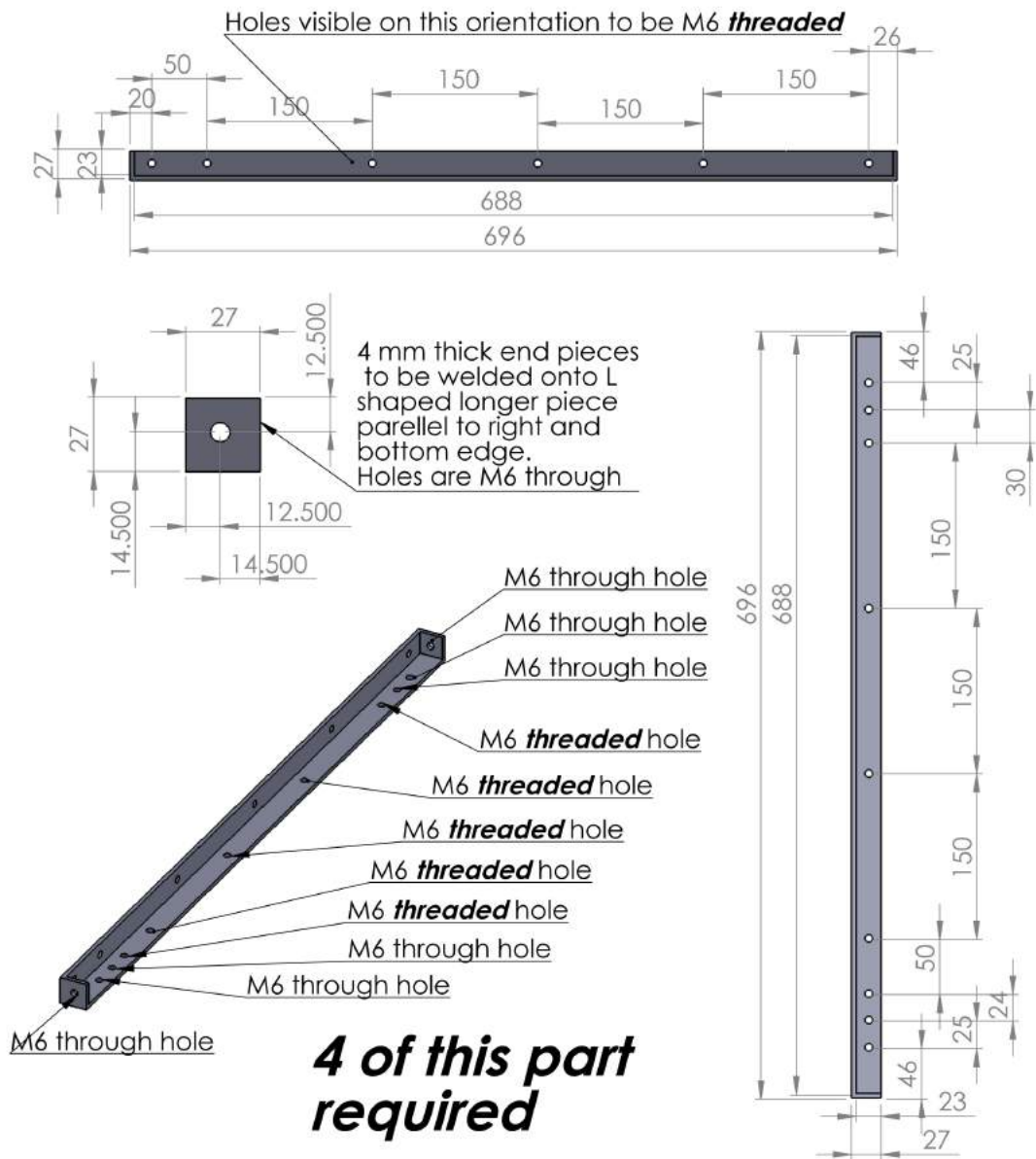


Figure B.23: The corner posts of the Faraday cage. The threaded holes are for installing the main panels and the through holes are so that these corner posts can be connected to the bottom and top corner pieces which hold the frames together.

***4 of this part  
required***

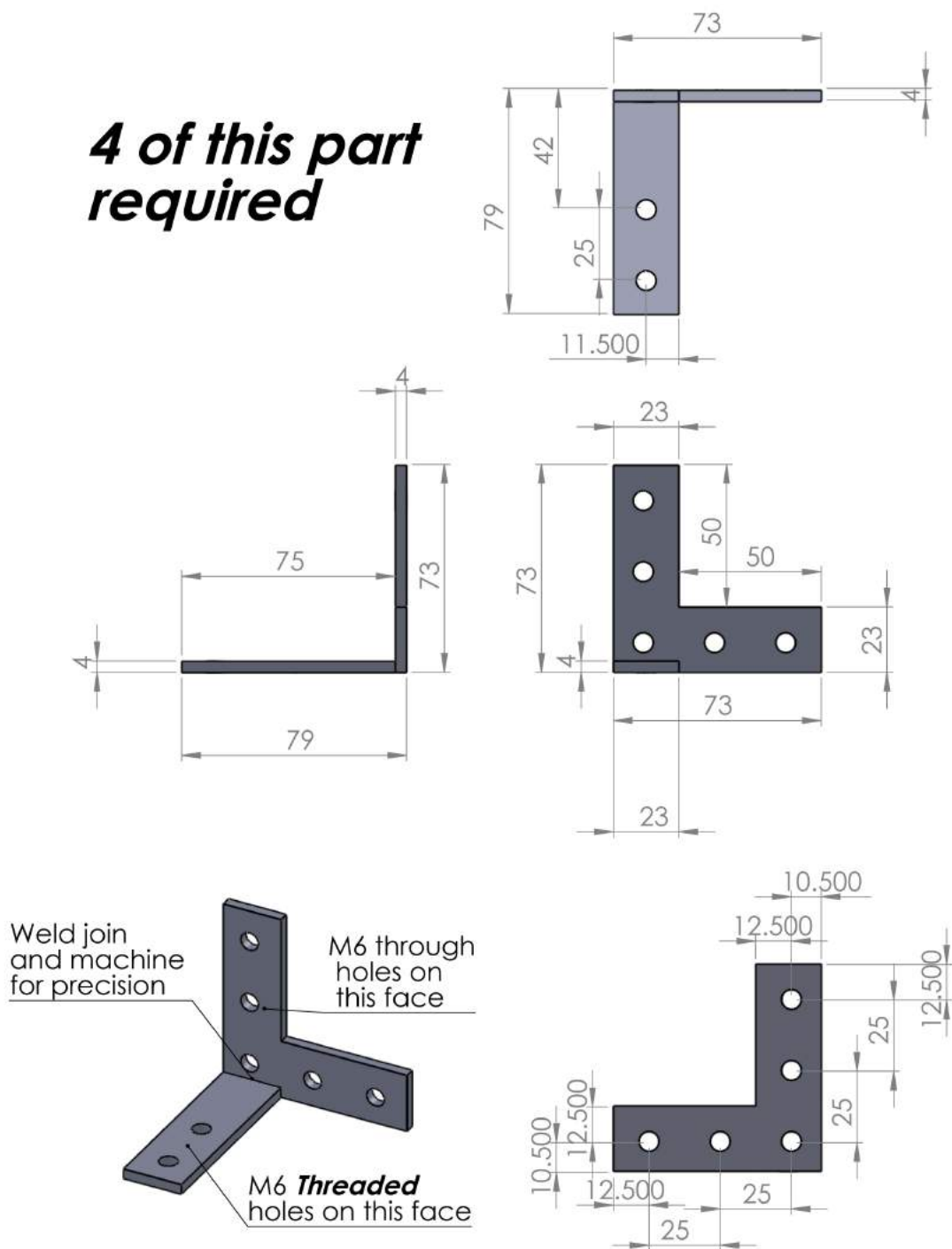


Figure B.24: The bottom corner pieces which secure the corner posts to the bottom frames of the cage. The through holes bolt through the bottom frames onto the experimental table. The threaded holes allow the corner posts to be secured in place.

***4 of this part  
required***

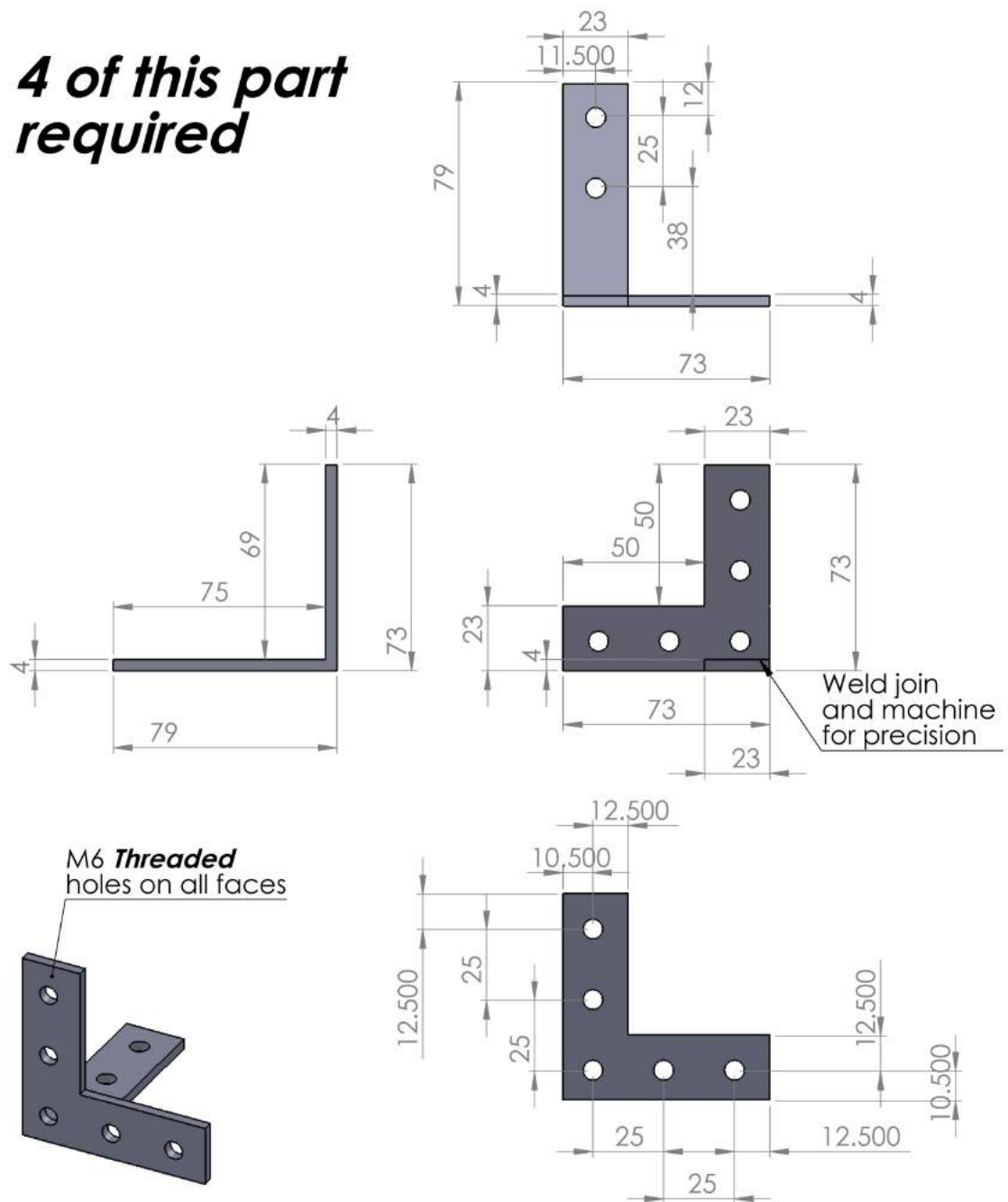


Figure B.25: The top corner pieces which secure the corner posts to the top frames of the cage. All holes are threaded because unlike the bottom corners, the experimental table cannot be used to secure the bolts in place.



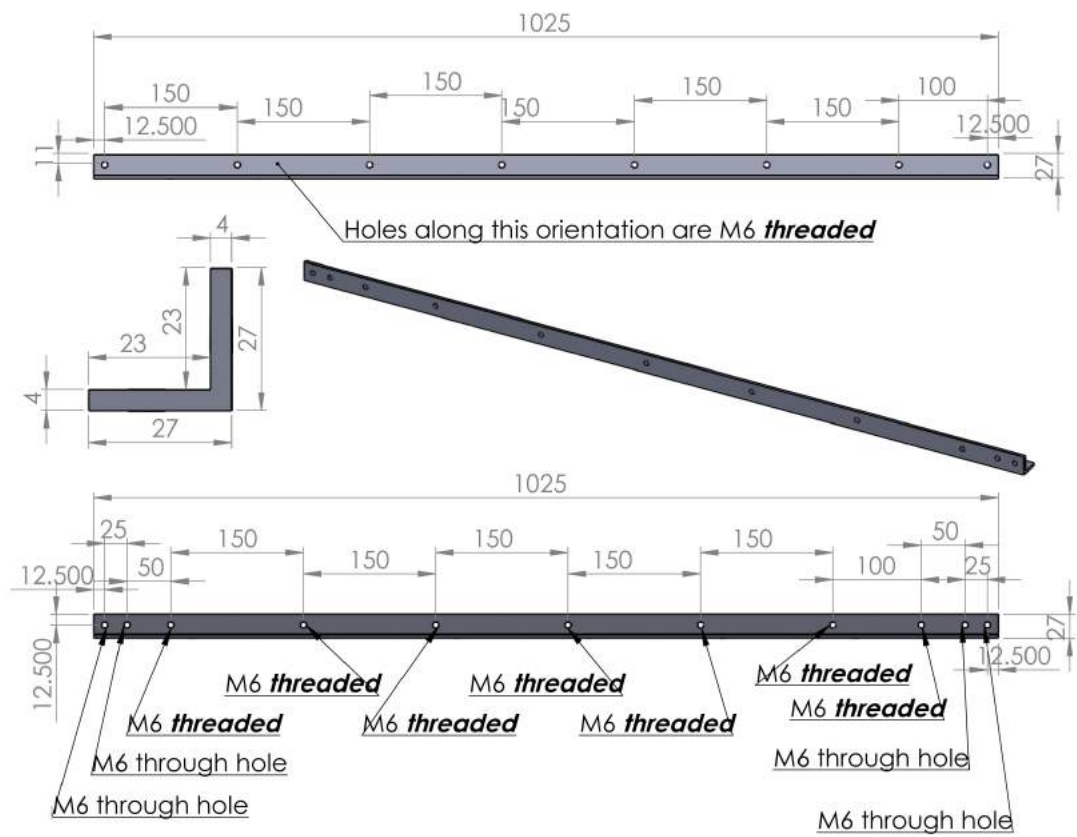


Figure B.26: Top frame 1 associated with Panel 1.



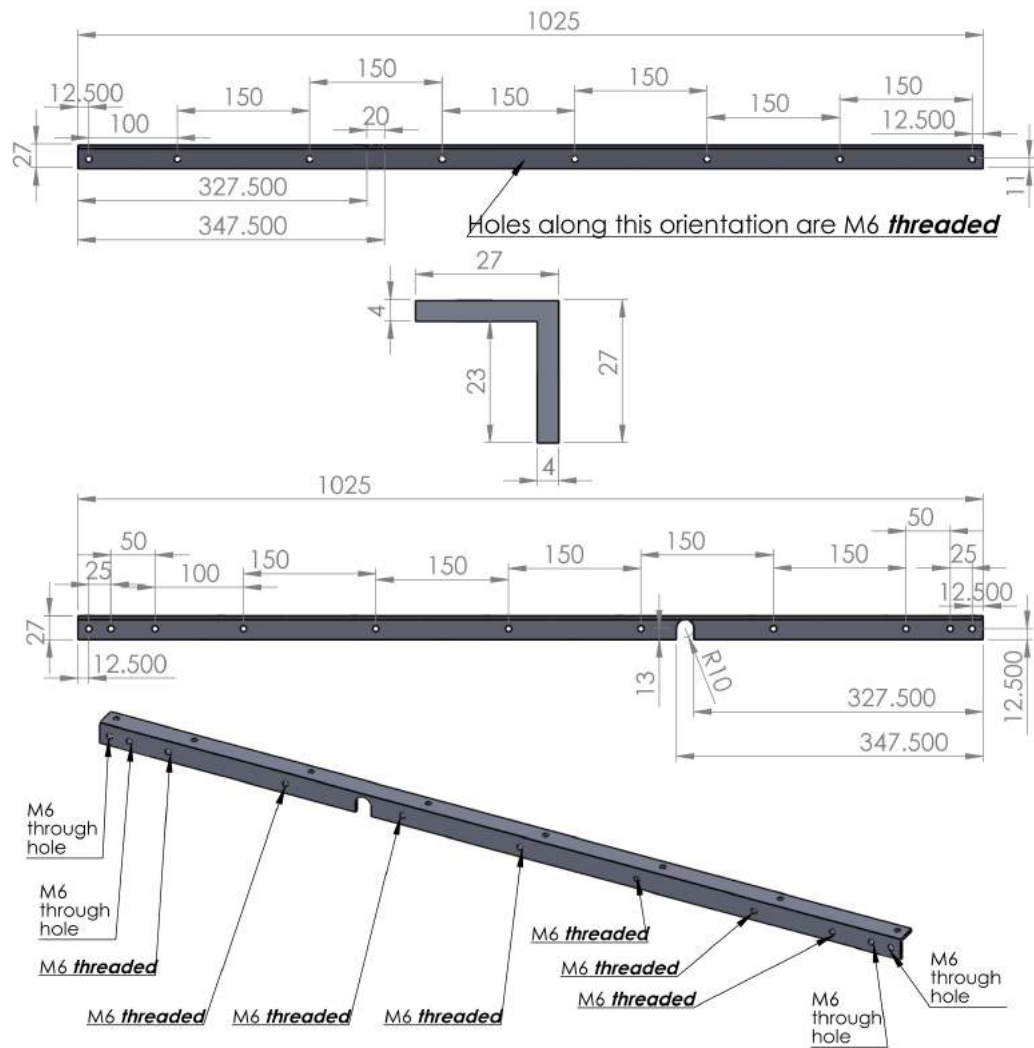


Figure B.28: Top frame 3 associated with Panel 3. There is a slot cut into this frame which allows the ion pump and gauge cables to exit the cage matching with the slot cut into the lid of the cage.

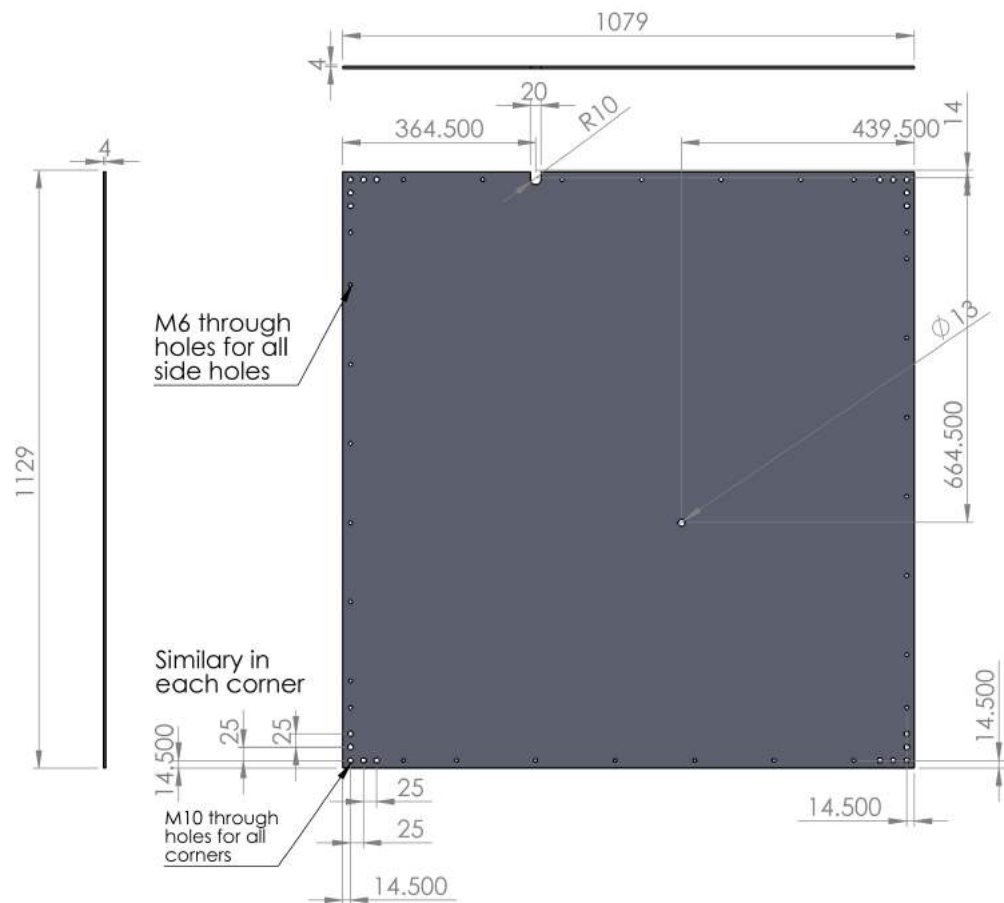


Figure B.29: Outside view of the Faraday cage lid showing the slot dimensions so that the ion pump and gauge cables can exit the system and the near-central hole into which a BNC connector is installed for the trap RF connection. The corner holes are larger so that the lid can fit over the heads of the M6 bolts that secure the top frames to the top corners.

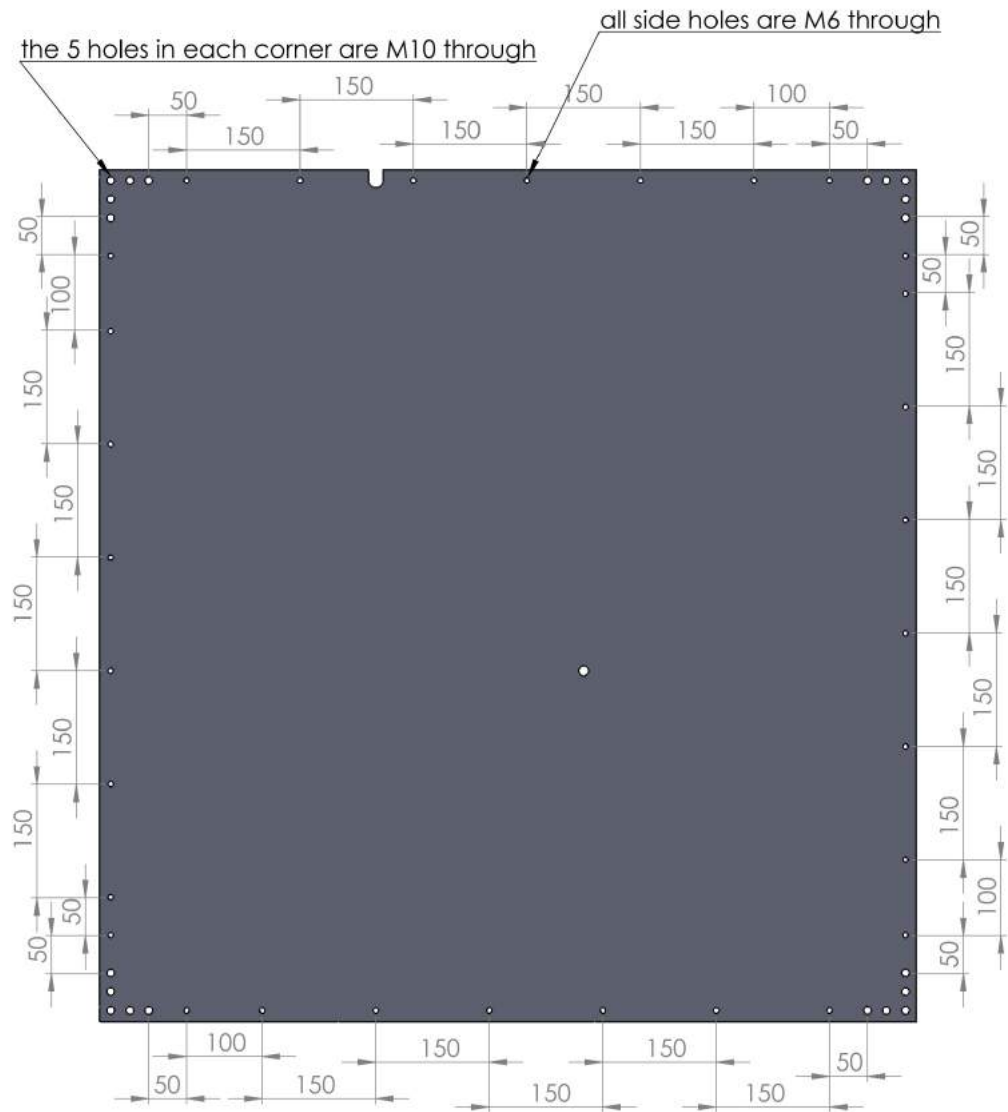


Figure B.30: Outside view of the Faraday cage lid showing the hole placement in order to secure it to the top frames of the inner frame structure.

## B.2 The alignment stage

This next group of technical drawings concerns the alignment stage that was discussed and constructed in Chapter 4. All of these parts are made of aluminium with the exception of the PTFE portion of the pump-activated chip tongue. The technical drawings of some parts have been omitted because of their extremely simple nature, such as an additional riser for the microscope translation stage mount shown in Figure B.32 and the PTFE spacers used to isolate the heating plate (the technical drawing of which is shown in Figure B.36) from the ThorLabs vertical translation stage; these dimensions can be taken from the corners of the heating plate.

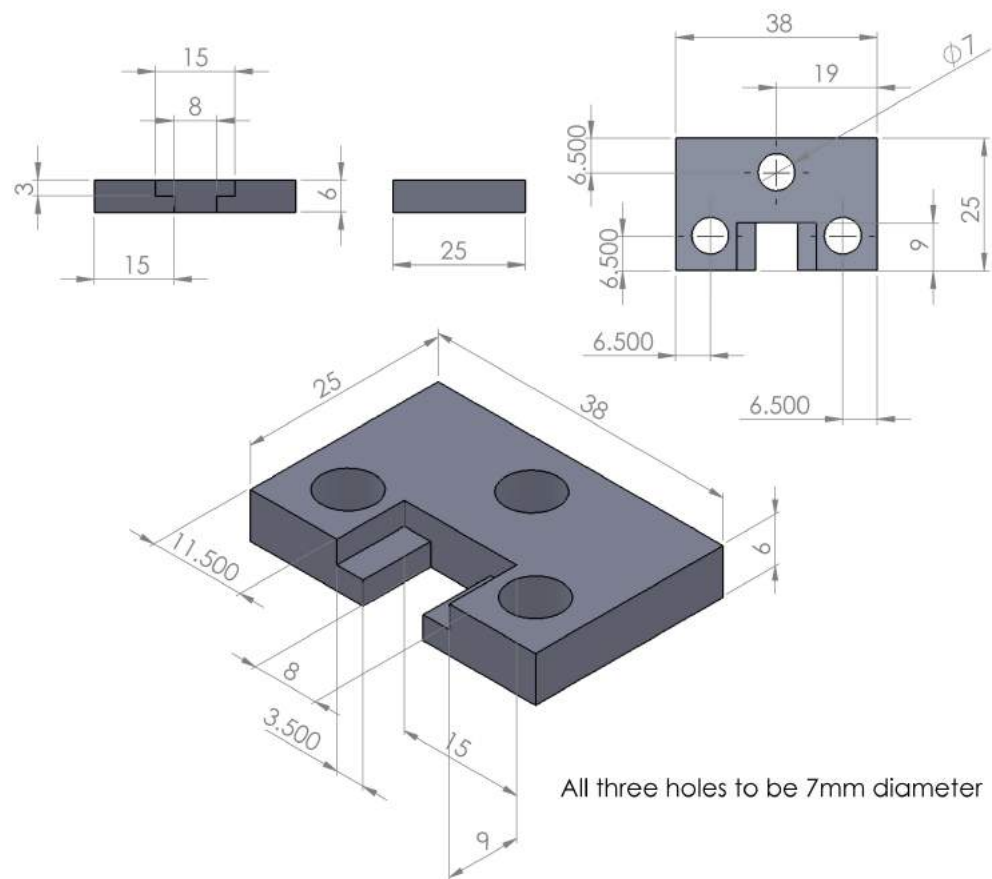


Figure B.31: The mount used in order to secure the digital USB microscope to a ThorLabs translation stage.

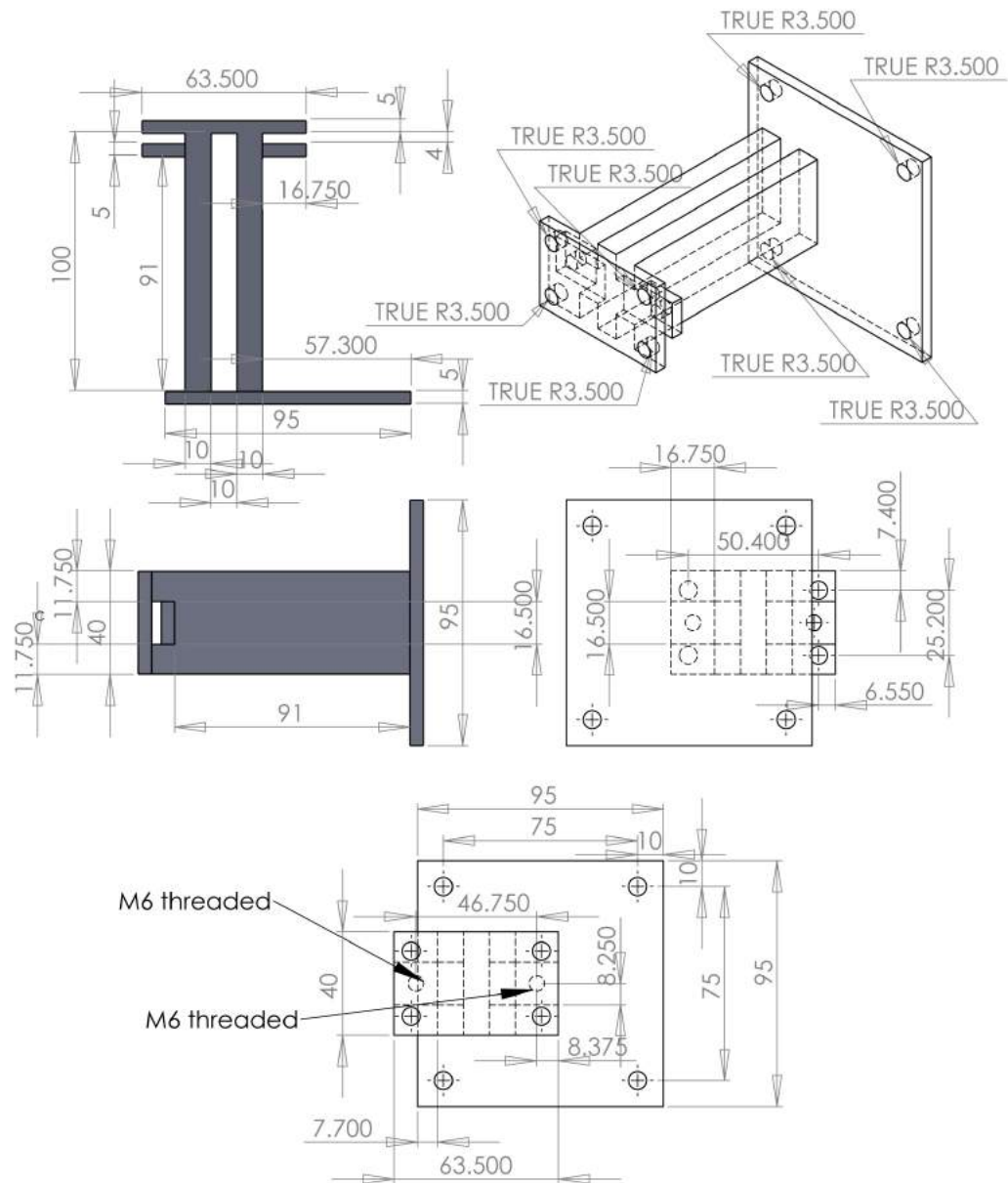


Figure B.32: The stand in order to raise the microscope translation stages above the chip and magnet alignment stages as shown in Figure 4.16 in Chapter 4. The chip tongues slot into the 16.5 mm wide, 4 mm thick gap underneath the top of the stage and are secured by tightening two M6 bolts into the threaded holes on the underside of this gap.

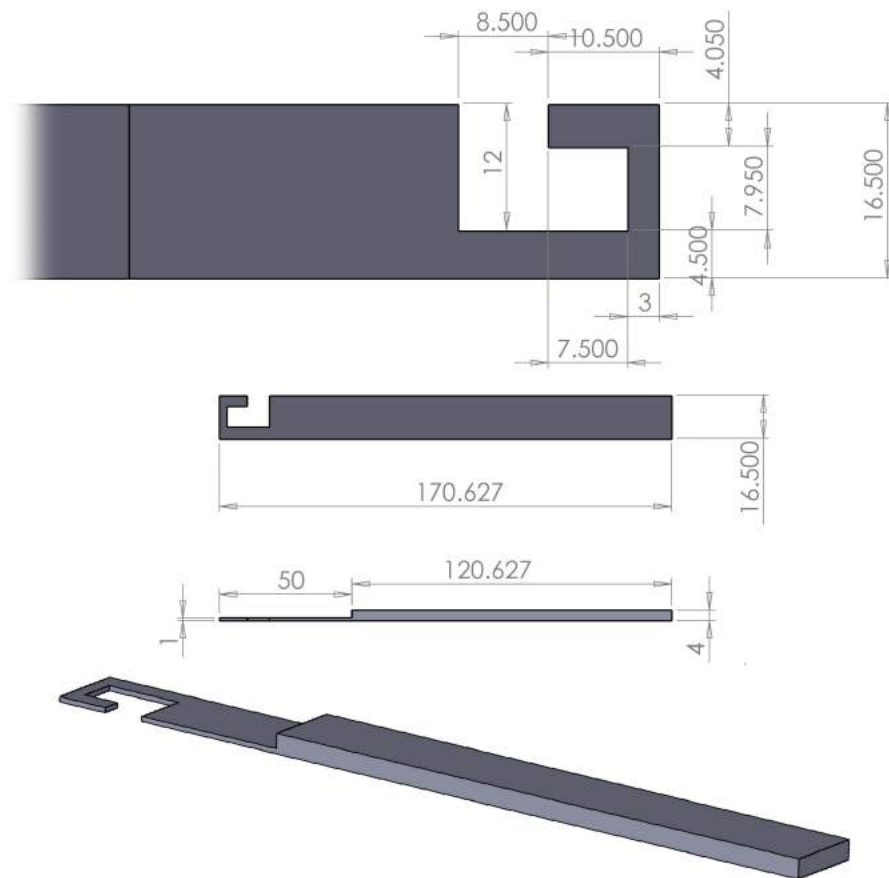


Figure B.33: The original suction-cup tape chip tongue design shown in Figure 4.12 (a) and (b) of Chapter 4.



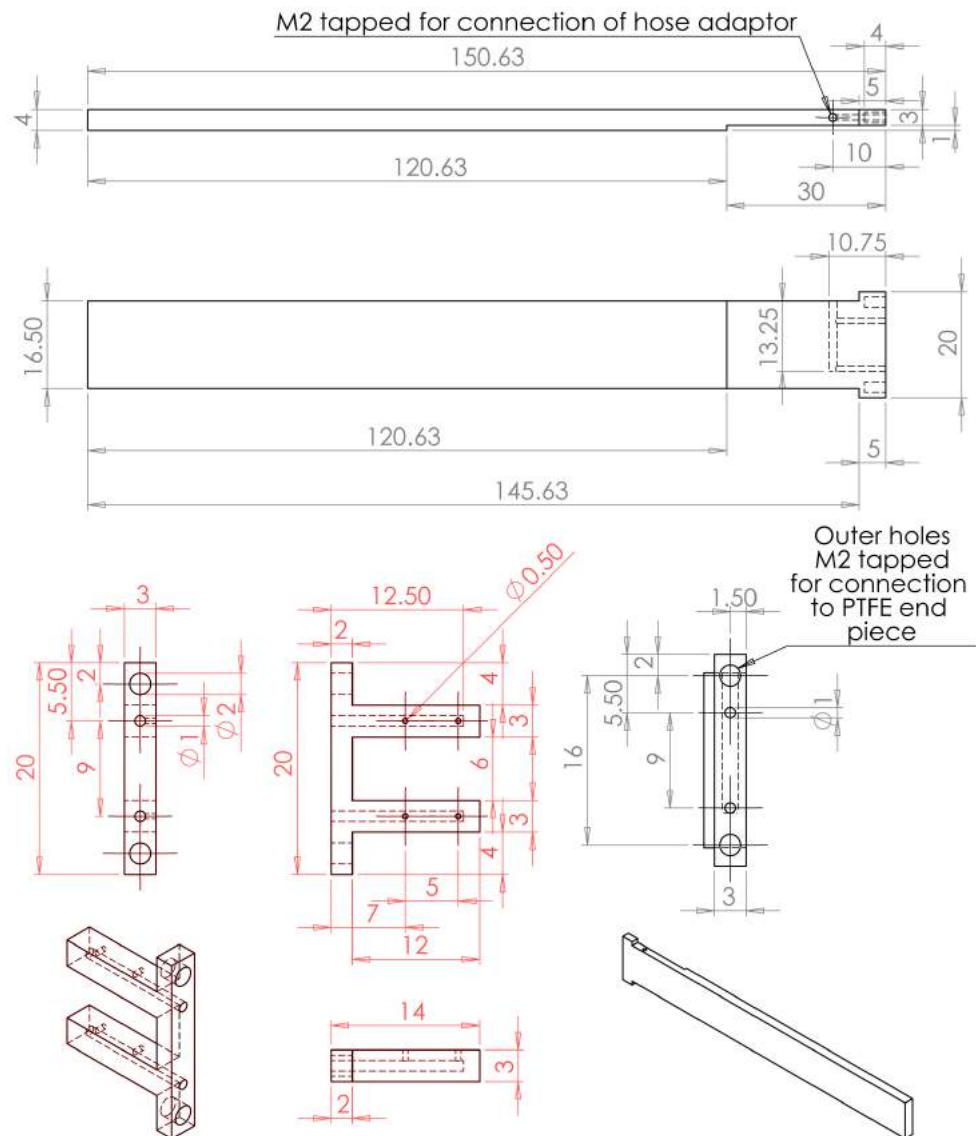


Figure B.34: The pump-activated chip tongue shown in Figure 4.12 (c) and (d) of Chapter 4. The PTFE portion of the tongue is shown in red and the remaining portion is aluminium. The real tongue is a mirror image of that shown in this technical drawing so that the suction comes from the opposite side. The suction hose adaptor screws into the threaded side hole of the tongue so that the pump can be connected.

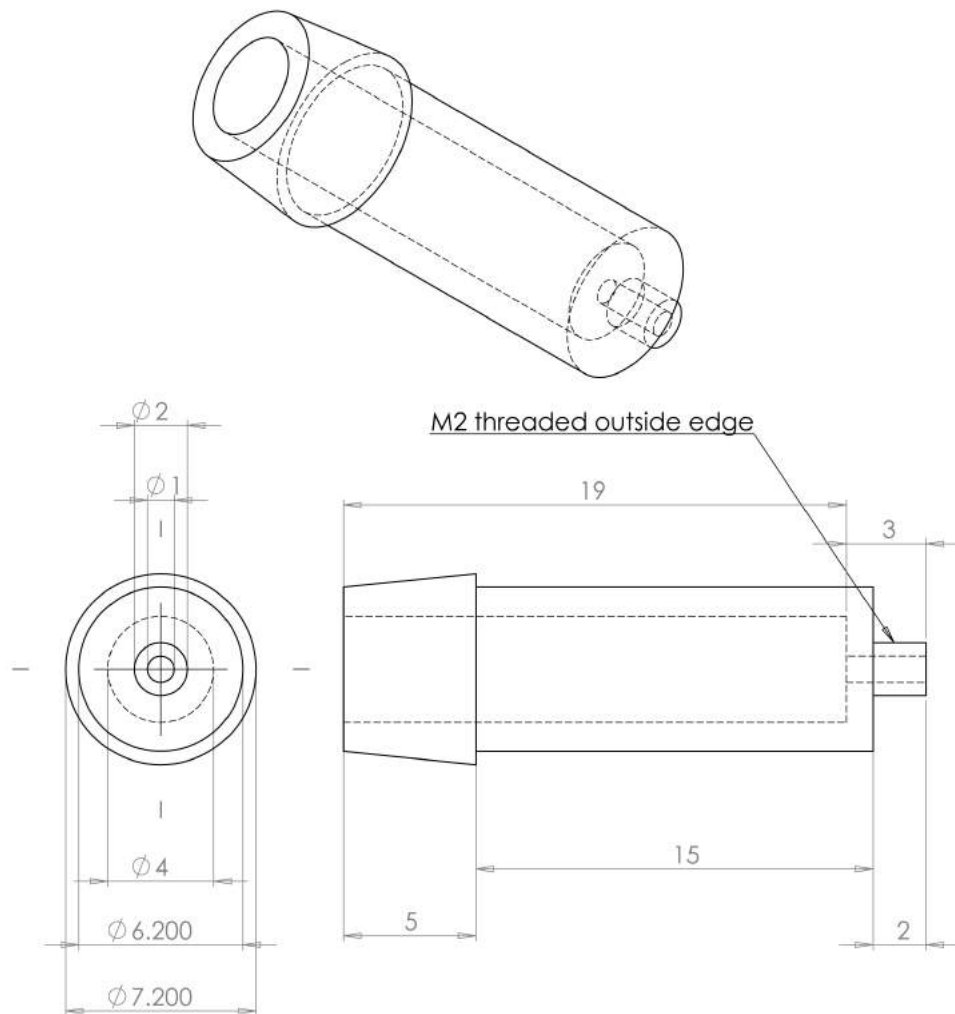


Figure B.35: The suction hose adaptor which allows the pump-activated chip tongue to be attached to a PVC tube compatible with the suction pump.

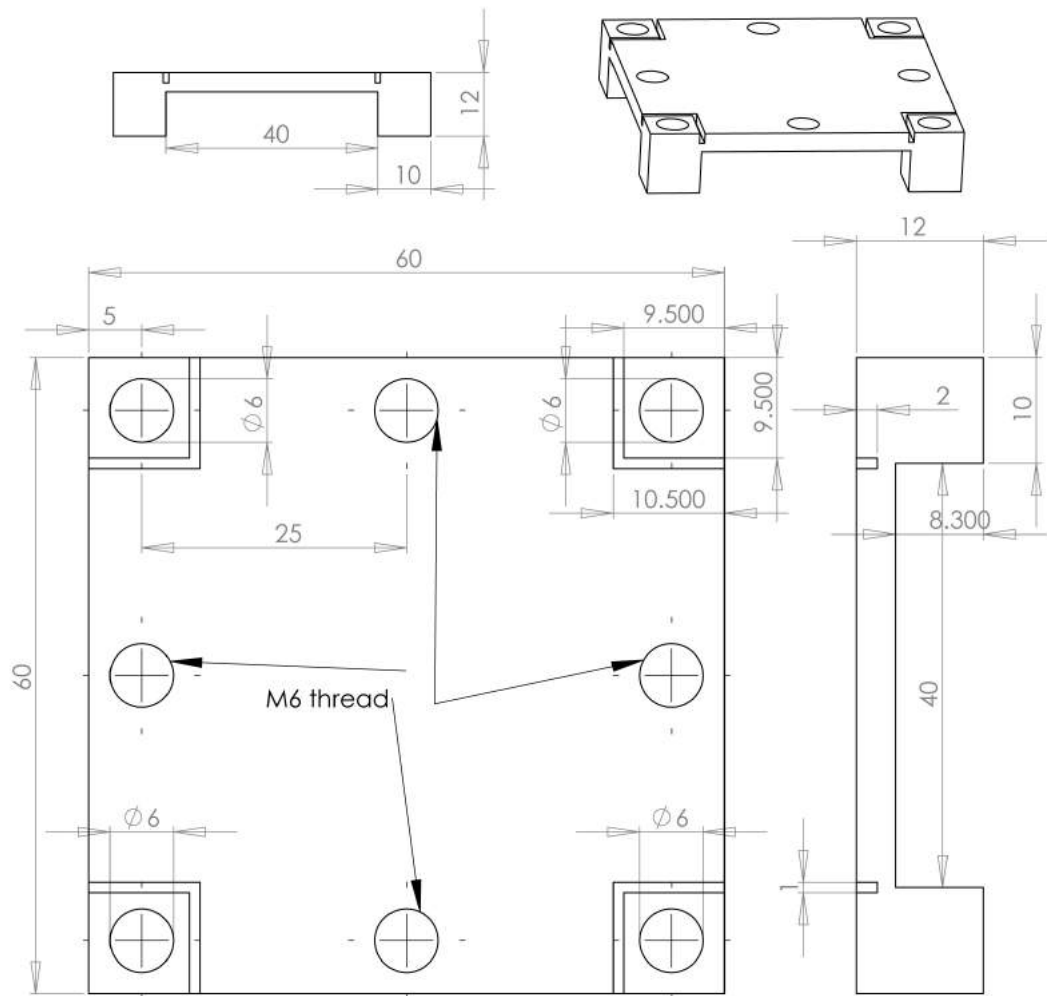


Figure B.36: The heating plate shown in Figure 4.15 of Chapter 4 which fits on top of the alignment stages shown in Figure 4.14. This heating plate was designed in conjunction with Dr Bjoern Lekitsch. The workshop altered this design for easier machining of the thermal isolation at the corners of the plate which can be seen in the previously mentioned figure. The threaded holes are in order to attach a small jig to hold the magnetic spacer in place during the alignment procedure. Though not shown on this drawing, two additional threaded holes were machined for mounting the DBK HP05-1/14-24 heating element of the plate.

### **B.3 Magnetic spacers, compensation magnetics, and coil mounts**

Finally, we come to the technical drawings for the magnetic apparatus constructed for the experimental setup discussed in Chapter 4. This includes the magnetic spacer frames which hold and position the magnets used to create the magnetic field gradient, as well as the compensation magnetics and the mounts used to keep them in place. An assembly of a magnetic spacer frame is shown in Figure B.37 and the figure-eight portion of each spacer is shown in Figures B.38 and B.39. The bottom/lid common to both spacers is shown in Figure B.40. As previously discussed, the magnetic spacer frames are made from oxygen free copper for UHV compatibility.

An assembly diagram of the large permanent magnet mount (shown in Figure 4.10 of Chapter 4) is shown in Figure B.41 with the corresponding technical drawings in Figures B.42 – B.48. These are made from aluminium with the exception of the magnet separators which are made of brass. This is held together using M6 brass studding that can be ordered from RS Components. The compensation coil formers are made from aluminium as are the parts used to secure them in place. As shown in Figure 4.4 of Chapter 4, these parts are also supplemented with M6 brass studding.

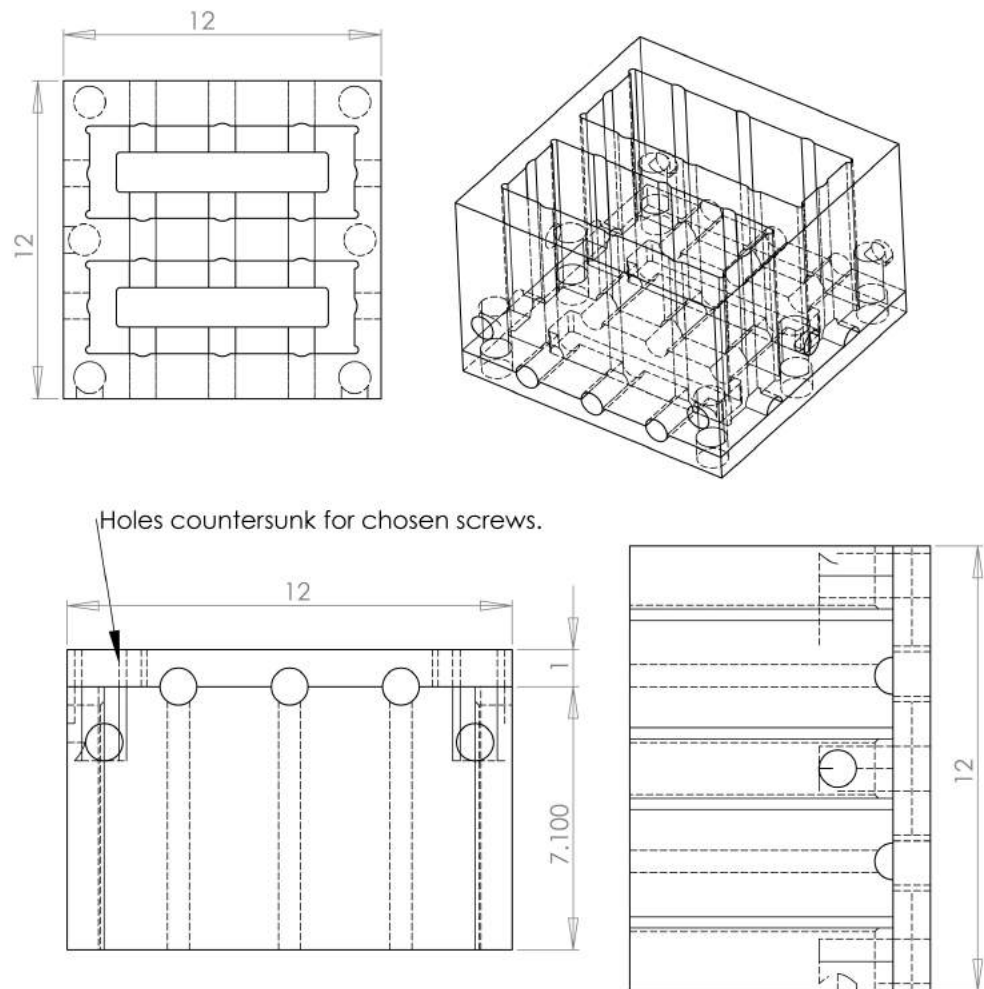


Figure B.37: An assembly drawing of a magnetic spacer comprised of the figure-eight and bottom parts shown in Figures B.38 and B.40 respectively.

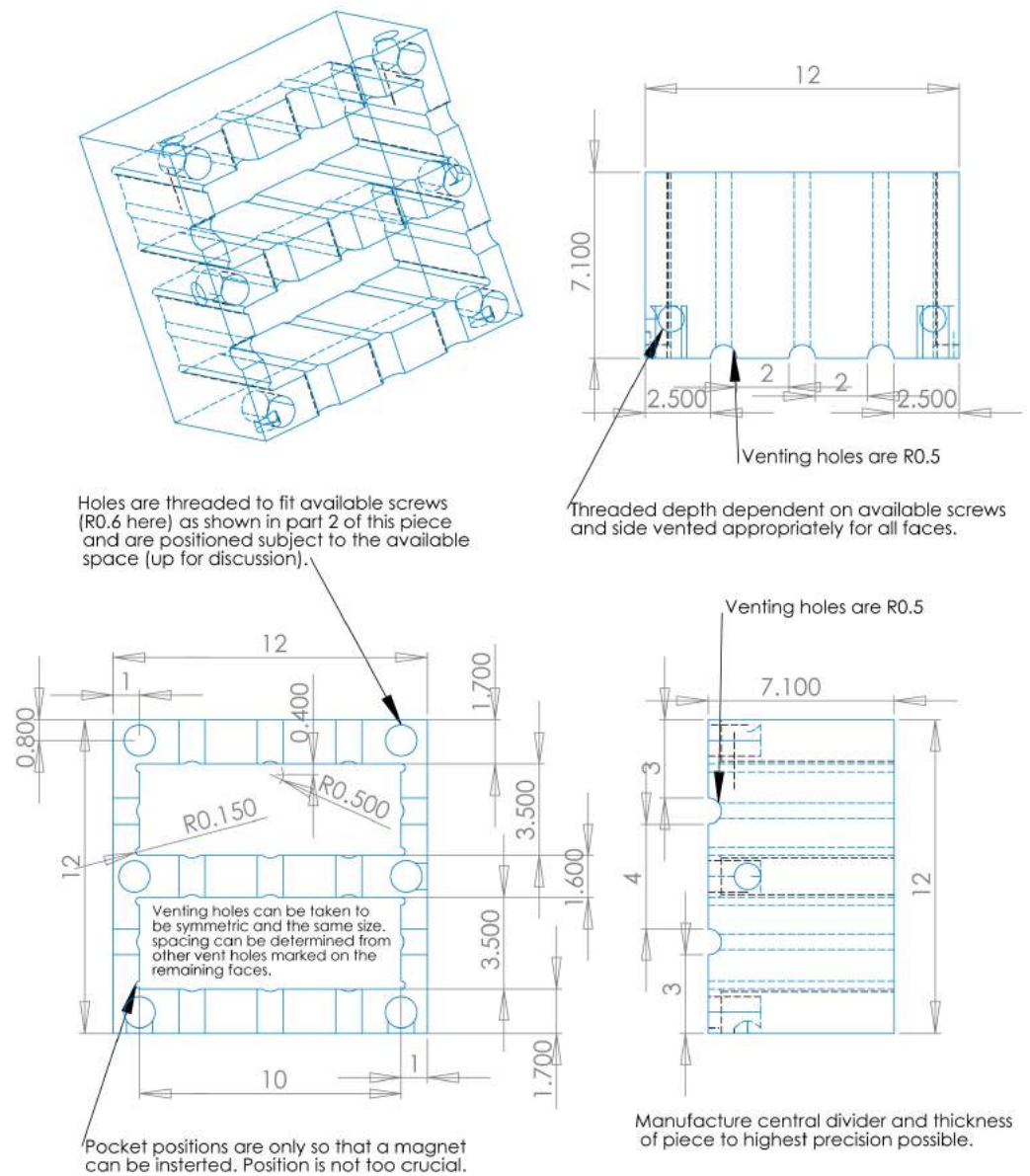


Figure B.38: The figure-eight of the high axial gradient spacer used in the axial gradient system. The real spacer is slightly altered from this design; side venting of the threaded holes was instead taken through to the top of the spacer in order to prevent trapped voids.

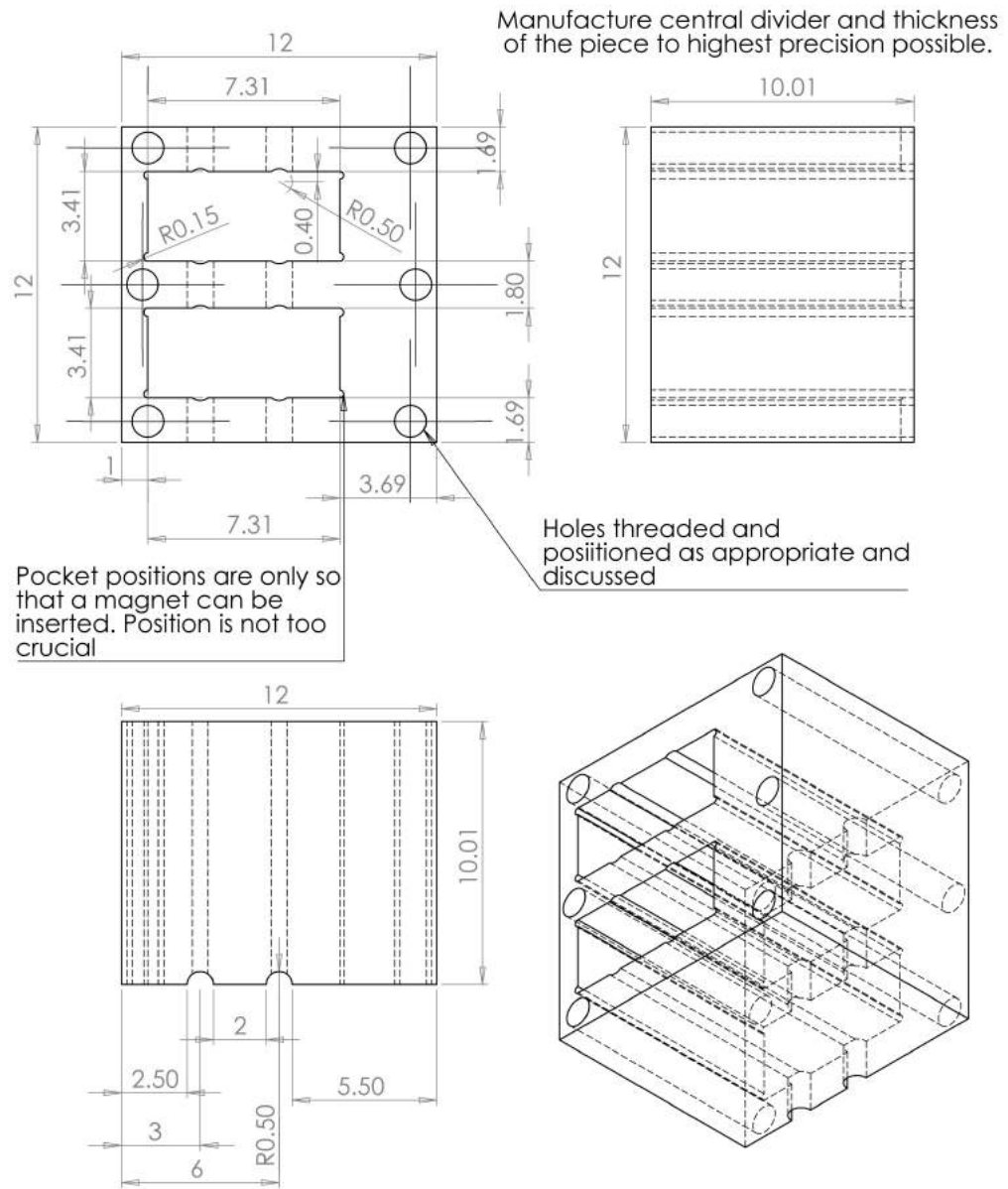


Figure B.39: The figure-eight of the offset magnet, high radial, small axial gradient spacer used in the radial gradient system. The venting holes in this diagram better reflect those manufactured for the spacer shown in Figure B.38.

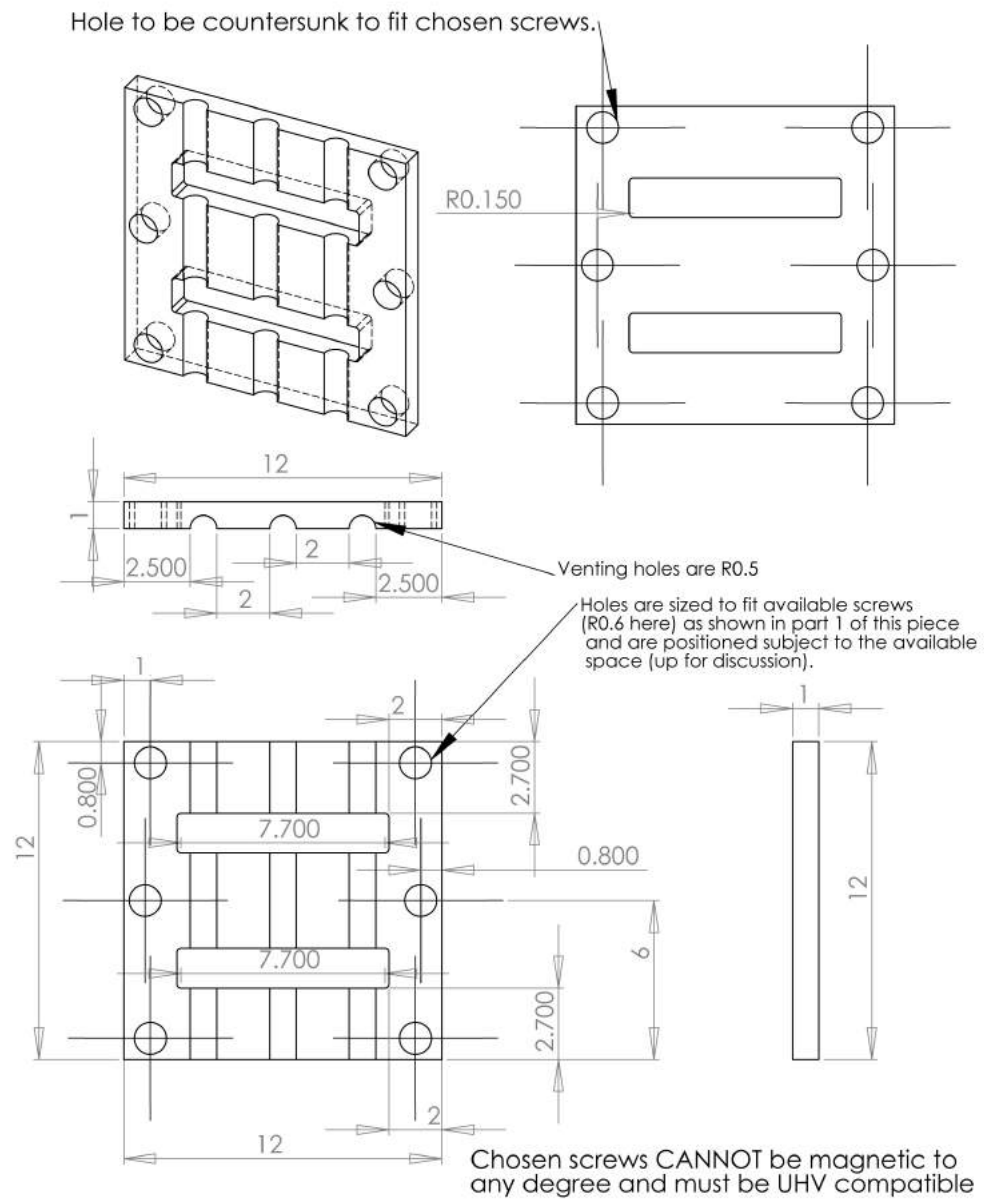


Figure B.40: The bottom/lid common to both spacers. The rectangular slots allow the magnets to be pushed out of the spacer without dismantling it if required.



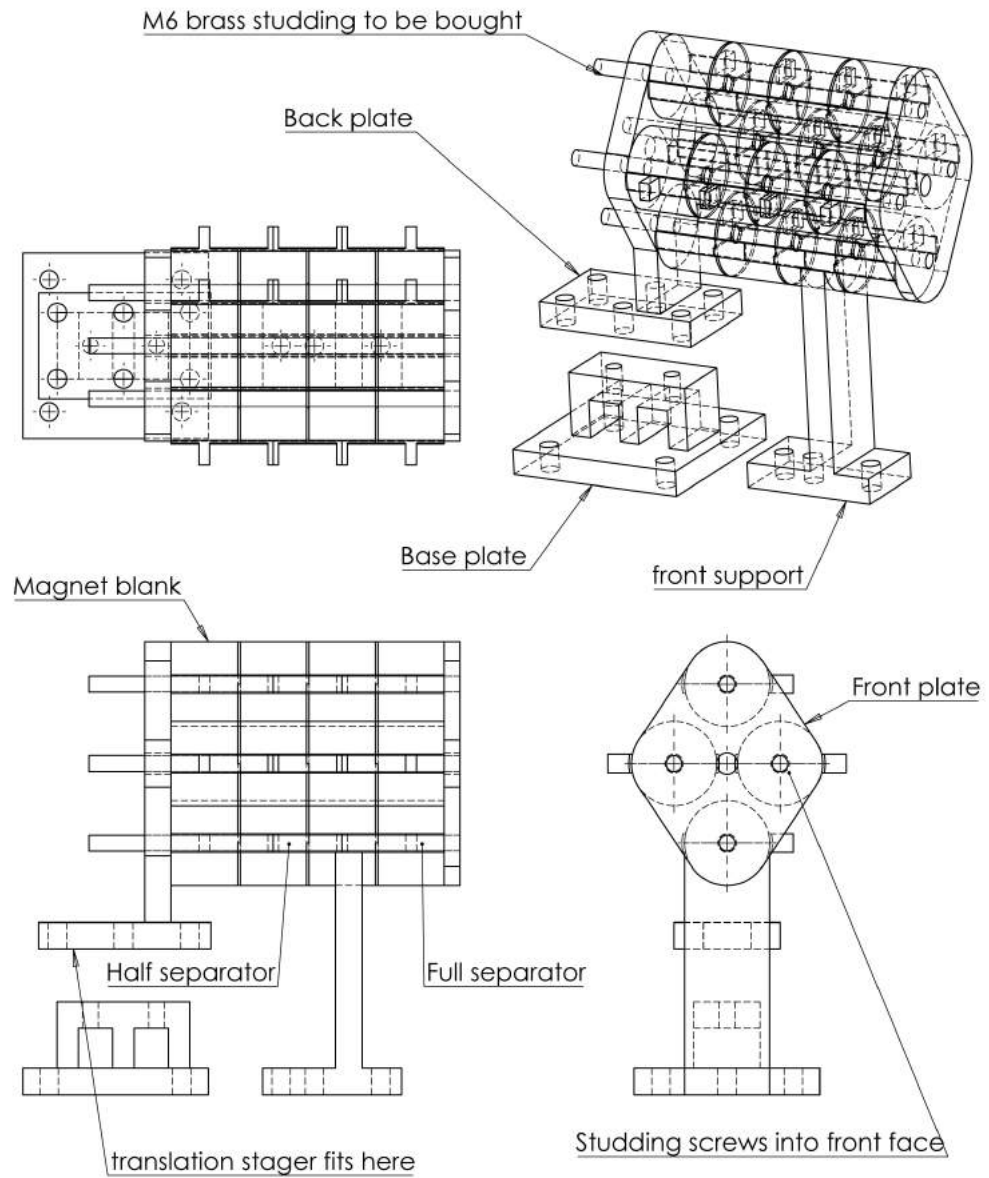


Figure B.41: An assembly drawing of the mount for the permanent magnet compensation setup shown in Figure 4.10 which is integrated with a ThorLabs PT1/M single-axis translation stage. The dimensions of individual parts are shown in Figures B.42 – B.48.

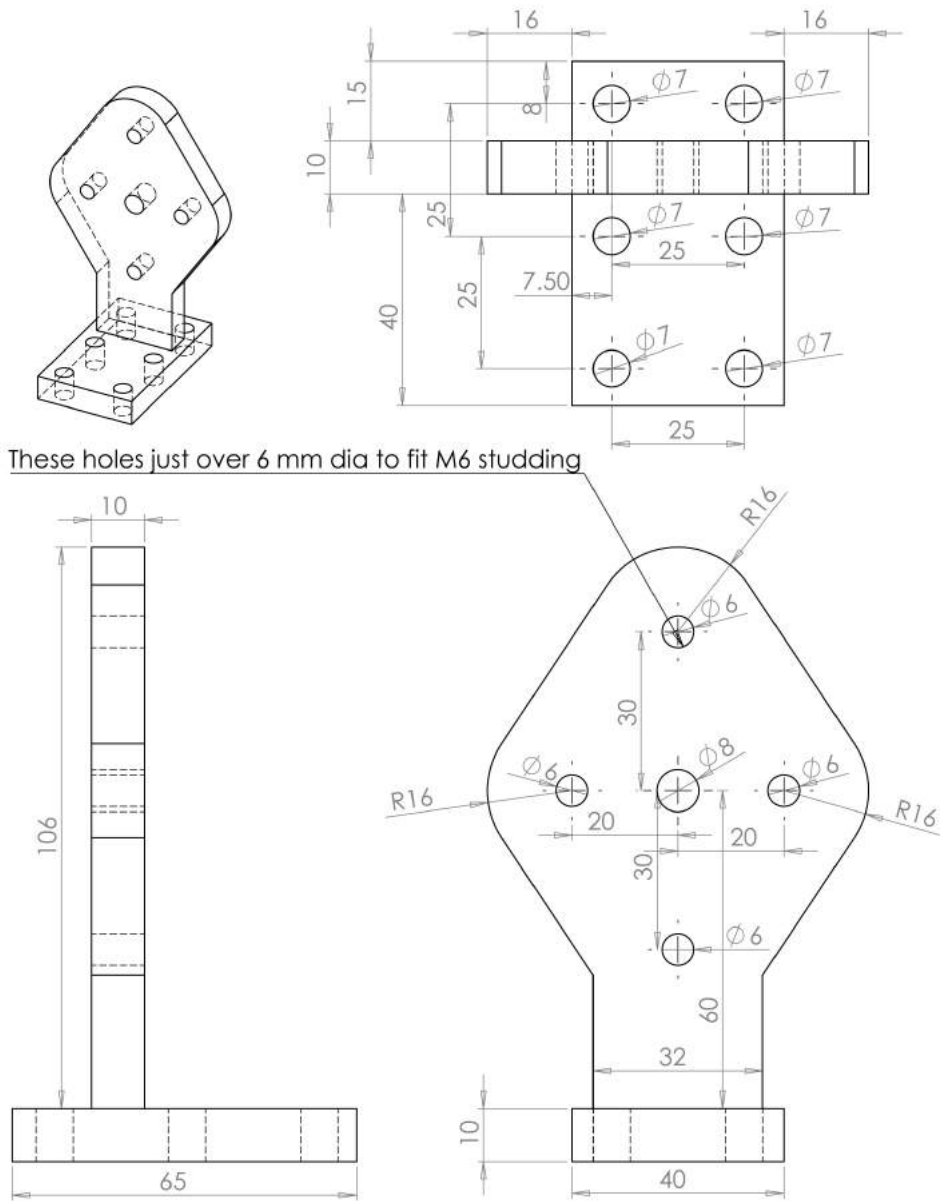


Figure B.42: The back plate of the magnet mount shown in Figure B.41.

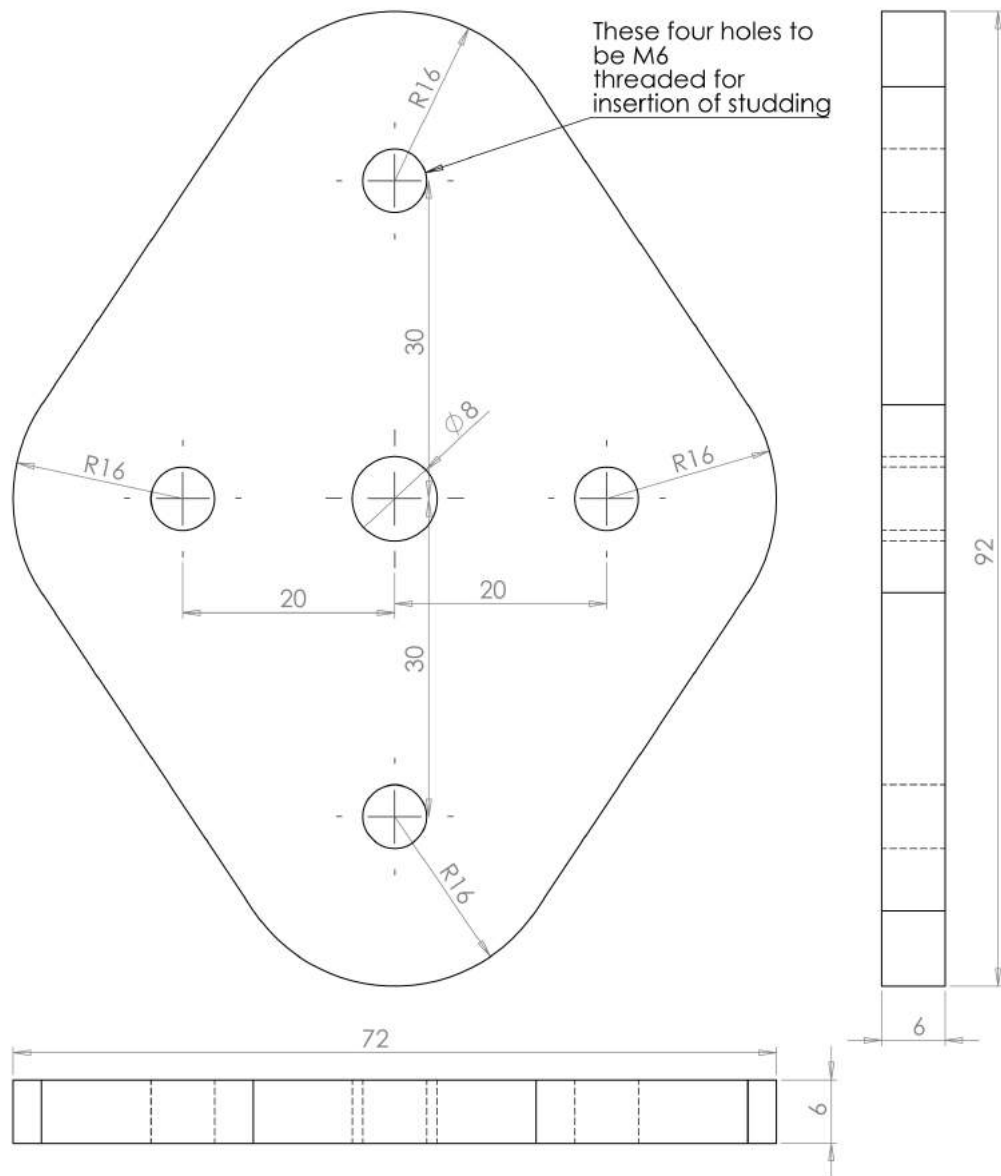


Figure B.43: The front plate of the magnet mount shown in Figure B.41.

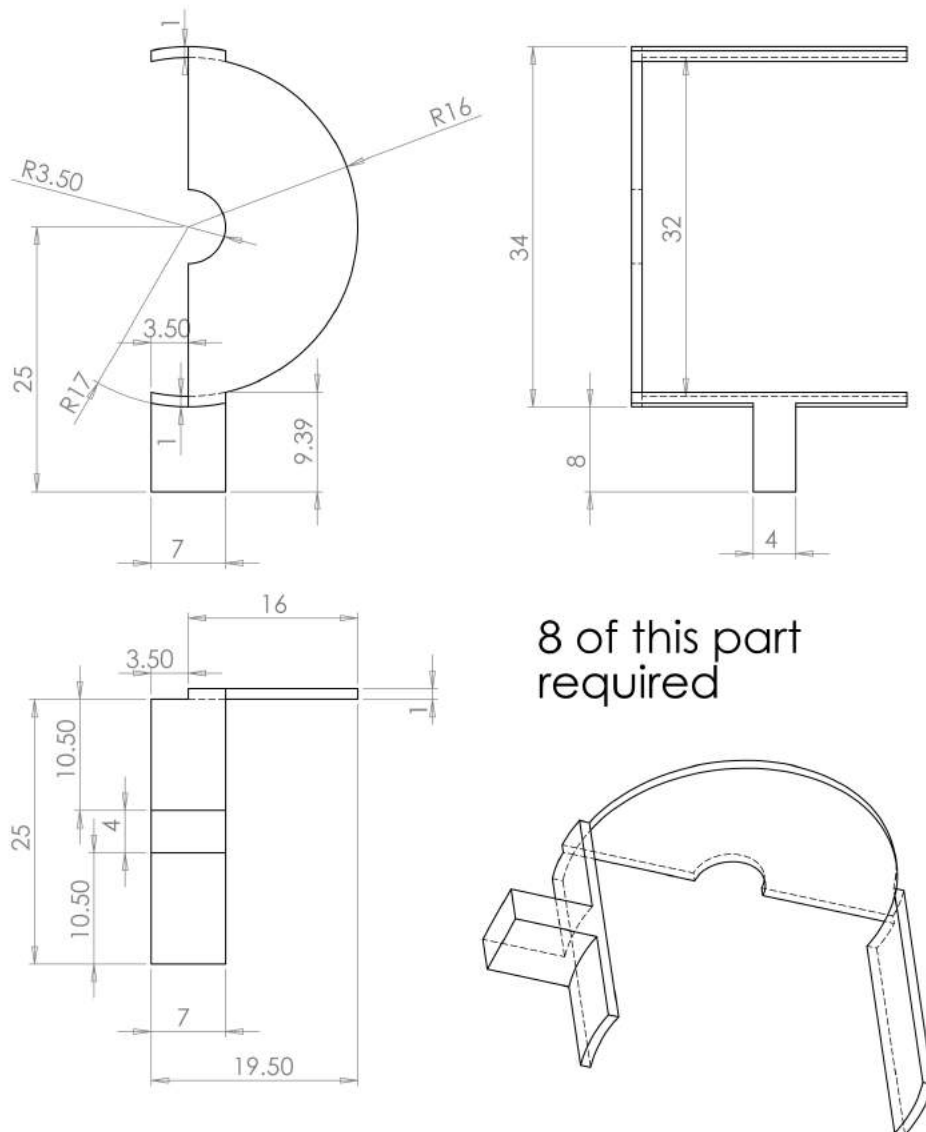


Figure B.44: A full separator which goes around the outermost magnets of each stack of four. The small tab can be used to pry the magnets apart if they need to be separated. These are made of brass which is stronger than the aluminium used for the rest of the stage.

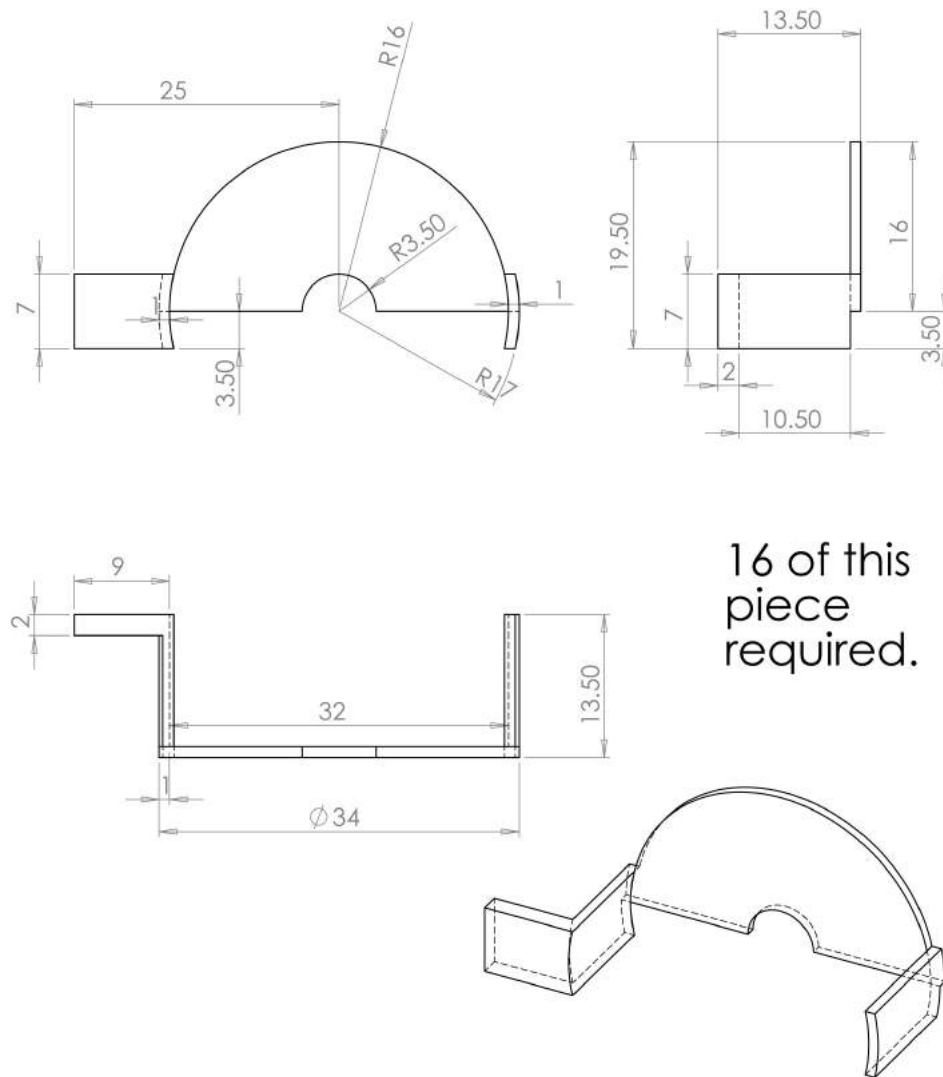


Figure B.45: A half separator which goes around the inner magnets of each stack of four. These are split as a magnet cannot be placed into a secure case without damaging it, thus the case is split into two sides which sit on either face of the magnet. The small tab can be used to pry the magnets apart if they need to be separated. These are made of brass which is stronger than the aluminium used for the rest of the stage.

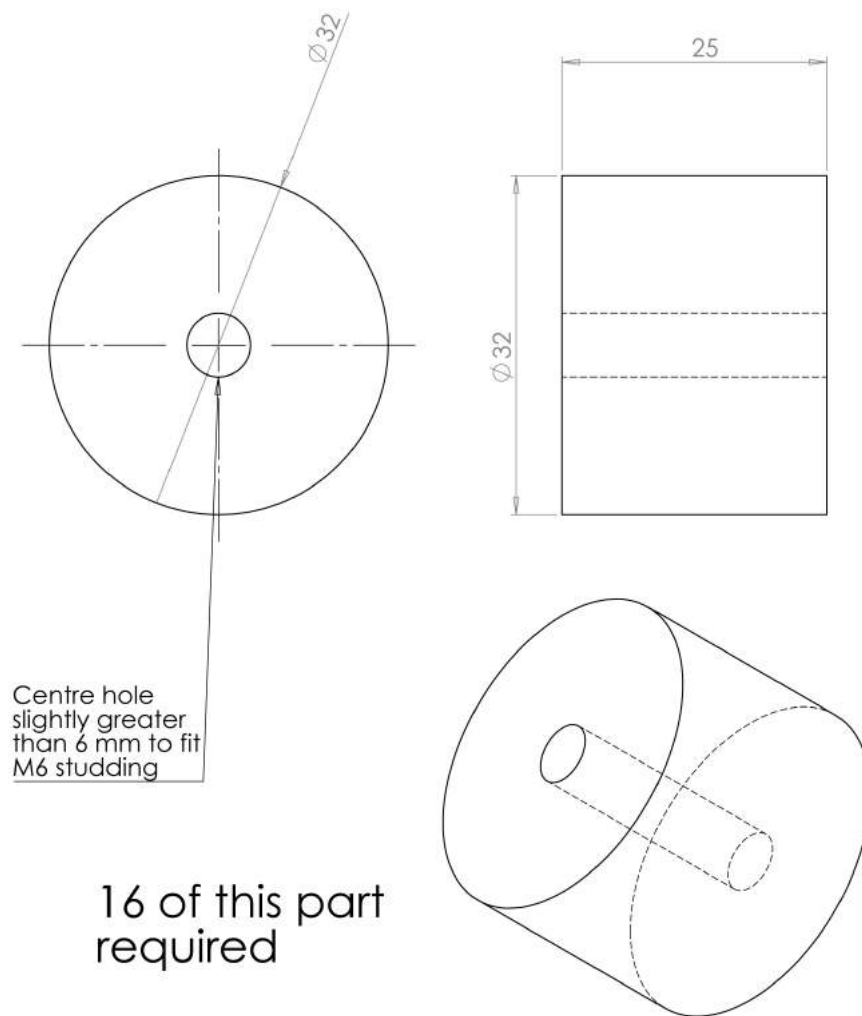


Figure B.46: An aluminium blank that can be used in place of a magnet if the stage is not required to be fully loaded.

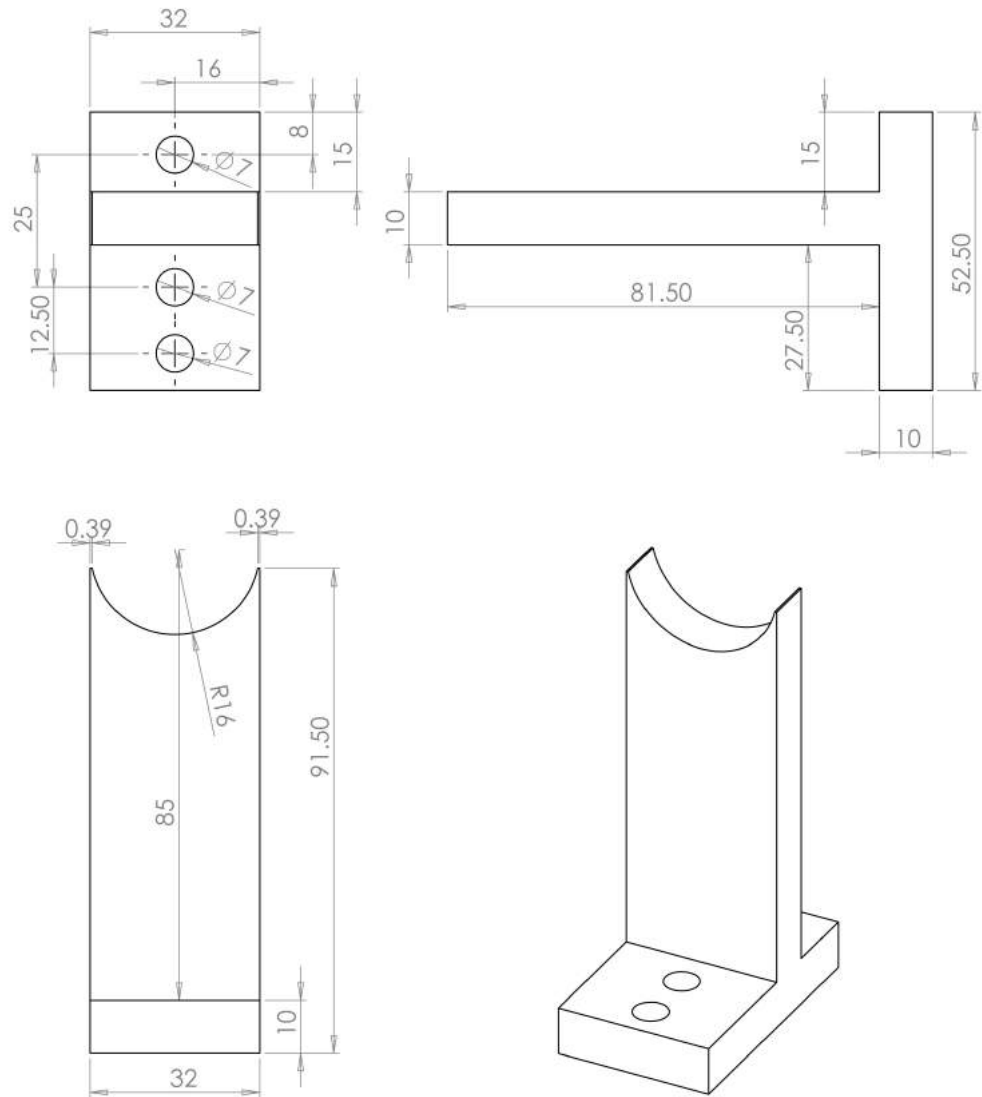


Figure B.47: The front support of the magnet mount shown in Figure B.41 which stops the stage overbalancing before being secured to the experimental table.

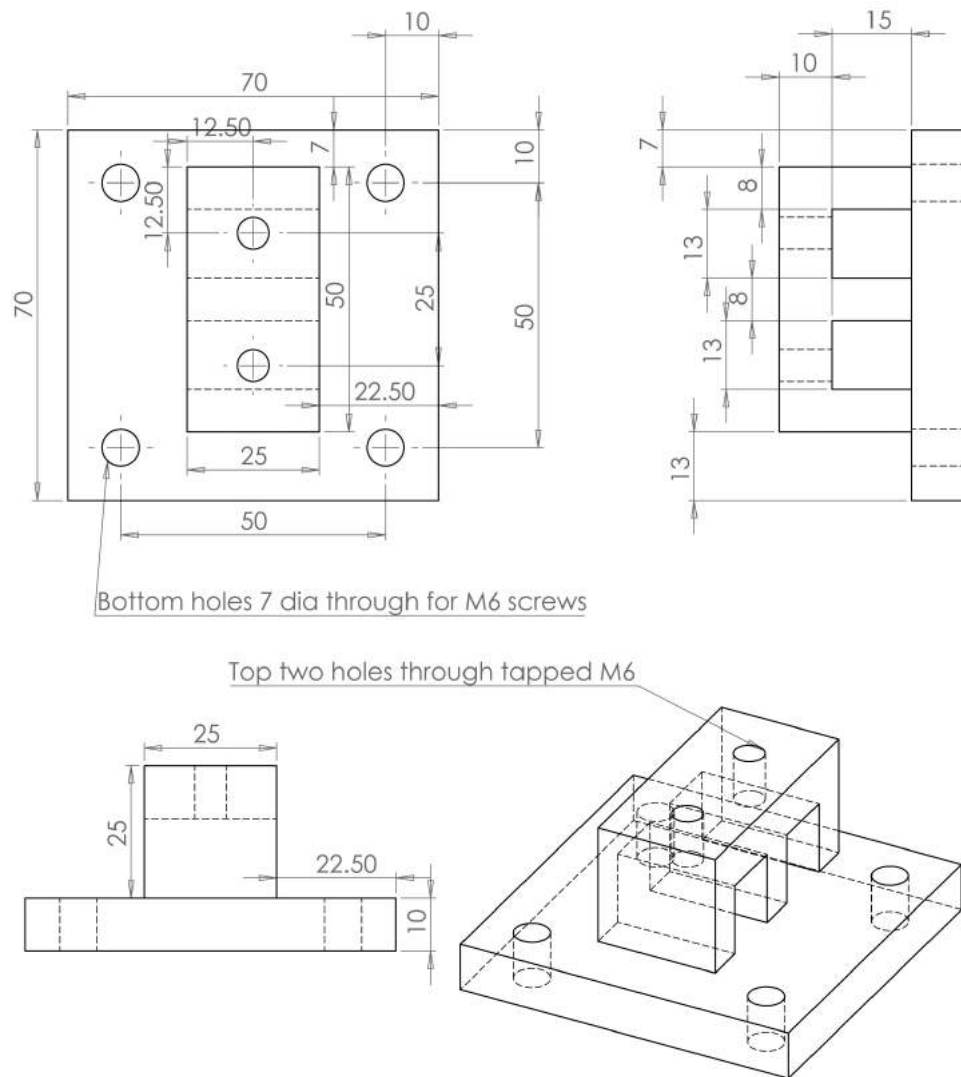


Figure B.48: The base plate of the magnet mount shown in Figure B.41 which is secured to the experimental table.



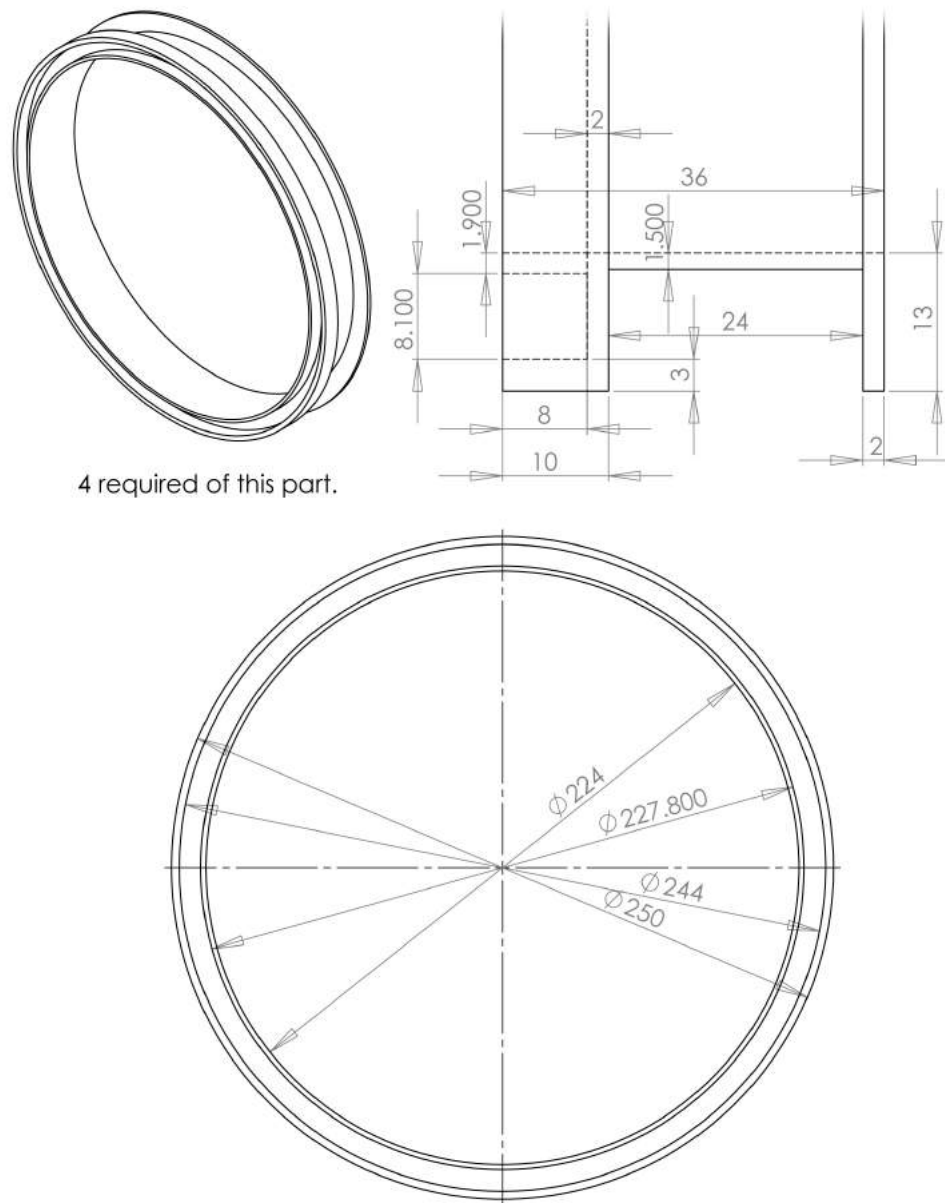


Figure B.49: The coil former of the primary compensation coils used for both vacuum systems discussed in Chapter 4. The channel in the side of the former is for retrofitting a water cooling pipe if need be. The only additional machining to this part is a small hole in the side of the former so that the wire can exit at the centre of the coil.

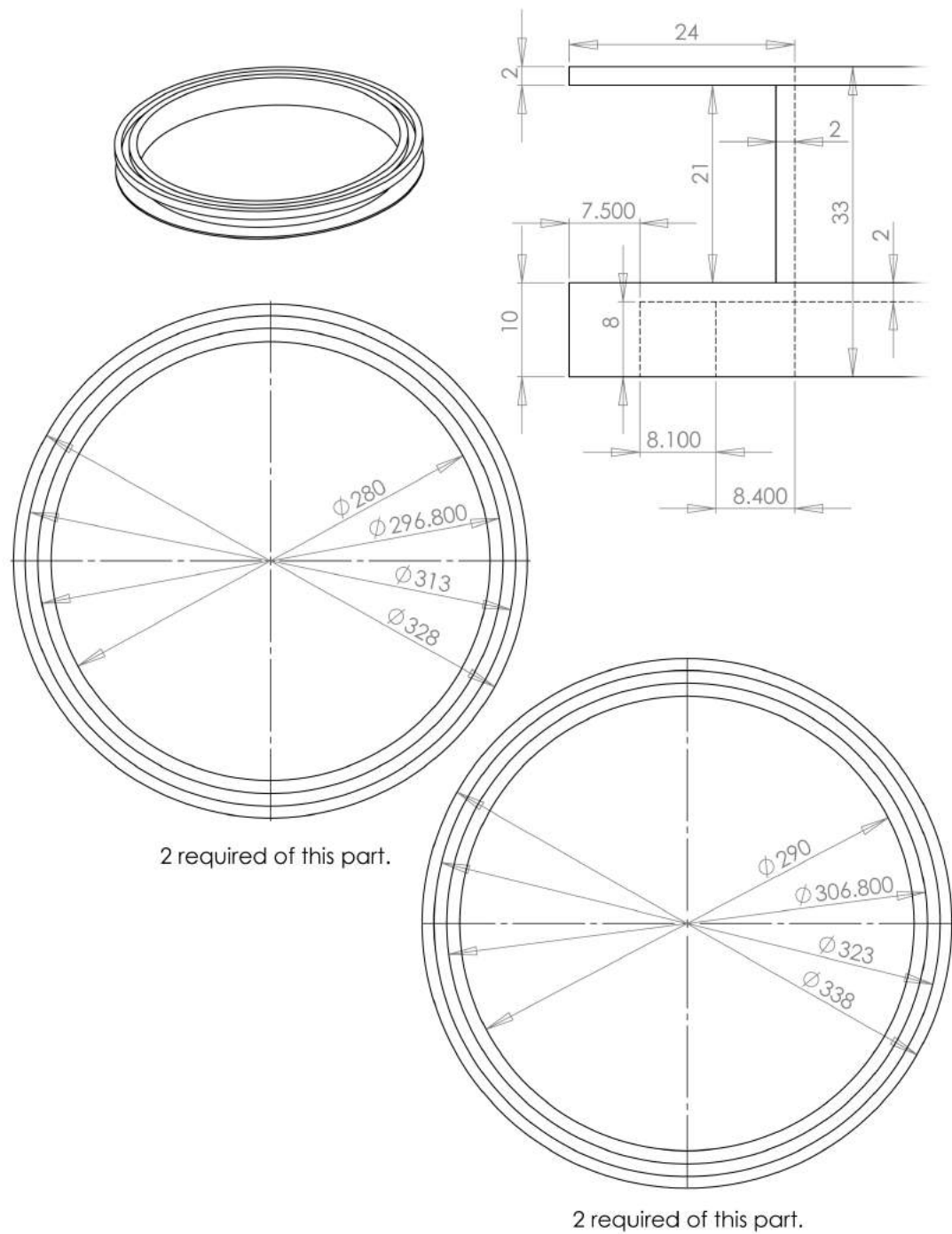


Figure B.50: The coil formers of the secondary compensation coils used for both vacuum systems discussed in Chapter 4; the larger diameter is for the radial gradient system. The channel in the side of the former is for retrofitting a water cooling pipe if need be. The only additional machining to this part is a small hole in the side of the former so that the wire can exit at the centre of the coil.

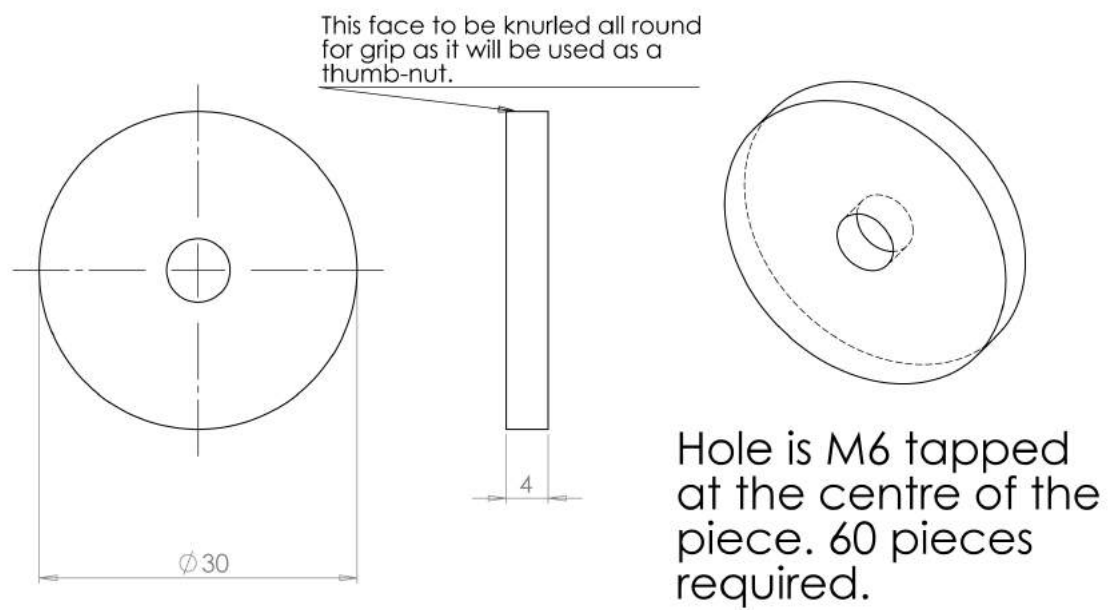


Figure B.51: A knurled thumbnut that is used to set the height or separation of the compensation coils. These are screwed onto brass studding which is interfaced with the mounts in Figures B.52 and B.53 as shown in Figure 4.4 in Chapter 4.

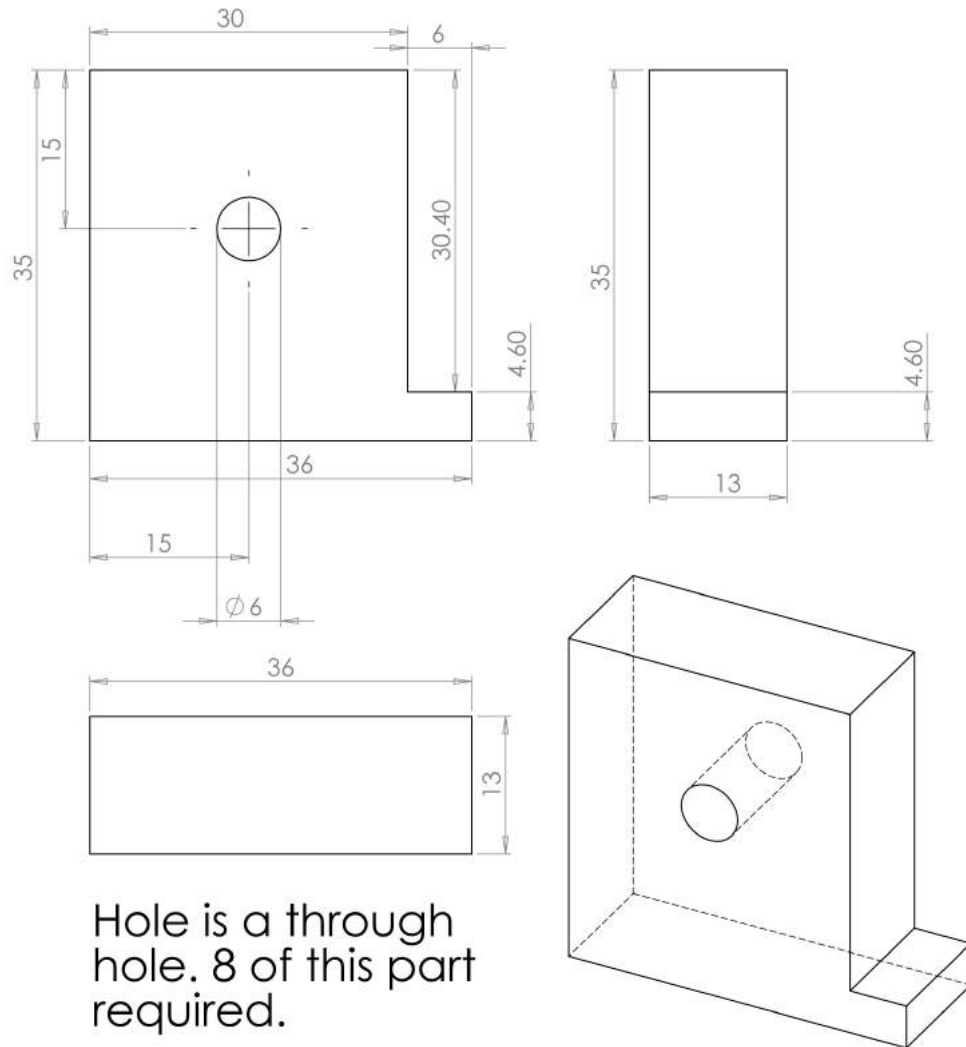
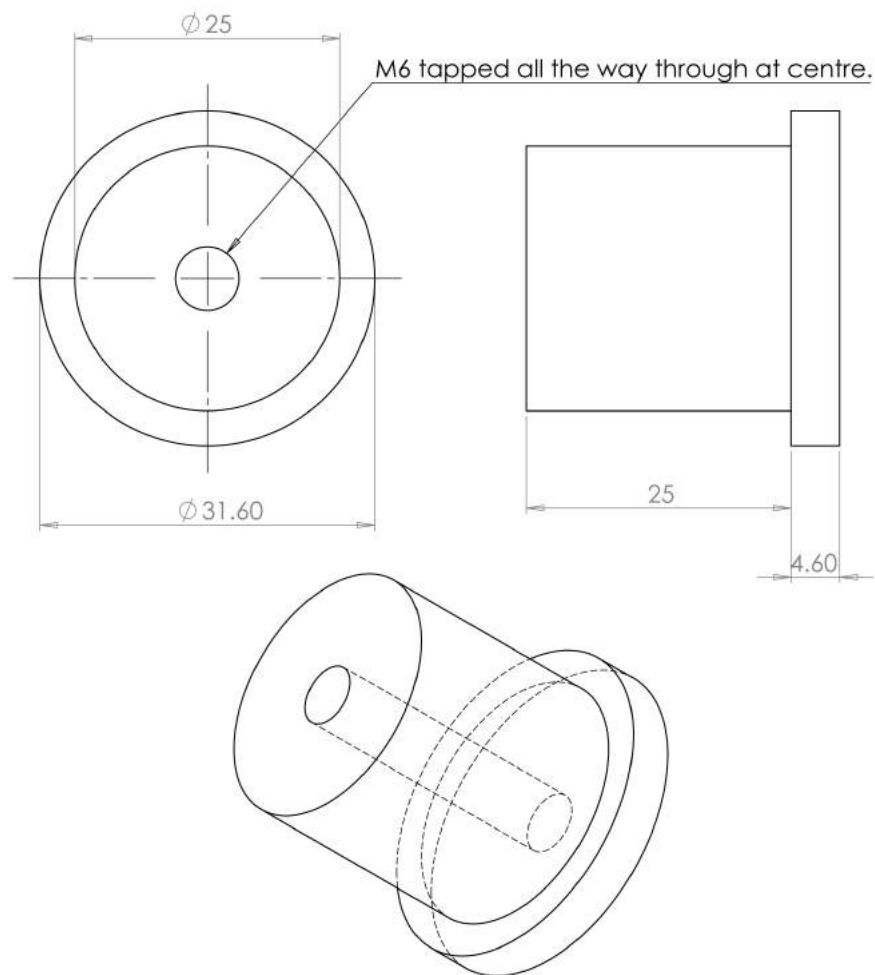


Figure B.52: A mount used for creating a horizontal rail from brass studding which can be used in conjunction with the thumbnuts to set the separation of the primary coils for each vacuum system. The small tab allows them to be clamped to the experimental table.



8 of this piece required

Figure B.53: An optics post style mount for securing the secondary coils. Brass studding is screwed into the post and the thumbnuts are used to set the height of the coils. Four posts are used for each vacuum system.